UNIVERSITEIT
GENT

Faculteit Wetenschappen
Vakgroep Geologie en Bodemkunde

Academiejaar 2000 - 2001

Gas hydrate stability and destabilisation processes in lacustrine and marine environments

Results from theoretical analyses and multi-frequency seismic investigations (part I)

Maarten Vanneste

Promotor: Prof. Dr. J.-P. Henriet
Co-Promotor: Prof. Dr. M. De Batist

Proefschrift ingediend bij de Faculteit Wetenschappen van de Universiteit Gent voor het verkrijgen van de graad van Doctor in de Wetenschappen

UNIVERSITEIT
GENT

Faculteit Wetenschappen

Vakgroep Geologie en Bodemkunde

Academiejaar 2000 - 2001

Gas hydrate stability and destabilisation processes in lacustrine and marine environments

---

Results from theoretical analyses and multi-frequency seismic investigations (part I)

Maarten Vanneste

Promotor: Prof. Dr. J.-P. Henriet
Co-Promotor: Prof. Dr. M. De Batist

Proefschrift ingediend bij de Faculteit Wetenschappen van de Universiteit Gent voor het verkrijgen van de graad van Doctor in de Wetenschappen

What did the deep sea say?

(Dave Alvin)

DANKWOORD

Alhoewel het doctoraatsonderzoek en het bijeenschrijven van het proefschrift een eenzame bezigheid blijkt, verdienen een heel aantal mensen een pluim voor bewezen diensten tijdens de afgelopen jaren. Het is niet voor niks dat hier een proefschrift ligt, dat ondertussen de halve wereldbol werd afgereisd van Siberië tot Antarctica. Een mens doet het ook niet allemaal alleen en dat is maar goed ook. Er werd geproefd van heel wat facetten van het leven, zowel in de persoonlijke als de wetenschappelijke levenssfeer. De opgedane ervaringen en beproevingen hebben vele deuren opengedaan waarvan er slechts af en toe weer eentje dichtviel.

Vooraleerst is er Prof. Dr. Jean-Pierre Henriet, promotor, die me de kans gaf de overstap te maken vanuit de Natuurkunde om vervolgens deze doctoraatstudie aan te vatten en in een volledig nieuwe wereld van Geologie-Geofysica ondergedompeld te worden. Hij introduceerde het onderzoek naar gashydraten in Gent, maakte het mogelijk om zowel expedities als diverse congressen en wetenschappelijke manifestaties bij te wonen en mee te helpen organiseren. Daarnaast is er nog zijn boeiende en uitgebreide ideeëngoed wat altijd wel van pas komt. Prof. Dr. Marc De Batist, co-promotor, wordt hartelijk bedankt voor het heroriënteren van het onderzoek richting de bijzondere hydraatproblematiek in het Baikalmeer, de opgedane ervaringen ter plaatse en de discussies omtrent het onderwerp. Een noodzakelijke en zeer gewaardeerde stap om het proefschrift tot een goed einde te brengen!

Daar het RCMG mijn vertrouwde uitvalsbasis was tijdens bijna 5 jaar als een aaneenschakeling van goede en minder goede dagen en waarbij spanningen niet uit te sluiten zijn, is ook een woordje van dank en appreciatie voor iedereen van het RCMG zonder uitzondering op zijn plaats. Wim V. wil ik speciaal bedanken voor de kennisoverdracht van data processing en de praktische kennis tijdens de expedities. Dat er zo af en toe eens over andere zaken werd gebabbeld, nam ik er graag bij. Dan is er Pieter VH die zich willens nillens moest bezighouden met mijn bijscholing richting Geologie, voor de vele computertoepassingen en het nalezen van een deel van dit manuscript. Marc F. was er dan weer om de vele administratieve en organisatorische problemen op te lossen, maar nog des te meer voor zijn positieve ingesteldheid, het samen organiseren van de gashydraat workshop en de kleine uitstapjes links en rechts tussendoor. De nauwe contacten met andere doctoraatstudenten maakten er soms een gezellig boeltje van, en zorgden tussen de wetenschap door voor noodzakelijke momenten van ontspanning. Er werden ook zeer intensieve contacten gelegd met bezoekende wetenschappers en een hele reeks thesisstudenten die de revue passeerden. Ook zij worden bedankt voor de interessante grensverleggende discussies en ware vriendschappen en soms late uurtjes ergens in de stad.

De diverse internationale samenwerkingsprojecten maakten het mogelijk de geest te verruimen en aldus een heel pak nieuwe ideeën op te doen. In dat kader wens ik mijn grote waardering op papier te zetten voor o.a. Dr. Aleksandr Yakovlevitch Golmshtok, Dr. Andrei Kremlev, vriend Dr. Serguei Bouriak, Prof. Dr. Jan Klerkx, Prof. Dr. Jürgen Mienert, Prof. Dr. Alan Judd, wijlen Prof. Dr. Gabriel Ginsburg, Oleg Khlystov, Dr. Achim Kopf, docenten tijdens de MIME intensieve cursus in Longhirst, ENAM2 partners, en de referees van wetenschappelijke artikels: Dr. George Spence, Dr. Martin Hovland, Prof. Dr. Karin Andreassen en een anonieme referee. Daarbij onthoud ik ook de vele expedities (Baikal, Porcupine, 70-daagse bezinning in de Weddell Zee, Antarctica): met dank aan het wetenschappelijk personeel, ingenieurs, kapiteins, bemanning en verantwoordelijken op R.V. Belgica, Titov, Vereshchagin, Polarstern, Prof. Logachev.

Speciale aandacht gaat ook uit naar een hele reeks vrienden waarop steeds gerekend kon worden doorheen de jaren. De centrale persoon is uiteraard Steph. Ze was en is er altijd zowel als mens als wetenschapper en

moest hoogstwaarschijnlijk de grootste last dragen tijdens de laatste maanden en de spanning die daarbij kwam kijken. De manier waarop ze daarmee omging, maakt een mens gelukkig. Daarnaast in willekeurige volgorde, voor evidente redenen en niet in het minst wegens het missen van een aantal belangrijke aangelegenheden: Ma & Pa, broer & schoonzus, zus, Peter, Tom, Jan, Christine & Pierre, Pieter VB, Hospita Olga, 't Gebed, Arthur & Declan en de nobele bekenden die blijkbaar even in vergetelheid geraakt zijn tijdens het bijeenpennen van deze lofbetuiging (met excuus).

Tot slot wens ik het IWT te bedanken voor de financiële steun in de vorm van de doctoraatsbeurs.

Maarten

Part 1

Chapter 1

State of the Art & Rationale of this research project (p. 1)

Chapter 2

Sensitivity of the gas hydrate stability field and destabilization processes (p. 23)

Part 2

Chapter 3

Multi-frequency acoustic imaging of hydrate-bearing sediments in Lake Baikal (p. 118)

Chapter 4

Variability of the vertical extent of the gas hydrate stability field in Lake Baikal (p. 159)

Chapter 5

Inferred gas hydrates and clay diapirs near the Storegga Slide on the southern edge of the Vøring Plateau, offshore Norway (p. 208)

Chapter 1

State of the Art & Rationale of this research project

1.0
Introduction: Aspects of natural gas hydrates

The present-day volume of atmospheric methane is estimated to be approximately 1.7 ppmv [*Thorpe, 1996*] or $4.9 \cdot 10^{12}$ kg [*Kvenvolden, 1998*]. Recent atmospheric research studies [*Raynaud et al., 1998; Watson et al., 1990*] point towards an annual increase of the atmospheric methane content with 1%. Ice core data from the last 220 ka indicate that the CH_4 concentration is characterised by significant fluctuations with a high degree of coherence with variations of the average temperatures (i.e. $\delta^{18}O$-variaties) [*Thorpe, 1996; Raynaud et al., 1998*]. Since methane is a much more efficient greenhouse gas as compared to carbon dioxide [*Lashof & Ahuja, 1990*], it is of great importance to locate possible methane reservoirs in nature and to investigate their stability under natural and anthropogenic influences. Especially the transfer of the greenhouse gases like methane to the troposphere and the stratosphere need to be considered. Several independent scientists [e.g. *Harvey & Huang, 1995; Paull et al., 1991; Leggett, 1990; Nisbet, 1990*] suggest that the destabilisation of naturally occurring gas hydrates gives an important contribution to the build-up of global atmospheric methane, and plays an important role in climatic changes.

Methane is known to occur in the natural environment in three different forms: dissolved in pore water, as free gas (bubbles from microscale to cm-scale) and in solid hydrate form. Gas hydrates are ice-like crystals of hydrogen-bonded water molecules enclosing individual low-molecular-weight gas molecules [*Kvenvolden, 1993a*]. These non-stoichiometric compounds were first discovered by Sir Davy in 1810 in the form of chlorine hydrates and were since then considered as a scientific curiosity in which gas and water are combined into one solid structure [*Sloan, 1998a*]. Due to their non-flowing nature, hydrates became a subject of debate within the hydrocarbon industry when they were first observed in pipelines in 1934. Meanwhile, scientists were busy identifying different hydrate compounds and their specific physico-chemical properties [*Sloan, 1998b*]. Only about 30 years ago, hydrates were observed under natural conditions and men realised that nature had predated man's hydrate fabrication by millions of years [*Makogon, 1965; Shipley et al., 1979*].

In nature, gas hydrates occur in the Earth's shallow subsurface (first hundreds of meters) within the pores of sedimentary rocks. Specific thermodynamic and gas-volume requirements dictate their stability conditions. Therefore, natural gas hydrate accumulations are mainly restricted to two regions: high-latitude permafrost areas (e.g. Messoyakha field, Russia [*Sloan, 1998a*] or Prudhoe Bay area, Alaska [*Collett, 1993*]) and deep oceanic regions in outer continental margins and slopes where cold bottom water is present [*Kvenvolden, 1993b; Hyndman & Spence, 1992;* e.g. ODP-leg 166, 164, 146,

131]. There is also evidence for the presence of gas hydrates in some deep-water inlands and marginal seas (e.g. Okhotsk, Black and Caspian Sea) [*Ginsburg & Soloviev, 1997*] and at tectonic plate junctures. Recently, gas hydrates were also retrieved from the sediments of Lake Baikal, a large continental rift lake in Siberia. This is the first – and up to now only – reported occurrence of gas hydrates in a confined fresh water basin [see also chapter 3-5]. In general, methane is by far the most abundant clathrated gas. In most cases, the gas enclosed in the hydrate structure is of biogenic origin, i.e. from microbial decay of organic matter. Sometimes, evidence of thermogenic gases is present in the hydrate structure [e.g. Gulf of Mexico, Caspian Sea].

The partial occupation of sediment pore spaces by gas hydrates severely influences the sediment's bulk properties. Fingerprints of hydrate accumulations are known to occur for seismic data acquisition (occurrence of typical reflectors, implications for calculating the geothermal field), hydraulics and fluid migration (permeability changes due to pore clogging), thermodynamics (typical stability conditions, latent heat of phase transitions) and geotechnics (influence on physical properties like shear strength), leading to the interest of academic research institutes and industrial companies.

One of the main characteristics of the gas hydrate structure is its huge **storage capacity** (see also below). The concentration of enclosed gas molecules in the clathrate cavities can be a factor of 6 higher than in an average gas-saturated porous medium [*Hovland & Judd, 1988*], but a little less than the density of a liquid hydrocarbon. This fact and the overall occurrence of hydrates form the basis for the global interest in all aspects of gas hydrate research. Especially its potential as a **future energy resource** [e.g. *Kvenvolden, 1993a, b, 1998*], as an important factor concerning **climate changes** [e.g. *Haq, 1993, Nisbet, 1990*] and as a plausible **submarine geohazard** in case of hydrate dissociation (e.g. Storegga Slide, offshore Norway [*Bugge et al., 1987 & 1988, Bouriak et al., 2000*]; Beaufort Sea margin [*Kayen & Lee, 1991*]) need to be mentioned.

To have a better point of view concerning the specific modes of accumulation of hydrates, we need to increase our knowledge of hydrate accumulation in the sediments, how - quantitatively and qualitatively - destabilisation can occur and what the consequences are. These topics are of primary importance for climate research, for future exploitation of these reservoirs as energy sources, for the slope (in-)stability of the sea floor and to reduce the risk factors inherent to offshore constructions and deep drilling projects in hydrate-rich areas. The research presented here tries to elucidate some of these topics. After more detailed discussions about the theoretical gas hydrate stability field and its sensitivity to environmental changes, we focus on the gas hydrate topic in Lake Baikal. Different acoustic tools (single-channel, multi-channel, several different acoustic sources and hence frequencies, OBH) were used to delineate the acoustic expression of gas hydrates and to evaluate the accumulation and distribution of gas hydrates. Also the lateral variability of the vertical extent of the hydrates in relation to heat flow measurements is analysed.

1.1
Microscopic and physico-chemical properties of gas hydrates

1.1.1
Microscopic structures, host and guest properties[1]

As mentioned before, **gas hydrates** are ice-like crystalline structures of gas molecules enclosed in cavities formed by hydrogen-bonded water molecules. Van der Waals bonds are linking the individual

[1] *The summary given here is mainly based on the monographs on natural gas hydrates of Sloan [1998a, 1998b]. Since most of the microscopic properties are not dealt with in this dissertation, the reader is referred to those manuscripts for more detailed information.*

gas (or guest) molecules and water molecules. The hydrogen bonds are responsible for the typical open hydrate structure. The stability of this structure is provided by the presence of gas molecules in about 85% of the cavities [*Sloan, 1998a*].

In nature, hydrates normally form in one of three repeating **crystal structures**: a cubic body-centred structure sI, a cubic diamond-packed structure sII, and a hexagonal structure sH. In table 1.1 [modified from *Sloan, 1998a*], the most important aspects of the different cavities in the mentioned hydrate structure and their geometry are presented. The 5^{12} cavity, i.e. a regular polygon composed of 12 faces of pentagons (pentagonal dodecahedron), is the basic component of these hydrate structures. Linking the vertices of the 5^{12} cavities gives the sI hydrate structure, while linking the faces results in sII. sH is more complicated: a layer of linked 5^{12} cavities is connected with layers of other kinds of cavities. Inside each cavity, a maximum of one guest molecule resides [*Sloan, 1998b*], although recently double occupancy of one cavity in sI and sII N_2-hydrates has been evidenced by neutron diffraction analysis [*Kuhs et al., 1996*].

The **size** and – to a lesser extent – the **geometry** of the enclosed guest molecules determine the cavity formed, and thus the kind of resulting hydrate structure. Molecules smaller than 3.5 Å are too small to form hydrates. Other molecules are too big to fit one or all of the cavities. sI-hydrate forms with small natural gas molecules of biogenic origin (CH_4, CO_2, H_2S, ...) found *in situ* in the deep ocean. sII forms when natural gases or oils contain molecules larger than C_2H_6 but smaller than C_5H_{12} and are in many cases related with seeps or faults. Those gases are mainly of thermogenic origin. In nature, there is usually between 1 and 20 mole % of C_3H_8 present in thermogenic hydrates. sH hydrates observed in the Gulf of Mexico [*Sassen & MacDonald, 1994*] can contain even larger molecules. The shape of the gas molecules is only important for sH hydrates. Furthermore, the guest molecules appear to be located preferentially off-centre in the cavity [*Sloan, 1998a*].

While sH hydrates are **mixed hydrates**, sI and sII hydrates can be **simple hydrates**, i.e. only one kind of guest molecules is present. sH hydrates require inclusions of a small occupant for the smaller cages but also larger molecules for the $5^{12}6^8$ cavities. For a simple hydrate to be stable, the size ratio of guest to cavity should exceed 0.76 [*Sloan, 1998a*]. If significantly less, the molecules will not stabilise the hydrate structure. When a molecule stabilises the small cavity of a structure, it will also enter the larger cavities of that structure, contributing further to its overall stability. Furthermore, the typical occupancy factor of the larger cavities is higher than that of the smaller cavity in sI hydrates. Large molecules can stabilise sI and sII hydrates by only saturating the large cavity. This is for example the case with pure ethane hydrates. The size of an individual ethane molecule is too large to fit the small 5^{12} cavities, so a sI hydrate is formed with only the bigger $5^{12}6^2$ cavities filled.

	hydrate structure						
	sI		***sII***		***sH***		
crystal system	cubic		cubic		hexagonal		
lattice parameter (Å)	12		17.3		12.3 / 10.2		
cavity	***small***	***large***	***small***	***large***	***small***	***medium***	***large***
description	5^{12}	$5^{12}6^2$	5^{12}	$5^{12}6^4$	5^{12}	$4^35^66^3$	$5^{12}6^8$
cavities/unit cell	2	6	16	8	3	2	1
average cavity radius (Å)	3.95	4.33	3.91	4.73	3.91	4.06	5.71
coordination number	20	24	20	28	20	20	36
water molecules/unit cell	46		136		34		

***Table 1.1**: Natural occurring hydrate structures and their cavities, from Sloan [1998a]*

The **fractional filling** of the cavities depends on thermodynamic conditions and, more important, of composition. The hydrate structure is non-stoichiometric, i.e. the ideal hydration number (i.e. the number corresponding to complete cavity filling) is not an integer value. The structural formula for pure methane hydrates is for example $CH_4 \cdot 5.75H_2O$, while the above-mentioned ethane hydrates are

represented by $C_2H_6 \cdot 7.66H_2O$. The fact that the ideal hydration number is an unrealistic upper-limit for cavity saturation enhances non-stoichiometric behaviour. This effect is stronger if the diameter of the guest molecules reaches the size of the cavity in which it has to be enclosed [*Sloan, 1998a*]. Small changes in composition can also force structural changes, due to the size and geometry of the molecules. This is for example the case if small amounts of propane are introduced in a pure methane vapour.

As can be seen from table 1.1, the three different hydrate structures occurring in nature are composed of about 82% of water and 18% of guest molecules. Due to the above-mentioned non-stoichiometry, the water fraction will be even higher. Therefore, the physico-chemical properties of gas hydrates are approximated by three heuristics [*Sloan, 1998b*]:

- ➔ The mechanical properties are similar to those of ice.
- ➔ The phase equilibrium conditions are determined by the guest and host properties.
- ➔ The thermal properties are set by the hydrogen-bonded crystals with cavity size ratios.

Properties of methane hydrates (sI) relative to ice are given in literature [e.g. *Sloan, 1998b; Rempel & Buffett, 1998; Tinivella, 1999*].

Hydrate formation kinetics is supposed to occur in different steps [*Sloan, 1998b*, and references therein]. In a first step, nucleation of a critical crystal radius is taking place, starting from a mixture with labile ring structures within favourable thermodynamical conditions. Water molecules will form labile clusters around dissolved guest molecules. Several clusters will then combine to grow unit hydrate cells. Once the dimensions of the cluster agglomerate reaches a critical value, growth of hydrates begins.

Using the figures given in table 1.1 in combination with the non-stoichiometric structural formula of pure methane hydrates ($CH_4 \cdot 5.75H_2O$), the hydrate gas expansion coefficient can be easily determined, supposing that the ideal gas law is applicable at STP conditions. Since a unit cell of pure methane hydrates is a cube with lattice parameter 12 Å, a unit cell comprises a volume of $1.728 \cdot 10^{-27}$ m³ and contains 8 CH_4 molecules (or $1.3285 \cdot 10^{-23}$ mole CH_4) and 46 H_2O molecules. One volume unit with only 90% filling of the cavities, contains in that case 6919 mole CH_4 or 155.08 m³ CH_4 (ideal gas law applied) and 796.38 kg H_2O, i.e.

$$1.00 \text{ m}^3 \text{ methane hydrate} \leftrightarrow 155.08 \text{ m}^3 \text{ CH}_4 + 0.80 \text{ m}^3 \text{ H}_2\text{O}$$
(STP conditions, 90% cavity filling)

Thus, the methane **hydrate gas expansion coefficient** is calculated to be approximately 155.1 (density of 907 kg/m³) and increases to 172.3 in case of a perfect hydrate crystal (density of 920 kg/m³). Similar values are obtained for the sII structure. These ratios show that the hydrated gas density is equivalent to a highly compressed gas, but slightly less than the density of a liquid hydrocarbon [*Hovland & Judd, 1988*]. Hence, the hydrate structure has a huge storage capacity of gas molecules. In other words, the 155.1 (172.3) m³ coincides with approximately 111.0 (123.3) kg of methane or 83.1 (92.3) kg of carbon per cubic meter massive hydrate. This explains the present-day interest of industrial companies in these structures and in their distribution and accumulation modes in nature.

1.1.2
Phase diagrams

At present more than 130 chemical compounds are known to form clathrate hydrates with water molecules [*Sloan, 1998a*], with each of them having their own specifications. In figure 1.1, a general pressure-temperature phase-diagram for small hydrocarbons, methane up to iso-butane, is presented. Each line represents a 3-phase equilibrium curve separating areas in which 2 phases (e.g. hydrate & saturated water, methane & pore water) co-exist. The theoretical zone of hydrate stability is found at the left of the 3-phase lines hydrate-ice-vapour, hydrate-water-vapour and hydrate-water-liquid

hydrocarbon. At the intersection of two 3-phase equilibrium lines, 4 phases co-exist. These positions in the PT-field are called quadruple points and are unique for each hydrate-forming compound. In the lower quadruple point, ice-hydrate-water-vapour co-exist, while in the upper quadruple point hydrate-water-liquid hydrocarbon-vapour co-exist. This upper point does not exist for all compounds, for example methane and nitrogen, since the vapour pressure critical temperature is too low. The lower quadruple point temperature lies for most hydrate forming compounds close to 0°C, but the pressure variability is high [*Sloan, 1998a*]. Other quadruple points exist as well, but are of no relevance to this research topic and are hence not discussed.

From the geological point of view, the 3-phase boundary hydrate-water-vapour is the most interesting since the thermodynamical conditions of stability are fulfilled in the shallow subsurface. Precise knowledge of the chemical composition plays a crucial role in determining equilibrium conditions for gas hydrates. This is clearly demonstrated in figure 1.2 showing several 3-phase hydrate-water-vapour equilibrium curves for diverse single and mixed hydrates in the 0-20°C temperature interval. The hydrate stability field is to be found in the upper left corner of the diagram, i.e. the area with higher pressures/lower temperatures relative to the equilibrium limit. Inclusion of small amounts of other molecules, in this case H_2S, seriously forces the equilibrium temperature to decrease at isobaric conditions, resulting in a broader stability window. The equilibrium data were calculated using the computer program CSMHYD [*Sloan, 1998a*].

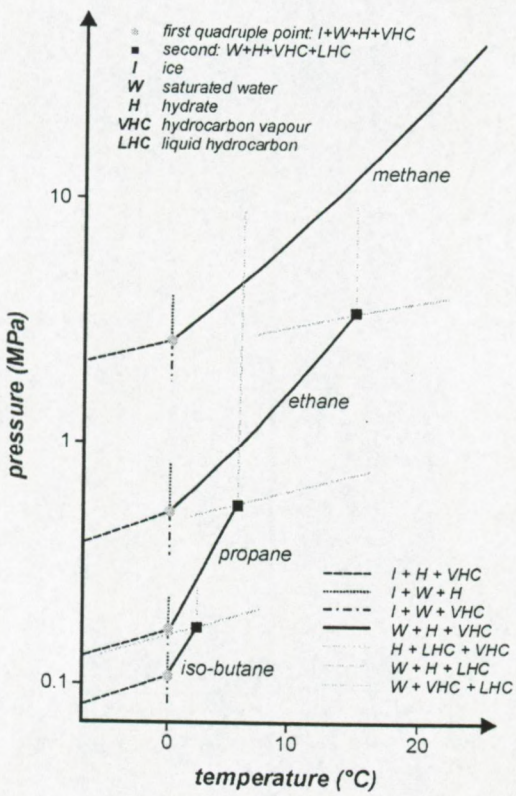

***Figure 1.1**: General phase diagram for simple hydrates (small hydrocarbons) with quadruple points, redrawn from Sloan [1998a]*

It is also worth noting that the vapour composition can significantly differ from the composition of the clathrated gas molecules. For example, some compounds are known for their favourable hydrate-forming behaviour, like H_2S [*Sloan, 1998a*]. This is clearly illustrated in table 1.2, giving the partial occupation numbers and the clathrated mole fractions of each compound of the systems discussed above. If the gas phase CH_4-H_2S contains only 1% of H_2S, almost 20% of the captured gas molecules appear to be H_2S. In case of 10% mole fraction in the vapour phase, over 70% of the enclosed gas is

H_2S. As can be seen from the pure hydrates in this table, the occupation number of the bigger cavity $5^{12}6^2$ of the sI hydrate structure appears to be higher than the saturation of the smaller cavity 5^{12}.

Impurities in the water also have an important influence on the equilibrium conditions. Salt ions for example shift the equilibrium boundary towards higher pressure and cannot be neglected in the porous media of the natural environment. Hydrates exclude all ions upon formation. A more accurate description of the different stability conditions in a fresh water and averaged salt water environment will be presented in the second chapter.

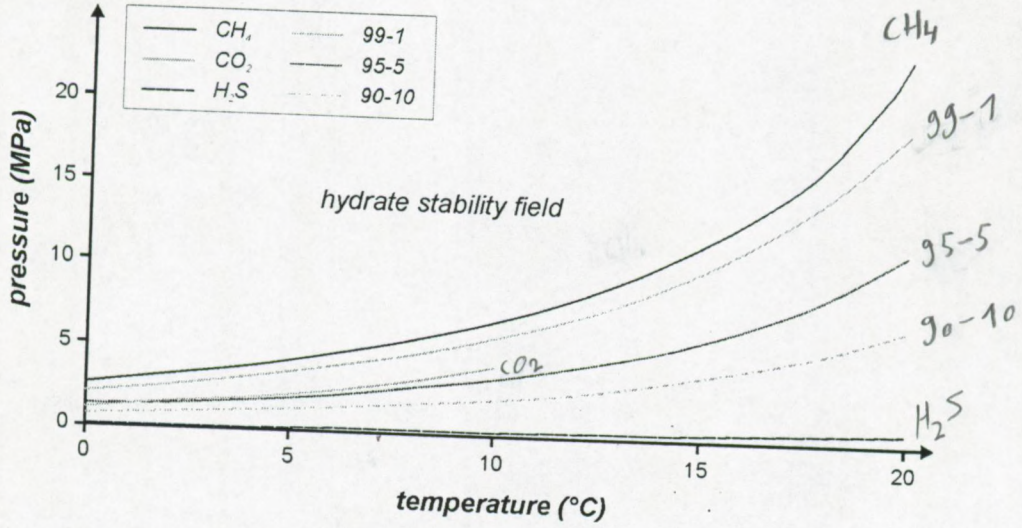

***Figure 1.2**: 3-phase equilibrium curves for diverse hydrate compositions.*

description	pure hydrates		
	H_2S	CH_4	CO_2
partial occupation of small 5^{12} cavity	0.9057	0.8699	0.7248
partial occupation of large $5^{12}6^2$ cavity	0.9701	0.9725	0.9808

description	mixed CH_4-H_2S hydrates		
	99-1	95-5	90-10
mole fraction CH_4 in gas phase	0.99	0.95	0.90
mole fraction H_2S in gas phase	0.01	0.05	0.10
CH_4-fraction in hydrate structure	0.8084	0.4626	0.2979
CH_4-occupation in small cavity	0.6340	0.3093	0.1802
CH_4-occupation in large cavity	0.8619	0.6108	0.4339
H_2S-fraction in hydrate structure	0.1916	0.5374	0.7021
H_2S-occupation in small cavity	0.2106	0.5543	0.6925
H_2S-occupation in large cavity	0.0836	0.3177	0.4870

***Table 1.2**: Differences between initial vapour composition and final hydrate gas compositions. Phase boundary conditions of these hydrates are shown in figure 1.2*

It is also worth noting that the vapour composition can significantly differ from the composition of the clathrated gas molecules. For example, some compounds are known for their favourable hydrate-forming behaviour, like H_2S [*Sloan, 1998a*]. This is clearly illustrated in table 1.2, giving the partial

occupation numbers and the clathrated mole fractions of each compound of the systems discussed above. If the gas phase CH_4-H_2S contains only 1% of H_2S, almost 20% of the captured gas molecules appear to be H_2S. In case of 10% mole fraction in the vapour phase, over 70% of the enclosed gas is H_2S. As can be seen from the pure hydrates in this table, the occupation number of the bigger cavity $5^{12}6^2$ of the sI hydrate structure appears to be higher than the saturation of the smaller cavity 5^{12}.

Impurities in the water also have an important influence on the equilibrium conditions. Salt ions for example shift the equilibrium boundary towards higher pressure and cannot be neglected in the porous media of the natural environment. Hydrates exclude all ions upon formation. A more accurate description of the different stability conditions in a fresh water and averaged salt water environment will be presented in the second chapter.

1.2
Geography, geology and geophysics of natural gas hydrates

1.2.1
Worldwide distribution of natural gas hydrates: geochemical and geophysical indicators

Highly simplified, one can state that for hydrates to accumulate in natural porous media, four heuristics are necessary, i.e. sufficient amounts of water molecules to form the hydrogen-bonded cavities, sufficient amounts of gas molecules to stabilise the open cavity structures, high enough pressure and low enough temperature [*Sloan, 1998a*].
When the pressure-temperature conditions are met for hydrate stability, it is the presence of a gas reservoir (i.e. in most cases CH_4) responsible for gas supply to the hydrate stability field, that will be the limiting factor for the presence of hydrates in sedimentary sections. It is known that the solubility of methane in sea water is rather low, only about 0.045 volumes of methane per volume of water at STP conditions [*Yamamoto et al., 1976; Zatsepina & Buffett, 1998; Ginsburg, 1998*]. This clearly means that the amount of methane necessary to stabilise the hydrate structure by far exceeds the solubility limit. Hence, an important gas reservoir is required to supply huge amounts of gases towards the stability field. In other words, the amount of organic matter needed for hydrate formation is very large as well. Under normal conditions, the methane solubility increases slightly with decreasing burial depth or temperature [*Ginsburg, 1998; Zatsepina & Buffett, 1998*]. In terms of hydrate stability however, the methane solubility is little affected by hydrostatic pressure, but is dictated essentially by the equilibrium pressure of hydrate formation, which is highly dependent on temperature. Solubility of CH4 in pore water generally decreases towards the sea floor within the hydrate stability zone [*Ginsburg, 1998*].

Also a certain minimum water depth of some hundreds of meters is necessary to assure hydrate stability. It is clear from the typical phase boundary diagrams that the thermodynamic stability conditions are the better, the deeper the overlying water column. The first hundreds of meters of sediments in the deep ocean obviously have favourable thermodynamic conditions for hydrate stability. At greater burial depths, the temperature rises too high for hydrates to remain stable. Hence, the intersection of the phase boundary curve with the sub-bottom temperature profile marks the base of the theoretical hydrate stability field (BHSF). In general, the sea floor acts as an upper-limit of hydrate occurrence, due to the buoyancy effect (hydrate is less dense than water, see also chapter 2). Hence, these hydrate particles will buoy up and will dissociate once they pass the equilibrium curve. According to the phase rule of Gibbs, the three phases hydrate – free gas – pore water (with dissolved gas) should co-exist at the equilibrium depth. In practise, a free gas zone (FGZ) with extent of a few m to a few tens of m is often thought to be present below the hydrate stability field [e.g. *Miller et al., 1991*], although this is not always confirmed from seismic data analysis [*Hyndman & Spence, 1992*]. A

schematic overview is shown in figure 1.3 for water depths of 1200 m and a geothermal gradient of 0.035 °C/m.

In this way, approximately 90% of the deep ocean is within the temperature-pressure interval in which hydrates can be stable. However, the occurrence of hydrate accumulations in oceanic settings seems to be restricted to continental margin and slope areas, as is clear from the overview map (figure 1.4). This behaviour is explained by the fact that biogenic or thermogenic hydrocarbon gas generation strongly depends on the total content of organic matter deposited in the sediments and on sedimentation rates, while both parameters tend to decrease seaward [*Ginsburg & Soloviev, 1997*]. Remarkably, at tectonic plate junctures where catalytic genesis of gas via Fischer-Tropsch synthesis cannot be excluded, hydrates are observed as well [*Szatmari, 1989*]. Direct and indirect evidence of hydrates is also provided from areas in the Okhotsk Sea, in inland seas (Black See, Caspian See) and recently Lake Baikal, a large continental rift lake in Central Siberia.

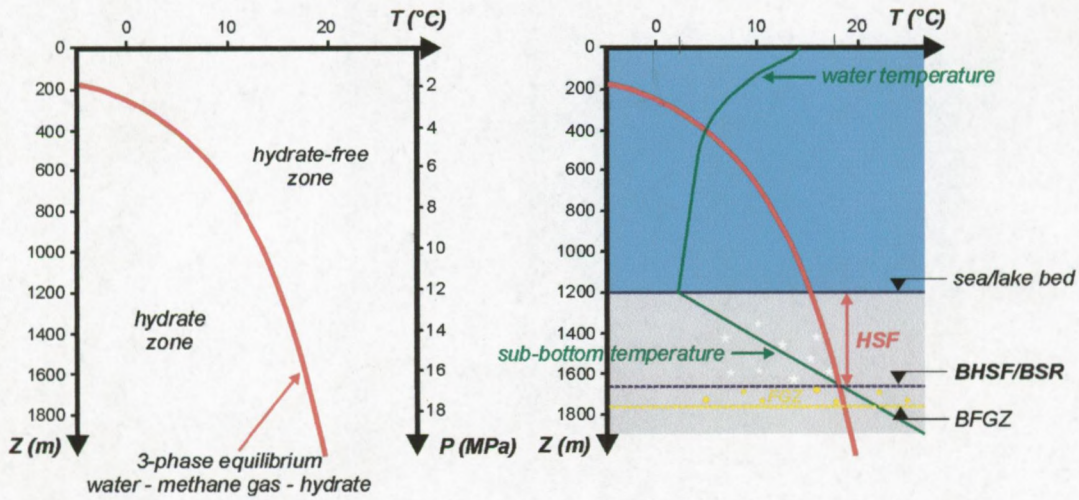

***Figure 1.3**: Sketch of the pressure-temperature stability conditions of pure methane hydrates in seawater (left) and theoretical extent of the hydrate stability field in sediments (right).*
BFGZ = Base of free gas zone

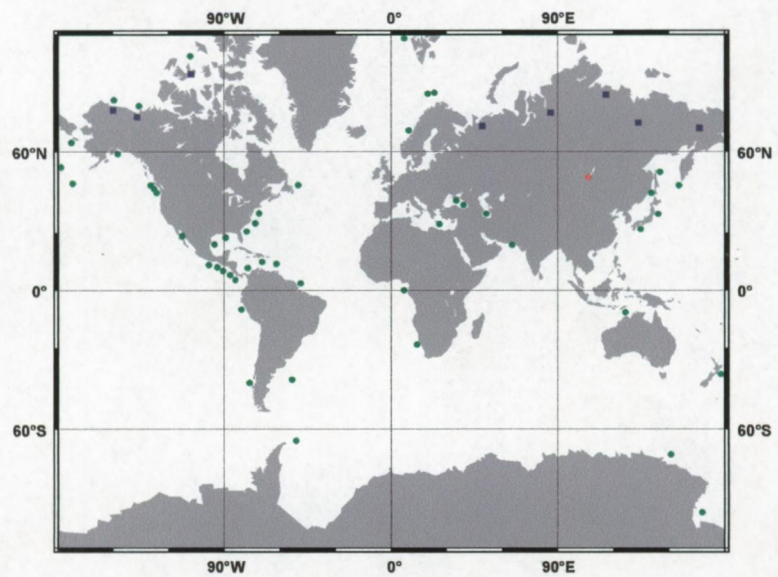

***Figure 1.4**: Overview map of direct and indirect hydrate occurrences in nature. The blue squares denote hydrate in permafrost areas while the green circles locate direct and inferred hydrate occurrences in continental margin areas. The red circle represents Lake Baikal, the only confined fresh water basin with both direct and indirect evidence of the presence of hydrate accumulations. Redrawn after Kvenvolden et al. [1998]*

Most of the locations where gas hydrates are believed to be present in the shallow subsurface are inferred indirectly, by the presence of a so-called bottom simulating reflection or BSR on low-resolution seismic profiles. Such a BSR is a high-amplitude polarity-reversed single reflector at the base of the hydrate stability field that often crosscuts the local stratigraphy. Such a reflection was originally thought to arise from the acoustic impedance contrast across the interface at the base of the hydrate stability field. Sonic velocity in pure hydrate is reported to be 3300-3800 m/s [*Whalley, 1980; Sloan, 1998b*]. Hence, above this boundary hydrate inclusions are responsible for higher than normal bulk compressional wave velocities, while under this interface free gas can be present with low sonic velocity. At present, more evidence becomes available that the BSR is due mainly to free gas trapped beneath the hydrate stability field rather than to the presence of hydrate just above the phase boundary [e.g. *Holbrook et al., 1996*].

It has to be mentioned that the HSZ is not identical to the *hydrate accumulation zone*. The former only defines a continuous range between the upper (most often the sea or lake bed, see also paragraph 2.3) and lower boundary of theoretical bulk equilibrium conditions, while the latter can be a discrete series of limited ranges in which hydrates factually accumulate, depending on the *in situ* conditions (water depletion, permeability, porous medium effects, gas supply rate...). For example, on the Blake Outer Ridge (figure 1.5) hydrate stability conditions are fulfilled for the upper 450 m of sediments, although no hydrates are observed within the first 190 m [*Thiery et al., 1998*].

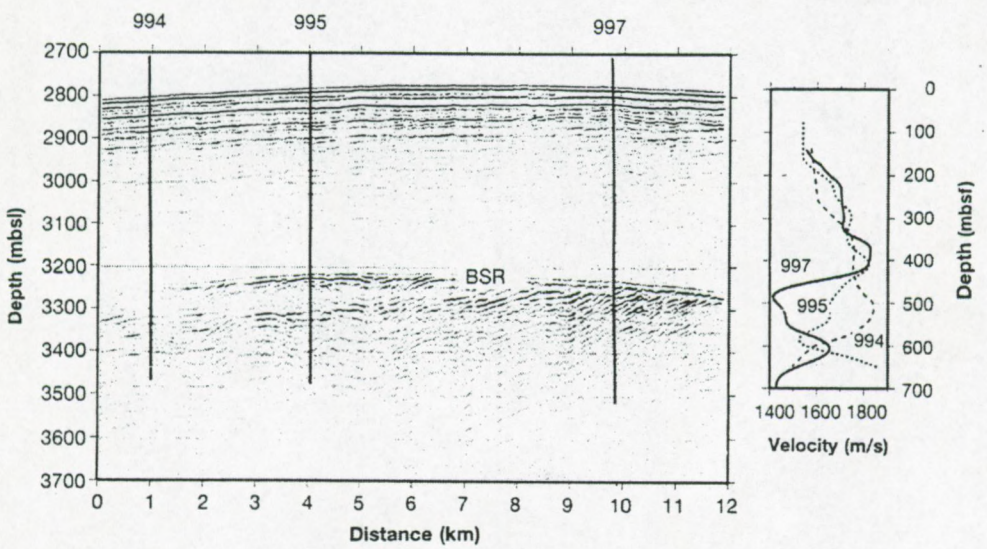

***Figure 1.5**: Typical BSR observed on a low-resolution acoustic profile from the Blake Outer Ridge, ODP Leg 164, with sub-bottom acoustic velocity profile. Taken from ODP website (http://www-odp.tamu.edu/)*

There are several examples of gas hydrate retrieval in oceanic settings without accompanying BSR. An example is shown in figure 1.5 from ODP Leg 164, site 994 (Blake Ridge). In this case, there is evidence of a transition zone between the base of the hydrate accumulation zone and the top of the free gas zone, while at the adjacent sites (995, 997) both interfaces coincide, so the acoustic impedance contrast gives rise to the reflection observed [*Wood & Ruppel, 2000*]. Also in Lake Baikal, hydrates were retrieved from the axial part of the Southern Basin although no BSR is observed at the drill site. A few km aside, a faint BSR is seen on medium-frequency acoustic profiles [*Vanneste et al., in press*]. This is also confirmed by recent physico-mathematical modelling: a transition zone can exist between the base of the hydrate accumulation zone and the top of the free gas zone [*Xu & Ruppel, 1999*].

Only in a limited number of cases, direct evidence of gas hydrate accumulations was provided by drilling or coring (DSDP/ODP e.g. offshore Peru, Mexico, Costa Rica, Guatemala, SE and W of US,

Japan, Gulf of Mexico, Black Sea, Caspian Sea, Okhotsk Sea, offshore California, Gulf of Mexico, Lake Baikal [e.g. *Kvenvolden, 1998* and references therein; *Kuzmin et al., 1998*].

While often the presence of a BSR indicates the base of the hydrate accumulation zone coinciding with the top of the free gas zone beneath the stability field, there is no evidence on acoustic profiles of the top of the hydrated section. This can be explained by a kind of gradationally decreasing accumulation mode from a maximum value at the basal limit, fading out at a certain level. In a few cases, a reflection from the base of the free gas zone underlying the hydrated section is observed [e.g. *Ecker et al., 1996*]. Advanced seimic tools to qualitatively as well as quantitatively analyse the response of partially hydrated sediments are used as well. Amongst those, especially AVO (amplitude vs offset) analysis, VSP (vertical seismic profiling) and wire-line logs (gamma ray, resistivity, caliper, spontaneous potential) are important [*Kvenvolden, 1998*]. More details of AVO analysis will be presented at a later stage.

Apart from a gas hydrate/free gas related BSR, there are other possibilities to generate a crosscutting BSR-like feature. The most obvious one is the reflection at a simple gas-water interface [*Sheriff & Geldart, 1995*]. Nevertheless, such a reflection will show positive polarity. According to *Hammond & Gaither* [*1983*], the diagenetic process of silica-rich sediments from Opal A to Opal CT or Opal CT to quartz can give rise to a BSR feature as well, again with positive polarity due to increasing acoustic impedance.
Next to geophysical tools, several geochemical methods are applied on cores in order to quantify the amount of hydrates. Especially isotopic analysis of carbon and oxygen, temperature and chlorinity measurements (pore water freshening related to hydrate dissociation during core recovery) are performed. The reader is referred to specialised literature concerning these topics.

1.2.2
Controls on growth and decay of gas hydrates

1.2.2a Modes of occurrence

In nature, hydrate inclusions appear in **4 different forms** [*Malone, 1985,* in *Sloan, 1998a*]: finely disseminated within pores (e.g. Mississippi canyon area in Gulf of Mexico), nodules (e.g. Green Canyon), layered (e.g. Blake-Bahama Ridge) and, only very occasionally, massive hydrates (> 95% of hydrates, Middle America Trench, DSDP-Leg 84, site 570). However, the mean maximum hydrate content of all retrieved gas hydrate samples is reported to be only 3% by volume of bulk sediment, while the mean maximum amount of free gas in sediments below the hydrate stability field is calculated to be only 5% [*Hovland et al., 1997*]. In the most prominent gas hydrate area, the 26000 km² Blake Ridge and Carolina Rise offshore southeastern USA, gas hydrate distribution is finely disseminated. Based on diverse geochemical and geophysical analysis tools, the volume of hydrate is estimated to be 2 to 3% throughout the hydrate accumulation zone [*Holbrook et al., 1996; Wood & Ruppel, 2000*].

As already stated, the gas clathrated in the hydrate structure can be of **biogenic** or **thermogenic** (e.g. Caspian Sea, Gulf of Mexico) origin. Biogenic methane results from microbial breakdown of organic matter common in shallow sediments. The sedimentation rate should exceed 30 m/My with a total organic carbon content higher than 0.5%. Thermogenic methane comes from thermal alteration of organic matter at depths and has migrated from deeper reservoirs [*Kvenvolden & Cooper, 1987*]. Discrimination between these two methane generation modes can be achieved via isotopic analyses on the clathrated gas in the recovered samples. Methane of biogenic origin has $\delta^{13}C$ isotopic value ranging from –85 and –60 ‰ relative to the PDB standard, while methane of thermogenic origin has values between –55 and –25 ‰. Also the ratio of the methane concentration to higher hydrocarbons differs significantly: biogenic: > 1000; thermogenic: < 100 [*Kvenvolden, 1993*]. For example, the gas hydrates in the Gulf of Mexico were found to be biogenic and sI if disseminated, and thermogenic and sII if more massive.

Of all **recovered hydrate samples**, approximately 70% were retrieved from sub-bottom depths well above (sometimes hundreds of meters) the three-phase equilibrium boundary, i.e. at lower *in situ* temperatures in the 2-phase region hydrate-water (methane-saturated). No samples were found below the calculated position of the BHSZ at the specific site [*Booth et al., 1998*]. These results give credibility to the suggestion that hydrates can form from methane-saturated water. It is unlikely to assume that all these hydrates once formed at the 3-phase equilibrium boundary, and moved upwards within the two-phase region [*Sloan, 1998b*]. Hence, hydrate nucleation from a single saturated liquid phase is evidenced in nature [*Booth et al., 1998*]. Obviously these hydrates are more stable than those found at the stability limit, or extra energy (and time) is necessary to start hydrate dissociation.

In literature, three important mechanisms explaining methane migration under natural conditions are distinguished [*Ginsburg, 1998*], i.e. a single-phase flow of porous water with dissolved methane, as free gas flows or by means of molecular diffusion as a result of random thermal movement along a concentration gradient. *Ginsburg* [*1998*] believes however that submarine gas hydrates mostly occur in discrete accumulations controlled by fluid migration. This is confirmed by *Booth et al.* [*1998*] who conclude that faults or vent systems have been found proximal to hydrates in nearly three-quarters of the samples contributing to their database. Often, authigenic carbonates – indicative of rapid fluid fluxes – are associated with gas hydrate zones [*Booth et al., 1998; Bohrmann et al., 1998*]. Also *Hovland et al.* [*1997*] put emphasis on a causal link between focussed and diffusive vertical fluid flows and the occurrence of hydrate accumulations. Furthermore, gas hydrates are sometimes associated with fluid escape features at the seabed, like pockmarks, diapiric structures and mud volcanoes [*Bouriak et al., 2000; Schmuck & Paull, 1993*]. Thermogenic hydrate accumulations are most often associated with seepages, faults, fissures and hence are more localised, while those lacking evident relation to seepage are mostly of biogenic origin and are more extensive (widespread BSRs) [*Ginsburg & Soloviev, 1997*]. The massive hydrate sample retrieved from the Middle America Trench (DSDP Leg 84) contained more heavy hydrocarbons than the surrounding hydrated cores and is thought to be closely linked with enhanced fluid flows. Also on the Blake Ridge on the US Atlantic passive margin, higher hydrate concentrations are attributed to increased fluid fluxes in faults [*Wood & Ruppel, 2000*].

1.2.2b Hydrate formation models

In literature, three models for gas hydrate formation in sedimentary sections are found:

- In a first model, *Claypool & Kaplan* [*1974*] propose that methane is generated *in situ* from microbial degradation of organic matter within the hydrate stability zone, in absence of oxygen and sulphates. Hydrate formation takes place concurrent with sedimentation processes. As the zone of hydrate occurrence deepens, part of this field may subside into a temperature field that is no longer favourable for hydrate stability. Hydrates will start to decompose, resulting in a free gas – (salt) water mixture within the pore spaces. If gas migration pathways are available, this free-coming gas can move back into the stability field where again hydrate formation can take place [*Kvenvolden, 1998*]. As a consequence, hydrates should be present throughout the entire stability zone, under which free gas can accumulate. Under the best conditions, it is suggested that maximum 4% of the pore volume can be filled with hydrates generated this way [*Minshull et al., 1994*].

- A second model [*Hyndman & Davis, 1992*] states that hydrates are formed by removal of gas molecules from upwelling saturated pore waters at the base of the hydrate stability field. In this case, the gas can either be biogenic or thermogenic. The drop of the gas solubility in rising pore water, being confronted with lower (hydrostatic) pressures and temperatures within the hydrate stability zone plays a crucial role in this theory [*Zatsepina & Buffett, 1998; Ginsburg & Soloviev, 1997*]. Here, gradational accumulation of hydrates from the base is expected, while no free gas needs to be present under the stability field.

➔ In a third model, free gas is supposed to migrate upward through zones of higher permeability (faults, fissures) due to buoyancy, capillary forces and overpressuring mechanisms [*Minshull et al., 1994*]. Hydrates start to form at nucleation or growth sites. Gas may come from either free migrating gas or from dissociated hydrates [*Sloan, 1998a*]. In this case, if hydrates block the porous medium and form a kind of seal, free gas will accumulate under the base of the hydrate stability field. After further sedimentation or subsidence, a new equilibrium position will be obtained, resulting in the decomposition of the previously stable but now unstable hydrate crystals. The free-coming gas again takes part in the migration cycle [*Paull et al., 1994*].

Ginsburg [*1998*] mentions that hydrates in nature presumably form in large voids from low-saline pore fluids. This is confirmed by theoretical investigations of the influence of porous medium effects on hydrate formation [*Clennel et al., 1999; Henry et al., 1999*]. Hydrate formation in natural porous media is a very slow process. According to results of physico-mathematical modelling using energy, mass and momentum conservation equations, *Rempel* [*1995*] showed that one needs a time span in the order of $2 \cdot 10^5$ years to reach a partial hydrate occupation of 1% of pore space at the base of the hydrate stability field, in case of the second hydrate formation model. Note that hydrate stability requires gas concentrations in the hydrate structure that are at least two orders of magnitude higher than the aqueous solubility (only a few methane molecules per thousand water molecules). Hydrate formation from a single phase will therefore need geological time spans. This means that sedimentation and subsidence processes need to be considered in evaluating the changes in hydrate stability conditions through geological time.

At present, modified models for hydrate formation and stability conditions in porous media are being presented, indicating that porous medium effects (capillary pressure, surface curvature) can have a significant influence on the gas hydrates stability and the kinetics of formation [e.g. *Clennell et al., 1999; Henry et al., 1999*]. Hydrate growth is inhibited in fine-grained sediments: a pore size may be smaller than the critical size necessary for hydrate nucleation at a specific temperature. Discrepancies between bulk conditions and thermodynamic properties of retrieved hydrate samples [*Ruppel, 1997*] support this theory.

1.3
General importance of natural gas hydrates

The general interest and importance of natural hydrates and hydrate research is - as already mentioned before - threefold: relevance to climate changes, relevance to world margin stability and its potential as a future clean energy resource.

1.3.1
Contribution to global climatic changes?

Global climate changes are at present always considered relative to sinks and sources of CO_2 (residence time approximately 200-250 years) comprising by far the biggest contribution to greenhouse warming, while the possible influence of CH_4 is largely neglected. The residence time of CH_4 is about 12-15 years, after which it oxidises to CO_2 and water and thus still has an impact on the radiative budget of the atmosphere [*Lashof & Ahuja, 1990*]. The greenhouse potential of CH_4 is a factor 3.7 (molar basis) or 10 (weight basis) higher relative to CO_2 [*Haq, 1998*]. The total amount of methane in the atmosphere ($4.9 \cdot 10^{12}$ kg) is estimated to be of the same order as the amount of methane stored in gas hydrate accumulations in the Arctic permafrost areas [*Kvenvolden, 1998*]. Next to that, natural hydrates appear to be accumulated at or close to their equilibrium limits. Therefore, several authors

[e.g. *Nisbet, 1990; Paull et al., 1991; Haq, 1993*] hypothesise that the sudden release in the atmosphere of methane coming from decomposing hydrate reservoirs in permafrost and deep ocean areas can severely affect the local or global climate system in an asymmetric positive-negative feedback mechanism [*Haq, 1993; 1998*]. While glaciation can be explained as Milankovich orbital forcing, deglacation tends to occur relatively abrupt and is associated with increased CH_4 and CO_2 levels in the palaeoclimatic record [*Raynaud et al., 1998*].

A possible causal link implies the combination of changes in the bottom water current (density, temperature, activity), sea level fluctuations, sensitivity of the hydrate equilibrium conditions, transfer of greenhouse gases from the sub-surface through the water column into the atmosphere and its atmospheric chemistry, ... for both the onshore and offshore hydrate accumulations. For more details of the theoretical stability sensitivity to climatic changes, I would like to refer to chapter 2. Highly simplified, it works as follows [e.g. *Haq, 1998;* and references therein]:

- ➔ The effect of sea level fall and/or glaciation is initially delayed in the high latitudes compared to low latitudes. In low- to mid-latitudes, the hydrostatic pressure reduction accompanying the eustatic sea level fall affects hydrate stability conditions at their base at several hundreds of meters sub-bottom depths on the margin and slope areas. As a consequence of overpressure build-up, reduced resistance and gravity, slumping can occur (see below) resulting in the release of significant amounts of methane that in turn move through the water column (low solubility) and finally enter the atmosphere.
- ➔ Such an evolution represents a negative feedback mechanism to glacial cooling and the onset of warming conditions. This can lead to dissociation of permafrost hydrates and shallow marine hydrates. Hence, a new but positive feedback mechanism to warming is present and is thought to be responsible for the relatively abrupt and fast termination of glacial cycles [*Haq, 1993*].

It is worth noting that the impact of changing climatic conditions is different on continental or permafrost hydrate reservoirs and oceanic hydrate accumulations [*Kvenvolden, 1998*]. The rise in sea level during **global warming** due to melting of glaciers and polar ice caps increases the sub-surface hydrostatic pressure in oceanic sediments, a process that enhances hydrate stability conditions on continental margins, slopes and polar continental shelves. Meanwhile, onshore rising air temperatures may be responsible for decaying permafrost hydrate reservoirs at timescales of hundreds to thousands of years. The increasing water temperatures in deeper basins (negative in terms of hydrate stability) are thought to be offset by the pressure effect. On the shelf, this effect might be more noticeable in combination with higher sub-surface temperatures due to transgression of polar ocean over exposed colder continental shelf surface during sea level rise that may now offset the pressure effect. The growth of ice caps during **global cooling** on the other hand results in sea level fall and regression and hence pressure reduction (negative) and possibly hydrate dissociation. As polar shelves become colder, the cold temperatures eventually stabilise the hydrate accumulations. In polar regions, continental hydrates are buried under thicker ice loads (positive). Sea level fall induced hydrate dissociation in deeper-water areas and again methane release from sub-surface zones into the atmosphere can be possible [*Kvenvolden, 1998*].

More knowledge about the diverse accumulation modes of hydrates in sediments, how dissociation is initiated, and how the free-coming gas eventually migrates upwards through the sedimentary section to the sea or lake floor and is transferred through the overlying water column is necessary for several reason. First of all because of the causal link of climate changes vs. hydrate destabilisation. We need to mention here that perhaps a triggered decay of hydrate layers (e.g. by tectonic activity on continental margins and slopes) in a climatic stable period may contribute to changes in climate systems as well. This means that hydrate can become unstable under variable climatic conditions but they also can affect climate in a stable climatic situation. On the other hand, more knowledge of the typical accumulation of hydrates in sediments must give us more accurate and reliable estimates of the total amount of gases stored in the shallow geosphere. This will show us the role of clathrate hydrates in the global carbon cycle.

However, estimates of the effective influence of hydrate destabilisation on long-term climatic changes are still highly speculative [*Henriet & Mienert, 1998*]. *Thorpe* [*1996*] and *Thorpe et al.* [*1998*] modelled the possibility of a catastrophic hydrate release of methane at the termination of the last glaciation and its impact on global climate changes, and compared it with ice-core studies. Although the ice-core record is not inconsistent with this hypothesis, an extremely high methane pulse needs to be implied. Even in this case, the upper limit of the magnitude of this pulse only accounts for less than 15% of the supposed temperature shift at the deglaciation. More detailed studies of ice-cores revealed no evidence of any of these mentioned catastrophic events [*Raynaud et al., 1998*], but the resolution of the ice-core record may not be refined enough to decisively conclude this debate.

1.3.2
Gas hydrate dissociation as a geohazard?

Nowadays, the geotechnical aspects of hydrates in sediments and their dissociation are being studied. The general idea linking hydrate instability with mass wasting processes is the following. The mechanical behaviour of soils under their own weight is known to be highly dependent of the stress and pressure regime, especially of fluid phases [*Kenney, 1984*]. Whereas the sedimentary matrix can resist both normal and shear or tangential forces at the particle contacts, the fluid phase cannot support shear forces. The resistance to deformation (shear strength) is related to the normal forces transmitted at the particle contacts in terms of effective stress (total stress minus pore pressure). If overpressures of a fluid phase are being developed, part of the weight of the overburden will be supported by the fluids, resulting in reduced effective stresses between the grains and hence reduced shear strength. Once the total shear stress exceeds the critical shear strength, motion will be initiated along a failure plane.

In case of partially hydrate-saturated sediments, as will be discussed thoroughly, changing environmental conditions (pressure, temperature, sedimentation, sedimentation rates, erosion, with their own specific time scales) can shift the hydrate stability field and force part of the hydrate accumulations to dissociate at the base of their existence. Dependent on the balance between hydrate dissociation and overpressure dissipation, an overpressured gas and almost incompressible liquid phase can exist in the pore spaces at some hundreds of meter sub-bottom depth, replacing the solid hydrate volume. If the overpressure cannot dissipate fast enough due to the partially hydrate-saturated sediments above and reduced effective porosity and permeability, the fluids in the porous medium can exert power onto the surrounding (underconsolidated?) sediments. This leads to a drop of the shear strength or weakened cohesion. If the pore pressure attains the pressure exerted by the overlying column, the resistance of the skeleton disappears and liquefaction can occur. As a result of sliding or slumping, turbidity currents and debris flows may be generated or steep fault planes may develop [*Bjørlykke, 1989*].

There is evidence that mass wasting processes (e.g. slides and slumps) occurred in regions where gas hydrates are found or inferred from geophysical measurements. Some authors therefore suggest a causal link between hydrate dissociation and sediment failure on continental slope areas under the influence of gravity. This is for example the case offshore the USA (Blake Outer Ridge) where a huge collapse structure is attributed to hydrate dissociation [*Dillon et al., 1998*]. Also the Storegga Slide, offshore Norway and one of the biggest underwater landslides known is supposed to be related to hydrate dissociation and liquefaction [e.g. *Bugge et al., 1987; Mienert et al., 1998*]. *Bugge et al.* [*1987*] believe that an earthquake triggered the hydrate dissociation by sudden sub-bottom pressure changes. Whether hydrate dissociation contributes to further slope instability is controversial and highly depends on time scales and dissipation [*Bouriak et al., 2000*]. Pleistocene slope instability of the Beaufort margin is also related to hydrate decomposition [*Kayen & Lee, 1991*]. It is reasonable to assume that the collapse of hydrate-bearing sediments may lead to sudden and very fast release of methane from shallow sediments and the supply of methane to the atmosphere, and in this way effectively influence local or global climate changes as discussed before. Next to that, slope failures

appear to occur more frequently during sea level lowstand, i.e. a situation in which the pressure reduction can initiate hydrate decomposition. A sketch of such an event is presented in figure 1.6. This aspect is furthermore of fundamental importance for the offshore production, when human activity possibly can alter the *in situ* conditions of stability, resulting in similar mass wasting processes or site blow-outs.

1.3.3
Gas hydrate reservoirs as a future energy resource?

Although estimated amounts of carbon in hydrated form are speculative and highly uncertain, most recent estimates converge to a total mass of the order of magnitude of 10^{16} kg (a total volume of $1.9 \cdot 10^{16}$ m^3 of carbon, i.e. about $1.2 \cdot 10^{14}$ m^3 of hydrates) [*Kvenvolden, 1993a*]. Most researches determined the total reserves of carbon in marine sediments to be about two orders of magnitude greater than those in permafrost [*Kvenvolden, 1998; Sloan, 1998a*]. For example, *Harvey & Huang [1995]* report estimates of $2.4 \cdot 10^{16}$ kg in oceanic sediments and $0.8 \cdot 10^{16}$ kg in permafrost areas. If these estimates of the hydrate reservoirs hold true, these structures have a dominant position in the global carbon cycle. The only larger known carbon reservoir is completely disseminated in sedimentary rocks and hence unrecoverable (see table 1.3). It is however worth noting that *G. Ginsburg* [pers. comm., 1997] suggests that, due to incomplete knowledge of the exact setting of hydrate bearing sediments, these estimates may be of the order of two magnitudes too large. Still the hydrates might represent a huge amount of carbon and hence these structures can not longer be ignored in terms of the global carbon cycle [*Kvenvolden, 1988*].

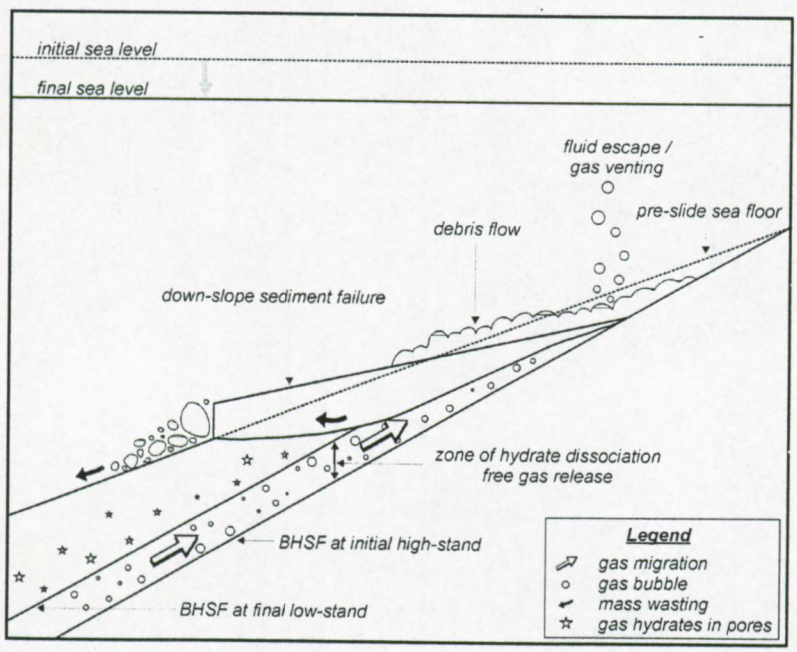

***Figure 1.6**: Gas hydrate dissociation vs. geohazard, redrawn from McIver [1982].*
BHSF = Base of Hydrate Stability Field

Because of these figures and the fact that less than 15% of the recovered energy is estimated to be necessary for dissociation [*Sloan, 1998a*], hydrated methane can possible represent an ecologically clean alternative for the largely reduced fossil fuel reservoirs. Industry hopes to find a way of safely exploiting the included gases in the next half a century. Therefore, large hydrate accumulations need to be found but also specific recovery techniques need to be developed since the reservoirs differ a lot from a gas or oil reservoir. But also the very dispersed character of the gas hydrate accumulations,

and the fact that these are in most cases not massive, only causes practical problems for accurate energy recovery. For example, one of the most successfully investigated hydrate-rich sites is the Blake Ridge area, off the SE United States. According to *Dickens et al. [1996]*, the total amount of carbon stored in the hydrate area is only of the order of 35 Gton.

At present, three different techniques for gas recovery from hydrate reservoirs in combination with horizontal drilling are being considered: thermal stimulation, depressurisation and inhibitor injection (or combination). The Messoyakha gas field in Siberia, discovered in the late 60's, represents a unique example of gas exploitation of microbial and thermogenic origin. 5.15 km^3 of gas has been produced from the hydrates by predominantly depressurisation [*Sloan, 1998*]. The hydrate stability limit in this permafrost region is about 800 m, i.e. about 300 m below the zone of permafrost conditions. A similar scenario is proposed to recover gas from hydrate accumulations on the North Slope of Alaska. Also Japanese scientists and engineers are developing plans to start exploiting gas hydrates from marine sediments.

Carbon reservoirs	***amount (Gton)***
marine biota	3
atmosphere	3.6
detritus	60
turf	500
dissolved organic matter in water	790
land biota	830
soil	1400
fossil fuel	5000
gas hydrates	**10000**
disperserd carbon	20000000

***Table 1.3**: Estimated amount of carbon stored in gas hydrates relative to other carbon reservoirs [Kvenvolden, 1998]*

1.4 Rationale of this research project

During this study, diverse aspects related to gas hydrates and their stability conditions in the natural environment have been investigated, knowing the guidelines mentioned in publications and summarised in this introductory chapter.

In the second chapter of this thesis, *Sensitivity of the gas hydrate stability field and possible destabilisation processes*, typical aspects of the evolution of the gas hydrate stability field, based on physical laws and their analytical mathematical expression, are discussed. Eustatic sea level fluctuations and changes in the bottom water temperature have their own completely different influence and rate on the stability behaviour of hydrate accumulations. Especially the time scale of the processes, the sub-bottom position of the gas hydrate stability limit, the water depth and the magnitudes of the changes are critical parameters during global climate change. A combination of both influences sometimes generates unexpected results, by which the one process is completely counterbalancing the other one with time. It will be shown that opposite working of both phenomena during climatic changes not always results in generally accepted ideas and that inversion can occur, both with time and with water depth. As a case study, the mediating methane hydrate hypothesis for the origin of large carbonate mud mound fields offshore Western Ireland [*Henriet et al., 1998; Henriet et al., accepted*] is investigated. Knowing that the gas hydrate layers are linked with directional fluid flows, that free-moving methane is not always captured within the solid hydrate structure when it

crosses the hydrate stability region and that sometimes hydrates are observed at the sea bed, the influence of buoyancy and the possibility of spontaneous uplift of (partially) hydrate-saturated sediments was investigated as well. This study allows us to define critical parameters as a function of porosity and densities of the different compounds before uplift can take place. Nevertheless, the results obtained clearly indicate that such an evolution is nearly impossible. As a last point is this chapter, the effect of destabilising hydrates on slope stability conditions and vice versa is briefly discussed. The effect depends on the pressure distribution assumed: overpressures appear to be a crucial point in this discussion. Fruitful co-operation with S. Bouriak from Moscow State University on seismic data in the Storegga Slide area, offshore Norway, resulted in a joint publication (Marine Geology) in which this topic is discussed as well [*Bouriak et al., 2000*]. Finally, also a few words are mentioned about the possible influence of dynamic aspects (basin subsidence, sedimentation, sediment erosion, compaction) onto the theoretical extent of hydrate accumulations.

The acoustic response of partially hydrate-saturated sediments and comparison of inferred and measured heat flow is discussed in the next chapters. Study area was Lake Baikal, a large continental rift lake in Central Siberia. Unfortunately, the main part of the seismic profiles only became available at the very end of the research project (August 1999).

The third chapter *Acoustic imaging of hydrate bearing sediments in Lake Baikal, Siberia* deals with the available geophysical data sets and the evidence of gas hydrates in this continental rift lake. The main part of this chapter is accepted for publication in *Marine Geology* [*Vanneste et al., in press*]. It is shown that the acquisition mode (frequency/wavelength, offset) strongly influences the acoustic image of the base of the hydrate stability field. On low-frequency data, the base of the gas hydrate stability field appears as a single, strong, polarity-reversed reflection that sometimes crosscuts the local stratigraphy. In a lot of cases, its sub-bottom position mimics the lake floor topography. On higher-frequency data, the picture looks rather different. On single airgun data, the BSR amplitude is smaller and its continuity decreases or even disappears. Watergun data (high-frequency) show a series of bright spots, each being part of an individual stratigraphic reflection. The up-dip terminations of these enhanced reflections are interpreted to represent a high-frequency picture of the BSR observed on nearly coincident low-resolution data and is nearly bottom simulating. This feature is explained by stratigraphically and/or lithologically-controlled free gas migration and accumulations beneath the hydrate stability field. Very-high-resolution sparker data cannot be used to unambiguously locate the base of hydrate stability. Within the inferred hydrate stability zone, amplitude blanking is often observed on most data sets, but is minimal on the MC seismic data. Evidence for free gas is provided by enhanced reflections beneath the BSR, the high reflection coefficients of the BSR, the sudden drop of instantaneous frequency across the BSR/enhanced reflections, the increase of reflection amplitude with offset or angle of incidence (AVO) and the presence of a low-velocity zone observed on OBH data. Thickness of the free gas zone is limited to a few m to a few tens of m. The frequency dependent behaviour of the BSR amplitude is explained in terms of horizontal and vertical resolution, and hence the volume sampled that gives rise to acoustic reflection in relation with the succession of gas-containing and gas-free sediment layers. The high amplitude observed on stacked data originates from the contribution of the high amplitudes recorded in the far-offset channels due to the AVO effect. Unique seismic profiles were acquired across the BDP-97 drilling site. Hydrates were retrieved from sub-surface sections without any acoustic characteristic feature indicative for hydrate occurrence. Using the Baikal-99 seismic data from the Southern Basin in combination with results from BDP-97, the first estimate of the total amount of carbon stored in the gas hydrates of Lake Baikal is estimated. The Baikal gas hydrate reservoir does – in my opinion – not have a future economic potential [*Vanneste et al., in press*].

The fourth chapter *Variability of the vertical extent of the gas hydrate stability field in Lake Baikal* continues with the same topic. The main difference lies in the fact that here the anomalous behaviour of the reflection at the base of the GHSF is investigated. Detailed re-interpretation of the low-frequency multi-channel airgun-array data revealed local variations in the vertical extent of the GHSF, resulting in "bumps" of the BSR which occur totally independent of any lake floor morphology but appear to be linked with structural features. The magnitude of these irregularities can be over 200 m. Reflection

seismic profiles, side-scan sonar imagery, heat flow measurements, echo-sounding and CTD-measurements were acquired in the zone of irregular behaviour. These data reveal a kind of hydrate ridge terminating at an antithetic fault. Within this area, active fluid escape structures characterised by elevated heat flow values but no temperature anomalies within their plumes are observed. Inferred heat flow is compared with measured heat flow values showing both zones of reasonable and poor correlation, exceeding the estimated errors on both the measurement and calculation procedures. The unique behaviour of hydrates and free gas accumulations occurs in the immediate vicinity of a major intra-basinal fault zone with active fluid escape features and heat flow anomalies at the lake bed. This suggests the presence of structurally-controlled upward fluid flows that could locally influence the hydrate stability conditions. A model for explaining the hydrate distribution observed, is presented in which as a result of active tectonics warmer water in injected into fault zones, spreading out in the sediments. Once the hydrate stability field is reached, the thermal pulse forces hydrates to dissociate on relatively fast, and excess pore pressure is built-up. If this overpressure cannot dissipate fast enough, hydraulic fracturing may occur and the gas-rich mud will percolate through the hydrate stability field. Part of the escaping gas can be re-hydrated while the remainder will escape at the lake floor. In this way, the fluid escape structures find their origin in hydrate dissociation related to tectonic activity. At present, these results are being incorporated for forthcoming publications.

The fifth chapter is the above-mentioned manuscript *Inferred gas hydrates and clay diapirs near the Storegga Slide on the southern edge of the Vøring Plateau, offshore Norway* published in *Marine Geology*, discussing part of the TTR8 (1998) airgun lines with side-scan sonar data and paleontological analyses. Two separated zones of inferred hydrate occurrence are delineated on seismic data, of which the upslope zone coincides with a region of high backscatter patches (pockmarks, dome-like elevations) on side-scan sonar data. The presence of enhanced reflections in the intermediate zone suggests that both zones are linked. A hydrate formation model is then proposed to explain this behaviour. In this paper, the authors provide for the first time a method to estimate roughly the internal fluid migration velocity (by combining seismic data and results from published theoretical modelling studies), once indirect evidence of gas hydrates is observed in the area of factual mass removal. The influence of hydrate dissociation to further slope instability in the area is discussed as well.

Finally, general conclusions (chapter 6) are drawn and guidelines for further research are mentioned. A summary in Dutch (chapter 7) is also included.

Several user-defined computer programs for PC platforms were written. Three main programs (labelled program_1.exe, program_2.exe, Bai_hyd.exe) are enclosed to allow the user/reader to analyse theoretically the behaviour of the basal limits of hydrate stability under natural conditions. Outlines are given throughout the text.

There were also several contributions to other scientific papers published or submitted that were not included in this thesis. The most important ones are:

Bushenkov, Y.N., Kremlev, A.N., Golmshtok, A.Y. & Vanneste, M. [1998]. *Estimation of physical properties of bottom sedimentary deposits.* Bulletin of the Novosibirsk Computing Centre, Series: Mathematical modelling in Geophysics, issue 4, 65-74.

Henriet, J.-P., De Mol, B., Pillen, S., Vanneste, M., Van Rooij, D., Versteeg, W., Croker, P., Shannon, P., Unnithan, V., Bouriak, S. & Chachkine, P. [1998]. *Gas hydrate crystals may help build reefs.* Scientific Correspondence, Nature, **391**, 648-649

Henriet, J.-P, De Mol, B., Vanneste, M., Huvenne, V., Van Rooij, D. & "Porcupine-Belgica" 97, 98 & 99 shipboard parties [accepted]. *Carbonate mounds and slope failures in the Porcupine Basin: a development model involving past fluid venting.* Special Publication, Geological Society of London.

Kremlev, A.N., Golmshtok, A.J., Vanneste, M., De Batist, M. & Bushenkov, Y.N. [submitted]. *Estimation of gas hydrate quantity in submarine deposits from seismic data.* Proceedings of the Indo-Russian workshop on gas hydrates.

Other manuscripts are presently being prepared, especially on the Lake Baikal gas hydrate topic.

A significant part of the first year of the Ph.D. research was devoted to organising an international conference on natural gas hydrates in Gent, Belgium. Convenors were Prof. Dr. J.-P. Henriet (RCMG, Univ. of Gent) and Prof. Dr. J. Mienert (GEOMAR; now at IBG, Univ. of Tromsø). Some of the world's most prominent hydrate researchers like Dr. K. Kvenvolden (USGS), Prof. Dr. E. Sloan (Colorado School of Mines) and the late Prof. Dr. G. Ginsburg (St. Petersburg) took part in a 1-day tutorial session. The next two days were filled with presentations of recent research advances covering results from ODP-164, physico-mathematical modelling, seismic tomography, climatology, ice-core analysis... Next to that, during the last years several close co-operations with some thesis students resulted in Master Theses. Especially the work of Tanja Fouquet (Gas hydrate induced lake degassing: Lake Nyos), Kristof Van Belle (Gas and gas hydrate induced slope destabilisation in lacustrine environments) and Kristof De Meersman (Reflectie- en refractie-seismiek in het Baikalmeer, Siberië) need to be mentioned.

References

Bjørlykke, K. [1989]. *Sedimentology and Petroleum Geology.* Springer-Verlag, Berlin Heidelberg, pp. 363.

Bohrmann, G., Greinert, J., Suess, E. & Torres, M. [1998]. *Authigenic carbonates form the Cascadia subduction zone and their relation to gas hydrate stability.* Geology, 26 (7), 647-650.

Booth, J.S., Winters, W.J., Dillon, W.P., Clennell, M.B. & Rowe, M.M. [1998]. *Major occurrences and reservoir concepts of marine clathrate hydrates: implications of field evidence.* in Gas hydrates: relevance to world margin stability and climatic change [Ed. J.-P. Henriet & J. Mienert], p. 113-128.

Bouriak, S., Vanneste, M. & Saoutkine, A. [2000]. *Inferred gas hydrates and clay diapirs near the Storegga Slide on the southern edge of the Vøring Plateau, offshore Norway.* Marine Geology, 163, 125-148.

Bugge, T., Befring, S., Belderson, R.H., Eidvin, Jansen, E., Kenyon, N.H., Holtedahl, H. & Sejrup, H.P. [1987]. *A giant three-stage submarine slide off Norway.* Geo-Marine Letters, 7, 191-198.

Bugge, T., Belderson, R.H. & Kenyon, N.H. [1988]. *The Storegga slide.* Philosophical Transactions of the Royal Society of London, A 325, 357-388.

Bushenkov, Y.N., Kremlev, A.N., Golmshtok, A.Y. & Vanneste, M. [1998]. *Estimation of physical properties of bottom sedimentary deposits.* Bulletin of the Novosibirsk Computing Centre, Series: Mathematical modelling in Geophysics, issue 4, 65-74.

Claypool, G.E. & Kaplan, I.R. [1974]. *The origin and distribution of methane in marine sediments,* in *Methane in marine sediments,* 99-139.

Clennell, M.B., Hovland, M., Booth, J., Henry, P. & Winters, P. [1999]. *Formation of natural gas hydrates in marine sediments: 1. Conceptual model of gas hydrate growth conditioned by host sediment properties.* Journal of Geophysical Research, 104 (B10), 22985-23003.

Collett, T.S. [1993]. *Natural gas production from Arctic gas hydrates.* in The future of energy gases, USGS professional paper 1570, 299-311.

Dickens, G.R., Wallace, P., Paull, C.K. & the ODP Leg 164 Scientific Party, 1996. *In-situ methane quantities across a bottom simulating reflector on Blake Ridge.* presentation at First Master Workshop Gas hydrates: Relevance to world margin stability and climatic change, Henriet, J.-P. & Mienert, J., Gent, abstract book, 14-15.

Dillon, W.P., Danforth, W.W., Hutchinson, D.R., Drury, R.M., Taylor, M.H. & Booth, J.S. [1998]. *Evidence of faulting related to dissociation of gas hydrate and release of methane off the southeastern United States.* in Henriet, J.P. & Mienert, J. (eds.), *Gas hydrates: relevance to world margin stability and climatic changes,* Special Publication of the Geological Society of London, 293-302.

Ecker, C., Lumley, D., Dvorkin, J. & Nur, A. [1996]. *Structure of hydrated sediment from seismic and rock physics.* in Proceedings of the Second International Conference on Natural Gas Hydrates, eds. Monfort et al., Toulouse, 491-498.

Ginsburg, G.D. [1998]. *Gas hydrate accumulation in deep water marine sediments.* in Gas hydrates: relevance to world margin stability and climatic change [Ed. J.-P. Henriet & J. Mienert], p. 51-62.

Ginsburg, G.D. & Soloviev, V.A. [1997]. *Methane migration within the submarine gas hydrate stability zone under deep water conditions.* Marine Geology, 137, 49-57.

Hamilton, E.L. [1972]. *Reflection coefficients and bottom losses at normal incidence computed from sediment properties.* Geophysics, 38, 2276-1180.

Hammond, R.D. & Gaither, J.R. [1983]. *Anomalous seismic character – Bering Sea Shelf.* Geophysics, 48, 590-605.

Haq, B.U. [1993]. *Deep-sea response to eustatic change and significance of gas hydrates for continental margin stratigraphy.* Special Publication of the International Association of Sedimentologists, 18, 93-106.

Haq, B.U. [1998]. *Natural gas hydrates: searching for the long-term climatic and slope stability records.* in Gas hydrates: relevance to world margin stability and climatic change [Ed. J.-P. Henriet & J. Mienert], p. 303-318.

Harvey, L. & Huang, Z. [1995]. *Evaluation of the potential impact of methane clathrate destabilisation on future global warming.* Journal of Geophysical Research, v100 (D2), 2905-2926.

Henriet, J.-P., De Mol, B., Pillen, S., Vanneste, M., Van Rooij, D., Versteeg, W., Croker, P., Shannon, P., Unnithan, V., Bouriak, S. & Chachkine, P. [1998]. *Gas hydrate crystals may help build reefs.* Nature, 391, 648-649.

Henriet, J.-P, De Mol, B., Vanneste, M., Huvenne, V., Van Rooij, D. & "Porcupine-Belgica" 97, 98 & 99 shipboard parties [accepted]. *Carbonate mounds and slope failures in the Porcupine Basin: a development model involving past fluid venting.* Special Publication, Geological Society of London.

Henriet, J.P. & Mienert, J. [1998]. *Gas hydrates: the Gent debates. Outlook on research horizons and strategies.* in Gas hydrates: relevance to world margin stability and climatic change [Ed. J.-P. Henriet & J. Mienert], p. 1-8.

Henry, P., Thomas, M.& Clennell, M.B. [1999]. *Formation of natural gas hydrates in marine sediments: 2. Thermodynamic calculations of stability conditions in porous media. Journal of Geophysical Research.* 104 (B10), 23004-23022.

Holbrook, W.S., Hoskins, H., Wood, W.T., Stephen, R.A., Lizzarralde, D., and the Leg 164 Science Party [1996]. *Methane gas-hydrate and free gas on the Blake Ridge from vertical seismic profiling.* Science, 273, 1840–1843.

Hovland, M. & Judd, A.G. [1988]. *Seabed pockmarks and seepages: impact on geology, biology and the marine environment.* Graham & Trotman Ltd., London, pp. 293.

Hovland, M., Gallagher, J.W., Clennell, W.B. & Lekvan, K. [1997]. *Gas hydrate and free gas volumes in marine sediments: Example from the Niger delta front.* Marine and Petroleum Geology, 14 (3), 245-255.

Hyndman, R.D. & Davis, E.E. [1992]. *A mechanism for the formation of methane hydrate and seafloor bottom simulating reflectors by vertical fluid expulsion,* JGR, **97** (B5), 7025-7041.

Hyndman, R.D. & Spence, G.D. [1992]. *A seismic study of methane hydrate marine bottom simulating reflectors.* Journal of the Geophysical Research, 97 (B5), 6683-6698.

Kayen, R.E. & Lee, H.J. [1991]. *Pleistocene slope instability of gas hydrate-laden sediment on the Beaufort sea margin.* Marine Geotechnology, 10, 125-141.

Kenney, C. [1984]. *Properties and behaviours of soils relevant to slope instability.* in Slope instability (eds. Brunsden, D. & Prior, D.B.), John Wiley & Sons Ltd., 27-65.

Kuhs, W., Chazallon, B., Radaelli, P., Pauer, F. & Kipfstuhl, J. [1996]. *Raman Spectroscopic and neutron diffraction studies on natural and synthetic clathrates of air and nitrogen.* In Proceedings of the 2nd international conference on natural gas hydrates (ed. J.P. Monfort), p. 9.

Kuzmin, M.I., Kalmychkov, G.V., Geletij, V.F., Gnilusha, V.A., Goreglyad, A.V., Khakhaev, B.N., Pevzner, L.A., Kavai, T., Ioshida, N., Duchkov, A.D., Ponomarchuk, V.A., Kontorovich, A.E., Bazhin, N.M., Mahov, G.A., Dyadin, Yu.A., Kuznetsov, F.A, Larionov, E.G., Manakov, A.Yu., Smolyakov, B.S., Mandelbaum, M.M. & Zheleznyakov, N.K., 1998. *First find of gas hydrates in sediments of Lake Baikal* (in Russian). Doklady Akademii Nauk, 362, 541-543.

Kvenvolden, K.A. & Cooper, A.K. [1987]. *Natural gas hydrates of the offshore Circum-Pacific margin: a future energy resource?* in Transactions of the 4th Circum-Pacific Energy and Mineral Resources Conference (ed. M. Horn), chapter 24, 285-297.

Kvenvolden, K.A. [1988]. *Methane hydrates and global climate.* Global Biogeochemical Cycles, 2 (3), 221-229.

Kvenvolden, K.A. [1993a]. *Gas hydrates: geological perspective and global change.* Review of Geophysics, 31 (2), 173-187.

Kvenvolden, K.A. [1993b]. *Gas hydrates as a potential energy resource – a review of their methane content.* USGS professional paper 1570, 555-561.

Kvenvolden. K.A. [1998]. *A primer on the geological occurrence of gas hydrate.* in Gas hydrates: relevance to world margin stability and climatic change [Ed. J.-P. Henriet & J. Mienert], p. 9-30.

Lashof, D.A. & Ahuja, D.R. [1990]. *Relative contribution of greenhouse gas emissions to global warming.* Nature, v344, 529-531.

Leggett, J. [1990]. *The nature of the greenhouse threat.* in Global warming, the Greenpeace report, (Leggett, J., ed.), Oxford University Press, 14-43.

Makogon, Y.F. [1965]. *Hydrate formation in gas bearing beds under permafrost conditions.* Gazov. Promst., 14.

McIver, R.D. [1982]. *Role of naturally occurring gas hydrates in sediment transport.* American Association of Petroleum Geologists Bulletin, 66 (6), 789-792.

Mienert, J., Posewang, J. & Baumann, M. [1998]. *Gas hydrates along the north-eastern Atlantic margin: possible hydrate bound margin instabilities and possible release of methane.* in Henriet, J.-P. & Mienert, J. (eds); *Gas hydrates: Relevance to world margin stability and climatic change*, Geological Society of London, Special Publication, **137**, 275-291.

Miller, J.J., Lee, M.W. & von Huene, R. [1991]. *An analysis of a seismic reflection from the base of a gas hydrate zone, offshore Peru.* American Association of Petroleum Geologists Bulletin, 75, 910-924.

Minshull, T.A., Singh, S.C. & Westbrook, G.K. [1994]. *Seismic velocity structure at a gas hydrate reflector, offshore western Colombia, from full waveform inversion.* JGR, 99 (B3), 4715-4734 [GH].

Nisbett, E.G. [1990]. *The end of an ice age.* Canadian Journal of Earth Sciences, v27 (1), 148-157.

Paull, C.K., Ussler III, W. & Dillon, W.P. [1991]. *Is the extent of glaciation limited by marine gas hydrates?* Geophysical Research Letters, v18, 432-434.

Paull, C.K., Ussler III, W. & Borowski, W.S. [1994]. *Sources of biogenic methane to form marine gas hydrates.* in Annals of the New York Academy of Sciences, 715, International Conference on Natural Gas Hydrates, Eds. Sloan et al., pp. 392-409.

Raynaud, D., Chappellaz, J. & Blunier, T. [1998]. *Ice-core record of atmospheric methane changes: relevance to climatic changes and possible gas hydrate resources.* in Gas hydrates: relevance to world margin stability and climatic change [Ed. J.-P. Henriet & J. Mienert], p. 327-331.

Rempel, A.W. [1995]. *Mathematical models of hydrate accumulation.* Unpublished M.Sc. Thesis, University of British Columbia.

Rempel, A.W. & Buffett, B.A. [1998]. *Mathematical models of gas hydrate accumulation.* In Henriet, J.-P. & Mienert, J. (eds); *Gas hydrates: Relevance to world margin stability and climatic change*, Geological Society of London, Special Publication, **137**, 63-74.

Ruppel, C. [1997]. *Anomalous cold temperatures observed at the base of the hydrate stability zone on the US Atlantic passive margin.* Geology, 25 (8), 699-702.

Sassen, R. & MacDonald, I.R. [1994]. *Evidence for structure H hydrate, Gulf of Mexico continental slope.* Organic Geochemistry, 22 (6), 1029.

Schmuck, E.A. & Paull, C.K. [1993]. *Evidence for gas accumulation associated with diapirism and gas hydrates at the head of the Cape Fear slide*, Geo-Marine Letters, **13**, 145-152.

Sheriff, R.E. & Geldart, L.P., 1995. *Exploration Seismology.* Cambridge University Press, Cambridge, 592 pp.

Shipley, T.H., Houston, M.K., Buffler, R.T., Shaub, F.J., McMillen, K.J., Ladd, J.W. & Worzel, J.L. [1979]. *Seismic reflection evidence for the widespread occurrence of possible gas hydrate horizons on continental slopes and rises.* American Association of Petroleum Geologists Bulletin, 63, 2201-2213.

Sloan, E.D. Jr. [1998a]. *Clathrate hydrates of natural gases.* Second edition, revised and expanded, Marcel Dekker Inc., New York & Basel, pp. 705.

Sloan, E.D. Jr. [1998b]. *Physical/chemical properties of gas hydrates and application to world margin stability and climatic change.* in Gas hydrates: relevance to world margin stability and climatic change [Ed. J.-P. Henriet & J. Mienert], p. 31-50.

Szatmari, P. [1989]. *Petroleum formation by Fischer-Tropsch synthesis in plate tectonics.* American Association of Petroleum Geologists Bulletin, **73** (8), 989-998.

Thiery, R., Bakker, R., Monnin, C. & the Shipboard Scientific Party of ODP Leg 164 [1998]. *Geochemistry of gas hydrates and associated fluids in the sediments of a passive continental margin. Preliminary results.* in Henriet, J.-P. & Mienert, J. (eds); *Gas hydrates: Relevance to world margin stability and climatic change*, Geological Society of London, Special Publication, **137**, 275-291.

Thorpe, R. [1996]. *Can methane-driven deglaciation provide a plausible account of the end of the last ice age?* Unpublished Ph.D.-dissertation, Cambridge University, pp. 193.

Thorpe, R.B., Pyle, J.A.& Nisbet, E.G. [1998]. *What does the ice-core record imply concerning the maximum climatic impact of possible gas hydrate release at Termination 1A?* in Gas hydrates: relevance to world margin stability and climatic change [Ed. J.-P. Henriet & J. Mienert], p. 319-326.

Tinivella, U. [1999]. *A method for estimating gas hydrate and free gas concentrations in marine sediments.* Bollettino di Geofisica Teoretica et Applicata, **40** (1), 19-30.

Vanneste, M., De Batist, M., Golmshtok, A. & Kremlev, A. & Versteeg, W. [in press]. *Multi-frequency seismic study of the gas hydrate bearing sediments in Lake Baikal, Siberia.* Marine Geology.

Watson, R. T., Rodhe, H., Oeschger, H. & Siegenthaler, U. [1990]. *Greenhouse gases and aerosols,* in Climate change, the IPCC Scientific Assessment (Houghton, J. T., Jenkins, G. J. & Ephraums, J. J., eds.). Cambridge University Press, 1-40.

Whalley, E. [1980]. *Speed of longitudinal sound in clathrate hydrates.* Journal of Geophysical Research, 85 (B5), 2539-2542.

Wood, W.T. & Ruppel, C. [2000]. *Seismic and thermal investigations of the Blake Ridge gas hydrate area: a synthesis.* in Paull, C.K. et al. (eds.), Proceedings of the Ocean Drilling Program, Scientific Results, volume 164, 253-264.

Xu, W. & Ruppel, C. [1999]. *Predicting the occurrence, distribution and evolution of methane gas hydrates in porous marine sediment.* Journal of Geophysical Research, 104, 5081-5096.

Yamamoto, S., Alcauskas, J.B. & Croziers, T.E. [1976]. *Solubility of methane in distilled water and sea water.* Journal of Chemical and Engineering Data, 21, 78-80.

Zatsepina, O.Y. & Buffet, B.A. [1998]. *Thermodynamic conditions for the stability of gas hydrate in the seafloor.* Journal of Geophysical Research, 103 (B10), 24127-24139.

Chapter 2

Sensitivity of the gas hydrate stability field and possible destabilisation processes

2.0 Introduction

In this section, emphasis is placed on different naturally occurring scenarios altering the vertical extent of the gas hydrate stability field or zone (HSZ) in the natural environment. The stability limit of hydrates is situated at a certain sub-bottom depth were the temperature exceeds the formation temperature of hydrates at *in situ* pressure. Above this zone, the hydrates are more stable, i.e. one needs energy input first to move the hydrates towards their stability limits, and then extra energy to start dissociation. In this chapter, both qualitative analyses and quantitative results of the changes in the stability conditions of pure methane hydrates due to a variety of environmental changes are presented. All results are based on an analytical expression of the three-phase hydrate-water-gas equilibrium equation. The modelling resulted in several mathematical expressions that were implemented in self-written programs (program_1 and program_2 are enclosed) to delineate the base of the stability limit for various hydrates under variable conditions of sea level and bottom water temperatures. Since it is impossible to analyse all possible combinations of parameters occurring, these programs then allow the user to determine the extent/the change of extent in a situation more relevant for his/her own subject or area. The figures (and the theoretical analysis) are intended to provide the reader useful and easily understandable information of what can be expected in a specific basin with methane hydrate occurrence. The different options of the program are discussed throughout the text and are summarised in the conclusions.

In the first instance, eustatic sea level changes are considered. The fluctuation of the global sea level since the Pleistocene is well documented. *Haq* [*1993*] mentioned that hydrates are supposed to have accumulated under natural conditions since at least the Eocene (approximately 55 Ma BP) and since then climate underwent important and sometimes fast changes. On a shorter time scale, a very-high-resolution curve since the last glacial maximum (LGM) was established by *Fairbanks* [*1989*] and *Fleming et al.* [*1998*]. In this work, the relative sea level curve of *Fleming et al.* [*1998*] is used. Pure sea level fall will initiate decomposition of the gas hydrates located at the BHSZ while sea level rise will result in more favourable hydrate conditions. A model is proposed to calculate the changes in the

HSZ, based on theoretical hydrate equilibrium curves, steady-state geothermal gradients and a known pore pressure distribution.

Also the temperature dependence on the evolution of the HSZ is discussed. Important differences with the pressure influence are noticed. For example, the time scale of the interacting process can differ considerably. The pressure-induced effect is assumed to take place immediately via the interconnected pore spaces, while a change in the bottom water temperature only gradually penetrates through the sediments until hydrate accumulations are influenced. The modelling performed is restricted to three different time-dependent variations of the bottom water temperature, i.e. sudden bottom temperature change, linear change with time and bottom temperature oscillation. Quantitative analysis of these situations shows that the primary variables are the amplitude of the fluctuation of the bottom water temperature, the time since this shift took place and the sub-bottom depth of the stability limit. Theoretical curves clearly show the temperature dependence as a function of time and penetration depth. This process can lead to both bottom-up and top-down destabilisation processes, depending on time, depth and amplitude of the temperature change.

Both climatic influences mentioned above are taking place concurrently. Most of the time the one process is counteracting the other. Therefore, a discrete time panel is investigated, using the detailed sea level curve of *Fleming et al.* [*1998*] and estimates of the bottom water temperature changes. The behaviour appears to be highly dependent on the time scale, water depth, the amplitudes of the changes and the geothermal gradient. Some surprising results are obtained. The theoretical models are then applied to a single-channel high-resolution seismic data set (used to determine bathymetry in close connection with the navigation files) acquired with R.V. Belgica during 1997-1999 offshore Western Ireland to study the theoretical spatial and vertical extent of methane hydrates under varying climatic conditions. This modelling was done in order to support the hydrate mediation hypothesis proposed in *Henriet et al.* [*1998*].

Spontaneous uplift of partially hydrated sediments, as another destabilisation mechanism, is studied as well. This possibility is investigated since sometimes massive hydrates are retrieved (Middle America Trench, DSDP Leg 84, site 570) while in some other places hydrates are observed at the sea bed (Gulf of Mexico). In the latter case, a cycling period of 8 months of the Current Loop might have consequences for the stability of these hydrates and the chemosynthetic biota. On the other hand, the sudden uplift of H_2S rich hydrates is proposed as a plausible hypothesis to explain the Lake Nyos disaster in Cameroon, 1986 [*Rodgers & Yevi, 1996*]. The results obtained from the mathematical formalism however are negative due to the fact that the density difference between the pore fluids and hydrate inclusions is rather small (approximately 10%), so spontaneous uplift of sediments almost fully saturated with hydrates is very unlikely to occur.

In a final part of this topic, the influence of subsidence, continuous sedimentation and mass wasting events onto the extent of the HSZ is discussed. Acoustic profiles acquired during the Training Through Research 8 expedition (1998) in the Storegga Slide area allowed to investigate the influence of the sudden removal of part of the sedimentary section on the hydrate stability conditions. Pore pressure assumptions appear to play an important role.

2.1
The methane hydrate stability field in the natural environment

2.1.1
Methane hydrate stability conditions and equations in fresh and salt water

Gas hydrates in marine sediments are observed within the shallow subsurface. At these depths, the sediments are likely to be unconsolidated and have a granular structure [*Ecker et al., 1998*]. The HSZ is defined as that part of a geological section where hydrates can exist under *in situ* conditions of pressure, temperature and chemical-mineral composition [*Ginsburg & Soloviev, 1997*]. This zone is limited from above by the sea floor due to buoyancy of the hydrate particles (hydrates are less dense than fresh- or seawater). This was already illustrated in figure 1.3.

To determine the extent of the HSZ in reality, accurate knowledge of chemical compositions, pore water salinity, bottom water temperatures, sub-bottom temperature profiles (geothermal gradients) and pore pressure gradients is necessary. Since CH_4 is by far the most abundant clathrated gas [*Kvenvolden, 1998*], it is common practice to locate the base of the HSZ (BHSZ) at the intersection of the sub-bottom temperature profile and the 3-phase equilibrium curve of the CH_4 – (sea-) water – hydrate mixture.

For the investigation of the marine and lacustrine hydrate stability conditions and its sensitivity to environmental changes, the three-phase equilibrium phase boundary of hydrate, fresh or sea water and methane gas plays a central role. The phase boundary equations used in this study were estimated from the CSMHYD hydrate phase equilibrium program of *Sloan* [*1998*] and checked, whenever possible, with experimental data compiled from literature [e.g. *Dickens & Quinby-Hunt, 1994*]. For different temperature values within the interval between the first quadruple point (approximately 0°C) and 25°C, the 3-phase equilibrium pressure value was calculated. A logarithmic analytical equation relating the equilibrium pressure P_{eq} with equilibrium temperature T_{eq} of the following form is proposed to fit the calculations:

$$\log P_{eq} = a + b \cdot T_{eq} + c \cdot T_{eq}^2 \qquad [1]$$

In this equation, pressure is expressed in MPa (but scaled to 1 MPa), while temperature is expressed in °C. Inversion of this formula to equilibrium temperature as a function of equilibrium pressure leads to ($c \neq 0$):

$$T_{eq} = \frac{-b + \sqrt{b^2 + 4c\left(\log P_{eq} - a\right)}}{2c} \qquad [1']$$

after discrimination of the negative result since only positive temperatures were taken into account. In general, if temperature is less than 0°C, equation [1] will not hold any longer. A lot of hydrate forming gases appear to have their first quadruple point close to 0°C with each of them having their own specific stability pressure (see also chapter 1). Crossing this thermodynamic point will result in other co-existing phases. A new 3-phase equilibrium boundary at temperatures less than the quadruple point temperature will be a co-existence of hydrate, ice and gas. Hence, a different boundary equation needs to be established. Nevertheless, in this manuscript only the above three phase boundary equation for methane – water (salt or fresh) – hydrate will be used.

The coefficients a, b and c are determined by the method of least squares, i.e. the best-fit curve such that the sum of the squares of the difference between the data points and the curve is minimal. These coefficients strictly depend upon the salinity of the porous water in which the hydrate forms. In nature, the salinity in the ocean basins varies in general between 33 and 38‰ with an mean salinity of 35‰ [*Allaby & Allaby, 1999*], while also recently hydrates were retrieved from Lake Baikal with salinity of only 0.76‰, i.e. a factor of 50 less than the average value. For a pure CH_4 – fresh water – hydrate phase, these coefficients are:

$$\begin{cases} a = 0.419626 \\ b = 0.039326\,°C^{-1} \\ c = 0.000299\,°C^{-2} \end{cases} \qquad R^2 = 0.999893 \qquad [2]$$

R^2 denotes the regression coefficient, being a reference to the fitting quality. This quantity is defined as follows:

$$R^2 = 1 - m \cdot \sum_{j=1}^{m} (y_j - y_j)^2 \quad \left[m \cdot \left(\sum_{j=1}^{m} y_j^2 \right) - \left(\sum_{j=1}^{m} y_j \right)^2 \right]$$

with $y_j \equiv a + b \cdot T_{eq,j} + c \cdot T_{eq,j}^2$ the theoretical best fit value in point j

and $\overline{y}_j \equiv \log(P_{eq,j})$

As this coefficient approaches unity, the analytical expression will give highly accurate results within the temperature interval. Higher degrees of the polynome can hence be ignored. For calculating the stability limits in the marine environment, typical ocean salinity of 35‰ is used, with density of 1025.67 $kg \cdot m^{-3}$. The same procedure as above is applied here. As a result, slightly different equilibrium coefficients are obtained:

$$\begin{cases} a = 0.478626 \\ b = 0.040094\,°C^{-1} \\ c = 0.000309\,°C^{-2} \end{cases} \qquad R^2 = 0.999925 \qquad [2']$$

A difference here is that the 3-phase boundary extends further towards negative temperatures in a salt-water environment. Salt ions will be excluded upon hydrate formation and act as a chemical inhibitor. The quadruple point of salt-water methane hydrates is approximately –2°C, determined using the CSMHYD program of *Sloan [1998]*. The relationship above is therefore valid for temperatures between –2 and 25°C.

These analytical phase boundary equations are shown in figure 2.1. The HSZ lies at the upper left corner of the pressure-temperature window, i.e. at those conditions of higher pressure or lower temperature relative to the equivalent phase boundary or equilibrium conditions. As can be seen, the stability conditions in salt water are stricter (inhibitor), so that the stability field is smaller: at the same temperature, higher pressure is required for hydrate stability (at the same pressure, lower temperature is required) compared to the conditions for fresh water methane hydrate accumulations.

Figure 1.3 (previous chapter) depicts the vertical extent of the HSZ in the natural environment at 1200 m water depth with an average geothermal gradient of 0.035°C·m^{-1}, assuming hydrostatic pressure to be valid within the pore spaces of the shallow subsurface. The basal limit in the macroscopic approach (bulk conditions, ignoring porous medium effects) coincides with the intersection of the 3-phase

equilibrium boundary and the sub-bottom temperature profile. Under the base of the stability field, i.e. at higher temperature, free gas migrating (as free gas or dissolved) from deeper parts of the basin may accumulate, due to reduced permeability at the base of the stability field. Within the HSZ, only part of the pore spaces is hydrate-saturated, typically a few percent [*Hovland et al., 1997*]. From deep drilling results, it is known that in most cases hydrate is not found throughout the entire HSZ but most probably in a zone concentrated just above its stability limit. In these cases, a gradational decrease of saturation factor with decreasing sub-bottom depth is suggested. Also the different accumulation models give rise to different hydrate distributions in the sub-surface [*Rempel & Buffett, 1997*].

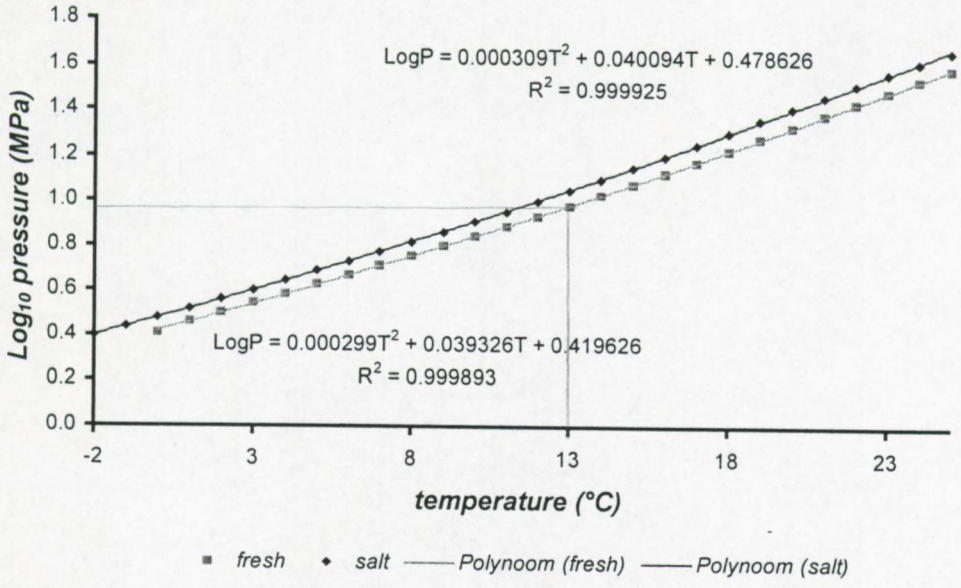

***Figure 2.1**: Pure water and average salt water – hydrate – methane 3-phase equilibrium conditions, determined using the program CSMHYD of Sloan [1998] and program_1.exe. Experimental data of Dickens & Quinby-Hunt [1994] are given as well. The HSZ lies in the upper left corner of the pressure-temperature domain, i.e. at higher pressures or lower temperatures than the equilibrium conditions.*

2.1.2
Determining the vertical extent of the methane HSZ: programs

For determining the vertical extent of the methane hydrate stability, the above-mentioned equation [1, 1'] has to be solved, in agreement with the assumed sub-bottom temperature profile and pore pressure distribution. Several authors suggest that overpressures only occur very occasionally at shallow burial depth [e.g. *Hyndman & Davis, 1992; Dickens & Quinby-Hunt, 1994; Ecker et al., 1998*], so for the hydrate accumulation zone, the pore pressure distribution is considered to be (nearly) hydrostatic, thus a function of the height of the total (water depth + sub-bottom depth) overlying water column. The temperature profile is most often supposed to increase linearly with increasing burial depth, expressed as a geothermal gradient, starting from a fixed reference temperature at the seabed.

In terms of formulas, we have:

→ Hydrostatic pressure (expressed in MPa) distribution as a function of height of the water column H (expressed in m) and sub-bottom depth z (also expressed in m) (P_{atm}, average atmospheric pressure taken to be 0.101325 MPa), with fluid density ρ_f:

$$P\langle z,H\rangle = P_{atm} + \rho_f g(H+z)\cdot 10^{-6} \qquad [3]$$

→ Linear sub-bottom temperature profile T (expressed in °C) as a function of sub-bottom depth z with constant slope or gradient G (expressed in °C·m^{-1}) and sea bed temperature T_0:

$$T\langle z\rangle = T_0 + G \cdot z \qquad [4]$$

→ And the phase boundary equation [1] or [1']

$$LogP_{eq}\langle T_{eq}\rangle = a + b \cdot T_{eq} + c \cdot T_{eq}^2 \qquad \text{or} \qquad T_{eq}\langle P_{eq}\rangle = \frac{-b + \sqrt{b^2 + 4c\left(LogP_{eq} - a\right)}}{2c}$$

The HSZ is hence that part of the subsurface fulfilling the following relationship :

$$T\ z \leq T_{eq}\ P_{eq}\ z \qquad z \geq 0 \qquad [5]$$

The above analytical 3-phase equilibrium curve (with specific coefficients of interest for the user) can then be used to determine the vertical extent of the stability field in sedimentary sections. This implies that the base of the partially hydrated section is supposed to coincide with the top of the free gas section, according to the Gibbs phase rule[1]. Using the above formulas, it becomes clear that for the above-mentioned set of equations, an implicit dependence on sub-bottom depth arises. This explains why the stability limit cannot be calculated straightforward. To solve this problem, a graphic solution can be used as presented in figure 1.3 (previous chapter). For easier applications, a general computer program (program_1) with an iterative approach for common PC platforms is written in TP-language in order to determine the evolution of the HSZ between two discrete time slices with several user-defined parameters. Here some specifications about these programs are mentioned. The reader is referred to the discussion of this chapter for an overview of the sub-programs. Below, some general aspects of the methodology are explained.

→ The programs allow the user to apply the pre-defined coefficients for pure methane in fresh water [2] (option A) or salt water [2'] (option B). Situations can also be analysed for other hydrate compositions for which the 3-phase equilibrium curve can be written in the general form of [1]. Therefore, the user can define new coefficients (option C) or let the program determine those coefficients (option D) by giving couples of 3-phase equilibrium pressure and temperature (min. 3, max. 300). The method of least squares is used. These coefficients will be used throughout the entire procedure until the user returns to the main page where other coefficients can be defined.

→ One of the options of the main program deals with a simple *conversion* from 3-phase equilibrium temperature to equilibrium pressure (or vice versa) and is performed using the three-phase equilibrium formulas mentioned above [1, 1', 2, 2']. Since the regression coefficient of the phase boundary equation in general lies close to unity, errors during conversion are very small for bulk conditions. However, for user-defined compositions (option C & D of the program) this coincidence between data points and the curve might be less accurate. Also the minimum required water depth or critical depth (see §2.1.4) is calculated for specific bottom water temperatures, or vice versa, the maximum temperature to guarantee hydrate stability at the sea or lake bottom at specific water depth is determined.

[1] Note that discrepancies are found to occur in nature. Recent modelling [*Xu & Ruppel, 1999*] showed that (1) the base of the hydrate accumulation zone often lies at shallower sub-bottom depth than the BHSZ, (2) a disparity can be present between the top of the hydrate stability zone (usually the sea or lake floor) and the top of the hydrate accumulation zone and (3) a transition zone can exist between the top of the free gas zone and the base of the hydrate accumulation zone, dependent of fluid fluxes.

➔ For determining the sub-bottom depths of the hydrate stability limit under steady-state bulk conditions (hydrostatic pressure), the water depth of the basin, the geothermal gradient and the bottom water temperature are user-defined parameters. The critical bottom temperature at present water depth and the critical water depth at present bottom temperature are calculated. If the given water depth exceeds the critical depth, the uppermost sedimentary section falls within the HSZ. In this case, the base of the stability field is determined via an iterative approach. The *in situ* pressure and temperature are calculated for specific sub-bottom depths and compared to the necessary 3-phase equilibrium conditions. When the difference between the *in situ* theoretical stability conditions and the *in situ* thermodynamic bulk conditions (sub-bottom temperature profile and pore pressure distribution) vanishes, the limit of stability is reached, and the iterative approach comes to a halt. The error using this procedure is determined by the depth interval used in the iterative approach, i.e. 0.1 m sub-bottom depth (bulk conditions). As a result, the sub-bottom depth of the hydrate stability limit, the total depth of the stability limit and the *in situ* equilibrium pressure-temperature conditions are given. A similar but inverted approach is used in the next option, in which a total depth below sea or lake level is converted into sub-bottom depths, using the bottom water temperature and the geothermal gradient given by the user.

➔ Further options include the calculation of the variability of the HSZ with changing sea level (see section 2.2) and bottom water temperature variation (section 2.3). A second program (*program_2.exe*) offers the possibility to analyse the influence of combined pressure-temperature changes (section 2.4). The time scale of the acting process and a time delay option are then introduced. A standard thermal diffusivity parameter can be interchanged with a user defined value. These functions will be explained in the paragraphs 2.2-2.4. A third program (*bai_hyd.exe*) deals with the calculation of the conductive heat flow for Lake Baikal conditions using the two-way travel time of the lake floor reflection and the reflection at the BHSZ. Also the inverse, the determination of the vertical extent of the HSZ based on heat flow can be performed. The methodology is outlined in chapter 4 but closely resembles the approach used in this chapter.

The analytical equilibrium equation is used throughout this entire chapter for different applications and situations. Most of the figures included are based on the results of such a calculation procedure in several expanded programs with focus on different parameters or variables (time scale, sea level fluctuation, bottom water temperature change, geothermal gradient, ...) by means of programming loops. These programs typically generate output text files with series of results, that in turn were used to make graphics or figures and contouring. The numerical values used to make the figures throughout this chapter are not imported in this text.

The results shown here are purely theoretical analyses based on the algorithm explained above. It is important to stress that these conditions for hydrate stability are bulk conditions without taking into consideration small scale *in situ* deviations of temperature and pressure conditions due to hydrate formation/dissociation and subsequent latent heat of crystallisation (heat release)/dissociation (heat supply from surroundings) or the size of the porous medium (capillary effects).

2.1.3
Extent of the HSZ as a function of geothermal gradient and bottom water temperature

In general, the theoretical BHSZ viewed on a transect from the shelf into the deep ocean basin (3000 m water depth) is presented in figure 2.2 for bottom water temperature of 1°C and a geothermal gradient of 0.050°C·m^{-1}. In the interval between 0 and 3000 m water depths, the extent of the stability field was calculated with steps of 5 m water depth. Except for relatively shallow water depths (< 1000 m), the limit of theoretical hydrate occurrence varies almost linearly with the height of the overlying water column. At shallow water depths, the extent changes faster, and will hence be more sensitive to environmental changes. In basins with warmer bottom waters and/or higher geothermal gradients,

the extent will be less. Furthermore for warmer bottom waters, the minimum water depth within overall stability conditions will be found at greater water depths.

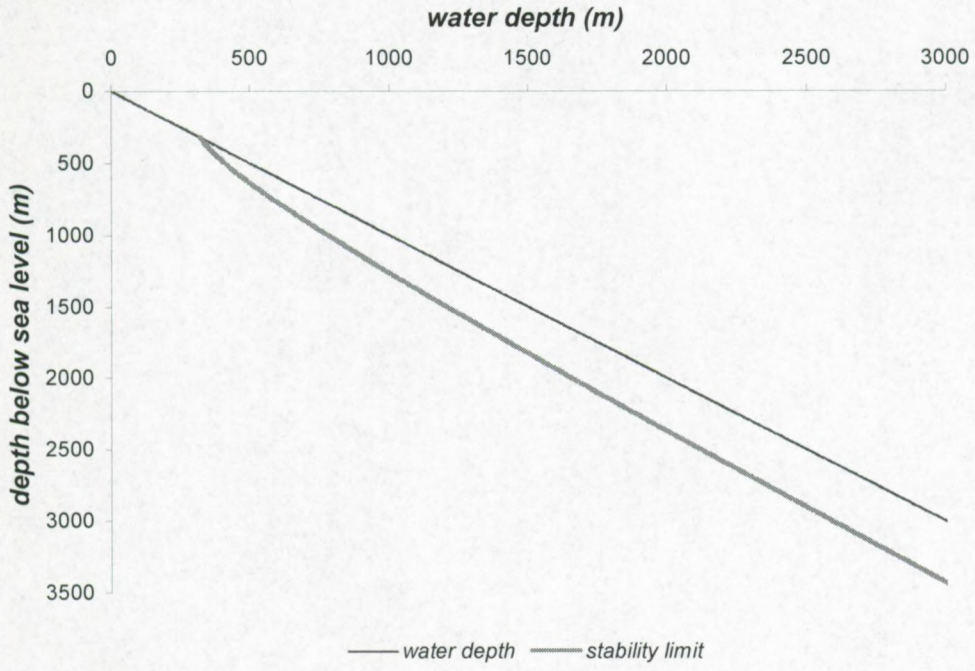

Figure 2.2: *Illustration of the base of the theoretical methane HSZ at 1 °C bottom temperature and a geothermal gradient of 0.050°C·m^{-1} on a transect from the continent into the deep ocean.*

Here, the influence of the geothermal gradient and bottom water temperature on the extent of the HSZ is discussed and numerical results will be presented. The author would like to mention that the results and figures are of interest to see differences in different geographic areas with different conditions, especially the combination of both for discrete water depth. Under steady-state thermal conditions both properties can be treated as a constant parameter, and hence at one and the same place and time no variation will occur. The figures hence are only meant to give the reader an idea to what extent hydrates can be stable in the subsurface in different geological settings characterised by different geothermal regimes. In this way they represent a guide to obtain relatively fast qualitative and quantitative ideas of the variability of the extent of the hydrate stability limits. All results are obtained using the analytical phase boundary equation in diverse self-written programs based on the methodology outlined above. The basic program included allows to calculate the extent for bulk conditions using hydrostatic pressure if all necessary details are available.

2.1.3a As a function of geothermal gradient or heat flow

Up to now, only discrete values of geothermal gradients G were taken into account. Accurate knowledge of the sub-bottom temperature profile is necessary to obtain information about the extent of the stability field. Subsurface temperature depends on local heat flow q_{HF} and heat conductivity λ. In the simplest case, one-dimensional pure conductive heat flow without internal heat production or consumption is linked to the geothermal gradient and the sub-bottom temperature profile [4] as follows:

$$q_{HF} = \lambda G \qquad [6]$$

ignoring the sign difference between common upward heat flow and downward temperature increase (increasing burial depth). Typical values of thermal conductivity of bulk shallow sediments fall in the range of 1 to 1.3 $W \cdot °C^{-1} \cdot m^{-1}$ and are treated here as a constant value. In the case of Lake Baikal however, the thermal conductivity is known to increase slightly with increasing burial depths [*Duchkov & Kazantsev, 1996; Golmshtok et al., 1997*].

From pure observation of the phase boundary diagram, one can see that the higher the heat flow value, the shallower the hydrate stability limit will be. In figure 2.3, the sub-bottom depth of the BHSZ is expressed as a function of geothermal gradients between 0.020 and 0.200°C·m^{-1} for discrete water depths covered by bottom water masses at 1°C temperature. Pore pressure is assumed to be hydrostatic. The equilibrium sub-bottom depth of the methane hydrate phase is calculated by applying a computer program based on the algorithm explained above. During the calculation procedure, the geothermal gradient ranges between 0.020 and 0.2000°C·m^{-1} with intervals of 0.0001°·m^{-1}. Water depths were chosen to increase with intervals of 20 m between 500 and 4000 m, of which only selected water depths are displayed here.

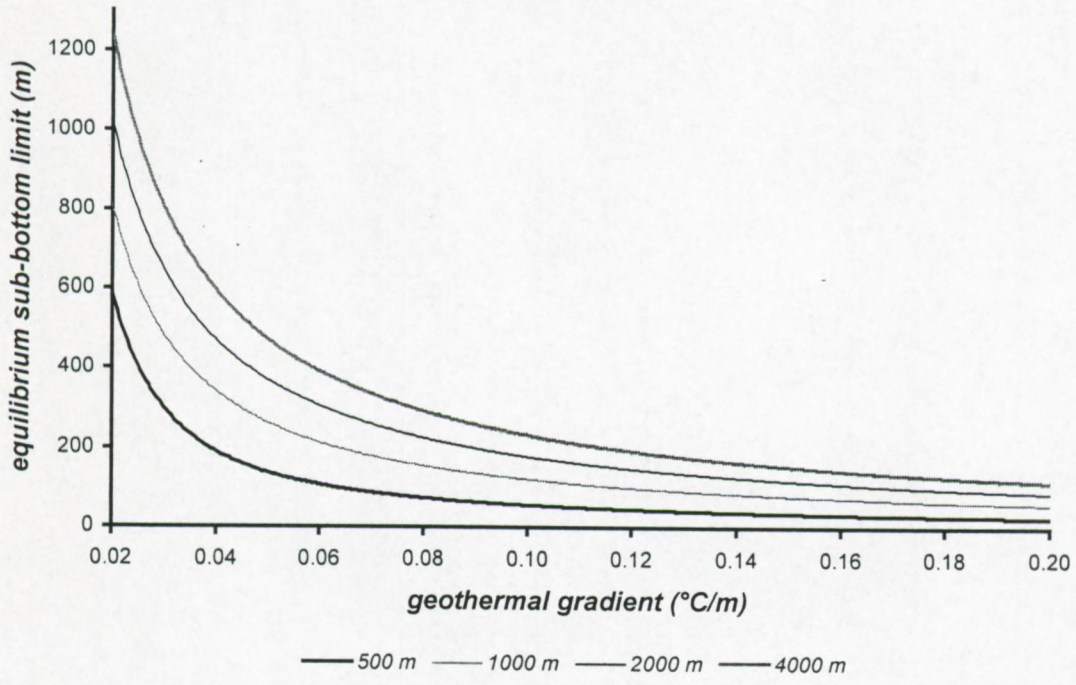

***Figure 2.3**: Equilibrium sub-bottom limit of methane hydrates in an average salt water environment for different water depths as a function of geothermal gradient. Pore pressure is assumed to be pure hydrostatic, bottom water temperature is 1°C.*

This figure illustrates that the pure methane hydrate stability zone in oceanic settings is larger for small geothermal gradients or heat flow values and deep water basins, while numerical results of the difference can easily be read from the figure. Average geothermal gradients are 0.035-0.050°C·m^{-1} [*Allaby & Allaby, 1999*]. Values of 0.024-0.038°C·m^{-1} are found for the Porcupine Basin, offshore Western Ireland [*Croker & Shannon, 1987*] while higher values of 0.050-0.056°C·m^{-1} are reported from the vicinity of the Storegga Slide area, Norwegian margin [*Mienert et al., 1998; Bouriak et al., 2000*]. Hence, in the remaining part of this study these values will be used as reference geothermal gradients or as typical values, in order to discuss the variability and sensitivity of the HSZ.

An application can be found in places with spatially limited anomalous behaviour, relative to the background values. For example, mud volcanoes normally are characterised by an increasing heat flow towards the central part of the volcano. If the volcano lies well within hydrate equilibrium conditions, then the sub-bottom depth of the hydrate stability limit will change considerably close to the volcano. This is for example the case for the Håkon Mosby Mud Volcano offshore Western Norway [*Eldholm et al., 1999*] in which hydrates are observed at the sea bed.

Also in Lake Baikal, direct and indirect evidence of hydrate occurrence is present. Since the lake occupies the central part of the Baikal Rift Zone, it is characterised by a complex fault pattern and a highly variable heat flow. Bottom water temperatures in the lake's basins are 3.2 (Central) to 3.4°C (Southern) [*Golmshtok, pers. Comm.*] in water depths between 700 and 1500 m. A similar figure as figure 2.3 but for fresh water basins then indicates that the equilibrium limit of hydrate stability can easily vary to over several tens of meters sub-bottom depth as a function of the heat flow or geothermal gradient measured. This is analysed in more detail in chapter 4.

2.1.3b As a function of bottom water temperature

Although naturally occurring hydrate accumulations are primarily temperature-controlled [*Kvenvolden, 1998*], a minimum water depth is needed to assure hydrate stability, as can be seen from figure 2.1. This minimum pressure value or height of the water column can be easily expressed as a function of bottom water temperature, using the analytical phase boundary equation. The minimum necessary water depth will hence be that value at which the pressure reaches the hydrate equilibrium pressure for the present bottom water temperature, i.e. a situation in which hydrates can be present at the seabed. Hence, the pressure can be easily converted into water depths. These conditions are labelled as critical water depths or critical temperatures.

For pure methane hydrates, the minimum water depth as a function of bottom water temperature between 0 and 25°C is given in figure 2.4 for both the fresh water and average salt water environments. For areas characterised by cold bottom water temperatures, methane hydrates will be stable at water depths exceeding 300 m. For example, the high-salinity Antarctic Bottom Water (AABW) formed in the Weddell and Ross Seas, and the North Atlantic Deep Water (NADW) formed in the Norwegian Sea have typical temperatures between –2 and –0.4°C res. 1 and 2.5°C [*Allaby & Allaby; 1999*]. Temperate bottom water mass temperatures of 7.5°C need a minimum water depth of 650 m. Hydrate stability with bottom water temperatures of 15°C (subtropical waters) is only guaranteed at water depths exceeding 1200 m (fresh water) or 1400 m (salt water). It will be shown in paragraph 2.3 that these so-called critical temperatures are of importance for analysing the behaviour of the HSZ for changing temperature regimes.

The vertical extent of the HSZ is then calculated as a function of bottom water temperatures for discrete water depths and geothermal gradient parameters. The result is shown in figure 2.5. Water depths are 500, 1000, 2000, 3000 and 4000 m for geothermal gradients of 0.050°C·m^{-1}. It is observed that the maximum sub-bottom depth of HSZ decreases almost linearly with increasing bottom water temperature, until the temperature is too high for the present water depths. At higher water depths, the relationship becomes more linear. Regression correlation coefficients are 0.9995 (H = 500 m) to 1 (H >2000). Also for increasing water depths, the slope of the curve is decreasing.

2.1.3c Iso-equilibrium depth maps of the methane hydrate stability limit

A combination of variable heat flow or geothermal gradients with variable bottom water temperature is performed for the pure methane – salt water – hydrate phase boundary, according to the analytical phase boundary equation. The whole calculation procedure of the self-written program is as follows.

The geothermal gradient ranges from 0.02000 and 0.10000°C·m^{-1} with steps of 0.00025°C·m^{-1} between successive calculations, while the sea bed temperature covers the interval between –1.50 to 10.00°C with steps of 0.25°C. For each couple of geothermal gradient and bottom water temperature, the bulk equilibrium limit below the sea bed is calculated for discrete water depths. For each water depth, a set of iso-equilibrium depths for methane hydrate occurrence was obtained for 15087 samples and was then contoured using surfer software with triangulation/linear interpolation between adjacent values. Examples of this procedure are represented in figure 2.6a. At 500 m water depth, hydrates cannot be stable if bottom water temperature exceeds 5.54°C.

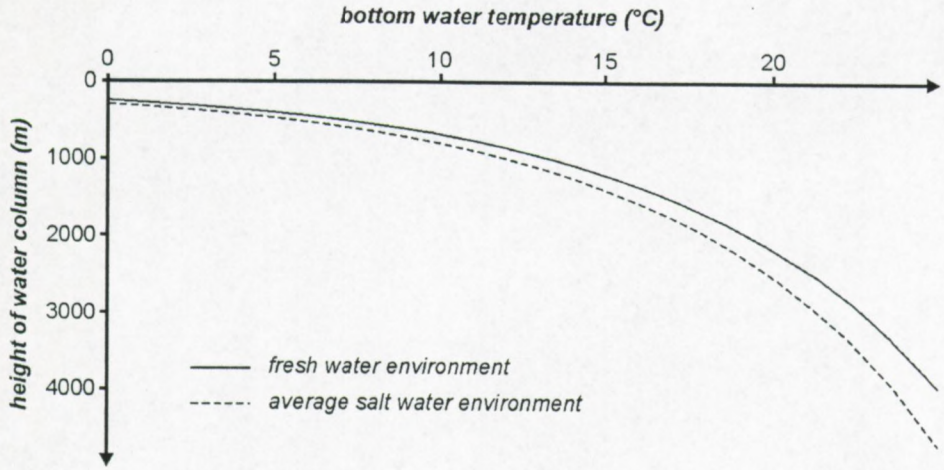

***Figure 2.4**: Minimum water depth for methane hydrate stability as a function of bottom water temperature in a fresh and average salt water environment*

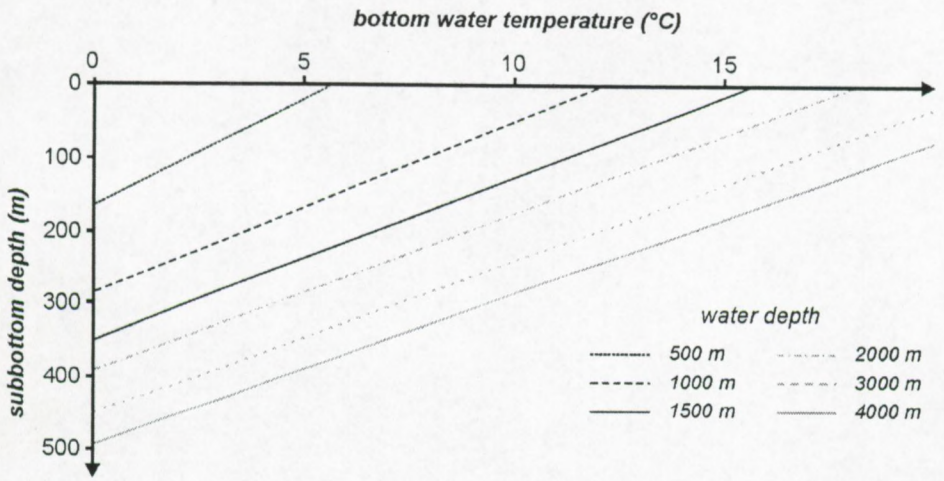

***Figure 2.5**: Variation of the hydrate stability limit for discrete water depth, as a function of bottom water temperature with geothermal gradient of 0.050°C·m^{-1}*

The advantage of such figures is that, assuming a linear sub-bottom temperature profile with non-variable bottom water temperature, one easily can check to what depth pure methane hydrates can be stable in an average salt water environment, once some details (T_0, G) are known. Figures 2.2 and 2.4 are in fact cross-sections of these contour plots. A second application of such figures is that, if one knows the sub-bottom depth of the methane hydrate stability limit (e.g. from seismic data analysis) and the bottom water temperature, one can rapidly estimate the local geothermal gradient.

Exactly the same approach is used to create contour plots for methane hydrate limits in fresh water environments as well, with bottom water temperatures ranging from 0 up to 10°C. Figure 2.6b then is the fresh water counterpart of figure 2.6a. These figures can be used for example for the Lake Baikal gas hydrate study. The salinity of 0.76‰ of the water in Lake Baikal does not result in a shift of the 3-phase equilibrium curve relative to pure methane hydrates in pure fresh water. Hydrate stability requires bottom water temperatures less than 6.77°C at 500 m water depth.
Figure 2.6c gives iso-sub-bottom depth lines for pure methane hydrates for average salt water environments. Only the iso-equilibrium depths for geothermal gradients between 0.0300 and 0.1000°C·m^{-1} are shown here. Linear interpolation is done in intervals of 20 m water depths and 0.0005°C·m^{-1}. This figure is similar to figure 2.3a, since figure 2.2a represent a transect of figure 2.6b.

Iso-depths of the theoretical bulk methane hydrate stability limit calculated for variable salt water depths (500 to 4000 m, with 20 m interval) and bottom water temperatures (-1 to 10°C) are shown in figure 2.6d. Geothermal gradient was 0.050°C·m^{-1}. Interpolation windows had dimensions of 20 m (water depth) by 0.2°C (temperature). Figure 2.5 is in fact a transect of this figure.

2.1.4
Pore pressure deviations and heat flow aspects

Since hydrates form in the pore spaces, one must take into account the *in situ* pore pressure to determine stability conditions. Typically, BSRs are observed no deeper than several hundreds of meters below the sea floor. At these depths, the sediments is most likely to be unconsolidated having a granular structure [*Hamilton, 1971; Ecker et al., 1998*]. Hence, the pore pressure will be close to hydrostatic.

If however, the pore pressure is not hydrostatic, the depth of the 3-phase boundary will be different. In general, the pore pressure of sediment depositions is assumed to lie in between of the pure hydrostatic pressure, i.e. the pore fluids only support the overlying water column, and the lithostatic pressure, i.e. also the matrix is partially supported by the fluids. Therefore, this uncertainty means basically that one needs to take into account both end members (hydrostatic as a minimum, lithostatic as a maximum). The real extent of the HSZ will then lie in between the calculated values.

If the pore pressure is higher than hydrostatic, the pore fluid is capable of performing work. One of the reasons for increased pore pressures to occur is to be found in sediment compaction, resulting most often in an upward fluid flow. Incorporating this phenomenon for determining the hydrate stability limit is more difficult since accurate information of the actual *in situ* conditions of small scale pressure and temperature is needed.

(next page)

Figure 2.6a *(above): Lines of iso-sub-bottom depths of the hydrate stability limit (20 m intervals) for discrete water depths with variable geothermal gradients and bottom water temperatures in an average salt water environment (salinity 3.35%).*

Figure 2.6b *(below): Lines of iso-sub-bottom depths of the hydrate stability limit (20 m interval) for discrete water depths with variable geothermal gradients and bottom water temperatures in a fresh water (e.g. Lake Baikal, Siberia) environment.*

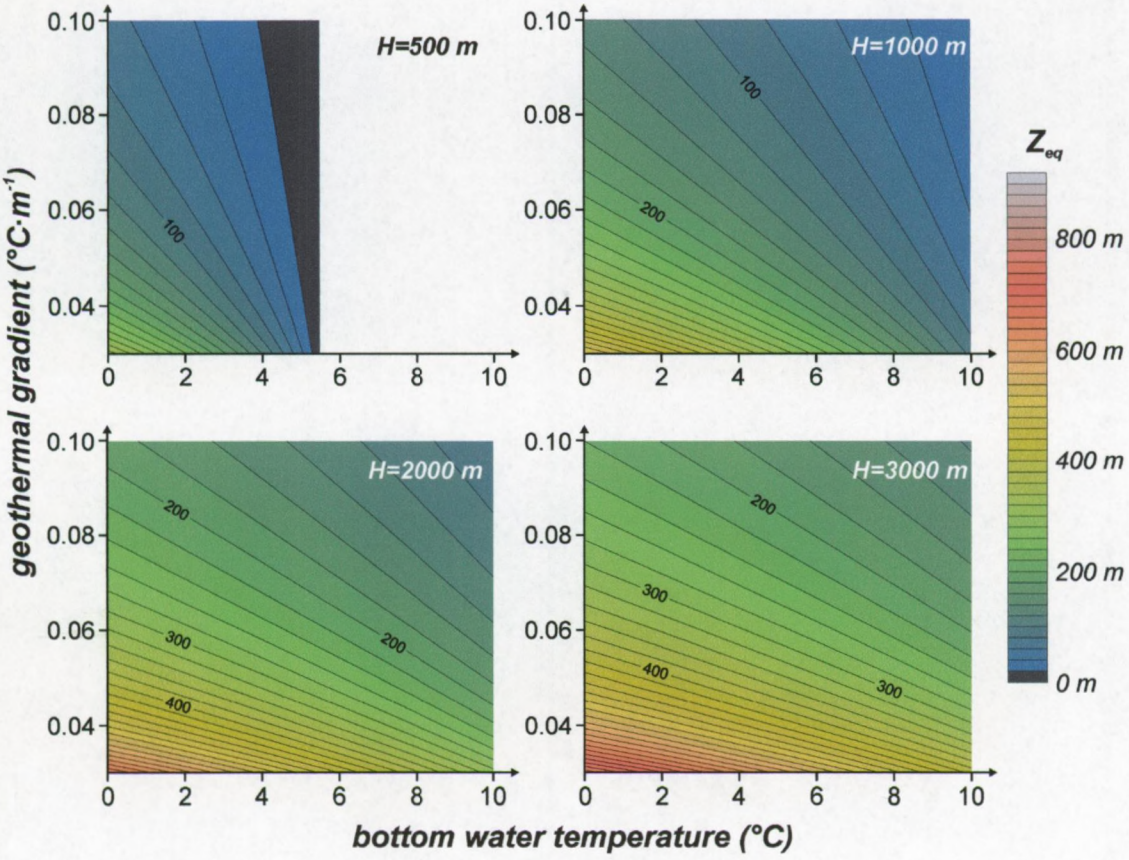
H=500 m
H=1000 m
H=2000 m
H=3000 m
geothermal gradient (°C·m-1)
bottom water temperature (°C)
Zeq
800 m
600 m
400 m
200 m
0 m

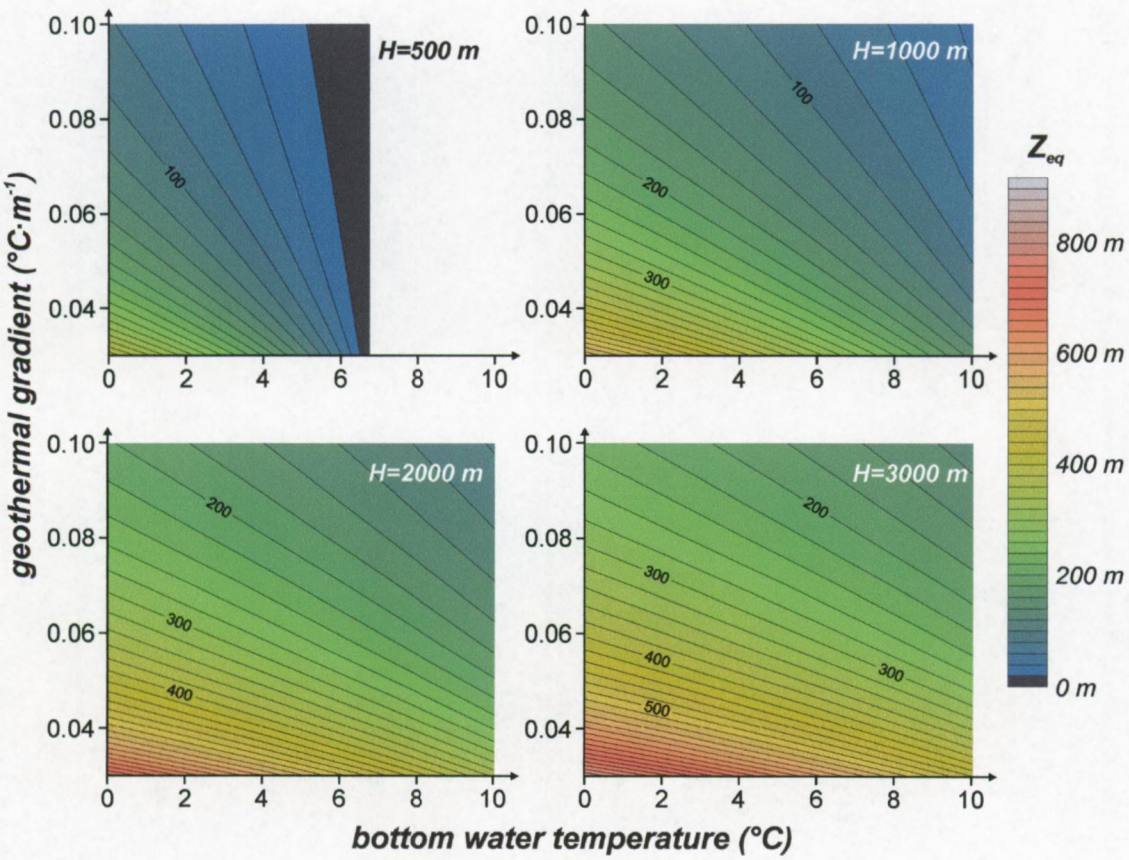
H=500 m
H=1000 m
H=2000 m
H=3000 m
geothermal gradient (°C·m-1)
bottom water temperature (°C)
Zeq
800 m
600 m
400 m
200 m
0 m

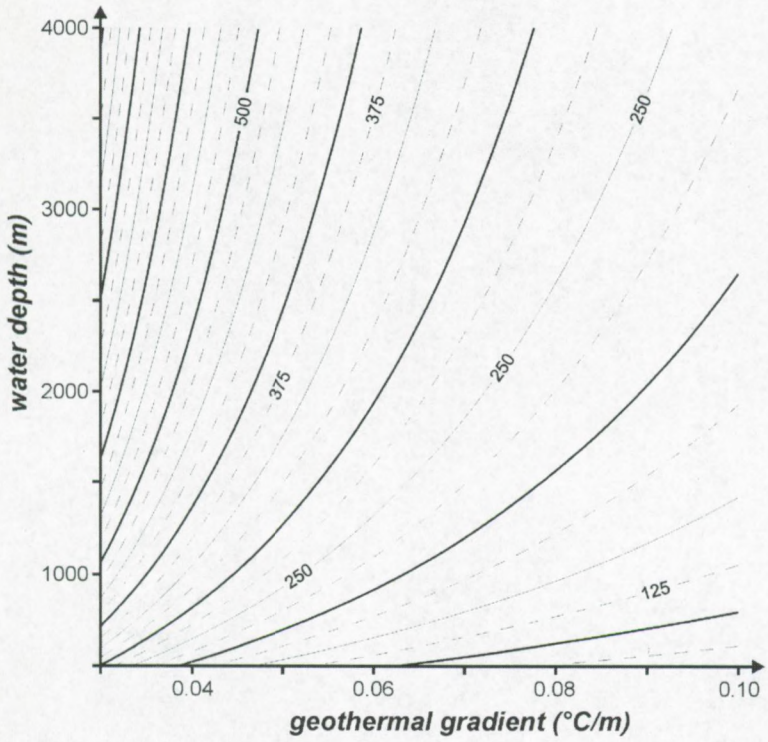

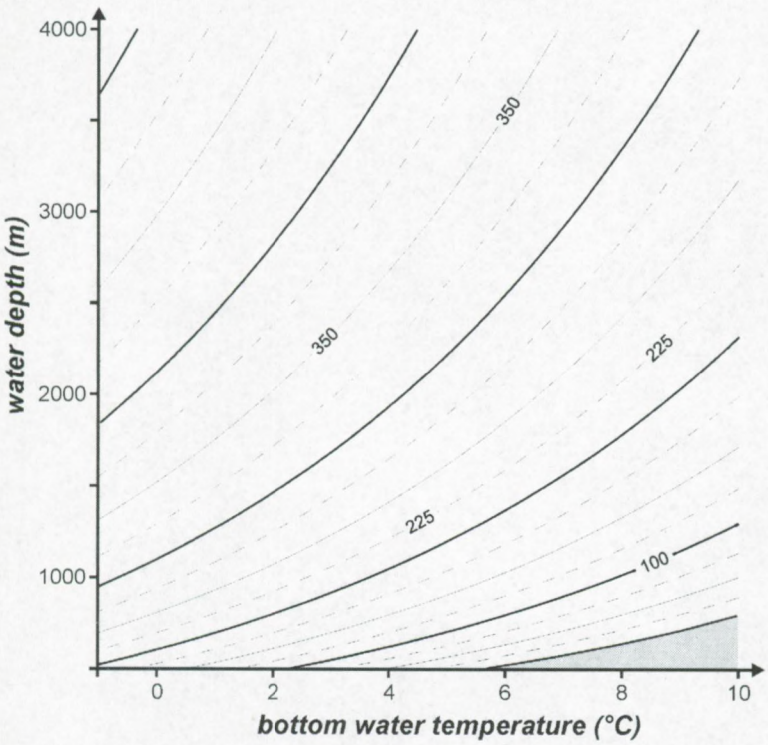

Figure 2.6c *(above): Iso-equilibrium sub-bottom depths (25 m interval) for pure methane hydrates in an average salt water environment with bottom water temperature of 1 °C. Pore pressure is assumed to be hydrostatic.*
Figure 2.6d *(below): Iso-equilibrium sub-bottom depths (25 m interval) for pure methane hydrates in an average salt water environment with geothermal gradient of 0.050°C·m^{-1}. Pore pressure is assumed to be hydrostatic. The grey zone marks the area that falls outside the stability field.*

However, for small internal fluid migration no significant shift of the hydrate equilibrium curve from the hydrostatic approach will occur (see also paragraph 2.5). Occasionally, extreme high pore

pressures can occur. If the pore pressure for example exceeds the lithostatic pressure, the sediments will expand and fractures can form (i.e. hydrofracturing) [*Bjørlykke, 1989*], providing pathways for overpressure to dissipate. It will be shown in paragraph 2.6 that pore pressure in excess of hydrostatic pressure is important for discussing the relevance of slope instability in relation to hydrate dissociation on the Norwegian Continental margin.

In case of lithostatic pore pressure, the density of the sedimentary matrix and the porosity behaviour vs. depth need to be included. The difference between the hydrostatic and lithostatic approach is presented in figure 2.7, for a bottom water temperature of 3°C and a geothermal gradient of 0.035°C·m^{-1}. A typical matrix density of 2500 kg·m^{-3} is used. In general, hydrates are only present in relatively small amounts [*Hovland et al., 1997*], so a contribution of hydrates in calculating the bulk density can be neglected. Water depth is 1500 m. Porosity is assumed to decrease with sub-bottom depth according to Athy's law, with a compaction parameter k of 0.000473 m^{-1} and a maximum porosity ϕ_0 of 65% at the seabed, a situation typical for the sediment accumulations in Lake Baikal [*Golmshtok et al, 1997*]. The compaction coefficient depends almost solely on the type of sediments. The value used here is a typical value for clay-sandstone layers [*Golmshtok et al., 2000*]. Porosity and bulk density without hydrate saturation are:

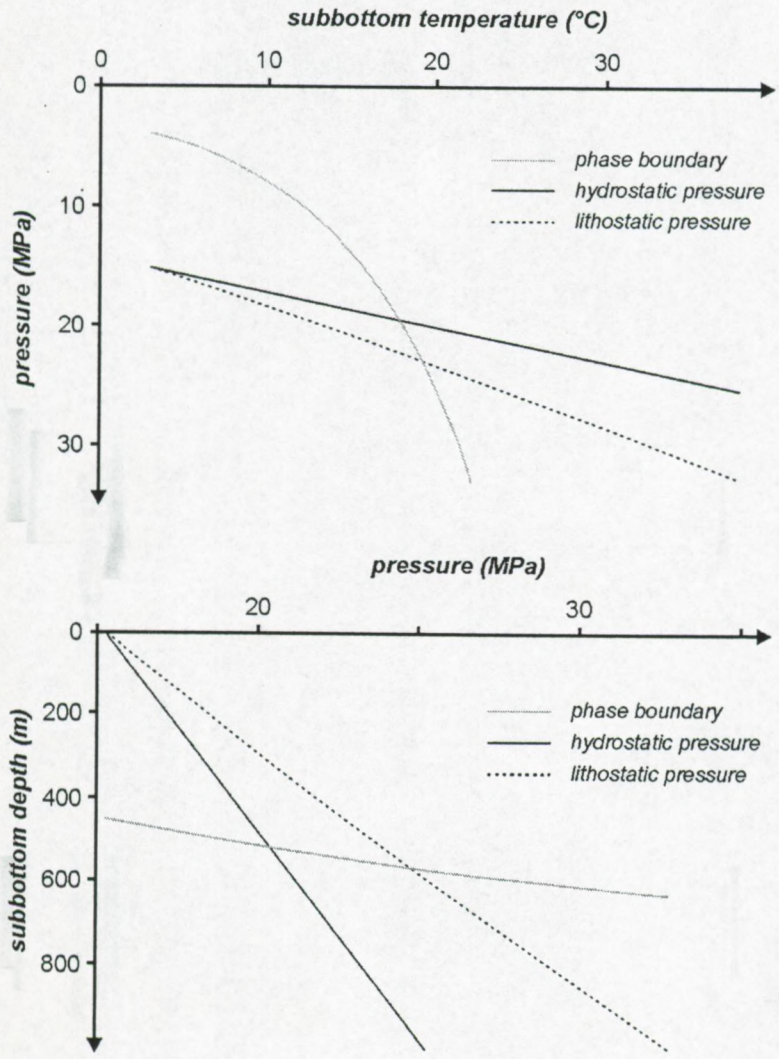

***Figure 2.7**: Influence of the pressure approach (hydrostatic vs. lithostatic) onto the extent of the methane HSZ at 1500 m water depth, geothermal gradient of 0.035°C·m^{-1}, and porosity decrease according to Athy's law. Temperature is linked to sub-bottom depth.*

$$\phi\langle z\rangle = \phi_0 \exp(-k \cdot z) \quad [6]$$

$$\rho\langle z\rangle = [1-\phi\langle z\rangle]\rho_m + \phi\langle z\rangle\rho_f \quad [7]$$

with ρ_m the density of the skeleton. Lithostatic pressure (expressed in MPa) can then be written as:

$$P_{lith}\langle z,H\rangle = P\langle 0,H\rangle + 10^{-6}\int_{\omega=0}^{\omega=z}\rho\langle\omega\rangle g d\omega$$
$$= P\langle 0,H\rangle + 10^{-6} g\left\{\rho_m z + \phi_0 \frac{\rho_m-\rho_f}{k}[\exp(-k\cdot z)-1]\right\} \quad [8]$$

using formula [3].

This figure clearly illustrates that the determination of the sub-bottom position is highly dependent of the pressure distribution function. In this case, a difference of almost 40 m sub-bottom depth is observed. The difference in the vertical extent of the HSZ calculated using both pressure approaches of course also depends on the bottom water temperature and the geothermal gradient. This is illustrated in figure 2.8 for variable bottom water temperatures (1, 3, 5, 7°C) with a fixed geothermal gradient of 0.035°C·m^{-1} (a) and for variable geothermal gradients (0.035, 0.050 and 0.070°C·m^{-1}) with a fixed bottom water temperature of 5°C (b). The water depth varies from 1000 to 4000 m.

These figures illustrate that the difference between the lithostatic and hydrostatic approach for determining the base of the theoretical HSZ becomes smaller into the deep basins. The higher the bottom water temperature and/or the geothermal gradient or heat flow, the smaller the error will be in using a different pressure approach.

This is an important feature if one wants to use the presence of a bottom-simulating reflector on seismic data as a temperature reference. After velocity analysis is carried out on multi-channel data, the sub-bottom depth and hence pressure at the BSR can be calculated. The use of hydrostatic or lithostatic pressure will lead to other *in situ* equilibrium temperatures, so other geothermal gradients or heat flow values. For example, *Yamano et al. [1982]* use the lithostatic approach, while most other researchers assume hydrostatic pressure to be more realistic [*Hyndman & Davis, 1992*]. In case of Lake Baikal (see chapter 4) pressure differences of approximately 5 to 10% are observed at mean sub-bottom depths of the methane hydrate stability limit, resulting in heat flow differences of less than 5% (see chapter 4). Together with S. Bouriak (Moscow State University) a similar analysis was performed using single-channel seismic data in the immediate neighbourhood of the Storegga Slide area, offshore Norway (TTR8 survey, 1998). For this study, a regression equation for the sub-bottom velocity profile [*Hamilton, 1980*] was compared with results from neighbouring ODP sites (Leg 104, sites 642-644) [*Eldholm et al., 1987; 1989*]. Heat flow differences of less than 10% were calculated as a result of the different pressure approach [*Bouriak et al., 2000*].

In this work, the pore pressure distribution is always assumed to be hydrostatic, except otherwise mentioned. This is also the case for the programs written. Only for the analysis of the behaviour and distribution of the hydrate accumulations in Lake Baikal (chapter 3, 4), both approaches are used.

2.1.5
Sensitivity of the HSZ: evolutionary tracks

As is clearly observed from the analytical 3-phase boundary curve, the extent of the HSZ in nature will be sensitive to changes in pressure, temperature or composition. A quantitative analysis of pressure and temperature changes for pure methane hydrates is given in the next sections of this chapter. A

qualitative sketch of these situations can be easily represented in diagrams as shown in figure 2.9 for evolution towards more stable conditions, i.e. lower *in situ* temperature or higher *in situ* pressure (a) or for evolution towards less stable conditions, i.e. higher *in situ* temperature or lower *in situ* pressure (b). These diagrams are useful but lack accurate details of the real impact of environmental changes on the behaviour of the hydrate stability limit in nature. It is worth noting that, for hydrate dissociation to occur, the *in situ* conditions first have to evolve towards the stability limit.

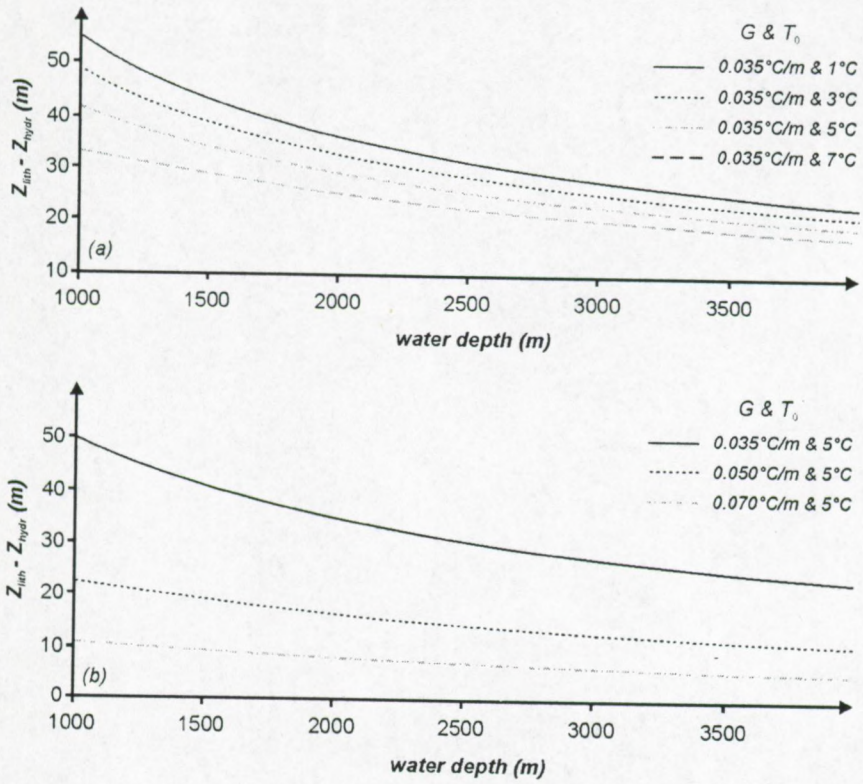

***Figure 2.8**: Influence of the pore pressure assumption on the determination of the vertical extent of the hydrate stability limit. The difference between the lithostatic (Athy's law for Lake Baikal conditions) and the hydrostatic approach is expressed as a function of water depth for fixed geothermal gradient G and variable bottom water temperatures T_0 (a) and for fixed bottom water temperature T_0 but changing geothermal gradients G (b).*

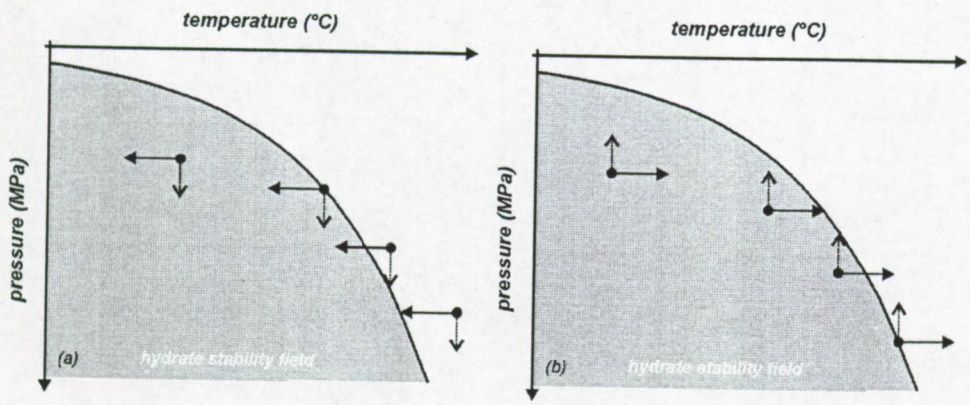

***Figure 2.9**: Sketch of the evolution with time for in situ conditions as a result of pure pressure or temperature changes relative to the gas hydrate 3-phase equilibrium curve.(a) represent the evolution towards more stable conditions, while (b) represents the opposite.*

2.2.1
Theoretical aspects

First of all, the dependence of the gas HSZ during sea level changes is discussed. Eustatic sea level changes are known to occur since at least hundreds of millions of years. The amplitude of such variations can be up to some hundreds of meters. One of the reasons for global sea level fluctuations may be the change of the volume of the oceanic basins, basically caused by tectonic and isostatic processes, e.g. swelling and shrinking of mid-oceanic ridges or eruptions of large volumes of basalts from mantle plume activity [*Leeder, 1999*]. These mechanisms are slow-acting processes. More important in our discussion is the relatively fast sea level changes resulting from the growth or decay of ice caps [e.g. *Leeder, 1999; Bjørlykke, 1989*]. It is known that during the last 800 ka, progression from high-stand to low-stand situation (regression) is considerably slower than the relatively short smooth step from low-stand to high-stand (transgression) [*Leeder, 1999*]. Deglaciation is believed to be tuned by *Milankovitch* orbital forcing, but this principle cannot explain the rapid shift to interglacial conditions. Deglaciation periods are associated with rapid increases of methane and carbon dioxide in the atmosphere [*Haq, 1998*]. This observation suggests a plausible link with hydrate dissociation and subsequent release into the water column and later across the water-air interface, perhaps triggering climate or climatic changes [e.g. *Nisbet, 1990; Paull et al., 1991; Haq, 1993; 1998*].

In this discussion, the high-resolution relative sea level curve of *Fleming et al.* [*1998*] covering the last 210 ka will be used (figure 2.10). Especially the sea level changes since the Last Glacial Maximum (LGM) are well established. Since the LGM, the most pronounced sea level increase took place between 17 ka and 6 ka BP. Since then, only a small change (a few meters) occurred. At the LGM, the average sea level was approximately 118-125 m lower than at present. Such a sea level change results in a water pressure change of approximately 1.2 MPa. As is clear from a methane hydrate phase diagram and the evolutionary tracks shown in figure 2.7, increasing pressure will lead to more stable hydrate conditions in a constant geothermal field. In case that the pressure drops, conditions become less favourable and part of the hydrates will dissociate. The pore spaces are in general considered to be interconnected and permeable in the uppermost sediment section, so water level fluctuations are supposed to be immediately translated into changing pore pressures.

Here, quantitative results for the amplitude of the extension or shrinking of the HSZ will be presented in relation to the amplitude of the sea level change. These results are obtained after careful analysis of the analytical phase boundary equation, and applying the algorithm explained in the previous paragraph. Since at present only one freshwater basin with indirect and direct evidence of gas hydrates is known (i.e. Lake Baikal, Siberia) [*Golmshtok et al., 1997; Kuzmin et al., 1998; Vanneste et al., in press*], the discussion is carried out for average salt water environments (salinity: 3.35%, density 1025.67 $kg \cdot m^{-3}$) and will not be repeated for fresh water basins. The trends will however be the same, with slightly different amplitudes of the changes.

In case only the pressure has changed due to sea level fluctuations, so that the geothermal regime is not altered, an estimate of the vertical shrinking (sea level drop) or expansion (sea level increase) can be derived from the analytic phase boundary equations. Initially, the sub-bottom depth of the BHSZ is determined by (taken from §2.1 [1, 1'])

$$z_1 = \frac{T_{eq,1} - T_0}{G} = \frac{1}{2cG}\left[-b + \sqrt{b^2 + 4c \cdot \left(LogP_{eq,1} - a\right)}\right] - \frac{T_0}{G} \qquad [1]$$

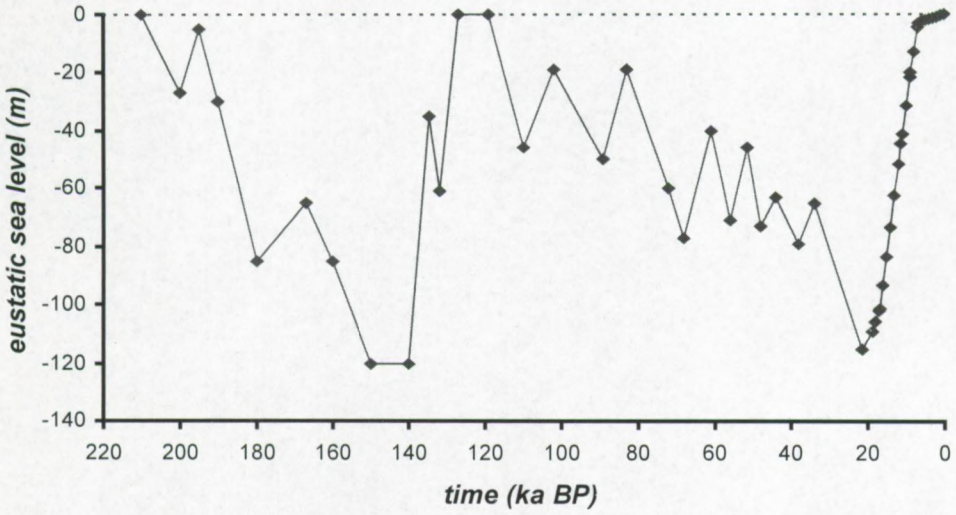

***Figure 2.10**: Relative sea level curve over the last 210 ka, from Fleming et al. [1998]*

Finally, after the sea level change, the pressure conditions will be different and a new equilibrium limit will be established or

$$z_2 = \frac{T_{eq,2} - T_0}{G} = \frac{1}{2cG}\left[-b + \sqrt{b^2 + 4c \cdot \left(LogP_{eq,2} - a\right)}\right] - \frac{T_0}{G} \qquad [1']$$

The change in sub-bottom depth of the hydrate limit can be written as [*Vanneste, 1997*]:

$$\Delta z = z_2 - z_1 = \frac{1}{2cG}\left[\sqrt{b^2 + 4c \cdot \left(LogP_{eq,2} - a\right)} - \sqrt{b^2 + 4c \cdot \left(LogP_{eq,1} - a\right)}\right] \qquad [2]$$

Positive values of the difference indicate increased stability since the limit will lie deeper into the sediments. Negative values indicate a smaller extent of the HSZ. Obviously, this methodology allows us to determine quantitative results of the sensitivity of the stability limit under eustatic sea level changes. In the remaining part of this paragraph, diverse applications of this formula with different parameters will be discussed.

One needs to be cautious in applying this formula for the following reason. The hydrostatic pressure change as a result of the variation of the water level causes the HSZ to shift but this pressure change is not identical to the change of *in situ* equilibrium pressures. Some examples for discrete water depths are given in table 2.1. In all cases, pore pressure distribution is supposed to be hydrostatic. The equilibrium pressure change has in all cases a higher magnitude than the pressure change due to sea level variation.

The variability of the hydrate stability limit, as expressed by formula [2], can be theoretically analysed as a function of the different parameters occurring, i.e. height of the overlying water column, bottom water temperature, geothermal gradient or the amplitude of eustatic sea level change. In the next paragraphs, the variability is discussed in more detail. Again, a series of comparative figures is generated, based on the same algorithms, including extra information concerning the pressure change.

2.2.1a Variability of the hydrate stability limit during sea level changes along the continental margin and slope into the deep basin

	A	B	C	D
initial situation				
geothermal gradient (°C/m)	0.035	0.035	0.050	0.050
bottom water temperature (°C)	3.00	3.00	0.00	2.10
water depth (m)	1000.0	1000.0	4000.0	2542.0
subbottom equilibrium limit (m)	330.3	330.3	492.8	382.3
total depth equilibrium limit (m)	1330.3	1330.3	4492.8	2924.3
in situ equilibrium temperature (°C)	14.56	14.56	25.64	21.21
in situ equilibrium pressure (MPa)	13.49	13.49	45.31	29.52
final situation				
geothermal gradient (°C/m)	0.035	0.035	0.050	0.050
bottom water temperature (°C)	3.00	3.00	0.00	2.10
sea level change (m)	120.0	-120.0	-120.0	-30.0
water depth (m)	1120.0	880.0	3880.0	2512.0
subbottom equilibrium limit (m)	356.3	300.0	488.4	380.5
total depth equilibrium limit (m)	1476.3	1180.0	4368.4	2892.5
in situ equilibrium temperature (°C)	15.49	13.50	24.42	21.12
in situ equilibrium pressure (MPa)	14.96	11.97	44.05	29.20
differences				
hydrostatic pressure change (Mpa)	1.21	-1.21	-1.21	-0.30
equilibrium subbottom depth difference (m)	26.0	-30.3	-4.4	-1.8
equilibrium total depth difference (m)	146.0	-150.3	-124.4	-31.8
equilibrium temperature difference (°C)	0.93	-1.06	-1.22	-0.09
equilibrium pressure difference (Mpa)	1.47	-1.52	-1.26	-0.32

Table 2.1*: Examples of the change of the extent of the methane hydrate stability under eustatic sea level changes in a constant geothermal field for 4 different situations labelled A, B, C and D. The equilibrium pressure difference has a higher amplitude than the hydrostatic pressure change caused by the sea level variation, a trend decreasing with increasing overlying water column.*

As a first snapshot illustrates the change of the stability field with increasing hydrostatic pressure, due to sea level rises according to formula [2], as a function of initial water depths (figure 2.11). Bottom water temperature was 3°C and geothermal gradient was $0.035°C \cdot m^{-1}$. Basically, this figure (and the next one) can be considered as general slope profiles, on which the total depth below sea level of the hydrate stability limit in the initial and final situation is given. The thick blue line represents the change in sub-bottom depth, expressed on the right vertical axis. Positive values of the change indicate a downward shift, or an increase of the hydrate stability limit to deeper sediment sections. These are inversely plotted to show the relative downward movement of the stability limit. Negative values indicate an upward shift or decrease of the extent of the stability field. This is reflected in figure 2.12 in the case of a sea level fall of 120 m.

The changes are most significant at shallow water depths and fade out into the deep basins. On the overall figure 2.11, the change of the extent of the HSZ in deep basins cannot be resolved. Highest amplitudes are observed near the critical water depths. Peak amplitude is about 144 m.

Several authors point out that, on average, the vertical extent of the HSZ during major glacial regressions (comparable with the situation at the LGM) since the Pleistocene was reduced by about 20 m [*Kayen & Lee, 1991; Paull et al., 1996; Kvenvolden, 1998*]. The above figure gives very similar results for initial water depths of more than 1200 m, but it also states that this effect is highly dependent on topography, since especially in shallower water areas the influence is much more pronounced, the more because of the typical shelf-upper slope topography. Hence, shallow water depths appear as critical zones in which sea level changes have the biggest influence on hydrate stability conditions.

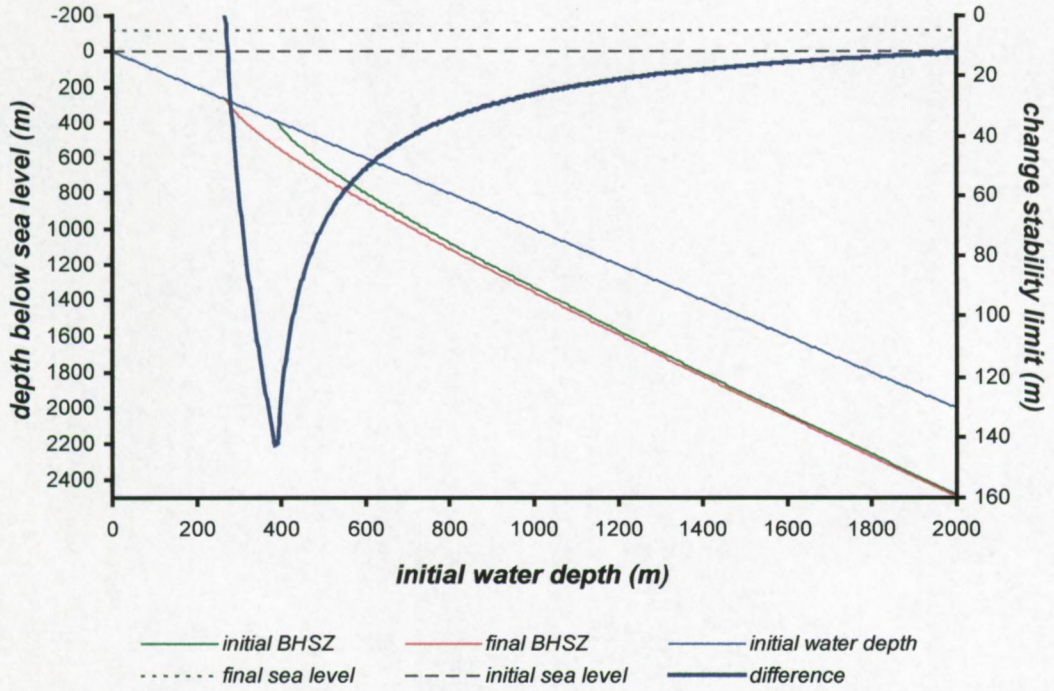

***Figure 2.11**: Change of the vertical extent of the HSZ as a function of initial water depths in case of a eustatic sea level rise of 120 m, a situation similar to the sea level change between the LGM and present-day. The base of the theoretical HSZ subsides deeper into the sedimentary section due to the water pressure increase.*

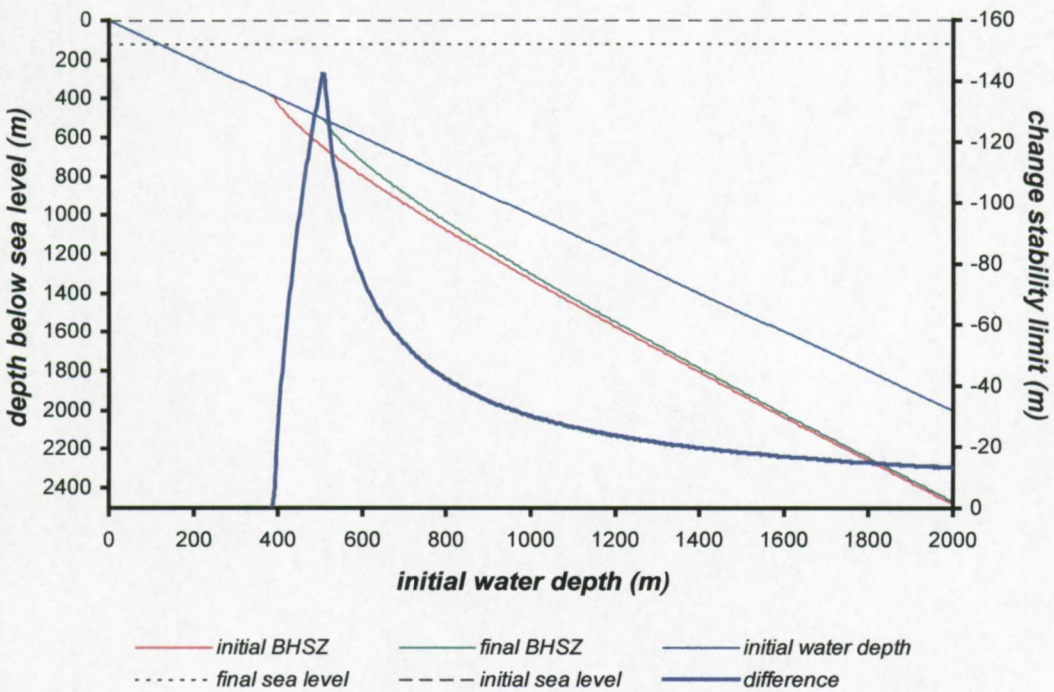

***Figure 2.12**: Change of the vertical extent of the HSZ as a function of initial water depths in case of a eustatic sea level fall of 120 m amplitude, a situation similar to the sea level change between 210 and 150 ka BP, or the inverse situation of figure 2.11. The BHSZ migrates upwards into the sedimentary section due to the water pressure drop.*

Since the LGM forms a kind of reference in literature, the evolution from present to the LGM and hence a relative sea level drop of approximately 120 m was chosen for further analyses. Smaller sea

level fluctuations will result in a very similar behaviour of the stability limit, with obviously smaller amplitude. Since the slope profiles for other sea level changes show the same qualitative trend, these are not included. Even the effect of very small sea level changes will theoretically lead to shifts in hydrate stability conditions towards deep oceanic basins. For example, it is calculated that since the last 2 ka (1 m rise) the extent of the stability field grew with about 0.5 m at 500 m water depths, bottom water temperatures of 1°C and geothermal gradient of 0.050°C·m^{-1}. In deep basins (> 2000 m water depth), the difference is less than 10 cm.

2.2.1b influence of the amplitude of sea level fluctuations in a uniform geothermal field

An overview illustration of the influence of sea level changes with amplitudes varying between –150 and 150 m for water depths ranging from 500 to 4000 m and a combination of a 1°C bottom water temperature and a geothermal gradients of 0.050°C·m^{-1} is presented in figure 2.13a and b. Data were determined for every 20 m of water depth interval and 5 m of relative sea level change. Iso-lines of the amplitude of the equilibrium limit change are drawn with intervals of 2.5 m (a) and 5 m (b). From this figure, it is seen that the amplitude of the change of the stability limit is not an odd function of sea level change at specific initial water depths. The same situation for discrete water depths is sketched in figure 2.14 for geothermal gradients of 0.050°C·m^{-1} and bottom water temperature of 1°C (labelled A) or 3°C (labelled B). While shifts over vertical distances of more than 50 m occur at shallow water depths, the effect will be an order of magnitude less in deep basins.

2.2.1c Effect of the present bottom water temperature

For water depths exceeding 1000 m there is almost no influence of the actual bottom water temperature on the amplitude of the change of the stability limit due to sea level changes, if the geothermal gradient is not altered (0.050°C·m^{-1}). While the difference between the change of the extent of hydrate stability for bottom temperatures of 1°C res. 3°C for initial water depths of 500 m varies from 15 (112 m sea level drop) to 7 m (150 m rise), at 750 m initial water depths the difference is reduced to approximately 2.5 to 2.0 m over the same interval of sea level changes (figure 2.14). On the same figure, the curves for initial depths of 1000 and 2000 m for situation B would completely mask those of situation A. Hence, in terms of changes of the hydrate stability limit in natural sediments during sea level changes, the bottom temperature appears more important in relatively shallow basins.

One detailed example is shown in figure 2.15 (geothermal gradient = 0.050°C·m^{-1}, sea level fall = 120 m). Iso-lines of the change of the methane hydrate stability limit as a function of variable bottom water temperatures between –1 and 10°C are drawn with 2 m interval (a) or 10 m interval (b). This figure (a) supports the observation that for deep basins, the influence of the bottom water temperature on the variation of the stability limit due to sea level fluctuations is only of minor importance. The difference will only be slightly higher with higher bottom water temperatures (approximately 5% increase from bottom temperature of 1°C to 7°C at 2000 m water depth). The situation in shallower basins however is more complicated. The change is bigger at shallower depths and at lower bottom temperatures. A cross-section of figure 2.15 at 3°C results in a slope profile very similar (other geothermal gradient used) to the one presented in figure 2.12. The reduction of the stability field in the first instance at constant bottom temperature for increasing sea level is then explained by the presence of the critical water depth.

Some examples for discrete water depths (500, 1000, 2000 and 4000 m) and variable bottom temperature – thus cross-sections of figure 2.15 but with a geothermal gradient as used in figure 2.12 – are presented in figure 2.16. This figure explains better the variation at shallow depths and low temperatures.

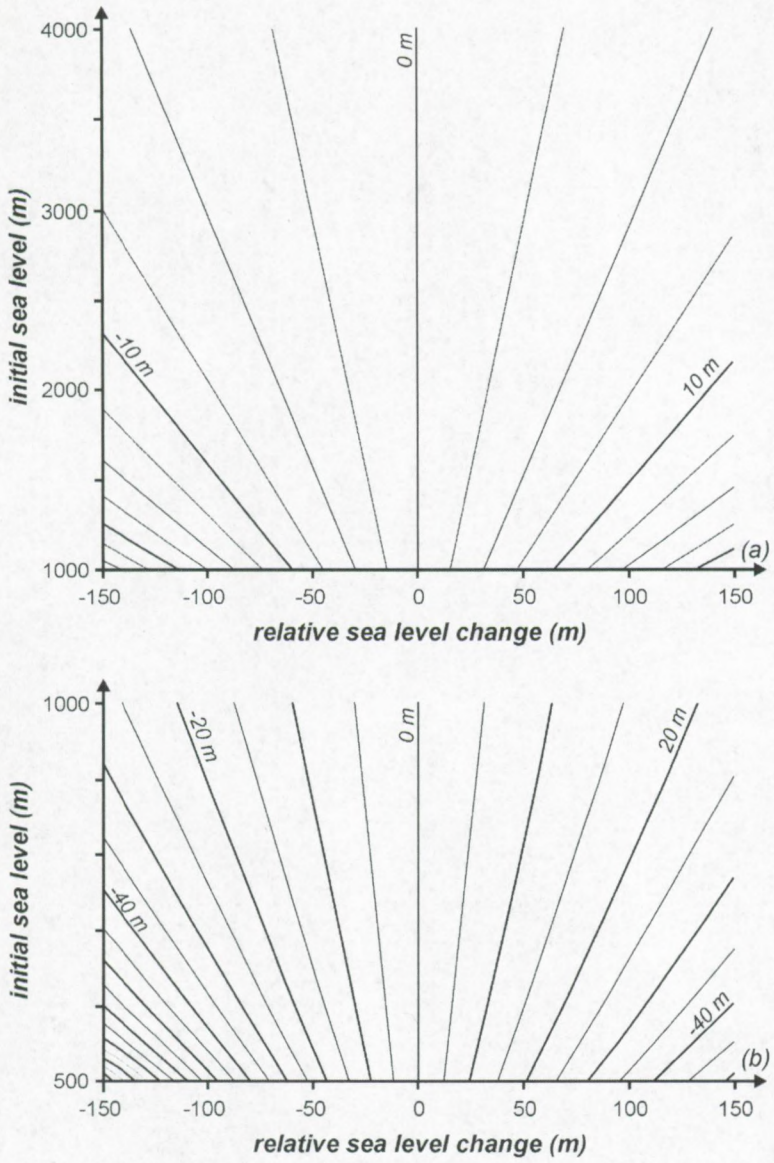

***Figure 2.13**: Influence of variable sea level changes on the extent of the methane hydrate stability limit in average sea water environments. (a) iso-lines of the amplitude of the change for water depths ranging from 1000 to 4000 m with bottom water temperature of 1°C and geothermal gradient of 0.050°C·m^{-1}; (b) same situation for water depths between 500 and 1000 m.*

2.2.1d Effect of the present geothermal gradient

The amplitude of the shift of the stability limit due to sea level fluctuations also depends on the local geothermal field. The variability of the limit of hydrate stability as a function of geothermal gradient for selected discrete water depths is given in figure 2.17. The amplitude of the sea level regression was 120 m during calculation. Bottom water temperature is 1°C. These results show that the higher the geothermal gradient or heat flow in the area of hydrate occurrence, the smaller the difference between the initial and final stability limit due to such a sea level fall. Curves connecting points of equal variation of the stability limit due to a 120 m sea level regression as a function of geothermal gradient are then shown in figure 2.18, assuming a bottom temperature of 1°C. During calculation, windows of 20 m water depth were combined with windows of 0.0005°C·m-1 of geothermal gradient. This figure is also characterised by the high sensitivity of the stability limit at shallow water depths and low geothermal fields.

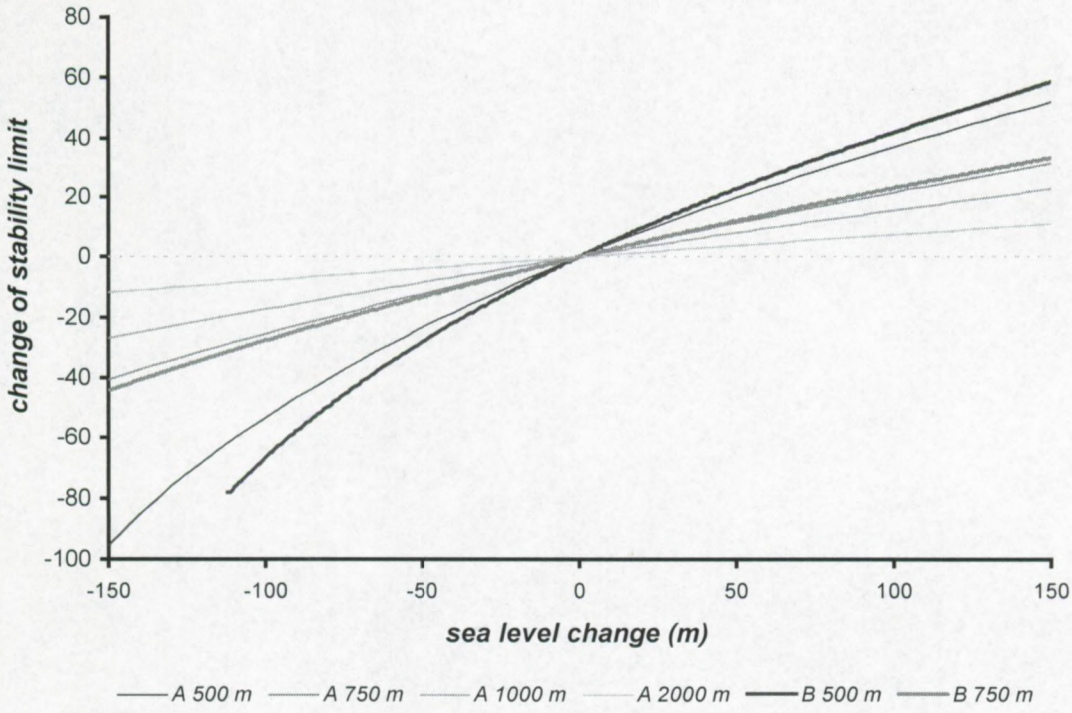

***Figure 2.14**: Change of the extent of the stability limit at some discrete water depths characterized by bottom water temperatures of 1°C (A) or 3°C (B) and geothermal gradients of 0.050°C·m^{-1}.*

It is important to mention that a pressure-induced shift of the HSZ toward less favourable conditions affects the hydrates at their stability limit, resulting in hydrate dissociation at the base of the initial hydrate stability zone over a depth range of cm up to tens of m. Pressure induced hydrate decomposition is therefore called a bottom-up destabilisation. It is worth noting that changes of the parameters will only result in quantitative differences, showing the same qualitative behaviour as discussed.

2.2.2
Application: Evolution of the HSZ under influence of eustatic sea level fluctuations during the last 210 ka

The above situation just describes a few snapshots of changes between two discrete moments in time. The evolution of the extent of the HSZ during the last 210 ka as a consequence of pure eustatic sea level changes according to the sea level curve of *Fleming et al.* [*1998*] is investigated as well as under steady-state geothermal conditions. Since only bulk conditions of the theoretical extent of the stability field are considered supposing permeable strata above the hydrate stability limit, the rate of change is not important. The average rate of change during the last 210 ka for the intervals of the *Fleming* sea level curve varies and has a peak amplitude of 15 m·ka^{-1}. In a first stage, the sub-bottom depth of the methane HSZ was calculated for every peak of the sea level curve for discrete water depths and fixed geothermal gradients. The extent was determined using a similar program that uses the numerical values of the discrete sea level fluctuations from *Fleming et al.* [*1998*] as an input file, and calculates the stability limit with the same procedure as discussed above (geothermal gradient and bottom water temperature are user-defined parameters), taking into consideration relative sea level fluctuations. Obviously, since the present-day sea level appears to be the maximum over the last 210 ka, the extent of the stability field of natural gas hydrates reaches maximum sub-bottom depths.

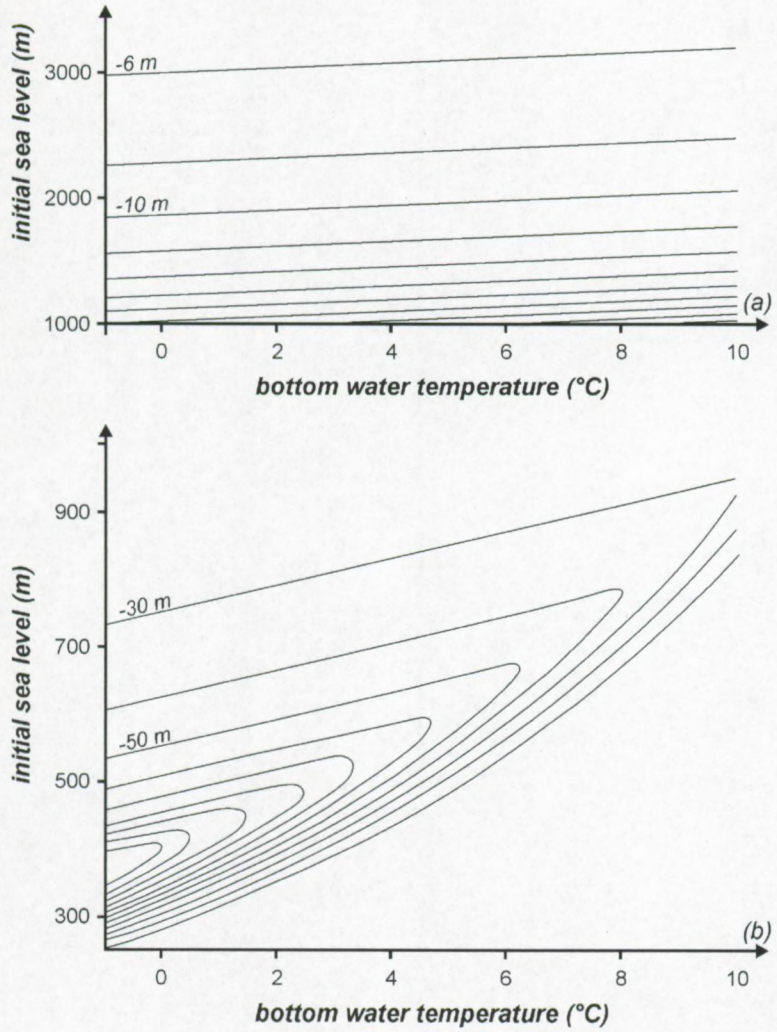

***Figure 2.15**: Shrinking of the vertical extent of the HSZ due to sea level falls of 120 m as a function of bottom water temperature. Geothermal gradient was 0.050°C·m^{-1}. (a) situation between 1000 and 3000 m with 2 m intervals; (b) situation between 250 and 1000 m, with 10 m interval.*

An example of the evolution of the hydrate stability field under fixed geothermal conditions during the last 210 ka is given in figure 2.19a using a geothermal gradient of 0.050°C/m and a 1°C bottom water temperature for variable initial water depths between 250 and 4000 m. Water depth interval during calculation was 5 m. The trend closely follows the eustatic sea level curve shown in figure 2.10. Transects of this figure for discrete water depths of 1000, 2000, 3000 and 4000 m are given in figure 2.19b. The rate of change of the vertical extent of the HSZ for these discrete water depths is shown in figure 2.19c.

These figures only represent a very limited spectrum of the possible variations of the methane HSZ in an average salt water environment with specified geothermal parameters. The program included allows the user to determine the change of the stability field with different values of sea level change, bottom water temperature and geothermal gradient for methane hydrates in both a fresh and salt water environment, as well as for other hydrate compositions that obey a similar analytical phase boundary equation.

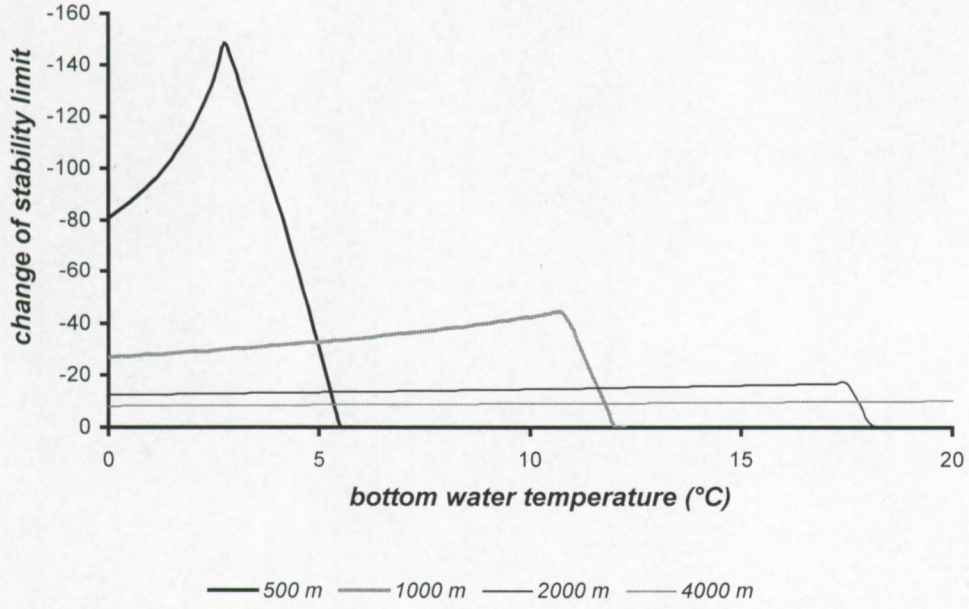

***Figure 2.16**: Variation of the methane hydrate stability limit for discrete water depths as a function bottom temperature, as a result of a 120 m sea level drop. Geothermal gradient was 0.035°C·m⁻¹.*

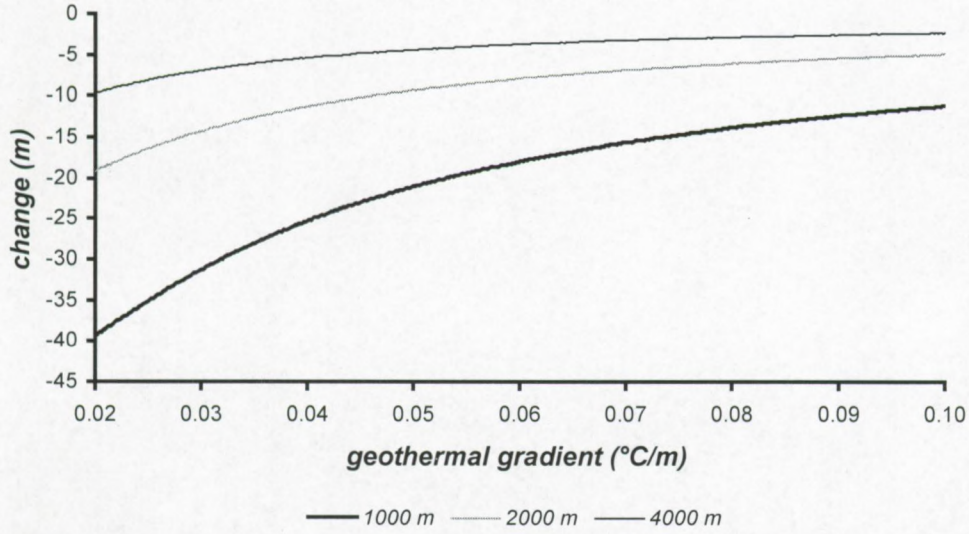

***Figure 2.17**: Variability of the extent of the methane HSZ due to a sea level fall of 120 m, as a function of geothermal gradient for discrete initial water depths of 1000, 2000 and 4000 m. A uniform bottom water temperature of 1°C was assumed during calculation.*

Using these figures, it again becomes clear that the variability of the hydrate stability limit closely follows the amplitude of the eustatic sea level curve with time showing an inverted trend. Even within the deep oceanic basins, the sea level changes documented since 210 ka BP are reflected within the variability of the extent of the HSZ but with much smaller amplitude. The amplitude of the variation is the highest in the shelf and upper slope areas where fluctuations of more than 20 meter are observed, while in the deep basins (> 3000 m) differences of only a few meters occur. In those shallow areas, the rate of change – thus the sensitivity to sea level changes – is much higher as well.

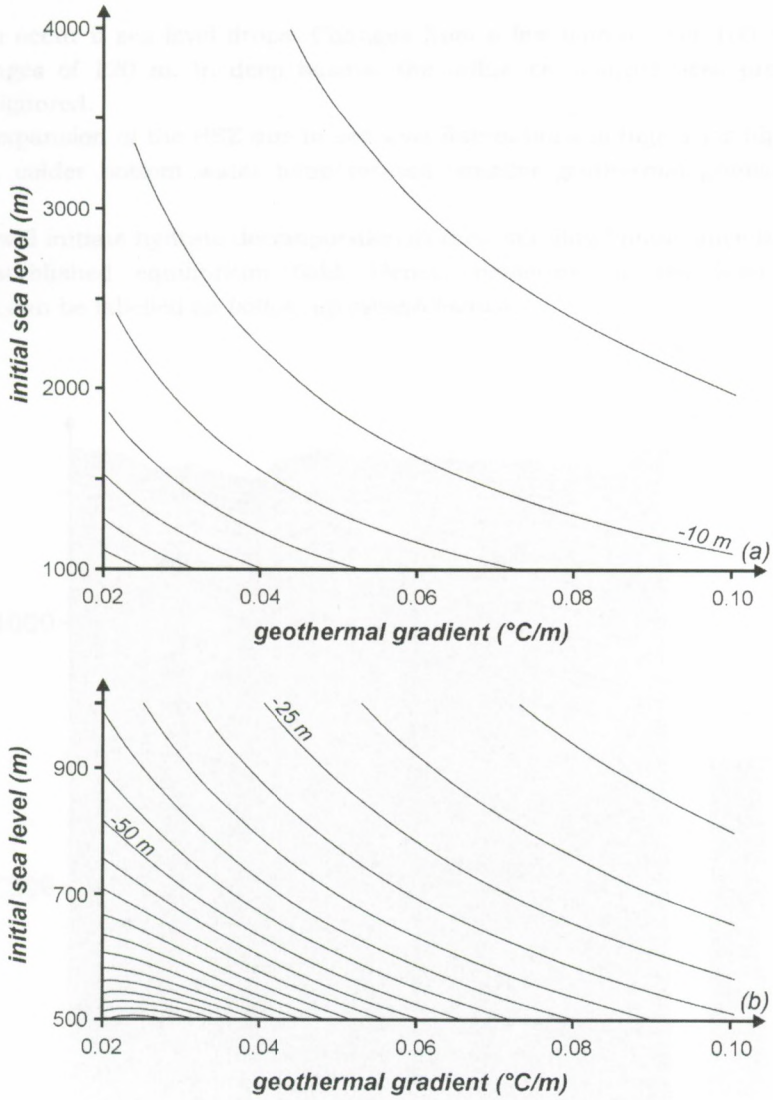

***Figure 2.18**: Variation of the methane HSZ caused by a 120 m sea level fall with bottom temperature of 1 °C, as a function of geothermal gradient. Interval distance is 5 m.*

2.2.3
Conclusions: sea level changes vs. hydrate stability

In this paragraph, a detailed discussion of the influence of eustatic sea level changes on the extent of the theoretical methane HSZ is presented, based on an analytical expression of the 3-phase methane hydrate equilibrium curve. Not only qualitative pictures are shown, but also quantitative results and numerical values are presented throughout this chapter, illustrating the effect of the diverse parameters occurring. A few striking facts related to sea level fluctuations and the variability of the hydrate stability limits can be summarised as follows:

- ➔ The influence of sea level changes on hydrate stability conditions is equivalent to shifting the 3-phase equilibrium curve according to the pressure change when superimposed on a cross-section of the sub-surface.
- ➔ Pure sea level rise results in deepening of the hydrate stability limit in the sedimentary section. Pure sea level fall results in reduced hydrate stability. Theoretically and considering pure hydrostatic pressure distribution within the sediments, even the smallest change of sea level will influence the extent of the HSZ.
- ➔ The shift of the stability limit is strongly dependent of the amplitude of the sea level change and the overlying water column. On the shelf and slope areas dramatic changes of the stability

conditions can occur if sea level drops. Changes from a few tens to over 100 m are observed for sea level changes of 120 m. In deep basins, the influence is much less pronounced and can sometimes be ignored.

➔ Shrinking or expansion of the HSZ due to sea level fluctuations is higher for higher-amplitude sea level changes, colder bottom water temperatures, smaller geothermal gradients and shallower water areas.

➔ Sea level falls will initiate hydrate decomposition at their stability limits, since this zone falls out of the newly established equilibrium field. Hence, pressure- or sea level induced hydrate decomposition can be labelled as *bottom-up destabilisation*.

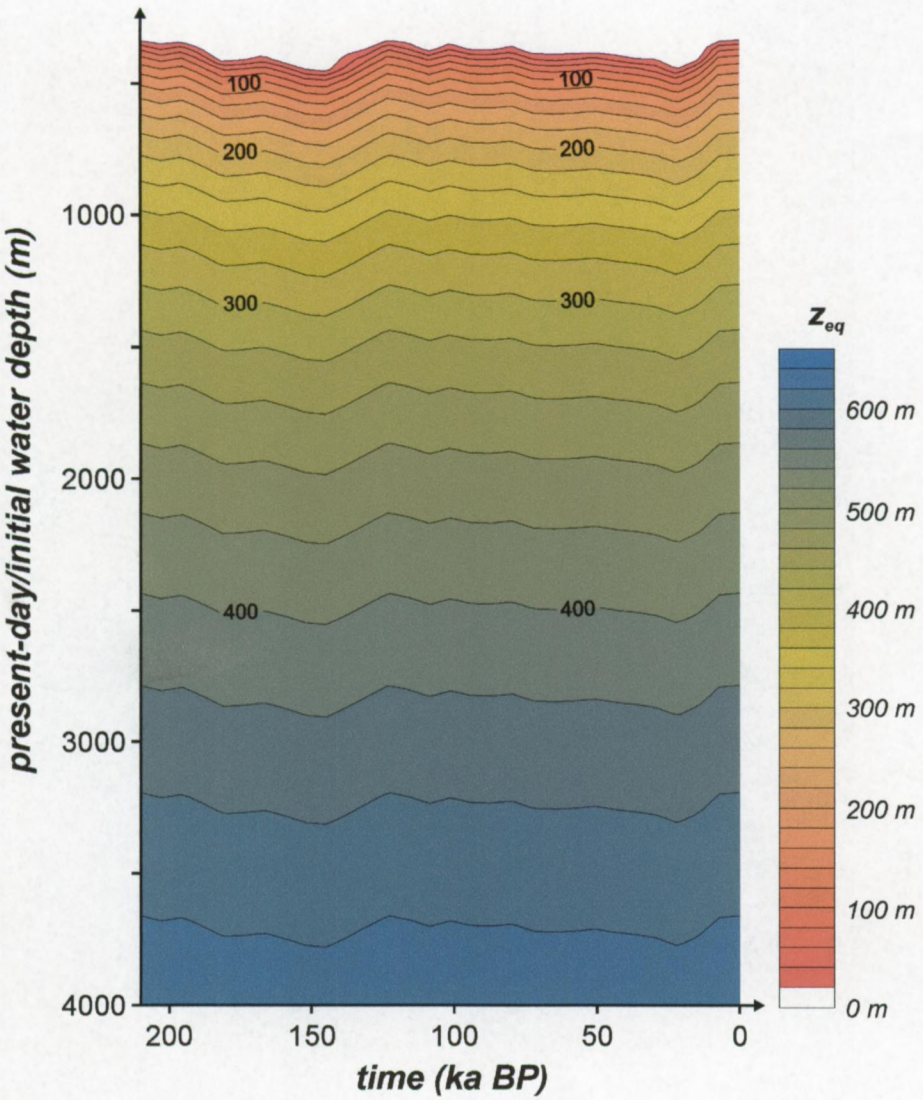

***Figure 2.19a**: Evolution of iso-sub-bottom depths of the limit of the HSZ during the last 210 ka, according to the sea level curve of Fleming et al. [1998]. Geothermal gradient was 0.050°C·m-1, bottom water temperature was 1°C. More details are shown in figures 10b & 10c*

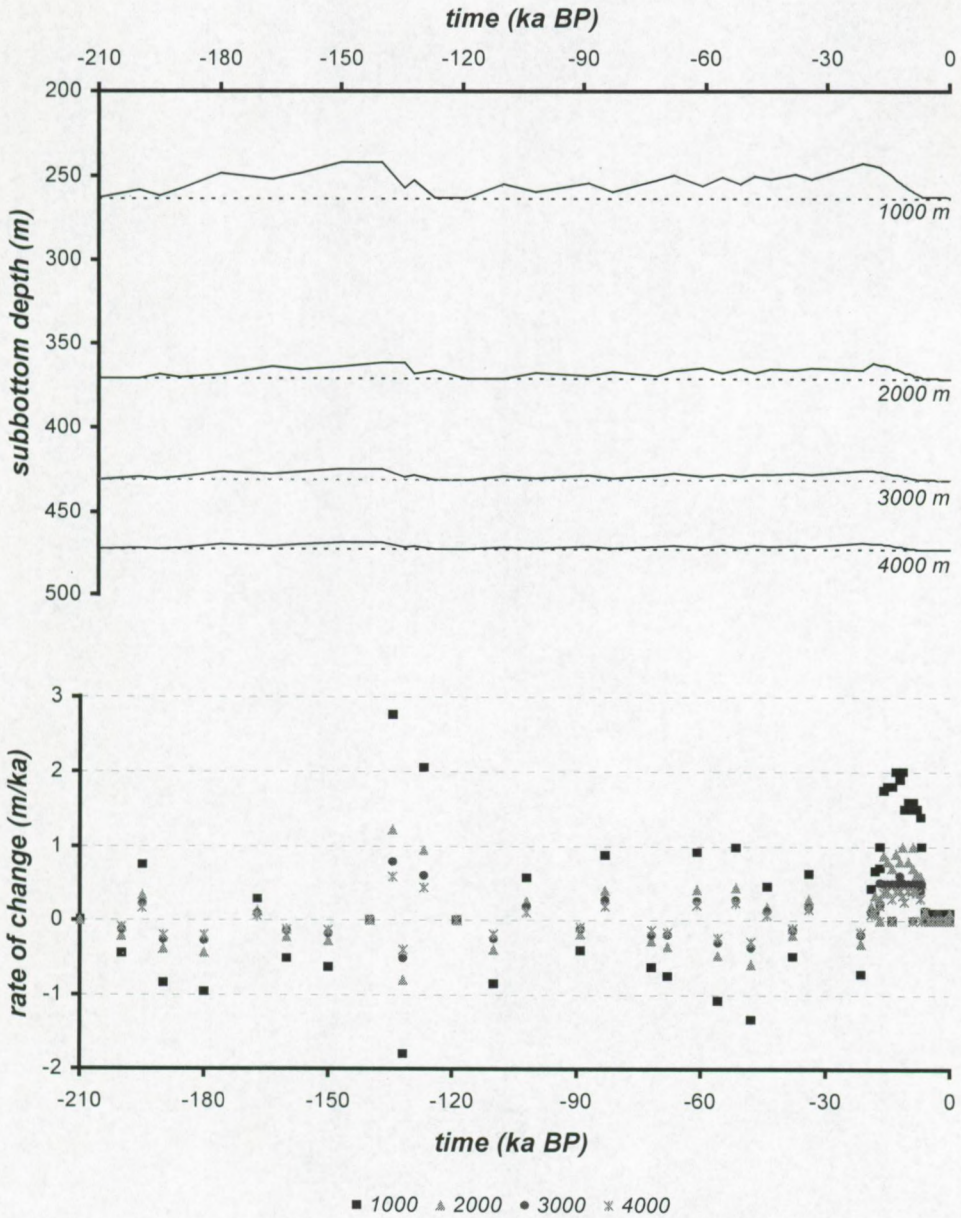

***Figure 2.19b, c**: Variation of the methane hydrate stability limit since 210 ka BP for discrete water depths (b, above) and the mean rate of change of the stability limit during the same time span for the same discrete water depths (c, below). The geothermal field used during calculation was the same as for figure 2.19a.*

2.3
Effect of fluctuations of the sub-bottom temperature profile on the extent of the HSZ

2.3.1
Theoretical aspects: sub-bottom temperature profiles

In this section, fluctuations of the bottom water temperature and subsequent curvature of the sub-bottom temperature profile with time is discussed in respect to the extent of the methane HSZ. The key question is in how far a thermal pulse exposed at the seabed will penetrate the subsurface and alter the *in situ* hydrate stability conditions with time. While pressure reduction causes an upward shift of the hydrate stability limit, and hence, basically initiates hydrate dissociation at their equilibrium limits, a temperature pulse of the bottom water can also influence shallower hydrates. Therefore, the amplitude of the thermal pulse is of importance. Most recovered hydrate samples were retrieved form a sediment section well above the phase boundary, i.e. at lower *in situ* temperatures [*Booth et al., 1998*]. Hence it is important to consider hydrates throughout the entire section. No pressure-induced effects are taken into consideration at present. In this case, thermal dissociation of hydrates in oceanic or lacustrine sediments requires in the first place heating of the porous medium until the hydrate equilibrium limit is reached. At that time, decomposition of the hydrate structure can occur, requiring extra heat for dissociation defined as being the enthalpy change to decompose the hydrate phase to a vapour and aqueous phase. Note that in case of changing bottom water temperatures, the position of the 3-phase equilibrium curve is not altered due to the temperature change when superimposed on a cross-section of the sub-surface.

As mentioned before, in case of interconnected pore spaces, sea level changes lead to an immediate effect on the (hydrostatic) pore pressure distribution. Thermal pulses related to variations in bottom water temperature on the other hand will need time to penetrate the subsurface and influence the geothermal gradient. The thermal regime of the uppermost sediment section is controlled by the thermal properties of the sediments and the heat flow coming from deeper parts of the basin. In an ideal homogeneous medium with constant surface temperature T_0, the sub-bottom temperature profile is a linear function of burial depth with temperature gradient G.

$$T_{st}\langle z\rangle = T_0 + G \cdot z \qquad [1]$$

with
- G the geothermal gradient
- T_0 the bottom water temperature
- z the sub-bottom depth

This equation represents a steady-state situation, i.e. a situation with fixed geothermal gradient and where bottom water temperature was maintained over a longer time relative to temperature changes. Sudden or gradual fluctuation of bottom water temperature forces the system to leave the steady-state condition and the linear approximation. The sub-bottom temperature profile will be modified (curved), but not at a constant rate. The one-dimensional new sub-bottom temperature profile can then be considered as a disturbance of the primary steady-state conditions:

$$T\langle z,t\rangle = T_{st}\langle z\rangle + \Omega\langle z,t\rangle \qquad [2]$$

with $\Omega\langle z,t\rangle$ the deviation from the steady-state situation as a function of time t and burial depth z in the sediments. In order to solve the above equation, different boundary condition have to be imposed as follows (seabed: $z = 0$, assume z positive at burial depth):

$$T\langle z,0\rangle = T_{st}\langle z\rangle \qquad z \geq 0 \qquad [3]$$

$$\Omega\langle 0,t\rangle = \tau\langle t\rangle \qquad t \geq 0 \qquad [4]$$

$$\Omega\langle z,0\rangle = 0 \qquad z \geq 0 \qquad [5]$$

Equation [3] states that in the initial phase the sub-bottom temperature profile is the steady-state condition. Equation [4] represents the bottom water temperature change with time-variable amplitude τ. Equation [5] states that the change of the sub-bottom temperature profile in the initial phase is zero, and it is a consequence of equation [3]. Assuming an isotropic, continuous and homogeneous medium without mass movement or energy production/consumption, the governing one-dimensional heat flow equations are:

$$\frac{\partial}{\partial t}T\langle z,t\rangle = \frac{\lambda}{\rho c}\frac{\partial^2}{\partial z^2}T\langle z,t\rangle \quad \text{or} \quad \frac{\partial}{\partial t}\Omega\langle z,t\rangle = \frac{\lambda}{\rho c}\frac{\partial^2}{\partial z^2}\Omega\langle z,t\rangle \qquad [6]$$

or $$\left[\frac{\partial^2}{\partial z^2} - \frac{1}{\bar{\kappa}}\frac{\partial}{\partial t}\right]T\langle z,t\rangle = 0 \qquad \left[\frac{\partial^2}{\partial z^2} - \frac{1}{\bar{\kappa}}\frac{\partial}{\partial t}\right]\Omega\langle z,t\rangle = 0$$

with $$\bar{\kappa} = \frac{\lambda}{\rho c}$$

with $\bar{\kappa}$ the thermal diffusivity of the medium, as the ratio of the thermal conductivity and the product of the density and the heat capacity. In this chapter, a thermal diffusivity representative for marine sediments of 4.3·10-7 $m^2 \cdot s^{-1}$ was used [*Rempel & Buffett, 1998*].
In three dimensions, equation [6] is written as

$$\left[\vec{\nabla}^2 - \frac{1}{\bar{\kappa}}\frac{\partial}{\partial t}\right]T\langle \vec{\mathbf{r}},t\rangle = 0 \quad \text{or} \quad \left[\vec{\nabla}^2 - \frac{1}{\bar{\kappa}}\frac{\partial}{\partial t}\right]\Omega\langle \vec{\mathbf{r}},t\rangle = 0 \qquad [6']$$

The steady-state equation [1] obviously is a solution of the one-dimensional heat flow equation [6].

The effect of changing bottom water temperatures upon the sub-bottom temperature profile can be written as follows [*Carslaw & Jaeger, 1959*]:

$$\Omega\langle z,t\rangle = \Delta T \cdot \Gamma\left(\frac{n}{2}+1\right)\cdot t^{n/2}\cdot 2^n \cdot i^n Erfc\left(\frac{z}{2\sqrt{\bar{\kappa}t}}\right) \qquad [7]$$

with $$Erfc(x) = \frac{2}{\sqrt{\pi}}\int_x^{+\infty}\exp\left(-y^2\right)dy = 1 - Erf(x) = 1 - \frac{2}{\sqrt{\pi}}\left[\sum_{n\geq 0}\frac{(-1)^n}{(2n+1)}\frac{x^{2n+1}}{n!}\right] \qquad [8]$$

$$i^n Erfc(x) = \int_x^{+\infty} i^{(n-1)}Erfc(\chi)d\chi \qquad n = 1, 2, \ldots \qquad [8']$$

and $$\Gamma(\zeta) \equiv \int_0^{\infty}\exp(-\chi)\cdot\chi^{\zeta-1}d\chi = \lim_{m\to+\infty}\frac{1\cdot 2\cdot\ldots\cdot m}{\zeta\cdot(\zeta+1)\cdot(\zeta+2)\cdot\ldots\cdot(\zeta+m)}m^{\zeta} \qquad [9]$$

i^nErfc is the repeated integral of the complementary error function while Γ is the gamma-function [*Arfken, 1985*]. The explicit dependence of the temperature profile on time is a striking feature in the discussion of the effect of bottom temperature changes onto the methane hydrate stability evolution with time. In this case, the porous medium is considered to be a good approximation of a solid, with averaged thermal properties.

Here, only three specific solutions of the above equation that can describe a wide range of features observed in nature will be discussed. The first one is a sudden discontinuous step of the bottom water

temperature that can be used for those situations in which the temperature change is significantly faster than other environmental or geological changes. The second solution is a linear change of the bottom temperature with time as a simplified situation for non-instantaneous temperature changes. Finally, periodic temperature fluctuations are introduced, a phenomenon relevant for basins with known seasonal or longer terms bottom water circulation processes.

Due to the fact that the temperature profile is no longer a linear function of burial depth, a similar approach as was used in the previous paragraph discussing the influence of sea level changes on the stability limit given by equations [1, 2] cannot be used. Nevertheless, the same but modified algorithm can be applied.

2.3.1a Instantaneous discontinuous temperature change

During the last deglaciation and Holocene, there is evidence from shallow sediment cores of very rapid deep-water temperature fluctuations. These changes may be due to fast changes in the conveyor belt mechanism [*Bianchi & McCave, 1999*], i.e. a complex circulation of water masses with different densities (salt) and heat budgets, important for global climate conditions. Modelling suggested that the North Atlantic Deep Water (NADW) is a non-linear system which is highly sensitive to changes in freshwater forcing [*Rahmstorf, 1995*]. For example, sudden injections of freshwater into the North Atlantic [*Manabe & Stouffer, 1995*] can trigger important changes in the flow pattern of NADW and hence the climate. If this current pattern covering the world's ocean basins comes to a halt, it would take hundreds to thousands of years for the currents to be reinstated [*Broecker, 1995*]. Meanwhile, the bottom will be swept by water masses with different temperatures. *Kennett et al.* [*2000*] found evidence of dramatic warming in upper intermediate waters in the Santa Barbara Basin during the first decades of interglacials and interstadials, in concert with rapid atmospheric methane increases. The temperature is related to deep-sea thermohaline circulation patterns. Bottom water temperatures were warmer during interstadials and colder during stadials with rapid changes at the transitions. The amplitude change can be several degrees, and can occur within a time span of decades [e.g. *Haq, 1998*]. Oscillations of the benthic $\delta^{13}C$ reflect extreme environmental changes, explained by changing CH_4 gradients [*Kennett et al., 2000*].

Since gas hydrates have strict thermodynamical stability conditions and are located close to areas with prominent bottom water variability (just a few tens to hundreds of meters sub-bottom depth on continental margin and slope areas), such fluctuations of the bottom water mass will have an impact on the extent of the HSZ with time.

Having this in mind, bottom water temperature fluctuations from polar to temperate (or inverse) temperatures can be considered to occur with full amplitude at a certain moment, relative to geological time scales. A sudden discontinuous change of surface temperature with amplitude ΔT at time t_0 is described by the following equation:

$$\tau(t) = \begin{cases} T_0 & t < t_0 \\ T_0 + \Delta T & t \geq t_0 \end{cases} \quad \text{for} \qquad [10]$$

Then, a solution of the governing differential equation [6] starting from a steady-state geothermal field is written as:

$$T\langle z,t\rangle = T_0 + G \cdot z + \Delta T \cdot Erfc\left(\frac{z}{2\sqrt{\kappa t}}\right) \qquad [11]$$

i.e. equation [7] with n=0. The complementary error function *Erfc* is characterised by a fast decrease of amplitude with increasing positive arguments. If the argument exceeds ±2.35, the complementary

error function vanishes, i.e. the difference between the initial and final *in situ* temperature will be less than 1‰ of the amplitude of the bottom temperature change. Formula [11] indicates that at fixed times $t > t_0$, the bottom water temperature change will fade out within deeper sedimentary units (increasing z values) and will approach asymptotically the steady-state linear profile. If the time scale approaches infinity for finite burial depths, the argument of the complementary error function approaches zero, thus the temperature profile evolves towards a new steady-state situation with the same geothermal gradient but with new steady bottom water temperature being the sum of the initial bottom water temperature T_0 and the amplitude of the temperature change ΔT.

The behaviour of a changing geothermal field due to sudden temperature changes is independent of the water depth of the basins in which the temperature change occurs, while the equilibrium depth does depend on water depth. An important difference with the influence of sea level changes lies in the fact that even small sea level fluctuations will have an effect on the stability limit from the continental margin into deep oceanic or lacustrine basin while temperature changes might or might not influence the basal limit of hydrate stability. Hence, a different behaviour is expected concerning the behaviour of the BHSZ. The general idea is that in deep basins the BHSZ lies deeper, so more time is needed to influence the stability conditions. For example, using the same thermal diffusivity value as before, deviations between the new geotherm and the original linear temperature profile can be neglected for sub-bottom depths of 60 m after 10 years, 175 m after 100 years and 550 m after 1000 years. Higher thermal diffusivity values will lead to higher amplitude of the temperature pulse penetrating the subsurface at a given time, i.e. the penetration goes faster.

A few typical temperature curves for some discrete time delays since the initiation of the thermal pulse from 3 to 7.5°C (cold to temperate conditions) res. 3 to 1°C (cold to polar conditions) is shown in figure 2.20 res. figure 2.21 for shallow water basins of 500 m depth and geothermal gradients of 0.050°C/m. Shortly after the change, the sub-bottom temperature profile will be highly curved in its uppermost part. The average temperature gradients will highly differ in different sedimentary sequences, since positive and negative gradients can occur. After a sufficiently long time, the profile will be much smoother again, and only resulting in a normal positive gradient, if no other thermal disturbance occurs.

Adding the analytical pressure-temperature phase boundary equation gives a qualitative image of the behaviour of the HSZ. A rather different situation of the HSZ is observed compared to the effect of pure eustatic sea level changes in case of such an instantaneous temperature rise. Depending of the amplitude of the temperature increase and the water depth, destabilisation can then occur either at the top or the base or throughout the entire interval of initial stability conditions. Hence, this situation is more complicated than sea level fluctuations in which only the base of the stability field is touched.

In order to determine quantitative results of the influence of changing bottom water temperatures onto the extent of the HSZ, the newly established sub-bottom temperature profile at time t has to be included in the algorithm[1]. During the analysis and programming, different critical parameters were defined (see also figure 2.22) and are calculated in the included program.

➔ *Critical temperature*
The first feature is the *critical temperature* linked to the height of the water column, and already used in paragraph 2.1. The critical temperature is defined as the unique hydrate equilibrium temperature at the pressure at the seabed.

[1] *The complementary error function and repeated integral forms are not defined in the available programming language version of TP, hence these functions are approximated by the series up to its 200th term according to [9] or their recurrence formula is used. Deviations or misfits are less than 0.5% relative to the error function for the first 2000 m of sub-bottom depth for average thermal diffusivity values.*

If the new bottom temperature is lower than this critical value, hydrates can be stable from their basal stability limit up to the lake floor or seabed. Analysis of the mathematical expression of the newly established temperature curve shows that only one intersection of the new temperature profile and the phase boundary exists. In this case, within time first the hydrates stored near the initial stability limit will be altered, and this base will migrate upwards (increasing bottom water temperature) or downwards (decreasing bottom water temperature).

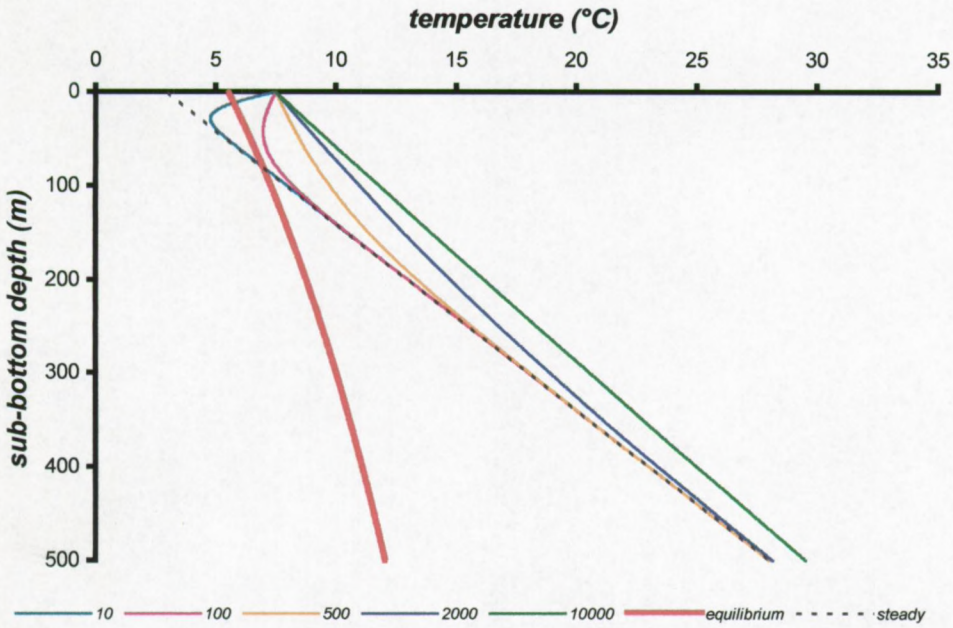

***Figure 2.20**: Sub-bottom temperature profiles and methane hydrate equilibrium curve during a sudden bottom water temperature increase from 3 to 7.5°C/m for different time slices.*

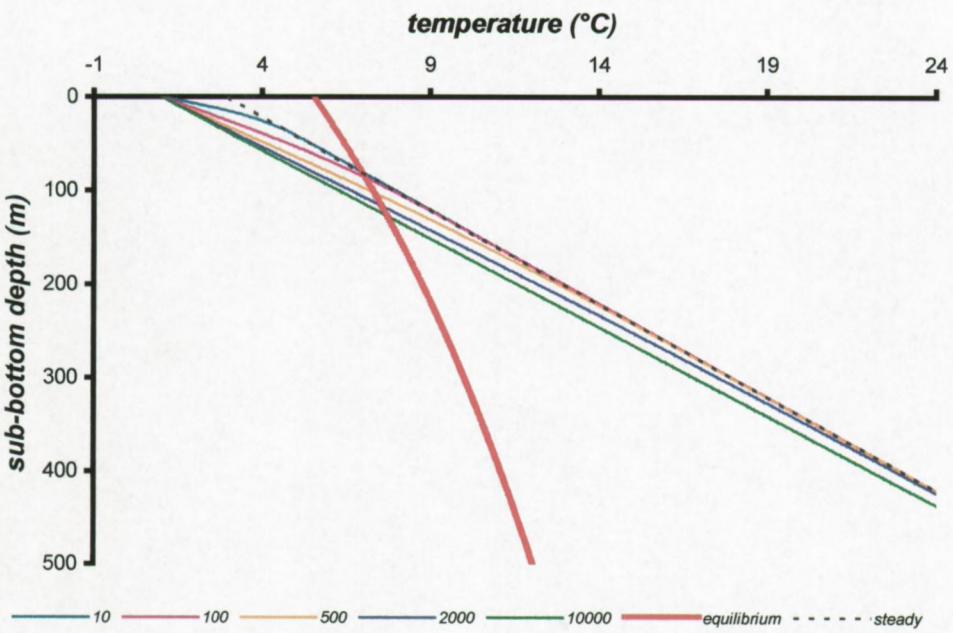

***Figure 2.21**: Sub-bottom temperature profiles and methane hydrate equilibrium curve during a sudden bottom water temperature decrease from 3 to 1°C/m for different time slices.*

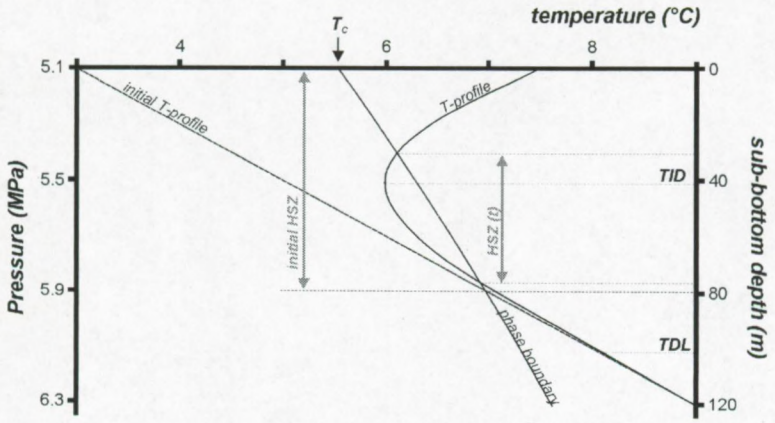

***Figure 2.22**: Change of the vertical extent of the HSZ after 40 years, supposing a sudden temperature rise from 3 to 7.5°C in a 500 m deep salt water basin. Also the parameters defined for facilitating the programming loops (critical temperature T_C, temperature deviation limit TDL, temperature inversion depth TID) are indicated for this particular case.*

If the new bottom temperature is higher than the critical value for the present water depth, the curved pattern at relatively shallow sub-bottom depths (first tens of meters) can cause local non-equilibrium conditions at the top of the stability field or throughout the entire pre-change stability field. At short time scales (years to tens of years), two intersections of the 3-phase equilibrium curve and the temperature profile can occur. With time, these intersections can disappear leaving a hydrate-free sediment section. If possible, the upper boundary of the stability field is determined as well, as the point in which physically the same basic equilibrium conditions are fulfilled.
It is obvious that this parameter depends on the hydrate composition and structure. Using the analytical phase boundary equation, the accuracy of this parameter is very high.

➔ *Temperature deviation limit*

A second parameter introduced, is the so-called *temperature deviation limit depth*. At this sub-bottom depth, the difference between the initial steady-state linear and final curved temperature profile vanishes (i.e. becomes less than 0.05°C). This parameter is determined with an accuracy of 0.5 m sub-bottom depth. Hence, at greater depths the initial steady-state linear temperature profile is valid and can be used for determining the stability limit. This value in used to minimise the calculation procedure and is very efficient for small time scales. No changes of the basal limit of the HSZ will occur as long as the deviation limit is smaller than the initial equilibrium limit. This parameter is directly related to the changing temperature conditions and is independent of water depth. Its position deepens with time. It is obvious from figure 2.22 that the deviation limit depth migrates deeper with time. This parameter also depends on the thermal diffusivity value used. For higher values, the deviation limit of the sub-bottom temperature profile will lie deeper in the sediments than that at lower values, independent of the hydrate structure or composition. This parameter is also independent of the initial geothermal gradient used.

➔ *Inversion depth*

A third parameter is the *inversion depth* for the final curved temperature profile, being defined as the depth at which the temperature profile changes from negative to positive interval (accuracy of 0.1 m) gradient values. If the *in situ* equilibrium temperature at the inversion depth is smaller than the temperature at this depth, then no hydrate stability is achieved in the entire section. Also this parameter is independent of water depth. This parameter is not relevant in the case of a temperature profile that is uniformly increasing with increasing burial depth and is in this case identically zero. This is the case for increasing bottom water temperatures after a sufficiently long time period, and it is always the case with decreasing bottom water temperatures. Higher res. lower thermal diffusivity values will result in higher res. lower values of inversion depths of the sub-bottom temperature profile at the same time. If the inversion depth is found at a certain sub-

bottom depth, then – dependent on the critical water depth/critical bottom temperature – *top-down dissociation* of hydrates is possible. Obviously, the inversion depth is smaller than the temperature deviation limit.

Figure 2.23 depicts the variability of the vertical extent of the HSZ if the bottom water temperature suddenly rises from 3 to 7.5°C. The situation is shown for a very short time period of 65 years following the temperature change. Water depth is again 500 m. Calculation was performed for every single year. Negative values of the change are still interpreted as an upward migration of the hydrate stability limit. In this case, especially the stability in the uppermost part of the sediments appears very sensitive to such a change. Only after more than 30 years, the basal limit of stability field is reached, and the stability limit decreases sharply. The green curve represents the change with time of the entire stability window, i.e. taking into account both the superficial and basal effects. However, it is questionable whether the bottom water fluctuation time can still be considered as immediate and with full amplitude on year scale. The effect of *bottom water temperature decrease* from 3 to 1°C – also shown in the figure 2.23 – over the same period of time results in increasing sub-bottom depths of stability from 29 years on. After 65 years the stability has increased with almost 4 m.

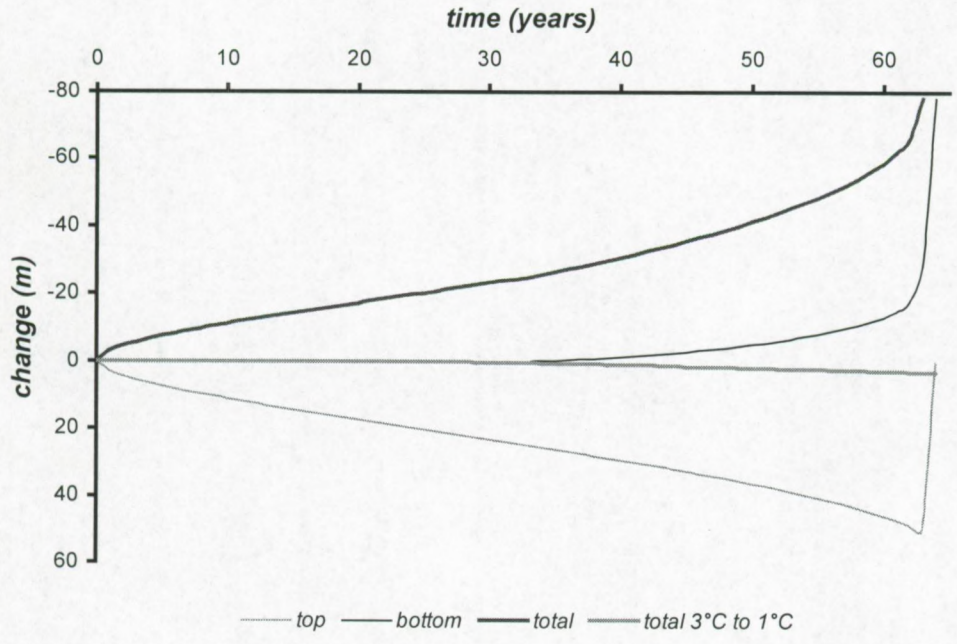

***Figure 2.23**: Sensitivity of the HSZ with time in a 500 m deep water basin, if bottom water temperature suddenly rises from 3 to 7.5°C. "top" represents the changes at the lake or sea bed (top-down destabilisation) while "bottom" shows the changes at the basal limit (bottom-up). "total" represents the total shrinking of the stability field caused by the temperature change. "total 3°C to 1°C" shows the variation of the stability field if the bottom water temperature decreases from 3°C to 1°C.*

As mentioned before, in deeper water basins the effect on the basal limit will be strongly delayed due to the increasing burial depth of the initial stability limit. The effect at the top of the sediment section will also be different, in the sense that in deeper basins the critical temperature is considerably higher (see figure 2.4), meaning that one needs much higher bottom water temperatures for having a similar top-down dissociation. Hence, the change at the surface is only important in shallow water areas.

Figure 2.24 shows the change of the basal limit of the HSZ as a function of time in case of a sudden bottom water temperature change from 3 to 7.5°C (i.e. the same situation as above) for different water depths. Note that the time scale is now of a different order of magnitude compared to figure 2.23. On this longer-term record, the change of the basal equilibrium limit occurs rather fast and is

predominantly taking place shortly but not immediately after the bottom water temperature change. The first 100 years after the temperature pulse, no change of the basal limit of the theoretical hydrate occurrence is present. Then, the main shift of the stability limit for a 650 m deep basin is observed between 100 and 1000 years after the change. For deeper basins, the delay is even bigger. In other terms, the rate of change of the stability field is lower in deeper basins. Next to that, the amplitude of the change is also considerably lower in deeper water areas but can still reach several tens of meters for deep basins. At longer time scales, the variation slows down, i.e. the sub-bottom temperature profile approaches new steady-state conditions.

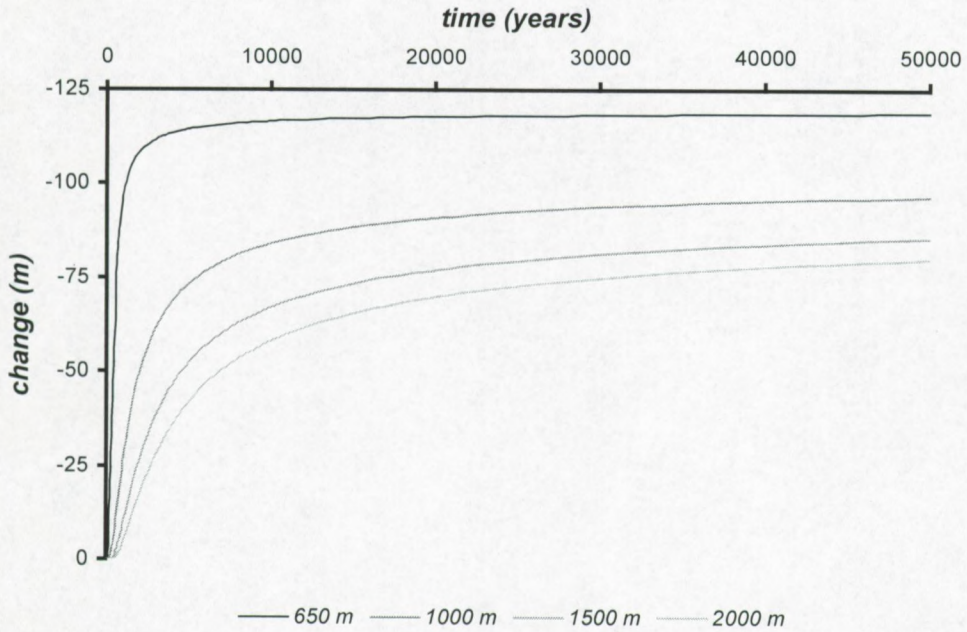

***Figure 2.24a**: Shrinking of the vertical extent of the BHSZ with time for discrete water depths (650, 1000, 1500 & 2000 m), as a result of the sudden bottom water temperature increase from 3 to 7.5°C.*

As is seen, the shift of the basal stability limit due to a sudden temperature change can be of the same order of magnitude relative to the shift caused by sea level fluctuations. Figure 2.24b represents the similar situation for a temperature decrease from 3 to 1°C. Results are similar as for the temperature rise mentioned above.

The program included can be used to investigate the influence of any arbitrary combination of parameters for both fresh and average salt water environments and a variety of analytical phase boundary coefficients. Selecting this option of the program, once the thermal diffusivity value is defined, various situations with specific initial temperature, final temperature, steady-state geothermal gradient and water depth can be analysed.

2.3.1b Linear bottom temperature change with time

Knowing that bottom water temperature changes occurring with full amplitude at a specific time are not always realistic in geology and hence cannot be used for all geological situations and processes, hydrate stability conditions were investigated as well in the situation of a linear bottom water temperature change with time. A gradual change of the bottom water temperature requires a different solution of the differential equation [6] and other boundary conditions. The simplest case of a linear bottom temperature pulse with amplitude ΔT between times 0 and Δt is written as:

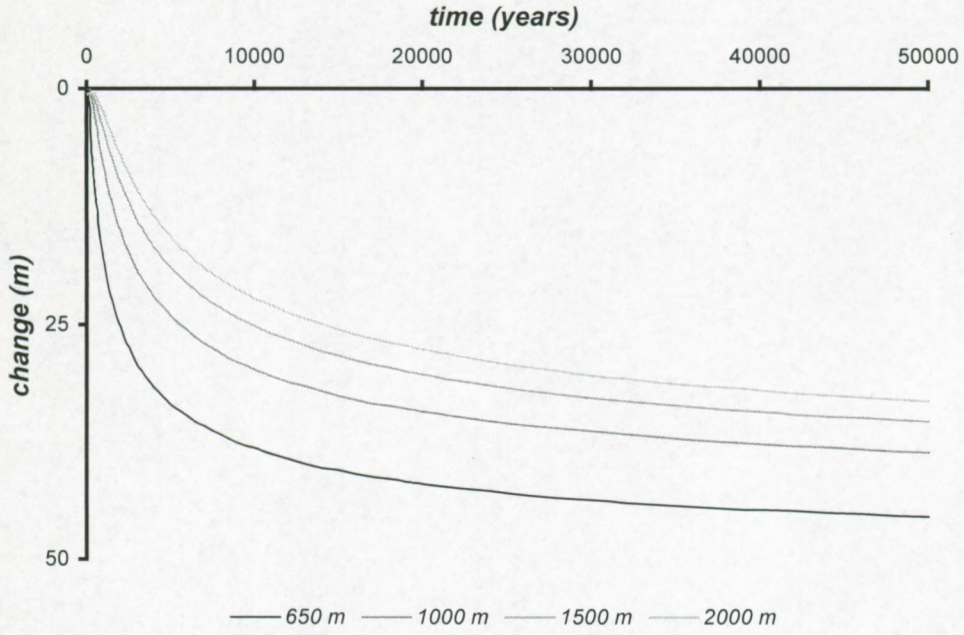

***Figure 2.24b**: Expansion of the vertical extent of the BHSZ with time for discrete water depths (650, 1000, 1500 & 2000 m), as a result of the sudden bottom water temperature decrease from 3 to 1°C.*

$$\tau\langle t\rangle = \Omega\langle 0,t\rangle = \begin{cases} \Delta T \cdot \dfrac{t}{\Delta t} = \alpha \cdot t & 0 \le t \le \Delta t \\ 0 & t \le 0 \because t \ge \Delta t \end{cases}$$

Resulting in a final divergence of the steady-state temperature profile:

$$\Omega\langle z, t \le \Delta t\rangle = 4\alpha \cdot t \cdot i^2 Erfc\left(\frac{z}{2\sqrt{\kappa t}}\right)$$
$$= \alpha \cdot t \cdot \left[\left(1 + \frac{z^2}{2\kappa t}\right) \cdot Erfc\left(\frac{z}{2\sqrt{\kappa t}}\right) - \frac{z}{\sqrt{\pi \kappa t}} \cdot \exp\left(-\frac{z^2}{4\kappa t}\right)\right] \quad [12]$$

$$\Omega\langle z, t \ge \Delta t\rangle = 4 \cdot \Delta T \cdot i^2 Erfc\left(\frac{z}{2\sqrt{\kappa t}}\right)$$
$$= \Delta T \cdot \left[\left(1 + \frac{z^2}{2\kappa t}\right) \cdot Erfc\left(\frac{z}{2\sqrt{\kappa t}}\right) - \frac{z}{\sqrt{\pi \kappa t}} \cdot \exp\left(-\frac{z^2}{4\kappa t}\right)\right] \quad [12']$$

$$\zeta = \frac{z}{2\sqrt{\kappa t}}$$

i.e. equation [7] with n=2 and *a* the rate of change of the bottom water temperature. Here, the general recurrence relation for the repeated integrals for error functions was used. Formula [12] describes the evolution with time of the sub-bottom temperature profile within the time interval of the temperature change. [12'] then describes the profile at a later stage, once the temperature change has occurred with full amplitude. Analysis of the sub-bottom temperature profile reveals that, if the bottom water temperature increases with time, the *in situ* sub-bottom temperature profile will be higher than or equal to the initial steady-state temperature profile. In other words, the initial *in situ* steady-state condition is a minimum *in situ* temperature in case of temperature rise. If bottom water temperature

decreases, a similar but opposite reasoning is valid. Furthermore, the *in situ* change of the temperature will be always less than in case of an instantaneous change of temperature at the bottom, described in the previous paragraph.

Here also specific points similar to those defined in the previous paragraph can be defined. As a consequence, in this case also top-down destabilisation of hydrates is theoretically possible with time, if the conditions approach the critical temperature and depth conditions, so this phenomenon is restricted to relatively shallow basins. However, if the rate of change at the bottom is rather slow, then such a top-down destabilisation will not occur even within shallow basins. This can easily be understood, knowing that the faster the temperature change happens with full amplitude, the closer the linear change approaches the instantaneous change. Having this in mind, this option does not take into account fast changes of the temperature at the bottom. The limit value of the temperature divergence terms [12] or [12'] approaches zero for small t, so the situation is close to the initial temperature profile. At very long time scales (>> time scale of the temperature change), the temperature curve evolves towards new steady-state equilibrium conditions with constant fixed geothermal gradient identical to the initial value and the final bottom water temperature. If the bottom water temperature change is very slow, then the temperature curve behaves almost linearly with burial depth.

An example is given in figure 2.25 for a bottom water temperature rate of change of $0.0045°C \cdot a^{-1}$ during 1000 years in an average salt water basin of 500 m water depth. The situation with a linear bottom water temperature decrease with a rate of $0.002°C \cdot a^{-1}$ is shown in figure 2.26. The initial geothermal gradient in both cases is taken to be $0.050°C \cdot m^{-1}$.

The shrinking/extension of the vertical extent of the methane HSZ in a 500 m deep basin if the temperature linearly increases during 1000 years as in figures 2.25 and 2.26, is shown in figure 2.27. Note that the rate of change is different. Once the temperature change at the sea bed is complete, the change of the stability field with time varies slower and almost linearly. The initial steady-state equilibrium limit is found at 79 m sub-bottom depth. The inverse plotting of the y-axis again has the intention of clearly showing the movement of the base of the stability field relative to the lake or sea bed.

For deeper basins, the change will be smaller since the hydrate stability limit will lie deeper into the sediments. Some results of the equilibrium sub-bottom depths for pure methane hydrates in an average salt water environment using the same parameters as above (linear temperature rise from 3 to 7.5°C over a time span of 1000 years) but for deeper water basins are summarised in Table 2.2.

The fact that the evolution of the theoretical base of the methane hydrate strongly depends on the time scale, the amplitude of the bottom temperature change and the rate of change and hence strongly depends on local conditions makes it difficult to generate overview pictures since too many assumptions have to be made. Therefore, such figures were not made. The program included however can easily provide the necessary information for specific changes. The user can then analyse the behaviour of the HSZ for various initial and final bottom water temperatures, steady-state geothermal gradients, rates of change of the bottom water temperature, times of interest after the initiation of the temperature change using a standard thermal diffusivity or define a new value. The reader is therefore invited to use this program for more detailed and relevant situations.

2.3.1c Bottom temperature oscillations

A final specific aspect of thermal disturbances of steady-state conditions mentioned here, is the case of oscillating bottom water temperatures. It is known that especially in relatively shallow basins, seasonal fluctuations of bottom water temperatures can occur. A theoretical approximation of oscillating bottom water temperatures with frequency f and the final temperature profile with depth can then be written as follows [*Carslaw & Jaeger, 1959*]:

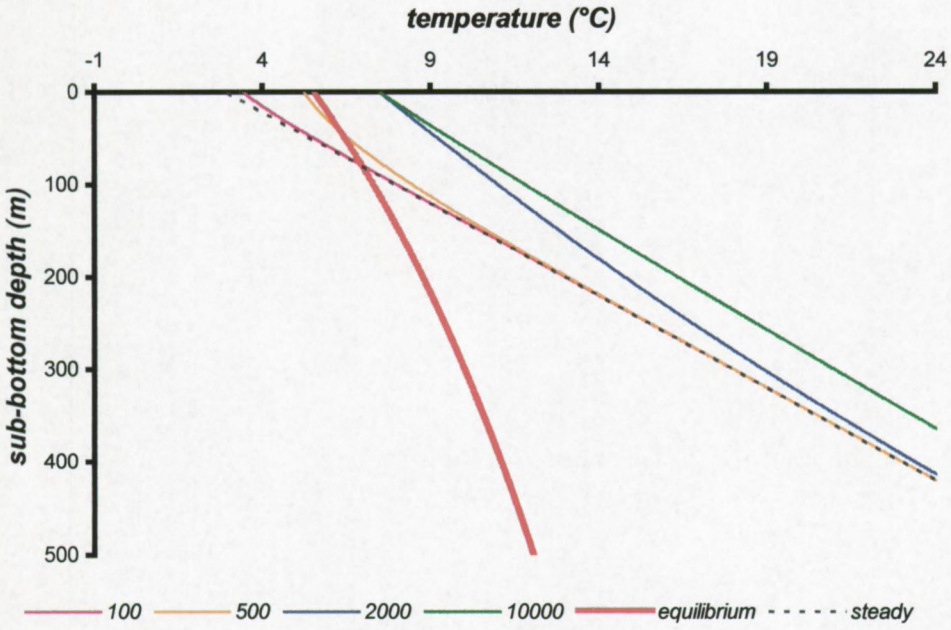

***Figure 2.25**: Influence of a linear bottom water temperature increase from 3.0 to 7.5°C over a period of 1000 years on the theoretical methane hydrate stability limit. Water depth is 500 m. The situation is shown for the initial situation and 100, 500, 1000 and 10000 years after the initiation of the temperature change.*

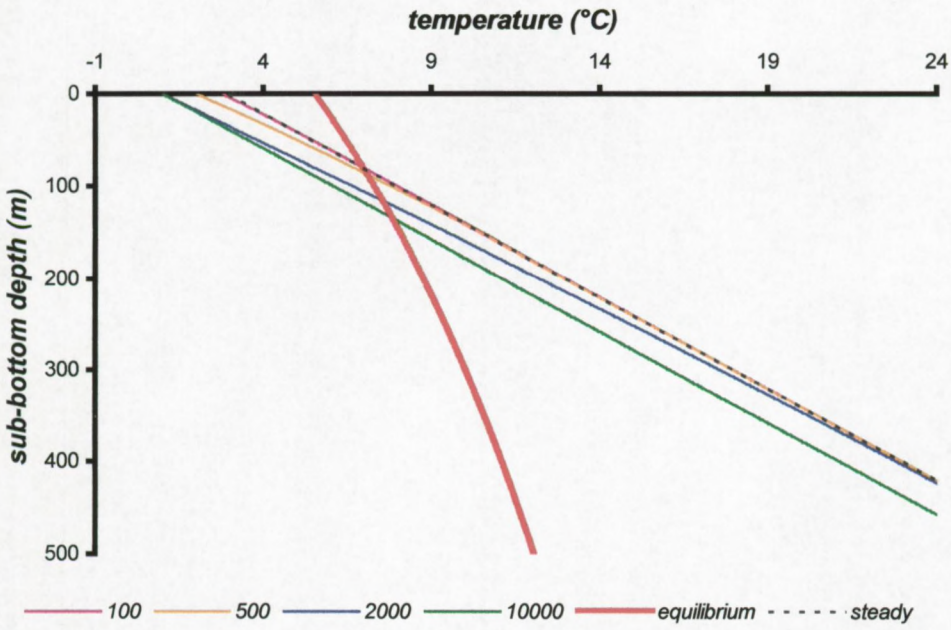

***Figure 2.26**: Influence of a linear bottom water temperature decrease from 3.0 to 1°C, i.e. opposite to situation of figure 2.25 using the same parameters. Rate of change of the bottom water temperature is –0.002°C/yr.*

$$\tau\langle t\rangle \propto \cos(\omega \cdot t - \varepsilon) = \cos(2\pi f \cdot t - \varepsilon) \quad [13]$$

$$T\langle z,t\rangle \propto \exp\left(-\sqrt{\frac{\omega}{2\kappa}} \cdot z\right) \cdot \cos\left(\omega \cdot t - \sqrt{\frac{\omega}{2\kappa}} \cdot z - \varepsilon\right) \quad [14]$$

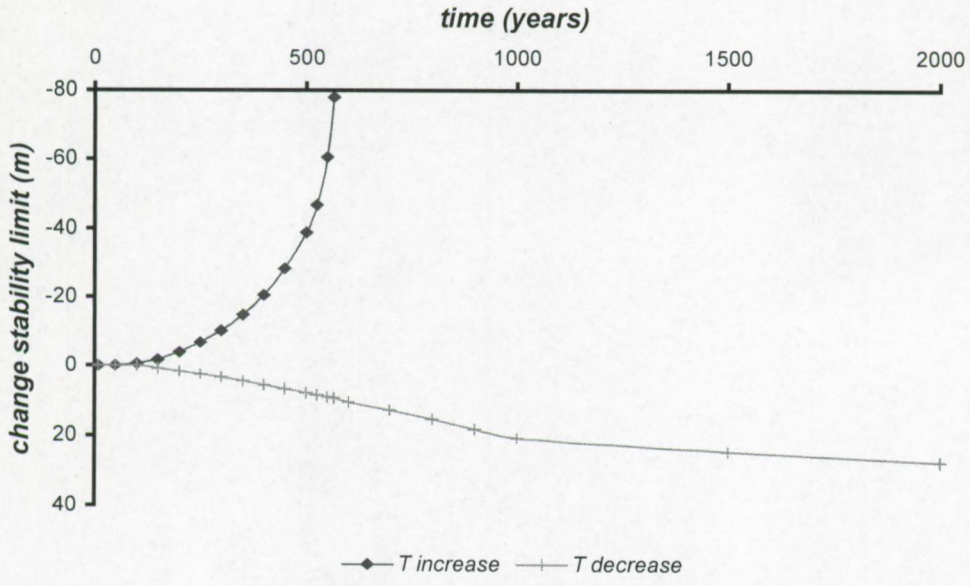

***Figure 2.27**: Change of the basal limit of the methane HSZ with time in a 500 m deep salt water basin. Bottom water temperature linearly increases from 3.0 to 7.5°C res. decreases from 3.0 to 1.0°C during 1000 years.*

time (years)	quantity	water depth (m) 1000	2000	3000	4000
0	bottom temperature (°C)	3	3	3	3
	equilibrium depth (m)	216.0	327.3	388.7	431.2
	average gradient (°C/m)	0.05	0.05	0.05	0.05
100	bottom temperature (°C)	3.45	3.45	3.45	3.45
	equilibrium depth (m)	216.0	327.3	388.7	431.2
	difference (m)	0.0	0.0	0.0	0.0
	average gradient (°C/m)	0.0480	0.0486	0.0489	0.0490
1000	bottom temperature (°C)	7.5	7.5	7.5	7.5
	equilibrium depth (m)	207.3	326.1	388.7	431.2
	difference (m)	-8.7	-1.2	0.0	0.0
	average gradient (°C/m)	0.0301	0.0364	0.0384	0.0396
10000	bottom temperature (°C)	7.5	7.5	7.5	7.5
	equilibrium depth (m)	150.9	291.0	361.6	409.0
	difference (m)	-65.1	-36.3	-27.1	-22.2
	average gradient (°C/m)	0.0387	0.0404	0.0411	0.0416
10000	bottom temperature (°C)	7.5	7.5	7.5	7.5
	equilibrium depth (m)	121.8	251.8	320.1	366.7
	difference (m)	-94.2	-75.5	-68.6	-64.5
	average gradient (°C/m)	0.0495	0.0461	0.0462	0.0462

***Table 2.2**: Examples illustrating the influence of gradual bottom water temperature change from 3.0 to 7.5°C over a period of 1000 years on the theoretical methane hydrate stability conditions in an average fresh water basin, for diverse water depths and time scales.*

Equation [13] represents an oscillating temperature wave with wavelength λ defined by

$$\lambda = \pi\sqrt{\frac{8\bar{\kappa}}{\omega}} = 2\sqrt{\frac{\pi\bar{\kappa}}{f}} \qquad [15]$$

From the above formula, it is clear that the amplitude of the temperature pulse rapidly diminishes with increasing burial depth and that this aspect is dependent of the pulsation frequency. The

amplitude obviously falls off more rapidly for large frequencies. The waves are strongly attenuated since at a distance of one wavelength below the sea or lake bed, the amplitude is reduced by a factor of $\exp(-2\pi) = 1.87 \cdot 10^{-3}$. In case of single yearly oscillations (period of $31.536 \cdot 10^7$ s) of the bottom water temperature, the frequency is $3.171 \cdot 10^{-9}$ Hz. The wavelength of the oscillation is then approximately only 13 m, supposing the same diffusivity parameter as used above. In general the temperature pulse coming from oscillations on a yearly base will not penetrate deep enough to touch the hydrates at several hundreds of meters sub-bottom depth. Short-term changes are even more restricted to the upper part of the sediment section. Here also the amplitude and the time frame of the thermal pulse are important in this discussion, together with the water depth and its critical equilibrium temperature.

The program included also has the option to determine the variability of the hydrate stability limit in case of oscillating bottom water temperatures according to equations [13] and [14]. The different parameters here are the thermal diffusivity, mean bottom water temperature, amplitude of the temperature change at the sea or lake floor, the mean geothermal gradient, the present water depth, the oscillation period and the time of interest.

A few examples for yearly oscillation of the bottom water temperature with surface amplitude of 2°C (mean temperature 5°C and mean geothermal gradient of $0.050°C \cdot m^{-1}$) and the effect on the stability limit are shown in figure 2.28. Water depth is taken to be 500 m, leading to a critical temperature of 5.54°C, well within the range of the bottom temperature change. The situation is sketched after 0.25, 0.35, 0.50 and 0.75 years, with phase of $\pi/2$.

The influence of periodic oscillations of the bottom water temperature is now considered for Lake Baikal conditions. Hydrates were recently retrieved from 20 cm sub-bottom depth [*Klerkx, pers. Comm.*] in a small crater in the axial part of the Southern Basin. Water depths range from 1200 to 1400 m in this central part. As can be seen from figure 2.4 or calculated using the program included, these water depths require critical temperatures of approximately 15.0 res. 16.3°C in this fresh water basin. The present-day temperature is only 3.2-3.4°C, so temperature fluctuations of the order of 12°C are necessary before dissociation of hydrates accumulations close to the lake bed as a consequence of fluctuations of bottom water temperature takes place.

But bottom water temperatures in the Baikal basins are believed to be very stable throughout the year. Divergence of the bottom water temperature is of the order of maximum 0.2°C [*Golmshtok et al., in press*]. Hence, such changes will not have any influence on the hydrate stability conditions since the water depth by far exceeds the necessary pressure requirements at the specific temperatures. The critical water depth at the present bottom water temperature is only 356 m.

In the Gulf of Mexico, such periodic fluctuations of bottom water temperature are known to be capable of locally destabilising hydrate accumulations at or close to the sea bed [*Milkov et al., in press*]. Shallow hydrate-rich spots are observed of both biogenic and thermogenic origin forming hydrate structures sI, sII and sH and are closely related to the presence of oil and gas seeps with chemosynthetic communities in water depths between 300 and 700 m. As shown above, especially in shallow basins the hydrate sensitivity to changes of water pressure or temperature is important since the thermodynamical conditions lie close to the critical values. Seasonal variations of the bottom water temperature are furthermore restricted to relatively shallow water depths. Bottom water temperature changes of approximately 1°C or even less can then be sufficient to initiate hydrate dissociation [*Milkov et al., in press*].

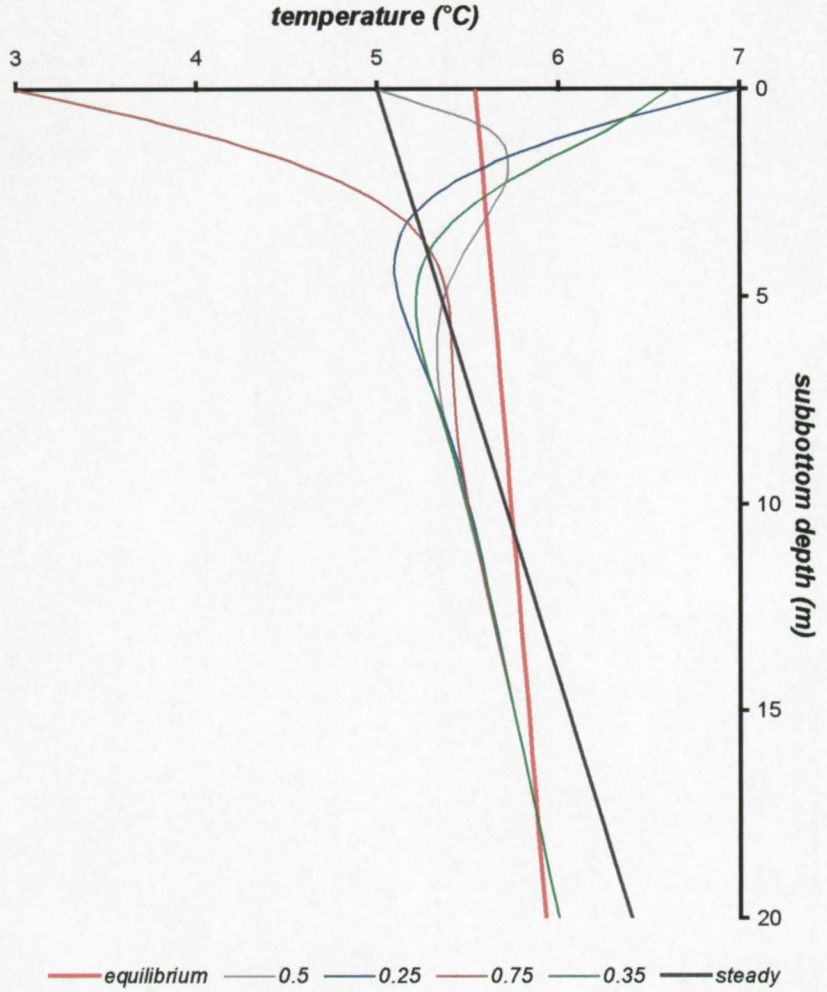

***Figure 2.28**: Influence of yearly bottom water temperature fluctuations with amplitude of 2°C at different times on the methane HSZ in a 500 m deep salt water basin with average bottom temperature of 5°C and geothermal gradient of 0.050°C·m^{-1}.*

An extra phenomenon of the Gulf of Mexico hydrate problem is the presence of warm-core eddies, associated with the Loop Current, propagating on the continental slope. The effect of such a current can be the sharp increase of temperature of several degrees at short time intervals (i.e. order of several months). In this case, other boundary conditions have to be applied. More details are provided in *Milkov et al.* [*in press*] and are not worked out here. Since this problem was not analysed, this situation is not included in the programs.

2.3.2
Discussion & Conclusions

2.3.2a Relevance to climatic changes

The figures shown in this paragraph clearly illustrate that changes of the bottom water temperature can have a significant effect on the theoretical extent of methane hydrate accumulations under natural conditions. Especially in shallow water areas (continental margins) where bottom water fluctuations do occur with higher amplitude [*Thiede, pers. comm.*], such changes should not be overlooked. For deeper basins however, long to very long time scales are required due to the increasing burial depth of

stability with increasing water depths. Hydrate dissociation due to increasing bottom water temperatures is a delayed effect, relative to the time of the initiation of the temperature fluctuation. The delay can be of the order of years to thousands of years.

The real-time sub-bottom temperature depends in the first instance on the thermal diffusivity and the amplitude and time scale of the bottom temperature change. The effect is also more pronounced for higher geothermal gradients or heat flow values. *Top-down dissociation* of hydrates can only occur in case of negative *in situ* interval geothermal gradients. Once the water depth exceeds the critical water depth related to the present bottom water temperature (or the final bottom temperature is less than the critical bottom temperature at present water depths), such a phenomenon will no longer be observed. This explains why such a *top-down dissociation* is only possible in relatively shallow basins. This effect is furthermore only important on a very short time scale, i.e. almost instantaneously on geological scale. Therefore, it is doubtful whether such process will occur under natural conditions although it is theoretically possible. For relatively deep basins only *bottom-up dissociation* is theoretically possible.

For very slow gradual changes of the bottom water temperature with time, the temperature profile will lie very close to a linear trend. Even for instantaneous changes, after a time lag of about 10 ka – i.e. half the period of the shortest term of the *Milankovitch* cycle – the sub-bottom temperature curve will be almost linear with burial depth within the first 1000 m of sediments. The thermal gradient will be slightly lower res. higher in case of bottom temperature increase res. decrease. Medium duration rapid climatic switches known as *Dansgaard-Oeschger* cycles occur within 1 to 5 ka [*Leeder, 1999*]. If these events are characterised by a shift of the bottom-water temperature, then the influence of previous changes might be important as well. In other words, the previous thermal pulse will still be active – although with reduced effect – and the situation would not return yet to approximate steady-state conditions before the initiation of the new thermal pulse. This case is more difficult and discrepancies can occur, dependent on the time scale and the amplitudes. For medium to short duration changes from A to C over B, careful analysis of the behaviour of the sub-bottom temperature profile between the different stages should be carried out and other boundary conditions will be present. While the evolution from A to B might be adequately described and studied by the methodology used in this chapter, the switch from the intermediate situation B to the final situation C will be more difficult since the intermediate conditions will not be in steady-state and should be worked out.

2.3.2b Relevance to continental margin and slope stability

It is also worth noting that a sudden discontinuous temperature change in relation to gas hydrate stability conditions is important in case of mass wasting processes, like for example the Storegga Slide [*Bugge et al., 1987; Bugge et al., 1988; Mienert et al., 1998; Bouriak et al., 2000*], the Beaufort Sea Margin [*Kayen & Lee, 1991*] or North Sulawesi [*Delisle et al., 1998*]. The removal of the uppermost sediments can be treated as an instantaneous thermal pulse with limited amplitude, dependent of the initial geothermal gradient and the thickness of the removed sediments. A "new" sea floor that was previously buried under several tens of meters of sediments, and hence had a higher temperature, will suddenly be washed by colder bottom currents. In this way, the occurring slide or slump can be considered as a cold front, since the assumed steady-state or linear temperature profile will be disturbed by the cold bottom water temperature. The reader is referred to section 2.6 for further details.

2.4.1
Theoretical aspects

For studying the impact of climate changes on the vertical extent of the HSZ in oceanic and lacustrine settings, the effects of pressure and temperature changes need to be combined. Here the real influence of the time scale of the interacting processes will become clear. In literature, the change of the vertical extent of the HSZ is in most cases solely expressed in terms of the initial situation and final situation, ignoring specific changes in between and often the influence of temperature changes is ignored [e.g. *Paull et al., 1991; Kvenvolden, 1998*]. It will be shown that the simulation from initial to final condition with varying temperature and pressure conditions is not straightforward when opposing processes are combined. For example, the extension of ice caps will result is global lowering of sea levels (negative effect in terms of hydrate stability) while at the same time bottom water currents can be enhanced. With time broader zones might then be spooled by colder bottom masses (positive effect in terms of hydrate stability).

The combination of pressure- and temperature-induced changes of the HSZ was also worked out using the same methodology as described in the previous paragraphs. Therefore, a few new parameters are introduced in program_2. One of these is the rate of the sea level change, a quantity that can be determined using the sea level curve of *Fleming* shown in figure 2.10. Typical values of this rate of change during the last 210 ka vary between 0.4 and 10 $m \cdot ka^{-1}$. While for pure sea level changes only the amplitude of the sea level fluctuation is of importance, this time dependence cannot be ignored any longer. In the program, only linear changes of sea level with time are taken into consideration. Another feature of interest is the delay being defined as the difference in time between the initiation of the sea level change relative to the start of the bottom water temperature change. This feature is incorporated into the program but will not be discussed here in detail since this parameter is only responsible for an offset of the one phenomenon to the other. Nevertheless, this parameter might be important.

2.4.1a Sea level changes combined with instantaneous bottom temperature change

A first particular example of the evolution with time of the hydrate stability limit in a 500 m deep salt water basin is given in figure 2.29 in case of instantaneous temperature change with full amplitude. This approach will result in maximum changes of the stability field, as was discussed in the previous paragraph. The black curve (situation A) illustrates the effect of a sudden bottom temperature drop from 3 to 1°C combined with a sea level drop of 120 m at a rate of 0.01 $m \cdot a^{-1}$. The initial steady-state equilibrium depth at these conditions is found at 79 m sub-bottom depth. The grey curve (situation B) on the other hand represents a sudden temperature drop from 0 to –1°C accompanied with a sea level decrease of 120 m with rate of 0.005 $m \cdot a^{-1}$. In this case, the initial equilibrium depth lies at 166 m sub-bottom depth.

A remarkable observation here is that indeed overturn happens, i.e. the system appears to move from the initial steady-state situation into more favourable conditions due to the temperature change. Maximum conditions are reached in situation A res. B at ± 2400 res. ± 3200 years (relative to the initiation of the pulses) and are dependent on the amplitude of the temperature decrease. Then, the influence of the sea level change becomes more and more important but at a lower rate and is responsible for the evolution towards less favourable conditions. Once the sea level change is completed (i.e. after 12 ka for situation A and 24 ka for situation B), only temperature effects play a role but the amplitude is already reduced by far. This results in slow subsidence of the equilibrium

limit. As a final result for shallow water depths at the above conditions, the pressure effect clearly is of higher importance at long time scales.

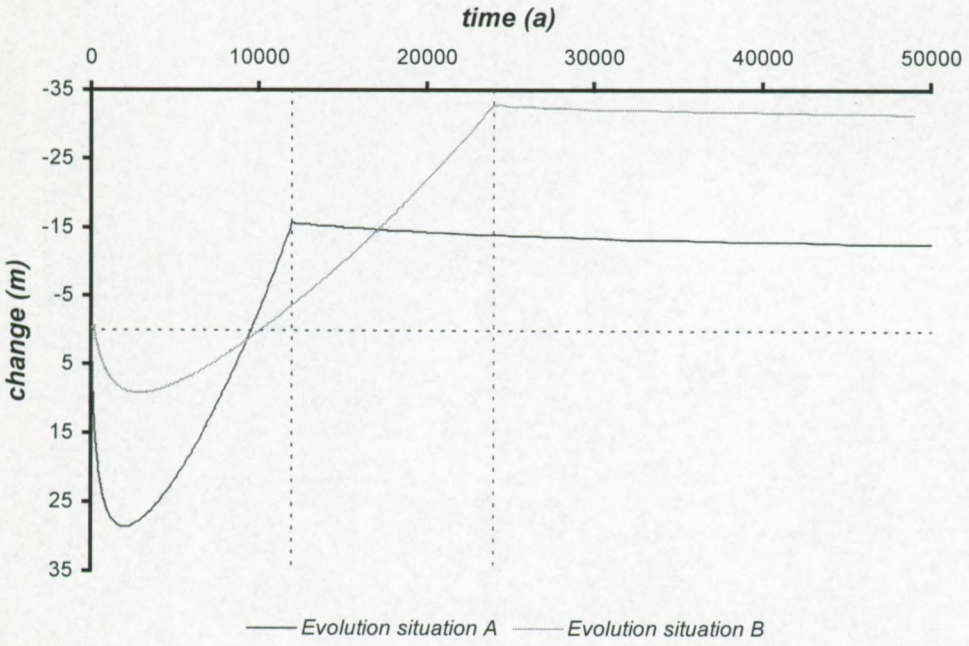

***Figure 2.29**: Evolution of the basal limit of the methane HSZ under gradual sea level decrease and a sudden bottom water temperature decrease in two different situations in a 500 m deep salt water basin. The vertical dashed lines represent the termination of the sea level changes.*

Another interesting feature that cannot be resolved on the figure is that on time scales at which the deviation limit is smaller than the steady-state equilibrium depth no temperature-effect can take place at the basal limit of hydrate stability since the thermal pulse did not have time enough to penetrate the subsurface that deep. Hence, only pressure changes are of importance during that period of about 50 years (situation A) res. 275 years (situation B) and this time lag depends on water depth and geothermal gradient. During this short period and in the above situations, the lower boundary of the stability field will migrate slightly upward over a few tens of cm during this period in which sea level changed with a magnitude of only 0.5 m (situation A) res. 1.4 m (situation B). Once the temperature pulse passes the steady-state equilibrium conditions, its effect offsets by far the pressure contribution.

In deeper basins under similar conditions of sudden temperature drop from 0 to –1°C in combination with gradual sea level fall at a rate of 0.005 $m \cdot a^{-1}$ starting at the same time, it will take longer before the thermal pulse reaches the stability limit (lying at greater depths). In a 2000 m deep oceanic basin with geothermal gradient of 0.050°C·m^{-1}, it will take approximately 1500 years before the system turns to more favourable conditions (figure 2.30). Here also the thickness of the zone in which hydrates theoretically can destabilise is limited to about 0.6 m located at the base of the initial stability field. But once the temperature pulse rules the game, a similar picture is obtained, as is shown in figure 2.30, but important differences are observed. First of all, the amplitude of the change of the stability limit is much less than in shallow water basins. Next, less favourable conditions are only present in the first period after the initiation of the change, while at longer times scales the temperature effect exceeds the influence of the continuing sea level drop. In this situation characterised by a very important sea level decrease equivalent to the difference between the present-day level and the level at the LGM, a 1°C temperature change at the sea bed will completely counteract and overrule the influence of sea level change, i.e. a result that qualitatively and quantitatively differs from the situation in shallower basins under identical environmental controls.

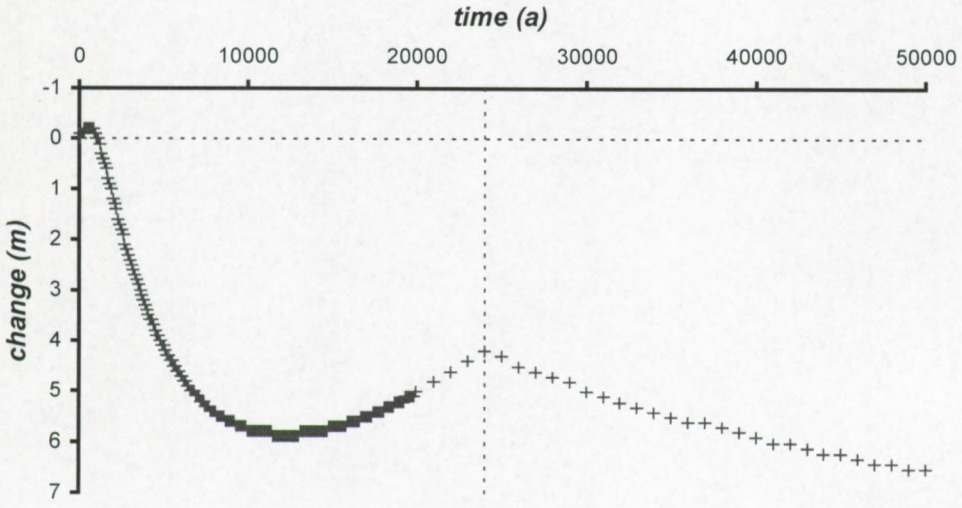

***Figure 2.30**: Evolution of the basal limit of the methane HSZ under gradual sea level decrease and a sudden bottom water temperature decrease in a 2000 m deep salt water basin. The duration of the sea level fall is 24000 years. The vertical dashed line represents the termination of sea level change.*

If the time lag between the initiation of the two individual processes (sea level change, bottom temperature change) is positive in a situation of decreasing bottom temperatures combined with sea level drops, then the dissociation process will be delayed or perhaps eliminated due to the temperature change. This means that during the first tens to hundreds of years, no changes will occur. On the other hand, if the delay is negative then the pressure effect takes place before the temperature effect starts. Then, the temporary dissociation in the first tens to hundreds of years will have a higher amplitude. At long time scales, the effect will fade out.

Now the opposite effects – a combination of increasing bottom water temperatures with sea level rise – are shortly discussed in similar situations as above, i.e. in a 500 and 2000 m average salt water basin. A 120 m sea level rise for example from the LGM up to now is considered but with linear sea level change of 0.005 $m \cdot a^{-1}$. The sudden bottom temperature rise from –1 to 0°C is supposed to take place at the initiation of the sea level change. The evolution of the basal limit of the methane HSZ under these variable conditions is illustrated in figure 2.31. The behaviour is qualitatively just the opposite of what is discussed above. This means, in the first instance but over a short time span the system evolves towards more favourable conditions due to the delayed effect of the thermal pulse while the sea level change is active. Then a period of less favourable conditions extends over approximately 10 ka (relative to the initial situation) after which the pressure effect takes over and is responsible for deepening of the theoretical stability limit. Note that the destabilisation during the first hundreds to thousands of years occurs faster than the return to more stable conditions. Note that, even with important sea level rise it is possible that the change is purely temperature-controlled and that destabilisation will occur. This is the case for deeper basins (2000 m).

2.4.1b Sea level changes combined with gradual temperature change

In a lot of geological situations, the bottom temperature profile can not easily be expressed as an instantaneous event. Considering the effect of gradual temperature changes combined with sea level changes, one knows already from the previous paragraph that the amplitude of the temperature effect will be reduced compared to instantaneous temperature changes. The same situations (500 and 2000 m deep average salt water basins, sea level changes over –120 m at a rate of 0.005 $m \cdot a^{-1}$) are investigated as above but temperature is supposed to change linearly from 0 to –1°C over 1 ka (short-

term relative to sea level change), 20 ka (about the same time scale of the sea level change) or 40 ka (longer time scale compared to time of sea level change). The evolution of the basal limit of the methane HSZ in a 500 res. 2000 m basin for these time scales of the temperature change is illustrated in figure 2.32 res. figure 2.33. From these figures, it is observed that for long time scales (> duration of the thermal pulse at the lake or sea bed), the change in the extent of the HSZ converges and is hence independent of the rate of change of bottom temperature. Thus, the rate of change is of minor importance at longer time scales compared to the amplitude of the temperature change. Comparing figure 2.32 with figure 2.29, it is also seen that at long time scales the situation is quantitatively rather similar to what is expected if bottom temperature changes suddenly. For example, a difference of only 2.5 m is present after 50000 years in a 500 m deep basin.

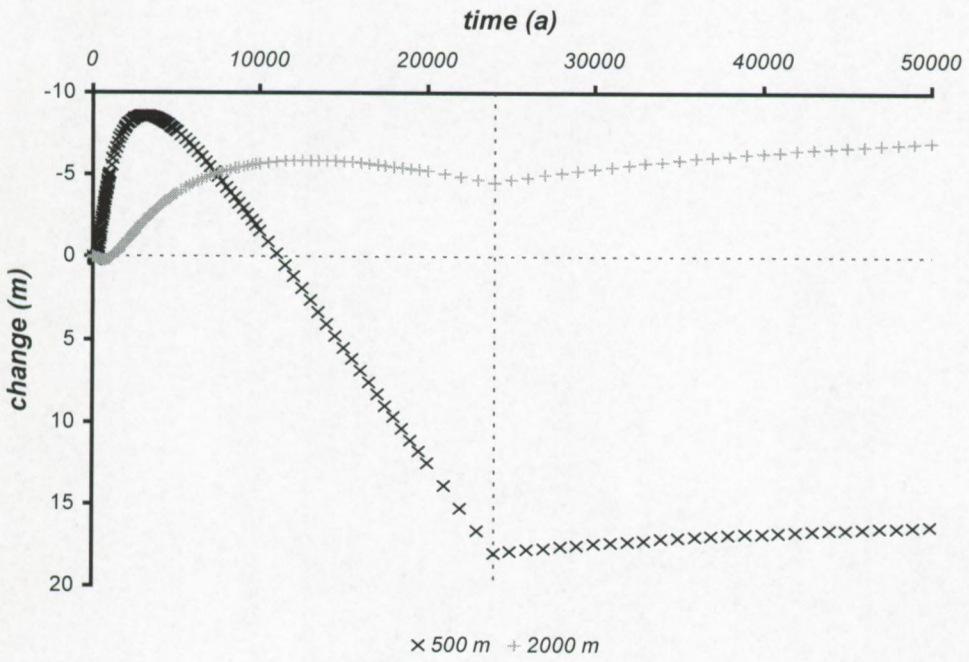

***Figure 2.31**: Evolution of the methane HSZ with time if bottom water temperature suddenly increases from –1 to 0°C while sea level slowly increases over 120 m at a rate of 0.005 m·a⁻¹. Water depth is 500 m or 2000 m.*

An important qualitative difference is that for slower changes (20 and 40 ka) of the bottom water temperature in shallow basins, the pressure-influence governs at all time scales (i.e. less favourable hydrate stability conditions compared to the initial situation in these examples), until the pressure change is completed, after which only the temperature effect is felt. Once the deviation limit is reached, the temperature pulse effectively affects the stability limit and the rate of change of the stability limit slows down due to the opposite working of reducing sea level and linearly diminishing bottom temperatures. Only for fast temperature changes, the evolution of the hydrate system changes first towards more favourable conditions until the sea level impact takes over resulting in inversion of the stability conditions. Also here, there is a very short period of reduced stability conditions at the initiation of the sea level change and the delayed working of the thermal pulse.

In deeper basins (figure 2.33 here 2000 m), the situation is different for short time scales of bottom water temperature change (1 ka). The phase of possible hydrate dissociation following immediately after the initiation of the sea level change lasts longer due to the delayed temperature effect in deeper parts of the basin. Once the thermal pulse penetrates deep enough, the temperature effect becomes more important than the pressure-induced effect. As a result, the system moves towards better stability conditions. After a while (approximately 12 ka in this situation) the pressure effect takes over again and results in the upward migration of the stability limit until the sea level reaches its final

level. Then, the changing sub-bottom temperature profile is the only mechanism still working and will force the system back into more favourable conditions. So, also in this case with important sea level drops of 120 m in deeper basins, in the end the system appears to evolve towards more favourable conditions compared to the initial situation due to the bottom water decrease while under the same conditions, the opposite is true in shallow basins (figure 2.32).

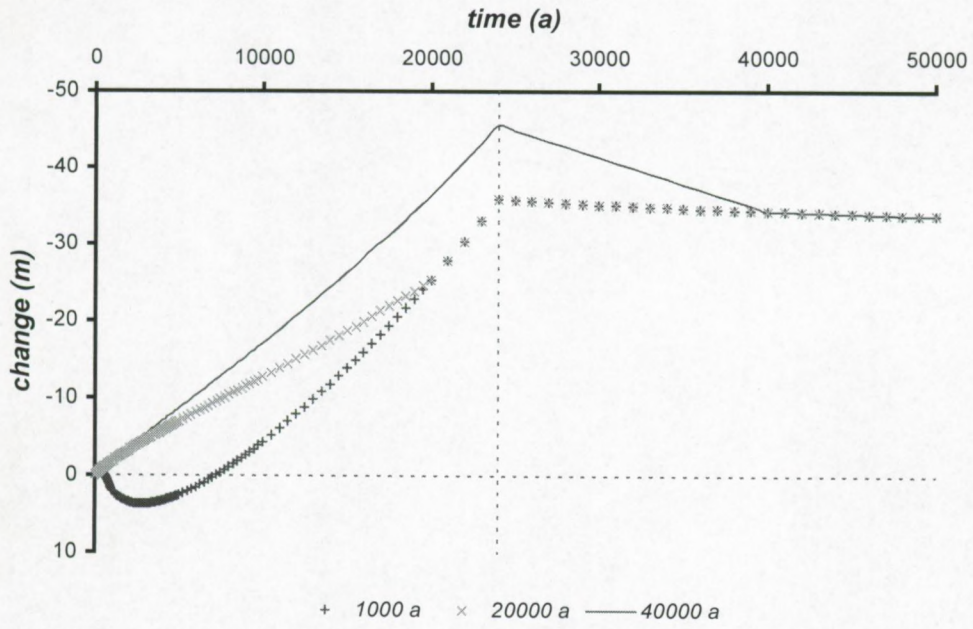

***Figure 2.32**: Evolution with time of the basal limit of the theoretical methane HSZ in a 500 m deep average salt water basin. Sea level is supposed to drop over 120 m at a rate of 0.005 m·a^{-1} while bottom water temperature decreases from 0 to −1 °C during 1000, 20000 or 40000 years.*

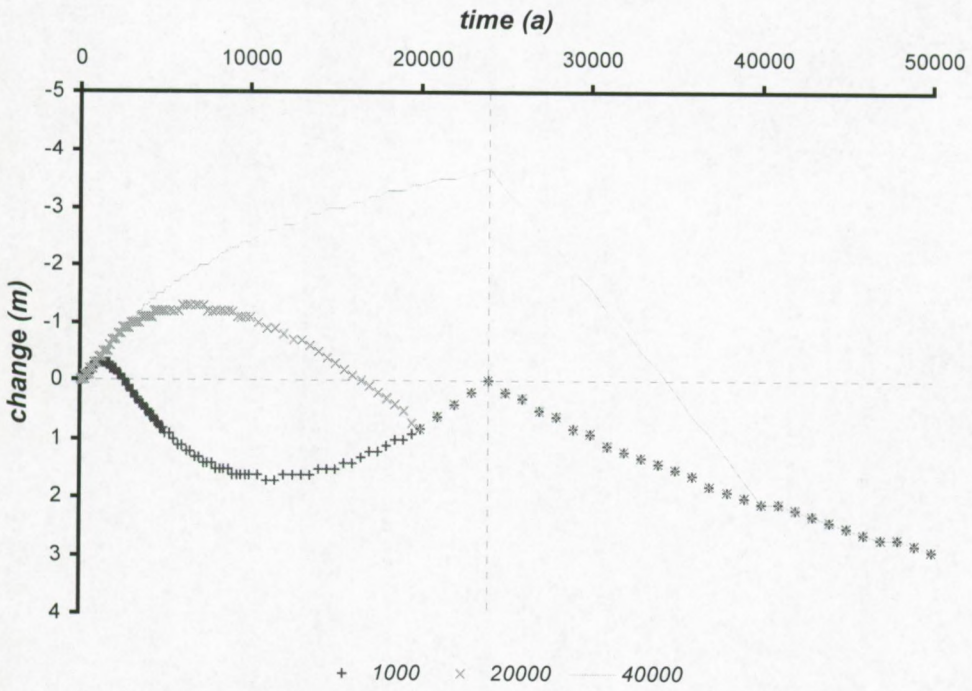

***Figure 2.33**: Evolution with time of the basal limit of the theoretical methane HSZ in a 2000 m deep average salt water basin. Conditions are similar to the figure above (sea level drop, bottom temperature decrease). The vertical dashed line represents the termination of sea level drop.*

For longer time scales of the bottom temperature change the situation can be different. For bottom temperature changes that take longer to be completed that the sea level change (e.g. 40 ka in this example), the system is clearly pressure dominated all time until the sea level has reached its final level. Then, the changing sub-bottom temperature profile is responsible for subsidence of the equilibrium limit. During approximately the first 35 ka, the system will be less favourable compared to the initial situation. If the time scale of both processes is of the same order of magnitude (e.g. 20 ka in this example), inversion between a pressure-dominated (first sequence of approximately 6.5 ka, third sequence between about 12 and 24 ka) and temperature-dominated processes (second sequence between approximately 6.5 and 12 ka, and last sequence after the sea level change is completed) do occur. The discontinuity jumps appearing in all three curves of figure 2.33 have about the same magnitude. Nevertheless in all three situations, the sea level fall of 120 m is not powerful enough to force long term hydrate destabilisation (> 35 ka) compared to the initial situation. In the long run, the temperature decrease of only 1°C dominates the system.

The opposite story (increasing sea level of 120 m combined with increasing bottom water temperature from –1 to 0°C, using the same rates of change) results in similar but opposite conclusions. Table 2.3 gives some selected results for a 500 and 2000 m water depth. The typical trend of the evolution is observed in those values and is therefore not repeated in figures like figure 2.33.

	time of interest (ka)					
water depth (m)	**500**	10	20	30	40	50
initial equilibrium sub-depth (m)	193.3	change of stability limit (m)				
duration of temperature change (ka)	1	3.7	16.9	21.4	20.3	19.7
duration of temperature change (ka)	20	10.9	16.9	21.4	20.3	19.7
duration of temperature change (ka)	40	14.4	25.1	25.8	20.3	19.7

	time of interest (ka)					
water depth (m)	**2000**	10	20	30	40	50
initial equilibrium sub-depth (m)	413.3	change of stability limit (m)				
duration of temperature change (ka)	1	-1.3	-0.7	-1.0	-2.3	-3.2
duration of temperature change (ka)	20	1.3	-0.7	-1.0	-2.3	-3.2
duration of temperature change (ka)	40	2.4	3.3	1.4	-2.3	-3.2

***Table 2.3**: Variation of the methane HSZ at selected times, as a result of gradual bottom water temperature increase from –1 to 0°C combined with a sea level change of 120 m at a rate of 0.005 m/a.*

As could be expected, only in shallow areas the system is pressure-dominated while at the same time in the deeper basin inversion occurs and finally the bottom temperature change is of primary importance, resulting in less favourable conditions. Note that the change of the stability limit differs by an order of magnitude.

Note also that such an evolution pattern depends on the delay between the sea level change relative to the initiation of the bottom temperature pulse. For positive delays, the situation will be kept at the initial equilibrium conditions longer until sea level change sets in or the thermal pulse reaches this limit. Such a temporary dissociation phase will be reduced or will disappear dependent on the effect. For negative delays, the situation will be very similar to the one sketched above, since the pressure effect will be the only one sensible for longer time scales.

2.4.2
Case study: the methane hydrate mediating hypothesis, Porcupine Seabight

As a first case study, the influence of climatic changes on the theoretical extent of methane hydrates in the sediments of Porcupine Seabight, offshore Western Ireland, is modelled.

2.4.2a Porcupine Seabight, offshore Western Ireland

The Porcupine Basin, lying to the west of Ireland, is a large basin containing a substantial thickness of Late Palaeozoic, Mesozoic and Cainozoic sediments. The evolution has been controlled by lithospheric stretching and cooling. Its rifting can be subdivided into a pre-rifting, a syn-rifting and a post-rifting phase [*Croker & Shannon, 1987*]. The Porcupine Basin consists of a north-south trending bathymetric low, the Porcupine Seabight gently sloping south. This bathymetric depression opens westwards onto the Porcupine Abyssal Plane. The Porcupine Seabight Basin is underlain by more than 10 km of Upper Palaeozoic-Cainozoic sediments. The Seabight is bounded by shallow platforms: the Irish continental shelf (E), Porcupine Bank and Ridge to the (N-NW) and Goban Spur (S). In the Porcupine Seabight, three water masses are present. East North Atlantic Water is presently extending to over 700 m water depth, overlying Mediterranean Water that in turn overlies Labrador Sea Water. Bottom water currents are highly variable from less than 16 $mm \cdot s^{-1}$ to over 100 $mm \cdot s^{-1}$ within a couple of hours combined with changes in current direction [*Vermeulen, 1996*].

Exploration in the Porcupine Basin began in 1970. Up to now, extensive acoustic profiles have been gathered in this area and several wells were drilled. Most of them have recorded flows of hydrocarbons. Light oils have accumulated at a number of stratigraphic horizons. The main oil-source horizons are thick Upper-Jurassic shales while gas source rocks exist principally in the Late Carboniferous [*Croker & Shannon, 1987*].

In this area, several seismic surveys have been carried out during the last 4 years by the RCMG, revealing the presence of deep water reefs. One of the most characteristic features on the profiles acquired is the presence of several kinds of transparent structures of which some occur in clusters, interpreted to be carbonate mounds. The diverse types of mounds were studied and divided into *Magellan mounds*, *Hovland mound* and *Belgica-Logachev mounds*, with their own specific characteristics [e.g. *Henriet et al., accepted; Henriet et al., 1998; Pillen, 1998, Van Rooij, 1998; Van Herreweghe, 1999*]. In the area of interest, only the first two mentioned kinds of mounds are observed, separated by a transition zone several km wide. This is illustrated in figure 2.34. Also two slide scars were identified on the high-resolution data acquired in 1998 [*Henriet et al., 1999; Almendinguer & Henriet, 1999*]. Here, only the main aspects of these structures will be mentioned. The reader is referred to the thesis work of e.g. *Pillen* [*1998*] for further information or typical acoustic profiles. At present, some publications about these structures, their seismic expression and their possible origin are being prepared by the RCMG.

2.4.2b Basic characteristics of Magellan and Hovland mounds

In the area covered by high-resolution acoustic profiles (see figure 2.35, approximately 3500 km^2) hundreds of *Magellan* mounds are observed. These features are recognised on high-resolution acoustic profiles by their homogeneous transparency with few weak chaotic internal reflections. Their structure is irregular. Often these features are observed in clusters. With a few exceptions, they all are buried under a package of recent sediments (drifts) that grows thicker upslope. Furthermore, they seem to be rooted to a common and virtually undisturbed horizon. Less than 3% of the *Magellan* mounds are (nearly) exposed at the sea bed. Sampling showed that these structures do contain coral fragments [TTR-result). The height of these mounds varies between 20 to 100 m while their width ranges from 100 to 500 m. A few mounds show some symmetry [*Pillen, 1998*]. The zone of occurrence of the *Magellan* mounds appears to be limited by the 500 m and 700 m isobath is this area. At its downslope boundary, a slide scar is observed as well. These structures do not show any correlation with deeper faults [*Henriet et al., 1998*]. The name *Magellan mounds* comes from an industrial research vessel that had discovered these phenomena a few months before the first high-resolution images were acquired by the RCMG with R.V. Belgica.

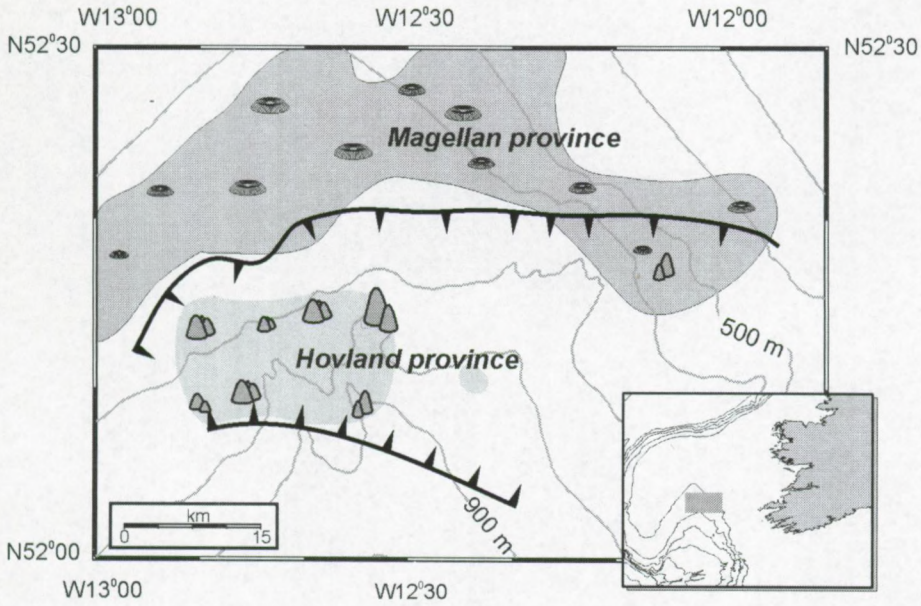

***Figure 2.34**: Bathymetry and location of the Magellan and Hovland province in Porcupine Seabight. Figure made by Alexei Almendinguer.*

Hovland mounds are located south of the *Magellan* mound area (6 to 8 km) at greater water depths up to 1000 m. They differ significantly from their *Magellan* counterparts and were first identified on industrial profiles by *Hovland et al.* [*1994*]. The width of the *Hovland* mounds varies between 100 to 1800 m. These structures rise out of the sea bed for more than 50 to 175 m. Most often, these mounds are lying in a deep moat. These structures are described as recent carbonate reefs and might have a causal relationship with underlying fault structures. *Hovland et al.* [*1994*] report that these knolls tend to be concentrated in areas where north-south trending normal faults in Tertiary and Upper-Cretaceous strata fade out, possibly due to the presence of east-northeast strike-slip faults. These features then provide possible fluid migration pathways. The presence of anomalously high-amplitude events on acoustic sections adjacent to the faults and below the base of the knolls may possibly represent gas-charged sediments. Interstitial gas sampled from the mounds is – although highly variable – predominantly methane of thermogenic origin. It is suspected that the large degree of variation in this methane concentration reflects both active seepage and methane consumption by biological activity [*Hovland et al., 1994*]. Thus, the development and location of the organic rich mounds may be closely related to focused seepage of light hydrocarbons from the subsurface. Dating indicated that the final stage of mound development is possibly of Upper-Pleistocene age (12-13 ka BP) [*Hovland et al., 1994*]. On the other hand, *De Mol et al.* [*1999*] report that gas analyses of the pore fluids in the *Hovland* mound province do not display real anomalies, and conclude that recent evolution of the mounds is most likely to be controlled by favourable ocean circulation or currents, changes of the water masses and changes of nutrient supply.

Furthermore, gravity cores, box cores and grab samples on a few *Hovland* mounds and on a single outcropping mound in the *Magellan* province have recovered carbonate-rich clay with extensive deep-water colonial coral debris (*Lophelia pertusa, Madrepora oculata*) [*Henriet et al., 1998; De Mol et al., 1999*].

2.4.2c Methane hydrate mediating hypothesis

The genesis and evolution of these structures and whether the different types of mounds are related is not clear at present. Recently, a hydrate-mediating hypothesis is proposed to explain some of the features observed, linking fluid migration, hydrate growth and decay under climatic changes and the

presence of slide scarps [*Henriet et al., 1999; Pillen, 1998; Henriet et al., accepted*]. The modelling as shown here was used for these manuscripts. In this hypothesis, it is proposed that the sudden onset and near-synchronous decay of the *Magellan* province with its numerous reefs implies a regional and transient degassing event. There, a specific role is played by the growth and decay of the gas hydrate layer in the area, under influence of sea level changes and bottom temperature fluctuations. The upslope boundary of the *Magellan* province where the reef structures fade out, follows depth contours, supporting the idea of a pressure control on the extension of the hydrates and mounds.

Under glacial conditions, hydrates may form or a present hydrate layer may grow since the Porcupine sea bed was swept by much colder bottom waters. Gases are supposed to migrate (dissolved or as free gas) from deeper reservoirs or source rocks through faults and fissures. Once they enter the stability window, they are captured in the solid hydrate structures. When such a hydrate layer at a later stage starts to decompose in warmer postglacial waters, it could have funnelled methane via seeps to shallower sediments and possibly the ocean. In the immediate neighbourhood of these fluid migration pathways, bioherms may have grown under dominantly bacterial processes. Once the source of the upwelling gas ran out, the bioherms got buried due to continuous sedimentation. Due to hydrate dissociation, the release of huge amounts of gas could also lead to the build-up of increased pore pressure. Such a mechanism might be thought of being responsible for slumping or sliding or the formation of pockmarks in the area.

2.4.2d Modelling: theoretical extent of the HSZ

The question of mound genesis or evolution and the relationship with hydrocarbon migration and slide scars in the area lies beyond the scope of this study. At present, several people from the RCMG are working on this topic. My contribution is hence restricted to the modelling of the theoretical extent (and its evolution) of methane hydrates in the area as a fundamental support for the hypothesis.

The main problem with this hypothesis, is the lack of evidence of hydrates in the area although there is evidence for the presence of gases. Porcupine Basin is considered to represent an important hydrocarbon province. The presence of carbonates [*De Mol, pers. comm.*] and pockmarks [*Wheeler et al., 1998*] might further give indirect evidence of important fluid migration and recent gas escape from the shallow subsurface [*Hovland & Judd, 1988*]. The wells drilled in the basin also showed the presence of hydrocarbon flows [*Croker & Shannon, 1987*]. Although several hundreds of km of high-resolution acoustic profiles (sparker source) are acquired in the area, no single line shows the presence of an anomalous reflection that could be interpreted to represent the BHSZ, as is the case in other areas with known hydrate occurrence (e.g. Cascadia, Oregon, Storegga, Blake Ridge, Lake Baikal, ...). In general, such a typical reflection should be present at the boundary between partially hydrate-rich sediments above and free gas-containing sediments below, resulting in an important acoustic impedance drop across this interface, and hence a negative polarity reflection on acoustic profiles. The fact that the horizontal and vertical resolution of this data set is very high (< 1 m res. 60 m at 750 m water depth), makes it hard for the purpose of BSR detection. This means, low-resolution data are necessary before any conclusion can be drawn [*Vanneste et al., in press*]. But even on paper copies of some industrial data (courtesy of Statoil) no evidence is observed. Analyses of recently acquired seismic data in the nearby Belgica mound area indicate the presence of few negative polarity reflections observed at the sides of buried mound features, under which the acoustic frequency drops significantly. Whether this is due to free gas accumulation is not clear at present [*Guidard et al., 2000*]. Similar analyses are currently being performed on the data within the *Magellan-Hovland* area.

Nevertheless, the data acquired during recent high-resolution surveys (1997-99) in Porcupine bight are now used to delineate the zones of theoretical past or potential present occurrence of methane hydrates in the shallow subsurface of Porcupine Bight, by means of the methodology worked out in the previous paragraphs. The sensitivity of this basin was investigated under glacial and interglacial conditions, i.e. a situation of combined bottom water temperature changes and sea level variations. Due to a lack of accurate information, several assumptions have been made.

In the first instance, the bathymetry in the *Magellan*-area has been determined using the sea bed reflection with careful navigation control. Along several acoustic lines in the area, the sea floor reflection was digitised. Conversion from two-way travel time to depth below sea level was performed using an average acoustic water velocity of 1500 $m \cdot s^{-1}$. Data and results are then imported in Surfer software for contouring. The data grid was contoured using triangulation with linear interpolation. The bathymetry based on the seismic profiles in the area is presented in figure 2.35. Contouring interval was 100 m. The data points used are also shown. This bathymetry information is then used as input file in one of the programs in order to calculate the theoretical extent of the methane HSZ and its evolution.

➔ *Present-day situation*

According to the numerical database *Levitus* [*1982*], no single bottom-water temperature can be used in the Porcupine Bight area. Present-day bottom water temperatures in Porcupine Seabight appear to be related to water depth. At 250 m water depth, bottom temperature is approximately 10.5°C while at 1000 m a value of 8°C is reported from the Southern limit of the bight. In this model, this variation as a function of water depth is incorporated by assuming that the bottom water temperature linearly decreases with increasing water depth, based on the temperature values at 250 and 1000 m water depth as appropriate boundary conditions. Hence, the bottom water temperature can be written as follows:

$$T_0\langle H\rangle = \alpha_0 + \alpha_1 \cdot H$$

with $\alpha_0 = \frac{34}{3}$ and $\alpha_1 = -\frac{1}{300}$

and H the height of the water column. a_0 is expressed in °C, a_1 in $°C \cdot m^{-1}$. Using these bottom temperature values at minimum res. maximum water depth of the area of interest, the critical water depth for pure methane hydrates in an averaged salt water environment to be stable is calculated to be 843 res. 645 m. Using the bottom water gradient with water depth, then hydrates can at present only be stable within the deeper part of this area, starting from the critical water depths of about 714 m, i.e. out of the *Magellan* province (limited by 500 and 700 m isobath). This bottom temperature behaviour as a function of water depth is responsible for much better hydrate stability conditions at increasing water depth, since both the bottom temperature is lower and the water pressure is higher.

Croker & Shannon [*1987*] present results from analysis of the subsurface temperature in available wells (23 at that time) in the Porcupine Basin. A few of those wells lie in the immediate neighbourhood of the grid of acoustic profiles acquired and are useful in this discussion. The mean geothermal gradients range from 0.024 to $0.038°C \cdot m^{-1}$, with an average of $0.030°C \cdot m^{-1}$ that will be used in this study. The geothermal gradient shows a relatively consistent increase towards the centre of the basin.

Knowing the bottom water distribution in the *Magellan-Hovland* area and this average geothermal gradient value, the theoretical extent of the methane HSZ can now be calculated under present-day conditions. For all data points the sub-bottom depth of the HSZ was calculated using the methodology outlined in the previous paragraphs. The results of the basal limit of hydrate occurrence were then contoured using the same gridding method and are represented in figure 2.36. Note that the spatial gradient of the equilibrium depth is rather high. Iso-sub-bottom depth lines are drawn for every 20 m sub-bottom depth.

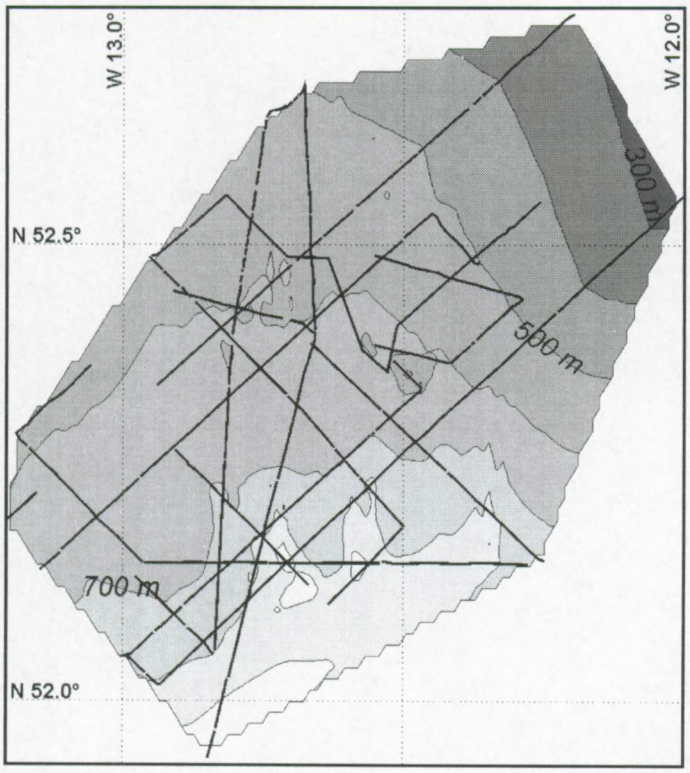

***Figure 2.35**: Bathymetry of the Magellan-Hovland province, Porcupine Bight offshore Western Ireland, inferred from single-channel acoustic profiles. Contour interval is 100 m. Data points of calculation are shown. In total, 59402 points were used for all calculations, contouring and mapping.*

➔ *Situation during glacial conditions: the Last Glacial Maximum*

There is evidence for floating ice during the Pleistocene on the Irish Continental shelf and on Porcupine Ridge (NW of Porcupine Seabight), where characteristic patterns of glacial scour marks are recorded from side scan sonar data in water depths less than 500 m. Those marks are typically a few m to a few tens of m wide and a few m thick. The examples found on the Porcupine Ridge are most probably generated during the last glacial (or late glacial) period and represent the southernmost occurrence of such features in the North Atlantic [*Vermeulen, 1996*]. Plough marks – being sea bed depressions of a few m deep and several tens of m wide due to moving icebergs – are also observed to the north of Porcupine Bight [*Henriet, pers. comm.*]. These observations provide evidence for the presence of large ice caps extending from the polar region over Scandinavia, Scotland and part of Ireland during recent geological time (LGM, previous glacial maximum). Under these conditions, it is reasonable to assume that local bottom water temperatures at those times were very close present-day bottom temperatures in polar regions like the Norwegian Continental Margin or the Greenland Sea, i.e. 0°C or even less.

Now consider the situation between the present-day situation and the LGM, separated by a time span of approximately 21.5 ka according to the sea level curve of *Fleming et al.* [*1998*] shown in figure 2.10. Since the LGM, sea level rose over a height of about 120 m while a difference in bottom water temperature with magnitude of 8 to 10.5°C seems reasonable. Furthermore, during the last 8 ka sea level rose only very slowly compared to the change in the period between 17 and 8 ka BP. Under these conditions, it is supposed that the bottom water temperature change was completed at 8 ka BP.

Calculating back in time to the LGM, the initial geothermal gradient that approximately coincides with the present-day situation in the shallow subsurface (first hundreds of meters, typical depth of hydrate stability limit) at a central point in the area taken to be the 700 m isobath at present-day temperatures of 9°C is determined to be about $0.045°C \cdot m^{-1}$. This is illustrated in figure 2.37.

For clarity, the steady-state initial geothermal situation is assumed to coincide with the LGM with bottom water temperatures of 0°C and a geothermal gradient of 0.045°C·m^{-1}. With the onset of warmer climatic conditions at 21.5 ka BP, sea level starts to rise accompanied by a gradual bottom temperature increase during 13500 ka until the present-day value is reached. In this case, there is no delay between sea level and temperature change. The rate of bottom temperature change is then 0.67°C·ka^{-1}. From figure 2.37 it is seen that the steady-state present-day temperature profile used above lies close to the real sub-bottom temperature profile starting from 21.5 ka caused by a gradual temperature increase from 0 to 9°C over 13.5 ka. The accuracy is better than 5 to 10 m difference in sub-bottom depth but increases rather fast at depths exceeding 350 m. As discussed before, the sensitivity of the basal limit of the HSZ will highly depend on the initial sub-bottom equilibrium depth calculated for steady-state conditions. Using one of the included programs, the deepest limit of the methane HSZ at 1000 m water depth and a geothermal gradient of 0.045°C·m^{-1} will be located at 323 m sub-bottom depth, so this approximation is reasonable for discussing the evolution of the methane hydrate stability limit. Note that such an approximation will be better for smaller amplitudes of the bottom temperature change and for smaller rates of change.

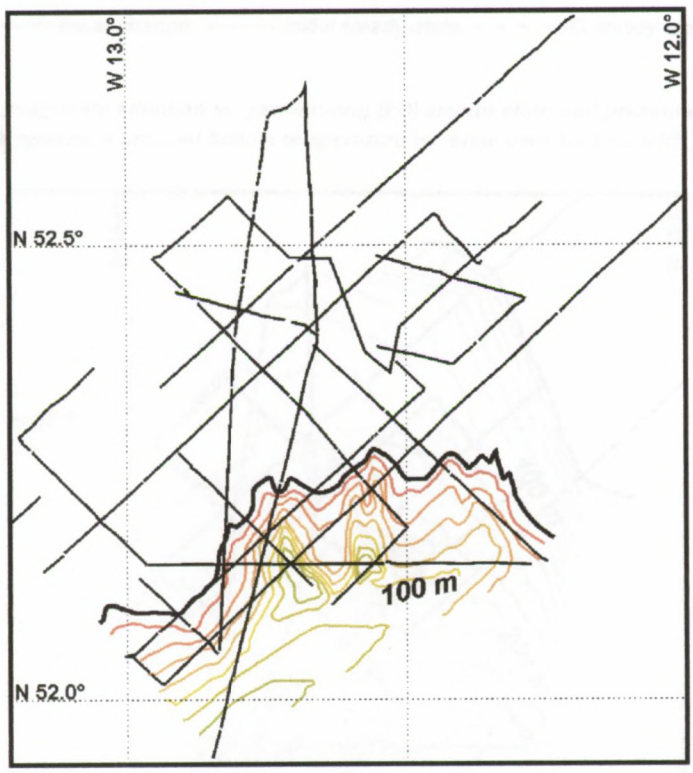

***Figure 2.36**: Present-day theoretical spatial and vertical extent of the 3-phase equilibrium depth of the methane HSZ in the Magellan-Hovland area, offshore Western Ireland. Interval is 20 m sub-bottom depth. The black thick line denotes the critical water depth (717 m).*

Knowing the bottom water distribution in the *Magellan-Hovland* area and this average geothermal gradient value, the theoretical extent of the methane HSZ can now be calculated under present-day conditions. For all data points the sub-bottom depth of the HSZ was calculated using the methodology outlined in the previous paragraphs. The results of the basal limit of hydrate occurrence were then contoured using the same gridding method and are represented in figure 2.36. Note that the spatial gradient of the equilibrium depth is rather high. Iso-sub-bottom depth lines are drawn for every 20 m sub-bottom depth.

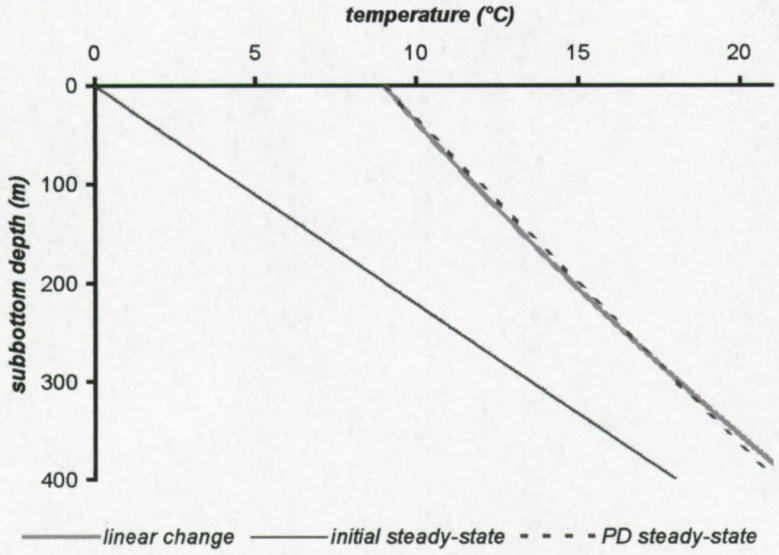

***Figure 2.37**: Initial steady-state situation vs. present-day (PD) steady-state and present-day curved sub-bottom temperature profile supposing a gradual bottom temperature increase over 13.5 ka with full amplitude of 9°C.*

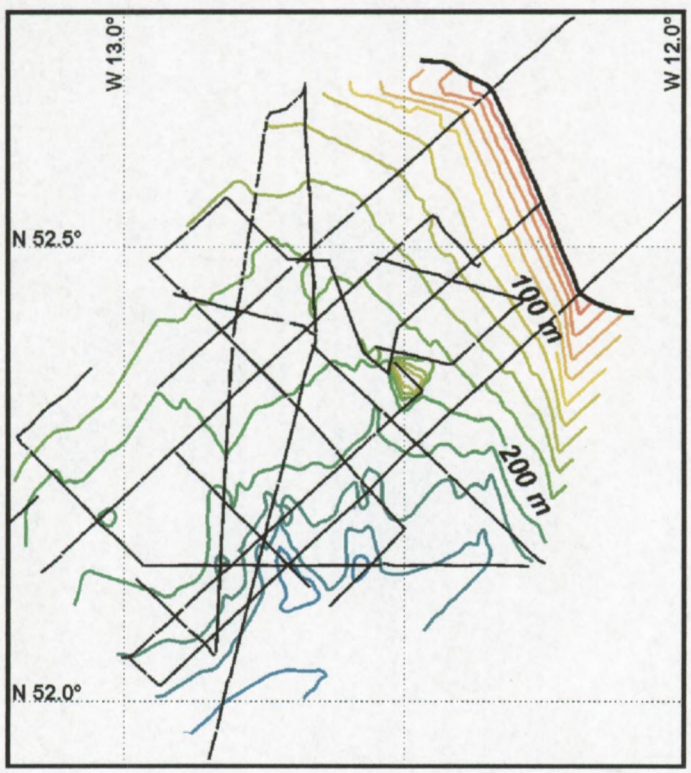

***Figure 2.38**: Theoretical spatial and vertical extent of the 3-phase equilibrium depth of the methane HSZ in the Magellan-Hovland area, offshore Western Ireland, for geothermal conditions estimated to be valid at the LGM. The thick black line marks the critical water depth for methane hydrate stability in the area at the LGM. Contouring interval is 20 m sub-bottom depth. Colour bar is identical to the one used in figure 2.36.*

➔ *Situation in between the LGM and the present day: inversion?*

The delayed effect of the bottom temperature change relative to the sea level fluctuation will also result here in an asymmetric evolution of the spatial and vertical extent of the HSZ. Thus temperature-

induced upward migration of the basal limit of the stability window will take place at earlier times in the shallower part while in the deeper part pressure-induced subsidence of the stability limit can be present, combined with global continuous pressure effects. This is illustrated in the examples given in table 2.4. It is seen that in the shallow part of the *Magellan-Hovland* area, the evolution is strictly temperature-dominated. In the deeper part, on short time scales (1 ka) the slow sea level rise forces the system into more favourable conditions. The amplitude is restricted to about 1 m. At longer time scales, the pressure-effect turns out to be less important relative to the temperature-induced destabilisation within the entire area.

initial water depth (m)	**500**	***time of interest since change (ka)***				
initial equilibrium depth (m)	186.4	0.0	1.0	5.0	10.0	21,5 = PD
real time water depth (m)		500.0	505.6	527.9	555.8	620.0
real time bottom temperature (°C)		0.00	0.59	2.96	5.93	8.00
final equilibrium depth (m)		186.4	186.3	140.2	0.0	0.0
difference (m)		0.0	-0.1	-46.2	-186.4	-186.4

initial water depth (m)	**880**	***time of interest since change (ka)***				
initial equilibrium depth (m)	317.8	0.0	1.0	5.0	10.0	21,5 = PD
real time water depth (m)		880.0	885.6	907.9	935.8	1000.0
real time bottom temperature (°C)		0.00	0.72	3.58	7.16	9.67
final equilibrium depth (m)		186.4	187.6	173.9	128.1	64.8
difference (m)		0.0	1.2	-12.5	-58.3	-121.6

***Table 2.4**: Some examples for discrete water depths (500, 880 m) of the evolution of the basal limit of the methane hydrate stability since the LGM. It is supposed that the temperature rose from 0.00°C up to 9,67°C (top) res. 8.00°C during a time span of 13.5 ka. Sea level started to increase at a rate of 5.58 m/ka from the LGM up to now.*

2.4.3 Discussion & Conclusions

In this paragraph, emphasis was placed on the different behaviour and combination of sea level induced and bottom temperature induced variations of the spatial and vertical extent of the methane HSZ in the *Magellan-Hovland* area. Due to the complex combination of time scales and amplitude of changes occurring with their importance for local geothermal conditions and very limited relevant data, the modelling was restricted for the period since the LGM, about 21.5 ka BP. This by no means excludes the possibility of similar events of growing or decaying hydrate accumulations in this area during geological times, but the lack of accurate data does not allow me to draw any conclusions for earlier time scales.

The high amplitude of the sea level change, being the maximum sea level rise since at least the last 210 ka, does not appear to be strong enough to move the system into better stability conditions. The evolution of the HSZ in this relatively shallow area is very sensitive to climatically-controlled bottom temperature changes that overrule the pressure-induced stabilising effect. Note that several assumptions were made during the analysis. The most important aspects are summarised here.

- The present-day bottom temperature distribution was modelled by a pure linear dependency of present-day water depths and differences with real bottom temperature cannot be ignored. This will result in small changes for the present-day extent of the stability field.

- Knowing the average present-day geothermal gradient, the situation at the LGM was estimated. This results in palaeo-geothermal gradients that vary between 0.043 to 0.046°C·m^{-1}, depending on the point of reference used. If one uses a shallower res. deeper point of reference, the initial geothermal gradient is bigger res. smaller. As an average value, a palaeo-geothermal gradient of 0.045°C·m^{-1} was used in order to delineate the extent of the methane HSZ at the LGM. As a reference the 700 m isobath was taken with bottom temperature of 9°C. Independent from the

initial geothermal gradient used, the geothermal gradient changed significantly over the last 21.5 ka in the model (on average a decrease of 33%).

→ There is a difference of several m sub-bottom depth of the stability limit using the average present-day conditions compared to the calculation using the modelling described in this chapter. This observation illustrates that the model should be refined in the future.

→ A uniform bottom water temperature of 0°C was assumed to be present at the LGM. Present-day bottom water temperatures in polar regions can be even lower. For example, the Antarctic Bottom Water (AABW) formed in the Weddell and Ross Seas has typical bottom temperatures between –2 and –0.4°C [*Allaby & Allaby; 1999*]. Bottom water masses on the Norwegian continental margin and slope are typically around 0°C [*Mienert et al., 1998*].

→ Full amplitude of the change in bottom water temperature is considered to have taken place during the major regression period (± 13.5 ka). In reality, this evolution might be significantly different. Unfortunately, no data were available to check. If the rate of temperature change with time is higher, then the inversion in the deeper part (cf. Table 2.4) will occur earlier. This means that the amplitude of the change of the basal limit will be lower since the sea level change is smaller at shorter times. The higher the temperature's rate of change, the faster the thermal pulse reaches the *in situ* stability limit. The standard thermal diffusivity parameter was used in this modelling and might not stroke with reality.

→ The amplitude of the changes that can be expected in the *Magellan-Hovland* area since the LGM appears to be strongly dominated by the temperature effect. The evolution towards better stability conditions invoked by the sea level change are by far offset by the evolution towards worse stability conditions caused by the drastic bottom temperature change.

→ Having this in mind, a few words need to be mentioned about the time scale. Although the modelling was performed for a well documented period between the LGM and the present-day situation, the acoustic data show evidence that this episode should have taken place before the LGM. The fact that the *Magellan* mounds are buried under a package of sediments of several meters to tens of meters, while these mounds are up to 100 m high, means that sedimentation rate should be extremely large if this event took place since the LGM. According to *D. Long* [*pers. comm.*], an extensive sub-horizontal reflection is observed just beneath (couple of m) the base of the *Magellan* mounds. This horizon has been mapped during BGS site surveys as "the near base Quaternary horizon". Based on well prognosis, the sedimentation rates through the Neogene and Quaternary are rather low (0.046 $m \cdot ka^{-1}$ res. 0.073 $m \cdot ka^{-1}$) [*D. Long, pers. comm.*]. However, if the base of the *Magellan* mounds is located at about 21.5 ka BP, then the sedimentation rate for most of the Quaternary would have to be only 0.011 $m \cdot ka^{-1}$ and sharply increase to over 5 $m \cdot ka^{-1}$ since the LGM. Hence, if the hydrate mediating event took place earlier in the Quaternary, then a more uniform rate of sedimentation could be envisaged. Nevertheless, since this area appears to be subject to major bottom temperature oscillations within short time spans that are not restricted to the most recent geological time scale the temperature effect is most probably of higher importance than the (also large amplitude) sea level changes.

→ Although several assumptions and suggestions were made, the results show that at present the spatial extent of the methane hydrate stability in the *Magellan-Hovland* province is restricted to the deepest part of the area. Under glacial conditions, the extent was much larger. Knowing that climate underwent important and sometimes fast changes, one can assume that similar climatic oscillations also occurred during the past. One can further assume that – also in other shallow areas – hydrate accumulations (if any) will be very sensitive to changing environmental controls. Especially the effect of sea level changes needs to be combined with details about the bottom water temperature changes before any conclusion can be drawn. But in all cases, especially gas hydrate accumulations in relatively shallow water areas show the highest degree of sensitivity to environmental changes.

2.5
Quantitative estimation of the buoyancy effect on (partially) hydrated sediments

As mentioned in the introduction, the density of pure gas hydrates is approximately 900-920 kg/m^3 and is thus smaller than the average density of pore fluids (1000 to 1030 kg/m^3) saturating the sedimentary section. This means that the hydrate particles are subject to buoyancy, which will result in an upward acting force. Especially for these sites were hydrates are observed at or very close to the sea or lake floor (e.g. Gulf of Mexico, Oregon Hydrate Ridge) or in mud volcanoes (e.g. the Håkon Mosby Mud Volcano in the Norway-Greenland Sea or in the Black Sea), this phenomenon is important. These hydrate occurrences are related to fluid discharge sites (seeps, faults, mud volcanism). It is worth noting that seafloor hydrates undergo rapid dissolution. They can be maintained at the sea floor only due to a high rate of upward migration of gas saturated waters. High diffusion and dispersion of methane in the seawater however hinders the formation of hydrates at the seabed [*Egorov et al., 1999*].

Here, quantitative theoretical estimations in a simplified situation are made for determining the minimum content of gas hydrates in the shallow subsurface before spontaneous uplift occurs of this part of the sediment column. Therefore, a mathematical formalism needs to be developed, based on averaged properties (densities) of the constituting parts of the section. Using the results of this methodology, a critical evaluation is brought of the proposed hypothesis for the catastrophic density-driven overturn in Lake Nyos, a crater lake on an extinct volcano in Cameroon, 1986 [*Rodgers & Yevi, 1996*].

2.5.1
Situation

Assume a porous, permeable and isotropic medium completely saturated with an incompressible homogeneous fluid. This means on the one hand that the mathematical formalism is reduced to simple vector equations without tensors, and on the other hand that no free gas and gas concentration gradients are present. Free gas percolation through the HSZ is ignored here. Furthermore, gas hydrate occupies part of the pore spaces. No explicit time dependence of the entire system is taken into consideration, i.e. a steady-state situation without sedimentation and subsidence. Also heat flow is believed to be constant. Internal fluid flow, as a result of local total energy differences, can occur and is the driving force of shear forces. The primary energies in this case are the potential energy, the pressure energy and the thermal energy. The composition of the pore water is identical to the composition of the overlying water mass.

2.5.2
Density of pure hydrates and bulk sediment

Knowing the fractional filling of each type of cavity in the hydrate structure, the exact density of pure methane hydrates can be determined, based upon the properties of a unit crystal cell. The necessary parameters are mentioned in table 1.1. The density of pure hydrates then, is defined as follows [*Sloan, 1998*]:

$$\rho_h = N_A^{-1} V_{cell}^{-1} \left[N_w W_w + \sum_{j=1}^{c} \sum_{i=1}^{n} y_{ij} \upsilon_i W_j \right] \qquad [1]$$

with N_w number of water molecules per unit cell

N_A Avogadro's number

V_{cell} volume of a unit cell

W_j molecular weight of component j

n number of cavity types per unit cell

c number of components in hydrate phase

y_{ij} fractional occupation of cavity i by component j

υ_i number of type i cavities per water molecule in unit cell

The fractional occupation of the cavities for the pure methane hydrate structure differs for fresh vs. salt water environments. For the interval between 0 and 25°C, the cavity occupation numbers and calculated density is shown in figure 2.39. The density of salt water hydrates appears to be only slightly higher than the density of fresh water hydrates due to the higher saturation values, and hence will not make any difference for buoyancy. The big cavities have a higher saturation value than the small cavities, as was already mentioned in the introduction. The increase of density with increasing temperature is not significant. An average density of 915 kg/m^3 will be used in this study. Situations in which other cavity saturation values will lead to slightly different critical conditions for uplift to occur, but as is shown, this does not change the density in a significant way.

The bulk density of fluid-saturated, partially hydrated sediments can be expressed as a weighted equation of the densities of the constituting parts, i.e. the grain skeleton, the pore fluids and the hydrates, taking into consideration the volumetric distribution. The following relationship is obtained:

$$\rho = (1-\phi)\rho_m + \phi\left[S\rho_h + (1-S)\rho_f\right] \qquad [2]$$

with ϕ total porosity of the sedimentary unit

S partial hydrate occupation of the pore space

ρ_m density of the sedimentary skeleton or matrix

ρ_f density of the saturating incompressible pore fluid

ρ_h density of pure hydrates, defined by [1]

This relationship can be easily rewritten in a solid part comprising the skeleton and the hydrate particles and a fluid part, enclosed in the effective pore space ϕ_{eff}, i.e. the total pore space minus the fractional hydrate space.

$$\rho = (1-\phi)\rho_m + \phi_h\rho_h + \phi_{eff}\rho_f = (1-\phi_{eff})\rho_s + \phi_{eff}\rho_f \qquad [3]$$

with $$\rho_s = \frac{1}{1-\phi_{eff}}\left[(1-\phi)\rho_m + \phi_h\rho_h\right] = \rho_m - \frac{\rho_m - \rho_h}{1-\phi_{eff}}\phi_h \qquad [4]$$

$\phi_h = \phi S$ fraction of hydrate in bulk sediment

$\phi_{eff} = \phi(1-S)$ fraction of pore fluid in bulk sediment

$\phi = \phi_{eff} + \phi_h$

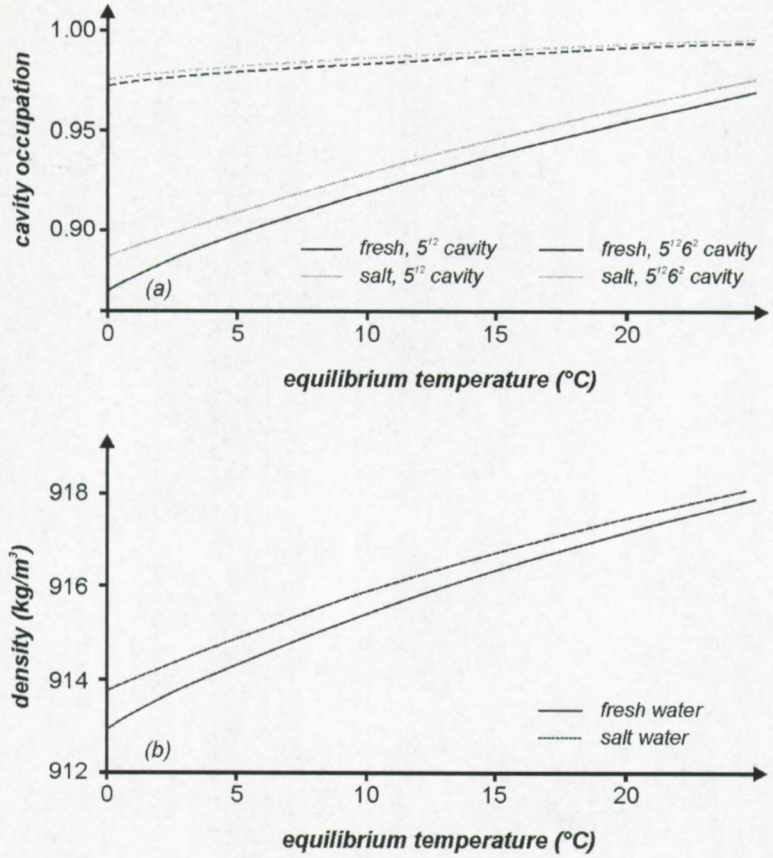

***Figure 2.39**: Cavity occupation (a) and density (b) for pure methane hydrates in a fresh water and average salt water environment for equilibrium temperatures between 0 and 25°C. Cavity occupation numbers were determined using the program CSMHYD [Sloan, 1998]*

Figure 2.40 shows the effect of hydrate saturation on the bulk density using formula [2] and the effective porosity. Also the density of the solid part of the section (i.e. sedimentary matrix and hydrate in pore space) is given. The density of the skeleton was 2500 kg/m^3 with a primary porosity of 60%. Generally, the porosity is a function of sub-bottom depth and decreases with increasing burial depth of the sediments due to compaction (e.g. Athy's law). This is not taken into consideration in this model.

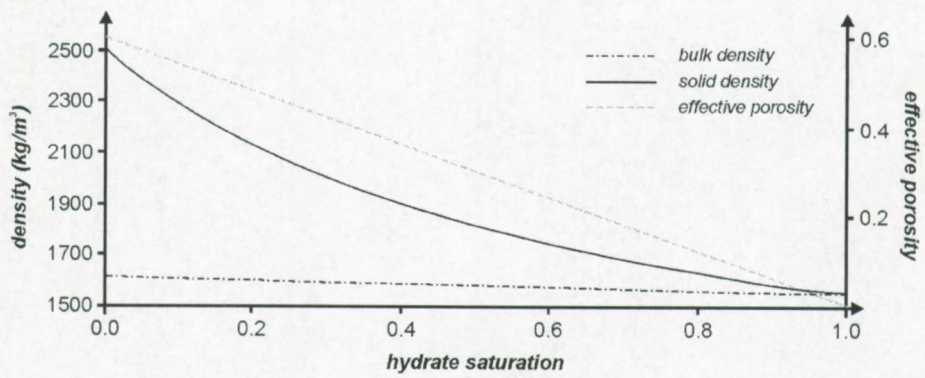

***Figure 2.40**: Bulk sediment density, density of the solids (grains and hydrate) and effective porosity as a function of hydrate saturation of the pore space. Density of the grain skeleton is assumed to be 2500 kg/m^3, the porosity is 60%.*

2.5.3
Total force per unit volume of porous medium

The most important driving forces for fluid flow are sedimentary compaction, buoyancy and gravity [*Lawrence & Cornford, 1995*]. When fluid flow in porous media is considered, the fluid exerts forces on the solid particles present, in our case the matrix and the hydrates accumulated in the pore space, assuming that these are in equilibrium and fixed before the flow was initiated. Three forces need to be considered in this case. First of all, gravity is acting on all objects. The density difference between the hydrate particles and the fluid gives rise to uplift or buoyancy, and finally, due to the fluid displacement, shear force or fluid seepage need to be included.

2.5.3a Weight of the solids (grains and hydrate)

Gravity is acting on all solid objects into the vertical downward direction:

$$\vec{F}_{grav,m} = -\gamma_m (1-\phi)\vec{e}_z = -\gamma_m (1-\phi)\vec{\nabla} z \qquad [5]$$

$$\vec{F}_{grav,h} = -\gamma_h \phi_h \vec{e}_z = -\gamma_h \phi_h \vec{\nabla} z \qquad [5']$$

which leads to the total gravity force on the solid particles:

$$\vec{F}_{grav} = \sum_j \vec{F}_{grav,j} = -\left[\gamma_m (1-\phi) + \phi_h \gamma_h\right]\vec{\nabla} z = -(1-\phi_{eff})\gamma_s \vec{\nabla} z \qquad [6]$$

Here, γ_j represents the specific weight (density multiplied with gravitation acceleration) of component *j*.

2.5.3b Buoyancy or uplift force

Uplift is caused by density gradients in a mixed system and is mainly controlled by temperature and salinity, both of which usually increase with increasing burial depth [*Lawrence & Cornford, 1995*]. These forces will naturally lead to convectional fluid flow. The result is equal to the resultant of the fluid pressure in the pore spaces P_p acting on the solid particles [*Bear, 1972*]. For the matrix and hydrate parts, the buoyant forces can be written as follows:

$$\vec{F}_{buoy,m} = -(1-\phi)\vec{\nabla} P_p \qquad [7]$$

$$\vec{F}_{buoy,m} = -\phi_h \vec{\nabla} P_p \qquad [7']$$

The total effect of buoyancy is:

$$\vec{F}_{buoy} = \sum_j \vec{F}_{buoy,j} = -(1-\phi_{eff})\vec{\nabla} P_p \qquad [8]$$

2.5.3c Seepage or shear force

The driving force allowing fluids to flow through a porous medium is the hydraulic head. Movement is causing friction at the fluid-solid contact area, leading to energy dissipation. In this way, a force is exerted on the solids by the passing fluid in the direction of the fluid displacement. Darcy's empirical law expresses fluid flow (at low Reynold's numbers):

$$\vec{q} = K\vec{J} = -K\vec{\nabla}\varphi = -K\vec{\nabla}\left(z + \frac{P_p}{\gamma_f}\right) \quad [9]$$

with $\vec{q}$ fluid discharge or Darcy-velocity

$\vec{J}$ hydraulic gradient

K hydraulic conductivity, assumed to be univariant, i.e. a scalar unit

φ hydraulic head

For fluid flow to take place, the pressure gradient has to be non-hydrostatic. The hydraulic conductivity expresses the ease with which fluid migrates through a porous medium, so it depends both on matrix and fluid properties [*Bear, 1972*].

The average fluid velocity vector is related to the Darcy-velocity by

$$\vec{v} = \frac{\vec{q}}{\phi_{eff}} \quad [10]$$

The net force exerted on a fluid element – and acting on the solid particles as shear force – in a porous medium is composed of the spatial pore pressure variability and gravity and can be written:

$$\vec{F}_{seep} = \phi_{eff}\gamma_f\vec{J} = \frac{\phi_{eff}\gamma_f}{K}\vec{q} = -\phi_{eff}\gamma_f\vec{\nabla}\left(z + \frac{P_p}{\gamma_f}\right) = -\phi_{eff}\gamma_f\vec{\nabla}z - \phi_{eff}\vec{\nabla}P_p \quad [11]$$

2.5.3d Total force per unit of porous medium

The superposition principle states that the total interacting force on the solid particles is the vector sum of the independent parts:

$$\vec{F} = \sum_j \vec{F}_j$$

$$\vec{F} = -\left[\gamma_m(1-\phi) + \gamma_h\phi_h + \gamma_f\phi_{eff}\right]\vec{\nabla}z - \vec{\nabla}P_p = -\gamma\vec{\nabla}z - \vec{\nabla}P_p \quad [12]$$

or $$\vec{F} = -(1-\phi_{eff})\gamma_s\vec{\nabla}z - (1-\phi_{eff})\vec{\nabla}P_p + \phi_{eff}\gamma_f\vec{J} \quad [12']$$

or in terms of a force potential

$$\vec{F} = -\vec{\nabla}\xi \qquad \text{with} \qquad \xi = \phi_{eff}\gamma_f\varphi + (1-\phi_{eff})(P_p + \gamma_s z) \quad [13]$$

The specific submerged weight of the solid particles is denoted as γ^* and is defined as:

$$\gamma^* = \gamma - \gamma_f = (1-\phi_{eff})(\gamma_s - \gamma_f) = \gamma_m^* - \gamma_h^* \quad [14]$$

with $\gamma_m^* = (1-\phi)(\gamma_m - \gamma_f)$

$\gamma_h^* = \phi_h(\gamma_h - \gamma_f)$

So the total force (and its three components) can alternatively be written:

$$\vec{F} = \gamma_f \vec{J} - \gamma^* \vec{\nabla} z \qquad [15]$$

$$F_X = \gamma_f J_X = -\frac{\partial P_p}{\partial x} = -\gamma_f \frac{\partial \varphi}{\partial x}$$

$$F_Y = \gamma_f J_Y = -\frac{\partial P_p}{\partial y} = -\gamma_f \frac{\partial \varphi}{\partial y}$$

$$F_Z = -\gamma^* + \gamma_f J_Z = -\gamma - \frac{\partial P_p}{\partial z} = -\gamma^* - \gamma_f \frac{\partial \varphi}{\partial z}$$

or using a second force potential

$$\vec{F} = -\vec{\nabla}\chi \qquad \text{with} \qquad \chi = \gamma_f \varphi + \gamma^* z \qquad [16]$$

2.5.4

Interpretation and discussion

Due to the superposition principle of vector calculus, the three components of the total force can be treated individually. The main component for this discussion is the vertical acting one, since this net force will define a kind of threshold fractional occupation of hydrates, before buoyancy is effectively resulting into an upward motion of part of the sedimentary section. For defining the diverse appearing parameters in an unambiguous way and getting a clear overview of the relative importance of these, the discussion is split up into different parts. In every subparagraph, the x- and y-dependence of the total force, which are only dependent on the partial derivatives of the pore pressure in these directions, will be mentioned. It is evident that, if the pore pressure is purely hydrostatic (i.e. the pressure results only from the entire overlying water column) or lithostatic (i.e. the fluids support the sedimentary matrix) there is no net force acting in the horizontal plane, as is clearly seen from [14]. The presence of fluid movement however, will change the pore pressure distribution, so this dependence can no longer be ignored.

2.5.4a Critical hydrate saturation factors and ratios

The system is in equilibrium as the total acting force is zero. More specific using [15], this means that the pore pressure is not dependent on the spatial variables x and y and that the vertical component is zero as well. In this case, the following condition has to be fulfilled:

$$F_z = -\left(1-\phi_{eff}\right)\left(\gamma_s + \vec{\nabla} P_P\right) + \phi_{eff}\gamma_f J_z = -\gamma - \frac{\partial P_P}{\partial z} = -\gamma^* + \gamma_f J_z = 0 \qquad [17]$$

In the simplest situation without internal fluid flow $\vec{J} \equiv 0$, the minimum condition for spontaneous uplift of partially hydrated sediments occurs once a positive vertical component of the total force is present. This means once the bulk submerged weight is less than zero, or in other words, once the density of the fluid phase exceeds the bulk density:

$$-\gamma^* = \gamma_f - \gamma = \gamma_h^* - \gamma_m^* > 0 \qquad [18]$$

In terms of hydrate saturation of the pore space, this means:

$$\phi_h\left(\gamma_h - \gamma_f\right) > \left(1-\phi\right)\left(\gamma_m - \gamma_f\right) \quad \Rightarrow \quad 1 \geq S > \frac{1-\phi}{\phi}\frac{\gamma_m - \gamma_f}{\gamma_f - \gamma_h} \geq 0 \qquad [19]$$

The critical hydrate saturation factor is shown in figure 2.41. It appears that this condition can only be fulfilled at extreme high values of porosity (more than 93% of porous medium). Matrix density was taken to be 2500 kg/m³. At lower matrix densities, the necessary conditions are weaker, for denser grain material the conditions are stricter.

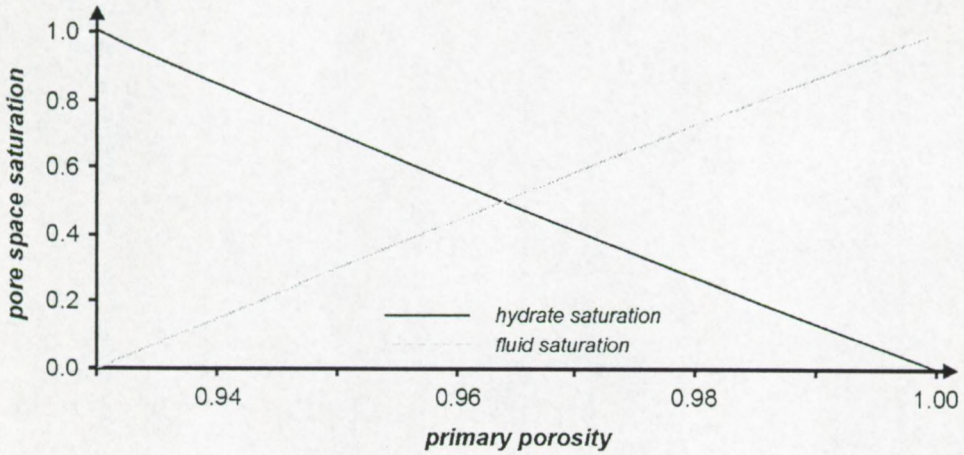

***Figure 2.41**: Minimum hydrate and maximum fluid saturation of porous volume allowing spontaneous uplift of sediments to occur, according to formula [17]. Matrix density was assumed to be 2500kg/m³. Almost pure methane hydrates should be present for uplift to occur since the minimum primary porosity needs to exceed 93% in this situation.*

For example, if the porosity is 98%, for spontaneous uplift to occur the section has to be composed of more than 27% of hydrate and less than 71% of pore fluids. At 94% porosity, the hydrate phase has to exceed 80% and the fluid phase less than 14%.

Formula [19] also leads to a value of the ratio α of the hydrate fraction to the grain fraction of the bulk sediments for uplift to occur, once a critical value α_{cr} is exceeded:

$$\alpha \equiv \frac{\phi_h}{1-\phi} > \frac{\gamma_m - \gamma_f}{\gamma_f - \gamma_h} \equiv \alpha_{cr} \qquad [20]$$

Hence, the critical ratio α_{cr} equals 13.32, which means that the hydrate fraction needs to be at least a factor of 13.32 larger than the grain's fraction for upward movement to occur. Matrix densities of only 1600 kg/m³ require a critical fraction of 5.2. This critical value as a function of matrix density is given in figure 2.42. The ratio α is always positive or zero and has no upper limit. It approaches infinity when the primary porosity approaches unity. At that time, the medium can no longer be considered as a porous medium.

A similar equation can be obtained, combining formulas [4], [14] and [18] (and the fact that the effective pore space is less than 100%). This results in the following boundary condition for uplift to occur:

$$\rho_s = \rho_m - \frac{\phi_h}{1-\phi_{eff}}(\rho_m - \rho_h) < \rho_f \qquad [21]$$

thus that the density of the solids (hydrate and grains) has to be less than the pore fluid density. The ratio β of the hydrate fraction to the solid fraction must satisfy the relation:

$$\beta \equiv \frac{\phi_h}{1-\phi_{eff}} > \frac{\rho_m - \rho_f}{\rho_m - \rho_h} \equiv \beta_{cr} \qquad [22]$$

Using the same density values as before, the limit lies at 0.93, or again 93% of the solid fraction has to be hydrate. This also leads to extreme high porosity values (hydrate is supposed to be located in the porous space) with almost no skeleton. Grain densities of only 1600 kg/m³ result in 84%. Also this critical ratio is given in figure 2.42, as a function of matrix density. The β ratio value falls between 0 (no hydrate) and 1 (pure hydrate).

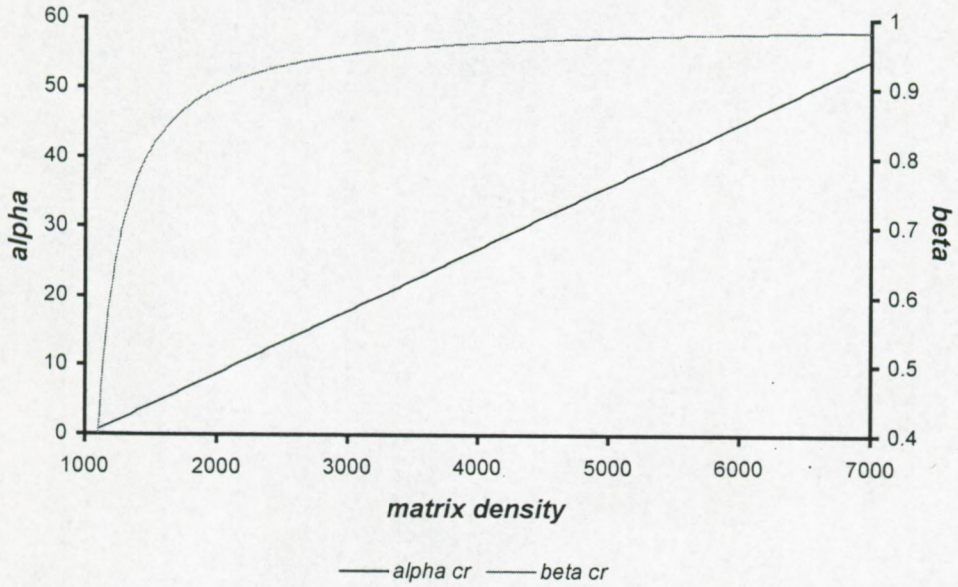

***Figure 2.42**: Minimum conditions of the ratio α_{cr} of the hydrate fraction to the skeleton fraction, and the ratio β_{cr} of the hydrate fraction to the solid fraction (skeleton and hydrates) as a function of matrix density. In every case, for spontaneous uplift of partially hydrate-saturated sedimentary sections to occur, values exceeding these minimum values need to be present. Hence, the hydrate fraction has to be extremely high.*

2.5.4b Application: massive hydrate recovery during DSDP-Leg84, Middle America Trench

If massive hydrates are found well within the sedimentary section, spontaneous uplift is not readily to occur due to an overburden weight of on average denser sediments although the above relations might hold true. For example, in the Middle America Trench massive hydrates were observed at approximately 250 m sub-bottom depth at water depths of 1718 m. The "massive" samples were taken from an almost pure hydrate block of 3 to 4 m thickness. The sample contained over 95% of sI-hydrate and less than 5% of sediments, hence no effective porosity was present. The density bulk of the sample was approximately 1050 kg/m³ [*Sloan, 1998*]. This results in a grain density of 3615 kg/m³. Even in this extreme case of hydrate saturation, the α and β ratios of the hydrate content relative to the matrix fraction res. solid fraction as defined in [20] and [22] are less than the critical value:

$\alpha = 19.0 < 23.4 = \alpha_{cr}$
$\beta = 0.950 < 0.959 = \beta_{cr}$

Hence, no uplift can occur due to the high average grain density. Grain densities suitable for uplift can be determined, using the known values of the hydrate fraction ratios α and β determined from the known bulk distribution (95% hydrate, 5% sediment and no fluid). This can be done by plotting the critical values as a function of variable matrix density, starting from the calculated real grain density, as is shown in figure 2.43. It appears that the maximum grain density for allowing instability with

this hydrate concentration equals 3128.4 kg/m^3 (figure 2.43), significantly less than the actual density.

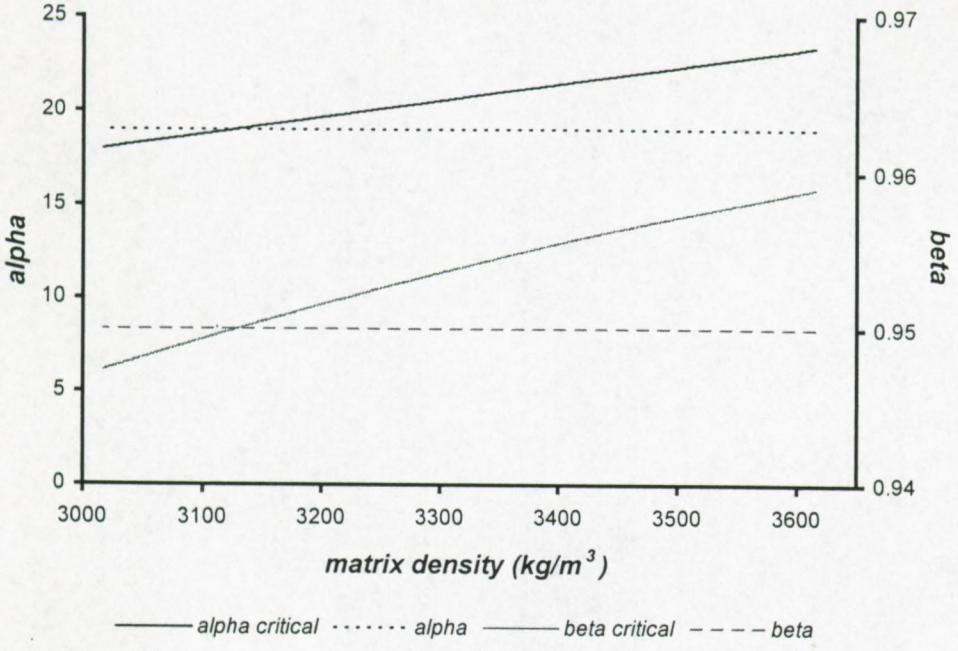

***Figure 2.43**: Variation of both hydrate saturation critical factors α_{cr} and β_{cr} as a function of the density of the sedimentary matrix. Ideal conditions appear when these curves cross the respective values α and β determined from knowledge of the hydrate distribution (95% hydrate, 5% sediment, no fluid) of the massive hydrate recovered during DSDP Leg 84 (site 570), i.e. at 3128 kg/m^3, significantly less than the observed density.*

Even if the density of the grains should be less than this critical value, uplift of fully saturated hydrated samples at a certain sub-bottom depth will not occur easily, due to the overburden weight of the sedimentary section above with less hydrate.

2.5.4c Uplift of massive hydrate samples at the seabed

The buoyancy of hydrate samples found at or in the immediate vicinity of the seabed is a special situation of the above-mentioned case. The vertical component of the total force per unit volume [17] is always directed upward and has a constant value that only depends on the density difference between hydrate and water.

$$F_z = -\gamma^* = \gamma_f - \gamma_h > 0 \qquad [23]$$

The Newtonian laws of motion then result in a constant upward acceleration of a pure hydrate sample:

$$\rho_h \frac{d^2 z}{dt^2} = (\rho_f - \rho_h) g > 0 \qquad [24]$$

And finally the travel path time for released hydrate samples through the water column of height H (figure 2.44):

$$\Delta t = \sqrt{\frac{2\rho_h H}{(\rho_f - \rho_h)g}} \qquad [24']$$

Typical time scales for this process is less than 1 minute for water depths up to 2000 m. Once the hydrate crystals pass the HSZ border in the water column (see figure 1.3) the structure will dissociate. The free coming gas will dissolve in the surrounding water or will migrate upward in the form of gas bubbles. If hydrates remain at the seabed, a bounding pressure between the hydrate and the surrounding sediment particles has to exceed the buoyant pressure at depth H [*Lerche and Bagirov, 1998*] (figure 2.44):

$$P_{bond} \geq P_{buoy}\langle H \rangle = (\gamma_f - \gamma_h)H \qquad [25]$$

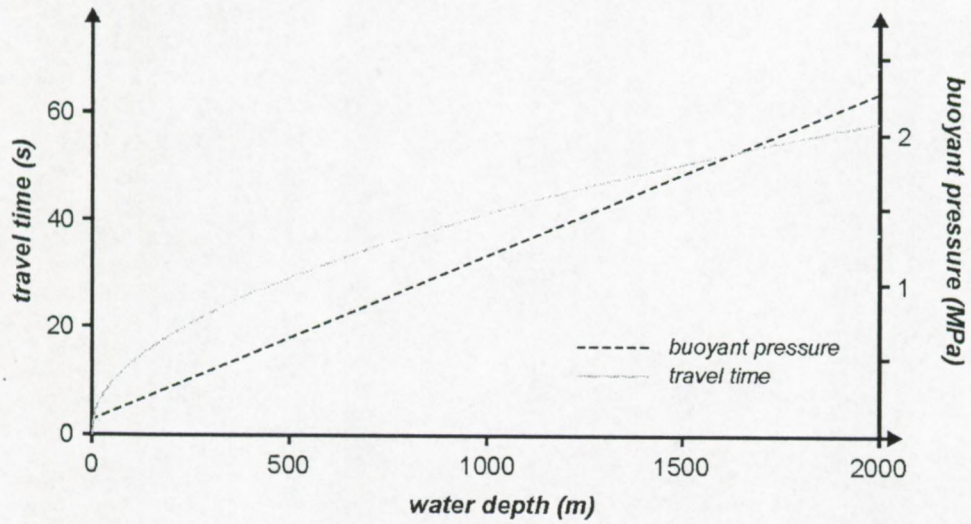

***Figure 2.44**: Travel time for uprising hydrate crystals and buoyant critical pressure for remaining hydrates at the seabed, as a function of water depth.*

Individual hydrate particles observed at some depth from the seabed, will also undergo buoyancy. However, due to the random grain size distribution and most probably a pure upward acting force, these hydrates might find serious difficulties in travelling towards the water column. This is dependent on the size of the hydrate particle, the distance to the seabed, and the pore size distribution.

2.5.4d Influence of internal fluid migration

In case of fluid migration, $\vec{J} \neq 0$ and the three components of the total active force will generally not vanish. The two components of this force in a horizontal plane are only influenced by their respective space co-ordinate x and y. The pore pressure will hence be dependent on these variables as well. This movement however does not alter the vertical component. Hence, the horizontal spatial dependence of the pore pressure will be ignored in further analyses. For the vertical component, equation [17] needs to be solved:

$$F_z = -(1-\phi_{eff})(\gamma_s + \vec{\nabla} P_p) + \phi_{eff}\gamma_f J_z = -\gamma - \frac{\partial P_p}{\partial z} = -\gamma^* + \gamma_f J_z \qquad [17]$$

Internal fluid flow will obviously alter the system's pore pressure distribution, which will be no longer hydrostatic and hence will alter the *in situ* stability conditions compared to the simplified situation in

paragraph 2.1. It is known that the deviation from hydrostatic pressure drives fluid flow, and can find its origin in compaction or sealing effects within the sediments. Supposing that the fluid density of the porous medium is the same as the density of the overlying water column, the pore pressure distribution can be written as:

$$P_P\langle z \geq 0, H \geq 0, J_z \rangle = P_0 + \gamma_f (z + H) + \gamma_f \int_0^z J_z dz \qquad [26]$$

or $P_P = P_0 + \gamma_f \cdot (z + H) + \gamma_f z J_z$

if J_z is independent of z

with P_0 atmospheric pressure at the water-air interface (0.101325 MPa)
z burial depth
H height of the water column

Overpressures are present as the fluid flow rises, while lower pressures exist in downward flow.

Equation [17] makes it furthermore possible to define a critical hydraulic gradient as a limiting value for movement to take place:

$$J_{cr} = \frac{\gamma^*}{\gamma_f} = \frac{(1-\phi)\gamma_m + \phi_h \gamma_h - (1-\phi_{eff})\gamma_f}{\gamma_f} \qquad [27]$$

If the vertical component of the hydraulic gradient is equal to this critical value, the system is in equilibrium. Smaller values indicate downward movement, bigger values indicate upward movement. Whenever in vertical upward fluid flow ($J_z > 0$), the force component F_z is directed downward ($F_z < 0$), the soil is stable. If $F_z > 0$, an upward acting force is present and the soil loses its stability. This happens as

$$J_z > J_{cr} = \frac{\gamma^*}{\gamma_f} \qquad [28]$$

The critical gradient depends on porosity and hydrate saturation S of the pore spaces, but also on the density of the sedimentary matrix. Figure 2.45a presents the critical gradient as a function of hydrate saturation of porous volume. Porosity is assumed to be 60% and the density of the sedimentary matrix is 2500 kg/m^3. Also the bulk density of the sediments is given as a function of hydrate saturation of the pore spaces. Typical values of the critical gradient vary between 0.5 and 0.6. For lower skeleton densities, the values for the critical gradient are smaller as well. For example, if the density is 2000 res. 1500 kg/m^3, then the critical gradient is calculated to be approximately 0.35 res. 0.15.

Figure 2.45b illustrates the dependence of the critical gradient of the grain density, supposing a fractional filling of porous volume with hydrates of 5%. The critical gradient was calculated for densities between 1100 to 4000 kg·m^{-3} with intervals of 10 kg·m^{-3}. Porosity was 60%.

Typical hydraulic conductivity values of pervious and semi-pervious sediments lie between 10^{-2} for sands and 10^{-8} m/s for very fine sand or silt [*Bear, 1972*]. With a common compaction-driven internal fluid migration velocity of $3.17 \cdot 10^{-11}$ m/s (i.e. 1 mm/year) [*Rempel & Buffett, 1998*], Darcy's law [9] results in hydraulic gradients between 10^{-11} to 10^{-3}, thus several orders of magnitude smaller than the necessary critical value. Even with fluid displacement rates of a factor 10 higher, the pore pressure elevation due to the fluid flow is in both cases very close to the hydrostatic pressure distribution (figure 2.46). No significant deviations from the stability field will be observed (a couple of meters, which falls within the range of accuracy of the applied method). With the low conductivity value, the curve cannot be resolved from the hydrostatic pressure. Remarkably, if the critical hydraulic gradient is reached, the pore pressure will even exceed the lithostatic pressure with the above-mentioned

assumptions of density and porosity sub-bottom profiles. Such a situation is not believed to be realistic, and hence, spontaneous uplift of partially hydrated sediments will not occur, except perhaps in extreme cases of exceptional fluid displacement rates.

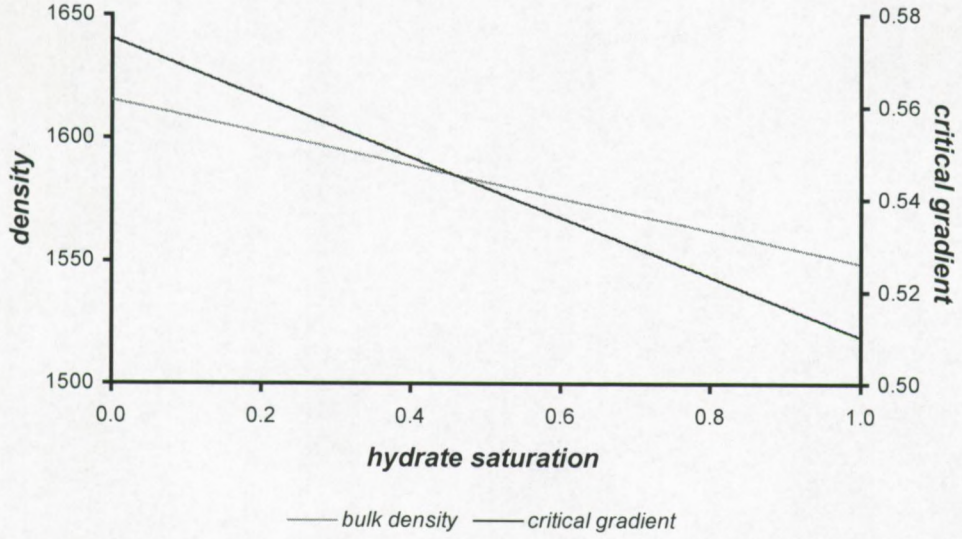

***Figure 2.45a**: Bulk density and critical gradient as a function of hydrate saturation of the pore space. Primary porosity is 60%, the density of the skeleton is 2500 kg/m³.*

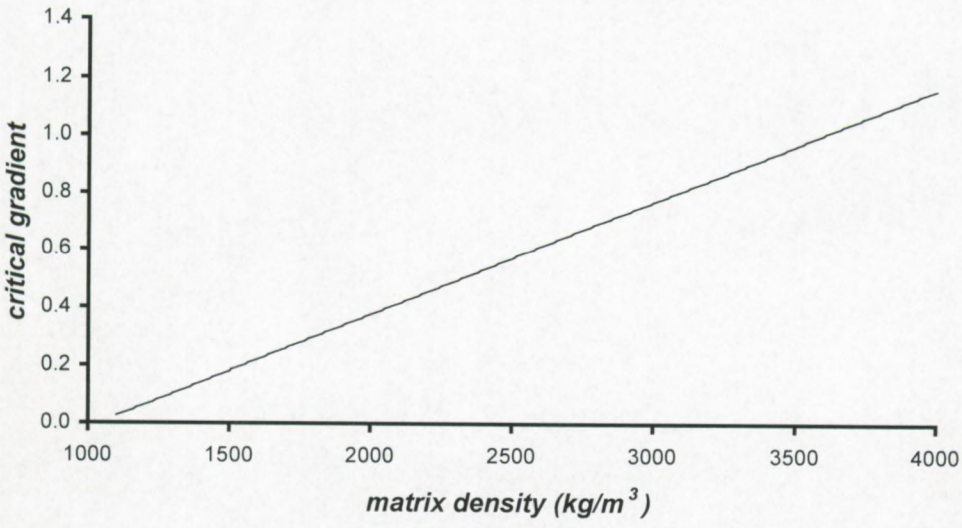

***Figure 2.45b**: Critical gradient as a function of matrix density, with 60% porosity and a partial filling of porous volume with hydrate of 5%.*

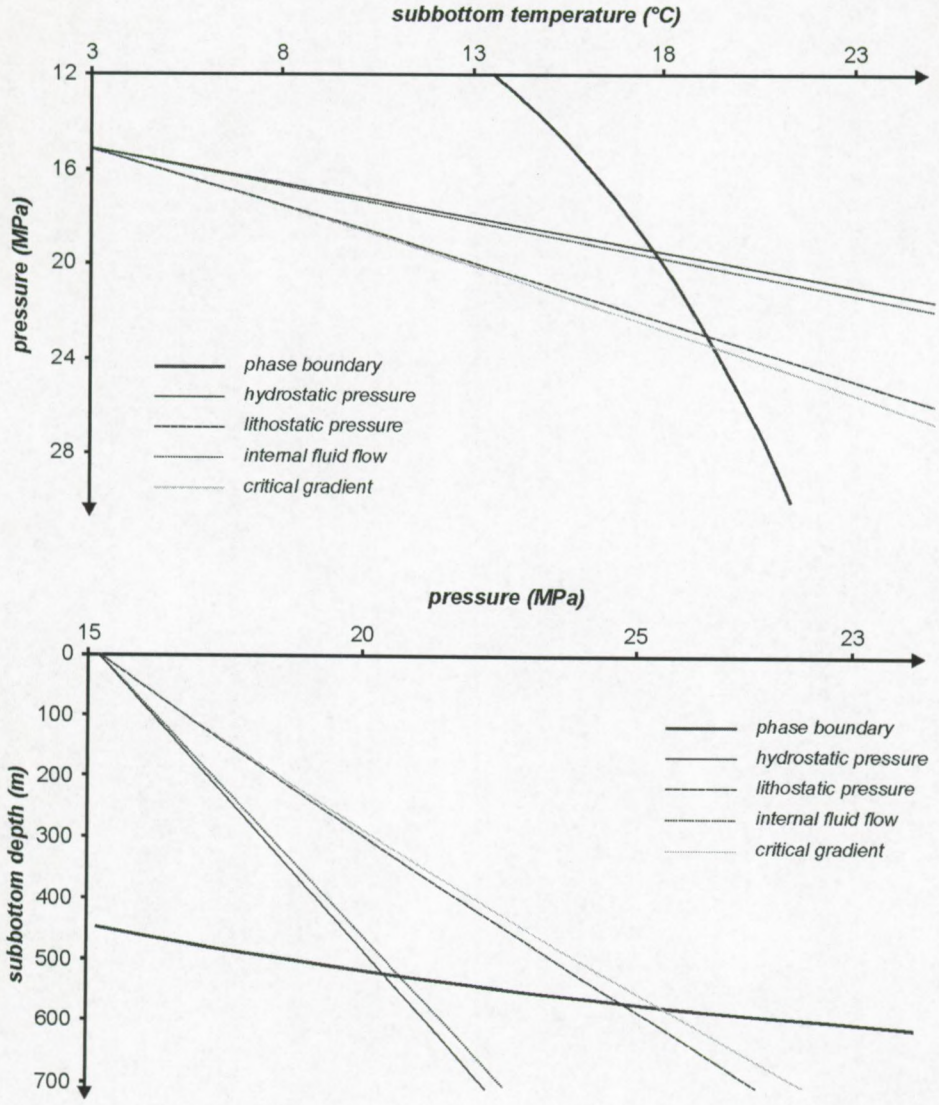

***Figure 2.46**: Influence of fluid migration onto the extent of the HSZ at water depths of 1500 m and geothermal gradient of 0.035°C/m. Fluid migration velocity was assumed to be 1 cm/year. At the critical gradient, values exceeding the lithostatic pressure result.*

2.5.5
Application: the Lake Nyos disaster

Note: more details about geochemistry and limnology are compiled in Fouquet [1999].

Lake Nyos is a 208 m deep asymmetric crater lake with a 10-20 m platform located at about 1100 m above sea level and has a surface area of 1.4 km^2. It lies on an extinct volcano along the still active 1600 km long Cameroon Volcanic Line. Precipitation is high in the area, and during the rain season the local fault systems can be easily saturated with meteoric water. The oldest volcanic activity dates back to 30 Ma BP. Two fault systems cross in the immediate neighbourhood of the lake. The lake itself is formed by a series of phreatomagnetic eruptions [*Barberi et al., 1989*]. The water column is stratified: three water masses are recognised below the thermocline (2-13 m) and have different densities due to slightly different temperatures and dissolved components. The deeper water (> 50 m) is anoxic. Dissolved gas is mainly CO_2, with minor concentrations of N_2 and CH_4. Next to that, traces gases like Ar, CO and H_2S were detected [*Kling et al., 1989*]. Dissolved CO_2 accounts for most of the increasing water density with depth, while the solubility increases with increasing pressures. This

density profile is explained by the slow leakage of magmatic CO_2 [*Zhang, 1996*]. Inversion of the regime can result in spontaneous lake degassing... [*Chau et al., 1996*].

In August 1986, a massive jet of water and gas erupted from Lake Nyos. Reaching a height of over 100 m, the heavy lethal gas displaced the air below it and swept down the slope, asphyxiating 1746 people in the villages below the lake [*Ladbury, 1996*]. The volume of the gas cloud was estimated to be 40-60 m^3 [*Freeth, 1992; in Rodgers & Yevi, 1996*] to 170±50 m^3 [*Chau et al., 1996*] and 1200 m^3 [*Kling et al., 1987*]. This was however not the first of that kind of eruption. A few years earlier, a similar event with smaller impact took place in Lake Monoun, also located along the Cameroon Volcanic Line. Geochemical analyses pointed out that the CO_2 released was mainly of magmatic origin ($\delta^{13}C$ values of –3.4 to –2.2‰). At present, three alternative scenarios are proposed, i.e. the limnic hypothesis (degassing in the lake water), the volcanic hypothesis (eruption of high temperature gases from beneath the lake floor combined with volcanic activity) and eruption of gases that had been accumulated within the sediments [e.g. *Fouquet, 1999 for more details*]. The most plausible explanation is the *limnic hypothesis*, i.e. the dramatic density-driven overturn of supersaturated CO_2-containing water masses although the triggering mechanism (thermal or mechanical) is yet unknown [e.g. *Kling et al., 1989*] but is supposed to be initiated at the lake bottom [*Chau et al., 1996*]. As a result, the CO_2-rich water is forced to well up causing dissolved gas to come out of solution. Buoyancy then finishes the job... Nevertheless, the triggering mechanism is yet not well understood. Landslides, seismic shocks, water mixing and turbulence, cold meteoric water inflow are considered [see *Fouquet, 1999*].

Another theory states that the triggering could have been the spontaneous uplift of massive hydrates from the lake bed [*Rodgers & Yevi, 1996*]. The formation of hydrates in the shallow sub-surface will reduce the effective porosity and most probably also the permeability of the sediments. In case of continuous internal fluid migration through the major and minor fault systems, the hydrated sediments might form a trap, resulting in storage of overpressured fluids underneath it. With increasing overpressure within the pore spaces, the stability of the sediments becomes critical and small external triggering can force failure to occur. As a consequence, the formerly captured gases are released into the water column and finally into the atmosphere.

As was shown in the first chapter, hydrates have the ability to store huge amounts of H_2S relative to the free gas concentration. Especially the presence of H_2S is important in this discussion. Symptoms of the victims clearly indicated that the exsolved gas contained sulphurous irritant components while these are not present in the water column [*Rodgers & Yevi, 1996*]. As mentioned, H_2S readily forms gas hydrates. *Rodgers & Yevi* [*1996*] calculated that at local thermodynamical conditions at the lake bed (bottom water temperature is approximately 23.5°C [*Kling et al., 1989*]) mixed hydrates of CO_2, CH_4 and H_2S can be stable with different concentrations. This was verified by *Fouquet* [*1999*]. At these thermo-dynamical conditions at the lake bed, the gas phase should consist of 55.5% of H_2S [e.g. *Fouquet, 1999*]. This percentage will give rise to an occluded H_2S concentration exceeding 90% in the solid hydrate structure. This means that most of the H_2S will be clathrated in the pore spaces, without leaking into the water column. As mentioned, H_2S is only found as a trace gas in the lake water, with a concentration less than 0.2‰ mole fraction [*Giggenbach et al., 1991; Kling et al., 1989*] while at the lake bed, the gas is almost pure CO_2.

Unfortunately, very little is known about the sediments on the bed of Lake Nyos and almost nothing about their physical properties due to severe problems during sampling of both water and sediments. The few retrieved samples contained disturbed sediments. No *in situ* measurements of physical properties have been undertaken up till now. Also the use of high-resolution seismics failed since the acoustic energy was absorbed or the acoustic source was not powerful enough [*S. Freeth, pers. comm.*]. So it is difficult to check the methodology outlined above. *Kling et al.* [*1987*] mention that the flat plain at 208 m water depth is formed of silt and mud of unknown (but most probably very thin) thickness. One sediment sample from the bottom indicated the presence of feldspar, quartz, biotite and kaolinite without fresh volcanic constituents [*Kling et al., 1987*].

Assume a rather low grain density for fine-grained silt or clays of 1450 $kg \cdot m^{-3}$ [*Carmichael, 1982*]. Using formula [1] the density of possible hydrates using a diversity of H_2S, CO_2 and CH_4 compositions falls between 875 and 925 $kg \cdot m^{-3}$. The density of the pore fluid is taken to be the same as the water density at the lake bottom, shown in *Fouquet* [*1999*] from *Kanari* [*1989*], i.e. 1002.2 kg/m^3. In this approximation, the critical alpha- and beta-values are calculated to be 3.52 res. 0.78. In other terms, the solid should consist of approximately 78% of hydrate and a maximum of 22% of sediment for uplift to occur. The porosity at the lake bed has to be very high as well.

Such a spontaneous uplift of sediments is rather unlikely to happen. It is doubtful whether sufficient amounts of gases can be transported and incorporated into hydrate structures at or close to the lake bed without escaping within the overlying water column. Furthermore, massive samples of hydrates found in nature are rare, except in places with known very high fluid displacement rates like mud volcanoes. If hydrates form at the seabed, there needs to be a binding force as well to keep them down against their buoyancy. The formation of almost pure hydrate layers with reasonable spatial dimensions in sediments is not easily understood. In that case, the formation of hydrates should be thought of being responsible for moving aside part of the sediments, while most often the fluids to be incorporated in the hydrate structure come from deeper parts of the sedimentary basin. If the sediments are moved upward due to hydrate formation, spontaneous uplift will be inhibited, because the hydrates are buried by denser sediments.

Rodgers & Yevi [*1996*] suppose that these gases migrate from deeper parts. They finally got stored into the solid hydrate form well below the water contact, so no H_2S will escape in the water column. But then the problem arises how the hydrates can disturb the sediments in a way they move the sediments apart at depth and fill the gap created. Next to that, the fact that Lake Nyos is a very young lake (< 1000 a) [*Schenker & Dietrich, 1986; Kling et al., 1987*] only a few meters to a few tens of meters of sediments are present at the lake bed [*S. Freeth, pers. comm.*]. Mixing of the upper sediment layers (< 2 m) is supposed to have taken place at the time of the disaster [*Piboule et al., 1990*]. If hydrates crystallise from migrating saturated pore waters it will take geological time scales to form massive hydrates. Physico-mathematical modelling showed that, for 1% of pore spaces to be filled with hydrates, one needs about 200 ka in a normal compaction-driven internal fluid migration field [*Rempel & Buffett, 1997*]. Hence, even for high fluid displacement rates, full saturation of pore spaces with hydrates will take over 2 Ma. It is furthermore important to stress once more that massive gas hydrates are rare. This represents in my opinion a gap in the theory. It is most doubtful whether the very small amount of deposited sediments can store sufficient gas molecules and hydrates and what would be the origin of the molecules in this young lake?

In the above paragraphs, the influence of naturally occurring climatic fluctuations and its effects on the vertical extent of the HSZ was investigated in a static sediment section, i.e. ignoring several important geological processes like sedimentation, sediment removal (slides, slumps, debris flows) and subsidence. While sedimentation and basin subsidence can most probably be considered as long-scale continuous processes with time (with variable amplitude), mass wasting processes occur suddenly with full amplitude. Also these processes obviously will be responsible for a changing thermodynamical environment at a specific time scale. In this section, the main influences of these processes on the evolution of the hydrate stability limit are being discussed on a purely qualitative level due to a lack of experimental or published data, except for the influence of slope failure on the Norwegian margin, based on seismic data acquired with R.V. Professor Logachev during the TTR8-expedition (1998). These aspects are just mentioned for completeness to the subject.

2.6.1
Mass wasting events in hydrate provinces: the Storegga Slide

2.6.1a Relation between hydrate dissociation and slope stability

It is generally believed that the decomposition of gas hydrates can play a role in mass wasting events on the continental slopes by weakening the mechanical strength of sediments. This is for example the case for the Storegga slide offshore Norway [*Bugge et al., 1987*], on the Beaufort Sea margin [*Kayen & Lee, 1991*] and offshore southeastern United States [*Dillon et al., 1998*]. Unfortunately, no unambiguous theory is available up till now and the proposed models lack experimental evidence.

The general idea is the following. As mentioned in the previous chapter, for the pure methane hydrate structure with 90% of the cavities filled with methane molecules, it is calculated that at standard temperature and pressure conditions, one volume of hydrate releases approximately 0.8 volumes of water and 155 volumes of gases (see chapter 1). This means, for *in situ* conditions with conservation of pore volume [note: the hydrates are considered to be part of the pore space], that the 155 volumes of gas need to be compressed into 0.2 volumes of pore space. It is obvious that this process can lead to the creation of overpressures in the pore spaces in which hydrate decomposition takes place, if no lateral or vertical dissipation of the excess pore fluid takes place. The presence of free gases may result in a decrease of shear strength. If this zone of weakness is located at some tens to hundreds of meters in inclined slope sediments, the interacting gravity can induce slope failures, initiated by the hydrate decomposition.

2.6.1b The Storegga Slide, offshore Norway

The Storegga Slide is known as one of the biggest underwater mass wasting events. The slide is up to 450 m thick and the total displaced volume of sediments is estimated to be of the order of 5500 km^3 [*Bugge et al., 1987*]. The headwall, being the steepest part of the slide, has an average gradient of 10-20°. Based on seismic profiles, sediment samples and Gloria side-scan sonar data, *Bugge et al.* [*1987, 1988*] defined three main stages of sliding events (with additional minor slides) of which the first one - between 30 ka and 50 ka BP - was the most important one.

This first mass wasting event moved in the form of a debris flow and extended into the abyssal plane, about 800 km further west relative to the headwall, comprising the entire slide scar area. The mobilised sediments are believed to be relatively soft, fine grained Plio-Quaternary clays [*Bugge et al., 1987*]. The last two major slides (8-6 ka BP) cut deeper into the more consolidated sediments in the

central part of the first slide area. The deposits contain some large, almost undisturbed sediment units. The deposits of the second slide are the most extensive and far-travelled [*Bugge et al., 1987*]. The third event only disturbed the central and upper part of the slide scar.

The occurrence of BSRs interpreted to represent the BHSZ on the Vøring Plateau and their possible relationship with the initiation of the Storegga Slide on the Norwegian shelf edge have previously been reported [*Bugge et al., 1988*; *Mienert et al., 1998*]. *Bugge et al.* [*1987*] hypothesised that the main triggering mechanism for the slides was likely to have been earthquake loading with a possible contribution of ice loading for the first slide event. After the observation that the inferred gas hydrates are located at the same depth of part of the gliding plane, decomposition of hydrates may have contributed to the triggering of the slides, after an earthquake suddenly reshaped the pore pressure distribution in the sedimentary column, leading to liquefaction [*Bugge et al., 1987*] and weakening of the sediments.

A detailed description and interpretation of a series of single-channel airgun profiles (TTR-8 expedition, 1998) with clear evidence of the BHSZ in the form of a BSR was worked out in close collaboration with S. Bouriak from Moscow State University and was recently published [*Bouriak et al., 2000*]. A full copy is added in the fifth chapter of this dissertation. Here, more details are presented about the hydrate stability aspects and influence of the mass wasting process. In the paper, sea level changes since the Storegga Slide were ignored. Here, the evolution of the theoretical extent of the methane hydrate stability since the sliding event is presented, by means of a combination of bottom temperature changes and pressure changes. The paper (see last chapter) furthermore presents a formation model for the occurrence of two spatially separated zones of inferred hydrate accumulation by 3-D fluid migration in combination with diapirism in the upper zone. Next to that, the repositioning of the BSR within the slide scar area to newly established present-day equilibrium conditions was used to derive internal fluid migration velocity in the area.

2.6.1c Hydrate stability conditions: hydrostatic pressure distribution

The possible influences of sliding, and in particular the Storegga Slide events, on gas hydrate destabilisation and/or vice versa have been actively discussed. For instance, *Bugge et al.* [*1987*] and *Jansen et al.* [*1987*] proposed gas hydrate decomposition due to earthquake agitation of sediments as one of the most likely triggering mechanisms for the Storegga Slide. *Mienert et al.* [*1998*] noticed that, as a consequence of earthquakes or mass wasting events which provoke gas hydrate to decompose, the consequent release of gases and water in the pore space would exceed the volume that was previously occupied by the solid gas hydrate structure. This leads to - eventually drastically - increased pore pressures, facilitating further sliding. Next to that, the rapid release of methane during major slide events in coincidence with gas hydrate dissociation might have serious implications for the marine methane cycle and possibly for the global climate system [*Lammers et al., 1995a, 1995b*]. Thus, any quantitative estimates of these effects are of significant interest.

During the summer of 1998, single-channel airgun acoustic profiles were acquired across the Storegga Slide scarp, offshore Norway [see last chapter, and *Bouriak et al., 2000*] with clear evidence of BSRs in two separated zones. Acoustic inversion pointed out that the different BSRs are most probably related to a gas hydrate – free gas interface since a significant acoustic velocity drop was observed to be present across this boundary. Having observed BSRs inside the slide scar area and below slide deposits, it seems possible to estimate how sliding could affect the gas hydrate stability in this area. It should be emphasised that such procedure strongly depends on the assumptions made about the pore pressure distribution.

In case of hydrostatic pore pressure distribution, no sliding nor earthquake would affect the overall hydrate stability:

➔ After removal of the uppermost sediment of the seafloor, the hydrostatic pore pressure would remain unchanged since this value only depends on the height of the entire overlying water

column, and not of the amount of sediments deposited at this location. This is clearly an *in situ* isobaric process.

→ Immediately after the slide, the seafloor is now formed by sediments initially exposed at higher temperatures due to burial under the suddenly removed sediments. The temperature difference existing between the seabed and the bottom water mass will cause a gradual decrease of the sub-bottom temperature profile. As a consequence, the base of the GHSF will slowly move deeper into the sediments, until a new equilibrium position is reached. In this case, the hydrate stability conditions are always guaranteed. The *in situ* conditions at the pre-slide equilibrium limit will not be changed immediately, so this situation (*in situ*) is also isothermal.

The temperature effect with time now depends on the thickness of the removed sediments and the geothermal gradient that appears to be relatively uniform within the area [*Bouriak et al., 2000*]. In order to determine the time scale of the evolution of the pre-slide stability limit to the post-slide and present-day equilibrium limit, line PSAT96 (figure 2.47) was used to calculate the thickness of the removed sediment layer. Along this line, two locations were selected for further analyses: at the slide scarp with present-day water depth of 910 m (point 1) and 15 km further down-slope at present-day water depths of 1260 m (point 2). At the first location, approximately 85 m (114 ms TWTT) of sediments was removed, while at the second location still 30 m (39 ms TWTT) of sediment was removed.

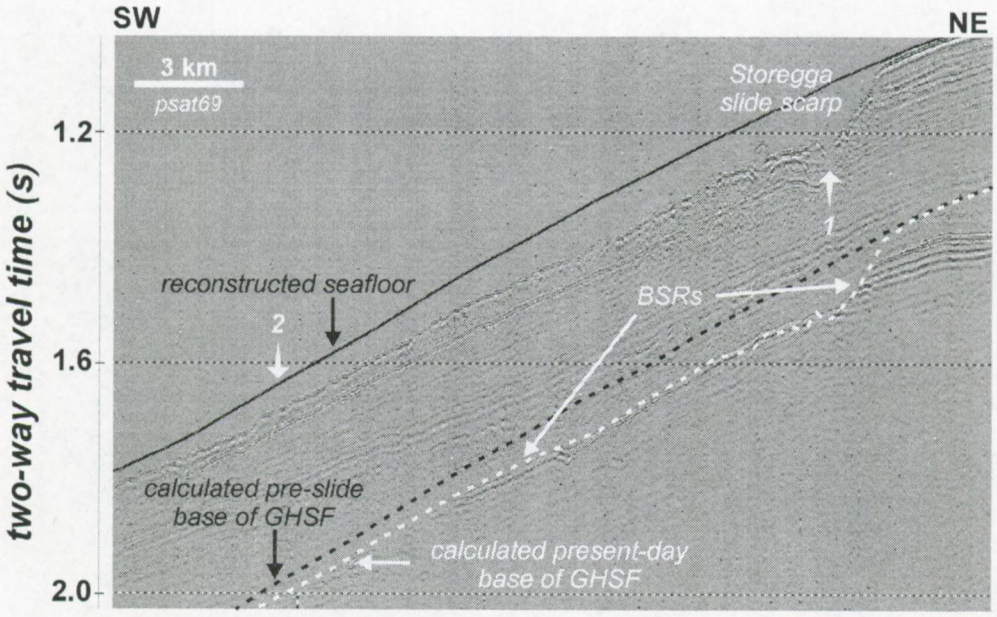

***Figure 2.47**: Single-channel airgun profile PSAT69 acquired during the TTR8 expedition (1998). A BSR is observed below the slide scarp and within the slide area. This profile is used to determine the thickness of removed sediments after reconstructing the paleo-seafloor. Locations 1 and 2 mentioned in the text are indicated.*

Concerning the delayed temperature effect on the hydrate stability conditions, the slide event can be considered as generating a variable temperature disturbance that fades out down-slope in the slide area. Using the hydrostatic pressure distribution, the steady-state geothermal field was calculated to be 0.0515°C·m^{-1} outside the slide area [*Bouriak et al., 2000*] while the bottom water temperature is approximately 0°C [e.g. *Mienert et al., 1998; Thiede et al., 1989*]. Similar geothermal gradients were reported by *Mienert et al.* [*1998*] for this area. Before the sliding took place, the entire area is assumed to have had a uniform geothermal field. At the slide scarp (location 1), the temperature pulse has a magnitude of 4.38°C while at the second location the magnitude is 1.55°C using the linear sub-bottom temperature profile. In both cases, the disturbance has the effect of a sudden arrival of a cold front since the sediments are initially exposed at their respective steady-state temperature and suddenly are

washed by much colder bottom water currents. It was furthermore assumed that the mass wasting process does not affect the local water temperature.

The sensitivity of the extent of the theoretical HSZ due to this temperature effect can then be determined, applying the methodology outlined in §2.3. In other words, the BHSZ will slowly deepen (no pressure effect!) but with variable magnitude along the acoustic section due to the variable thickness of sediments removed and hence the spatial variation of the thermal pulse. This evolution is shown in figure 2.48 for both locations covering a time period of 50 ka, i.e. about the time that passed by since the first Storegga Slide [*Bugge et al., 1987*]. The difference between 30 and 50 ka appears to be only 5 m for location 1 and 2 m for location 2. Note that at present no changes of sea level are taken into consideration.

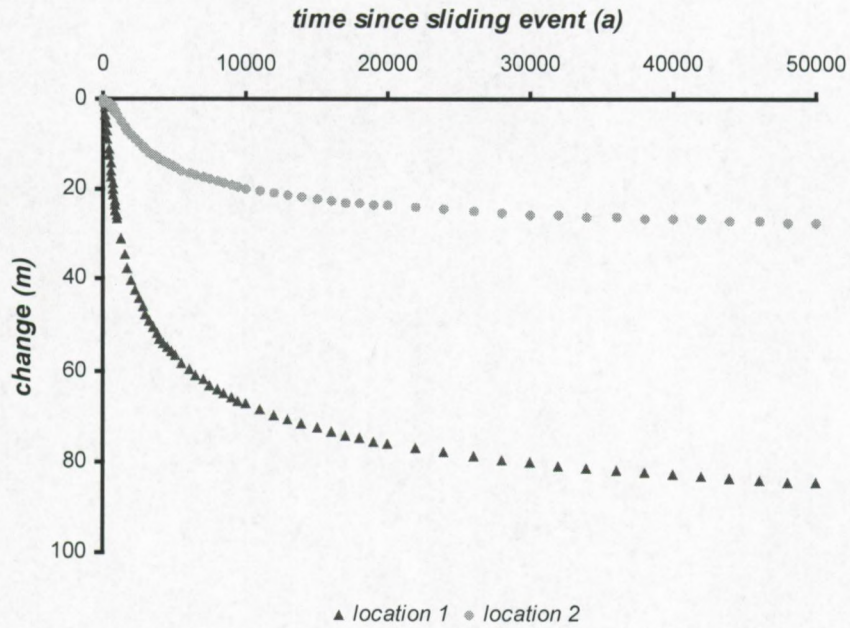

***Figure 2.48**: Evolution with time of the BHSZ after the slide took place, assuming hydrostatic pore pressure distribution*

Also the mean geothermal gradient over the hydrate stability interval varies due to the sliding and the subsequent temperature effect. After 50 ka, the difference between the initial and final geothermal gradient is only 0.0031°C·m^{-1} (location 1) res. 0.0012°C·m^{-1} (location 2). As a consequence, the deepening of the new stability limit with time has about the same order of magnitude as the thickness of the removed sediments.

As a conclusion, an arbitrary point within the initial HSZ or at equilibrium condition at total depth Z below sea level will slowly evolve towards more favourable stability conditions, as shown in figure 2.49. This process is delayed relative to the slide. Points initially falling out of the stability field, can migrate towards stable conditions as well, depending on the thickness of the removed sediments.

2.6.1d Hydrate stability conditions: lithostatic pressure distribution

The removal of the uppermost part of the sediments automatically reduces the lithostatic pressure immediately at the pre-slide equilibrium depth without changing the hydrostatic pressure. As a consequence of the sliding, the mean lithostatic pressure effect within the remaining sedimentary body at burial depth z will be reduced by the following term:

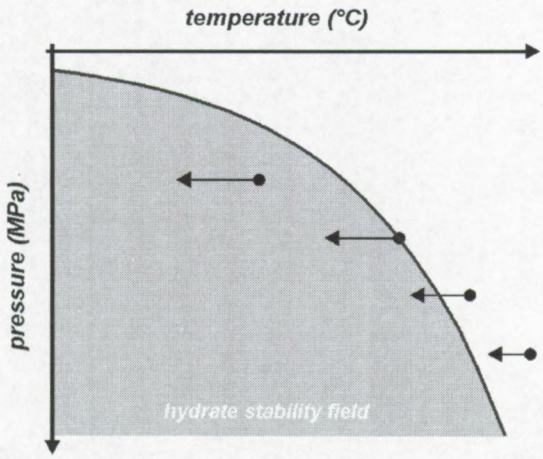

***Figure 2.49**: Sketch of the evolutionary track of different points within and outside the stability region as a result of mass wasting processes, supposing hydrostatic pore pressure distribution.*

$$\Delta P_{lith}\langle z\rangle = g\cdot(\rho_{sw} - \rho_{bulk})\cdot\Delta h$$

with ρ_{sw} sea water density (1025 kg·m^{-3})
ρ_{bulk} mean bulk density (1800 kg·m^{-3})
Δh change of local water depth due to sliding (m)

and is independent of burial depth. Substituting the calculated thickness of the removed sediments at the two locations on the acoustic section PSAT69, the instantaneous pressure reduction is approximately -0.65 MPa at the slide scarp and -0.23 MPa at a distance of 15 km. This pressure reduction will be responsible for a sudden *in situ* hydrate instability while the *in situ* temperature conditions will not be altered immediately similar to the hydrostatic pressure approach. The use of lithostatic pressure to determine the local geothermal field using the TTR8 seismic reflection data set instead of the hydrostatic pressure also resulted in slightly higher heat flow. The geothermal gradient turned out to be 0.0558°C·m^{-1} [*Bouriak et al., 2000*]. This also means that the amplitude of the cold front will be slightly higher for this approach, i.e. 4.74°C for the first location and 1.62°C for the second location.

Using the methane hydrate pressure-temperature analytical phase boundary equation [see §2.1], the theoretical extent of the stability field in the pre-slide situation and the instantaneous post-slide situation was analysed. A sketch of these together with the present-day situation in which the temperature effect becomes of primary importance is presented in figure 2.50. Table 2.5 then gives the impact of the sliding event for the two locations shown on profile PSAT69. Note that at present the influence of hydrate dissociation on pore pressure due to the overburden pressure reduction is not taken into account.

The evolution with time of arbitrary points at fixed depth below sea level within and outside the initial stability field assuming lithostatic pressure is represented in figure 2.51. In this case, first an instantaneous isothermal depressurisation takes place, followed by a slow delayed isobaric temperature reduction. In this situation, it is supposed that the hydrate will adapt immediately according to the overall bulk conditions. This means, it is supposed that no thermal or pressure effects related to phase changes (latent heat, creation of overpressure during hydrate dissociation) take place.

At those two locations, it will take different time scales before the thermal pulse acting with different amplitude will influence the medium at depth. The temperature effect will anyhow force the system

back into more favourable conditions. At the slide scarp (location 1), the thermal deviation limit reaches the equilibrium sub-bottom depth after 175 years since the slide event. At that time, the pressure-induced dissociation will be opposed by the thermal pulse. A few tens of years later, the thermal pulse penetrates the initial conditions and the system evolves towards more favourable conditions relative to the initial situation before the slide. At location two, the thermal disturbance caused by the slide has a much smaller amplitude and the equilibrium depth lies deeper within the sediments. There, it will take approximately 1000 years before the thermal pulse is active in terms of hydrate stability conditions.

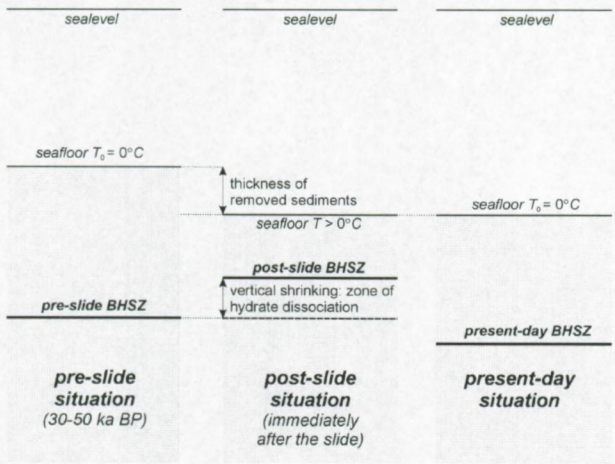

***Figure 2.50**: Sketch of the influence of the slide effect on the sub-bottom position of the BHSZ. The pre-slide, post-slide and present-day situations of the vertical extent of the HSZ are shown using the lithostatic pressure approach. Assuming hydrostatic pressure distribution, the system will move slowly but directly from the initial phase towards the present-day situation, i.e. without intermediate upward migration of the stability limit.*

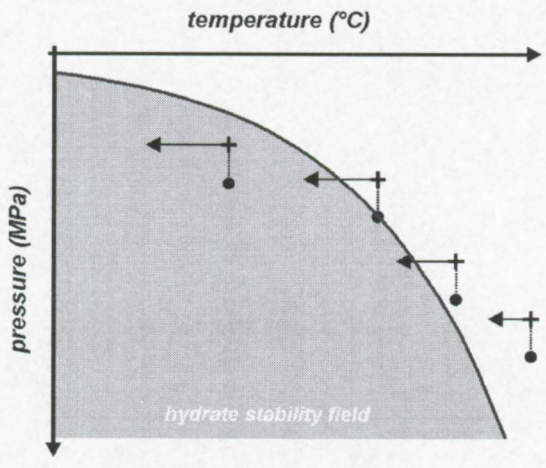

***Figure 2.51**: Sketch of the evolutionary track of different points within and outside the stability region as a result of mass wasting processes, supposing lithostatic pore pressure distribution.*

The same procedure was then carried out for the entire area where BSRs occur within the slide area: the paleo-seafloor (i.e. the situation before the first Storegga Slide event) was reconstructed using the available acoustic profiles and the position of the base of the GHSF before sliding was calculated within the area. The calculated thickness of that part of the initial GHSF falling out of the newly established GHSF in the intermediate situation just after the sliding is shown on figure 2.52, assuming lithostatic pore pressure distribution. However, it should be noted here that, even if we do assume excess fluid pore pressure at sub-bottom depths less than 300 m, the pore pressure in reality would still hardly reach the lithostatic one. Also the mean bulk density used for the section within the

HSZ will be a maximum value for this area. Thus, this calculated thickness is clearly overestimated, and even in this case, beside the areas directly below the escarpment, the average vertical shrinking of the GHSF due to the slide event seems to be less than 4 m. The biggest influence of the mass wasting event is observed at the headwall of the slide where approximately 6-10 m of the sedimentary section falls out of the newly established stability field.

	location 1	location 2
pre-slide conditions		
water depth (m)	825.0	1230.0
geothermal gradient (°C/m)	0.0558	0.0558
bottom water temperature (°C)	0.00	0.00
sea floor temperature (°C)	0.00	0.00
subbottom equilibrium limit (m)	253.6	304.8
depth below sea level (m)	1078.6	1534.8
in situ lithostatic equilibrium pressure (MPa)	12.88	17.86
in situ equilibrium temperature (°C)	14.15	17.01
in situ post-slide conditions		
water depth (m)	910.0	1260.0
thickness of removed sediments (m)	85.0	29.0
geothermal gradient (°C/m)	0.0558	0.0558
bottom water temperature (°C)	0.00	0.00
sea floor temperature (°C)	4.74	1.62
subbottom depth (m)	168.6	274.8
depth below sea level (m)	1078.6	1534.8
in situ lithostatic pressure (MPa)	12.23	17.62
in situ temperature (°C)	14.15	17.01
new post-slide equilibrium conditions		
water depth (m)	910.0	1260.0
subbottom equilibrium limit (m)	158.0	273.6
depth below sea level (m)	1068.0	1533.6
in situ lithostatic equilibrium pressure (MPa)	12.05	17.61
in situ equilibrium temperature (°C)	13.55	16.88
equilibrium pressure difference (MPa)	-0.83	-0.25
equilibrium temperature difference (°C)	-0.60	-0.13
difference equilibrium limit (total depth) (m)	-10.6	-1.2

***Table 2.5**: Influence of the sliding event on the hydrate stability conditions at locations 1 and 2, using the lithostatic pressure approach. A sketch of the situation is presented in figure 2.50.*

The total volume of sediments that was released from the GHSF due to down-slope mass movement according to figure 2.52 was calculated to be 4.13×10^8 m^3. The volume of sediments that remained undisturbed above the paleo-GHSF base is estimated to be 2.79×10^{10} m^3. *Hovland et al. [1997]* mention a fractional occupation of less than 10% (maximum) of the pore spaces with hydrates as the most common value taken from literature. Knowing this partial hydrate filling factor and assuming an average porosity of 50%, the total volume of dissociated hydrates due to sliding is estimated as 2×10^7 m^3. The volumetric gas expansion factor for hydrate dissociation was already determined in the first chapter, using the properties and dimensions of a unit cell for hydrate structure I, i.e. the methane hydrate structure. If methane molecules are present in 90% of the cavities, one volume of gas hydrate yields approximately 0.8 volumes of water and 150 volumes of free gas at STP conditions. However, to make a maximum possible estimate, we assume the cavities to be fully saturated, and correspondingly the maximum theoretical gas expansion factor of 164 [*Kvenvolden, 1998*]. Then, the total amount of destabilised gas hydrates in this area would release 33.8×10^8 m^3 gas and 1.6×10^7 m^3 water at STP conditions. At *in situ* pressures of more than 10 MPa the volume of released gas would not exceed approximately 3×10^7 m^3, due to the high compressibility of the gas. Here, we ignored the volume decrease caused by the temperature difference between standard temperature (20°C) and *in situ* hydrate equilibrium temperature, typically around 10-15°C. Possible partial dissolution of the released gas in the released water was also disregarded. Thus, at *in situ* pressures, the initial volume of 2×10^7

m^3 of dissociating gas hydrate releases in total $4.6x10^7$ m^3 of gas and water. In other words, an excess pore volume of $2.6x10^7$ m^3 needs to be redistributed through $1.4x10^{10}$ m^3 of pore spaces of the undisturbed sediments above the inferred paleo-BSR. This leads to a pore pressure increase of only 0.2%, which can - in our opinion - hardly be considered as a relevant contribution to further slope instability.

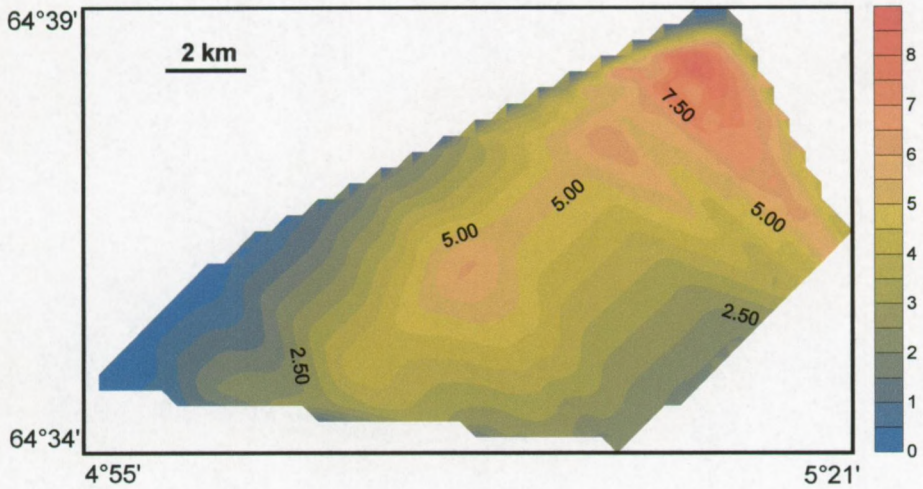

***Figure 2.52**: The calculated thickness (0.5 m intervals) of the initially gas-hydrate layer which could fall out of the HSZ due to sliding within the area where the "lower-slope BSR" was observed below the slide deposits. Lithostatic pressure distribution was assumed.*

If the same excess volume is considered to be distributed not within the whole volume of sediment above, but just within a thin layer at the initial BSR locations, the calculated pore pressure increase would be much higher. However, the only thing needed for the overpressure to dissipate through non-ideal impermeable media is sufficient time. The *in situ* dissociation of gas hydrates is supposed to be a slow process, since with consuming heat and increasing pore pressure, dissociation tends to shift the PT conditions back into equilibrium values. Furthermore, we disregarded the fact that excess pore pressure is the driving force for internal 3D fluid migration (Darcy's law), thus lateral fluid displacement can take place as well. Some volume of these migrating fluids can be exhausted with time towards the seafloor so forming a pathway for release of excess pressure. So we believe that at least the order of the estimation is quite reasonable and reliable.

Of course, these estimates exclude by no means more complicated mechanisms or models in which the dissociation of gas hydrate effectively affects the slope stability. For instance, liquefaction or the release of active fresh water into the clayey environment of the glacial/interglacial sedimentary sequence can stimulate formation of so-called "fast clays", leading to sediment failure. However, at least the most straightforward and simple mechanism of sliding vs. hydrate-dissociation interrelation will most likely not to be considered seriously in this region. In fact, the independence of the observation of the "lower-slope BSR" on weather there was sliding above it or not, is in itself indirect evidence of minor, if any, relevance of the sliding to gas hydrate dissociation and vice versa.

2.6.1e Influence of sea level changes following the first Storegga Slide event

For being correct, sea level changes should be taken into consideration as well. Suppose now that the mass wasting event evidenced by the acoustic profiles is the first Storegga Slide event taking place between 50 to 30 ka BP and that this erosion process is the only disturbance of the local geothermal regime since the slide. In other words, during the last tens of thousands of years, the bottom water

temperature in the area is assumed to have remained invariable. Then, the evolution of the methane hydrate stability limit is still sensitive to sea level changes while the stabilising effect of the thermal pulse continues and deepens within the subsurface. This system of changing sea levels according to the sea level curve of *Fleming et al. [1998]* in combination with the results obtained above is now investigated for location 1 and 2.

For the initial situation taken to be 48 ka BP, the relative sea level position is –73 m [*Fleming et al., 1998*] with bottom temperature of 0°C. Table 2.6 gives an overview of the situation in location 1 and 2 just before (equilibrium limit) and just after (*in situ* pre-slide equilibrium position and newly established bulk equilibrium limit) the sliding event. Comparison with table 2.5 learns that the influence of the sea level change is rather small. This means that the analysis of the contribution to further slope instability – although determined neglecting eustatic sea level changes – is still valid. The evolution of the vertical extent of the HSZ with time as a consequence of the mass wasting event is determined for all peak values of the eustatic sea level curve since 48 ka BP (time 0). The result is presented in figure 2.53 for using the lithostatic pressure approach (see above).

Note the important difference between the bulk equilibrium sub-bottom depth and total depth just before and immediately after the slide. While the difference in total equilibrium depth below sea level just before and after the erosion is of the order of a few to 10 m, the difference in sub-bottom depth can be an order of magnitude bigger, dependent on the thickness of removed sediments and the fact that the *in situ* temperature does not change in concert with the slide event. These figures also illustrate the relative importance of sea level changes and bottom temperature changes. At the moment of the slide, the system is pressure-dominated and a discontinuity occurs. After 175 res. 1000 years, the temperature effect positive for hydrate stability become sensible. After about 13 ka, the sub-bottom depth only varies slightly with changing sea level. Since the LGM (here about 37 ka), the methane hydrate equilibrium depth subsided over a distance of ±8 m (location 1) res. ±5 m (location 2), i.e. about twice the variation shown in figure 2.48 without taking into consideration eustatic sea level changes. The situation is rather similar using hydrostatic pressure, except that in this case pressure-effect caused by sliding is not present.

2.6.1f Conclusions

The most striking results of this study are the following:

- ➔ Excess pore pressures are a prerequisite for gas hydrate dissociation as a consequence of slope failure.
- ➔ It is determined that the shrinking of the vertical extent of the HSZ due to sliding and hence *lithostatic* pressure reduction in the area is of the order of a few m. After (some) hundreds of years, this effect is opposed by the penetration of the thermal pulse.
- ➔ At present, the thermal effect is almost completed. Sea level rice since the LGM is responsible for further subsidence of the stability field.
- ➔ The fact that there is evidence of a BSR at the present-day equilibrium conditions below and within the slide scar means that hydrate formation continued during recent times. Enough gas molecules were clathrated at depths below the pre-slide position of equilibrium.
- ➔ Taking into account global sea level changes since the slide event and ignoring other possible bottom temperature fluctuations but the sliding, shows that only minor differences occur at present. The difference of the stability limit with and without sea level fluctuations lies in the order of a few m.
- ➔ Note that the influence is determined using lithostatic pressure approach while the real pore pressure will fall in between of the hydrostatic and lithostatic one. Hence, the estimates presented here will be maximum values of what can be expected.

	location 1	location 2
pre-slide conditions		
water depth (m)	752.0	1157.0
geothermal gradient (°C/m)	0.0558	0.0558
bottom water temperature (°C)	0.00	0.00
sea floor temperature (°C)	0.00	0.00
subbottom equilibrium limit (m)	242.3	297.9
depth below sea level (m)	994.3	1454.9
in situ lithostatic equilibrium pressure (MPa)	11.95	17.00
in situ equilibrium temperature (°C)	13.52	16.62
in situ post-slide conditions		
water depth (m)	837.0	1186.0
thickness of removed sediments (m)	85.0	29.0
geothermal gradient (°C/m)	0.0558	0.0558
bottom water temperature (°C)	0.00	0.00
sea floor temperature (°C)	4.74	1.62
subbottom depth (m)	157.3	268.9
depth below sea level (m)	994.3	1454.9
in situ lithostatic pressure (MPa)	10.72	16.34
in situ temperature (°C)	13.52	16.62
new post-slide equilibrium conditions		
water depth (m)	837.0	1186.0
subbottom equilibrium limit (m)	145.4	266.5
depth below sea level (m)	982.4	1452.5
in situ lithostatic equilibrium pressure (MPa)	11.09	16.74
in situ equilibrium temperature (°C)	12.85	16.49
equilibrium pressure difference (MPa)	-0.86	-0.26
equilibrium temperature difference (°C)	-0.67	-0.13
difference equilibrium limit (total depth) (m)	-11.9	-2.4

***Table 2.6**: Influence of the sliding event on the hydrate stability conditions at locations 1 and 2, using the lithostatic pressure approach. Values were corrected for a relative eustatic sea level of –73 m around 48 ka BP (first Storegga Slide).*

2.6.2
Influence of basin subsidence and sediment deposition on hydrate stability

Variations in the sedimentary medium and typical porous medium effect can also lead to changes in the vertical extent of the hydrate stability. The most important aspects are sediment compaction, basin subsidence, sedimentation and capillarity and need to be incorporated into modelling for correctness. Since no detailed analysis of the influence of these quantities was performed, only the basic ideas will be mentioned here with some references to relevant papers.

Sedimentation can affect both the temperature profile (heat flow) and the pressure distribution, dependent on the sedimentation rate. There appears to be a progressive increase in sedimentation rate with decreasing geological age of the sediments, with an overall average of about 22 cm·ka^{-1} [*Bates & Jackson, 1980*]. Sediment deposition will in general result in reduced geothermal gradients and hence heat flow, since particles from warmer upper levels of the water column are introduced. Typical sedimentation rates for the Porcupine Basin res. Lake Baikal are 4.6 to 7.3 cm·ka^{-1} [*D. Long, pers. comm.*] res. 16 to 120 cm·ka^{-1} [*Edgington et al., 1991*], i.e. differences of a factor of 25 are not impossible.

High sedimentation rates will in general create zones of overpressure in the sediments [*Dimakis et al., 2000*] while the newly deposited sediments will only gradually warm up by heat coming from the deep basins [*Bjørlykke, 1989; Lerche & Bagirov, 1998*]. This will result in lower geothermal gradients within the shallow subsurface, and a significant time span is required before the base of the stability field will be altered. The generation of overpressure is favourable for *in situ* hydrate conditions, but one cannot forget that partial decomposition of hydrates in porous media may give rise to elevated overpressures

as well. For *small sedimentation rates*, the sub-bottom temperature profile will adapt in concert with sedimentation. As a consequence, the basal limit of hydrate stability will slowly move upward. Excess pore pressure due to hydrate dissociation at the base will most probably dissipate with time through small-scale migration pathways. Assuming a constant heat flux q from great depths, then the surface heat flow q_{sed} at time t in an area with rate of sedimentation v will be [*Jones, 1999*]:

$$q_{sed}\langle t\rangle = q_0\left[1 - 4i^2 erfc\left(0.5 \cdot v \cdot \sqrt{\frac{t}{\kappa}}\right)\right]$$

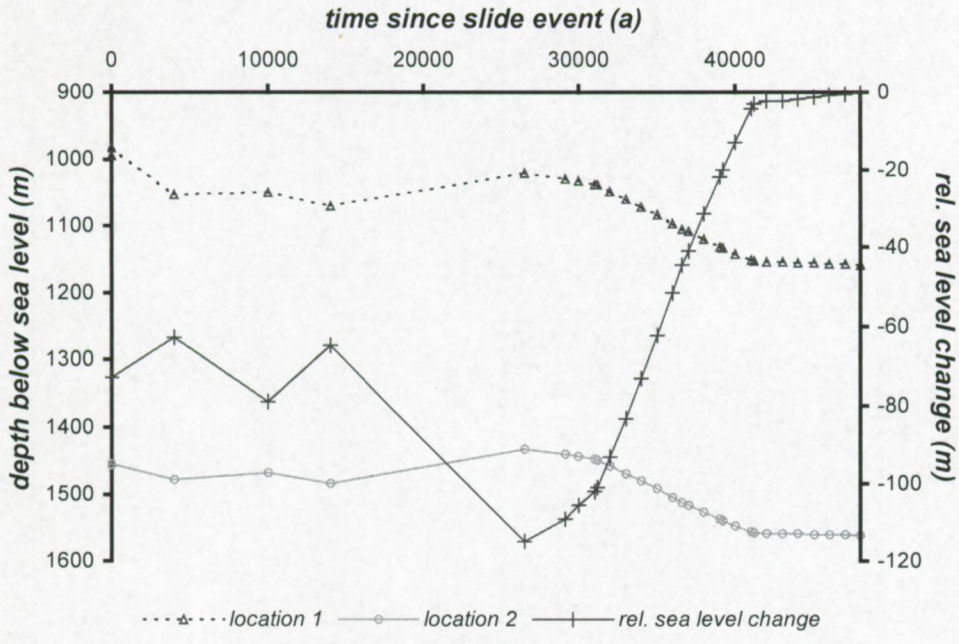

(a)

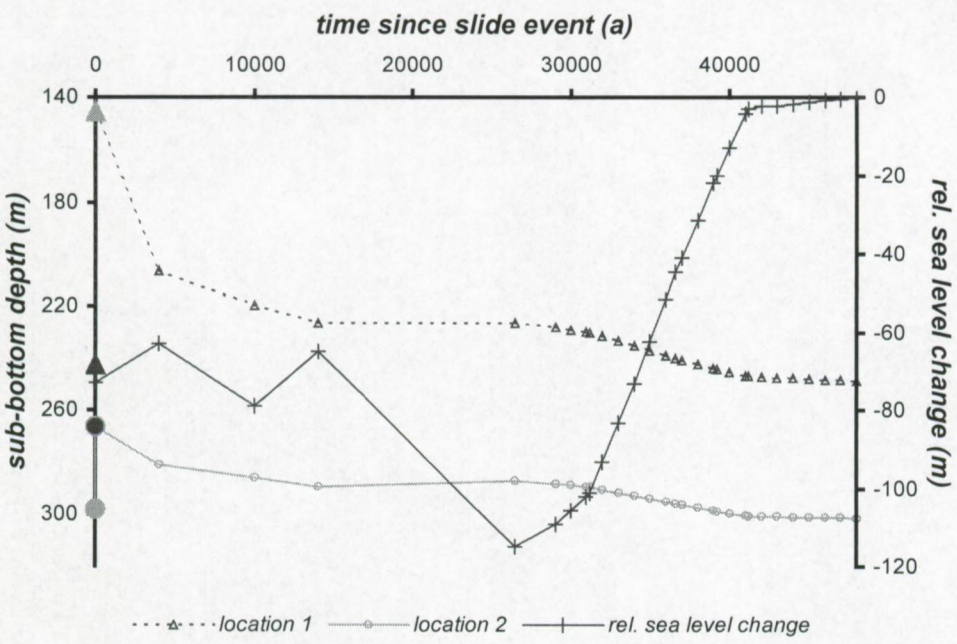

(b)

***Figure 2.53**: Evolution of the vertical extent of the methane HSZ during the last 48 ka BP, as a consequence of the slide event and eustatic sea level changes. Snapshots are shown for both location 1 at the slide scarp and location 2 15 km further down-slope. (a) total depth of the equilibrium limit below sea level and relative sea level, (b) sub-bottom equilibrium depth.*

Since the time scale of the process is important, not only fixed or temporary pore pressures but also their evolution with time will be important. Serious efforts were undertaken by e.g. *Luo & Vasseur* [*1993, 1995*], *Schneider* [*1997*], *Schneider et al.* [*1993, 1994, 1996*]. They formulate the pore pressure evolution in terms of mass conservation equations and momentum equation linking quantities like Darcy flow or percolation/migration velocity, effective stress, porosity reduction with depth, compressibility of fluid and matrix, densities, thermal fluid expansion, permeability, viscosity, temperature, sources or sinks, ... This hydrodynamic equation is rather complex and is up to now not included in the discussion of hydrate stability conditions and its variation with time.

Tectonic uplift represents an isothermal pressure decrease and will hence result in hydrate dissociation at their base of stability and release of free gas, that can possibly be recycled within the overlying hydrated section dependent on permeability and hence lithology. A more detailed discussion is given by *Von Huene & Pecher* [*1999*].

Sediment movement or *erosion* (e.g. slides, slumps, debris flows) also influences the local geothermal gradient, as is explained above in case of the Storegga Slide event. Erosion removes the uppermost colder strata and exposes warmer strata at the new sea bed. As a result the geothermal gradient will increase. With time, the base of the stability field will subside into the sediments over a limited distance.

Basin subsidence or a gradual downward settling of the sea or lake bed occurs and is in general a slow process that takes place on geological time scales. Average rates of subsidence are about 0.001 $m \cdot a^{-1}$ [*Leeder, 1999*]. Higher subsidence rates will create more sediment accommodation space. If sedimentation persists, this will lead to higher compaction. Subsidence will give rise to slowly increasing hydrostatic pressure at constant sea level. Hence, more favourable hydrate stability conditions will occur. Nevertheless, the time scale of such a process makes that this feature is of minor importance in comparison to sea level fluctuations that occur relatively fast with higher amplitude. Hydrate accumulation in polar regions or glacial settings will also be sensitive to *isostatic effects*. The present-day isostatic rebound of Fenno-Scandinavian shield is of the order 0.01 $m \cdot a^{-1}$ [*Benn & Evans, 1998*]. Extra corrections need to be introduced for determining the evolution of the hydrate stability limit in polar settings over long periods.

In nature, discrepancies between the observed base of the stability zone and its theoretical stability position do occur in some places [*Ruppel, 1997*]. Such differences are best explained by porous medium effects. Especially capillarity as a result of surface tension in small pores is thought of being responsible for deviations. The porous medium influences the gas hydrate equilibrium and the kinetics of hydrate formation. The kinetic effect lies in the fact that a pore size may be less than a gas hydrate critical nucleus size at a given temperature. In this case, for hydrate formation to start, more overcooling or oversaturation is required [*Sloan, 1998*]. It is evident that hydrate formation in coarse-grained sediments has an advantage over fine-grained sediments. The reader is referred to some excellent papers recently published on that topic for further information [e.g. *Henry et al., 1999; Clennell et al., 1999*].

Next to that, the base of the hydrate accumulation zone does not necessarily (1) coincide with the base of the theoretical HSZ and (2) coincide with the top of the gas-charged sediments [*Xu & Ruppel, 1999*]. A transition zone without free gas and without hydrate can be present below the hydrate accumulation zone and above the free gas zone. Still the intersection of the sub-bottom temperature profile with the phase boundary is denotes as the gas hydrate stability limit and at the same time the potential upper limit for free gas, but the system is also controlled by other factors (e.g. energy flux, mass flux, critical fluid migration rates, saturation).

2.7.1
Outline of the computer programs 1-2

The programs included provide the user with a helpful tool for analysing the extent of the HSZ under natural conditions and varying environmental controls, according to the equations used in this chapter. All scenarios are based upon the analytical phase boundary equation for a specific hydrate composition. This obviously means that the program is not at all restricted to pure methane hydrates, although all examples given throughout this chapter are worked out using this option. Here, only a basic summary is written down. The reader is referred to the main text for further details and governing formulas.

➔ The first step in the program is the definition of this phase boundary equation that has to fit the particular equation [1]. Standard coefficients for pure methane hydrates in both fresh water and average salt water environments are given for temperatures ranging from approximately the first quadruple point up to 25°C, i.e. a reasonable estimate of the upper temperature limit in hydrate-rich sediments. If the gas composition of interest differs from pure methane, then the program offers the possibility to define one's own coefficients in two ways. The first one uses coefficients given straight by the user or taken from literature [e.g. *Bakker, 1998*], while the second one uses input couples (minimum of 3, maximum of 300) of 3-phase equilibrium temperature (expressed in °C) and pressure (in MPa) values and applies the method of least squares. These data can for example be retrieved from the hydrate stability program CSMHYD of *Sloan [1998]*. In the last two cases, the user needs to define the fluid density as well. The returned coefficients will be used throughout the entire program, for all options and selections made until new equilibrium conditions are given by the user, i.e. by turning back to the first menu page and starting all over again. The coefficients are written in a temporary text file (phase_1 or phase_2) which will be overwritten every time the program is started up. During one session, the coefficients of the diverse sequences are written down every time they change. At the same time, the window displays the values of the coefficients, the regression coefficient, temperature interval and water density.

➔ The next window then gives an overview of the diverse options of the main outline of program_1. This is represented here, with attention for sub-programs related to the diverse topic. The parameters occurring are written italic between brackets. Also output results are given.

A. Conversion of equilibrium pressure to equilibrium temperature or vice versa
   - Determination of the 3-phase equilibrium pressure at specific equilibrium temperature
     Output: *equilibrium pressure, equivalent water depth*
   - Determination of the 3-phase equilibrium temperature at specific equilibrium pressure
     Output: *equilibrium temperature*

B. Determination of the critical water depth or critical temperature for stability
   - Determination of the critical water depth for stability at the sea or lake bed at specific bottom water temperature
     Output: *equilibrium pressure, critical or equivalent water depth*
   - Determination of the critical temperature for stability at the sea or lake bed at specific water depth of the basin
     Output: *hydrostatic pressure at bottom, equivalent equilibrium temperature*

C. Determination of the sub-bottom equilibrium depth under steady-state conditions (*water depth, geothermal gradient, bottom water temperature*)
Output: *critical water depth, sub-bottom depth of the stability limit, total depth of stability limit, in situ equilibrium temperature, in situ equilibrium pressure*

D. Conversion from total depth below water level to sub-bottom depth of the equilibrium limit (*total depth, geothermal gradient, bottom water temperature*)
Output: *critical water depth, sub-bottom depth of the stability limit, water depth, in situ equilibrium temperature, in site equilibrium pressure*

E. Sensitivity of the HSZ as a consequence of pure sea level changes (*initial water depth, bottom temperature, steady-state geothermal gradient, amplitude of sea level change*)
Output: *critical water depth, initial and final sub-bottom and total depth of the stability limit, difference of sub-bottom and total depth due to sea level change, in situ initial and final equilibrium temperature, in situ initial and final equilibrium pressure*

F. Sensitivity of the HSZ as a consequence of pure bottom temperature changes (*thermal diffusivity, water depth, initial steady-state geothermal gradient, initial bottom water temperature, time of interest since the initiation of the bottom temperature change*)
- Instantaneous bottom temperature change (*final bottom water temperature*)
- Linear bottom temperature change with time (*final bottom water temperature, time scale of bottom water temperature change*)
- Bottom temperature oscillation with time (*amplitude of temperature oscillation, oscillation period, phase of oscillation*)

Output: *initial and final critical water depth, critical temperature, initial and final sub-bottom equilibrium and total depth, real-time bottom temperature, in situ equilibrium temperature, in situ equilibrium pressure, average geothermal gradient, top-depth of stability field, wavelength, temperature deviation limit, temperature inversion depth.*

→ *Program_2* is based on exactly the same algorithms and procedure, with that difference that the pressure- and temperature-induced effects are combined. Parameters that can be defined by the user are: *initial water depth, initial steady-state geothermal gradient, initial bottom water temperature, magnitude of temperature change, rate or period of temperature change, amplitude of sea level change, rate of sea level change, thermal diffusivity and the delay between the initiation of the bottom water temperature change and the sea level change.* The sensitivity can be determined for various hydrate compositions, as is the case in program_1 since different regression coefficients can be used.
Output: *critical temperature, critical water depths, initial and final equilibrium depth, difference due to combined pressure and temperature change, final in situ equilibrium temperature, final in situ equilibrium pressure, average geothermal gradient, top-depth of stability field, temperature deviation limit, temperature inversion depth*

→ A third program *bai_hyd.exe* deals with heat flow determination based on the observation of a reflection at the base of the stability field, specifically worked out for the Southern and Central Baikal Basins, Siberia (option A) or the inverse process, i.e. determining the vertical extent of the HSZ for both hydrostatic and lithostatic pressure distribution based on heat flow information (option B). All information is provided in chapter 4.
Output: *bottom water temperature, critical water depth, two-way travel time sub-bottom depth, water velocity, water depth (m and ms TWTT), sub-bottom depth and total depth below lake level of stability limit (m and ms TWTT), in situ hydrostatic and lithostatic equilibrium pressure, equivalent equilibrium temperatures, mean geothermal gradient, heat flow, in situ thermal conductivity, in situ porosity, in situ bulk density*

→ Note that the investigation of the sensitivity of the HSZ under variable temperature conditions is a time-consuming process.

➔ The accuracy of the calculation procedure of the equilibrium sub-bottom depth under hydrostatic pressure conditions in all procedures is of the order of 0.1 m, being the interval value of the iterative approach. Conversion from equilibrium temperature to equilibrium pressure or vice versa is performed with high accuracy, since the R^2 value approaches unity.

➔ This program gives the user a quick reference to what extent natural gas hydrates can be stable within shallow marine or lacustrine sediment sections, and gives a first idea of the sensitivity of the bulk conditions during environmental changes. However, in reality significant differences can be observed from real-time stability limits relative to these theoretical estimation. It is of importance to stress that only bulk conditions are taken into account, i.e. no contribution of the porous medium is considered or changes from the hydrostatic pore pressure profile (except for the part about Lake Baikal where both the hydrostatic and lithostatic effects are taken into account). Physico-chemical conditions (conservation of mass, energy, latent heat of phase transitions) are also ignored in the program since emphasis was placed on the sensitivity of the HSZ under variable climatic changes. Next to that, the variety of situations is always worked out starting from initial steady-state geothermal conditions so one needs to be cautious anyway to apply the program to whatever situation. The user should be aware of this.

The same procedures were also implemented in MS Excel to generate a graphical representation of this program that shows the initial and real time sub-bottom temperature profile, the initial and real time phase boundary (taking into consideration the sea level change with time) and the initial and real time equilibrium limit. Also in this program, all parameters can be changed by the user. Additionally, results using a lithostatic pressure approach are also worked out (constant bulk density with depth or according to Athy's law) in this file.

2.7.2
Conclusions

In this chapter, a thorough discussion of the sensitivity of the methane HSZ to climatic and environmental changes is presented. Although only methane hydrates were considered, qualitative results will be very similar for other hydrate forming gases, with different quantitative results since the stability conditions will be different. The programs included can easily be used for other hydrate compositions with a similar 3-phase equilibrium behaviour and analytical expression. The analytical phase boundary equation and its application play the key role in investigating the sensitivity of the bulk HSZ under variable conditions. Hydrostatic pressure was in most cases assumed to be valid for partially hydrate saturated sediments.

Although all results were obtained for simplified situations with a lot of assumptions (pure hydrostatic pore pressure distribution, no porous medium effects, ideal initial geothermal conditions, no latent heat effects, fixed hydrate composition, no desalination, no pore pressure evolution with time) the results are believed to represent a realistic picture of what can be expected under natural conditions. The most important conclusions can be summarised as follows.

➔ Pure sea level falls res. rises are responsible for reduced res. increased hydrate stability conditions. It is supposed that sea level changes are immediately transmitted into changes of pore pressure. In case of perfect interconnected and permeable sediments, even the smallest change of sea level will induce small changes of the stability limit from the margin into the deep basin very shortly after the change. The amplitude of the change is bigger for higher-amplitude sea level changes, in shallower basins, for lower bottom water temperatures and smaller geothermal gradients. Furthermore, sea level changes influence hydrate conditions at their basal limit (e.g. *bottom-up destabilisation*). The effect of pure sea level changes can have amplitudes ranging from cm scale to over 100 m for sea level changes recorded during the last 210 ka. General figures were

generated that can be used to obtain reasonable and fast estimates of the sub-bottom depth of the stability limit as a function of diverse parameters.

→ Pure changes of bottom water temperature can be responsible for both *top-down destabilisation* and *bottom-up destabilisation*. The effect is more important in shallow areas, for higher temperature changes, for higher rates of change of the thermal disturbance, and higher heat flow or geothermal gradients. Temperature-induced effects furthermore are delayed, since the thermal pulse needs years to hundreds of years to penetrate into the sediments until the equilibrium conditions are reached. The amplitude of the change can be of the same order of magnitude as pressure-induced effects.

→ Theoretical hydrate stability conditions are highly sensitive to both pressure- and temperature changes especially in shallow basins. Also top-down destabilisation initiated by fast bottom temperature increase can only occur in relatively shallow basins, dependent on the hydrate compositions and their critical conditions. The change due to sea level or temperature fluctuations is reduced by about one order of magnitude moving from a 500 m deep basin into the deep ocean at water depths exceeding 2000 m. At relatively long time scales compared to the bottom temperature change, the rate of temperature change is of no importance.

→ Whether there is a causal link between the higher sensitivity of shallow basins to hydrate destabilisation and the occurrence in recent geological times of numerous mass wasting events in continental marginal areas (e.g. Norwegian margin and slope) within this higher risk zone is not yet proved, but is striking.

→ Accurate knowledge about the effective pressure and temperature changes and their time scale is necessary to obtain a realistic picture of the sensitivity of hydrate stability conditions. Hydrate conditions can evolve from favourable to less favourable situations and vice versa from time to time during single environmental changes consisting of e.g. a combination of bottom water temperature increase and sea level rise. In those cases, inversion can occur with time and with depth of the basin. It is shown that important sea level changes might be offset even by small bottom water temperature changes on medium to long time scales, a feature also dependent on water depth. This means that one cannot simply state that sea level drop automatically forces the system into less favourable hydrate stability conditions if no temperature information is taken into account. Such procedure was successfully applied to the *Magellan-Hovland* mound province in order to investigate and model the influence of climatic changes during glacial-interglacial transitions in this basin. Theoretically, the spatial extent of methane hydrates can cover almost the entire zone of observed buried Magellan mound under glacial conditions. During interglacials, the hydrate zone will be restricted to the deeper part of the basin, a phenomenon that is fully attributed to the high-amplitude increase of the bottom water temperature, independent of the favourable sea level change.

→ Sediment erosion like slumping or sliding can be considered as a process in which the bottom temperature suddenly decreases by the down-slope movement of the uppermost sediment section. With time the situation obviously will lead to subsidence of the equilibrium limit. A second case study as a combination of temperature- and pressure-induced effects on the hydrate stability conditions was performed using seismic data acquired in the Storegga Slide area, offshore Norway. Now the assumed pressure distribution is of importance for modelling.
Using hydrostatic pressure, the *in situ* conditions are not immediately altered by the slide event. After a while (hundreds of years, depending on temperature change) the theoretical equilibrium depth will subside in concert with the favourable *in situ* temperature conditions. No hydrate destabilisation occurs.
In case of lithostatic pressure, the slide is responsible for sudden pressure reduction forcing dissociation (less favourable bulk conditions) within a zone of a few m at the base of the pre-slide stability field. This unstable phase will last for hundreds of years. With time, the temperature effect takes over and will result in better *in situ* conditions.

Documented sea level changes since the slide act as a second-order effect: changes of only a few m of sub-bottom are calculated. At present, the thermal effect is completed and sea level changes become more important. The presence of a BSR below the slide scarp and within the slide area provides indirect evidence for significant sub-bottom gas-rich fluid migration for allowing hydrate formation at the newly established equilibrium limit.
The balance between the time scale of the thermal pulse relative to the time scale of the hydrate decomposition process and the dissipation of overpressure, i.e. the variation of the sub-bottom temperature profile relative to the variation of the *in situ* pore pressure profile, becomes important concerning hydrate accumulations in relation to slope stability.

➔ Spontaneous uplift of partially hydrate-saturated sediments is unlikely to happen due to the small res. big density difference of pure hydrates relative to the density of average fresh- or sea water res. the sedimentary matrix. Only almost pure hydrate samples located very close to the lake or sea bed will be able to rise by buoyancy. If not, a binding force should be present. The critical values seriously limit the possibility for uplift of partially hydrate-saturated sediments. Hence, the hydrate hypothesis for explaining the Lake Nyos disaster is in my opinion not realistic.

References

Allaby, A. & Allaby, M. [1999]. *Oxford dictionary of Earth Sciences.* Oxford University Press, Second Edition, Oxford, pp. 619.

Almendinguer, A. & Henriet, J.-P. [1999]. *Onset of current-induced sedimentation in the northern Porcupine Seabight: seismic evidence.* Abstract Book, North-East Atlantic slope Processes: multi-disciplinary approaches, Southampton Oceanography Centre, January 1999, p.12.

Arfken, G. [1985]. *Mathematical Methods for Physicists.* Academic Press, San Diego, pp. 985.

Bakker, R.J. [1998]. *Improvements in clathrate modelling II: the H_2O-CO_2-CH_4-N_2-C_2H_6 fluid system.* . in Henriet, J.P. & Mienert, J. (eds.), *Gas hydrates: relevance to world margin stability and climatic changes,* Special Publication of the Geological Society of London, 75-105.

Barberi, F., Chelini, W., Marinelli, G. & Martini, M. [1989]. *The gas cloud of Lake Nyos (Cameroon, 1986): Results of the Italian Technical Mission.* J. Volcanol. Geotherm. Res., **39**, 125-134.

Bates, R.L. & Jackson, J.A. [1980]. *Glossary of Geology.* second edition, American Geological Institute, pp. 751.

Bear, J. [1972]. *Dynamics of fluids in porous media.* Dover Publications Inc., New York, pp. 764.

Benn,D.I. & Evans, D.J.A. [1998]. *Glaciers & Glaciation.* Arnold Publishers, London, pp. 734.

Bianchi, G.G. & McCave, I.N. [1999]. *Holocene periodicity in North Atlantic climate and deep-ocean flow south of Iceland.* Nature, **397**, 515-517.

Bjørlykke, K. [1989]. *Sedimentology and Petroleum Geology.* Springer-Verlag, Berlin Heidelberg, p. 363.

Booth, J.S., Winters, W.J., Dillon, W.P., Clennell, M.B. & Rowe, M.M. [1998]. *Major occurrences and reservoir concepts of marine clathrate hydrates: implications of field evidence.* in Henriet, J.P. & Mienert, J. (eds.), *Gas hydrates: relevance to world margin stability and climatic changes,* Special Publication of the Geological Society of London, 113-127.

Bouriak, S., Vanneste, M. & Saoutkine, A. [2000]. *Inferred gas hydrates and clay diapirs near the Storegga slide on the southern edge of the Vøring Plateau, offshore Norway.* Marine Geology, **163**, 125-148.

Broecker, W.S. [1995]. *Chaotic climate.* Scientific American, November, 44-50.

Bugge, T., Befring, S., Belderson, R.H., Eidvin, Jansen, E., Kenyon, N.H., Holtedahl, H. & Sejrup, H.P. [1987]. *A giant three-stage submarine slide off Norway.* Geo-Marine Letters, **7**, 191-198.

Bugge, T., Belderson, R.H. & Kenyon, N.H. [1988]. *The Storegga slide.* Philosophical Transactions of the Royal Society of London, A **325**, 357-388.

Carmichael, R.S. [1982]. *Handbook of physical properties of rocks, volume II.* CRC Press, pp. 345.

Carslaw, H.S. & Jaeger, J.C. [1959]. *Conduction of heats in solids.* Oxford University Press, Oxford, pp. 510.

Chau, H.F., Kwok, P.K. & Mak, L. [1996]. *A model of gas buildup and release in crater lakes.* Journal of Geophysical Research, **101** (B12), 28253-28263.

Clennell, M.B., Hovland, M., Booth, J., Henry, P. & Winters, P. [1999]. *Formation of natural gas hydrates in marine sediments: 1. Conceptual model of gas hydrate growth conditioned by host sediment properties.* Journal of Geophysical Research, 104 (B10), 22985-23003.

Croker, P.F. & Shannon, P.M. [1987]. *The evolution and hydrocarbon prospectivity of the Porcupine Basin, offshore Ireland.* in *Petroleum Geology of North West Europe*, chapter 54, 633-642.

Delisle, G., Beiersdorf, H., Neben, S. & Steinmann, D. [1998]. *The geothermal field of the North Sulawesi accretionary wedge and a model on BSR migration in unstable depositional environments.* in Henriet, J.P. & Mienert, J. (eds.), *Gas hydrates: relevance to world margin stability and climatic changes*, Special Publication of the Geological Society of London, 267-274.

De Mol, B., Heyrman, J., Haarr, G., Henriet, J.-P., Swennen, R., Van Ranst, E. & The Belgica and Prof. Logachev Shipboard Parties [1999]. *Sedimentological analysis of the Hovland mound area.* Abstract Book, North-East Atlantic slope Processes: multi-disciplinary approaches, Southampton Oceanography Centre, January 1999, p.27.

Dickens, G.R. & Quinby-Hunt, M.S. [1994]. *Methane hydrate stability in seawater.* Geophysical Research Letters, **21** (19), 2115-2118.

Dillon, W.P., Danforth, W.W., Hutchinson, D.R., Drury, R.M., Taylor, M.H. & Booth, J.S. [1998]. *Evidence of faulting related to dissociation of gas hydrate and release of methane off the southeastern United States.* in Henriet, J.P. & Mienert, J. (eds.), *Gas hydrates: relevance to world margin stability and climatic changes*, Special Publication of the Geological Society of London, 293-302.

Dimakis, P., Elverhøi, A., Høeg, K, Solheim, A., Harbitz, C., Laberg, J.S., Vorren, T.O. & Marr, J. [2000]. *Submarine slope instability on high-latitude glaciated Svalbard-Barents Sea margin.* Marine Geology, **162**, 303-316.

Duchkov, A.D. & Kazantsev, S.A. [1996]. *Temperature measurement in the first underwater boreholes in Lake Baikal.* Russian Geology and Geophysics, **37** (6), 94-102.

Ecker, C., Dvorkin, J. & Nur, A. [1998]. *Sediments with gas hydrates: internal structure from seismic AVO.* Geophysics, **63** (5), 1659-1669.

Edgington, D.N., Klump, J.V., Robbins, J.A., Kusner, Y.S., Pampura, V.D. & Sandimirov, I.V., 1991. *Sedimentation rates, residence times and radionuclide inventories in Lake Baikal from ^{137}Cs and ^{210}Pb in sediment cores.* Nature, **350**, 601-604.

Egorov, A.V., Crane, K., Vogt, P.R. && Rozhkov, A.N. [1999]. *Gas hydrates that outcrop on the sea floor: stability models.* Geo-Marine Letters, **19**, 68-75.

Eldholm, O., Thiede, J. & Taylor, E. [1987]. Proceedings of the Ocean Drilling Program, initial reports, Leg **104**, College Station, TX (Ocean Drilling Program).

Eldholm, O., Thiede, J. & Taylor, E. et al. [1989]. *Proceedings of the Ocean Drilling Program, Scientific Results,* Leg **104**, College Station, TX (Ocean Drilling Program).

Eldholm, O., Sundvor, E., Vogt, P.R., Hjelstuen, B.O., Crane, K., Nilsen, A.K. & Gladczenko, T.P. [1999]. *SW Barents Sea continental margin heat flow and Håkon Mosby Mud Volcano.* Geo-Marine Letters, **19**, 29-37.

Fairbanks, R.G. [1989]. *A 17,000-year glacio-eustatic sea level record: influence of glacial melting rates on the Younger Dryas event and deep-ocean circulation.* Nature, **342**, 637-642.

Fleming, K., Johnston, P., Zwartz, D., Yokoyama, Y., Lambeck, K. & Chappell, J. [1998]. *Refining the eustatic sea-level curve since the Last Glacial Maximum using far- and intermediate-field sites*, Earth & Planetary Science Letters. **163**, 327-342.

Fouquet, T. [1999]. *Gas hydrate induced lake degassing: Lake Nyos.* unpublished Master Thesis, Vrije Universiteit Brussel, pp. 148.

Giggenbach, W.F., Sano, Y. & Schmincke. H.U. [1991]. *CO2-rich gases from Lake Nyos and Monoun, Cameroon; Laacher Sea, Germany; Dieng, Indonesia; and Mt. Gambier, Australia – Variations on a common theme.* J. Volcanol. Geotherm. Res., **45**, 311-323.

Ginsburg, G.D. & Soloviev, V.A. [1997]. *Methane migration within the submarine gas hydrate stability zone under deep water conditions.* Marine Geology, **137**, 49-57.

Golmshtok, A.Y., Duchkov, A.D., Hutchinson, D.R. & Khanukayev, S.B. [1997]. *Estimation of the heat flow on Lake Baikal based on seismic data of gas hydrates layer low boundary.* Russian Geology and Geophysics, 10.

Golmshtok, A.Y., Duchkov, A.D., Hutchinson, D.R. & Khanukayev, S.B. [2000]. *Heat flow and gas hydrates of the Baikal Rift Zone.* International Journal of Earth Sciences, **89**, 193-211.

Guidard, S., Vanneste, M., Henriet, J.-P. & Versteeg, W. [2000]. *The Belgica mound province, offshore Western Ireland: results from deep-towed and surface-towed reflection seismic data.* Abstract, AGU 2000 Fall Meeting.

Haq, B.U. [1993]. *Deep-sea response to eustatic change and significance of gas hydrates for continental margin stratigraphy.* Special publication of the International Association of Sedimentologists, **18**, 93-106.

Haq, B.U. [1998]. *Natural gas hydrates: searching for the long-term climatic and slope stability records.* in Henriet, J.P. & Mienert, J. (eds.), *Gas hydrates: relevance to world margin stability and climatic changes*, Special Publication of the Geological Society of London, 303-318.

Hamilton, E.L. [1971]. *Elastic properties of marine sediments.* Journal of Geophysical Research, **76** (2), 579-604.

Hamilton, E.L. [1980]. *Geo-acoustic modelling of the seafloor.* Journal of the Acoustical Society of America, **68** (5), 1313-1340.

Henriet, J.-P., De Mol, B., Pillen, S., Vanneste, M., Van Rooij, D., Versteeg, W., Croker, P., Shannon, P., Unnithan, V., Bouriak, S. & Chachkine, P. [1998]. *Gas hydrate crystals may help build reefs.* Scientific Correspondence, Nature, **391**, 648-649

Henriet, J.-P, De Mol, B., Vanneste, M., Huvenne, V., Van Rooij, D. & "Porcupine-Belgica" 97, 98 & 99 shipboard parties [accepted]. *Carbonate mounds and slope failures in the Porcupine Basin: a development model involving past fluid venting.* Special Publication, Geological Society of London.

Henriet, J.-P., De Mol, B., McDonnell, A., Pillen, S., Vanneste, M., Almendinguer, A., Chachkine, P., Van Herreweghe, K., Van Rooij, D. & the Porcupine-Belgica 98 Shipboard Party [1999]. *Imbricated cratering events and recent mud volcanism in the mound provinces of the Porcupine Basin SW of Ireland: coincidence, cohabitation or connection?* Abstract Book, North-East Atlantic slope Processes: multi-disciplinary approaches, Southampton Oceanography Centre, January 1999, p.40.

Henry, P., Thomas, M.& Clennell, M.B. [1999]. *Formation of natural gas hydrates in marine sediments: 2. Thermodynamic calculations of stability conditions in porous media.* Journal of Geophysical Research, 104 (B10), 23004-23022.

Hovland, M. & Judd, A. [1988]. *Sea bed pockmarks and seepages: impact on geology, biology and the marine environment.* Graham & Trotman, Sterling House, London, pp. 293.

Hovland, M., Croker, P.F. & Martin, M [1994]. *Fault-associated seabed mounds (carbonate knolls?) off Western Ireland and north-west Australia.* Marine and Petroleum Geology, **11**, 232-246.

Hovland, M., Gallagher, J.W., Clennell, W.B. & Lekvan, K. [1997]. *Gas hydrate and free gas volumes in marine sediments: Example from the Niger delta front.* Marine and Petroleum Geology, 14 (3), 245-255.

Hyndman, R.D. & Davis, E.E. [1992]. *A mechanism for the formation of methane hydrate and seafloor bottom simulating reflectors by vertical fluid expulsion.* Journal of Geophysical Research, **97** (B5), 7025-7041.

Jansen, E., Befring, S., Bugge, T., Eidvin, T. Holtedahl, H. & Sejrup, H.P. [1987]. *Large submarine slides on the Norwegian continental margin: sediments, transport and timing.* Marine Geology, **78**, 77-107.

Jones, E.J.W. [1999]. *Marine Geophysics.* John Wiley & Sons Ltd, pp. 466.

Kanari, S. [1989]. *An inference on the proces of gasoutburst from Lake Nyos, Cameroon.* J. Volcanol. Geotherm. Res., **39**, 135-149.

Kayen, R, & Lee, H. [1991]. *Pleistocene slope instability of gas hydrate-laden sediment on the Beaufort Sea Margin.* Marine Geotechnology, **10**, 125-141.

Kennett, J.P., Cannariato, K.G., Hendy, I.L. & Behl, R.J. [2000]. *Carbon isotopic evidence for methane hydrate instability during Quaternary interstadials.* Science, **288**, 7 april, 128-133.

Kling, G.W., Clark, M.A., Compton, H.R., Devine, J.D., Evans, W.C., Humphrey, A.M., Koenigsberg, E.J., Lockwood, J.P., Tuttle, M.L. & Wagner, G.N. [1987]. *The 1986 Lake Nyos gas disaster in Cameroon, West Africa.*

Kling, G.W., Tuttle, M.L. & Evans, W.C. [1989]. *The evolution of the thermal structure and water chemistry of Lake Nyos.* J. Volcanol. Geotherm. Res., **39**, 151-165.

Kuzmin, M.I., Kalmychkov, G.V., Geletij, V.F., Gnilusha, V.A., Goreglyad, A.V., Khakhaev, B.N., Pevzner, L.A., Kavai, T., Ioshida, N., Duchkov, A.D., Ponomarchuk, V.A., Kontorovich, A.E., Bazhin, N.M., Mahov, G.A., Dyadin, Yu.A., Kuznetsov, F.A, Larionov, E.G., Manakov, A.Yu., Smolyakov, B.S., Mandelbaum, M.M. & Zheleznyakov, N.K. [1998]. *First find of gas hydrates in sediments of Lake Baikal* (in Russian), Doklady Akademii Nauk, **362**, 541-543.

Kvenvolden. K.A. [1998]. *A primer on the geological occurrence of gas hydrate.* in *Gas hydrates: relevance to world margin stability and climatic change* [Ed. J.-P. Henriet & J. Mienert], p. 9-30.

Ladbury, R. [1996]. *Model sheds light on a tragedy and a new type of eruption.* Physics Today, may 1996, 20-22.

Lammers, S., Suess, E. & Hovland, M. [1995a]. *A large methane plume east of Bear Island (Barents Sea): implications for the marine methane cycle.* Geologischen Rundsch, **84**, 56-66 [Clim].

Lammers, S., Suess, E., Mansurov, M.N. & Anikiev, V.V. [1995b]. *Variations of atmospheric methane supply from the Sea of Okhotsk induced by the seasonal ice cover.* Global Biogeochemical Cycle, **9** (3), 351-358.

Lawrence, S.R. & Cornford, C. [1995]. *Basin geofluids.* Basin Research, **7**, 1-7.

Leeder, M. [1999]. *Sedimentology and sedimentary basins: from turbulence to tectonics.* Blackwell Science Ltd., pp. 592.

Lerche, I. & Bagirov, E. [1998]. *Guide to gas hydrate stability in various geological settings.* Marine and Petroleum Geology, **15**, 427-437.

Levitus, S. [1982]. *Climatological Atlas of the World.* NOAA/ERL GFDL Professional Paper 13, Princeton, N.J., pp. 173, website http://ferret..wrc.noaa.gov/las/

Luo, X. & Vasseur, G. [1993]. *Contributions of compaction and aquathermal pressuring to geopressure and the influence of environmental conditions (reply).* AAPG Bulletin, **77** (11), 2011-2014.

Luo, X. & Vasseur, G. [1995]. *Modelling of pore pressure evolution associated with sedimentation and uplift in sedimentary basins.* Basin Research, **7**, 35-52.

Manabe, S. & Stouffer, R.J. [1995]. *Simulation of abrupt climate change induced by freshwater input to the North Atlantic Ocean.* Nature, **378**, 165-167.

Mienert, J., Posewang, J. & Baumann, M. [1998]. *Gas hydrates along the north-eastern Atlantic margin: possible hydrate bound margin instabilities and possible release of methane.* in Henriet, J.-P. & Mienert, J. (eds); *Gas hydrates: Relevance to world margin stability and climatic change,* Geological Society of London, Special Publication, **137**, 275-291.

Milkov, A.V., Sassen, R., Novikova, I. & Mikhailov , E. [in press]. *Modelling the influence of bottom water temperature on shallow gas hydrate stability, Gulf of Mexico continental slope.* AAPG Bull..

Nisbet, E.G. [1990]. *The end of the ice age.* Canadian Journal of Earth Sciences, **27**, 148-157.

Paull, C.K., Buelow, W.J., Ussler III, W. & Borowski, W.S. [1996]. *Increased continental margin slumping frequency during sea level lowstands above gas hydrate-bearing sediments.* Geology, **24** (2), 143-146.

Paull, C.K., Ussler III, W. & Dillon, W.P. [1991]. *Is the extent of glaciation limited by marine gas hydrates?* Geophysical Research Letters, **18** (3), 432-434.

Piboule, M., Pourchet. M., Bouchez, R., Amosse, J., Brenac, P. Maley, J., Pinglot, J.F. & Vincent, C. [1990]. *Radiometric studies of Lake Nyos (Cameroon) sediments: evidence of strong. mixing and excess ^{210}Pb.* J. Volcanol. Geotherm. Res., **42**, 363-372.

Pillen, S. [1998]. *Detailkartering en seismische analyse van de Magellan-mounds in het Porcupine Bekken, ten zuidwesten van Ierland.* unpublished MSc. Thesis, Renard Centre of Marine Geology, University of Gent, Belgium, pp. 89.

Rahmstorf, S. [1995]. *Bifurcations of the Atlantic thermohaline circulation in response to changes in the hydrological cycle.* Nature, **378**, 145-149.

Rempel, A.W. & Buffett, B.A. [1997]. *Formation and accumulation of gas hydrate in porous media.* Journal of Geophysical Research, **102** (B5), 10151-10164.

Rempel, A.W. & Buffett, B.A. [1998]. *Mathematical models of gas hydrate accumulations.* in Henriet, J.-P. & Mienert, J. (eds); *Gas hydrates: Relevance to world margin stability and climatic change,* Geological Society of London, Special Publication, 137, 63-74.

Rodgers, R. & Yevi, G. [1996]. *Hydrate theory explains Lake Nyos disaster,* in *Proceedings of the 2nd international conference on natural gas hydrates.* Toulouse, 2-6 June, 477-486.

Ruppel, C. [1997]. *Anomalous cold temperatures observed at the base of the hydrate stability zone on the US Atlantic passive margin.* Geology, 25 (8), 699-702.

Schenker, F. & Dietrich, V.J. [1986]. *The Lake Nyos gas catastrophe (Cameroon): a magmatical interpretation.* Schweiz. Mineral. Petrogr. Mitt., **66**, 343-384.

Schneider, F.J.S. [1997]. *Compaction model for fluid overpressure and porosity predictions at basin scale.* in GeoFluids II, Second International Conference on Fluid Evolution, Migration and Interaction in Sedimentary Basins and Orogenic Belts (Belfast), Extended abstracts volume, 227-230.

Schneider, F., Bouteca, M. & Vasseur, G. [1994]. *Validity of the porosity/effective stress concept in sedimentary basin modelling.* First Break, **12** (6), 321-326 [stapel].

Schneider, F., Potdevin, J.L., Wolf, S. & Faille, I. [1996]. *Mechanical and chemical compaction model for sedimentary basin simulators.* Tectonophysics, **263**, 307-317.

Schneider, F., Burrus, J. & Wolf, S. [1993]. *Modelling overpressures by effective-stress/porosity relationships in low-permeability rocks: empirical artifice or physical reality?* in *Basin Modelling: Advances and Applications* (ed. Doré *et al.*), NPF Special Publication, **3**, 333-341, Elsevier, Amsterdam.

Sloan, E.D. Jr. [1998]. *Clathrate hydrates of natural gases.* Marcel Dekker Inc., 2nd edition, New York, pp. 705.

Thiede, J., Eldholm, O. Taylor, E. [1989]. *Variability of Cenozoic Norwegian-Greenland Sea paleoceanography and northern hemisphere paleoclimate.* in Eldholm, O., Thiede, J., Taylor, E. et al. (Eds.). *Proceedings of the Ocean Drilling Program*, Scientific Results, Leg 104, Ocean Drilling Program, College Station, TX, 1067-1118.

Thiery, R., Bakker, R., Monnin, C. & the Shipboard Scientific Party of ODP Leg 164 [1998]. *Geochemistry of gas hydrates and associated fluids in the sediments of a passive continental margin. Preliminary results.* in Henriet, J.-P. & Mienert, J. (eds); *Gas hydrates: Relevance to world margin stability and climatic change*, Geological Society of London, Special Publication, **137**, 275-291.

Van Herreweghe, K. [1999]. *Sequentiestratigrafie met hoog-resolutie seismiek van de Belgica Mound zone in het Porcupine Bekken, ten zuidwesten van Ierland.* unpublished licentiate thesis, University of Gent, Belgium, pp. 76.

Vanneste, M. [1997]. *Theoretische en experimentele studie van de destabilisatie van methaanhydraten in de zeebodem.* IWT rapport, pp. 35, unpublished (in Dutch).

Vanneste, M., Poort. J., De Batist, M., Henriet, J.-P. & Klerkx, J. [1998]. *Characteristics of the gas hydrate stability field in relation to spatial heat flow variations in the sediments of the Selenga Delta, Lake Baikal.* Active Tectonic Continental Basins, Gent, Abstract Book.

Vanneste, M., De Batist, M., Golmshtok, A., Kremlev, A. & Versteeg, W. [in press]. *Multi-frequency seismic study of gas hydrate bearing sediments in Lake Baikal, Siberia.* Marine Geology.

Van Rooij, D. [1998]. *Sequentie-stratigrafie met hoog-resolutie seismiek aan de rand van de Keltische Zee en het Porcupine Bekken, ten zuidwesten van Ierland.* unpublished MSc. Thesis, Renard Centre of Marine Geology, University of Gent, Belgium, pp. 103.

Vermeulen, N.J. [1996]. *Hydrography, surface geology and geomorphology of the deep water sedimentary basins to the West of Ireland.* Marine Resource Series, **2**, pp. 41.

Von Huene, R. & Pecher, I. [1999]. *Vertical tectonics and the origin of BSRs along the Peru margin.* Earth and Planetary Science Letters, **166**, 47-55.

Wheeler, A., Degryse. C., Limonov, A. & Kenyon, N. [1998]. *Oretech side scan sonar data: the northern Porcupine Seabight.* in Cold water carbonate mounds and sediment transport on the Northeast Atlangic Margin, IOC Technical Series, **52**, p. 40-58.

Wood, W.T. & Ruppel, C. [2000]. *Seismic and thermal investigations of the Blake Ridge gas hydrate area: a synthesis.* in Paull, C.K. et al. (eds.), *Proceedings of the Ocean Drilling Program, Scientific Results*, volume **164**, 253-264.

Xu, W. & Ruppel, C. [1999]. *Predicting the occurrence, distribution and evolution of methane gas hydrates in porous marine sediment.* Journal of Geophysical Research, **104**, 5081-5096.

Yamano, M., Uyeda, S., Aoki, Y. & Shipley, T.H. [1982]. *Estimates of heat flow derived from gas hydrates.* Geology, **10**, 339-343.

Zhang, Y. [1996]. *Dynamics of CO_2-driven lake eruptions.* Nature, **379**, 57-59.

UNIVERSITEIT
GENT

Faculteit Wetenschappen
Vakgroep Geologie en Bodemkunde

Academiejaar 2000 - 2001

Gas hydrate stability and destabilisation processes in lacustrine and marine environments

Results from theoretical analyses and multi-frequency seismic investigations (part II)

Maarten Vanneste

Promotor: Prof. Dr. J.-P. Henriet
Co-Promotor: Prof. Dr. M. De Batist

Proefschrift ingediend bij de Faculteit Wetenschappen van de Universiteit Gent voor het verkrijgen van de graad van Doctor in de Wetenschappen

UNIVERSITEIT
GENT

Faculteit Wetenschappen

Vakgroep Geologie en Bodemkunde

Academiejaar 2000 - 2001

Gas hydrate stability and destabilisation processes in lacustrine and marine environments

---

Results from theoretical analyses and multi-frequency seismic investigations (part II)

Maarten Vanneste

Promotor: Prof. Dr. J.-P. Henriet
Co-Promotor: Prof. Dr. M. De Batist

Proefschrift ingediend bij de Faculteit Wetenschappen van de Universiteit Gent voor het verkrijgen van de graad van Doctor in de Wetenschappen

Part 1

Chapter 1

State of the Art & Rationale of this research project (p. 1)

Chapter 2

Sensitivity of the gas hydrate stability field and destabilization processes (p. 23)

Part 2

Chapter 3

Multi-frequency acoustic imaging of hydrate-bearing sediments in Lake Baikal (p. 118)

Chapter 4

Variability of the vertical extent of the gas hydrate stability field in Lake Baikal (p. 159)

Chapter 5

Inferred gas hydrates and clay diapirs near the Storegga Slide on the southern edge of the Vøring Plateau, offshore Norway (p. 208)

Chapter 3

Multi-frequency acoustic investigation of hydrate-bearing sediments in Lake Baikal, Siberia

3.0 Abstract

In this chapter, the frequency-dependent behaviour of the acoustic characteristics of methane hydrate-bearing sediments in Lake Baikal (Siberia) is presented and discussed. Five different types of seismic data (airgun-array, two types of single airguns, watergun and sparker) encompassing a frequency bandwidth from 10 to 1000 Hz are used. On low-frequency airgun-array data, the base of the hydrate stability zone is observed as a high-amplitude bottom-simulating reflection (BSR) with reversed polarity. The amplitude and continuity of the BSR decrease or even disappear on medium- to high-frequency data, a feature explained in terms of vertical and horizontal resolution. The increasing reflection amplitude of the BSR with increasing offset, the calculated reflection coefficient of the BSR and the occurrence of enhanced reflections below the BSR suggest the presence of free gas below the hydrate stability zone. The observation of some enhanced negative-polarity reflections extending above the BSR may be interpreted as an indication for free gas co-existing with hydrates within the hydrate stability zone. Amplitude blanking above the BSR is highly variable while the BSR itself appears to act as a low-pass frequency filter for medium- to high-frequency data.

New single-channel airgun profiles provide the first seismic information from the BDP-97 deep drilling site, at which hydrate-bearing sediments were retrieved at about 200 m above the base of the local hydrate stability zone. At the drilling site there are no seismic characteristics indicative of the presence of hydrates. Combination of the drilling and seismic information has allowed me to make a rough estimation of the volume of hydrates and carbon stored in the sediments of Lake Baikal, which leads us to conclude that the Lake Baikal gas hydrate reservoirs do not form a prospective energy resource.
Emphasis is placed on the analysis and interpretation of a series of different seismic data sets, and on investigating the acoustic characteristics of the hydrate-bearing sediments in the Southern and Central Baikal Basins. More specifically, it aims to:

1. present the different seismic data sets (low-frequency airgun-array, medium-frequency single airgun, high-frequency watergun, very-high-frequency sparker) covering a broad frequency range from 10 to 1000 Hz,

2. present and describe the typical frequency-dependent response of the BHSZ and its lateral continuity,
3. discuss the observed reflection-amplitude characteristics, like reflection coefficients of the BSR, offset-dependence of the BSRs reflection amplitude, amplitude effects in the hydrate-bearing section, and acoustic frequency filtering effects at the BHSZ,
4. better constrain the limits of the HSZ where no clear BSR is observed, by means of reflection amplitude variations,
5. use the above observations and interpretations to provide for the first time a rough quantitative estimate of the hydrate distribution in the Southern and Central Baikal Basins.

3.1 Introduction: acoustic imaging of hydrate-bearing sediments

Local accumulations of gas hydrates are mainly inferred indirectly from the presence of a distinct reflection observed on low-frequency seismic data. The main characteristics of this typical reflection are as follows:

- The reflection normally ***crosscuts the local stratigraphy***, indicating that it represents not a simple stratigraphic or lithological boundary, but deals with changing physical or chemical properties of the bulk sediments or in the pore spaces [e.g. *Kvenvolden, 1998; Hyndman & Spence, 1992; Shipley et al., 1979*].

- The reflection mimics the sea or lake floor morphology. This means that its sub-bottom position is primarily temperature-controlled. This characteristic feature justifies the name ***bottom-simulating reflector*** or **BSR** [e.g. *Kvenvolden, 1998*].

- The signature of the reflector shows ***reversed polarity***, relative to the sea or lake floor reflector. This point towards negative relative acoustic impedance contrasts across this interface.

- ***Origin of the BSR***: The BSR was long assumed to represent the base of gas hydrate-bearing sediments. In this way, the reflection originates from the acoustic impedance contrast across an interface between partially hydrated sediments with high compressional wave velocity above, and gas-charged sediments with lower velocity below. Present-day insights (ODP 141, 146 and especially 164) indicate that the BSR is mainly due to free gas trapped beneath the hydrate stability zone, rather than to the presence of hydrate just above the phase boundary [e.g. *Bangs et al., 1993; MacKay et al., 1994; Holbrook et al., 1996; Wood & Ruppel, 2000*]. Free gas has a strong effect on acoustic reflectivity that the effect of hydrate saturation is most often hidden [*Von Huene & Pecher, 1999*]. If the top of the free gas zone does not coincide with the base of the hydrate accumulation zone, it is possible that no BSR is present on acoustic sections. This is observed on e.g. Blake Outer Ridge [*Paull et al., 1998*], the Peru Margin [*Von Huene & Pecher, 1999*], Lake Baikal [*Vanneste et al., in press*].

- Often ***amplitude blanking*** – i.e. relative diminishing of reflection amplitude – is observed above the BSR [e.g. *Shipley et al., 1979*]. This feature was considered to confer important information about the partial hydrate occupancy of the pore spaces [*Lee et al., 1993*]. Again, results from the Blake Ridge ODP Leg 164 show that the low reflectance above the BSR is readily explained as the naturally low background reflectance of a uniform sedimentary section [*Holbrook et al., 1996*]. It will be shown here that hydrates can be present in the porous medium without visible amplitude effects [*Vanneste et al., in press*].

- In general, the position of the BSR coincides well with the 3-phase ***theoretical hydrate equilibrium conditions*** in porous media, although important shifts are known to occur [*Clennell et al., 1999; Henry et al., 1999; Guerin et al., 1999; Ruppel, 1997*]. Recent physico-mathematical modelling showed that a hydrate-free and gas-free transition zone of several meters to tens of meters thickness can exist between the base of the hydrate accumulation zone and the top of the free gas zone, while at the same time the base of the hydrate accumulation zone does not necessarily coincides with the base of the hydrate stability field/zone (BHSZ), depending on gas supply rates and conservation equations [*Xu & Ruppel, 1999*]. Once the gas supply rate exceeds a critical value, the base of the hydrate accumulation zone will coincide with the top of the free gas zone and the acoustic impedance contrast will give rise to the BSR [*Xu & Ruppel, 1999, Wood & Ruppel, 2000*].

- The BSR is a ***single reflector***, indicating that – at the used frequencies – the BHSZ is a sharp interface [*Hyndman & Spence, 1992*].

- No reflection is recognised arising from an interface at the ***top of the hydrate accumulation zone***, indicating that hydrate saturation of the pore spaces most probably gradually decreases with decreasing burial depth [*Hyndman & Davis, 1992*] or that it extends from its basal limit up to the sea or lake floor. Only in a few cases, a reflection is observed arising from the base of the free gas layer beneath the stability field [*Ecker et al., 1996*].

- In many cases, there is direct and indirect evidence of ***free gas occurrence*** below the BHSZ [e.g. *Holbrook et al., 1996; Bouriak et al., 2000; Spence et al., in press; Sain et al., 2000*].

These typical reflections are observed on acoustic profiles acquired worldwide, especially in continental slope areas. Note that hydrate accumulations can be present without giving rise to a BSR at its base on seismic profiles: in some places hydrates are retrieved from cores during ODP drillings in areas without BSRs on the seismic records. This was for example the case in ODP Leg 164 site 994 on the Blake Ridge [*Paull et al., 1998*]. In this area the theoretical stability conditions are fulfilled for approximately the upper 450 m of sediments. No gas hydrates have been sampled from the first 190 m below the seabed [*Thiery et al., 1998*]. In the case of Lake Baikal, a very faint BSR feature is present located away from the recovery site but not at the site [*Vanneste et al., in press*]. As will be shown, this might be a matter of acquisition frequency.

The offshore industrial companies in general use low-resolution seismic data, i.e. with a dominant frequency in the order of magnitude of 10 Hz. Seismic investigations of the hydrate accumulations at the Cascadia Margin, offshore Vancouver Island, performed by *Spence et al.* [*1995*] already showed that the BSR amplitude decreases with increasing frequencies. In their study, two different airguns were used with dominant frequencies between 60-90 Hz and 150-200 Hz. A high-frequency deep-tow source-receiver system was used on the Blake Outer Ridge and revealed one of the first high-resolution features of hydrate-bearing sediments [*Rowe & Gettrust, 1993*]. In this case, the frequency ranged between 250 and 650 Hz, i.e. approximately the same as with the RCMG very-high resolution CENTIPEDE sparker system [see previous chapter].

During this study, seismic data covering a broad acoustic frequency range were available, from low- to very-high-resolution acquired in Lake Baikal, a continental rift basin in Central Siberia. It will be shown and explained why the base of the GHSF has a different acoustic response as a function of the frequency used and other aspects of the seismic acquisition layout. At present, these results are submitted for publication in Marine Geology [*Vanneste et al., in press*]. The observations and results will be highlighted here in greater detail. Remarkably, there is evidence of local anomalies in the extent of the HSZ. These anomalies appear to be closely linked with the variable heat flow pattern, typical for rift basins. This topic is further discussed in the next chapter and will be translated into another publication.

3.2
Geological setting of Lake Baikal

Lake Baikal, being more than 650 km long and on average 50 km wide, is the world's deepest (1637 m) and most voluminous lake (23000 km^3), containing approximately 20% of the world-wide reserve of fresh water [*Galaziy, 1993*] (salinity 0.76‰, average sea water salinity is 33.5‰ [*Dickens & Quinby-Hunt, 1994*]). The lake occupies part of the tectonically active Baikal Rift Zone [*Zonenshain et al., 1990; Logachev, 1993*]. Small basins occur along the entire length of the rift zone, but three major rift basins developed in its central part and form the present-day Lake Baikal: the Southern, Central and Northern Baikal Basins (figure 3.1a). These basins are highly asymmetric half-grabens, with major steeply dipping border faults especially on their western side [*Hutchinson et al., 1992*]. The deep basins are separated by two fault-controlled structural highs or accommodation zones: the Academician Ridge Accommodation Zone between the Northern and Central Baikal Basins, and the Selenga Delta Saddle between the Central and Southern Baikal Basins. MC data reveal that the Selenga Delta is underlain by a complex of deformed basement blocks [*Scholz & Hutchinson, in press*]. One of the most important structural features in the Southern Basin is the Posolskaya Bank, a basement ridge with a thick sequence of sediments on top, trending NE, oblique to the main border fault and belonging to the Selenga Delta accomodation zone. This structure is bounded at the SE by a steep slope corresponding to the active Posolskaya fault zone with displacement of more than 1 km [*Klerkx et al., 2000*] (figure 3.1b).

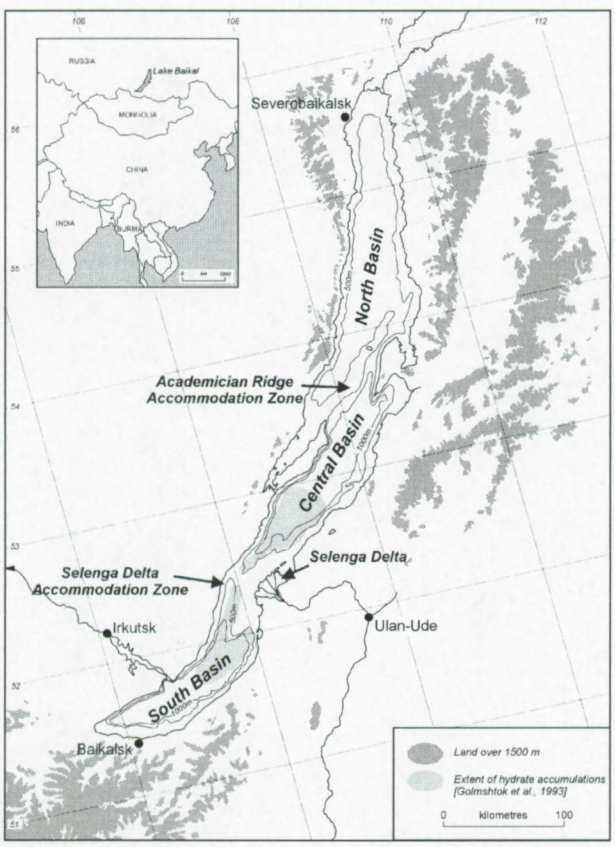

***Figure 3.1a**: Map of Lake Baikal, Central Siberia. The area with inferred hydrate occurrences in the Southern and Central Baikal Basins [Golmshtok et al., 1997] is indicated in grey.*

Rift development is thought to have occurred during four principal phases: Early Miocene (or earlier), Late-Miocene, Late-Pliocene, and Pleistocene [*Golmshtok et al., 2000*]. The first phase is associated with the formation of both the Southern and Central Basins, the second one with the formation of the Northern Basin. The third and fourth phases are characterised by a drastic increase in contrasting movements along the faults. Faulting in the sedimentary section can be divided into three main intervals. Firstly, faulting associated with the initial rifting of the basin; secondly, faulting associated with the second phase of subsidence; and finally, faulting that offsets the sediment surface [*Golmshtok et al,. 2000*; and references therein).

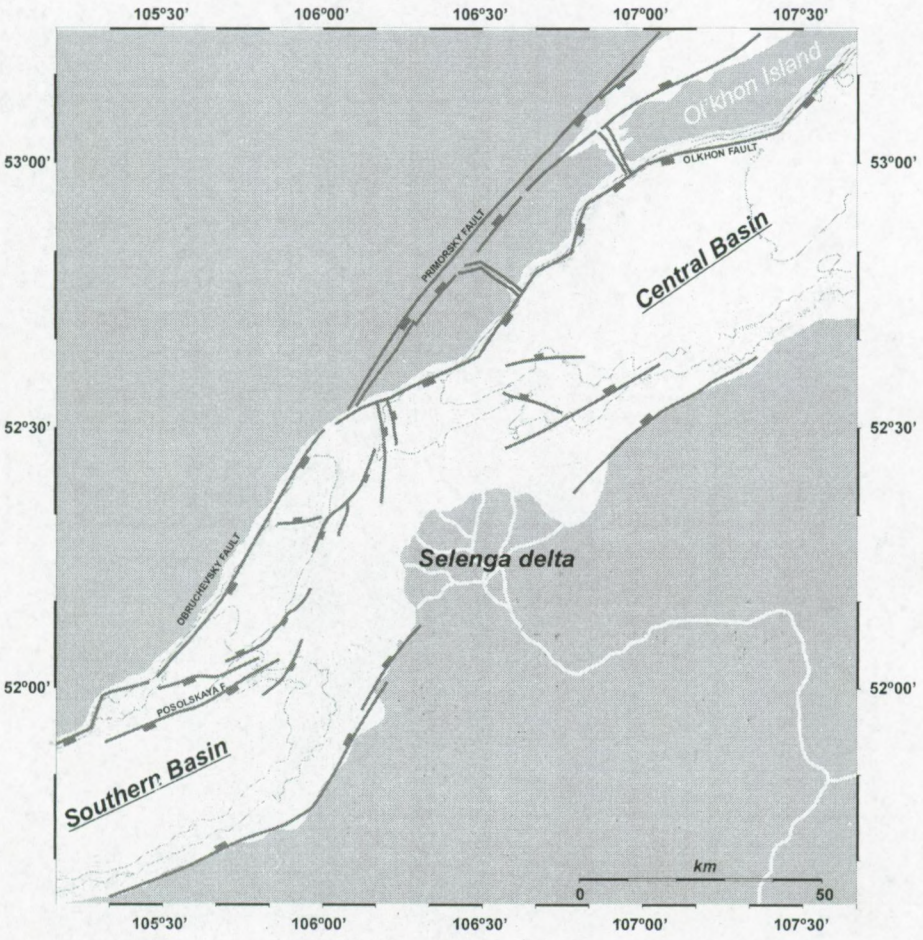

***Figure 3.1b**: Map of the study area (Southern and Central Baikal Basins) with its bathymetry and its main structural features compiled from literature [e.g. Scholz & Hutchinson, in press] by P. Van Rensbergen.*

The deep lake basins are underlain by in general thick sediment accumulations that can be sub-divided into three first-order stratigraphic packages: Late Cretaceous to Oligocene, Late Oligocene to Early Pliocene and Late Pliocene to Quaternary [*Zonenshain et al., 1992; Mats, 1993*]. The thickness of these deposits exceeds 8 km in the Southern and Central Basins [*Scholz et al., 1993*] but can vary significantly in each basin. In the Northern Basin, sediment deposition started only in the Late Miocene [*Keller et al., 1995*] and, hence, the sedimentary infill is less thick. Sediment cores have shown that the upper package consists of a unit of Holocene diatomaceous, hemipelagic mud with some thin turbidites, while the underlying Pleistocene glacial units are mainly clays interbedded with thicker and coarser turbidite layers [*Nelson et al., 1998*]. Shallow structural highs, like the Academician Ridge, receive little clastic sediment and accumulate regular alternations of diatomaceous ooze and fine clay layers [*Grachev et al., 1998*]. Sedimentation rates in Lake Baikal derived from core analyses vary from 16 cm/ka (Northern Baikal Basin) to 30-70 cm/ka (Southern

Baikal Basin), with maximum values of 120 cm/ka measured in front of the Selenga Delta, where sediments are also enriched in organic matter [*Edgington et al., 1991*].

One of the main characteristics of the Baikal Basins is the presence of a complex pattern of active fault zones and folding structures, and of a highly variable heat flow [*Poort et al., 1998*]. Measured heat-flow values are reported to vary between 40 ± 6 to 195 ± 25 mW/m^2 and show a general decreasing trend in SSE-NNW direction [*Poort et al., 1998*]. On smaller scale (order of km), strong heat flow fluctuations with a magnitude of 30-40 mW/m^2 are reported to occur almost everywhere on the lake bed. Locally, at intersections between the regional border fault and transverse faults, extreme high values of up to 8.6 W/m^2 were measured [*Golubev et al., 1993*]. Therefore, hydrothermal activity and a convective heat-flow component are considered to be present.

3.3
Gas hydrates in Lake Baikal

The occurrence of hydrates in the sediments of Lake Baikal was first suggested by the presence of a distinct BSR on multi-channel seismic reflection profiles acquired during a Russian survey in 1989 [*Hutchinson et al., 1991*]. More details became available in 1992 during a follow-up seismic survey conducted jointly by Russian and American teams [*Golmshtok et al., 1997*]. On these profiles, the BSR appears with reversed polarity and crosscuts the slightly dipping stratigraphic boundaries, especially with significant vertical exaggeration. Using these data, *Golmshtok et al.* [*1997*] mapped the extent and thickness of the hydrate accumulations in the Baikal Basins. Clear indications for hydrate occurrences were found in the Southern and Central Baikal Basins, in the area around the Selenga Delta, while none were observed in the North Baikal Basin (figure 3.1). The thickness of the hydrate-stability zone (HSZ), inferred from the seismic data, ranges between 35 and 450 m [*Golmshtok et al., 1997*].

Confirmation of the presence of hydrates in Lake Baikal was obtained in 1997 by deep drilling in the axial part of the Southern Baikal Basin (Baikal Drilling Project 1997 borehole; position N 51°47.9' – E 105°29.25'; water depth 1428 m, core length 224 m, see figure 3.2). This was the first – and up to now only – reported occurrence of gas hydrates in a confined fresh-water basin. Hydrate samples in coarse sandy turbidites were collected at 120 and 161 m sub-bottom depth [*Kuzmin et al., 1998*]. No information from intermediate depths is available due to poor core recovery. Also, the borehole did not penetrate to the BHSZ. The hydrates in the collected samples occupied approximately 10% of pore space [*Golubev, pers. comm.*]. Geochemical analyses of the samples showed that the enclosed gas molecules were mainly methane of biogenic origin (carbon isotopic composition $\delta^{13}C$ between -58 and -68 ‰). With bottom-water temperatures of 3.18°C (Central Baikal Basin) and 3.38°C (Southern Baikal Basin), the minimum water depth for methane hydrates to be stable is calculated using the equations of §2.1 to be 353 m and 359 m respectively. This is in agreement with the seismic observations of *Golmshtok et al.* [*1997*]. During the previous RCMG summer expedition 1999, a few seismic profiles were acquired crossing this BDP drilling site.

A few months ago during the winter of 1999-2000, shallow sediment cores were taken in the *Malen'kiy* crater (Southern Basin), in an area with evidence of gas seepage. Almost pure and massive methane hydrates were retrieved [*Klerkx, pers. comm.*] from the uppermost sediment layer (16-42 cm) [*Matveeva et al., 2000*]. At present, core analysis is being undertaken by the research group of V. Soloviev (St.-Petersburg). First results reveal very similar compositions as compared with the hydrates sampled at greater depth in the BDP site. Knowing the characteristics of the diverse data sets and their frequency content, the multi-channel airgun-array data are labelled low-resolution, relative to the medium-resolution single airgun lines, the high-resolution watergun and the very-high-resolution sparker profiles.

3.4
Seismic data acquisition and processing: technical details

Here, five different seismic data sets from the Southern and Central Baikal Basins, in the area around the Selenga Delta are presented. Location of the seismic profiles is shown in figure 3.2. The seismic sources used include an airgun-array system, two different single airguns (Ship & Impuls), a single watergun and a RCMG-made Centipede sparker source. They cover a frequency range between approximately 10 and 1000 Hz. Of these, only the airgun-array data were recorded in multi-channel (MC) mode. All data were specially processed or re-processed for this study. Technical information on data acquisition and processing is summarised in table 1 and table 2, and will be discussed below.

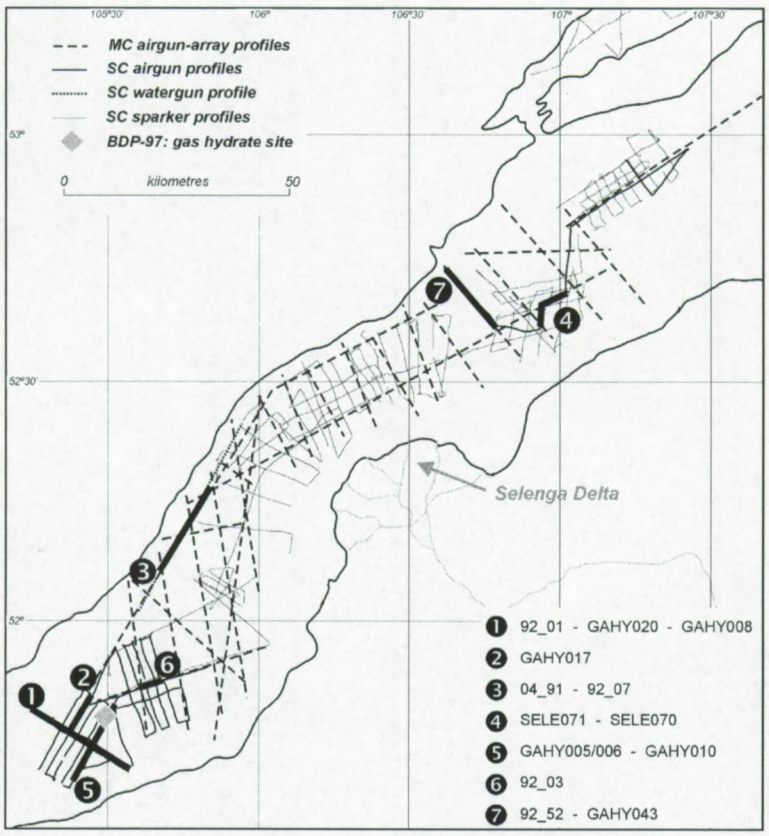

***Figure 3.2**: Location of the seismic profiles used in this study, and of the BDP-97 hydrate drilling site. The profiles shown in this chapter are marked.*

3.4.1
Seismic data acquisition

3.4.1a Multi-channel low-resolution airgun-array data

The MC airgun-array data were collected in 1992 by a joint Russian-American team involving the Shirshov Institute of Oceanology (Gelendzhik, Russia), the Limnological Institute (Irkutsk, Russia), the U.S. Geological Survey and a number of U.S. universities [*Nichols et al., 1992; Klitgord et al., 1993; Scholz et al., 1993*]. The aims of this survey were to map the deep geological features and structures in Lake Baikal, in combination with global change perspectives.

Only the first three seconds of a selection of these lines were available for this study via the INTAS-1915 project. The low-resolution data were recorded with a 96-channel streamer with an active length of 2400 m (2375 m between the centres of the first and last recording channel units). The individual recording channels consist of equally-spaced (0.75 m) series of 31 hydrophones resulting in an individual array length of 22.5 m. Spacing between the centres of successive groups is 25 m. The data-acquisition geometry results in 24-fold CDP gathers. Sampling interval was 4 ms. The airgun-array was specially designed to reduce the bubble effect inherent to that kind of acoustic source [*Golmshtok, pers. comm.*]. Offsets range from 495 m (nearest channel) to 2870 m (furthest channel), leading to angles of incidence between approximately 10° and 50° for typical depths of the Baikal basins. Nominal frequency f of the signals determined from spectral analysis is 39 Hz leading to vertical resolution of 10 m. Shot interval was 23-25 s (approximately 50 m). The fact that only the first 3 s of data were available for this study makes that the BSR and underlying reflections are not present in the far-offset channels in the common midpoint gather. As a result, the accuracy of picking of horizons is not high enough to obtain a detailed sub-bottom acoustic velocity profile for determining the possible velocity effects associated with the interface between partially hydrate-saturated sediments above and gas-charged sediments below.

Lateral resolution is determined by the width of the first Fresnel zone [e.g. *Yilmaz, 1987; Sheriff & Geldart, 1995*]. Ignoring the small submersion depth of the source and receiver relative to the water depth, then the following formula is used to calculate the lateral resolution at offset x for dominant wavelength λ:

$$R_{fresnel}\langle x\rangle = 2\sqrt{\left(1-\frac{H^2}{(H+\lambda/4)^2}\right)\cdot\left(\frac{x^2}{4}+\left(H+\frac{\lambda}{4}\right)^2\right)} \qquad [1]$$

with $\lambda \cdot f = v$

This formula can be slightly simplified by taking into consideration the fact that the nominal wavelength of the acoustic wave is in general considerably smaller than the height of the water column. Thus, one gets:

$$R_{fresnel}\langle x\rangle \cong \sqrt{2\lambda H\cdot\left(H^2+\frac{\lambda H}{4}\right)^{-1}\cdot\left(\frac{x^2}{4}+H^2+\frac{\lambda H}{2}\right)} \qquad [1']$$

As a result the horizontal resolution of the MC data ranges from 300 m (minimum offset) to 465 m (maximum offset) at 1200 m water depth. Penetration depth of the full data (after CDP-stacking) is several seconds two-way travel time (TWTT).

3.4.1b Single-channel medium-resolution airgun data

In the summer of 1999, during a joint Belgian-Russian expedition involving the Renard Centre of Marine Geology (RCMG) and the Geophysical Survey, the Institute of Computational Mathematics and Mathematical Geophysics and the Institute of Geophysics (Novosibirsk, Russia), single-channel airgun profiles were acquired in selected areas in the Southern and Central Baikal Basins [*De Batist et al., 1999*]. The objectives were to acquire a whole set of new geological-geophysical data, in order to obtain more detailed knowledge about the probable link between the typical accumulation of hydrates, the geothermal regime and its spatial variability and the tectonic influence on the hydrate stability conditions in Lake Baikal [*Vanneste, 1999*].

Two types of airgun were used as acoustic sources: a 3.0 l Impuls-1 airgun and a 3.0 l Ship airgun. The guns were operated at 120 bar. These medium-resolution data were detected in a single-channel

(SC) streamer, towed at the surface and at a short offset from the source. Active length of this 10-hydrophone component receiver is 2.7 m. A variable analogue Krohn-Hite filter (20 – 10000 Hz) was used before the data were recorded digitally using Elics-Delph2 system at sampling frequencies of 2000 Hz.

The above formulas for calculating the radius of the Fresnel zone can easily be simplified for normal incidence data, resulting in:

$$R_{fresnel}\langle 0\rangle = 2\sqrt{\frac{\lambda}{2}\left(H+\frac{\lambda}{8}\right)} \cong \sqrt{2\lambda H} \qquad [2]$$

The vertical and horizontal resolution for the Impuls airgun (frequency range: 45-330 Hz) are approximately 3 m and 170 m respectively; for the Ship airgun (frequency range: 80-450 Hz) 1.6 m and 125 m respectively. The average penetration of the acoustic signal is about 500 ms TWTT. The coherence of the Ship data is not as good as that of the Impuls airgun, because of irregularities in the firing delay or triggering. Shot interval is 16 s (approximately 30 m).

3.4.1c Single-channel high-resolution watergun data

During two successive joint Russian-American seismic surveys (in 1991 and 1992) an extensive grid of SC watergun profiles was acquired in different parts of the lake. The data are published as part of an U.S. Geological Survey Open File Report [*Colman et al., 1996*]. The data were shot using a 0.246 l or 15 in^3 watergun towed at 1.2 m water depth to minimise the bubble effect and to reduce interference caused by the reflection from the water surface. A single-channel 200-element hydrophone system recorded the reflected signals at offsets of 180 m. The signals produced by the watergun have a frequency range of 100-650 Hz, and a peak frequency of approximately 330 Hz. Vertical resolution of these data is then approximately 1 m, while the lateral resolution is about 100 m at 1200 m water depth. The average penetration of the acoustic signal is about 500 ms TWTT. In total, about 3600 km of profiles were recorded [*Colman et al., 1996*]. For this study, only one watergun line 04_91 is used, located at the NW border of the Southern Baikal Basin, and in the immediate vicinity (almost parallel) to MC line 92_07.

The main objectives of this site survey were to identify and to map different sedimentary environments in the deep basins of Lake Baikal and to select the coring sites for paleoclimatic analyses, including the 1993 deep drilling site in the framework of the international Baikal Drilling Project [*Colman et al., 1996*].

3.4.1d Single-channel very-high-resolution sparker data

In 1997 and 1998, RCMG and the Limnological Institute (Irkutsk, Russia) collected a dense grid of SC very-high-resolution seismic profiles in the Selenga Delta area [*De Batist & Vanneste, 1997; Vanneste & De Batist, 1998*]. The data were shot using RCMG's Centipede fresh-water multi-electrode sparker, operated at 500 J, and a SC streamer. Both were towed at the lake surface and at a very short offset. The data were recorded digitally using a Elics-Delph2 system after analogue filtering. The frequency spectrum of the sparker signal ranges between 150 and 1000 Hz. The vertical and lateral resolution of these data then is less than 1 m and about 80 m respectively. Sub-bottom penetration is highly variable from line to line and does not exceed 350-400 ms TWTT. Shot interval was 3 s (approximately 6 m).

This expanded data set was acquired for several reasons. The main objective was the characterisation of hydrate-bearing sediments on very-high frequency data. Especially in the immediate area of the Selenga delta, the hydrate accumulations are reported to fall within the reach of the acquisition

system used. Next to that a detailed and high-resolution grid was acquired on both sides of the Selenga delta (south-western part in 1997, north-eastern part in 1998) to map the variable sedimentary infill during recent climatic cycles in this fault-controlled area [*De Batist & Vanneste, 1997; Vanneste & De Batist, 1998*]. More information concerning this topic is provided in the thesis of *Sandra* [*2000*] making use of the 1997 seismic profiles.

	airgun			***watergun***	***sparker***
	array	***impuls-1***	***ship***		
acquisition characteristics					
property of...	Golmshtok	RCMG	RCMG	USGS	RCMG
year(s) of acquisition	1992	1999	1999	1991-92	1997-1998
gun volume (l)	27.3	3	3	0.245	-
source energy	140 bar	120 bar	120 bar	200 bar	400-500 J
sampling interval (ms)	4	0.5	0.5	0.5	0.25
number of recording channels	96	1	1	1	1
CDP fold	24	1	1	1	1
source-receiver offset (m)	495-2895	± 25	± 25	±180	±25
angle of incidence	10-50°	< 1°	< 1°	< 5°	< 1°
frequency range (Hz)	7-110	45-330	80-450	100-650	150-1000
dominant frequency in water (Hz)	± 39	± 120	± 225	± 330	± 525
dominant wave length in water (m)	± 37	± 20	± 6.4	± 4.4	± 2.8
vertical resolution (m)	± 10	± 3	± 1.6	± 1.1	± 0.7
lateral resolution (m)	300-465	± 170	± 125	± 100	± 80
average penetration limits (m)	> 3000	± 700	± 500	± 500	< 400
processing characteristics					
CDP-sorting	x				
velocity analysis	x				
NMO-correction	x				
stacking	x				
correction for spherical divergence	x	x	x	x	x
inimum-phase predictive deconvolutio	x	x	x		
spectral analysis	x	x	x	x	x
amplitude analysis	x	x			
Butterworth band-pass filter	x	x	x	x	x
FK-filter				x	
automatic gain control (AGC)					

Table 3.1*: Summary of the acquisition layout and processing details of the acoustic data set used in this study. Lateral resolution (Fresnel zone) is determined for water depths of 1200 m. RCMG data are digitally recorded using Elics-Delph2 system.*

3.4.2
Seismic reflection data processing

3.4.2a General processing routine for single-channel seismic data

All seismic data processing was carried out on a Landmark ProMAX system at the RCMG. In general, before starting the processing flows, the frequency ranges of the acoustic sections were determined using spectral analysis performed on selected windows of approximately 100 shots and 500 ms for all data sets available for this study. In this way, both the strong lake floor reflection and the BHSZ are taken into account. This procedure determines the filter settings used.

In a next step, all data were submitted to additional processing routines, with the aim of enhancing the resolution and to restore the true amplitudes of the acoustic signals (no AGC scaling). This procedure involved: static header control, true amplitude recovery to correct for spherical divergence, applying minimum-phase predictive deconvolution to minimise bubble effects and to sharpen the wavelets (airgun data), *Butterworth* or *Ormsby* frequency filtering based on spectral analyses results for the specific source used, coherence and FK-filtering (watergun data) to suppress low-velocity backscatter effects. Burst and noise peaks were edited using a ProMAX macro.

The Ship airgun suffered from a variable triggering delay (few ms) that obviously reduces the data quality. This could often be removed by applying a modified swell filtering procedure. Such process was not necessary for the Impuls airgun data.

3.4.2b Multi-channel low-resolution airgun-array data

In a co-operative effort between the P.P. Shirshov Institute of Oceanology (Dr. A. Golmshtok) and RCMG, the first 3000 ms of a selected number of the MC airgun-array profiles were completely re-processed, involving a.o. CDP-sorting, velocity analysis, NMO-correction and stacking. From the Southern Basin, copies of the lines 92_01, 92_02, 92_03, 92_03A, 92_04 and the last part of 92_07 were available. From the Central Basin, this was the case for profiles 92_32, 92_34, 92_36 and 92_52.

All data are stored on CD in SEGY-format in demultiplexed form. In the first instance, the data were sorted by their field file identity number and sequence number in order to separate the real acoustic data from non-data (e.g. depth sensor information) that had to be removed. More specific, the 96-channel system represents 101 traces for a single shot. The first 5 channels appear to be double-traced of which only one of the two traces contains valuable acoustic information. The complete acoustic profile is then written to disk to facilitate further processing routines.

For a few MC airgun-array lines, several static header corrections had to be introduced to compensate variable recording delays. Analyses of the arrival times of the lake floor reflection and its first multiple in the near-offset channel allowed to determine this extra static header value in the different shot points along the lines. A first order delay of approximately 1100 ms was present on the lines 92_01 and 92_02. Smaller delays along the lines were about 20 ms from the one part relative to the other part of the acoustic section.

Some channels were also very weak and were killed. Also some shots generated by the guns had a very poor signal to noise ratio and were eliminated, not allowing them to have a significant influence on the stacking procedure. Missing shots were padded for obtaining a correct geometry layout for all MC data. An extra tool was used to detect and edit sample spikes and bursts. Spikes are removed by linear interpolation using neighbouring samples. Bursts (i.e. high-amplitude noise with long duration) are filtered out as well. For both, a ProMAX macro is used. The data were furthermore corrected for spherical divergence (true amplitude recovery). A dB/second curve was selected as a basis for spherical spreading. No corrections for inelastic attenuation were carried out.

Although the airgun geometry had the intention to reduce the bubble effect, a significant relative reversed polarity reflection was observed on all seismic lines following the primary reflections at about 125 ms TWTT. This was not conform the far-field tests performed before the expedition [*Golmshtok, pers. comm.*]. In order to remove this artefact, a minimum phase predictive deconvolution procedure was applied to the data. A second deconvolution was introduced to sharpen the wavelets. The prediction distance and operator length were determined from the autocorrelation.

In order to stack the data, the geometry layout was assigned for each line and the traces were binned. This procedure allows sorting the data into CDP gathers. Semblance velocity analysis and NMO corrections were performed. Finally, the data were bandpass frequency-filtered, using the *Butterworth* filter from 10 to 120 Hz, after spectral analysis. No time-variant filtering was considered. For

determining the reflection coefficients (section 5.5) in the near-offset channel of line 92_01, the data were band-pass filtered (10-90 Hz) and compensated for loss of amplitude due to wavefront spreading, based on the reciprocal of the travel path of the wavefront.

3.4.2c Specific processing tools

Next to these general processing steps, seismic attribute analyses were performed on the data set in Landmark ProMAX in order to further analyse the nature of the reflections. Amongst these, reflectivity strength plots, instantaneous phase plots (emphasising the continuity or coherence of weak reflections) and instantaneous frequency plots (temporal rate of change of the instantaneous phase, gives an idea about attenuation) were used frequently. Such attribute analyses are performed on true-amplitude-processed seismic sections. More details are given in *Yilmaz [1987]*.

3.5 Observations and results

3.5.1 Low- and medium-frequency imaging: airgun data

The BHSZ in Lake Baikal is, as is the case with most oceanic hydrate occurrences, expressed as a continuous high-amplitude bottom-simulating reflection on MCS profiles. Such a BSR can clearly be seen on profile 92_01 (figure 3.3a), a stacked profile from the central part of the Southern Baikal Basin. Vertical exaggeration of this profile is approximately 25:1. The BSR is roughly parallel to the flat lake floor and runs at approximately 340 ms TWTT sub-bottom depth. The reflection can be traced along the whole profile. Within the first 13 km of the profile (NW side), the continuous BSR clearly crosscuts the folded sedimentary units.

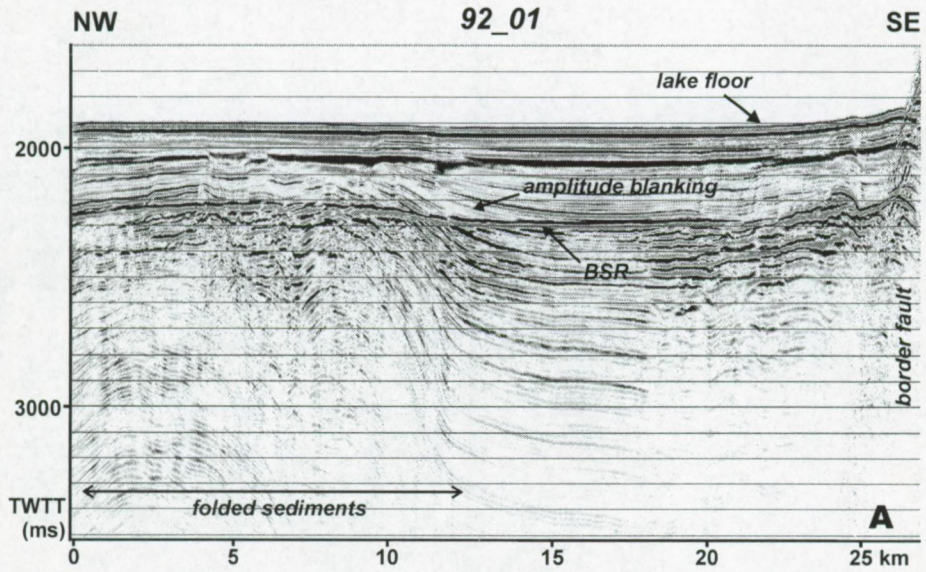

***Figure 3.3a**: Stacked low-resolution MC airgun-array profile 92_01 from the Southern Baikal Basin with clear evidence of a BSR. Coincident seismic profiles acquired with medium-resolution airguns are shown in figures 3c, 3d. For location, see figure 3.2.*

A zoom taken from the central part of this profile (figure 3.3b) shows the reversed polarity of the BSR (relative to the lake-floor reflection), indicating a drop in acoustic impedance across this interface. Since partial hydrate or free gas saturation of pore spaces only has a minor effect on bulk density, the change in acoustic impedance is most probably due to a velocity effect. Unfortunately the data do not allow us to obtain an accurate quantitative estimate of the compressional wave velocity drop at the BSR.

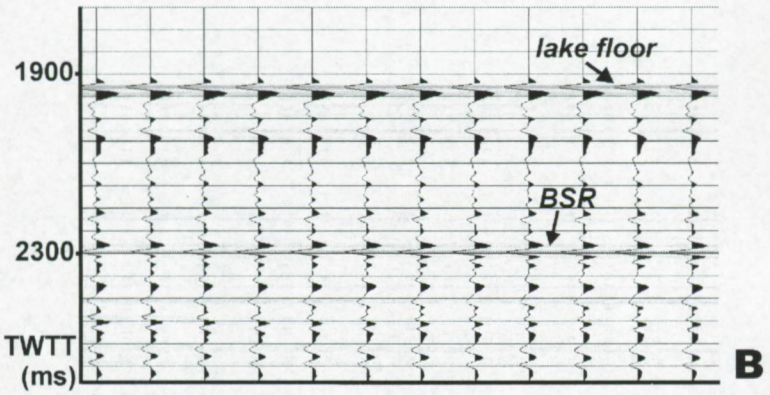

***Figure 3.3b**: Selection of traces from profile 92_01 illustrating the reversed polarity of the BSR relative to the lake floor reflection.*

The BSR is also imaged on the more or less coincident SC profiles GAHY020 (Impuls airgun, figure 3.3c) and GAHY008 (Ship airgun, figure 3.3d). On these higher-frequency profiles, several pseudo-vertical faults with small offsets can be identified within the fold structure. The amplitude of the BSR on these profiles is highly variable and in general weaker than on the low-resolution MC data. The BSR only appears as a clear reflection where it is crosscutting the dipping sediment layers at the border of the fold structure. Within the folded sedimentary section itself, the BSR is very weak. However, comparison with profile 92_01 (figure 3.3a) allows to trace the BSR across the structure, where it lies on top of a package of higher-amplitude reflectors (figure 3.3c). A few reflectors crossing the BSR at the border of the fold structure are characterised by high (enhanced) amplitudes just above the BSR, while the amplitude of most other reflectors in this interval is weak ("amplitude blanking"). A zoom of GAHY020 around SP 200, i.e. at the border of the fold, is shown in figure 3.3e. At the SE part of these lines, the BSR is faint to very faint within the sub-parallel sedimentation pattern.

Another clear example of a crosscutting BSR on a medium-frequency Ship airgun profile is observed on part of profile GAHY017 (figure 3.4), which crosses almost perpendicularly the above-described profiles (figure 3.3). This line continues in GAHY022 (see next chapter) approaching the Posolskaya fault to the NE. The BSR, which does not perfectly mimic the lake floor along this profile, is very distinct in the central part of the section displayed. Its continuity is affected neither by the dipping sediment layers nor by the small fault present at SP 480. Some stratigraphic reflections are enhanced just below the BSR, especially at the WSW-side of the section displayed. These terminate up-dip at the depth of the BSR feature. Amplitude blanking above the BSR is variable along this line. Along the SW part of the line (not displayed in figure 3.4), the BSR can hardly be discerned within the sub-parallel sedimentation pattern. Enhanced reflections are less evident as well.

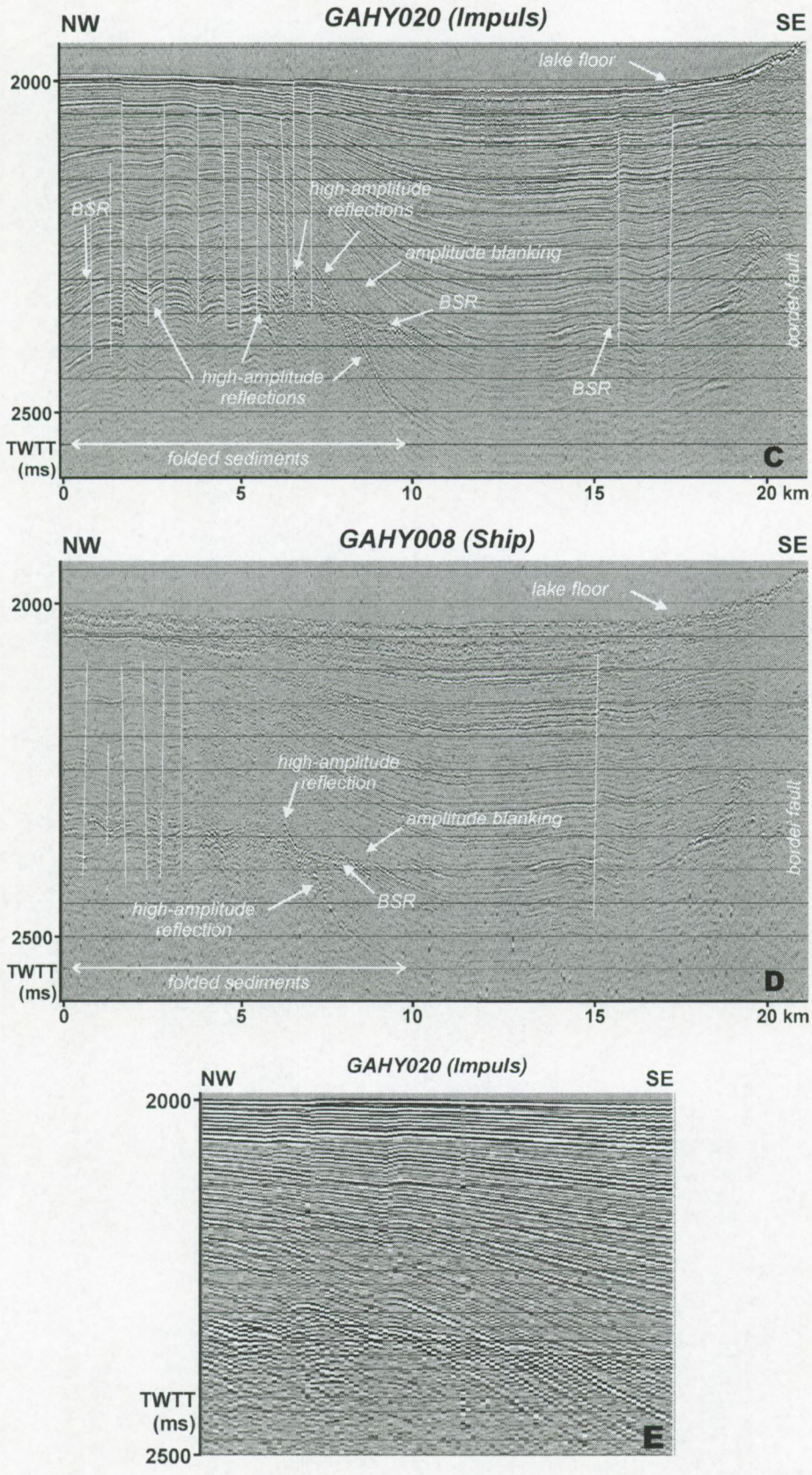

***Figure 3.3c, d, e**: Medium-frequency Impulse airgun line (c) and Ship airgun line (d) coincident with the stacked low-frequency profile shown above in the Southern Basin of Lake Baikal. Note that the amplitude of the BSR is reduced compared lower-frequency data. A zoom of the cross-cutting section of line GAHY020 is shown in figure 3.3e. For location, see figure 3.2.*

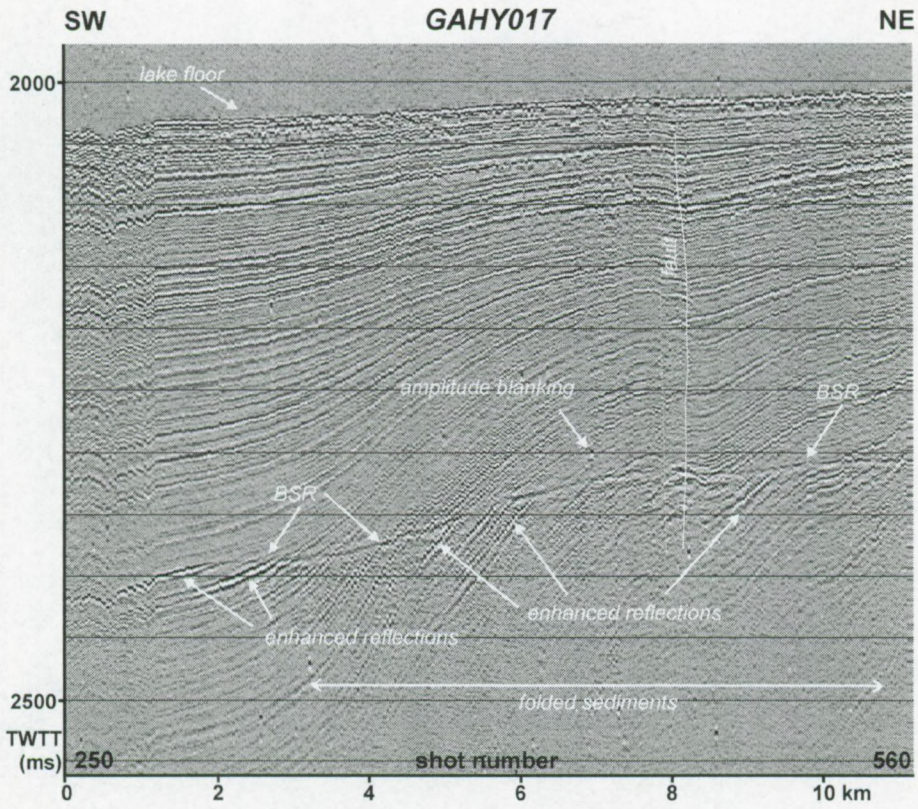

***Figure 3.4**: Part of a medium-frequency ship airgun line from the Southern Baikal Basin, showing a number of features typically associated with gas hydrates: a cross-cutting BSR, enhanced reflections beneath the BSR, amplitude blanking above. For location, see figure 3.2.*

Most of the MCS profiles in the Central and Southern basin of Lake Baikal reveal continuous acoustic features related to hydrates, as discussed above. Figure 3.5a shows perhaps the best BSR example (line 92_34) from the Central Baikal Basin. The lake floor along this profile is flat and regular, except at the SE part of the line characterised by one of the enormous fault systems. The reflection can be traced as a continuous bottom-simulating reflection, even within the fault structure extending to the SE. Its amplitude varies along the line and appears stronger in between of CDPs 1800-2050. In the middle of the line, a lake floor depression of ± 30 ms (> 20 m) deep and about 250 m wide is observed similar to pockmark features described in *Hovland & Judd [1988]*. No levees are observed at the sides of the depression while there is no evidence of fluid escape or plumes in the water column just above the lake bed. This depression does apparently not influence much of the low-frequency BSR image, although its reflection amplitude is slightly weaker beneath this event. The intermediate sediment layers between lake floor and BSR seem slightly disturbed. Note that not too many coherent reflections are present. Attenuation is more pronounced in this part compared to the other parts of the section and some amplitudes are smeared out. No clear evidence of major underlying faults or fluid migration pathways is found. However, the data are not conclusive to label this depression as a pockmark (e.g. side-scan sonar, echo-sound).

A parallel line 92_52 (± 19 km to the SW of 92_34, i.e. closer to the Selenga Delta) is presented in figure 3.5b. This profile is much more complex compared to its parallel line. Along this line, the continuous reflection mimics the more irregular and faulted lake floor topography between shot points 120 and 350. The amplitude of the BSR and amplitude blanking above are variable along this profile: if the lake floor morphology is less regular, the BSR appears fainter. The crosscutting character is less obvious in this case. Under the structural uplift at the beginning of the line (SE) and at the end (NW), no indirect evidence of hydrates is observed. Remarkably, an enhanced reflection with reversed polarity is observed at approximately 200 ms TWT sub-bottom depth between shot points 250-330. This enhanced reflector extends over a few km and lies well within the HSZ.

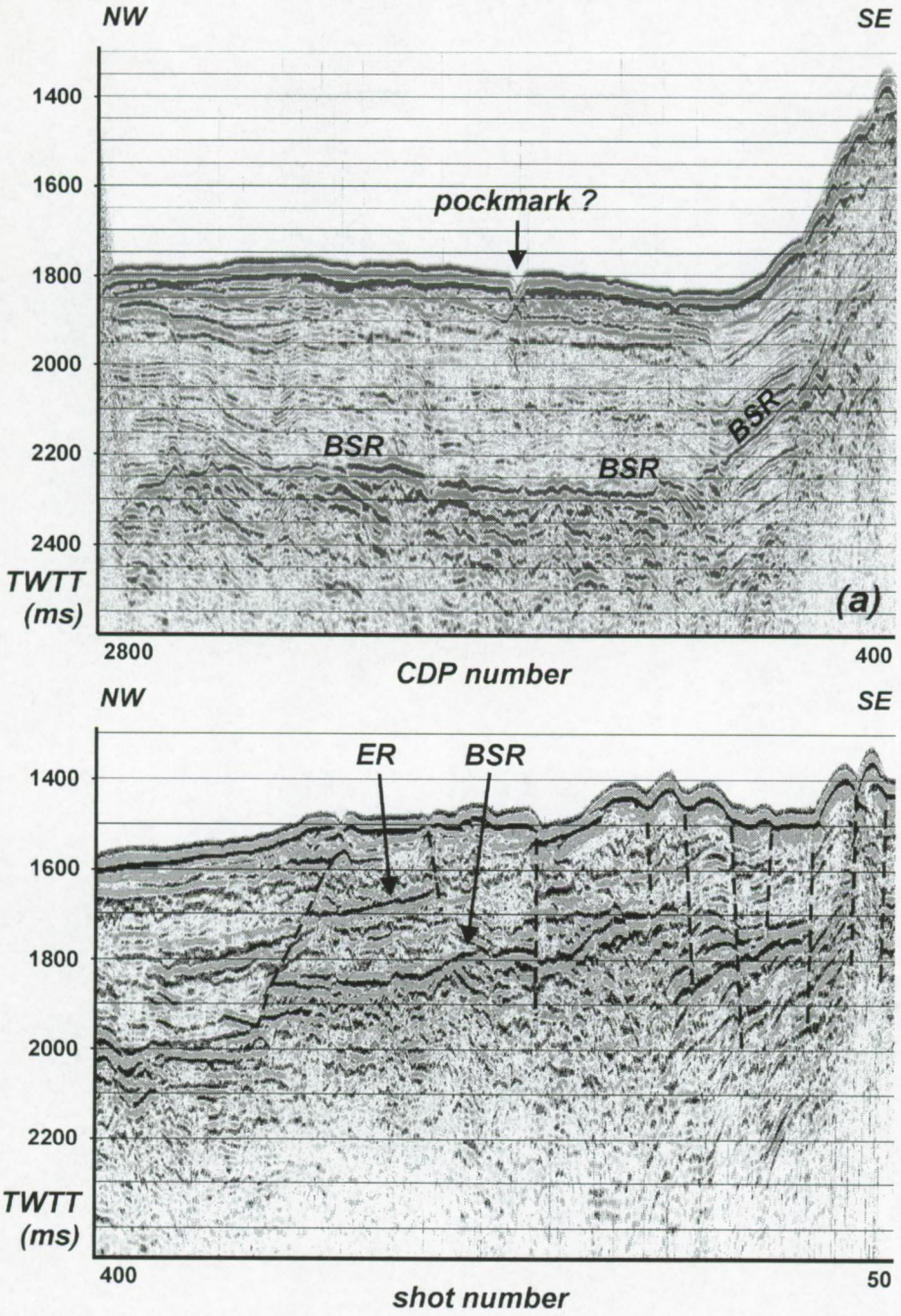

***Figure 3.5**: Parallel stacked MC lines 92_34 (a) and 92_52 (b) from the Central Baikal Basin. ER = enhanced reflection.*

3.5.2
High-frequency imaging: watergun data

A completely different image of the BHSZ is observed on higher-resolution seismic data. A good example is given on watergun line 04_91 (figure 3.6a), located in the Southern Baikal Basin. The most striking feature on this profile is a series of closely spaced, dipping, enhanced reflections or bright spots that all terminate up-dip at a sub-bottom depth of about 300 ms TWTT. The bright spots are all part of individual continuous stratigraphic boundaries that can be traced on both sides of the enhanced parts, as is evidenced by an instantaneous phase display of this section. This processing technique measures the continuity of coherent events and enhances in this way reflections with weak amplitudes [*Yilmaz, 1987; Sheriff & Geldart, 1995*]. Note that during the processing steps prior to this

attribute analysis, the amplitude and frequency content of the signals were preserved. Polarity analysis of these enhanced reflections suggests that their polarity is reversed compared to the lake floor reflection. The lateral extent and the amplitude of the bright spots varies. While sometimes no real amplitude anomaly is observed, other enhanced parts extend over hundreds of meters. The vertical extent is limited to a zone of about 50 ms TWTT. Amplitude blanking is present in the section above the enhanced reflections.

Figure 3.6b shows the shortest-offset (above) and largest-offset (below) channels of the nearly coincident lower-frequency profile 92_07. Especially on the latter, a high-amplitude BSR with all the typical characteristics can be seen. The BSR is still visible on the short-offset channel, although much weaker. It occurs at a sub-bottom depth of about 300 ms TWTT and forms the upper limit of a series of dipping, enhanced reflections. These observations indicate that the acoustic features observed on watergun profile 04_91 (Figure 3.6a) represent the high-frequency response of the BHSZ along this section. The interface at the top of the series of enhanced reflections still follows the lake-floor topography, but it does not appear as a distinct and continuous BSR as it does on lower-frequency data.

3.5.3
Very-high-frequency imaging: sparker data

During their study, *Rowe & Gettrust [1993]* reported that one of two high-resolution deeptow acoustic sections (250-650 Hz) is characterised by numerous closely-spaced reflections. They appear with rather high-amplitude and show reversed polarity at exactly the same sub-bottom depth as seen on multi-channel lower-resolution data. These reflections however are less coherent as known from low-frequency acoustic sections. The BSR is broken by high-angle normal faults responsible for small offsets. On a second profile, such a feature is not present. Sparker profiles acquired in the Baikal basins during the last years have a similar frequency content. From the dense grid of sparker data available in the different parts of Lake Baikal, some are nearly-coincident or cross lower-frequency data.

Some of the very-high-resolution sparker profiles SELE071 (figure 3.7a) and SELE070 (figure 3.7b) show yet another feature that may be or may not be related to the BHSZ or the top of free gas accumulation. These profiles are characterised by the presence of high-amplitude reflections jumping from one stratigraphic horizon to another and occur at an average sub-bottom depth of about 300-320 ms TWTT (figure 3.7). The enhanced reflections on the sparker lines seem to act as a kind of acoustic basement: i.e. where they occur, they completely block all acoustic energy and no reflections from below them can be detected. On nearby MC profiles the BSR is clearly visible and occurs at about the same sub-bottom depth (line MC 92_32) or slightly deeper within the sedimentary section (MC 92_34) so it is questionable whether these enhanced reflections can be related to gas hydrates.

It should be noted that the *maximum* sub-bottom penetration of the sparker signal in deep-water areas of Lake Baikal is limited to 350-400 ms TWTT but significant variations are observed from line to line. Several lines only show penetration of less than 200 ms. At the NE side of the Selenga Delta, the penetration of acoustic energy observed on three closely-spaced E-W directed sparker profiles located to the N of lines SELE070-071 (figure 3.7) decreases towards the centre of the lake (i.e. from S to N), from 350 to 200 ms TWTT. At the intersections of very-high-frequency sparker lines and stacked low-frequency airgun profiles, the BSR lies in most cases beneath the penetration limit of the sparker data. For example, line SELE077 does not reveal any acoustic features that can be related to free gas occurrence of partial hydrate saturation while line MC92_32 is characterised by a distinct BSR feature.

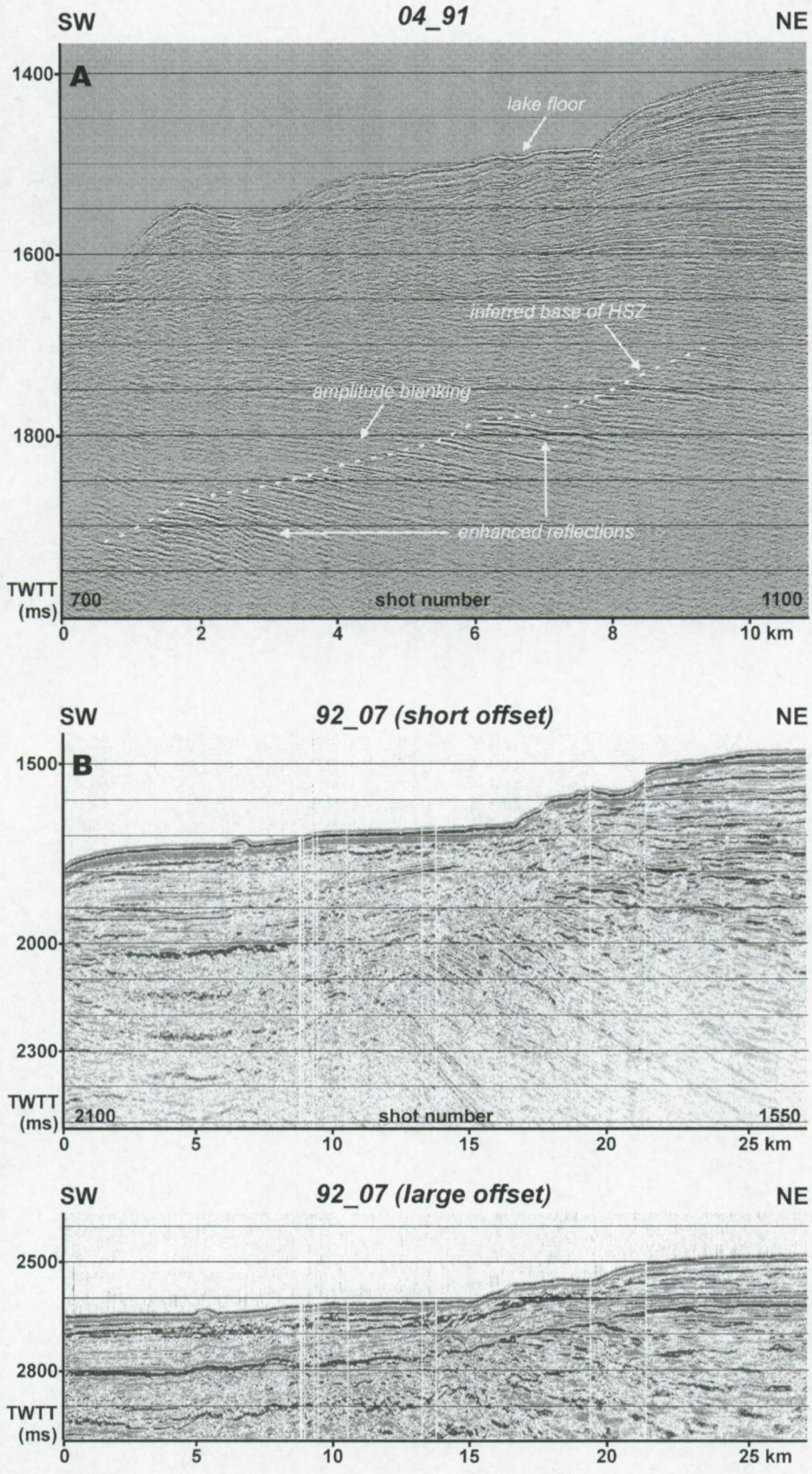

***Figure 3.6**: Nearly coincident seismic profiles acquired with different acoustic sources and acquisition layouts. (a) Watergun line 04_91, characterised by series of series of enhanced reflections termination at the base of the HSZ. (b) Short and large offset channels of low-resolution airgun-array profile 92_07 showing a distinct BSR. For location, see figure 3.2.*

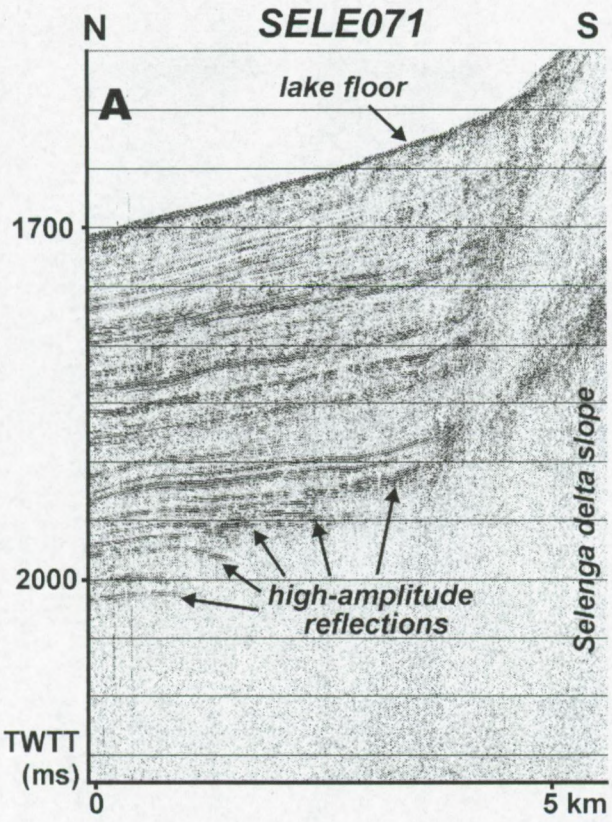

***Figure 3.7a**: Very-high resolution SC zero-offset sparker profile SELE071 showing the presence of enhanced reflections jumping from the one to the other horizon, and the acoustic-basement effect. For location, see figure 2.*

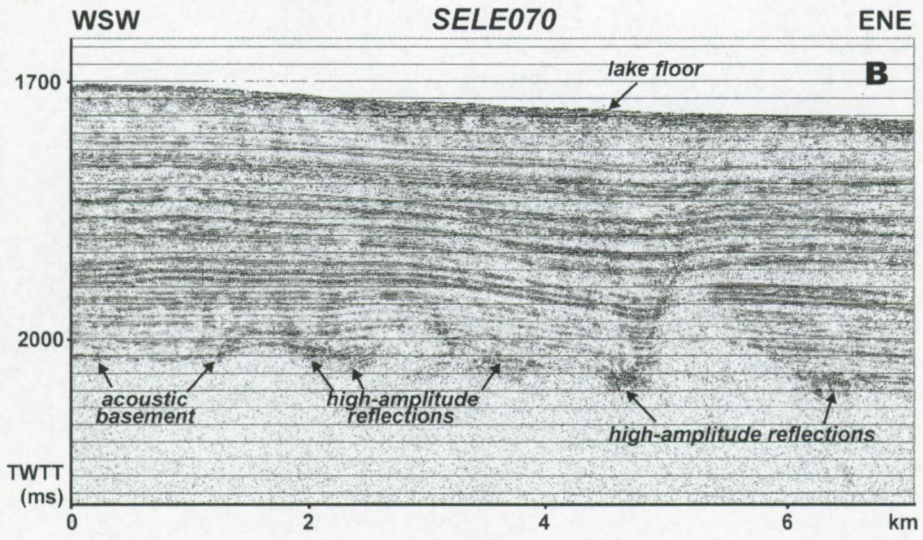

***Figure 3.7b**: Very-high-resolution SC sparker profile SELE070. For location, see figure 3.2.*

On other sparker profiles, diverse features are observed to occur near the penetration limit. Some show a rather continuous normal-amplitude reflection, others show very weak and irregular small reflections. None of these crosscut the local stratigraphic pattern. Polarity analyses of the sparker signals, especially of weak reflections, is furthermore not evident at all, so this does not contribute directly to this discussion. Comparison with nearby MC lines only gives information in the immediate neighbourhood of the cross points. It is therefore extremely difficult or even impossible to use these

very-high-frequency acoustic sparker profiles to unambiguously determine the position of the BHSZ, without any additional control of lower-frequency seismic data.

3.5.4
Seismic imaging of the HSZ at the BDP-97 site

A number of Ship airgun profiles were shot across the BDP-97 site: profile GAHY005/006 (figure 3.8a) and profile GAHY010 (figure 3.8b). On line GAHY005/006 the drilling site is located at SP 370; on line GAHY010 it is located near SP 150-160. On these profiles, only a very faint BSR is discerned in some parts of the sections. The BSR is visible to the NE and to the SW of the BDP drilling site, but is not present over a distance of several km in the vicinity of the site. Where present, the BSR is continuous, regular and crosscuts stratigraphic boundaries at a small angle at sub-bottom depths of 350-390 ms TWTT (figure 3.8). Some stratigraphic reflections below the BSR are slightly enhanced, and reflection amplitudes above the BSR are locally reduced.

Note that hydrate samples were retrieved close by from the sedimentary section well above the HSZ. Conversion from m- to ms-scale sub-bottom depth was performed using the Golmshtok velocity model [*Golmshtok et al., 1997*; see also next chapter]. In this way, the samples were recovered from 140 res. 187 ms TWTT sub-bottom depths, as shown in figure 3.8.

3.6
Discussion: acoustic characteristics of gas hydrate accumulations and free gas horizons

3.6.1
Amplitude blanking above the BHSZ

Amplitude blanking, or reduced acoustic reflection amplitude, is a common effect that has been described on seismic records from several well-studied gas hydrate provinces [e.g. *Shipley et al., 1979; Lee et al., 1993; Dillon et al., 1994; Hovland et al., 1997; Wood & Ruppel, 2000*]. It is usually observed in the section just above the BSR or the BHSZ. Even on high-resolution deep-tow data, a low-reflectivity zone is observed just above the BHSZ [*Rowe & Gettrust, 1993*]. Absence of internal reflection indicates lack of impedance contrasts within this medium. The effect is often attributed to the presence of gas hydrates in the pore spaces of the sediments that act as a kind of cement hereby reducing the velocity and density contrasts between the individual strata and hence damping the reflection amplitudes in that particular sedimentary section. It has therefore been argued that amplitude blanking can be used to estimate the amount of *in situ* hydrates in sediments [*Lee et al., 1993*] and to trace the BHSZ in areas or on seismic profiles without distinct BSR, i.e. especially on medium- to higher-frequency data.

On the other hand, *Ecker et al.* [*1998*] investigated and modelled physical properties of partially hydrated sediments. From their studies, hydrates appear to be located off the grains in the middle of the pore spaces, and hence do not cement the grains. Also *Hovland et al.* [*1997*] mention that acoustically transparent sediments are most probably not cemented by hydrates, but rather have a higher than normal water content. Results from ODP Leg 164 show that the low reflectance above the BSR is readily explained as the naturally low background reflectance of a uniform medium. In this way, the relation between amplitude blanking and hydrate saturation is not straightforward [*Holbrook et al., 1996*]. Most recent results from ODP Leg 164 suggest that other factors (energy scattering, paucity of nearly horizontal reflectors) might be important as well [*Wood & Ruppel, 2000*]. Seismic

profiles acquired in other areas with known hydrate occurrence (Cascadia margin, Makran accretionary prism) do not reveal evidence of blanking [*Spence et al., 1995; Sain et al., 2000*].

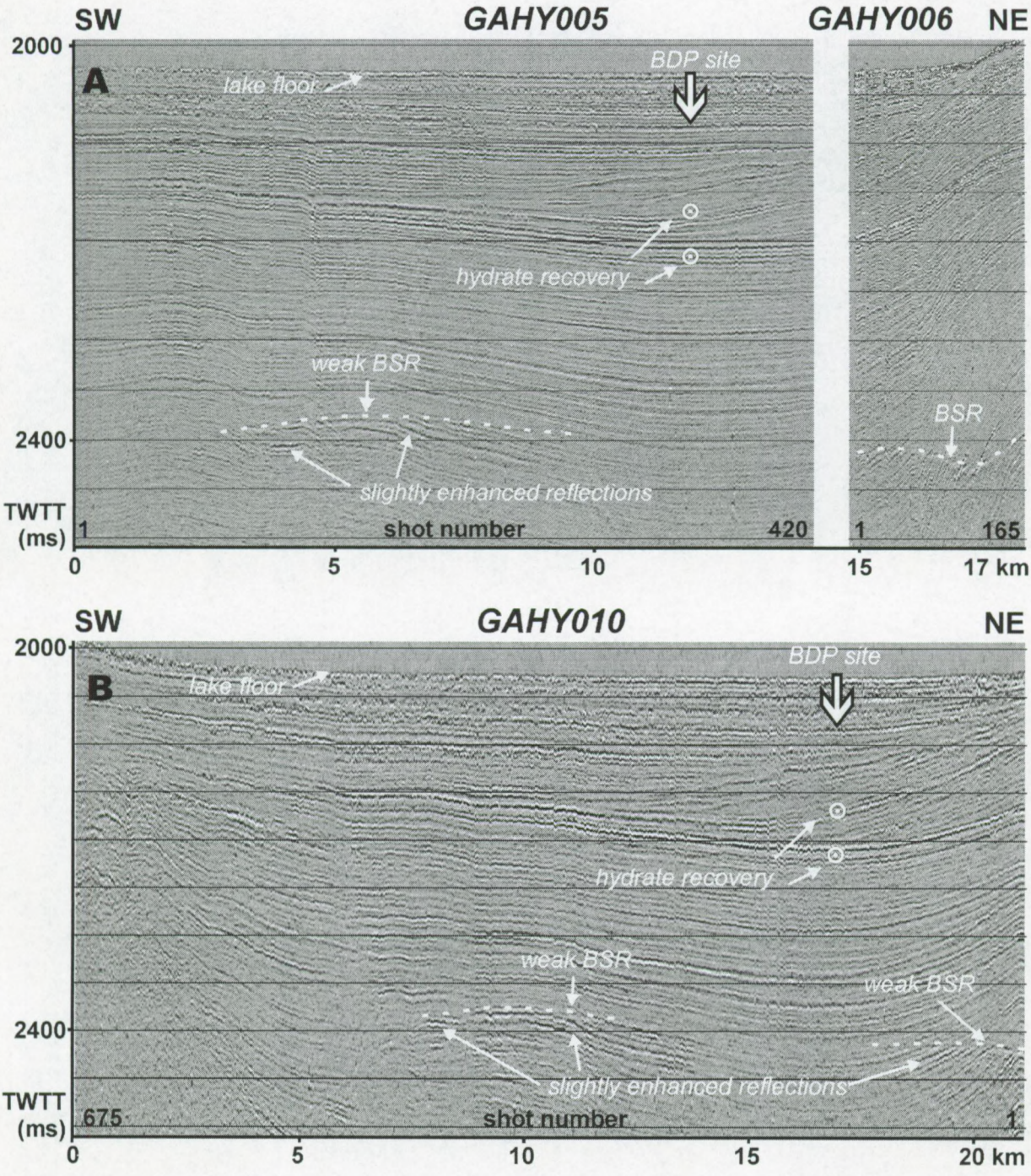

***Figure 3.8**: Medium-resolution SC Ship airgun profiles GAHY005-006 (a) and GAHY010 (b) across the BDP-97 hydrate drilling site. Only a very faint BSR can be observed along part of these profiles. No BSR is observed at the drill site. Note that the sub-bottom depths from which hydrates were retrieved lie well above the BHSZ. For location, see figure 3.2.*

Amplitude blanking is clearly observed on many of the seismic records from Lake Baikal and their respective reflection strength plots. In most cases it occurs in a limited zone just above the BSR or the BHSZ and fades out upwards. The intensity of the blanking effect also varies laterally. The effect is the

least evident on the MC airgun-array profiles, with exception of line MC92_34 (figure 3.5a). On profile 92_07 (figure 3.6b) some blanking can be observed on the shortest-offset channel (above). In contrast, the slightly higher-frequency SC airgun data show very distinct blanking effects, such as on profiles GAHY008 (figure 3.3c), GAHY020 (figure 3.3d) and GAHY017 (figure 3.4). The same applies to the SC watergun profile 04_91 (figure 3.6a). Since no automatic gain control (AGC) was applied to the data, this blanking cannot be related simply to the presence of enhanced reflections below the BSR.

Comparison of the drilling results with the seismic profiles through the BDP site (figure 3.7) illustrates that significant amounts of hydrates may also occur in sedimentary sections that are not characterised by amplitude blanking or any other acoustic anomaly. Note that at this site, hydrates were retrieved from about 200 m above their stability limit. This leads us to conclude that hydrate inclusion cannot be directly and unambiguously related with amplitude blanking.

3.6.2
Enhanced reflections below and above the BHSZ

Another common feature on seismic records from gas hydrate provinces is the presence of enhanced reflector segments or high-amplitude reflections below the BSR or the BHSZ [*Andreassen, 1995; Bouriak et al., 2000; Taylor et al., 2000; Wood & Ruppel, 2000*]. High-amplitude reflections are caused by significant acoustic impedance contrast due to physical and lithological properties across the interface. Under normal conditions, this will result in positive polarity reflections. When the acoustic impedance contrast is due to the presence of free gas beneath the interface, negative polarity reflections or "bright spots" will be generated. It is known that even a small amount of free gas in the pore spaces may cause a strong decrease in compressional wave velocity and thus in acoustic impedance [*Domenico, 1974; Sheriff & Geldart, 1995*]. The existence of free gas accumulations below BSRs has been confirmed at several locations by drilling [*Bangs et al., 1993; MacKay et al., 1994; Holbrook et al., 1996; Wood & Ruppel, 2000*]. Free gas may be trapped beneath partially-hydrate saturated sediment due to the reduced effective porosity and permeability above [*Ecker et al., 1998*].

Enhanced reflections or bright spots are characteristic for nearly all of the seismic records from Lake Baikal. They occur on some of the MC profiles (figure 3.5b), and are very common on the SC airgun profiles (figures 3c, 3d, 3e and 4) and on the SC watergun profiles (figure 3.6). In most of these examples, they do occur - as described above - just below the BSR or the BHSZ. Polarity analysis of the enhanced reflections suggests that they are reversed in polarity relative to the lake-floor reflection. They are therefore interpreted as a good indication for the presence of free gas accumulations below the BHSZ. Note that enhanced reflections basically appear if the inferred BHSZ/BSR is oblique to stratification.

The very characteristic enhanced reflector segments on the watergun line (figure 3.6) follow normal stratigraphic boundaries that are slightly inclined with respect to the BHSZ. The up-dip terminations of the bright spots line up regularly at what here is inferred to be the base of the overlying hydrate-enriched sediment section that effectively seals the gas-bearing strata by means of a permeability trap due to hydrate inclusions. The down-dip terminations are much less regular. Not all of the sediment layers in this section appear as enhanced reflections. These observations suggest a distinct stratigraphic and lithological control on the accumulation of the free gas below the BHSZ (preferentially in higher-porosity layers ?), and also on the migration of pore fluids within the sedimentary section.

On figures 3c, 3d, 3e (GAHY008-020) & 4 (GAHY017), some of the enhanced reflections extend to a certain height above the BSR, while the amplitude of the other reflectors in this interval is generally suppressed. For example, apparent polarity applied on the zoom of 3e shows that the enhanced reflection at the central part has negative polarity. In this case, this suggests that gases may locally migrate or seep into the HSZ. Migration pathways again appear to be primarily stratigraphically-controlled. These observations provide indirect evidence for the existence of a meta-stable situation in

which hydrates and free gases are present within the regional HSZ. This could be attributed to transient pulses of pore fluids with a slightly higher than background temperature causing a very localised shift in the HSZ. Alternatively, it could also be caused by stratigraphically (porosity and/or permeability?) controlled capillary effects which may also cause shifts in the HSZ in the order of several meters or tens of meters [*Henry et al., 1999; Clennell et al., 1999*].

The origin of the enhanced stratigraphic reflection with apparent reversed-polarity observed on line MC92_52 (figure 5b) is not obvious. It is unclear whether this impedance contrast is related to free gas presence at hydrate stability conditions or not. Faults are observed at the sides of this reversed polarity reflection and might form migration pathways.

Such negative-polarity features above the BSR, however, are not commonly observed on the data set discussed here, but only in a few cases. This is e.g. the case for line GAHY017, where a similar polarity analysis technique does not unambiguously prove negative polarity.

3.6.3
Attenuation and frequency filtering at the BHSZ

Using the multi-frequency data set, attenuation and acoustic frequency filtering effects were also investigated qualitatively. The amplitudes of events on a seismic record depend upon a multitude of factors. The most important attenuation mechanisms are divergence (due to wavefront spreading), absorption (conversion of acoustic energy into heat) and scattering (redistribution of acoustic energy in directions different from the propagation direction of the primary acoustic wave). Higher frequencies are preferentially attenuated. Furthermore, attenuation is known to increase substantially when the sediment is only partially-saturated. This effect is even more pronounced at high degrees of water saturation [e.g. *Sheriff & Geldart, 1995; Castagna et al., 1993*].

On the very-high-frequency sparker data (figure 3.7), the enhanced reflectors occurring close to the estimated depth of the HSZ (in this case 300-320 ms TWTT) appear as a kind of acoustic basement. No reflection arrivals could be recorded from below this level. Although the penetration limit of this very-high-frequency and relatively low-energy sparker signal in other areas of Lake Baikal [*De Batist & Vanneste, 1997; Vanneste & De Batist, 1998; Back et al., 1999*] is generally not much higher than 350-400 ms TWTT, the sudden and complete attenuation below the enhanced reflectors is quite striking as normally the amplitude of the signal tends to gradually decrease with depth.

On the low- to high-frequency data, a similar extreme effect is not observed. In the first instance, spectral analyses of the frequency content were performed on the different data sets in selected windows of 100 ms (averaged out over 100 shots) just above and below the hydrate accumulation zone. The results are also compared to the main window of 500 ms. On the medium- to high-frequency sections, small shifts towards lower main frequencies were observed across a clear BSR-feature.

Next to that, more detailed frequency analyses using colour-encoded displays of the acoustic instantaneous and response frequencies of SC airgun records and SC watergun line (ProMAX macros) reveal a shift to lower frequencies across the inferred base of HSZ. The displays are made for specially-designed RGB-combinations and contrasts to give the best picture quality. Unfortunately, such design is limited in ProMAX since the frequency band up to the Nyquist frequency is split up in intervals of uniform length. Investigation of the acoustic response of watergun line 04_91 (see figure 3.6a) results in an apparent reduced frequency content in the zone characterised by the series of enhanced reflections (figure 3.9a). Beneath this zone, the data are much more chaotic. Selected higher-frequency Ship (GAHY008, 010, 017) and lower-frequency Impuls (GAHY020, 021, 025) airgun data were also examined. On line GAHY008 (figure 3.3d) and GAHY017 (figure 3.4), one can see a similar behaviour as described above, i.e. a small shift of the frequency spectrum beneath the BSR (GAHY017 – figure 3.9b). Also for the lower-frequency airgun line GAHY020, the base of the inferred stability field appears to cut out the higher frequencies, similar to the observations along the coincident line GAHY008. For

line GAHY010 crossing the BDP drill site, the weak BSR does not result in obvious frequency shifts. The strength of the BSR and the enhanced reflections below has the highest impact on this behaviour. In zones of weaker BSR amplitude, this effect is less pronounced.

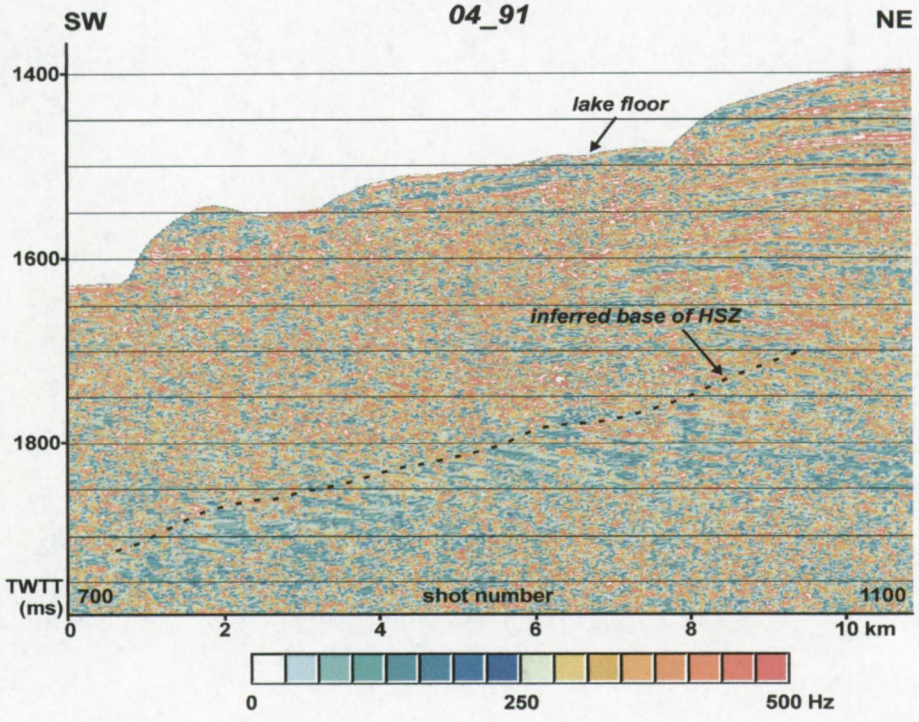

***Figure 3.9a**: Instantaneous frequency display of watergun line 04_91 (see also figure 3.6a).*

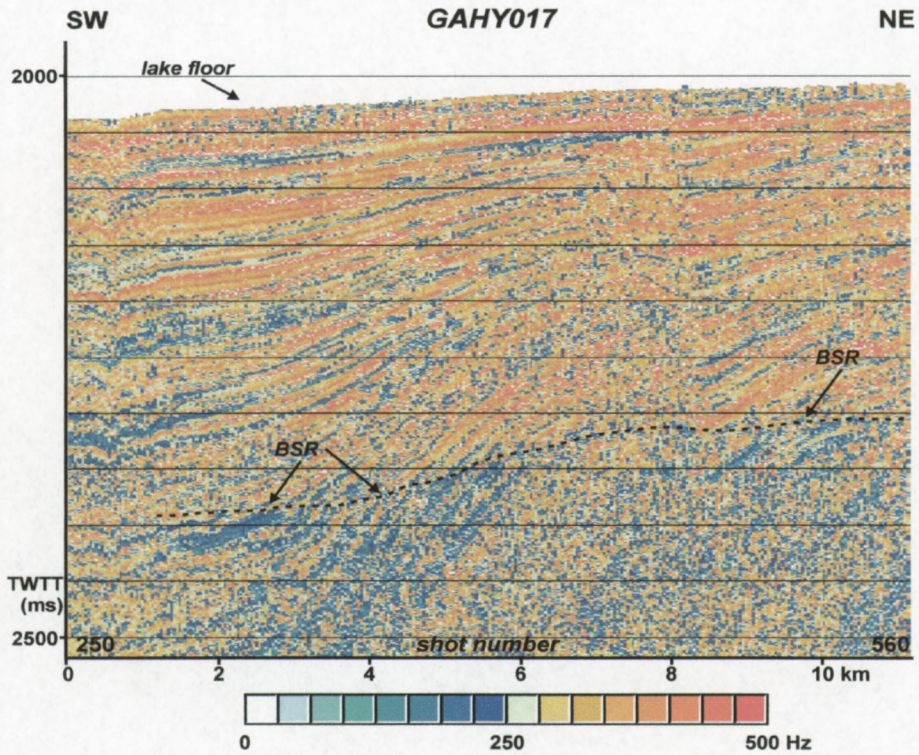

***Figure 3.9b**: Instantaneous frequency display of Ship airgun line GAHY017 (see also figure 3.4).*

On the low-frequency data, no frequency effect is visible at all, neither on the individual channels nor on the stacked sections. Analyses were performed on MC airgun-array profiles 92_01, 92_03, 92_07.

Medium- to high-frequency data sets appear more sensitive to attenuation across the BSR while at the same time absorption and scattering not necessarily affects low-frequency airgun-array signals. Energy scattering will occur once the wavelength of the incident pulses approaches the dimensions of the gas-enriched layer. Higher-frequency waveforms then become irregular and propagation will be different within this layer. For the low-frequency airgun-array data (larger wavelength), the gas-containing layer seems to be too small to have a visible influence. These observations confirm that the BHSZ behaves more effectively as a low-pass frequency filter for higher acquisition frequencies (single airguns, watergun, sparker).

3.6.4
BSR reflection coefficient

3.6.4a Multiple quotient method and formulas

Attempts were also undertaken to obtain a quantitative estimate of the reflection coefficient (i.e. a measure for the difference in elastic properties across the interface between two media) of the lake-floor reflection and of the BSR using the *multiple quotient method*. In this method [*Warner, 1990*], it is assumed that the amplitude of the lake-floor reflection is proportional to the lake floor's reflection coefficient and to an unknown factor describing the source and receiver geometry. The amplitude is furthermore inversely proportional to the travel path length of the acoustic wave. The unknown factor can easily be eliminated by comparing the primary lake-floor reflection with the first lake-floor multiple and by taking into account the difference in travel path length between them, and the reflection coefficient of the lake floor can hence be calculated. Amplitudes of other reflections are treated in the same way.

In terms of formulas, the following relationships are obtained, valid for normal incidence on a flat lake floor and assuming the water-air interface as a perfect mirror:

$$R_{P,lf}\langle \vartheta = 0 \rangle = \frac{v_{lf}\rho_{lf} - v_{water}\rho_{water}}{v_{lf}\rho_{lf} + v_{water}\rho_{water}} = -2\frac{A_{multiple}}{A_{lf}} \quad [3]$$

$$A_{lf} = \frac{kR_{P,lf}}{v_{water}t_{water}} \quad [4]$$

$$A_{multiple} = -\frac{kR_{P,lf}^2}{2v_{water}t_{water}} \quad [5]$$

$$R_{BHSF} = \frac{A_{BHSF}}{A_{lf}}\frac{t_{BHSF}\bar{v}}{t_{lf}v_{water}}\frac{R_{lf}}{1-R_{lf}^2} \quad [6]$$

with R reflection coefficient
A reflection amplitude as determined from ProMAX software package
t two-way travel time
v compressional wave velocity
and obvious indices.

3.6.4b Results along line 92_01, recording channel number 96

This method was first of all applied to a segment of the shortest-offset channel (offset 495 m) of MC airgun array profile 92_01, corrected for spherical divergence. This record is characterised by a regular

and continuous flat lake floor and BSR (stacked version is shown in figure 3.3). Because the reflections between the lake floor and the BSR are characterised by weaker amplitudes than the BSR feature, they were not taken into account in the calculation. Physically, this means that the sedimentary section between the lake floor and the BSR is considered to transmit the acoustic energy perfectly, i.e. without transmission loss due to reflections or absorption. For the sake of simplicity, we also assumed that the angle of incidence was nearly vertical (in fact, it was close to 10°). The amplitudes of the primary lake-floor reflection and its first multiple were measured for the first 450 shot points. The travel path length of the acoustic waves below the lake floor was calculated using the sub-bottom velocity model developed by *Golmshtok et al. [1997]*.

Along profile 92_01, the lake-floor reflection coefficient is on average about 0.197, while the BSR has a reflection coefficient of about –0.085, or –43 %. Comparable values were reported from BSR analyses from several oceanic settings [*Hyndman & Spence, 1992; Minshull et al., 1994; Andreassen et al., 1995; Kremlev et al., 1997*]. The lateral variability of both reflection coefficients along the selected profile segment is shown in figure 3.10. Fluctuations in the BSR reflection coefficient are significant, and show an inverse trend compared with the much smaller fluctuations of the lake-floor reflection coefficient. Around SP 275-366, the scattering is less significant. Average values along that segment are 0.146 for the lake floor, and –0.061 for the BSR. A ratio of –42 % is returned. Also along the first part of the section (first 200 shots), the lake floor reflection coefficient behaves rather invariable but is higher (0.231) than in the second part while the reflection coefficient of the BSR is still characterised by remarkable changes with mean value of –0.084 (-37%). Between shot point (SP) 200 and 250 data quality is reduced most probably due to weaker source signals.

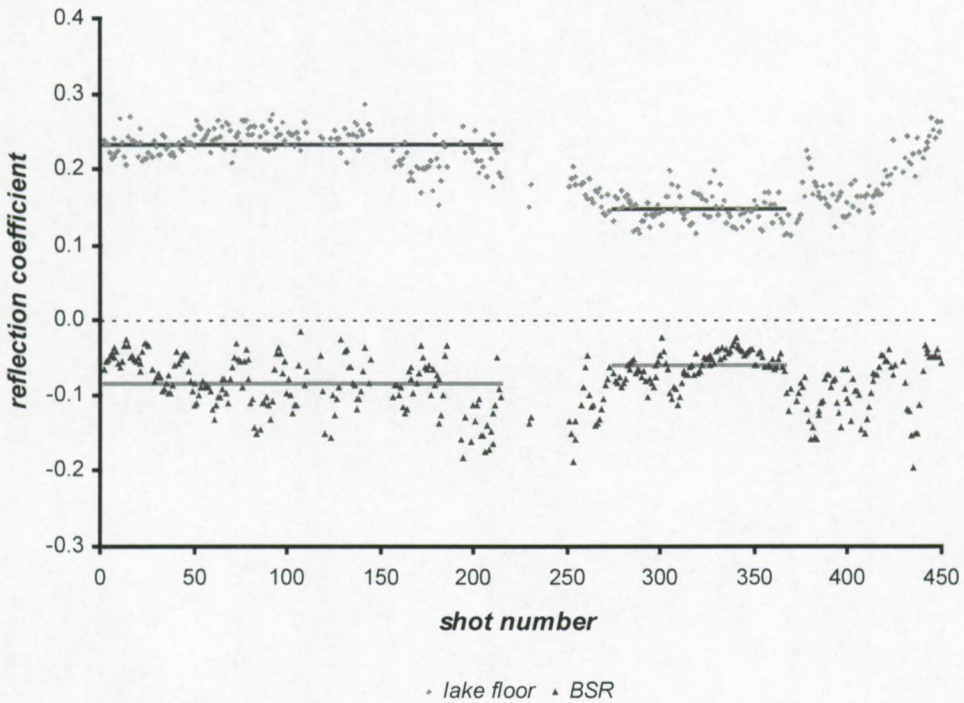

***Figure 3.10**: Reflection coefficient of lake floor and BSR along MC line 92_01, derived using the multiple quotient method (ignoring non-normal incidence). The scatter of the BSR reflection coefficient is remarkably higher than the lake floor coefficient. Mean values for some sections are shown as well. Plot direction is the same as in figure 3.3.*

3.6.4c Results along line GAHY020

The same procedure was then applied to a few points (SP 220-300) on the medium-resolution line GAHY020 that more or less coincides with MC line 92_01 also shown in figure 3.3 (zoom, figure 3.3e). As discussed before, the BSR reflection amplitude is highly variable and only appears as a clear

reflection where it is crosscutting the dipping stratigraphy at the border of the fold. On average, the lake floor res. BSR reflection coefficient in this section equals 0.139 res. –0.049 or –34%. This is slightly less than the values determined from the near-offset channel 96 of line 92_01.

3.6.4d Errors

Note that in this methodology several assumptions and simplifications were made. First of all, the medium in between of the lake floor and the BSR was considered to fully transmit the acoustic energy. In figure 3.2, reflections with weaker amplitude are present as well, so their transmission coefficients should be taken into account, resulting in a recursive method for solving this problem. Next to that, streamer directivity (see below) will only be of minor importance for the amplitude determination (±97.5%). Note that the array response will result in a systematic error almost identical for all data points. Finally, the non-normal incidence will have a certain influence as well for the airgun-array data. It is known that for non-normal incident acoustic waves, mode conversion from P- into S-waves occurs and that the amplitudes used for calculating the reflection coefficient should be determined based on the *Zoeppritz* equation or approximations [*Aki & Richards, 1980; Castagna, 1993; Shuey, 1985*]. For small angles of incidence, all of the energy will be in the reflected or transmitted P-waves and there are essentially no S-waves [*Sheriff & Geldart, 1995*]. At increasing angles of incidence, the relative importance of wave conversion becomes more and more important. The change of the P-wave reflection coefficient with respect to angle of incidence is then small at low angles [*Castagna, 1993*]. *Bushenkov et al.* [*1998*], using these MC data, also report that the deviation will be less than 4% for angles less than 25°. Hence, the above approximation will give a reasonable estimate for the reflection coefficient of the lake floor and the BSR.

3.6.4e Discussion & conclusion

The difference of the mean reflection coefficient in the first relative to the middle section observed in figure 3.10 of MC line 92_01 (figure 3.3a) is caused by relatively weaker amplitudes of both the lake floor reflection and its first multiple in the middle section. This is also reflected in the BSR reflection coefficients determined, based on formulas [3] and [6]. Note that around shot points 200-300, the dipping of the folded sediments is maximal and interference occurs. At the SE part of the profile, the sharp fault system is approached. There, the amplitude of the multiple reflection increases again. In this area (> shot point 450), the BSR cannot be traced any longer. On true amplitude plots of the medium-frequency line GAHY020, a similar response of the lake floor reflection and its first multiple is observed, being stronger in the zone characterised by the fold and much fainter in between the fault (SE) and the fold.

The reason for the scattering of the reflection coefficients and the reflection amplitudes observed cannot be explained by bathymetry since the lake floor topography is almost flat along the entire profile, with exception of the fault structure arising at the SE part. The enhanced reflection amplitudes appear to occur along that part of the section characterised by the folded sediment units where the BSR lies a few tens of ms TWTT shallower. At present, an unequivocal explanation for this behaviour is wanting. In my opinion, the most plausible explanation can be found in lateral changes of lithology (porosity, grain size, sediment type), possibly related to variations in bottom currents. Whether there may be a link between the folding and "harder" lake floor or not is unclear.

In terms of acoustic impedance contrasts, the reflection coefficient is written as:

$$R = \frac{Z_2 - Z_1}{Z_1 + Z_2} \qquad \text{or} \qquad \frac{Z_2}{Z_1} = \frac{1+R}{1-R} \qquad [7]$$

The lake floor (R = 0.197) represents an interface with relative impedance contrast of nearly 50%. The calculated reflection coefficients further imply a drop of mean acoustic impedance across the BSR of 15.5% (line 92_01) res. 9.4% (GAHY020). Since partial inclusion of hydrates or free gas within the pores will hardly reduce the bulk density, this effect can be almost fully attributed to a drop in acoustic velocity.

Using the methodology worked out in *Bushenkov et al.* [*1998*], the different physical properties of the lake floor sediments (density, porosity, compressional wave velocity) can now be estimated based on the value of the reflection coefficient. With the average result of 0.197, it is calculated that lake floor deposits should have an average density of approximately 1510 $kg \cdot m^{-3}$, a porosity of 70% and a compressional wave velocity of 1550 $m \cdot s^{-1}$. With the lake floor reflection coefficient of 0.231 determined for the folded sediment area, porosity is calculated to be 66%, also values typical for sandy-silty clays. In the other area with sub-parallel layering, a 78% porosity medium is returned indicating lake floor coverage with silty clays. The effective thickness – being defined as one fourth of the incident (dominant) wavelength of this layer – is then 4.8 m. With the reflection coefficient of 0.139 determined along line GAHY020, the lake floor porosity should be slightly less than 80%. Almost the same result is found using a sparker profile SELE022 (Baikal 1997 expedition) with lake floor reflection coefficient of 0.15.

Knowing these results and according to *Hamilton* [*1970*], the uppermost lake floor deposits may change from sandy-silty clays overlain by a very thin layer of silty clays. Note that this method only allows us to estimate the lake floor properties and is originally based on salt water environments with wave velocities of about 1500 $m \cdot s^{-1}$, i.e. higher than in the case of Lake Baikal.

Concerning the results obtained for the BSR, one can conclude that BSR originates from an acoustic interface characterised by a strong decrease in acoustic impedance, but they bring no conclusive evidence for the presence of free gas below the BSR.

3.6.5
BSR amplitude versus offset or AVO-analysis

3.6.5a Observations

The variation of the amplitude of acoustic reflections in function of offset or angle of incidence depends on the properties of the reflecting interface, i.e. on the difference in elastic properties between the two media separated by that interface. Increasing negative reflection amplitudes from a certain reflector with increasing offset point towards partial occupation of the pore spaces of the sediments with free gases just below that reflector [*Sheriff & Geldart, 1995; Ecker et al., 1998; Yuan et al., 1999*].

Displaying different channels of the low-resolution airgun-array data from Lake Baikal clearly demonstrates that the reflection amplitude of the BSR depends on the offset or angle of incidence. A reflectivity gather plot of the traces composing CDP 380 of line 92_03 clearly shows that the amplitude of the BSR is higher at large offsets/incident angles (figure 3.11). Reflection strength plots illustrate that this behaviour is not strictly limited to selected CDP gathers but extends over the entire profiles with BSR occurrence. Identical qualitative analyses performed on other MCS lines show a similar behaviour. These observations provide an additional argument confirming the presence of free gas accumulations below the BHSZ. Unfortunately, the observed offset-dependent amplitude characteristics could not be directly translated into absolute values of gas saturation, because no detailed sub-bottom compressional and shear-wave velocity information is currently available from the area.

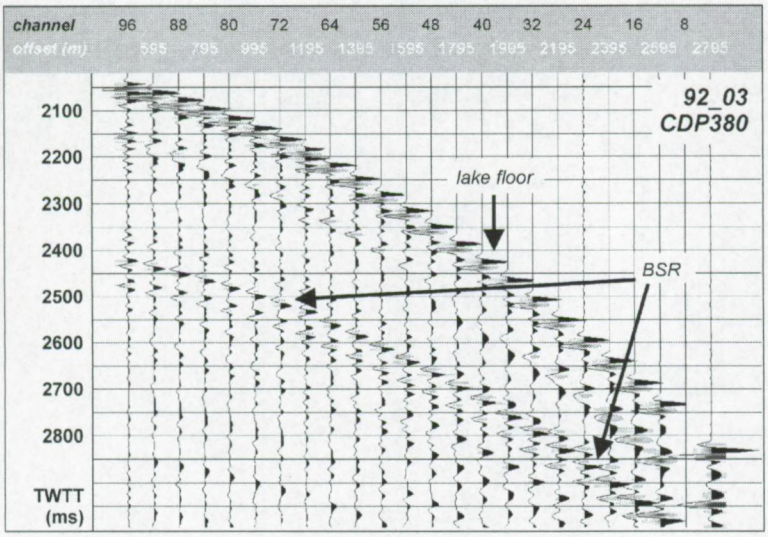

***Figure 3.11**: Reflectivity gather of CDP 380 of MC airgun-array profile 92_03 (Southern Baikal Basin) showing the increasing reflection amplitude of the BSR with increasing offsets or angles of incidence. This behaviour is attributed to the presence of free gas beneath the BSR. For location, see figure 3.2.*

In a way, this offset-dependent behaviour was already illustrated on figure 3.6c, which shows the difference in appearance (reflection strength, continuity, etc.) of the BSR between the short-offset channel display (above) and the large-offset display (below) of line MC92_07. On the large-offset display, the BSR occurs as a distinct and continuous high-amplitude reflection, while on the short-offset display it is more diffuse, less continuous and has lower amplitude.

The observation of increasing reflection amplitude with offset on all MCS data also explains why the BSR is generally much better expressed (higher-amplitude, more continuous) on stacked MCS profiles than on SC data obtained in the same frequency band-with. The stacked data will have a significant contribution of the larger-offset arrivals that will lead to a strong increase in BSR amplitude.

3.6.5b Correction for streamer directivity

Analyses of the AVO-effect attributed to free gas saturation have to be performed on true amplitude data. This means that to be correct also the directivity of the acquisition system (sources, receivers) has to be taken into account, so extra corrections need to be applied in order to obtain accurate results for BSR analysis [*Hyndman & Spence, 1992*]. Supposing that the source is considered as a point source, then only the influence of hydrophone array attenuation has to be investigated. The array response F depends on the dominant wave length of the acoustic pulses λ (or dominant frequency), the angle of incidence θ, the number of hydrophones n in the individual hydrophone groups and the distance Δ between the equally spaced hydrophones, according to the formula [*Hyndman & Spence, 1992; Sheriff & Geldart, 1995*]

$$F = \left| \frac{\sin\left(\pi n \frac{\Delta}{\lambda} \sin\theta\right)}{n \sin\left[\pi \frac{\Delta}{\lambda} \sin\theta\right]} \right| \qquad [8]$$

In case of the streamer array used on Lake Baikal, each recording channel consisted of an equally-spaced (distance of 0.75 m) series of 31 hydrophones resulting in an effective array length of 22.5 m and a distance of 25 m in between of the centres of each group. The array response for wavelengths of 35 m is illustrated in figure 3.12 as a function of offset/recording channel number and angle of

incidence for the specific case shown in figure 3.11. The amplitude reduction due to streamer array directivity is up to 32% at the far-offset groups of CDP-380. Dip corrections can be ignored for the lake floor reflection.

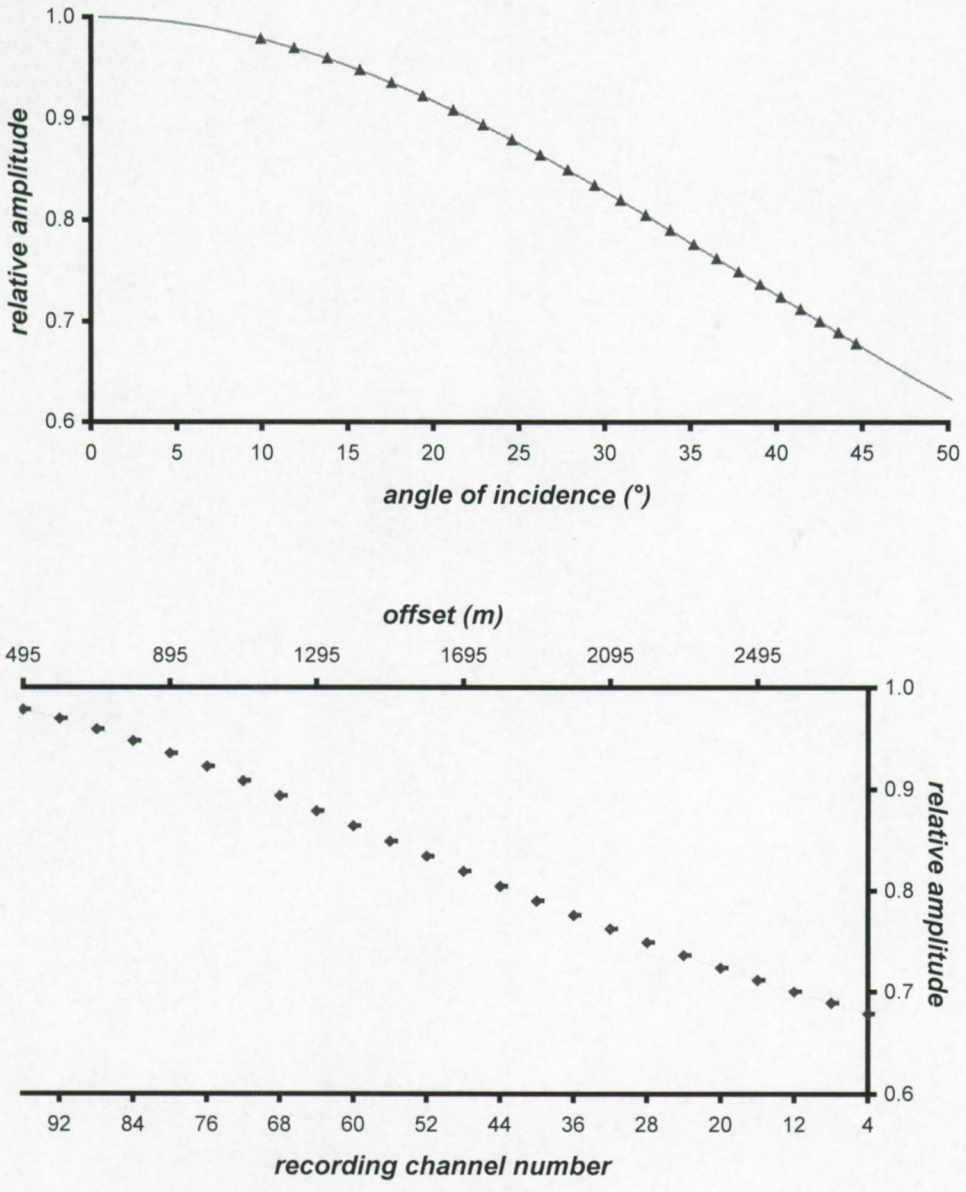

***Figure 3.12**: Array response or directivity of MC line 92_03 in CDP-380 (cf. figure 3.11) as a function of angle of incidence, with superposition of the different hydrophone groups (a) and as a function of recording channel number or offset (b) according to formula [3]. Note that the channels are numbered in reversed order.*

Airgun-array directivity was not taken into account since no detailed information was available. According to *Hyndman & Spence [1992]*, deviations can be significant.

3.6.5c Results

Reflection amplitudes were picked using *ProMAX* software of true-amplitude-processed seismic traces of 8 neighbouring CDPs along line MC92_03 where the lake floor as well as the BSR are more of less flat and where acoustic interference is minimal. To express the BSR AVO-effect quantitatively, these amplitudes were corrected for streamer directivity and spreading. Finally the amplitudes were

normalised for small offsets/angles of incidence (figure 3.13). The higher amplitude trend only appears at angles exceeding 25° or equivalent offset values 1400 m. Scattering also becomes stronger at farther offsets. On the Cascadia Margin, similar results are found [*Hyndman & Spence, 1992*] while slightly lower values for the Beaufort Sea were reported [*Andreassen et al., 1995*].

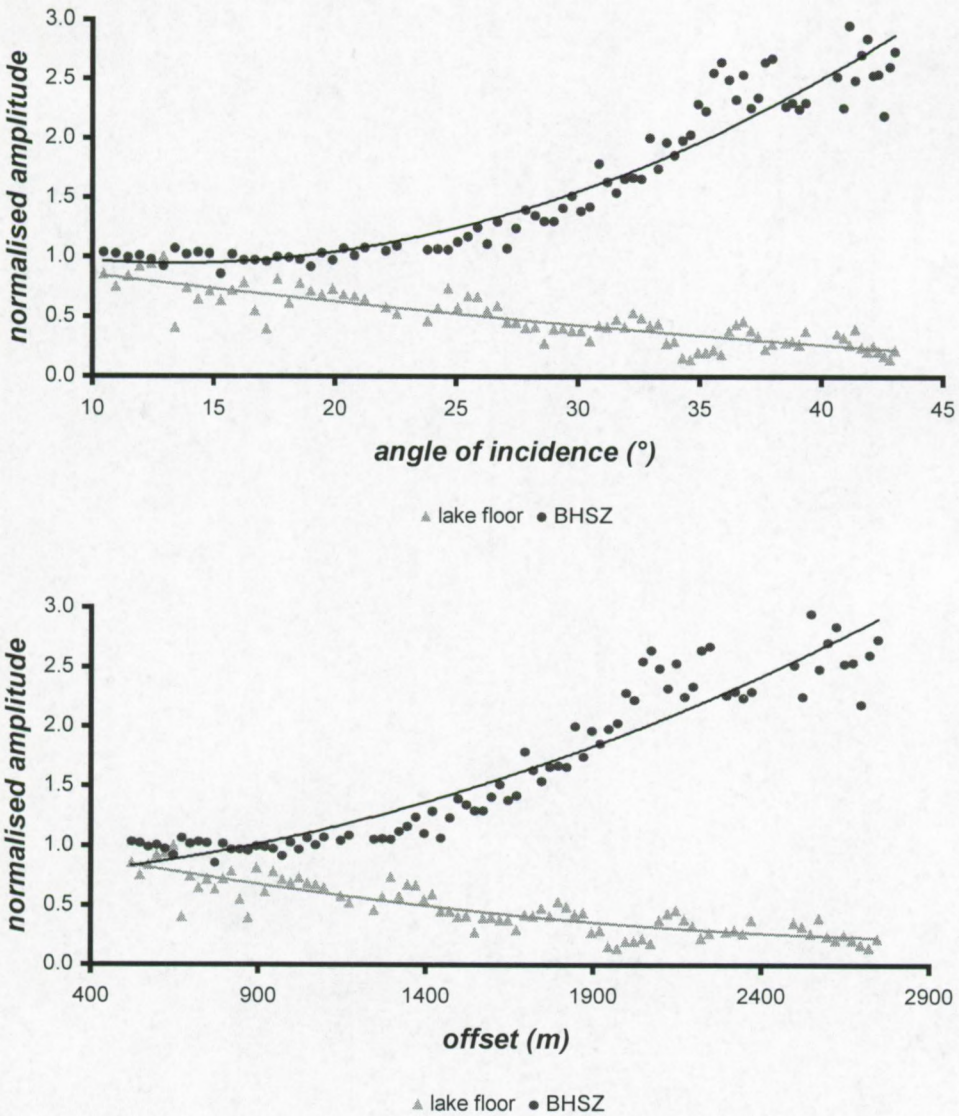

***Figure 3.13**: AVO results of 8 neighbouring CDPs (461-468), taken from line MC92_03. Amplitudes are normalised and corrected for spherical divergence and receiver directivity.*

These results could not be converted into estimates of the thickness of a free gas containing layer or partial hydrate distribution across the BSR. Waveform modelling should therefore be carried out, as worked out by *Hyndman & Spence* [*1992*] and *Andreassen et al.* [*1995*], based on appropriate *in situ* physical parameters (e.g. *Poisson's* ratio, acoustic wave velocities, densities and there contrasts across the BSR) and the (simplified) *Zoeppritz* equation [e.g. *Shuey, 1985*] for a variety of situations and accumulation modes of both free gas and hydrates. Such parameters are not yet available for Lake Baikal sediments. The nearly uniform increase of reflection amplitude with offset is – compared to the modelled trends shown in *Andreassen et al.* [*1995*] – most probably indicative for the presence of free gas beneath the BSR.

3.6.6
Thickness of free gas layer in Lake Baikal

Indirect evidences for the presence of gas-enriched sediments beneath the HSZ are abundant: increasing reflection amplitude with offset, sudden attenuation across the BSR/enhanced reflections on the medium- to high-frequency profiles, the presence of enhanced reflections beneath the BSR and the high reflection coefficients of the BSR. First attempts [*De Meersman, 2000*] to obtain a detailed sub-bottom velocity profile using Ocean Bottom Hydrophones (OBH – provided by GEOMAR, Kiel within the framework of EC-TMR programme) are compared with the *Golmshtok* background interval velocity profile (figure 3.13). The OBH profile shows a sharp decrease of interval velocity around 310 m sub-bottom depth. Unfortunately, no information is available from deeper reflections and only one OBH result was given. The low-velocity layer appears to be a few tens of m thick with the velocity being of the same order of magnitude as in the uppermost sediment layer. Compared with the *Golmshtok* velocity model [*Golmshtok et al., 1997*] derived from the MC 1992 data set, the interval velocity determined with OBH is less in the upper 130 m and is in good agreement in the interval between 130 and 300 m sub-bottom depths. The opposite is true for the OBH data vs. the Hamilton regression curve for terrigenous sediments (silt clays, turbidites, mudstone, shale) [*Hamilton, 1980*]. The velocity in the observed low-velocity layer is significantly lower compared to both the *Golmshtok* velocity model and *Hamilton's* regression curve and has about the same magnitude as in the uppermost sedimentary section. This anomalous behaviour can be explained by the presence of free gas, although the interval velocity is not lower than the velocity in the water column.

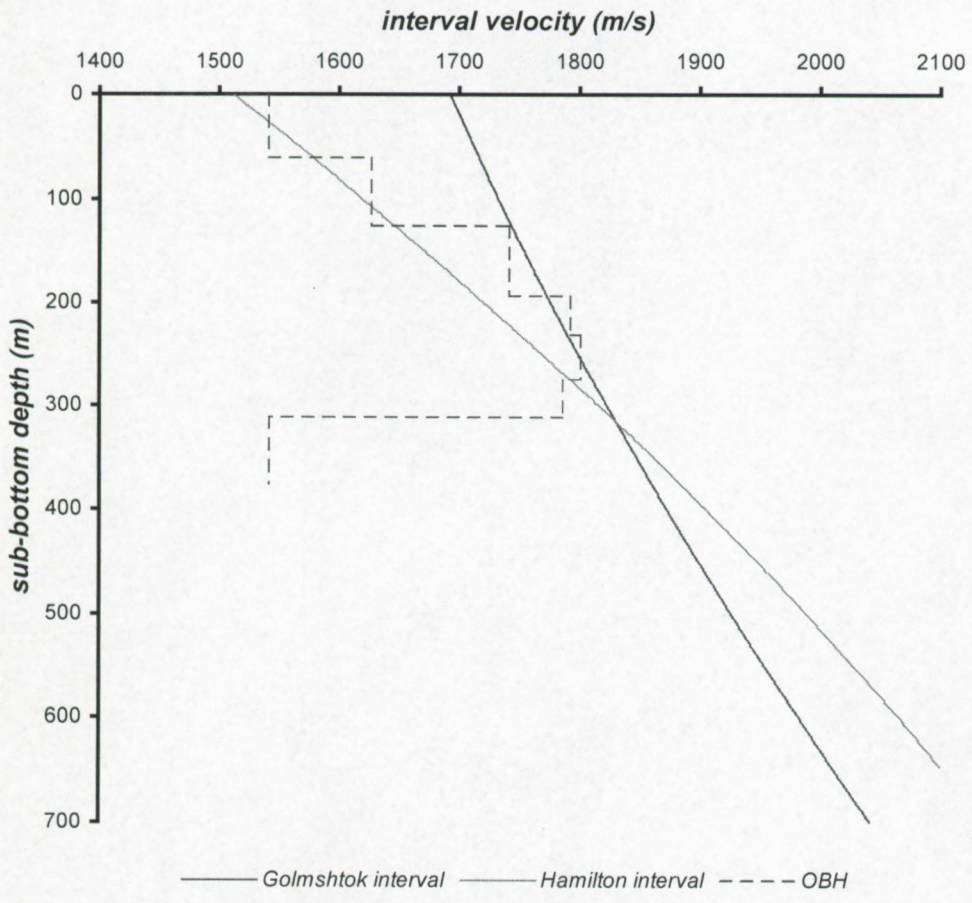

***Figure 3.14**: OBH sub-bottom interval velocity profile [De Meersman, 2000] vs. background reference profiles of Golmshtok et al. [1997] and Hamilton [1980].*

The sudden low-pass frequency filtering effect of the BSR/enhanced reflections on higher frequency data (figure 3.9) suggests that the free gas zone beneath the HSZ should extend over at least some meters to explain this behaviour. The series of bright spots observed on watergun line 04_91 (figure 3.6) is restricted to a certain depth range beneath the inferred HSZ. The individual stratigraphic boundaries – although rather faint – can be traced on both sides of the enhanced parts. The vertical extent of these bright spots is about 30 ms TWTT, or about 25 m. No free gas seems to be present in deeper parts.

Using the OBH interval velocities as shown in figure 3.14 with typical bulk density of 1732 $kg \cdot m^{-3}$ at about 300 m sub-bottom depths, then the reflection coefficient of the BSR considered as a pure velocity contrast is –0.073, i.e. the same order of magnitude as the values returned via the multiple quotient method. Both the velocities and the reflection coefficients are in good agreement with results obtained from the Cascadia Margin [*Spence et al., 1995*]. The lack of accurate data restrict the possibilities to estimate the amount of free gas beneath and hydrate above the BSR.

Hence, the interval of free gas occurrence beneath the HSZ appears to be limited to a few meters to tens of meters in Lake Baikal.

3.6.7
BSR characteristics and continuity: influence of acoustic frequency

The use of different acquisition frequencies off Vancouver Island (MC airgun-array, single airguns) already revealed a decreasing reflection continuity with increasing source frequency [*Spence et al., 1995*]. On high-frequency deeptow data from the same area, the BSR is rarely evident [*Gettrust et al., 1999*]. Our seismic data from Lake Baikal clearly illustrate that the BHSZ produces a distinctly different seismic image depending on the frequency of the acoustic signal and on the acquisition lay-out.

On low-frequency stacked MC airgun array the BHSZ is represented by a classic BSR, i.e. a continuous high-amplitude reflection with reversed polarity. On SC data in the same frequency bandwidth it appears still as a BSR but with much smaller amplitude. As discussed above, the difference in amplitude is easily explained by a contribution of the high-amplitude responses recorded in the larger-offset channels of the MCS data. On medium-frequency zero-offset SC airgun data, the amplitude and continuity of the BSR decreases even more and the BSR locally disappears. On higher-frequency data (SC watergun or sparker profiles), the BHSZ is no longer expressed as a single reflection, but it is characterised by a series of separate enhanced reflections that most probably mark the top of the free gas zone below the hydrate-bearing interval.

An explanation for the observed variability of reflection amplitude has to be found in differences in frequency-controlled lateral (Fresnel zone) and vertical resolution. At lower source frequencies, a larger volume of sub-surface is sampled than at higher frequencies, and also the physical properties that will contribute to generate a reflection will be averaged out over the larger volume. For higher frequency data, smaller volumes are sampled while also small-scale lateral variations (e.g. inhomogeneities) become more important once their dimensions are smaller than the respective resolution. This will result in reduced reflectivity and possibly decreasing signal to noise ratio. The fact that on higher-frequency data the BSR is weaker (or not present) indicates that the BHSZ is most probably not a regular interface.

A series of closely-spaced gas-bearing strata will be identifiable as separate events on higher-resolution records, but will merge to create only a single reflection on lower-resolution data at what would be the top of a gas-bearing sediment package. Along watergun line 04_91 (figure 3.6a), not all strata beneath the inferred base of hydrate stability appear as enhanced reflections. So free gas is thought to be present only within specific stratigraphic layers alternating with gas-free layers. If then the apparent horizontal distance between gas-containing strata exceeds the horizontal resolution, no

coherent reflection will be generated along the base of the stability limit since the impedance contrast will be much reduced due to the absence of gas along part of the section. This also confirms that the BSR has to be considered as a reflection arising from the top of gas-charged sediments.

3.7
Extent of the hydrate accumulation zone: constraints for volume estimations

3.7.1
Vertical extent of the hydrate accumulation zone: seismic data versus BDP results and implications for formation mechanism

Medium-resolution SC airgun profiles GAHY005/006 (figure 3.8a) and GAHY010 (figure 3.8b) were shot across the BDP-97 borehole site. A BSR is observed on parts of these profiles, but not in the immediate vicinity of the borehole. The lake floor is virtually flat along the entire profile, no faulting is observed and stratigraphy is not thought to be responsible for strong lateral variations in heat flow and pressure. It is therefore reasonable to assume that the BHSZ occurs at a more or less constant depth along the entire profile, i.e. at 350-390 ms TWT. Using the interval velocity model discussed in *Golmshtok et al. [1997]*, this equals a sub-bottom depth of 320-355 m. In the BDP-97 borehole, gas hydrates were retrieved from 120 and 161 m sub-bottom depth (i.e. 2170 ms and 2215 ms TWTT), thus well above the BHSZ. This indicates that the vertical extent of the hydrate accumulation zone reaches to at least 200 m above the BHSZ. Unfortunately, no results from intermediate depths are available due to poor core recovery. Also, the borehole did not penetrate to the BHSZ.

During shallow coring in the winter of 1999-2000, sediment samples with significant hydrate inclusions (see pictures, figure 3.15) were recovered from the first 50 cm of the elongated (800 m by 500 m) *Malen'kiy* crater [*Klerkx, pers. comm;, Soloviev, pers. comm.*], a shallow lake floor depression clearly observed on side-scan sonar data (for more details, see next chapter). Also seep activity (plumes) is observed coming from the crater. One core contained a 7 cm long almost pure hydrate sample while in others the hydrate appeared to be layered or more disseminated. Methane of biogenic origin is by far the most abundant enclosed gas component (> 99%) [*Soloviev, pers. comm.*]. Other shallow craters are found as well in this region, with similar characteristics but no attempt was undertaken to sample the lake floor sediments there. Whether the occurrence of hydrates at or just below the lake bed in the *Malen'kiy* crater is unique or typical for Lake Baikal is at present unknown. Also no high-reflectivity pattern as can be expected from a hydrate mat exposed at the lake bed was observed on the 30 kHz side-scan mosaic.

These observations indicate that sufficient amounts of stabilising gas molecules must have been present *in situ* for the formation of hydrates throughout the entire accumulation zone at least in some places, or that gas must have been supplied via fluid migration from below the HSZ. It is questionable if the organic matter content of the basin-floor turbidite sands and silts is high enough for in situ microbial generation of methane filling up to 10 % of porous volume. A process of methane enrichment by means of 3-D fluid migration along structural (e.g. through faults, which are very common in the Baikal rift basins) or stratigraphic pathways is proposed as an alternative and more plausible scenario for hydrate formation. Evidence of hydrate accumulation in rather massive form close to the lake bed further supports this hypothesis of focussed fluid flow.

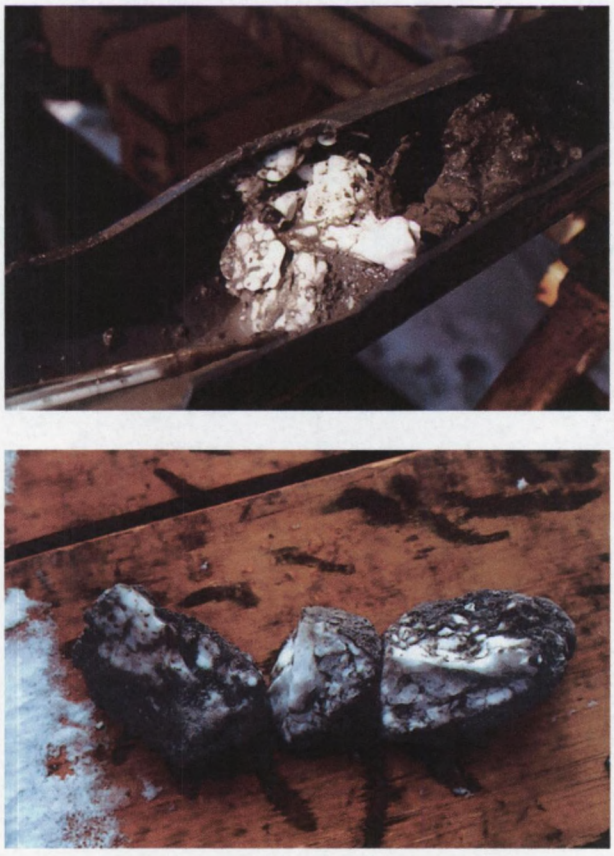

***Figure 3.15**: Pictures of gas hydrate containing sediments from the Malen'kiy crater (Southern Baikal Basin) from the lake bed, taken during the winter of 1999-2000, courtesy of Prof. J. Klerkx.(RMCA, Tervuren, Belgium)*

3.7.2
Lateral extent of the hydrate accumulation zone: estimates of quantities

The dense grid of medium-resolution SC airgun profiles around the BDP hydrate drilling site (Southern Baikal Basin, see figure 3.2), was used to estimate the amount of methane and carbon stored as hydrates in the shallow subsurface of the area. The depth of the lake floor and of the BSR (in ms TWTT) was picked in more than 800 points over an area of 700 km^2 and converted into sub-bottom depths. For this purpose, the velocity-depth model for Lake Baikal of *Golmshtok et al.* [*1997*] is used after modification into a relationship between sub-bottom two-way travel time and sub-bottom depth. More details are provided in the next chapter. The sub-bottom depth of the BSR in the area covered by the GAHY profiles varies from 160 to 455 m. The estimate presented here is based on the mean sub-bottom depth of the BSR of 303 m. At these depths, the porosity according to Athy's law (exponential decrease of porosity with burial depth) with the compaction parameters defined in *Golmshtok et al.* [*1997*] is approximately 56 %. In the studied area, then a volume of $206.69 \cdot 10^9$ m^3 of sediments is calculated to fall within the HSZ after converting the navigation details of the selected points into UTM projection.

It is further assumed that:

- ➔ Hydrates occur to at least 200 m above the BSR in the entire area, as is evidenced from the BDP-drilling results and seismic profiles GAHY005, 006, 010.
- ➔ No partial hydrate distribution with depth is taken into account, since insufficient data are available to build such a model. The partial hydrate saturation is taken to be 10 % of pore volume (BDP-1997) and valid within the hydrate accumulation zone. This value is also considered to be the maximum hydrate occupation of pore volume in the entire region. Such maximum value is reasonable for other areas as well [e.g. *Hovland et al., 1997*].

The total amount of hydrates in the study area can thus be calculated to be $7.58 \cdot 10^9$ m^3. Taking into account a hydrate gas expansion factor of 155 (see introduction), a maximum volume of $1.24 \cdot 10^{12}$ m^3 of methane at STP conditions is contained in the hydrated sediment layer.

Golmshtok et al. [1997], using the entire set of MC airgun-array profiles, mapped two zones of inferred hydrate accumulations, one NE and one W-SW of the Selenga Delta (figure 3.1) with a total area of roughly 4 to 6 times the size of our study area. Extrapolating our values over the entire area, the total amount of methane stored in the form of gas hydrates in the shallow sub-surface of Lake Baikal will not exceed $9 \cdot 10^{12}$ m^3 at STP (or 4.6 Gton carbon), under the above conditions and ignoring the contribution of local hydrate occurrence close to the lake bed. This is four orders of magnitude less than the estimated worldwide reserves of clathrated methane in submarine sediments (10000 Gton) [e.g. *Kvenvolden, 1998*] although this estimate might be exaggerated by an order of magnitude [*Ginsburg, pers. comm.*]. Furthermore, it is only about 13% of the estimated amount of carbon stored in the hydrate-rich sediments of Blake Ridge, on the Atlantic margin [35 Gton, *Dickens et al., 1996*]. Unfortunately, the BDP borehole had a very poor recovery and did not penetrate the BSR. Hence, no details are available about the distribution of hydrates in the vicinity of the BHSZ, and about variations in hydrate saturation throughout the HSZ. It is very likely that hydrate concentrations will increase towards the BHSZ, but due to insufficient information we did not take this into account in our calculations. We also did not take into account the presence of free gas below the HSZ for our volume estimations. The indirect evidence for free gas accumulation beneath the HSZ could not be translated into volumes.

The observation of two lobes with inferred hydrate occurrence symmetrical to the Selenga delta also suggests that this river provides the main input of organic matter which is later on degraded bacterially and finally incorporated in the solid hydrate structure.

3.8 Conclusions

- Lake Baikal is the first – and up to now only – confined fresh water basin with direct (drilling) and indirect (seismic) evidence for the presence of gas hydrates. Areas with hydrate accumulations are confined to deeper-water settings (> 580 m of water depth) almost symmetrical to the Selenga Delta, which is one of the main sources of organic matter for the Lake.

- The BHSZ is generally represented on MCS profiles by a distinct polarity-reversed BSR that cross-cuts other stratigraphic reflections and mimics the lake floor. Enhanced reflections occur commonly below the BSR and amplitude blanking can be observed above the BSR, but the effect fades out upwards and its intensity varies laterally. No seismic expression, neither of the upper boundary of the hydrate accumulation zone, nor from the lower boundary of the free-gas-containing layer below the HSZ, was found.

- The seismic expression of the BHSZ strongly depends on the frequency of the seismic signal and on the acquisition layout. Low-frequency MC airgun-array profiles (40 Hz) show all of the typical BSR characteristics. On medium-frequency SC airgun profiles (120 Hz), the amplitude and continuity of the BSR is much less explicit. The higher amplitude of the BSR on MC data can partially be explained by the acquisition lay-out which results in the recording of high-amplitude arrivals in the long-offset channels as a result of the AVO-effect at the top of the free-gas layer beneath the BHSZ. On higher-frequency records, such as the SC watergun profile (225-330 Hz), the BHSZ is no longer expressed as a single reflection, but rather as a facies change between high-amplitude (enhanced) reflections below and low-amplitude (blanked) reflections above. Very-high-

frequency SC sparker data (525 Hz) are often characterised by the sudden and complete absorption of acoustic energy beneath enhanced reflections.

→ The sparker data cannot be used to unambiguously determine the extent of the HSZ without lower frequency control. In most cases, the penetration is too limited. If not, no specific features are observed that can be directly related to hydrate saturation or free gas presence.

→ The presence of enhanced, polarity-reversed reflections below the BSR (on most data), increasing reflection amplitudes of the BSR with increasing offset (on low-frequency MC data), and average BSR reflection coefficients of -0.063 to -0.085 (–43 % of the lake-floor reflection coefficient) are interpreted as indirect evidence for the presence of free gas below the HSZ. Furthermore, the presence of a BSR acts as a low-pass frequency filter (i.e. sudden attenuation of higher frequencies) for the SC medium- to high-frequency data sets. Such behaviour is not observed on the low-frequency airgun-array data. First OBH results also demonstrate a sharp decrease in velocity at the BHSZ.

→ Free gas accumulates within specific strata beneath the HSZ, indicating that stratigraphy and lithology are major factors controlling the migration of fluids and the accumulation of free gas in the sedimentary section trapped by the hydrate boundary. The presence of some inverse-polarity enhanced reflections above the BSR suggests that in some places gases may locally migrate into the HSZ along stratigraphically-controlled pathways. Such features are not commonly observed but are interpreted as indirect evidence for the meta-stable co-existence of free gas and hydrates within the regional HSZ.

→ The BSR reflection amplitude depends on both vertical and horizontal (Fresnel zone) resolution representing a specific volume that gives rise to acoustic reflection. The higher the acoustic frequency, the smaller this volume and the more sensible the acoustic response is to small-scale lateral changes. In this way, alternating series of gas-containing and gas-free strata beneath the HSZ do not necessarily need to result in a coherent BSR feature especially on the higher-frequency profiles.

→ Significant amounts of hydrates (10 % of pore volume) can be present in the sub-surface without any apparent expression on seismic profiles: on SC airgun profiles, no BSR can be observed in the vicinity of the BDP-97 drilling site, and there is no acoustic blanking in the section from which the hydrate samples were collected. This indicates that the absence of the seismic characteristics indicative for the presence of hydrates (i.e. BSR, amplitude blanking) does not necessarily mean that hydrates are not present.

→ The extent of the hydrate accumulations and the total estimates of the amounts of methane or carbon stored as hydrates in the lake (4.6 Gton) show that the Baikal gas hydrates do not have any future economic potential.

References

Aki, K. & Richards, P.G. [1980]. *Quantitative seismology: theory and methods.* W.H. Freeman & Company, San Francisco, USA, pp. 912.

Andreassen, K. [1995]. *Seismic reflections associated with submarine gas hydrates.* Ph.D. thesis, University of Tromsø, Norway (ISBN 82-993804-0-5)

Andreassen, K., Hart, P.E. & Grantz, A. [1995]. *Seismic studies of a bottom simulating reflection related to gas hydrate beneath the continental margin of the Beaufort Sea.* Journal of Geophysical Research, **100**, 12659-12673.

Back, S., De Batist, M., Vanhauwaert, P. & Strecker, M. [1999]. *Quaternary depositional systems in Northern Lake Baikal, Siberia.* Journal of Geology, **107**, 1-12.

Bangs, N.L., Sawyer, D.S. & Golovchenko, X. [1993]. *Free gas at the base of the gas hydrate zone in the vicinity of the Chile Triple junction.* Geology, **21**, 905-908.

Bouriak, S., Vanneste, M. & Saoutkine, A. [2000]. *Inferred gas hydrates and clay diapirs near the Storegga Slide on the southern edge of the Voring Plateau, offshore Norway.* Marine Geology, **163**, 125-148.

Bushenkov, Y.N., Kremlev, A.N., Golmshtok, A.Y. & Vanneste, M. [1998]. *Estimation of physical properties of bottom sedimentary deposits.* Bulletin of the Novosibirsk Computing Centre, Series: Mathematical modelling in Geophysics, issue 4, 65-74.

Castagna, J.P. [1993]. *AVO Analysis – Tutorial and Review.* In Castagna, J.P. & Backus, M.M. (eds.), *Offset-dependent reflectivity – Theory and Practice of AVO Analysis*, Society of Exploration Geophysicists, Investigations in Geophysics, **8**, 3-36.

Castagna, J.P., Batzle, M.L. & Kan, T.K. [1993]. *Rock Physics – the link between rock properties and AVO response.* In Castagna, J.P. & Backus, M.M. (eds.), *Offset-dependent reflectivity – Theory and Practice of AVO Analysis.* Society of Exploration Geophysicists, Investigations in Geophysics, **8**, 135-171.

Clennell, M.B., Hovland, M., Booth, J., Henry, P. & Winters, P. [1999]. *Formation of natural gas hydrates in marine sediments: 1. Conceptual model of gas hydrate growth conditioned by host sediment properties.* Journal of Geophysical Research, **104**, 22985-23003.

Colman, S.M., Foster, D.S. & Hatton, J. [1996]. *High-resolution seismic reflection surveys of Lake Baikal, Siberia. 1990-1992.* U.S. Geological Survey Open-File Report 96-0274, 2 CD-roms.

De Batist, M., De Meersman, K., Hus, R. & Poort, J. [1999]. *Lake Baikal 1999.* Unpublished Expedition Report (on file at University of Gent). 11 pp.

De Batist, M. & Vanneste, M. [1997]. *Lake Baikal 1997 expedition report.* Unpublished Expedition Report (on file at University of Gent). 14 pp.

De Meersman, K. [2000]. *Reflectie- en refractieseismische studie van gashydraathoudende sedimenten in het Baikalmeer, Siberië.* Unpublished MSc thesis. RCMG, University of Gent, pp. 99.

Dickens, G.R. & Quinby-Hunt, M.S. [1994]. *Methane hydrate stability in seawater.* Geophysical Research Letters, **21** (19), 2115-2118.

Dickens, G.R., Wallace, P., Paull, C.K. & the ODP Leg 164 Scientific Party [1996]. *In-situ methane quantities across a bottom simulating reflector on Blake Ridge* [abstract]. Abstract Volume of First Master Workshop "Gas hydrates: Relevance to world margin stability and climatic change", Gent, 14-15.

Dillon, W.P., Lee, M.W. & Coleman, D.F., 1994. Identification of marine hydrates *in situ* and their distribution off the Atlantic Coast of the United States. In: Sloan, E.D. Jr., Happel, J. & Hnatow, M.A. (eds.) International Conference on Natural Gas Hydrates. *Annals of the New York Academy of Sciences*, **715**, 364-380.

Domenico, S.N., 1974. Effect of water saturation on seismic reflectivity and sand reservoirs encased in shale. *Geophysics*, **39**, 759-769.

Ecker, C., Lumley, D., Dvorkin, J. & Nur, A. [1996]. *Structure of hydrated sediment from seismic and rock physics.* in *Proceedings of the Second International Conference on Natural Gas Hydrates*, eds. Monfort et al., Toulouse, 491-498.

Ecker, C., Dvorkin, J. & Nur, A. [1998]. *Sediments with gas hydrates: internal structure from seismic AVO.* Geophysics, **63**, 1659-1669.

Edgington, D.N., Klump, J.V., Robbins, J.A., Kusner, Y.S., Pampura, V.D. & Sandimirov, I.V. [1991]. *Sedimentation rates, residence times and radionuclide inventories in Lake Baikal from 137Cs and 210Pb in sediment cores.* Nature, **350**, 601-604.

Galaziy, G.I. (ed.) [1993]. *Baikal Atlas (in Russian).* Federal Agency for Geodesy and Cartography, Moscow.

Gettrust, J., Wood, W., Lindwall, D., Chapman, R., Walia, R., Hannay, D., Spence, G., Louden, K., MacDonald, R. & Hyndman, R. [1999]. *New seismic study of deep sea gas hydrates: results in greatly improved resolution.* EOS Transactions of the American Geophysical Union, September 14, 439-440.

Golmshtok, A.Ya., Duchkov, A.D., Hutchinson, D.R., Khanukaev, S.B. & Elnikov, A.I. [1997]. *Estimation of heat flow on Baikal from seismic data on the lower boundary of the gas hydrate layer.* Russian Geology and Geophysics, **38**, 1714-1727.

Golmshtok, A.Y., Duchkov, A.D., Hutchinson, D.R. & Khanukayev, SB. (in press). *Heat flow and gas hydrates of the Baikal Rift zone.* Geologische Rundschau.

Golubev, V.A., Klerkx, J. & Kipfer, R. [1993]. *Heat-flow, hydrothermal vents and static stability of discharging thermal water in Lake Baikal (south-eastern Siberia).* Bulletin des Centres de recherches Exploration-Production Elf-Aquitaine, **17**, 53-65.

Grachev, M.A., Vorobyova, S.S., Likhoshway, Ye.V., Goldberg, E.L., Ziborova, G.A., Levina, O.V. & Khlystov, O.M. [1998]. *A high-resolution diatom record of the paleoclimates of East Siberia for the last 2.5 My from Lake*

Baikal. Quaternary Science Reviews, **17**, 1101-1106.

Guerin, G., Goldberg, D. & Meltser, A. [1999]. *Characterisation of in situ elastic properties of gas hydrate-bearing sediments on the Blake Ridge.* Journal of Geophysical Research, **104** (B8), 17781-17795.

Hamilton, E.L. [1970]. *Reflection coefficients and bottom losses at normal incidence computed from Pacific sediment properties.* Geophysics, **35**, No. 6, p. 995-1004.

Hamilton, E.L. [1980]. *Geo-acoustical modelling of the sea floor.* Journal of the Acoustical Society of America, **68** (5), 1313-1340.

Hamilton, E.L. & Bachman, R.T. [1982]. *Sound velocity and related properties of marine sediments.* Journal of the Acoustical Society of America, **72** (6), 1891-1904.

Henry, P., Thomas, M. & Clennell, M.B. [1999]. *Formation of natural gas hydrates in marine sediments: 2. Thermodynamic calculations of stability conditions in porous media.* Journal of Geophysical Research, **104**, 23004-23022.

Holbrook, W.S., Hoskins, H., Wood, W.T., Stephen, R.A. & Lizarralde, D. [1996]. *Methane hydrate and free gas on the Blake Ridge from vertical seismic profiling.* Science, **273**, 1840-1843.

Hovland, M., Gallagher, J.W., Clennell, M.B. & Lekvam, K. [1997]. *Gas hydrate and free gas volumes in marine sediments: example from the Niger Delta Front.* Marine and Petroleum Geology, **17** (3), 245-255.

Hovland, M. & Judd, A.D. [1988]. *Seabed pockmarks and seepages: impact on geology, biology and the marine environment.* Graham & Trotman, London, pp. 293.

Hutchinson, D.R., Golmshtok, A.J., Scholz, C.A., Moore, T.C., Lee, M.W. & Kuzmin, M. [1991]. *Bottom simulating reflector in Lake Baikal* [abstract]. Eos, Transactions American Geophysical Union, **72**, 307.

Hutchinson, D.R., Golmshtok, A.J., Zonenshain, L.P., Moore, T.C., Scholz, C.A. & Klitgord, K. [1992]. *Depositional and tectonic framework of the rift basins of Lake Baikal from multichannel seismic data.* Geology, **20**, 589-592.

Hyndman, R. & Davis, E. [1992]. *A mechanism for the formation of methane hydrate and seafloor bottom-simulating reflectors by vertical fluid expulsion.* Journal of Geophysical Research, **97**, 7025-7041.

Hyndman, R. & Spence, G. [1992]. *A seismic study of methane hydrate marine bottom simulating reflectors.* Journal of Geophysical Research, **97**, 6683-6698.

Keller, G.R., Bott, M.H.P., Wendlandt, R.F., Doser, D.I. & Morgan, P. [1995]. *The Baikal Rift system.* In: Olsen, K.H. (ed.) Continental rifts: evolution, structure, tectonics. *Developments in Geotectonics*, **25**, Elsevier Sciences B.V., Amsterdam. 325-339.

Klerkx, J., Hus, R., De Batist, M., Van Rensbergen, P. & Poort, J. [2000]. *The structural control of the methane venting area in the southern basin of Lake Baikal, Siberia.* in VI International Conference on Gas in Marine Sediments, St.-Petersburg, Abstract book, 57.

Klitgord, K.D., Golmshtok, A.Y., Scholz, C.A., Akentiev, L., Nichols, D., Schneider, C., McGill, J., Foster, D. & Unger, D. [1993]. *Seismic survey of Lake Baikal, Siberia. Cruise Report R.V. Balkhash.* U.S. Geological Survey Open-File Report OF-93-201, 25 pp.

Kremlev, A.N., Soloviev, V.A. & Ginsburg, G.D. [1997]. *Reflecting seismic horizon at the base of the submarine zone of gas hydrate stability.* Russian Geology and Geophysics, **38**, 1777-1788.

Kuzmin, M.I., Kalmychkov, G.V., Geletij, V.F., Gnilusha, V.A., Goreglyad, A.V., Khakhaev, B.N., Pevzner, L.A., Kavai, T., Ioshida, N., Duchkov, A.D., Ponomarchuk, V.A., Kontorovich, A.E., Bazhin, N.M., Mahov, G.A., Dyadin, Yu.A., Kuznetsov, F.A, Larionov, E.G., Manakov, A.Yu., Smolyakov, B.S., Mandelbaum, M.M. & Zheleznyakov, N.K. [1998]. *First find of gas hydrates in sediments of Lake Baikal* (in Russian), Doklady Akademii Nauk, **362**, 541-543.

Kvenvolden, K.A. [1998]. *A primer on the geological occurrence of gas hydrate.* In: Henriet, J.P. & Mienert, J. (eds.) Gas Hydrates. Relevance to world margin stability and climatic change. *Geological Society Special Publication*, **137**, 9-30.

Lee, M.W., Hutchinson, D.R., Dillon, W.P., Miller, J., Agena, W.F. & Swift, B.A. [1993]. *Method of estimating the amount of in situ gas hydrates in deep marine sediments.* Marine and Petroleum Geology, **10**, 493-506.

Logachev, N.A. [1993]. *History and geodynamics of the Lake Baikal Rift in the context of the Eastern Siberia Rift System: A review.* Bulletin des Centres de recherches Exploration-Production Elf-Aquitaine, **17**, 353-370.

MacKay, M.E., Jarrard, R.D., Westbrook, G.K. & Hyndman, R.D. [1994]. *Origin of bottom simulating reflectors: geophysical evidence from the Cascadia accretionary prism.* Geology, **22**, 459-462.

Mats, V.D. [1993]. *The structure and development of the Baikal rift depression,* Earth-Science Reviews, **34**, 81-118.

Matveeva, T.V., Kaulio, V.V., Mazurenko, L.L., Klerkx, J., Soloviev, V.A., Khlystov, O.M. & Kalmychkov, G.V. [2000]. *Geological and geochemical characteristic of near-bottom gas hydrate occurrence in the Southern Basin of Lake*

Baikal, Eastern Siberia. in VI International Conference on Gas in Marine Sediments, St.-Petersburg, Abstract book, 91-93.

Minshull, T., Singh, S. & Westbrook, G. [1994]. *Seismic velocity structure at a gas hydrate reflector, offshore western Colombia, from waveform inversion.* Journal of Geophysical Research, **99**, 4715-4734.

Nelson, C.H., Karabanov, E.B., Colman, S.M. & Escutia, C. [1998]. *Tectonic and sediment supply control of deep rift lake turbidite systems: Lake Baikal, Russia.* Geology, **27**, 163-166.

Nichols, D.R., Miller, G.K. & Akentiev, L.G. [1992]. *Seismic Survey of Lake Baikal, Siberia: Operational Technical Summary for the RV Balkash and RV Titov.* U.S. Geological Survey Open-File Report 93-0124, 21 pp.

Paull, C.K., Borowski, W.S., Rodriguez, N.M. & ODP Leg 164 Shipboard Scientific Party [1998]. *Marine gas hydrate inventory: preliminary results of ODP Leg 164 and implications for gas venting and slumping associated with the Blake Ridge gas hydrate field.* In: Henriet, J.P. & Mienert, J. (eds.) Gas Hydrates. Relevance to world margin stability and climatic change. *Geological Society Special Publication*, **137**, 153-160.

Poort, J., Golubev, V.A. & Polansky, O. [1998]. *The significance of the heat flow signal in Lake Baikal basin* [abstract]. Abstract Volume of the "Active Tectonic Continental Basins" Conference, Gent, 20.

Rowe, M.M. & Gettrust, J.F. [1993]. *Fine structure of methane hydrate bearing sediments on the Blake Outer Ridge as determined from deep-tow multichannel seismic data.* Journal of Geophysical Research, **98** (B1), 463-473.

Ruppel, C. [1997]. *Anomalous cold temperatures observed at the base of the gas hydrate stability zone on the US Atlantic passive margin.* Geology, **25** (8), 699-702.

Sain, K., Minshull, T.A., Singh, S.C. & Hobbs, R.W. [2000]. *Evidence for a thick free gas layer beneath the bottom-simulating reflector in the Makran accretionary prism.* Marine Geology, **164**, 3-12.

Sandra, A. [2000]. Unpublished MSc thesis, RCMG University of Gent.

Scholz, C.A. & Hutchinson, D.R. [2000]. *Stratigraphic and structural evolution of the Selenga Delta Accomodation Zone, Lake Baikal Rift, Siberia.* International Journal of Earth Sciences, **89**, 212-228.

Scholz, C.A., Klitgord, K.D., Hutchinson, D.R., Ten Brink, U.S., Zonenshain, L.P., Golmshtok, A.Y. and Moore, T.C. [1993]. *Results of 1992 Seismic Reflection Experiment in Lake Baikal.* Eos, Transactions American Geophysical Union, **74**, 465-470.

Sheriff, R.E. & Geldart, L.P. [1995]. *Exploration Seismology.* Cambridge University Press, Cambridge, 592 pp.

Shipley, T.H., Houston, M.K., Buffler, R.T., Shaub, F.J., McMillen, K.J., Ladd, J.W. & Worzel, J.L. [1979]. *Seismic reflection evidence for the widespread occurrence of possible gas-hydrate horizons on continental slopes and rises.* American Association of Petroleum Geologists Bulletin, **63**, 2204-2213.

Shuey, R.T. [1985]. *A simplification of the Zoeppritz equations.* Geophysics, **50**, 609-614.

Sloan, E.D. Jr. [1998]. *Clathrate hydrates of natural gases.* Second edition, Marcel Dekker Inc., New York. 703 pp.

Spence, G.D., Minshull, T.A. & Fink, C. [1995]. *Seismic studies of methane gas hydrate, offshore Vancouver Island.* Proceedings of the Ocean Drilling Program, Scientific Results, **146**, 163-174.

Spence, G.D., Hyndman, R.D., Chapman, N.R., Walia, R., Gettrust, J. & Edwards, R.N. [in press]. *Review of North Cascadia deep sea gas hydrates.* Annals of the New York Academy of Sciences, Third International Conference on Natural Gas Hydrates.

Taylor, M.H., Dillon, W.P. & Pecher, I.A. [2000]. *Trapping and migration of methane associated with the gas hydrate stability zone at the Blake Ridge Diapir: new insights from seismic data.* Marine Geology, **164**, 79-89.

Thiery, R., Bakker, R., Monnin, C. & the Shipboard Scientific Party of ODP Leg 164 [1998]. *Geochemistry of gas hydrates and associated fluids in the sediments of a passive continental margin: preliminary results of the ODP Leg 164 on the Blake Outer Ridge.* In: Henriet, J.P. & Mienert, J. (eds.) Gas Hydrates. Relevance to world margin stability and climatic change. *Geological Society Special Publication*, **137**, 161-166.

Vanneste, M. & De Batist, M. [1998]. *Lake Baikal 1998.* Unpublished Expedition Report (on file at University of Gent), 6 pp.

Vanneste, M. [1999]. *Lake Baikal 1999 expedition proposal.* Unpublished internal report (on file at University of Gent), 9 pp.

Vanneste, M., De Batist, M., Golmshtok, A. Kremlev, A. & Versteeg, W. [*in press*]. *Multi-frequency seismic study of the gas hydrate bearing sediments in Lake Baikal, Siberia.* Marine Geology.

Von Huene, R. & Pecher, I. [1999]. *Vertical tectonics and the origin of BSRs along the Peru margin.* Earth and Planetary Science Letters, **166**, 47-55.

Warner, M. [1990]. *Absolute reflection coefficients from deep seismic reflections.* Tectonophysics, **173**, 15-25.

Wood, W.T. & Ruppel, C. [2000]. *Seismic and thermal investigations of the Blake Ridge gas hydrate area: a synthesis.* In Paull, C.K. et al. (eds.) *Proceedings of the Ocean Drilling Program, Scientific Results*, volume **164**, 253-264.

Xu, W. & Ruppel, C. [1999]. Predicting the occurrence, distribution and evolution of methane gas hydrates in porous marine sediment, *Journal of Geophysical Research*, **104**, 5081-5096.

Yilmaz, Ö. [1987]. *Seismic data processing.* Society of Exploration Geophysicists, series: Investigation in Geophysics, volume 2; Tulsa, pp. 526.

Yuan, T., Spence, G.D., Hyndman, R.D., Minshull, T.A. & Singh, S.C. [1999]. *Seismic velocity studies of a gas hydrate bottom simulating reflector on the northern Cascadia continental margin: amplitude modelling and full waveform inversion.* Journal of Geophysical Research, **101**, 1179-1191.

Zonenshain, L.P., Golmshtok, A.Ya. & Hutchinson, D. [1992]. *The structure of Baikal rift* [in Russian]. Geotectonics, **5**, 63-77.

Zonenshain, L.P. , Kuzmin, M.I., Natapov, L.M. & Page, B.M. [1990]. *Geology of the USSR: a Plate-Tectonic Synthesis. AGU Geodynamics series*, **21**, 240 pp.

Chapter 4

Variability of the vertical extent of the gas hydrate stability field in Lake Baikal, Siberia

4.0 Introduction

During the summer of 1999, a multi-disciplinary scientific survey in Lake Baikal was organised by the RCMG in co-operation with various institutes. The main objective was to study and map the vertical and lateral variability of gas hydrate accumulations and gas seepage by means of medium-frequency single airgun reflection profiling, side-scan sonar imagery, echo-sounding, CTD and heat flow measurements [*Vanneste, 1999*]. In addition, OBH acquisition tools were deployed in two areas (5 deployments each, relative distance approximately 2 km) in the Southern Basin. This data set allows analyses of the behaviour of the hydrate stability zone (HSZ) on small lateral scales and data coverage bridges the gap in the low-resolution multi-channel data set acquired previously by Russian-American scientists especially in the central part of the Southern Baikal Basin. Heat flow measurements were performed based on the observations of the newly acquired seismic data and side-scan sonar images and thus are closely linked.

Emphasis lies on the multi-frequency reflection seismic data set acquired during the 1999 expedition in combination with heat flow measurements. Technical parameters about the reflection seismic data acquisition and processing and their influence on the expression of the BSR were already thoroughly discussed in the previous chapter and will not be repeated here. A side-scan sonar mosaic from the zone of inferred anomalies will be briefly discussed.

The first paragraph gives a complete and detailed overview of the methodology used to determine conductive heat flow based on the observation of a reflection at the BHSZ on seismic profiles for the specific case of Lake Baikal. The methodology is based on the sub-bottom velocity profile of *Golmshtok et al.* [*1997*] inverted into a relation of sub-bottom depth as a function of two-way travel time sub-bottom depth. Heat flow is calculated for both hydrostatic and lithostatic pressure distribution, assuming a simple porosity-depth law (*Athy*) with specific parameters determined for Lake Baikal sediments [*Golmshtok et al., 1997*]. The inverse method – determining the theoretical vertical extent of the HSZ from heat flow for both pressure assumptions – is discussed as well. The methodology was

also integrated into a computer program (Bai_hyd.exe). Using these relationships and equations, the theoretical vertical extent of methane hydrates in Lake Baikal is presented as a function of water depth and heat flow, using lithostatic and hydrostatic pressure distribution and expressed in depth below lake level and sub-bottom depth (both in m and ms TWTT scale). In order to analyse the errors inherent in this methodology on the final heat flow result, some purely theoretical models of hydrate saturation with depth and its influence on the sub-bottom velocity are compared with the hydrate-free reference profile of *Golmshtok et al. [1997]* and *Hamilton [1980]*, in combination with first OBH results.

In the second paragraph, a detailed description of the different available data sets and the anomalies observed is provided. The most striking event observed is the presence of a strong reflection or series of enhanced individual parts of lithological boundaries that no longer mimic the lake floor morphology, but are still interpreted to represent the BHSZ or top of the free gas accumulation zone. Several acoustic profiles acquired show such anomalies. Side-scan sonar images are also characterised by the presence of a clear fault structure across the central part of the basin, while a few semi-circular irregularities are observed in the proximity of this fault representing seepages or gas vents [*De Batist et al., in prep.*]. Heat flow measurements are presented as well, and converted into equivalent sub-bottom stability limits.

The next paragraphs then report analyses performed and results obtained from these data sets. Indirect evidence on the acoustic sections for free gas accumulation and migration within the zone of lateral variable hydrate distribution and accumulation are highlighted. Then, the relationships worked out in the first paragraph are applied to the acoustic data set to delineate the morphology of the present-day BHSZ and are compared with bathymetry deduced from the same data points. The anomalous behaviour of the BHSZ in the central part of the Southern Baikal Basin is discussed in terms of the behaviour generally expected using specific background heat flow values as a reference. This calculation procedure allows to estimate the magnitude of the local variations of sub-bottom depth taking into consideration the bathymetry effect on hydrate stability conditions. These analyses suggest that the vertical extent of hydrate stability evolves in two ways: both exceptionally shallow and deep compared to the observations in the area. Apparently these extremes are located very close the one to the other. Finally, measured heat flow is compared with inferred heat flow values in this area and along two specific seismic transects.

The discussion then deals with possible scenarios for explaining the observed behaviour with emphasis on the high-amplitude lateral variability observed.

4.1
Bottom-simulating reflections as a temperature reference: implications for the HSZ in Lake Baikal

The presence of a BSR on seismic profiles is the key indirect feature for gas hydrate occurrence in the shallow subsurface [e.g. *Kvenvolden, 1998*], although its absence does not necessarily rule out the presence of hydrate accumulations [e.g. *Paull et al., 1998 (ODP Leg 164, Blake Outer Ridge); Vanneste et al., in press (Lake Baikal)*]. The fact that this reflection in general mimics the sea or lake floor topography indicates that its position is primarily temperature-controlled and hence can be used to estimate the local geothermal field in a conductive medium [e.g. *Yamano et al., 1982; Bangs & Brown, 1995; Bouriak et al., 2000*]. In order to obtain quantitative results, one needs to take into account several assumptions or derive models, e.g. from seismic data or using empirical relationships.

Starting from seismic data, two-way travel time information has to be converted into sub-bottom depth. In other words, a sub-bottom velocity function is required. This can be done by velocity analysis performed with sophisticated seismic data processing software or by using average regression curves linking the sedimentation environment with sub-bottom profiles. In this discussion concerning Lake Baikal, results obtained by *Golmshtok et al. [1997]* applying the first method are used. An example of the second method is provided in *Bouriak et al. [2000]* in which we combined the *Hamilton* regression curve [*Hamilton, 1980*] with results from deep drilling and logging [ODP Leg 104, *Eldholm et al., 1987*]. Here also, a comparison is made with the Hamilton equation in combination with recently acquired ocean bottom hydrophone (OBH) results.

Once the sub-bottom depth of the basal limit of hydrate occurrence is known, this value is rather easily translated into hydrostatic or lithostatic pressures, after which *in situ* equilibrium temperature is taken from the 3-phase hydrate equilibrium curve discussed before. In a pure conductive medium the geothermal gradient and the sub-bottom thermal conductivity profile can then be combined to calculate the heat flow.

Such an approach will logically introduce errors inherent to the methodology and simplifications used therein. The most important ones are uncertainties about the density-porosity relation with depth, the velocity model used, the conversion of equilibrium conditions, assumptions about the hydrate and pore water composition, and the thermal conductivity profile. A brief discussion is presented about the influence of these uncertainties for the final results obtained.

4.1.1
Sub-bottom velocity profile for Lake Baikal

In a first step, the presence of an acoustic reflection interpreted to represent the BHSZ on an acoustic section (ms two-way travel time TWTT) has to be converted into its actual total depth below sea or lake level or the sub-bottom position (m). For this purpose, the sub-bottom interval velocity profile of *Golmshtok et al. [1997]* valid for both the Central and Southern Baikal Basins is used. This sub-bottom function is determined using MCS data acquired during 1992 by a joint Russian-American expedition and was used to map deep geological structures. The sonic velocity model is expressed as:

$$v\langle z\rangle = v_w + (v_m - v_w)\cdot \exp[-a_{lith}\cdot \exp(-k_c\cdot z)] \qquad [1]$$

with v_w = 1400 m·s^{-1} velocity in the water column
v_m = 6200 m·s^{-1} velocity in the sedimentary skeleton
a_{lith} = 2.80 coefficient depending on the sediment lithology
k_c = 0.000473 m^{-1} sediment compaction parameter, according to *Athy*'s law

The velocity of the sedimentary matrix corresponds to granite-gneiss massifs that surround the Baikal basins and is found in the crystalline basement below the sedimentary cover [*Golmshtok et al., 2000*]. The compaction parameter lies close to the average clay-sandstone value [*Hutchinson, 1985*]. The conformity between sub-bottom depth and two-way travel time using the above interval velocity model [1] is expressed as

$$t\langle H,z\rangle = t_0 + 2\cdot\int_0^z \frac{d\psi}{v\langle\psi\rangle} \qquad [2]$$

with $$t\langle H,0\rangle \equiv t_0 = 2\cdot\frac{H}{v_w}$$

For determining the relationship between the sub-bottom depth and the two-way travel time, the above equation was inverted. Using the trapezium rule for integration of [2] for discrete depth intervals,

$$t_\alpha = t_{\alpha-1} + \left(v_{\alpha-1}^{-1} + v_\alpha^{-1}\right)\cdot\left(z_\alpha - z_{\alpha-1}\right)$$

the sub-bottom depth vs. two-way travel time is finally written as follows:

$$z = \lambda_2 \cdot (t - t_0)^2 + \lambda_1 \cdot (t - t_0) \qquad R^2 = 1 \qquad [3]$$

with λ_1 = 0.8423 m·ms^{-1}
λ_2 = 0.0001 m·ms^{-2}
z sub-bottom depth (m)
t two-way travel time of the BSR on the (stacked) seismic profile (ms)
t_0 two-way travel time of the lake floor reflection on the stacked profile (ms)

Once the two-way travel time of the lake floor reflection and the BSR is known for the stacked or migrated section, the sub-bottom depth of the BSR is easily calculated with formula [3].

4.1.2
Hydrate equilibrium pressure and temperature determination

Depending on the assumed pore pressure distribution, the *in situ* thermodynamical stability conditions can be determined, combining the above-mentioned sub-bottom compressional wave velocity model and the analytical 3-phase equilibrium equation. In general, the real *in situ* pore pressure will lie somewhere in between of the lithostatic and hydrostatic pressure. In this chapter, heat flow inferred from the presence of a reflection at the BHSZ is worked out for both end-members, and will result in a maximum and minimum heat flow value.

Hydrostatic pressure at the 3-phase equilibrium boundary is simply computed as:

$$P_{hydr}\langle H,z\rangle = P_0 + 10^{-6}\cdot\rho_w g(H+z) \qquad [4]$$

and suggests freely communicating pore spaces. For typical Darcy velocities values (~ 1 mm·a^{-1}), the contribution of the fluid flow to pore pressure can be neglected. Lithostatic pressure depends on the gradual density increase with increasing burial depths due to compaction. For Lake Baikal conditions, *Golmshtok et al. [1997]* use *Athy*'s law with maximum porosity of 65% at the lake bed to incorporate density changes with depth. Porosity then decreases exponentially according to:

$$\phi\langle z\rangle = \phi_0 \cdot \exp(-k_c \cdot z) \qquad [5]$$

using the same compaction parameter as used for the sub-bottom velocity model. Lithostatic pressure at sub-bottom depth z is then written as (see figure 2.8):

$$P_{lith}\langle H,z\rangle = P_{hydr}\langle H,0\rangle + 10^{-6} g\cdot\int_{\mu=0}^{\mu=z}\rho\langle\mu\rangle d\mu$$
$$= P_{hydr}\langle H,0\rangle + 10^{-6} g\left\{\rho_m z + \phi_0\frac{\rho_m-\rho_f}{k_c}\left[\exp(-k_c\cdot z)-1\right]\right\} \qquad [6]$$

since $\rho\langle z\rangle = \left[1-\phi\langle z\rangle\right]\rho_m + \phi\langle z\rangle\rho_w$ [7]
and ρ_m = 2680 kg·m^{-3}

ρ_w = 1000 kg·m^{-3}

ignoring the partial occupation of gas hydrates in the pore spaces, as was the case for the sub-bottom velocity profile.

As a result, both the hydrostatic and lithostatic pressure are calculated for the sub-bottom depth of the basal limit of inferred hydrate occurrence. Since this reflection is supposed to coincide with local 3-phase equilibrium conditions for hydrate stability, the pressure value is easily translated into equilibrium temperature values, by means of the analytical phase boundary equation once the gas composition is known in this freshwater basin, as discussed in the second chapter.

In Lake Baikal, gas hydrates were both retrieved from deep drilling and shallow coring in the *Malen'kiy* crater, both in the Southern Baikal Basin. First geochemical analyses pointed out that the gas composition in the sI-clathrated structure was mainly biogenic methane (>99 %). Due to the uncertainty of the hydrate composition, all calculations are performed for pure methane hydrates in a freshwater (salinity 0.76‰) environment, with appropriate phase boundary equilibrium temperature:

$$T_{eq} = \frac{-b + \sqrt{b^2 + 4c\left(LogP_{eq} - a\right)}}{2c} \qquad \text{with} \quad \begin{cases} a = 0.419626 \\ b = 0.039326\,°C^{-1} \\ c = 0.000299\,°C^{-2} \end{cases} \qquad [8]$$

4.1.3
Determination of geothermal gradient and heat flow, using hydrate equilibrium conditions

Once the *in situ* equilibrium temperature and the lake bed temperature are known, the determination of the average geothermal gradient over the HSZ is straightforward:

$$G \equiv \frac{\partial T}{\partial z} = \frac{T_{eq}\langle z_{BHSF}\rangle - T_0}{z_{BHSF}} \qquad [9]$$

with T_0 bottom water temperature
z_{BHSF} sub-bottom depth of the BHSZ

The basic steady-state equation for one-dimensional conductive heat flow without sources or sinks is expressed as Fourier's law, here in absolute values:

$$q\langle z\rangle \equiv q = k\langle z\rangle \cdot \frac{\partial T}{\partial z} \qquad [10]$$

Under steady-state conditions, heat flow will be invariable with depth. Integration of this equation over the hydrate stability region leads to

$$T\langle z_{BHSF}\rangle - T_0 = \int_{\psi=0}^{\psi=z_{BHSF}} \frac{q\,d\psi}{k\langle\psi\rangle} = q \cdot \int_{\psi=0}^{\psi=z_{BHSF}} k^{-1}\langle\psi\rangle d\psi$$

or
$$q = \frac{T\langle z_{BHSF}\rangle - T_0}{\int_{\psi=0}^{\psi=z_{BHSF}} k^{-1}\langle\psi\rangle d\psi} \qquad [11]$$

and expresses the heat flow as a function of the thermal resistance integrated over the stability field.

For Lake Baikal, the thermal conductivity ($W \cdot m^{-1}K^{-1}$) in the uppermost layers increases slightly with burial depth [*Duchkov & Kazantsev, 1996*] according to:

$$k\langle z\rangle = k_1 + k_2 \cdot z \qquad [12]$$

with $k_1 = 1.05\ W \cdot m^{-1}K^{-1}$

$k_2 = 0.001\ W \cdot m^{-2}K^{-1}$

Importing this sub-bottom depth dependency of the thermal conductivity in equation [11] allows to write the conductive heat flow as follows:

$$q = \frac{T\langle z_{BHSF}\rangle - T_0}{\ln \frac{1050 + z_{BHSF}}{1050}} \qquad [13]$$

Due to the explicit dependency of the thermal conductivity on burial depth and the requirement for constant heat flow, the sub-bottom temperature profile will not be linear, but curved.

4.1.4
Inverse process: sub-bottom equilibrium depth calculation from heat flow measurements

Note that the same formulas can be used to analyse the inverse problem, i.e. deriving the hydrate equilibrium depth limit from heat flow measurements performed. Also here, an iterative approach is used similar to the one explained in chapter 2, but with different *in situ* temperature conditions as a function of steady-state heat flow q (expressed in $mW \cdot m^{-2}$) and sub-bottom thermal conductivity profile with depth [12]:

$$T\langle z\rangle = T_0 + q \cdot \ln\left(\frac{1.05 + 0.001 \cdot z}{1.05}\right) \le T_{eq}(z) \qquad z \ge 0 \qquad [14]$$

replacing equations [2.4, 2.5]. Due to the explicit sub-bottom depth dependence of the thermal conductivity and the constant heat flow requirement, the geothermal gradient will change with depth as well and the temperature profile will be curved. The method will result in different sub-bottom depths dependent of the pore pressure assumption. At a certain sub-bottom position, temperature will be too high for hydrate stability under hydrostatic conditions while at the same time the *in situ* temperature can be lower than the dissociation temperature at the prevailing lithostatic pressure.

4.1.5
Theoretical extent of methane hydrates in Lake Baikal

4.1.5a Principle of the program Bai_hyd.exe

One of the programs *bai_hyd.exe* included offers the possibility to calculate the heat flow using only the two-way travel time of the lake floor reflection and the reflection at the inferred base of hydrate occurrence, following the methodology outlined above. Also in this program, the user can define his or her own phase boundary coefficients or derive those coefficients based on equilibrium temperature-pressure couples, similar to the other programs. The situation is analysed for both hydrostatic and lithostatic pressure, based on the velocity, density, porosity and conductivity profiles given.

A second option is the calculation of the vertical extent of the HSZ – again for both pressure approaches – for specific heat flow values and water depths (ms TWTT or m), according to formula [14]. The same iterative method is applied as explained in chapter 2.

Output consists of the following quantities: water depth, sub-bottom depth of the stability limit, total depth of the stability limit (m and ms TWTT), *in situ* lithostatic and hydrostatic pressure, equivalent equilibrium temperatures, *in situ* porosity, *in situ* density and *in situ* thermal conductivity and mean geothermal gradient over the HSZ.

4.1.5b Extent of the methane HSZ in Lake Baikal

In Lake Baikal, the bottom water temperature is rather invariable during the year [*Golmshtok et al., 2000*]. In the Southern Baikal Basin, values of 3.38°C are measured for bottom water masses deeper than 700 m, while in the Central Baikal Basin the bottom water temperature is slightly less, 3.18°C. New CTD-measurements from the deeper part of the Southern Basin result in slightly lower temperatures of 3.370°C at 1000 m water depths and 3.361°C at the lake bottom, averaged over 8 CTDs. Some of them are shown in figure 4.1. Accuracy of the temperature measurements are 0.0001°C. Lateral variations are about 0.01°C. Location of the CTDs is given in table 4.1. At these temperatures, hydrates could theoretically be stable at water depths exceeding 356 m (Southern Basin) res. 350 m (Central Basin). *Golmshtok et al.* [*1997*] mapped out two zones of inferred hydrate occurrence, lying almost symmetrical to the Selenga Delta. In front of this delta structure, water depths are too shallow to assure hydrate stability. This observation suggests that the Selenga River supplies the main input of organic matter into the lake's basins.

Figure 4.2 sketches the theoretical extent of the methane HSZ in the Southern Baikal Basin as a function of both appropriate heat flow values and water depths based on results obtained from program *bai_hyd.exe*. The lithostatic res. hydrostatic approach is represented in figure 4.2a res. figure 4.2b. Intervals of the iso-sub-bottom lines are 25 m, as a result of a calculation procedure for 5 m water depths and 0.5 $mW \cdot m^{-2}$ heat flow interval steps or 25351 data points. The figures are very convenient to rapidly estimate the limits of theoretical occurrence of methane hydrates in Lake Baikal and offers the possibility to estimate a depth range of hydrate occurrence on seismic profiles. Over the entire water depth – heat flow domain represented in the figure, differences of the equilibrium limit between the two pressure approaches can be as high as 90 m. For the Central Baikal Basin, the thickness of the methane HSZ will be slightly thicker (order of m) due to the small difference in bottom water temperature.

Focusing on the link between heat flow data and seismic profiling, conversion of the entire data set to two-way travel times has higher applicability. The iso-sub-bottom lines for exactly the same heat flow – water depth domain covered as in figure 4.2 are converted in two-way travel times in figure 4.3. This figure can be very helpful to rapidly estimate the theoretical extent of methane hydrates and to locate its position on acoustic data sets without obvious occurrence of a BSR (e.g. high- to very-high-frequency profiles) in zones with available heat flow measurements in Lake Baikal. It gives the user at least an idea of the expected minimum (hydrostatic pressure) and maximum (lithostatic pressure) depth below lake level in ms TWTT of the stability limit at a given water depth and heat flow. For determining the extent of the stability field for a specific situation of water depth and heat flow, program *bai_hyd.exe* is appropriate.

4.1.6
Errors inherent to the methodology

The accuracy of the estimation of heat flow based on the observation of a BSR on seismic profiles depends on the errors made in the different parts, thus density profile, the sub-bottom velocity profile, pressure assumption, equilibrium condition conversion and thermal conductivity change with depth. Some of these parameters depend on lithology and will hence vary with sub-bottom depth and in specific locations. These aspects are not taken into consideration due to a lack of detailed information.

name	longitude (E)	latitude (N)
GH-01	105.7493	51.9539
GH-02	105.8092	51.9507
GH-03	105.6340	51.9186
GH-04	105.6300	51.9227
GH-05	105.6388	51.9181
GH-06	105.6408	51.9250
GH-07	105.6367	51.9198
GH-08	105.6370	51.9196
GH-09	105.6383	51.9193
GH-10	105.6325	51.9128
GH-11	105.5513	51.8801
GH-12	105.6260	51.8402

***Table 4.1**: CTD locations, Baikal-99 expedition.*

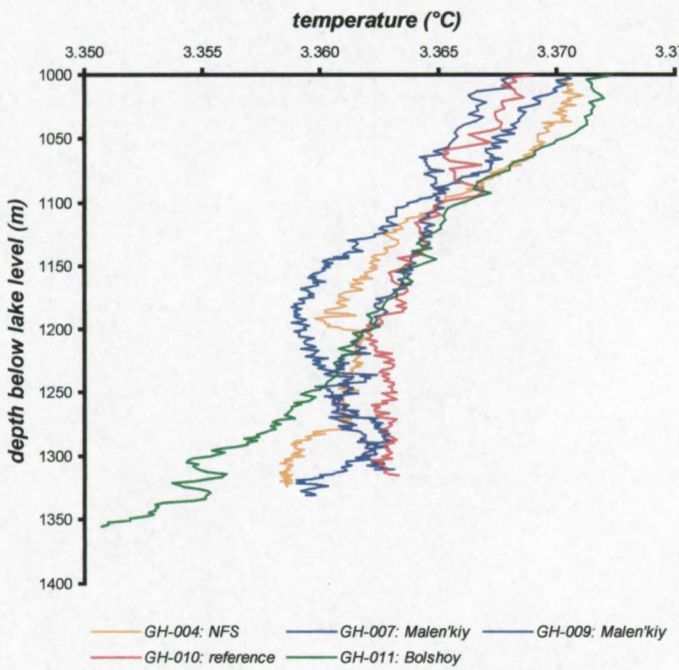

***Figure 4.1**: A few temperature profiles taken at specific locations in the Southern Baikal Basin used in the discussion.*

4.1.6a Density profile with depth

The partial occupancy of pore spaces by hydrate is of importance for the density profile with depth and hence *in situ* lithostatic pressure. Density was assumed to increase with depth according to *Athy*'s law [5] while effective porosity now depends on the *in situ* partial hydrate saturation h of the model. The generalised bulk density at depth is then written as:

$$\rho\langle z\rangle = \left[1-\phi\langle z\rangle\right]\rho_m + h\langle z\rangle\phi\langle z\rangle\rho_h + \left(1-h\langle z\rangle\right)\phi\langle z\rangle\rho_w \qquad [15]$$

Partial hydrate saturation h will result in slightly smaller densities than in a hydrate-free environment. For a 10% hydrate saturation at average BSR sub-bottom depths of 300 m, the density will be only 0.35% or approximately 5 kg·m^{-3} less than in a hydrate free medium and hence is only of minor importance. For a 30% hydrate saturation factor, the difference is about 1%. This will not influence final heat flow calculation. The uncertainty of the pressure profile with depth however can result in more important deviations.

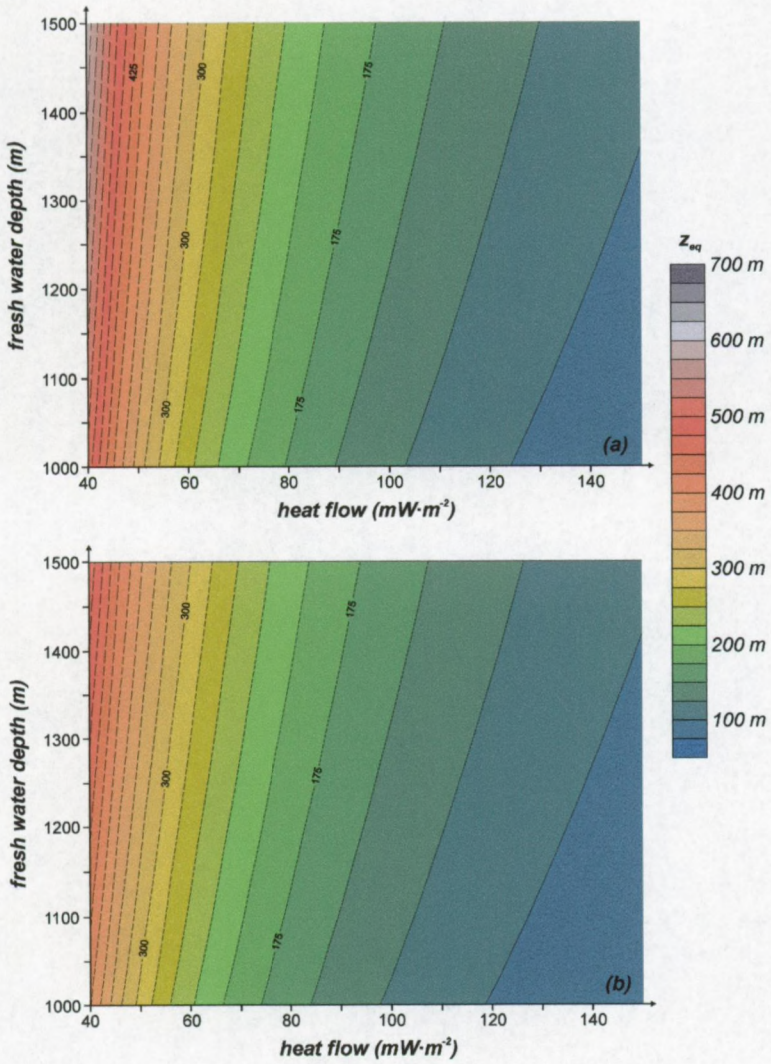

Figure 4.2: *Sub-bottom methane hydrate equilibrium limit under typical conditions of the Southern Baikal Basin (bottom water temperature 3.38°C), as a function of heat flow and water depths, for (a) lithostatic pressure distribution and (b) hydrostatic pressure distribution. Interval distance of the iso-lines is 25 m.*

4.1.6b Hydrate saturation vs. sub-bottom velocity profile: models for Lake Baikal

The next factor of uncertainty is the sub-bottom velocity profile used. The accuracy of the velocity profile is less than 50 m·s^{-1}. The error on sub-bottom depth determination then is less than 10 m [*Golmshtok et al., 2000*]. The average acoustic velocity in Baikal water is rather low (1400 m·s^{-1}). Analysis of several CDP gathers (x^2-t^2 method) of line 92_03 resulted in an average water velocity of 1405 ± 20 m·s^{-1}. These values are lower than velocities of ± 1430 m·s^{-1} at 1400 m water depth reported by *Sherstyankin & Kuymoua* [*1992*]. This also depends on the accuracy of picking of the reflections using *Landmark ProMAX* or *GES* software. These errors are within the order of magnitude of 10 ms TWTT for both the lake floor reflection and the BHSZ.

The velocity model ignores the effect of hydrate inclusion in and partial free gas saturation of the pore spaces on the compressional wave velocity. It is well known that the partial occupation of porous volume with hydrate res. free gas will increase res. decrease the bulk compressional wave velocity [e.g. *Whalley, 1980; Pearson et al., 1983; Hyndman & Spence, 1992; Singh & Minshull, 1994; Minshull et al., 1994; Yuan et al., 1996*]. Such effects are generally limited to a small layer of some tens of meters (or less) above the BHSZ. Depending on the amount of hydrates, the effect of partial hydrate saturation can be in the order of several hundreds of m·s^{-1} difference, relative to a lower background (hydrate-

free) interval velocity profile. In this approach, the *in situ* sub-bottom equilibrium depth will be underestimated resulting in lower than factual equivalent *in situ* temperature. The true influence of partial hydrate saturation above the BSR on the accuracy of the derivation of the geothermal gradient is however less sensitive to this effect, since the ratio of two bigger values is taken.

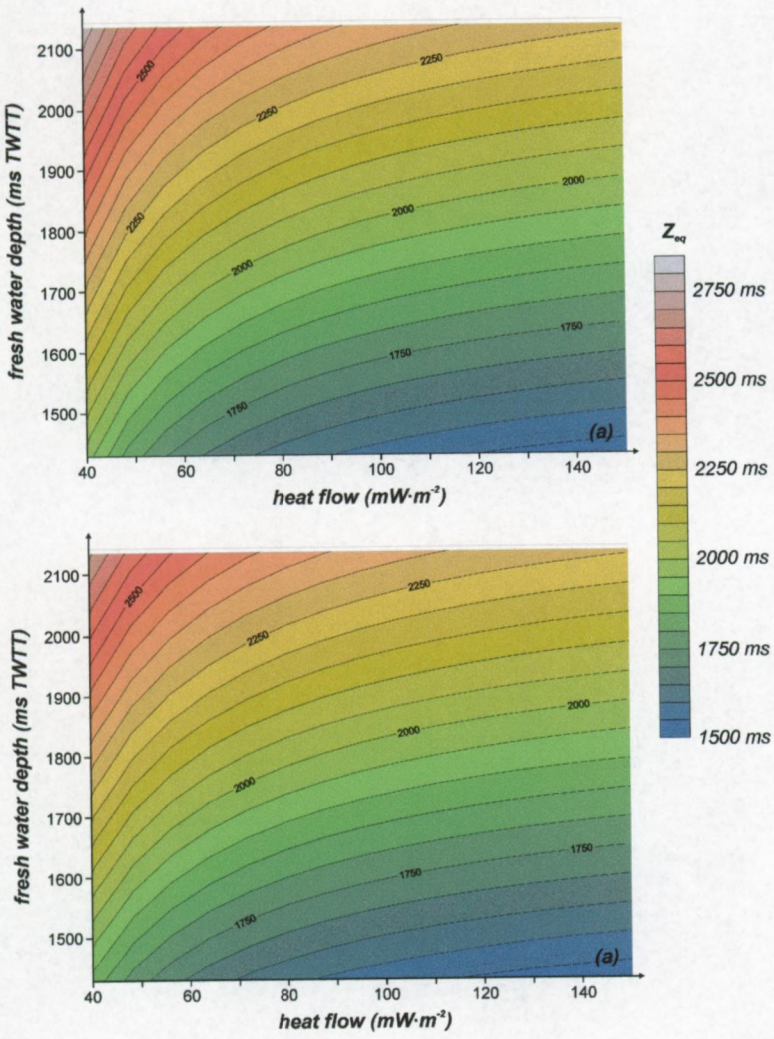

***Figure 4.3**: Two-way travel time from lake level to the BHSZ under typical conditions of the Southern Baikal Basin, as a function of heat flow and water depths (ms TWTT) for (a) lithostatic pressure and (b) hydrostatic pressure. Interval distance of the iso-lines is 50 ms.*

In a first attempt to estimate the effect of partial hydrate saturation on the inferred heat flow value, the *Golmshtok* velocity profile is used as a reference value valid in a hydrate-free medium, i.e. the reference velocity profile used in this study. Lack of knowledge about the distribution of hydrate with depth in Lake Baikal restricts this effort. Here, two modes of hydrate accumulation are considered. In the first model, hydrates are supposed to have accumulated gradationally above their stability limit: the hydrate volume fraction decreases exponentially with height above the BSR, in accordance with mathematical models of hydrate formation in sedimentary sections with mean internal fluid migration velocities [*Rempel & Buffett, 1998*]. In the second model, hydrate is supposed to have accumulated in a limited section of the sub-surface just above the BSR. Throughout this zone, hydrate saturation is fixed. In order to investigate the influence of hydrate saturation, an unusually high maximum hydrate saturation of 30% of porous volume is used. The presence of a low-velocity zone attributed to free gas occurrence beneath the hydrate stability limit is of no relevance here.

Interval velocity is expressed as a weighted mean of the three-phase time average equation of Wyllie [*Pearson et al., 1983*] and the three-phase *Wood* equation [*Tinivella, 1999*]. The interval velocity function with disseminated hydrate distribution for Lake Baikal is then written as:

$$\frac{1}{v_i} = \frac{A\phi(1-h)}{v_{wood}} + \frac{1-A\phi(1-h)}{v_{av}} \qquad \textit{Lee} \text{ equation [Lee et al., 1996]} \qquad [16]$$

with

$$\frac{1}{v_{av}} = \frac{1-\phi}{v_m} + \frac{\phi h}{v_h} + \frac{\phi(1-h)}{v_w} \qquad \text{time-average equation} \qquad [17]$$

$$\frac{1}{\rho v_{wood}^2} = \frac{1-\phi}{\rho_m v_m^2} + \frac{\phi h}{\rho_h v_h^2} + \frac{\phi(1-h)}{\rho_w v_w^2} \qquad \textit{Wood} \text{ equation} \qquad [18]$$

The weighting factor A – being function of porosity and hence sub-bottom depth – is derived by trial and error such that the hydrate-free interval velocity profile coincides almost perfectly with the *Golmshtok* interval velocity profile for the first 1000 m sub-bottom depth or:

$$A\langle z\rangle = 0.5204 + 0.0001 \cdot z - 2.5 \cdot 10^{-8} \cdot z^2 \qquad [19]$$

Now suppose mean conditions of the HSZ in the Southern Baikal Basin (water depth: 1400 m, sub-bottom stability limit: ± 350 ms TWTT) and an exponential increase of hydrate saturation from zero at the lake floor to 30% of pore volume at the stability limit (model 1). It is then calculated that the HSZ would lie about 20 m deeper than in the hydrate-free situation. Heat flow turns out to be 5% *lower* in case of partial hydrate saturation. In model 2, hydrate is located in the zone between 2285 and 2350 ms TWTT. The difference in equilibrium sub-bottom depth is then approximately 13 m, resulting in heat flow values that are 3% *lower* compared to the heat flow determined with the reference velocity profile. The sub-bottom interval velocity profiles for both models and the *Golmshtok* reference hydrate-free velocity model with its approximation according to equations [15-19], are shown in figure 4.4 Also the *Hamilton* curve for terrigeneous sediments is given [*Hamilton, 1980*].

Such hydrate accumulation modes might best be considered as extreme ones, since in general hydrates are mainly accumulating at their basal limit (model 2) but with lower partial hydrate saturation. Hence, the velocity effect induced by partial hydrate saturation will not generate significant errors.

Detailed analysis using OBH-data acquired during the 1999 expedition should be carried out in order to obtain a better sub-bottom velocity profile and get more information about the typical hydrate accumulation mode in the Southern Baikal Basin. A first attempt was undertaken by *De Meersman* [*2000*] in an area characterised by sub-parallel sedimentation (box 1, see below) coincident with line GAHY014, perpendicular to lines GAHY008-020 (see previous chapter, figure 3.3) and parallel to line GAHY017 (see previous chapter, figure 3.4). A faint BSR feature is observed along part of this profile at about 350 ms TWTT or 307 m sub-bottom depth. The first result from OBH data analysis was already shown in figure 3.14 and indicates that the interval velocities proposed by *Golmshtok et al.* [*1997*] are overestimated for the uppermost sedimentary section (first 100 m). Between 100 and 300 m, a good correlation exists. Whether this is due to a velocity effect related to partial hydrate occupation in this section is not clear. The significant velocity drop at the inferred BHSZ is most probably caused by free gas accumulations beneath the stability field and extends over a distance of a few tens of m. However, since no deeper reflections were picked, one has to be cautious with this interpretation. Nevertheless, the position of the upper boundary of this low-velocity layer coincides well with the normal BSR observed on the seismic line GAHY017. OBH velocity in the uppermost sedimentary layer is furthermore in good agreement with lake bottom velocities inferred from the magnitude of the lake floor reflection coefficient (see §3.6).

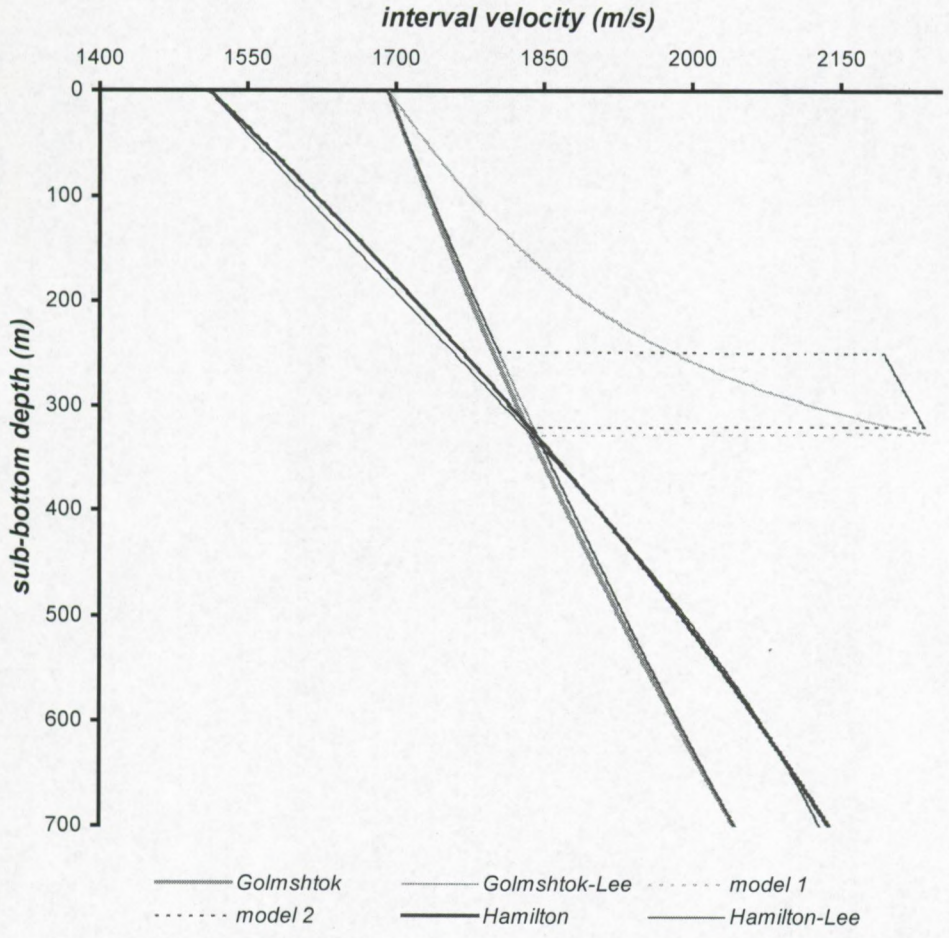

Figure 4.4: *Golmshtok and Hamilton interval velocity profiles as references vs. modelled profiles based on the Golmshtok profile.*

The discrepancy for shallow sediments between the OBH model and the *Golmshtok* velocity profile necessitates a comparison of the observed behaviour with the more general regression equation of *Hamilton* [*1980*] for terrigenous sediments (turbidites, silt clays, mudstone and shale):

$$v_{\text{int}}\langle t_s \rangle = -93 \cdot t_s^2 + 521 \cdot t_s + 1511 \qquad [20]$$

with t_s the sub-bottom two-way travel time (expressed in s). Converted into sub-bottom depth, one obtains:

$$v_{\text{int}}\langle z \rangle = -0.0003 \cdot z^2 + 1.1063 \cdot z + 1511 \qquad [21]$$

The OBH results are in good agreement with the *Hamilton* curve for the uppermost sediment section while in between of 130-300 m the *Golmshtok* curve gives a better approximation. In this way, it appears that the sub-bottom profile of *Golmshtok et al.* [*1997*] with very high lake floor interval velocity is valid in hydrate-rich areas and overestimated for hydrate-free areas. For the same point at 2000 ms TWTT water depth and 350 ms TWTT sub-bottom depth, heat flow based on the *Hamilton* regression relation is about 5% *higher* compared to its *Golmshtok* equivalent. Investigating the situation for both above-sketched models with the *Hamilton* function as a reference profile results in variations of less than 0.3% (model 1) res. 2.5% (model 2). The weighting factor *A* in case of the hydrate-free *Hamilton* regression equation was also determined by trial-and-error and resulted in the following expression:

$$A\,z = 1.0402 - 0.0019 \cdot z + 1.3 \cdot 10^{-6} \cdot z^2 + 2 \cdot 10^{-10} \cdot z^3 \qquad [22]$$

The best fit of the theoretical curves based on the *Hamilton* background reference profile with the first OBH results suggests a partial hydrate saturation of about 7-8% of porous volume within the sub-bottom depth interval of 125-195 m, and only 5% from 195 to 275 m. At deeper parts, the medium should be hydrate free although the upper boundary of the low-velocity layer lies slightly deeper (±307 m). Furthermore, several difficulties arose during OBH-data analyses due to inaccuracy of positioning and drift during deployment [*De Meersman, 2000*].

Magnitude of the maximum values agrees well with similar experiments (OBS) performed along the NE Atlantic margin [e.g. *Mienert et al., 1998*], while the velocity in the low-velocity layer seen seems higher in Lake Baikal than in their study. The interval velocities values across the BSR reported from the Cascadia margin [*Spence et al., 1995*] are similar to the OBH results from Lake Baikal. Velocity pull downs caused by higher than normal gas saturation are not supposed to have an influence on the sub-bottom velocity curve above the BSR. It is supposed that no significant amounts of methane gas have accumulated within the HSZ.

To summarise, the accuracy of heat flow determination due to the assumed velocity profile will be within 5 to 10% in our approach.

4.1.6c Phase boundary conditions and the influence of gas composition on heat flow

Conversion from equilibrium pressure to temperature using formula [8] will give highly accurate results, as was pointed out already in chapter 2, supposing that the hydrate composition is pure methane in a fresh water environment and that heat transport is purely conductive through sediments without porous medium effects. If not, the theoretical 3-phase equilibrium conditions may not be applicable [*Xu & Ruppel, 1999*]. Mass and energy transport will result in changing pore pressure and temperature profiles with depth. Typical fluid flows will in general not much alter the hydrostatic pore pressure profile but will be important in terms of temperature distribution. The data set available however does not allow extraction of detailed information on methane and heat supply rates within the sediments. Variations of porosity, grain size etc. can be another source of errors [*Clennell et al., 1999; Henry et al., 1999*].

The very low salinity in Lake Baikal water (0.76‰) does not give rise to deviations from the pure fresh water stability conditions. First geochemical analysis performed on both the deep drill hole (BDP-1997) and the samples retrieved from the *Malen'kiy* crater (winter 1999-2000) revealed only minor additions (< 1%) of CO_2 and C_2H_6 in the hydrate structure [*Golubev, pers. comm.; Klerkx, pers. comm.*]. Since the exact composition is at present unknown and due to their very small concentration, the hydrates in Lake Baikal are considered to be purely methane hydrates. The errors induced due to *in situ* temperature determination (other phase boundary conditions) are estimated by comparing "inferred" heat flow values at 5 locations of the Southern Baikal Basin for a few vapour compositions with 99% mole fraction of CH_4 (Table 4.2). Phase boundary equation coefficients and heat flow values were determined with program_1 (included), knowing the two-way travel time of the lake floor reflection and the inferred base of the stability field at these locations. Equilibrium conditions for selected pressure-temperature couples were determined with data couples from the CSMHYD program [*Sloan, 1998*] and imported in the program to determine the phase boundary coefficients using the method of least squares. The calculated heat flow values are slightly higher for mixed hydrates of CH_4, CO_2 and C_2H_6 in the vapour phase than for pure CH_4 hydrates, due to the slightly higher equilibrium temperature at depth. Stability conditions appear more sensitive to inclusion of C_2H_6 in the gas phase. Heat flow values are then maximum 2.5% *higher* than in case of pure methane hydrates.

Another important feature is the variability of bottom water temperature. In the zones of inferred hydrate occurrence, water depths in general exceed 700 m. At greater water depths, bottom water

temperatures are very stable. Divergence is maximum 0.1°C [*Golmshtok et al., 2000*]. This effect will not have any importance for hydrate stability conditions at depth or at the lake bed (see also chapter 2). The influence on geothermal gradient calculations can also be ignored: for mean BSR depths, deviations are about 0.00033°C/m or less than 1%.

	location 1	location 2	location 3	location 4	location 5
latitude	51.88900	51.88300	51.86877	51.91037	51.78555
longitude	105.56158	105.65105	105.57020	105.80048	105.47093
water depth (ms TWTT)	1945.3	1918.3	1971.7	1753.9	2045.1
water depth (m)	1361.7	1342.8	1380.2	1227.7	1431.5
BSR depth (ms TWTT)	2132.1	2427.2	2317.6	2090.2	2411.8
BSR depth (m)	1522.5	1797.3	1683.5	1522.3	1753.9
sub-bottom depth BSR (m)	160.8	454.5	303.3	294.6	322.4

		A	B	C	D
mole fraction (%)	CH_4	100.0	99.0	99.0	99.0
	CO_2	0.0	0.0	1.0	0.5
	C_2H_6	0.0	1.0	0.0	0.5
phase boundary coefficients	a	0.419626	0.389568	0.413199	0.401652
	b	0.039326	0.039920	0.039634	0.039731
	c	0.000299	0.000306	0.000292	0.000301
location 1	hydrostatic	95.95	98.44	96.39	97.43
	lithostatic	99.86	102.28	100.30	101.30
location 2	hydrostatic	42.00	42.91	42.17	42.54
	lithostatic	45.84	46.67	46.00	46.34
location 3	hydrostatic	57.32	58.65	57.56	58.11
	lithostatic	61.13	62.38	61.37	61.88
location 4	hydrostatic	55.28	56.72	55.54	56.14
	lithostatic	59.49	60.85	59.74	60.30
location 5	hydrostatic	55.64	56.87	55.87	56.38
	lithostatic	59.33	60.49	59.55	60.03

***Table 4.2**: Influence of small inclusions of CO_2 and/or C_2H_6 on heat flow based on the position of the BHSZ at 5 locations in the Southern Baikal Basin. The specific locations are the following: the one with the highest (1), lowest (2) and mean (3) inferred heat flow, shallowest (4) and deepest (5) point of inferred BSR occurrence on the seismic data grid.*

4.1.6d Thermal conductivity profile

The final calculation of heat flow depends on the thermal conductivity profile that is supposed to slightly increase with burial depth [12] according to *Duchkov & Kazantsev [1996]*. Since this relationship was obtained for a 100 m borehole while the hydrate accumulation boundary is on average located at more than 300 m sub-bottom depth, discrepancies can occur due to the extrapolation to deeper parts of the basin. Studies in other regions (Cascadia margin, Makran accretionary prism) reveal that the thermal conductivity does not behave linearly with sub-bottom depth [*Nobes et al., 1986; Ganguly et al., 2000; Kaul et al, 2000*] as was supposed in this study. Thermal conductivity will also depend on partial hydrate saturation and should be considered for the three-component system pore fluid – matrix – hydrate, knowing that the thermal conductivity of hydrate is low relative to pore water. This thermal conductivity curve is the factor with the highest degree of uncertainty.

4.1.6e Heat flow

In summary, in my opinion the error made in the entire procedure of determining local heat flow from BSR observation on seismic profiles seems limited to about 15% while the relative accuracy will be much higher. For the inverse process, i.e. determining the sub-bottom depth of the HSZ based on heat

flow measurements, two limiting values (hydrostatic and lithostatic pressure) are returned. For small heat flow values (40 $mW \cdot m^{-2}$), the difference and hence uncertainty of the result can be as high as 80-90 m while only 5 to 10 m of difference occurs at high heat flow values (100 $mW \cdot m^{-2}$) for pure methane hydrate, as shown in figures 4.2 and 4.3. This approach is also sensitive to similar changes in the sub-bottom velocity and thermal conductivity profile. The uncertainty due to the pressure distribution can induce significant errors, up to 30% between those two extreme values.

4.2
Observations from seismic reflection profiles, side-scan sonar imagery and heat flow data

During recent years, an expanded multi-disciplinary geophysical data set was acquired in the Central and especially the Southern Baikal Basins by the RCMG in close co-operation with several other Belgian (Royal Museum of Central Africa) and Russian institutes (Institute of Geology, Geophysics and Mineralogy, Institute of Computational Mathematics and Mathematical Geophysics, Institute of Limnology) and universities. In this discussion, multi-frequency seismic reflection profiles were used and combined with observations from side-scan sonar data and heat flow measurements, complemented with some results from echo sounding and CTD profiling. Emphasis lies on the medium-frequency seismic reflection profiles from the central part of the Southern Baikal Basin around the BDP-97 drilling site from which hydrates were retrieved. An overview picture of available data from the Southern Baikal Basin is shown in figure 4.5. The bathymetry deduced from the 1999 airgun reflection profiles is displayed in figure 4.6: the lake floor is gently dipping in SSW direction. For a detailed description of the seismic stratigraphy of the Southern Baikal Basin based on the seismic profiles acquired during the 1999 expedition, the reader is referred to the work of *De Meersman* [*2000*]. The discussion here is split up into the normal BSR features evidenced on the acoustic sections in box 1 (figure 4.6) and typical or anomalous features observed on data acquired in box 2 (figure 4.6), in combination with side-scan sonar coverage of part of this area.

The single-channel Ship and Impuls airgun GAHY-1999 profiles form the backbone of this study, but also available multi-channel airgun-array lines (92_02, 92_03, 92_03A, 92_04) are used. Location of all profiles is shown in figures 4.5 (Southern Basin). Profiles GAHY001-019 are acquired with the higher-frequency Ship airgun, profiles GAHY020-043 with the lower-frequency Impuls airgun. More technical details are provided in §3.4 (previous chapter). Unfortunately, the shorter profiles (GAHY011, 013, 016, 018, 024, 026, 029, 031, 033) are not useful for delineating the BHSZ. Line GAHY002 has a very poor signal to noise ratio and was omitted. The sparker data in the central part of the Southern Baikal Basin do not reveal prominent features that could be interpreted to represent the base of the hydrate stability field since the acoustic penetration is limited to typically 300 ms TWTT sub-bottom depth (see previous chapter). Furthermore, only a few sparker lines were acquired within the zone of inferred hydrate occurrence in the deeper part of the Southern Basin. Note that in front of the Selenga Delta, water depths are too shallow and/or temperatures are too high to ensure methane hydrate stability within the sub-surface. In the Central Baikal Basin, other features are observed by *Golmshtok et al.* [*2000*].

4.2.1
Normal BSR-features (box 1)

As shown in the previous chapter and in *Vanneste et al.* [*in press*], the general bottom-simulating behaviour is observed on several seismic profiles (92_01, GAHY008-GAHY020, GAHY005-006-010) from the Southern Baikal Basin. These lines are located in box 1 shown on figure 4.6.

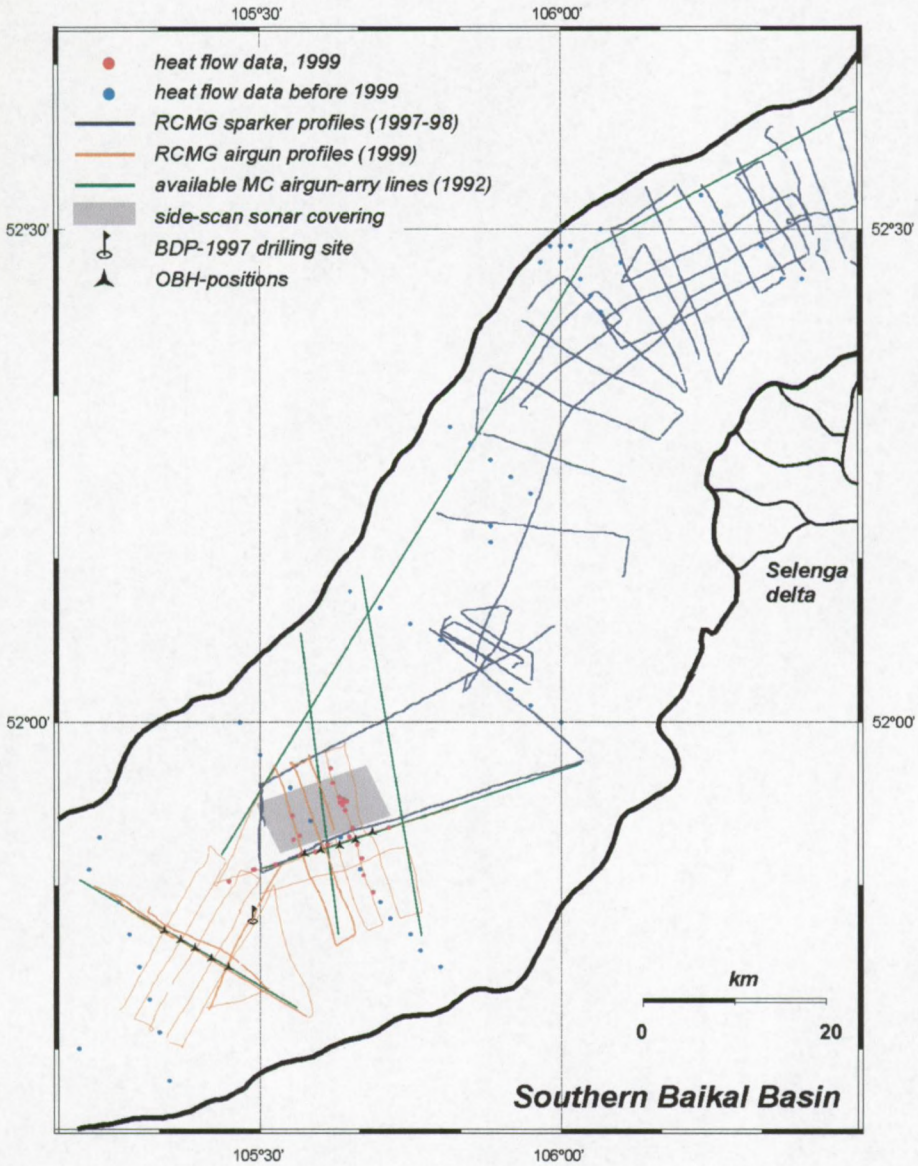

***Figure 4.5**: Seismic data tracks, side-scan sonar coverage, heat flow measurements, OBH positions and BDP-97 drilling site, in the Southern Baikal Basin, used in this study.*

The lines running in NW-SE direction (GAHY008, 020, MC92_01) are shown in figure 3.3 (previous chapter). The sedimentation pattern is folded over a distance of > 5 km at the NW side. Several pseudo-vertical faults with small offsets can be identified within the fold structure. The amplitude of the BSR on these profiles is highly variable and in general weaker than on the low-resolution MC data. The BSR only appears as a clear reflection on these medium-frequency profiles where it is crosscutting the dipping sediment layers at the border of the fold structure. Within the folded sedimentary section itself, the BSR is weak. A similar fold-crosscutting behaviour is observed along the parallel line GAHY001.

The southernmost of the NE-SW running lines GAHY005-006 and 010 (figure 3.8) cross the BDP-1997 drilling site. Here also the BSR is a rather weak feature that is not traceable along the entire sections. The BSR deepens slightly to the NE, independent of lake floor topography. This is also the case for line GAHY012. The three lines more to the N (GAHY014, 017, 019) show a similar sedimentation pattern, but to the NE side folding becomes more important (figure 3.4). Approaching the NE side of area 1, the BSR moves a little upwards within the folded strata. Also there, faults are present without effectively

disturbing the position of the BSR. On these three lines, the BSR is faint to invisible at the SW side (sub-parallel sedimentation) but is much more enhanced where it is crossing the folded sediments.

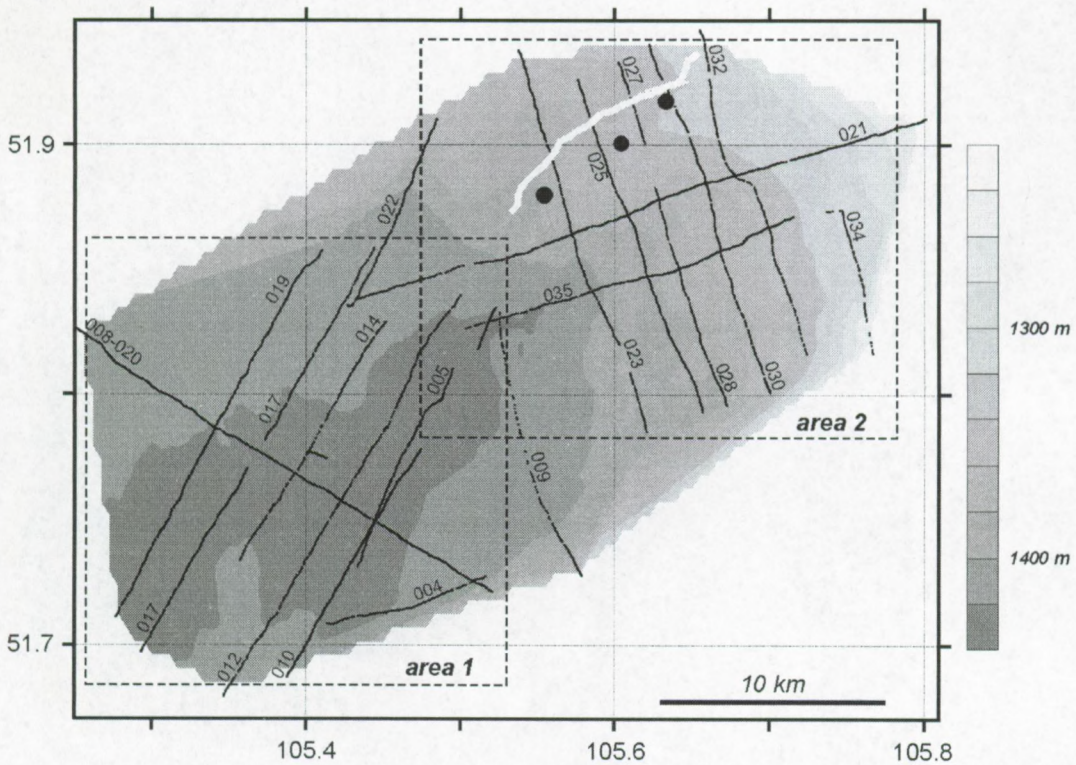

***Figure 4.6**: 20-m contours of the bathymetry of the axial part of the Southern Baikal Basin, deduced from 35 medium-frequency airgun profiles. The white line represents a fault clearly observed on side-scan sonar imagery and acoustic profiles. The black dots are fluid escape features. Line names of the selected data points from the GAHY expedition used for all calculations performed are shown.*

Irregularities of the acoustic expression of the BHSZ are only observed very occasionally on the profiles from area 1. The BSR feature on the short section GAHY006 is not really behaving as a BSR in the pure sense of the word (figure 3.8): this continuous reflection is undulating with small amplitude. On other lines (e.g. GAHY017 & GAHY005, 010) smooth variations of the BSR depth are observed as well. Folding appears to be of minor importance on the sub-bottom position of the BSR. At the same time, small offset faults in the area do not result in significant vertical shifts or discontinuities of the BSR feature. Acoustic energy penetration is reduced within the folded sediments.

Only on a few profiles or sections a distinct and continuous BSR is observed on the medium-frequency airgun data. Crosscutting the local stratigraphy is the primary indicator. Faint BSR features in this area are best recognised by the sudden termination of enhanced reflections, especially where the layering is only inclined at small angles relative to the BSR.

4.2.2
Side-scan sonar imagery and typical seismic reflection profiles (box 2)

Box 2 is located adjacent to box 1 to the NE. Side-scan sonar, reflection seismic data (Impuls airgun, MC airgun-array), CTD-profiles, echo-sounding and heat flow data are available from this region, situated south of the *Posolskaya* Bank with one of the major active intra-basinal fault zone, the *Posolskaya*-fault. Water depths area are approximately 1200 to 1400 m. The lake floor dips gently to the SW.

4.2.2a Side-scan sonar imagery: observation and interpretation

The "Sonic 3" side-scan sonar was provided by VNIIOkeangeologia of St.-Petersburg, Russia. The system was operated at 30 kHz and towed about 200 m above the lake floor. Data shown here (figure 4.7) are corrected for slant-range and track and are geo-referenced. A variable gain was applied to correct for spherical divergence [*De Batist, pers. comm.*]. Swath width of the system is approximately 2 km. The data acquisition was part of the multi-disciplinary research activities in Lake Baikal during the summer of 1999 [*De Batist et al., in prep*].

One of the most characteristic features is the presence of a ± 12 km long undulating fault structure running from SW to NE across the scanned area. This fault might be originally associated to the major *Posolskaya* fault situated to the N of the seismic grid. The seismic profiles (see below) evidence lake floor offsets up to 30 m. This fault splits up in NE and SE trending fault splays. Lake floor offsets related to this southern fault splay are smaller. South of this fault, four isolated semi-circular irregularities within the lake floor morphology are recognised. They line up nearly parallel to the intra-basinal fault. The structures were labelled "*Bolshoy*" (large), "*Stariy*" (old), "*Malyutka*" (very mall) and "*Malen'kiy*" (small). The central part of these irregular structures is depressed by several m. Diameter of the *Bolshoy* structure is about 1 km. Echo sounding revealed that *Bolshoy* rises about 28 m above the surroundings [*Van Rensbergen et al., 2000*]. The *Malen'kiy* structure – from which hydrates were retrieved during March 2000 and lying nearly on top of the southern fault splay – corresponds to an irregular surface with alternating highs and deeps, with maximum depth variations of 25 m [*Klerkx et al., 2000*] and a few hundreds of m in diameter.

The presence of acoustic non-transparent plumes in the water column immediately above three of these irregularities (*Bolshoy, Malen'kiy, Stariy*) reaching a height of 10-25 m [*De Batist et al., in prep.*] suggests intensive fluid escape from the lake floor. *Stariy* seems to be different from the others because of the high-reflectivity core (dark) while signal absorption (white) dominates in the central parts of the other irregularities. Echo sounding does not demonstrate large-scale seepage above the SW-NE trending fault.

CTD-measurements performed during the same expedition are not characterised by significant temperature anomalies in the water column straight above *Malen'kiy* and *Bolshoy* compared to an off-site reference profile, allowing us to label them cold seeps. Very small deviations (< 0.01°C differences) in the near-surface temperature profiles (200 m above lake bottom) however are present compared to the reference off-site temperature profile (see figure 4.1). The one temperature profile close to *Bolshoy* deviates more from the reference profile to smaller near-bottom temperature values. Another site of possible gas escape was recently identified ("*Novyi*"), based on CTD measurements, NE of the elongated structures already discussed [*Granin et al., 2000*].

4.2.2b Seismic reflection profiling

A stacked airgun-array line 92_03 (WSW-ENE) and a coincident zero-offset medium-resolution airgun line GAHY021 show a very clear example of a continuous oscillating strong reflection (figure 4.8). This rather bizarre behaviour occurs completely independent of the lake floor's morphology that is gently dipping in WSW direction. The difference between the lows and the highs taken from line GAHY021 exceeds 100 ms TWTT sub-bottom depths with oscillation wavelength of only a few km. The difference between the minimum and maximum two-way travel time sub-bottom depth along the entire line is about 250 ms TWTT.

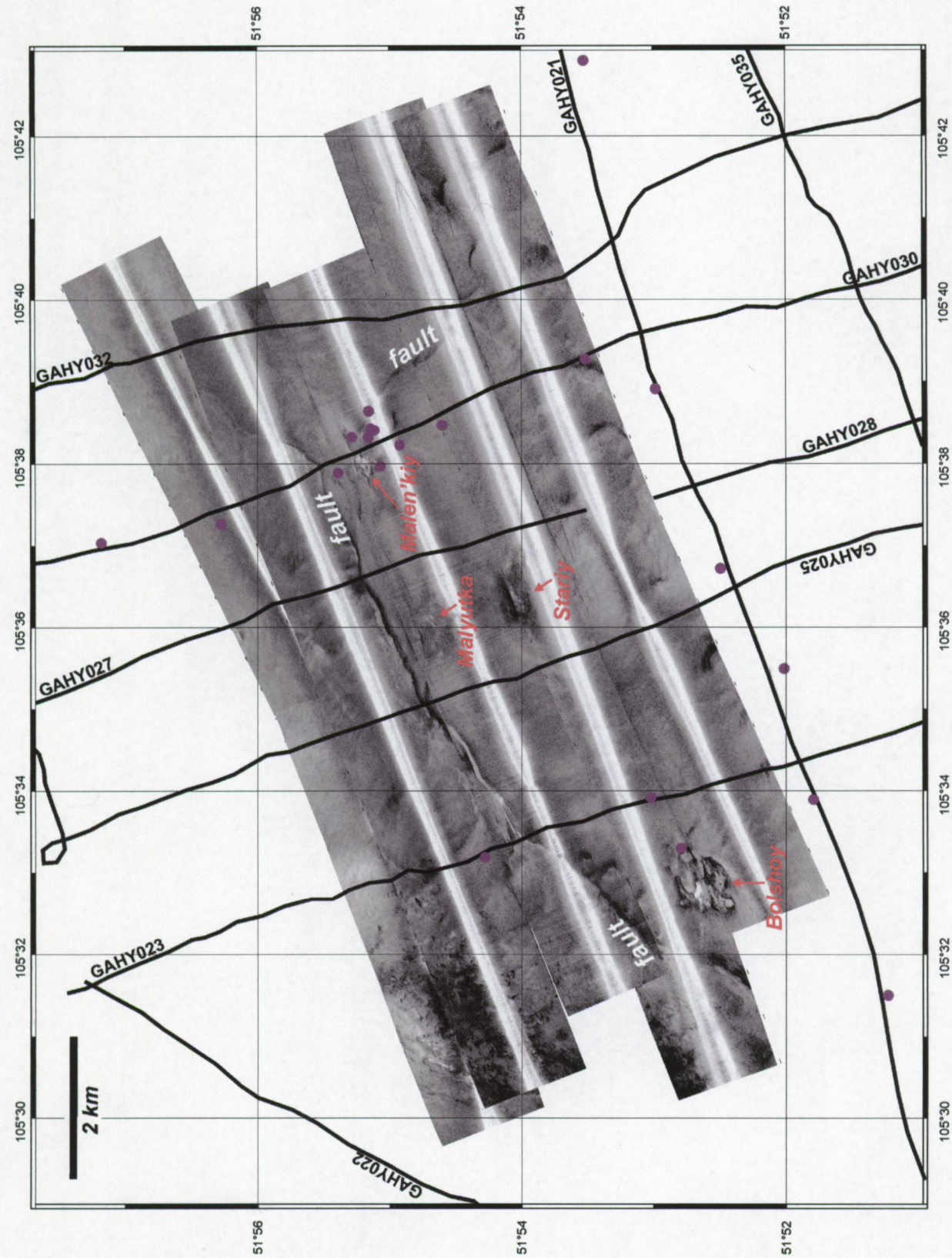

***Figure 4.7**: 30 kHz side-scan sonar mosaic (± 90 km² coverage) in the Southern Baikal Basin, with evidence of faults, cones, craters. Seismic profiles and heat flow locations (purple dots) are shown as well. All data shown here were acquired during the Baikal 1999 expedition.*

This oscillating reflection is characterised by its high reflection amplitude and reversed polarity while it is crosscutting the stratigraphic pattern. Amplitude blanking above and enhanced reflections below this interface are present. Such characteristics are often observed on acoustic sections from areas with known hydrate accumulations. Furthermore, this undulating reflection converts into a normal BSR on the prolongation of line 92_03. Therefore, this typical reflection is interpreted to represent the BHSZ. This was first suggested by *Golmshtok et al. [1997]* who observed faults beneath the local highs. The diffuse acoustic character however hampers the observation of fault structures. The discontinuity of the oscillating reflection towards the WSW is fault-related.

The coincident Impuls medium-frequency airgun line[1] GAHY021 (figure 4.8b) has very similar characteristics of what has been described in the previous chapter, compared to the low-frequency airgun-array line. The reflection amplitude is reduced and the continuity is less. Some reversed-polarity high-amplitude reflections cross this oscillating feature. Acoustic energy is attenuated beneath this feature. To the ENE, this typical reflection turns into a normal BSR feature. The lake floor morphology between SP 250-400 is characterised by wavy irregularities up to 15 m high, suggested to be sediment waves [*De Meersman, 2000*]. A coincident very-high-frequency CENTIPEDE sparker line was also acquired in 1997 but penetration was not deep enough to image the BHSZ.

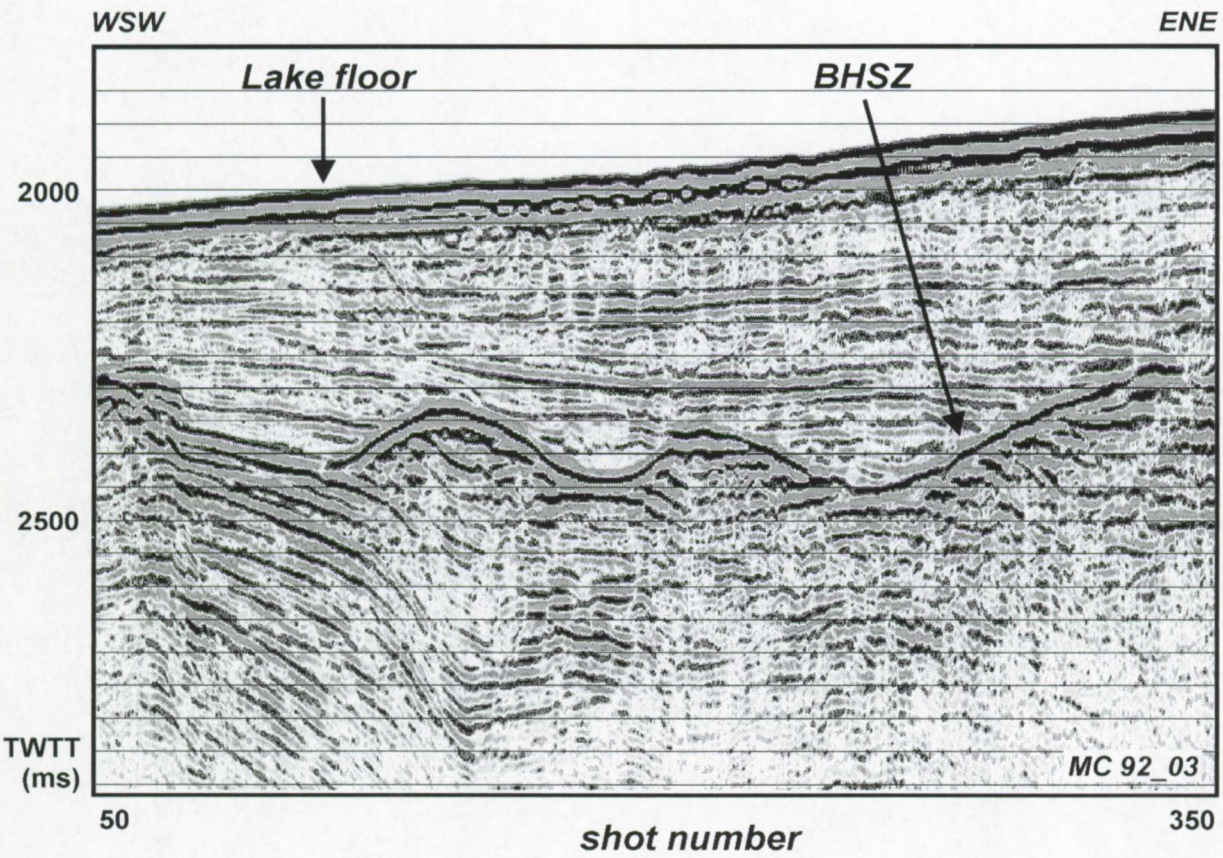

***Figure 4.8a**: Stacked profile MC92_03 characterised by a high-amplitude continuous oscillating reversed-polarity reflection from the Southern Baikal Basin.*

On line GAHY035 (figure 4.9), parallel to the S of line GAHY021 at a distance of approximately 3 km, neither a distinct BSR nor an undulating feature as described above can be observed. After checking the intersections with other profiles and performing instantaneous frequency analyses, the BHSZ is marked on top of some slightly enhanced reflections along this profile. The BHSZ is a BSR in the pure

[1] Shot interval of the SC airgun data res. MC airgun-array data is approximately 30-32 m res. 50 m.

sense of the word. One anomaly is observed around SP 120 at 350-400 ms TWTT sub-bottom depth. The continuity of the BSR is disrupted over a distance of ± 500 m. An enhanced reflection is elevated over 25 ms relative to the BSR, but no faults are observed. To the ENE end of this line, the BSR becomes shallower independent of lake floor morphology.

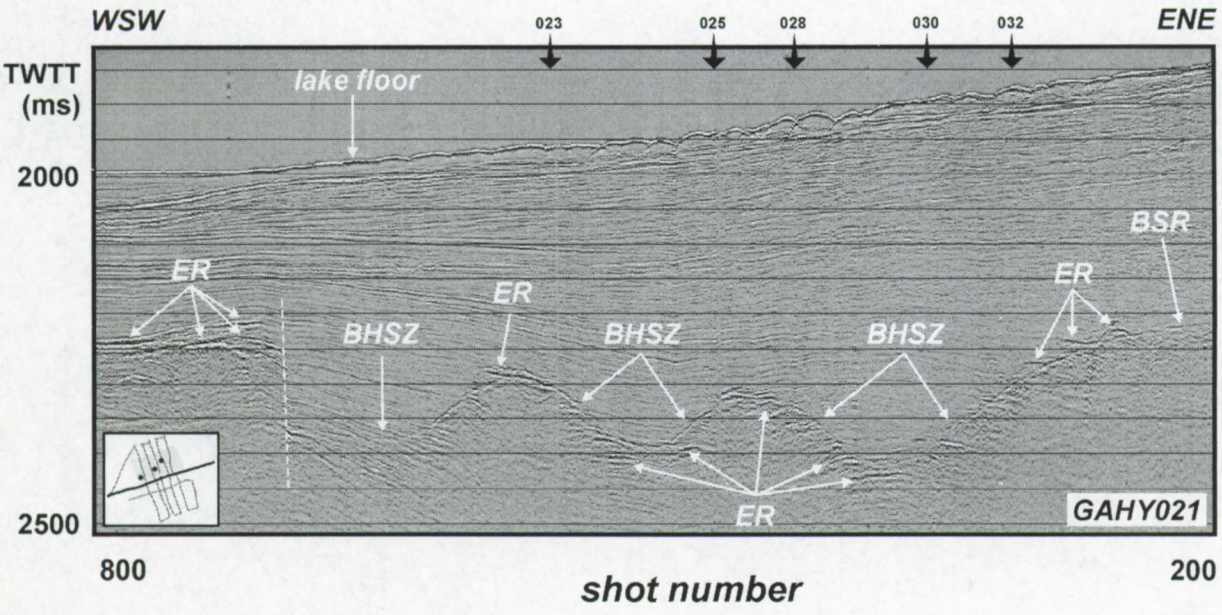

***Figure 4.8b**: Medium-frequency Impuls airgun profile GAHY021 coincident with line MC92_03 shown in figure 4.8a. Shot interval is approximately 30 m. The black arrows indicate the approximate location of the intersections with other GAHY profiles. The dashed white line represents discontinuities, e.g. faults.*

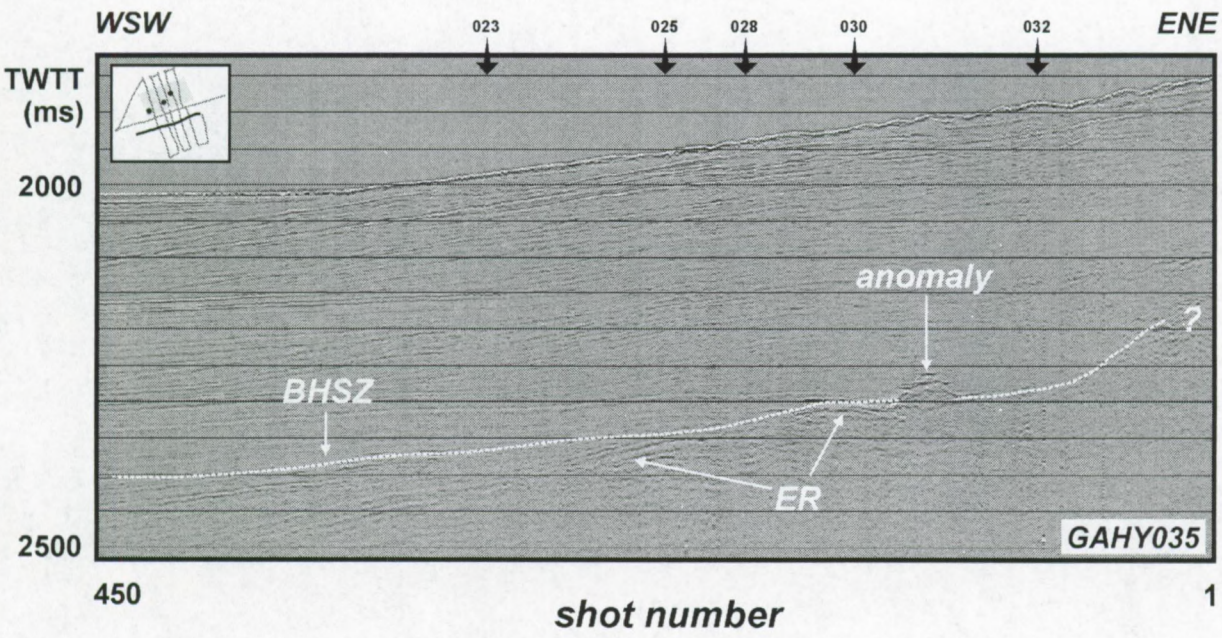

***Figure 4.9**: Impuls airgun line GAHY035, parallel to line GAHY021 (figure 4.8b). Along this line, the BHSZ is expressed as a very weak feature. Its bottom-simulating behaviour is only disrupted close to SP 120 and to the ENE edge. ER = enhanced reflection.*

The oscillating reflection on GAHY021 (figure 4.8) finds its continuation in a normal but weak BSR feature on line GAHY022 (figure 4.10). The BSR feature at the first part of this line (SP 1-280)

resembles the one observed on line GAHY017 (figure 3.3), i.e. inclined to stratigraphy but not perfectly mimicking the lake floor with slightly enhanced reflections below. Sub-bottom depth varies from 300 to 250 ms TWTT in this part. On the NE side of the profile in the direction of the *Posolskaya* Bank, the BSR disappears within a structural high. The BSR feature terminates in the immediate vicinity of a fault. Around SP 220, a package of enhanced reflections is observed, just above the BHSZ as evidenced by the BSR at both sides of this event. This package seems to be bounded by two faults.

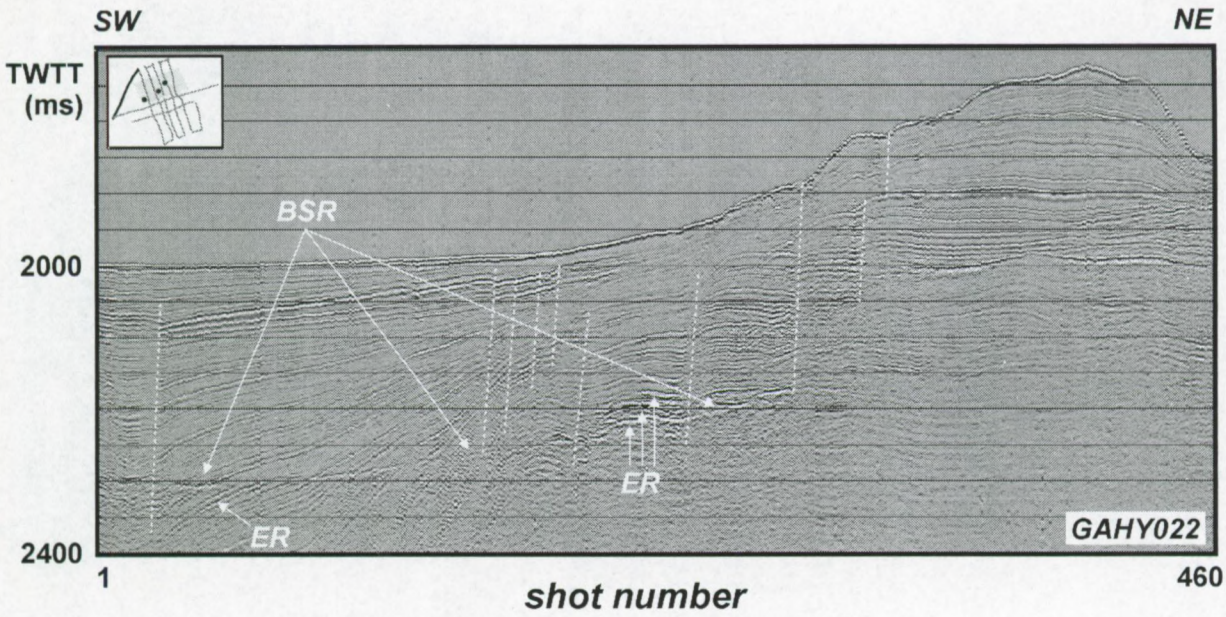

***Figure 4.10**: Impulse airgun line GAHY022, linking GAHY021 (WSW-ENE) with GAHY023 (NW-SE). The BSR observed coincides at the transition with the high-amplitude oscillating reflection on line GAHY021. ER = enhanced reflection.*

Different images are observed on the lines perpendicular to the lines GAHY021/MC92_03 and GAHY035. Five closely-spaced (distance about 2 km) nearly-parallel medium-resolution Impuls airgun lines (from W to E: GAHY023, 025, 027-028, 030 and 032) show similar characteristics. From these profiles, it is seen that the vertical offset of the fault diminishes to the E. In the area S of line GAHY021, a clear crosscutting BHSZ feature – not always perfectly mimicking the lake floor morphology – underlain by enhanced reflections is present on the NNW-SSE trending lines. Line GAHY028 gives a representative example of such a feature (figure 4.11). The BSR intersects around SP 20 with one of the local highs of the undulating anomalous reflection of GAHY021 (SP 445). This proves that the continuous but oscillating event on GAHY021 and MC92_03 can be considered as the BHSZ along these lines. The lake floor depression around SP 160 – also observed on lines GAHY025 (SP 130) and GAHY023 (SP 560) and MC92_02 – might represent a channel running nearly parallel to the SSE border fault.

A nearly identical BSR event is observed at the SSE part of lines GAHY025 (figure 4.12) and GAHY032. The amplitude of the reflection interpreted to represent the BHSZ varies from line to line: e.g. along line GAHY023, the reflection is very faint and irregular. On line GAHY025, the fault dip direction is opposite to the dip direction of the sedimentary strata that are cut. The fact that the dip direction of the fault is also opposite to the dip direction of the major *Posolskaya* fault, suggests a possible relationship. If so, this fault can be labelled as antithetic to *Posolskaya* [*Peacock et al., 2000*].

As can be seen from figure 4.7, *Bolshoy*, *Stariy* and *Malyutka* fall in between of the Impuls airgun seismic reflection profiles. Hence, the continuity and exact distribution of BSRs, BHSZ, high-reflectivity patches, etc. under or at the sides of these irregular features could not be investigated in

detail. Line GAHY030 (figure 4.13) is the only SC airgun profile in the immediate neighbourhood of one of those semi-circular irregularities observed on the side-scan sonar mosaic (figure 4.7). Line GAHY030 touches *Malen'kiy* at its eastern side. The acoustic anomaly indicates fluid escape from the lake bed. The southern fault splay lies within or at the sides of the acoustic transparent column but the plume masks its precise location. Beneath this fluid escape feature at the surface, the acoustic transparent zone might then represent a gas chimney or mud diapir, thus indicative of focussed fluid migration. At least this fluid escape feature appears to be directly related with anomalous hydrate accumulation or free gas presence/migration (enhanced reflections or bright spots) within the sediments.

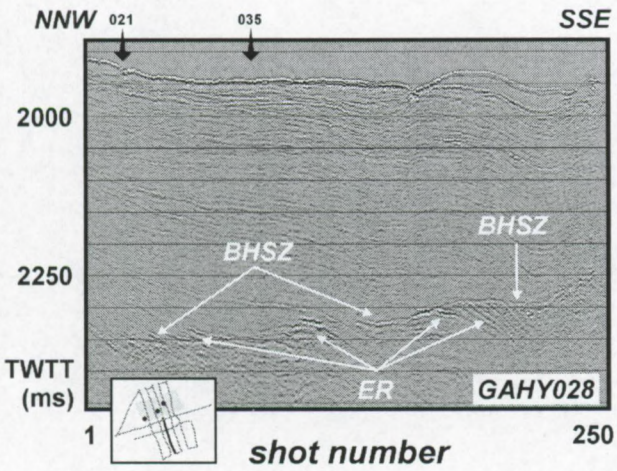

***Figure 4.11**: Airgun line GAHY028 perpendicular to and south of line GAHY021 with clear evidence of a BSR like feature.*

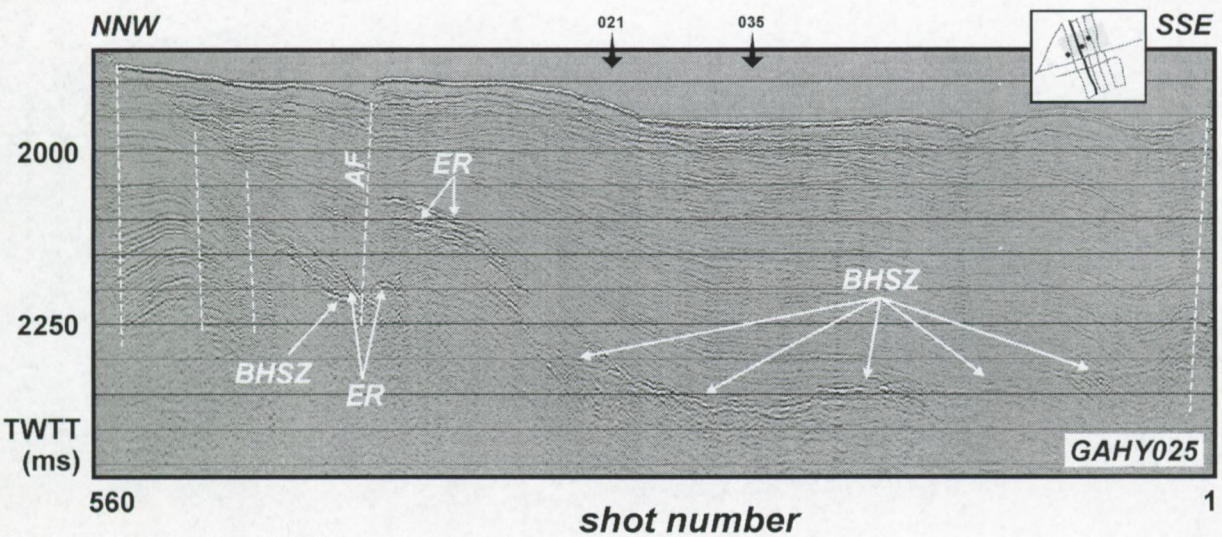

***Figure 4.12**: Profile GAHY025 parallel to GAHY028 (figure 4.11) and perpendicular to GAHY021 (figure 4.8b). AF = antithetic fault, ER = enhanced reflection.*

The inferred BHSZ at the SSE part of profile GAHY030 deviates much more from the BSR behaviour found on GAHY028. It deepens about 200 ms without any topographical control where it crosses line GAHY021 in one of the valleys of the BHSZ. A faint BSR-like feature can be discerned at the NNW side of the antithetic fault, much weaker than its SSE counterparts. In the intermediate zone, enhanced patches are observed at different sub-bottom depths.

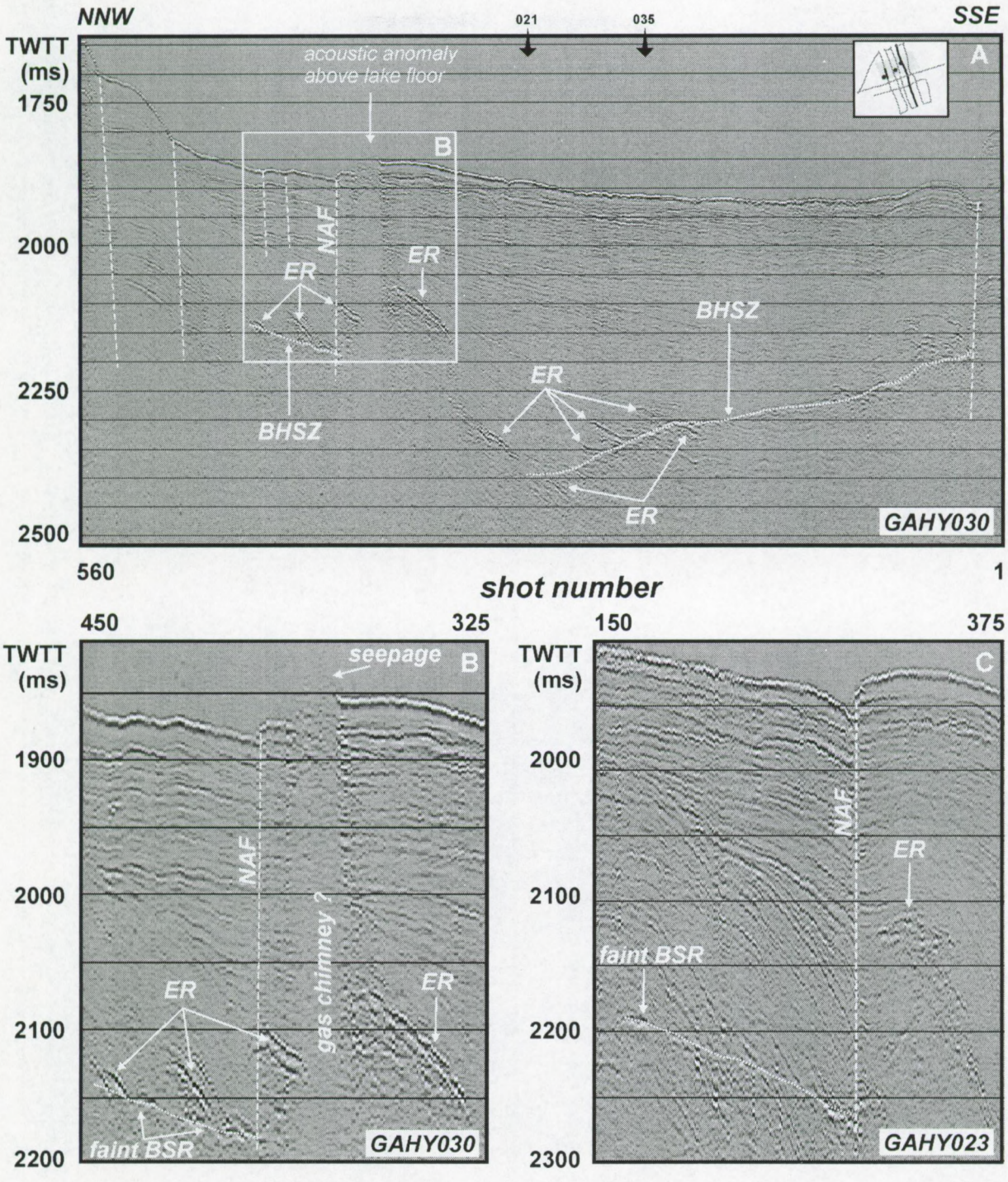

***Figure 4.13**: Profile GAHY030 perpendicular to GAHY021 (figure 4.8b) (A) and a zoom of the acoustic anomaly observed at the lake bed and enhanced reflections in the immediate neighbourhood of Malen'kiy (B). NAF = Northern antithetic fault splay, ER = enhanced reflection.*

Turning back to the MC seismic lines, then one low-frequency line running from S to N crosses the study area of inferred anomalies, i.e. line 92_02, and intersects lines GAHY025 (figure 4.12) and GAHY028. Checking the navigation of this profile with the SC seismic data reveals that this line most probably touches *Stariy*, appearing as a lake floor elevation. Aside *Stariy* (to the N) the much smoother lake floor elevation might represent *Malyutka*. Part of this profile S of *Posolskaya* is shown in figure 4.14. The BHSZ is – in contradiction to the observations on the medium-frequency profiles – a continuous event, starting from a BSR up-dipping towards its shallowest position under *Stariy*. This feature has much stronger reflection amplitude – although laterally variable – compared to other

stratigraphic boundaries (amplitude blanking above BHSZ). Its position nearly parallels the stratigraphy. The discontinuity around SP 300, N of *Stariy*, coincides with the fault structure. In between of *Stariy* and the fault structure, the acoustic section is chaotic. The high-amplitude event fades out towards the fault. Across the fault, a short BSR-like feature can be discerned. This feature disappears within the *Posolskaya* fault zone further N.

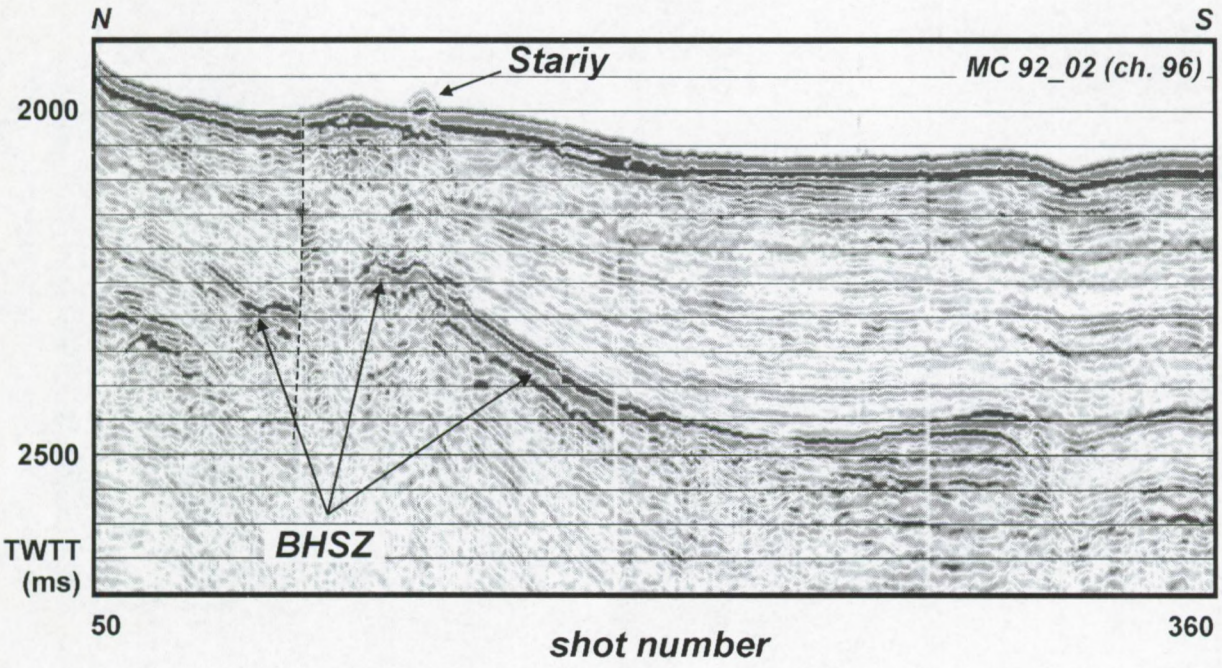

***Figure 4.14**: Part of MC 92_02 (shortest offset channel) across Stariy.*

MC seismic line 92_04 located at the E of the side-scan sonar coverage is characterised by a normal BSR feature. The nearly coincident medium-frequency line GAHY034 only gives evidence of a weak and slightly irregular BSR and enhanced reflections. The zone of up-doming BHSZ occurrence is hence limited to an area of about 175 km^2. Although the basal limit of hydrate stability is highly fluctuating in part of the Baikal Basins, no intersection of the BSR with the lake floor is observed on none of the data sets. Amplitude blanking is also highly variable along the seismic profiles.

4.2.3 Heat flow data

4.2.3a Heat flow measurements before 1999

Over the years, hundreds of heat flow measurements were taken in the upper meters of the sediments in Lake Baikal. Data compiled by *Golubev [1982]* in the Southern and Central Baikal Basin are given in table 4.3. Most measurements were performed along SE-NW running cross sections, using the "Golubev thermoprobe" [e.g. *Golubev, 1982*]. The measured heat flow has a very specific character in the Selenga delta and the southern basin of Lake Baikal: there is a general trend of decreasing heat flow in SSE - NNW direction (figure 4.15), but on a smaller scale strong fluctuations in heat flow occur over small distances almost everywhere at the lake floor. Measured heat flow values vary between the limits of 40 ± 6 and 195 ± 25 mW/m^2 while heat flow variations of 30-40 mW/m^2 over 3 to 4 km distance are recognized in several areas [*Golubev, 1982*].

Mean heat flow values are approximately 71 ± 21 mW·m^{-2}. In the Southern and Central Baikal Basins, heat flow of about 50 mW·m^{-2} is found along the western shores, while values up to 100-150 mW·m^{-2}

are measured along the eastern shores. At some places, extreme high heat flow values are measured considered to be related to hydrothermal activity (see figure 4.15). Furthermore, Lake Baikal is characterised by isolated heat flow anomalies that appear to be closely linked to intra-basin faults or fault zones [*Golubev et al., 1993; Poort, 2000*].

Only 11 heat flow measurements of this data set are more or less enclosed within our study area, of which 5 at the eastern rim of area 1 and only 3 close to the zone of inferred anomalies.

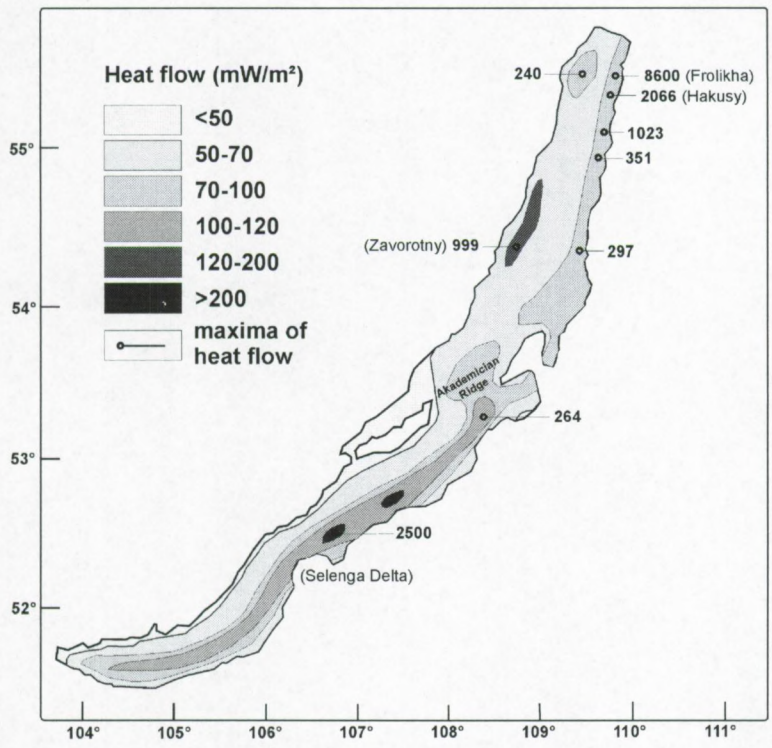

***Figure 4.15**: General heat flow trends in Lake Baikal, redrawn from Golubev [1993], from Poort [2000]*

4.2.3b Heat flow measurements acquired during the 1999 expedition

During the third leg of the Baikal-1999 expedition, geothermal data were collected in the Southern Baikal Basin, south of the *Posolskaya* Bank. Using the 2 m long GEOS-T thermoprobe, measurements of *in situ* temperatures and thermal conductivity were determined at 4 integrated depth intervals of 0.5 m. The instrumental error is 1-5% on the determined geothermal gradient, 5% on the thermal conductivity and 10% of the final heat flow value [*Poort, 2000*]. The heat-flow probe was developed by PALS company (Samara, Russia) and is property of the Royal Museum for Central Africa (RMCA, Tervuren, Belgium).

Investigated sites were selected based on the information provided by the reflection seismic and side-scan sonar data obtained during the first two legs of the expedition. Geothermal stations were chosen basically along two seismic profiles (GAHY021-series HFB and GAHY030-series HFA), and in the proximity of *Malen'kiy* observed on one of the seismic profiles (GAHY030) and on the side-scan sonar mosaic (figure 4.7). One more measurement was performed in *Bolshoy* and two along GAHY023 (series HFC). Measurements (compiled in table 4.4) range from 56 up to 165 $mW \cdot m^{-2}$. The highest values were obtained from *Malen'kiy* (HFA12-13: 112-65 $mW \cdot m^{-2}$) and *Bolshoy* (HFC-01: 110 $mW \cdot m^{-2}$).

station		longitude E °	latitude N °	depth (m)	heat flow (mW/m^2)	z hydro (m)	Z hydro (m)	z litho (m)	Z litho (m)	diff. (m)
175	C	106.683333	52.733333	1080	80	172	1252	186	1266	14
176	C	106.716667	52.716667	1060	96	137	1197	145	1205	9
177	C	106.750000	52.683333	1083	68	211	1294	231	1314	20
178	C	106.800000	52.633333	1120	73	198	1318	215	1335	17
179	C	106.833333	52.600000	980	87	144	1124	155	1135	11
180	C	106.883333	52.566667	672	48	218	890	277	949	59
87	C	106.783333	52.850000	1220	45	395	1615	454	1674	59
88	C	106.850000	52.783333	1225	66	239	1464	260	1485	21
89	C	106.883333	52.750000	1230	67	235	1465	255	1485	20
90	C	106.916667	52.716667	1245	82	185	1430	197	1442	12
91	C	106.950000	52.700000	1203	84	176	1379	187	1390	12
92	C	106.983333	52.666667	1155	98	142	1297	151	1306	8
24	C	107.416667	53.050000	1650	35	681	2331	796	2446	115
25	C	107.433333	53.016667	1600	47	437	2037	484	2084	47
26	C	107.450000	53.000000	1600	48	425	2025	469	2069	44
27	C	107.500000	52.933333	1650	62	310	1960	332	1982	22
28	C	107.533333	52.883333	1550	57	333	1883	361	1911	28
29	C	107.583333	52.816667	1350	69	241	1591	259	1609	18
30	C	107.616667	52.766667	700	90	98	798	109	809	11
12	C	104.916667	51.816667	1220	52	324	1544	363	1583	39
13	C	104.933333	51.766667	1240	90	165	1405	175	1415	10
14	C	104.950000	51.733333	1250	98	151	1401	159	1409	8
15	C	104.966667	51.683333	1300	99	153	1453	161	1461	8
16	C	105.000000	51.650000	1100	108	123	1223	129	1229	7
17	C	105.016667	51.600000	320	110	0	0	0	0	0
61	S	105.233333	51.883333	1378	69	240	1618	257	1635	18
62	S	105.216667	51.850000	1403	70	238	1641	255	1658	17
63	S	105.266667	51.816667	1369	83	191	1560	202	1571	11
64	S	105.283333	51.783333	1385	70	236	1621	253	1638	17
65	S	105.300000	51.750000	1384	75	217	1601	232	1616	14
66	S	105.316667	51.716667	1395	70	237	1632	254	1649	17
67	S	105.333333	51.683333	1380	64	263	1643	285	1665	21
68	S	105.350000	51.633333	1402	97	162	1564	169	1571	8
69	S	105.466667	52.000000	968	68	189	1157	209	1177	21
70	S	105.500000	51.966667	1155	65	229	1384	251	1406	22
71	S	105.550000	51.933333	1301	73	216	1517	231	1532	16
72	S	105.583333	51.900000	1339	85	183	1522	194	1533	11
73	S	105.633333	51.883333	1342	93	165	1507	174	1516	9
74	S	105.666667	51.850000	1349	95	162	1511	170	1519	8
75	S	105.700000	51.816667	1266	83	181	1447	193	1459	12
76	S	105.716667	51.800000	1240	70	220	1460	237	1477	18
77	S	105.750000	51.783333	963	68	188	1151	208	1171	21
78	S	105.766667	51.766667	801	111	87	888	94	895	7
79	S	105.800000	51.750000	293	85	0	0	0	0	0
168	S	105.650000	52.133333	965	52	268	1233	309	1274	41
169	S	105.700000	52.116667	1040	92	139	1188	148	1179	10
170	S	105.750000	52.100000	870	68	172	1042	193	1063	21
171	S	105.800000	52.083333	685	195	38	723	40	725	2
172	S	105.916667	52.033333	330	98	0	0	0	0	0
173	S	105.950000	52.016667	830	84	126	956	139	969	13
174	S	106.000000	52.000000	382	87	12	394	17	399	4

***Table 4.3**: Corrected heat flow measurement from Golubev [1982]. Data are converted into sub-bottom stability limits for both hydrostatic and lithostatic pressure distribution using bai_hyd.exe. S = Southern Baikal Basin, C = Central Baikal Basin, z = equilibrium sub-bottom depth, Z = equilibrium depth below lake level.*

Most of these new heat flow measurements were taken in zones of observed anomalies, while no heat flow stations were placed in box 1 of the study area where normal BSR features are present. Such measurements could have given better reference values along some seismic lines showing normal BSR features. For this, we have to rely on those measurements of *Golubev [1982]* in the study area. Raw data are used for comparison with inferred heat flow values. Away from the *Posolskaya* fault,

bathymetry is only gently dipping in the study area from 1220 to 1430 m and hence corrections for regional topography can be ignored. Corrections for regional topography and sedimentation using simplified models are estimated to be maximum -5% res. 10% [*Poort, pers. comm.*].

station	longitude E °	latitude N °	depth (m)	heat flow (mW/m^2)	z hydro (m)	Z hydro (m)	z litho (m)	Z litho (m)	diff. (m)
HFA03 S	105.640100	51.919100	1316	76.5	205	1521	219	1535	14
HFA04 S	105.616950	51.952920	1292	77.3	200	1492	214	1506	14
HFA05 S	105.620850	51.937930	1329	74.2	214	1543	229	1558	15
HFA06 S	105.631120	51.923280	1332	89.2	172	1504	182	1514	10
HFA07 S	105.640930	51.910200	1317	88.1	174	1491	184	1501	10
HFA08 S	105.654170	51.892230	1341	55.6	309	1650	340	1681	31
HFA11 S	105.636820	51.915570	1317	82.1	189	1506	200	1517	12
HFA12 S	105.638330	51.919450	1311	165.0	85	1396	88	1399	2
HFA13 S	105.638380	51.921530	1317	110.6	134	1451	139	1456	6
HFA14 S	105.639870	51.918700	1317	85.6	180	1497	190	1507	11
HFA15 S	105.643620	51.919430	1322	92.4	165	1487	173	1495	9
HFA16 S	105.632450	51.917920	1316	80.3	194	1510	206	1522	12
HFB01 S	105.714500	51.892370	1319	82.0	189	1508	201	1520	12
HFB02 S	105.648170	51.883420	1354	80.2	198	1552	210	1564	12
HFB03 S	105.611800	51.875330	1369	83.2	190	1559	202	1571	11
HFB04 S	105.591680	51.867400	1390	83.7	191	1581	202	1592	11
HFB05 S	105.565000	51.863770	1390	75.3	217	1607	231	1621	14
HFB06 S	105.525420	51.854450	1411	71.5	229	1640	245	1656	15
HFB08 S	105.448100	51.837200	1423	61.2	284	1707	308	1731	24
HFB09 S	105.490630	51.849330	1422	71.8	233	1655	249	1671	16
HFC01 S	105.555320	51.880320	1365	109.5	138	1503	144	1509	6
HFC02 S	105.553450	51.904870	1373	74.1	219	1592	234	1607	15
HFC03 S	105.565520	51.884080	1365	99.2	155	1520	162	1527	7

***Table 4.4**: Heat flow measurements acquired during the multi-disciplinary geophysical survey of Lake Baikal, 1999 in the Southern Baikal Basin. Data are converted into sub-bottom stability limits for both hydrostatic and lithostatic pressure distribution using bai_hyd.exe. z = equilibrium sub-bottom depth, Z = equilibrium depth below lake level. Series HFA coincides with GAHY030, HFB with GAHY021, HFC with GAHY023.*

4.3
Acoustic evidences for free gas accumulation and migration

In the first instance, the seismic data were analysed for specific features indicative of free gas occurrence or migration pathways. The basic results are briefly discussed here. The presence of BSRs or reflections interpreted as the BHSZ by their crosscutting character, reversed polarity and intersections with BSRs on other profiles, as discussed above is already indicative of free gas presence. Note also that the AVO response shown in the previous chapter was performed on line MC92_03, and hence illustrates that the reflection amplitude of the undulating reflection increases with increasing offset or angle of incidence. Such behaviour is indicative of the presence of free gas beneath the reflecting horizon, thus beneath the undulating reflection.

4.3.1
Enhanced reflections and inferred evidences for fluid migration: gas or gas hydrates?

As discussed in the previous chapter, enhanced stratigraphic reflections beneath the HSZ most probably point towards the presence of free gas, possibly trapped by a permeability barrier due to partial hydrate saturation. Such features occur frequently if the inferred BHSZ is inclined to stratigraphy. The data presented here have very similar characteristics.

While in box 1 only occasionally enhanced reflections penetrate the HSZ, the second box gives further evidence for significant presence and active focussed migration of gases throughout the entire hydrate stability field inferred from neighbouring sides. Active fluid escape features are evidenced on e.g. side-scan sonar data (figure 4.7), echo-sounding and on 1 medium-resolution airgun profile GAHY030 touching *Malen'kiy* (figure 4.13) by the presence of acoustic anomalies just above the lake floor and within the uppermost sedimentary section (chimney). MC Line 92_02 crosses one of the other inferred anomalies, *Stariy*. The local sub-surface is characterised by a chaotic facies in between this dome-like elevation and the antithetic fault structure. Similar characteristics are present beneath the oscillating reflection on MC 92_03, hence, the low seismic reflectivity is attributed to free gas presence. Reflection amplitude of the lake floor at *Stariy* is reduced without polarity reversal. No active seepage coming from *Stariy* is observed on the seismic profile but is evidenced on echo-sounding data. Such active fluid escape features however do not exclude the presence of hydrates. Ascending gas can percolate through the HSZ without being captured into solid hydrate structures [*Ginsburg & Soloviev, 1997*]. In the Okhotsk Sea for example, *Cranston et al.* [*1994*] determined that the amount of gas being captured is five orders of magnitude lower than the amounts of gas percolating through the HSZ. A similar scenario can happen here.

Within the immediate vicinity of the antithetic fault (SSE), the generally expected BSR feature is disrupted or disappears and gives way to several variable-amplitude high-reflectivity events on the SC airgun data. On lines GAHY023, 025, 027, 030 and 032 (figures 4.12 and 4.13), packages of enhanced reflections or bright spots often terminating at faults are present. Most of these high-reflectivity events appear with reversed polarity and are therefore interpreted to be indicative of free gas occurrence. From observation of these profiles alone, it is questionable whether hydrates above trap the gas or not, so these reflections should be related to gas to be correct. Line 92_02 (figure 4.14) with slightly different navigation heading and crossing *Stariy*, illustrates that lower-frequency seismic profiling does not reveal BHSZ reflection discontinuities in the same area. The different acoustic profiles do show the same trends, apart from the continuity. Thus, the acquisition frequency plays an important role concerning the acoustic expression and the lateral reflection continuity of the BHSZ within the zone of irregularities. As a result, the reflection at the BHSZ and the enhanced reflections might have the same origin, i.e. a gas hydrate – free gas interface, but the name BSR is definitely no longer appropriate. This comparison furthermore allows linking the enhanced reflections on the SC profiles with the fluid escape structures observed on the side-scan sonar. The dipping of the BHSZ in concert with stratigraphy can then result in gas migration along the base of inferred hydrate stability, i.e. towards the fluid escape features forming an ideal nearly-vertical conduit for gas escape from depth.

Finally, there are a number of bright spots crossing the BHSZ present on the medium-frequency acoustic sections acquired in box 2. Also here, the polarity of most of these high-amplitude events is reversed. Clear examples occur on line GAHY030 (figure 4.13a, b). They all represent a limited region of higher reflectivity of individual stratigraphic boundaries. This indicates that while fluid migration is observed to take place through or in the immediate neighbourhood of faults, migration within specific stratigraphic layers forms an important additional migration mechanism in the central part of the Southern Baikal Basin. Some of these enhanced reflections extend to some hundreds of m (lateral) and up to 50 ms (vertical) within the HSZ as evidenced by the underlying reduced BHSZ reflection. This can represent a meta-stable situation of the combined occurrence of hydrates and free gases within the regional HSZ caused by lithologically-controlled fluid migration within specific stratigraphic layers.

4.3.2
Attenuation along line GAHY021

The instantaneous frequency display (see also §3.6.3) of line GAHY021 (figure 4.16) clearly shows that there is a low-frequency shadow beneath the anomalous oscillating reflection (i.e. a shift towards blue colours). Attenuation is very typical for the GAHY profiles acquired in the second area, although these data were acquired with the lower-frequency airgun compared to the data in the first zone. In general, acoustic penetration should be deeper with the lower-frequency gun but this is obviously not the case.

This effect also takes place suddenly at depths of the enhanced reflection, while in general attenuation is a more gradual effect. Beneath the anomalous oscillating reflection or series of reflections, acoustic turbidity is often present, hampering the interpretation of the acoustic section beneath the inferred BHSZ. Also a frequency filtering effect is present but less pronounced beneath the inferred BHSZ of line GAHY035 (figure 4.9). This characteristic was very helpful to determine more accurately the BHSZ along this line due to the absence of a distinct BSR feature or series of enhanced reflections that terminate at a certain sub-bottom depth (see also previous chapter).

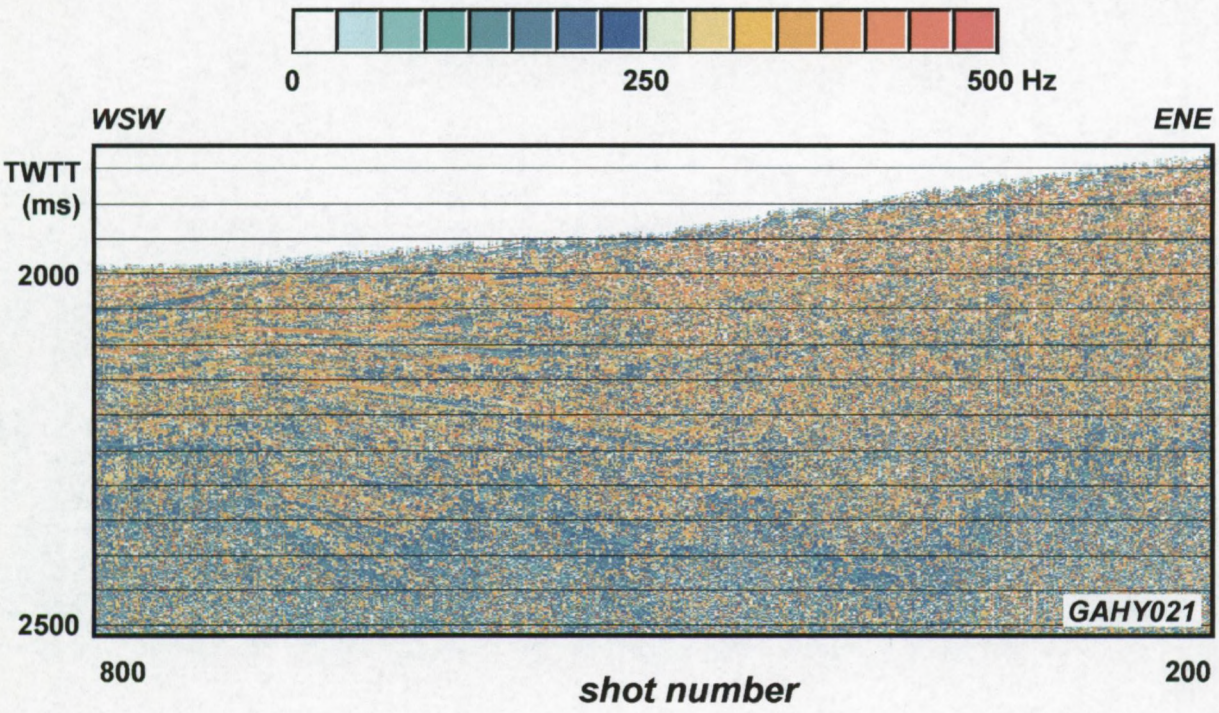

***Figure 4.16**: Instantaneous frequency display of line GAHY021 showing a clear drop of frequency content beneath the oscillating continuous reflection.*

4.3.3
Reflection coefficients along line MC92_03

Since only the first 3000 ms of the multi-channel lines were available, multiples are almost never present on these sections. Hence, another way for determining the reflection coefficient of this oscillating reflection has to be used but is based on exactly the same formulas mentioned before with this difference that the so-called geometry factor k is estimated from line MC92_01 while reflection amplitudes and travel times are read from the profile. Such a procedure is reasonable since the acquisition layout and material did not change from the one profile to the other. The geometry factor is taken to be the average value over the first 175 shots with good signal/noise ratio in the nearest recording channel of line 92_01 (see previous chapter). Accuracy of this method is less than the method used in the previous chapter.

The result along line MC92_03 is shown in figure 4.17 together with the bathymetry and the morphology of the undulating reflection. Scattering of the reflection coefficients of the base of the stability field and the lake floor appear to be rather high. Average values between shot points 50 and 300 are 0.171 (lake floor) and –0.076 (BHSZ), or –44.5%. Similar values were returned with the multiple quotient method for the near-offset channel of line MC92_01 (see previous chapter).

There seems to be a trend of increasing reflection coefficients at the local highs (= shallower) of the stability limit. In my opinion, the observed changing reflection coefficient in concert with the morphology of the stability limit cannot be solely explained by the fact that the travel path of the pulse is shorter and thus less vulnerable to attenuation mechanisms. Lateral variation of the free gas saturation beneath the reflection might form an alternative explanation. Migration of gas (within the plane of the profile) along the base of the oscillating stability field acting as a permeability barrier or trap in combination with migration within specific strata is then supposed to result in gas accumulation preferentially beneath the local highs, due to buoyancy under a lateral variable low-permeability interface.

Also on the medium-frequency airgun line GAHY021, higher reflection amplitudes are observed on the local highs of the BHSZ reflection.

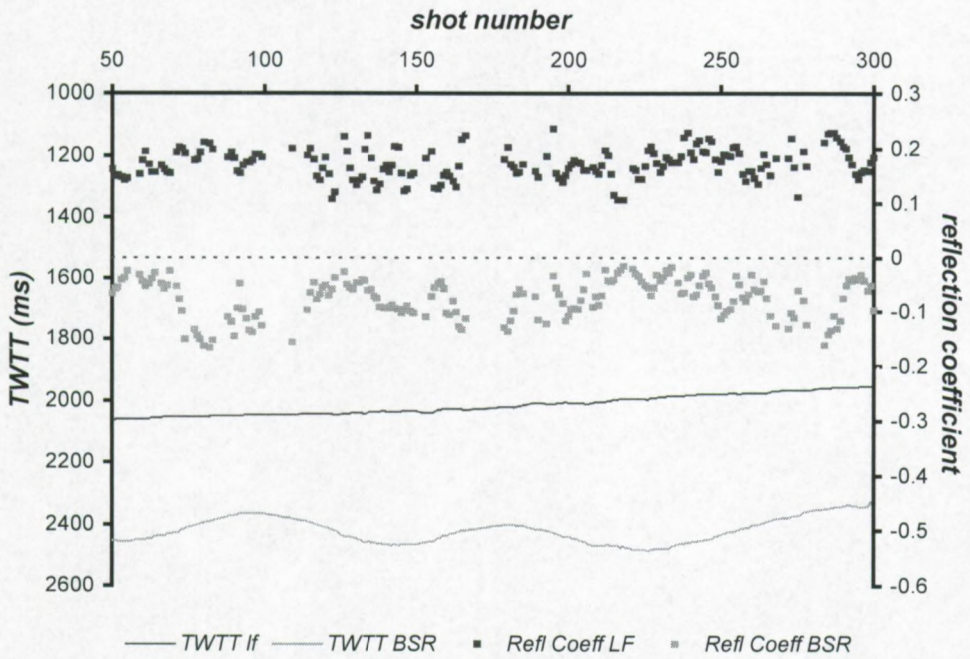

***Figure 4.17**: Two-way travel time of the lake floor and the anomalous reflection (solid lines) and their respective reflection coefficients (dots) for line MC92_03.*

4.3.4
Near lake bed hydrate occurrences in Malen'kiy and nature of the fluid escape features

All observed shallow sub-bottom gas hydrates are associated with fluid vents. Such have been found in the e.g. Caspian, Black and Okhotsk Seas [*Ginsburg, 1998*], the Gulf of Mexico [*Brooks et al., 1986*], Hydrate Ridge [*Bohrmann et al., 1998; Suess et al., 1999a*], offshore Norway [Håkon Mosby mud volcano, *Egorov et al., 1999*]. At these sites, hydrate accumulation is controlled by such fluid conduits as mud volcanoes, diapirs and faults.

Shallow coring in *Malen'kiy* also revealed the presence of almost pure methane hydrates of biogenic origin within the uppermost sedimentary section (20-40 cm depth) [*Klerkx, pers. comm.*]. This suggests that important amounts of methane (or other hydrate forming gases), hence high flux rates, must be supplied on a regular basis in order to form hydrates at the lake bed and enhanced local methane mass fractions in the Lake Baikal bottom waters. Whether this near-surface occurrence of gas hydrates is unique, is unclear since no information is available from the other irregular lake bed structures or from other parts of Lake Baikal.

Since only two seismic profiles are located within the immediate vicinity of the fluid escape features and due to limited navigation control, their real nature is unclear. *Van Rensbergen et al. [in prep.]* observe thin asymmetric sedimentary wedges just below the lake floor aside *Malen'kiy*, interpreted as mud flows and hence suggesting the irregularities to be recent mud volcanoes. Mud volcanoes are often associated with gas hydrates [*Milkov, 2000*] while fault-related hydrate dissociation and fluid escape into the water column is observed on several places [*Paull et al., 1995; Booth et al., 1998*].

4.4 Morphology of the BHSZ and its anomalous expression

NW-SE trending folding observed at the northern rim of area 1 does not have a significant effect on the position of the BHSZ, as it is observed on the acoustic sections (see e.g. MC92_01, GAHY008-020, figure 3.3). Within this folding, the BSR is situated maximally a few tens of ms TWTT shallower compared to the neighbouring part with sub-parallel stratigraphy while the lake floor is almost flat, but no important discontinuities of the BSR show up at pseudo-vertical small-offset faults within the uppermost sedimentary units.

Comparing the inferred depth below lake level and sub-bottom depth of the BHSZ contoured over the area (figure 4.18) with the bathymetry determined in exactly the same points (figure 4.6) clearly illustrates that the BSR morphology is strikingly different. The base of hydrate stability gets shallower towards the antithetic fault and *Posolskaya* (N) and towards the southern border fault zone, with maximum sub-bottom depths along the axis of the Southern Basin. The highest-amplitude variations are observed in the immediate neighbourhood of the antithetic fault, the semi-circular irregular structures observed on the side-scan sonar mosaic and the line with the high-amplitude oscillating reflection (GAHY021). To the S, E and W of this confined area, normal BSR featuress are observed. On the northern side of the fault in the direction of the *Posolskaya* fault, a faint BSR-like feature can be traced over some hundreds of m on several profiles. In the intermediate zone, the BSR appears to be disrupted and often only evidence for free gas occurrence (bright spots) is observed on medium-frequency profiles. Comparison with an airgun-array profile suggests that the BHSZ and the typical bright spots are most probably related.

The doming morphology of the BHSZ thus appears to be closely related to the presence of the antithetic fault and the fluid escape features. This is evidenced by MC line 92_02 crossing *Stariy* and line GAHY030 intersecting *Malen'kiy*. *Maluytka* and *Bolshoy* are situated in between of the seismic tracks (see figure 4.7). A distance of more than 1 km separates the medium-resolution seismic reflection profiles from these venting sites. On the profiles running nearly perpendicular to the fault (GAHY023, 025, 027-028, 030, 032) the reflection at the BHSZ seems to lose its continuity already a few km south of the fault, i.e. just across the intersection with GAHY021, approaching the zone of inferred lake floor seepages. Its position can also be depressed compared to its position further south (e.g. GAHY030) and north of the fault. The high reflectivity patches observed in the transition area between the zone of continuous BHSZ reflections (S) and the fault (N) are thrown up along faults with a vertical displacement exceeding the actual fault displacement. Hence, the irregular structures and the fault appear to have both a significant influence on the local hydrate stability conditions and their distribution and the accumulation and migration of gas, or vice versa.

The continuous but undulating reflection on a seismic line parallel to the side-scan sonar mosaic (GAHY021) is a bizarre and unique phenomenon. This feature seems to evolve to a normal (but much fainter) BSR about 3 km further south (GAHY035), thus further away from the seeps and fault structures. Comparison of the side-scan sonar imagery with line GAHY021 suggests that *Bolshoy* and *Stariy* might correspond well with two of the local uplifts (SP 600, 450) of the undulating high-amplitude reflection interpreted as the BHSZ. This is not the case for *Malen'kiy* but this structure is

separated more from line GAHY021. Such a link is however speculative, due to the lack of at least one more seismic profile parallel to line GAHY021 within the zone of irregularities. Furthermore, it should be noted that at the ENE part of this line, a normal BSR feature that suddenly starts to dip/oscillate around SP 220 is observed (figure 4.8b).

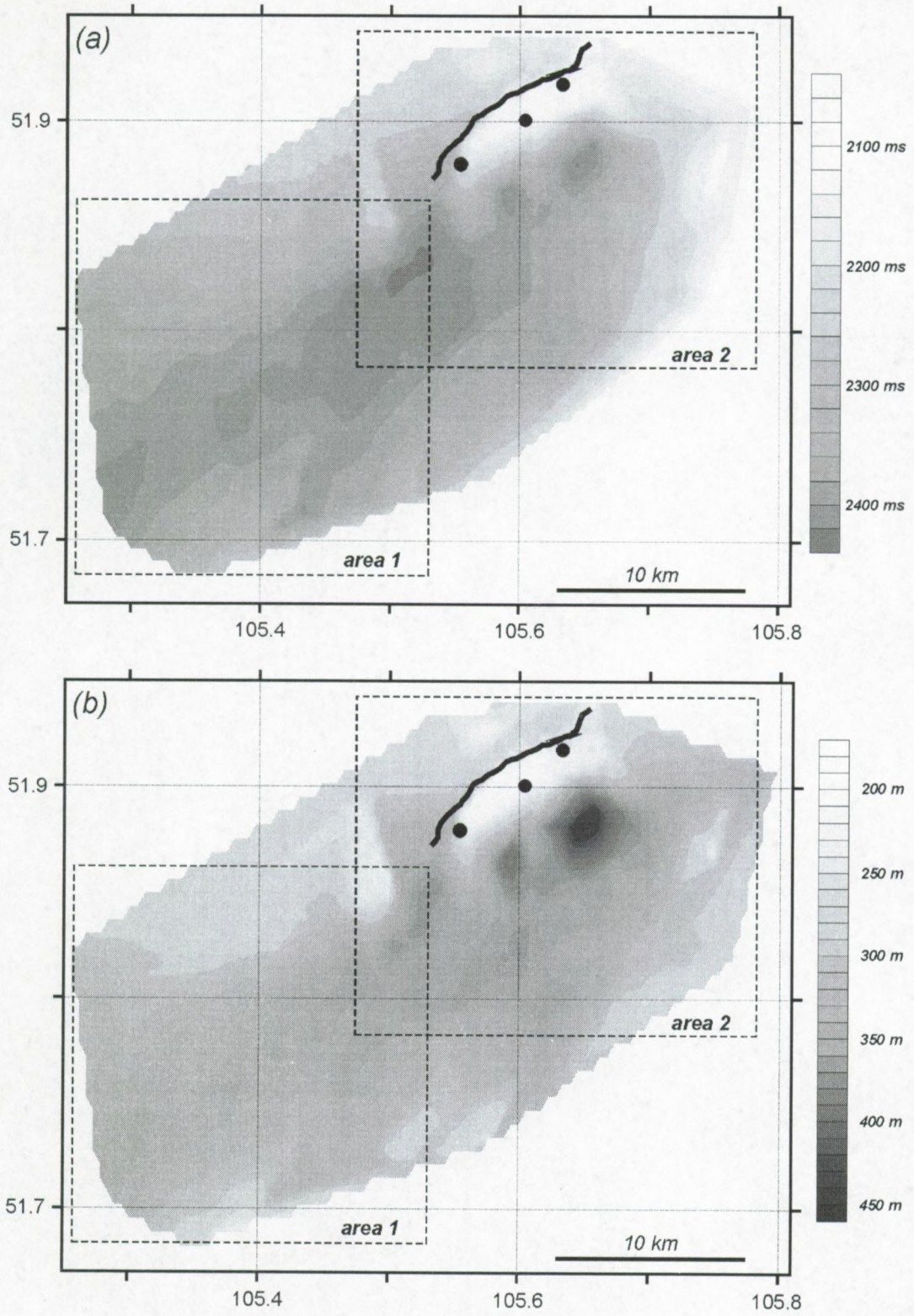

***Figure 4.18**: (a) Total depth (ms TWTT) below lake level of the basal limit of hydrate occurrence in the axial part of the Southern Baikal Basin, inferred from the GAHY-1999 reflection seismic profiles. Contour interval is 20 ms. (b) Conversion of total depth into sub-bottom depth (m) according to formulas [1-3] with contour intervals of 10 m.*

While the figures above clearly illustrate the lateral and vertical variation of the basal limit of hydrate occurrence, the magnitude of its anomalous behaviour is not exactly extracted from these figures due to the influence of bathymetry on hydrate stability conditions. Therefore, it is interesting to investigate the difference between the generally expected BSR behaviour and the observed variations of the BHSZ to obtain a rough estimate of the magnitude of the anomalous behaviour. The difficulty of such analysis lies in the observed heat flow trends and isolated heat flow anomalies in Baikal that cause the background or reference value to deviate from a uniform geothermal field approach.

Specific examples along lines GAHY021 res. GAHY030 are shown in figure 4.19 res. figure 4.20 using two different reference values being taken as the minimum inferred one in the entire area (close to the intersection of both seismic lines, but not at the deepest point of this part of Lake Baikal) and the mean value inferred from a parallel seismic line GAHY035 (figure 4.9) showing a weak but normal BSR at sub-bottom depths in agreement with the general trend (58 ± 4 $mW \cdot m^{-2}$). Anomalies of over 100-150 m sub-bottom depths over lateral distances of a few km are not rare. It is likely that these are caused by advective heat transport mechanisms. Remarkably, compared to the neighbouring BSR-behaviour, zones of exceptional deep subsidence of the BHSZ are present. Hence, these lows of the BHSZ have to be considered as an anomalous feature as well. At the ENE side of profile GAHY021 (figure 4.19), a good correlation exists with this heat flow inferred from line GAHY035. Only at the WSW side of the line, the BHSZ position lies shallower than expected. From this comparison, the lows appear to be more anomalous than the highs. This comparison suggests that there are both zones of anomalously deep and shallow extents of the HSZ.

4.5 Comparison of inferred vs. measured heat flow

The availability of heat flow measurements along the seismic profiles GAHY021 and GAHY030 provides a very interesting possibility to investigate the correlation between inferred and measured heat flow in this area of typical hydrate accumulation. The seismic data undoubtedly prove that the bottom-simulating principle of the reflection at the BHSZ is violated. A comparison of BHSZ-derived and measured heat flow values and its lateral variability might then give a rough idea of the magnitude of advective heat transport components or dewatering processes in the Baikal sedimentary section.

Table 4.5 resumes mean, minimum and maximum inferred heat flow values for the central part of the Southern Baikal Basin. Estimated heat flow values using the hydrostatic pressure assumption are 3.9 to 8.5% lower than those derived using lithostatic pressure. The average equilibrium pressure difference between the *in situ* hydrostatic and lithostatic equilibrium pressure approach (based on the *Golmshtok* velocity model) is in the order of 2 MPa (i.e. about 10%), resulting in an equilibrium temperature difference of slightly less than 1°C (approximately 5%).

A contour map of the calculated heat flow complemented with heat flow measurements is shown in figure 4.21. Only rarely the inferred (and interpolated) heat flow values exceed the measured ones. The highest heat flow measurements are found in *Malen'kiy* but repeated measurements in this specific area result in significant differences between 75-110 $mW \cdot m^{-2}$ with one exception of 165 $mW \cdot m^{-2}$. Whereas the lowest value is not atypical, the upper value clearly outstrips the other measurements in this part of the Southern Baikal Basin. It is however worth noting that similar to even much higher heat flow values are measured in other parts of the Lake, e.g. Northern Baikal Basin, NE of Selenga Delta (see figure 4.15), and in heat flow station G-171 [*Golubev, 1982*] to the NE of the side-scan sonar coverage (table 4.3).

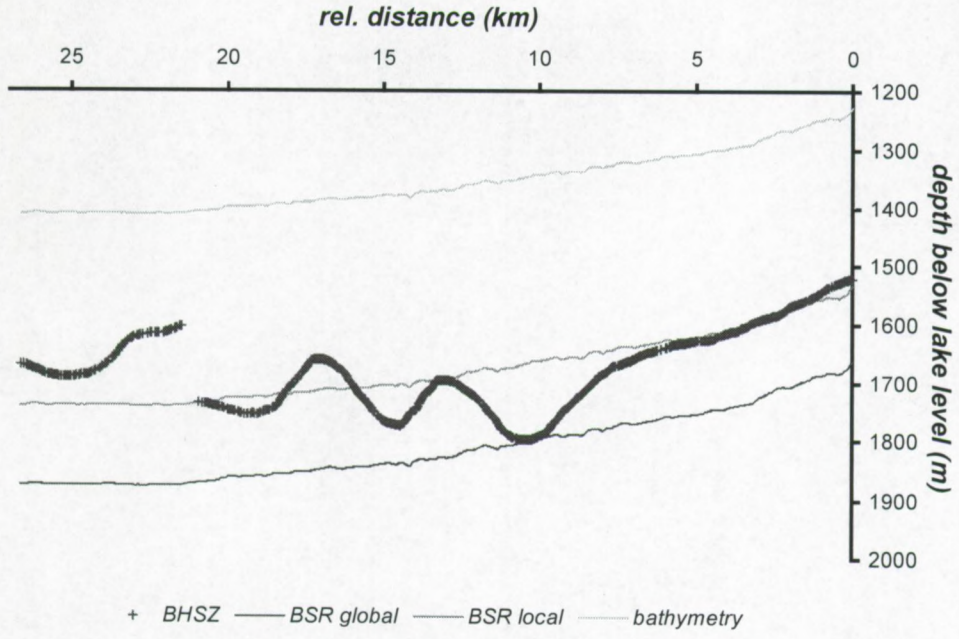

(a)

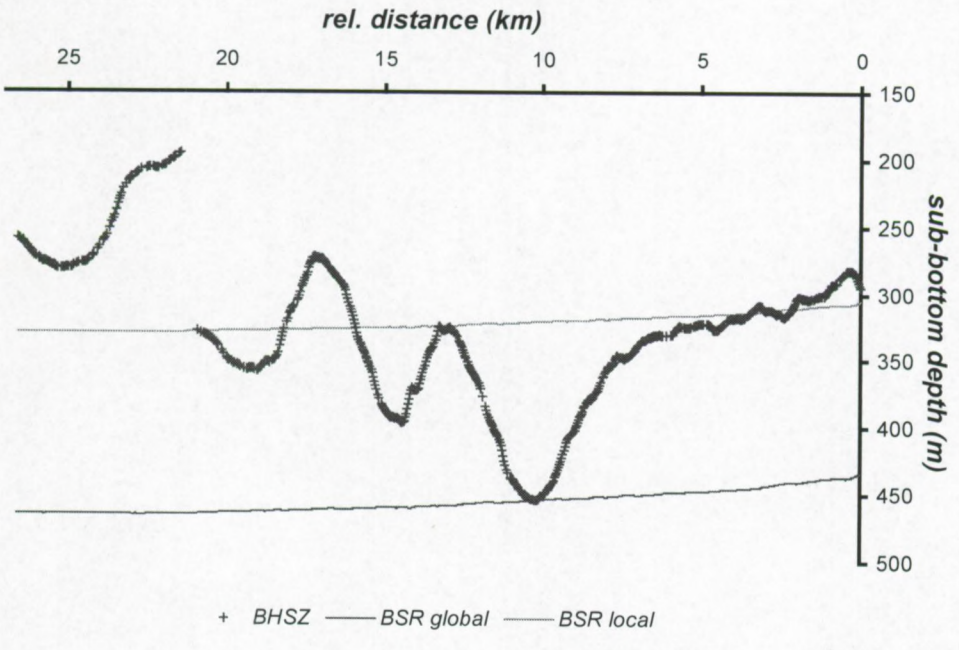

(b)

***Figure 4.19**: Magnitude of the "anomalous" behaviour of the BHSZ along line GAHY021 characterised by an undulating high-amplitude reflection, by comparing the observed sub-bottom depths with those determined in case of a global and local lateral invariant conductive heat flow. (a) total depths below lake level, (b) sub-bottom depths.*

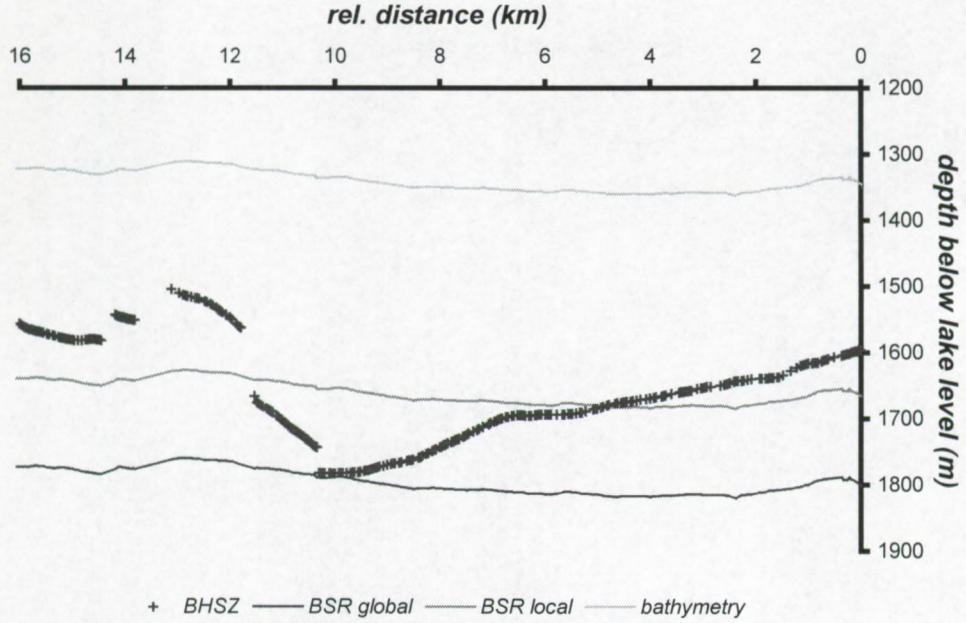

(a)

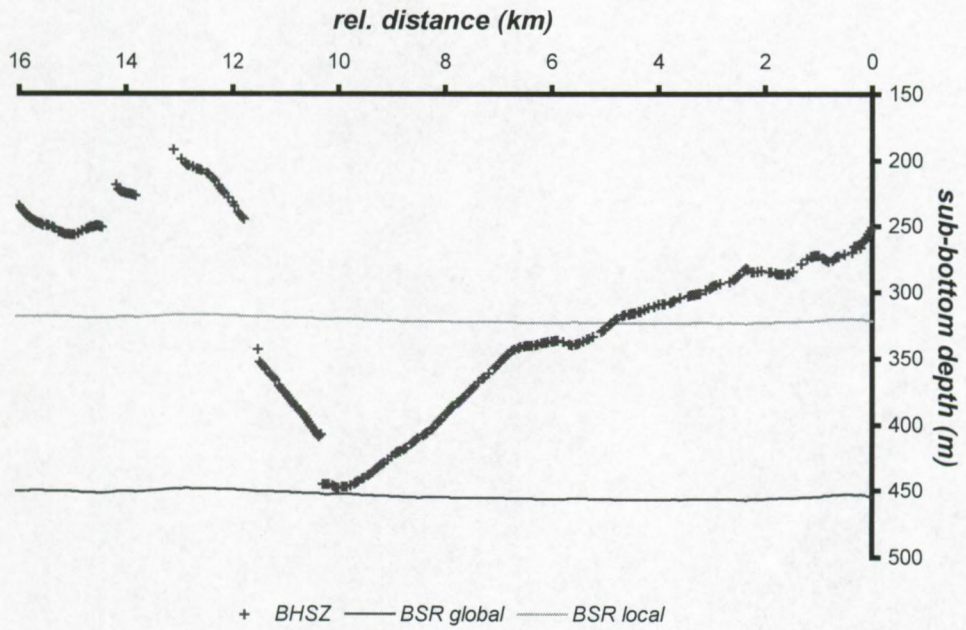

(b)

***Figure 4.20**: Magnitude of the "anomalous" behaviour of the BHSZ along line GAHY030 characterised by a fluid escape feature, by comparing the observed sub-bottom depths with those determined in case of lateral invariant conductive heat flow. (a) total depths below lake level, (b) sub-bottom depths.*

	parameter	unit	minimum	maximum	mean
	water depth	m	1227.7	1431.5	1398.9
	subbottom equilibrium limit	m	160.8	454.5	303.2
	equilibrium limit below lake level	m	1485.3	1798.7	1693.0
	in situ thermal conductivity	$W\ m^{-1}K^{-1}$	1.21	1.50	1.35
lithostatic	equilibrium pressure	MPa	16.23	20.85	18.69
	equilibrium temperature	°C	17.72	19.87	18.93
	geothermal gradient over stability field	$°C\ m^{-1}$	0.0363	0.0885	0.0524
	heat flow	$mW\ m^{-2}$	45.84	99.86	62.46
hydrostatic	equilibrium pressure	MPa	14.67	17.75	16.71
	equilibrium temperature	°C	16.84	18.49	17.97
	geothermal gradient over stability field	$°C\ m^{-1}$	0.0332	0.0850	0.0492
	heat flow	$mW\ m^{-2}$	42.00	95.94	58.67

***Table 4.5**: Mean, minimum and maximum values of the heat flow calculation process based on the inferred base of hydrate stability as observed on medium-frequency airgun profiles, acquired during the summer of 1999 in the Southern Baikal Basin. Mean values were determined over 5570 data points.*

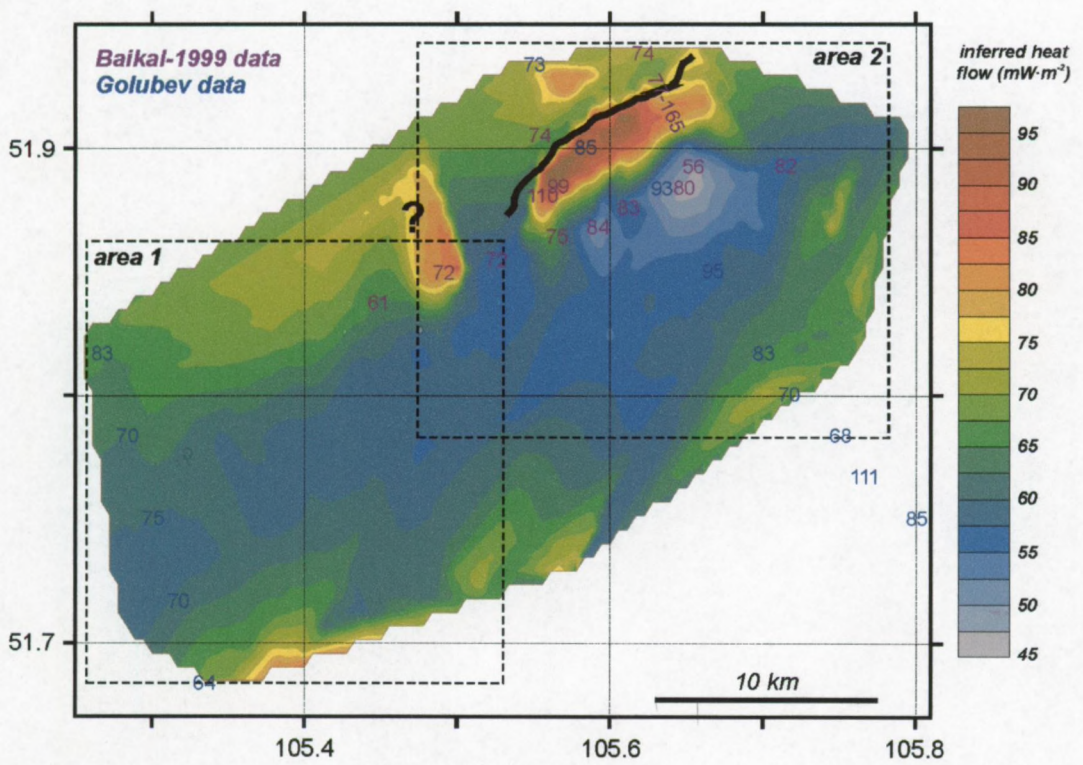

***Figure 4.21**: Inferred heat flow vs. heat flow measurements [Golubev, 1982 values in blue; Baikal-99 expedition results in pink]. The thick black line represents the antithetic fault structure. The zone of high inferred heat flow in the NE corner of area 1 and W of area 2 (see question mark) is an interpolation artefact due to poor data coverage in this part of the study area.*

Along GAHY021 (figure 4.22), deviations between measured and inferred heat flow are high, up to 40%, i.e. much more than the estimated error on both results. The heat flow measurements are higher than background values. Also the oscillating trend of this typical high-amplitude reflection is not directly translated within the nearly-coincident heat flow measurements. Along some sections of this line, inferred heat flow is exceptionally low (BHSZ lies exceptionally deep) for the area, while the local

highs give better results. In other words, extrapolation of measured heat flow with depth yields temperatures too high, compared to inferred values.

Much better correlation exists along GAHY030 (figure 4.23). The shape of the measured heat flow curve is typical for upward focused heat flow but its intensity suggests relatively cold temperatures (as is confirmed by CTD-profiling), compared to several hydrothermal venting sites observed elsewhere on the Lake Baikal lake floor [e.g. *Poort, 2000*]. Most important deviations occur where faults are present or fluid escape features exist, but the method based on conductive heat transport appears feasible.

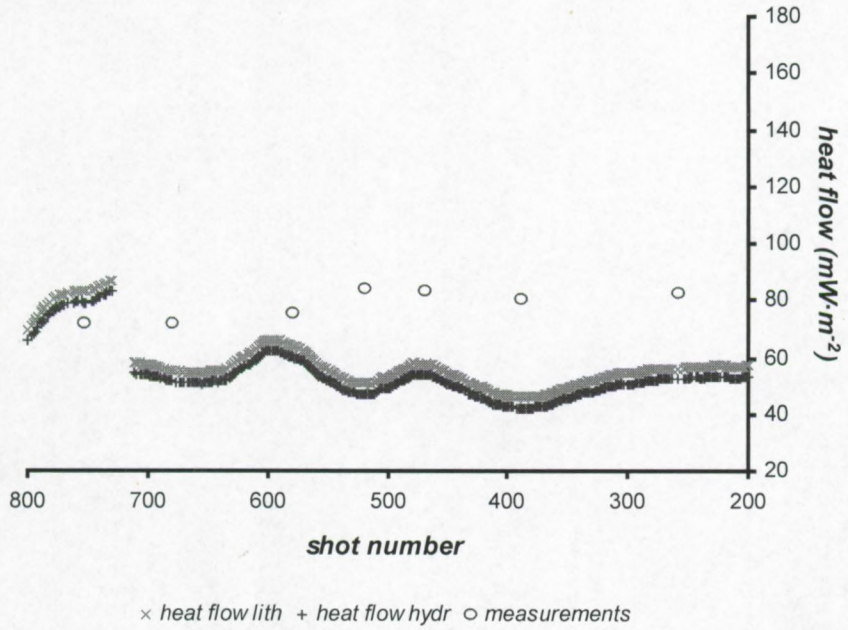

***Figure 4.22**: Measured (series HFB) and inferred heat flow along line GAHY021.*

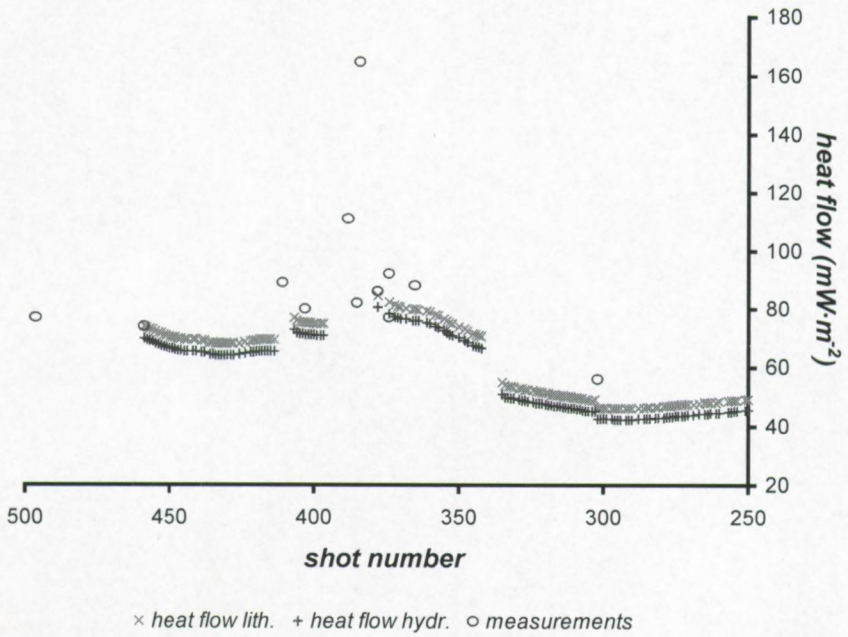

***Figure 4.23**: Measured (series HFA) and inferred heat flow along line GAHY030.*

Note that two heat flow measurements were taken close to the intersection of these two seismic lines, i.e. HFA08 (55.6 mW·m^{-2}) and HFB02 (80.2 mW·m^{-2}). The stations are located only ± 1 km apart. While

the former is in good agreement (slightly higher) with the inferred result from the seismic data, the latter lies significantly higher.

Three more heat flow values were measured, of which one is located in the immediate vicinity of *Bolshoy* and the others along GAHY023. A zoom of this seismic profile where both heat flow measurements were taken was already shown in figure 4.13c and details are given in table 4.6. For heat flow stations HFC02 and 03, the correlation between measured and inferred heat flow is very reasonable (< 15% difference). Station HFC03 is situated within the area of anomalous BSR behaviour (ENE of *Bolshoy*), similar to the acoustic section close to *Malen'kiy* (GAHY030), and hence most probably an area with enhanced or focused fluid migration. Station HFCO2 lies across the fault (N) and is lower but not anomalous compared to the heat flow trends. Heat flow measurements thus are elevated in the proximity of the elongated irregular lake floor structures. Four measurements by *Golubev* [*1982*] are located in region 1 of the study area and are also compared with inferred heat flow values. Mean inferred heat flow values in this region are 56-60 $mW \cdot m^{-2}$ and are in agreement with the general heat flow trends (50 to 70 $mW \cdot m^{-2}$).

In both areas, measured heat flow is in general higher compared to inferred heat flow values in this area. Deviations of 10 to 20 $mW \cdot m^{-2}$ are often present. Even in zone 1 where normal BSR features are observed suggesting spatial invariable geothermal conditions, such differences still occur in those few sampling points, but in this zone, correlation between seismics and heat flow data is poor. More detailed heat flow sampling in this zone should therefore be considered. These results are opposite to the observations of *Kaul et al.* [*2000*] on the Makran accretionary prism, where inferred heat flow appears to be higher than measured heat flow.

heat flow station	longitude E	latitude N	SP	depth m	BHSZ m	heat flow (mW/m^2) measured	hydr.	lith.
HFC02	105.55345	51.90487	253	1373	226	74.1	63.3	67.2
HFC03	105.56552	51.88408	334	1365	175	99.2	89.3	93.3
G-63	105.26667	51.81667	-	1369	280	83	61.7	65.4
G-65	105.30000	51.75000	-	1384	321	75	55.7	59.4
G-66	105.31667	51.71667	-	1395	319	70	55.9	59.6
G-67	105.33333	51.68333	-	1380	252	64	67.3	71.0

***Table 4.6**: Heat flow measurements (Baikal-99) vs. inferred heat flow values along line GAHY023 (above) and Golubev measurements in the study area (below). SP = shot point along seismic profile, BHSZ is sub-bottom depth.*

An explanation for the observed variations and the differences between measured and inferred heat flow is not simple and straightforward.

- ➔ Lateral variations of heat flow, both inferred and measured, are smaller in area 1 compared to area 2. Hence, in zone 1 heat transport occurs predominantly by conduction while in zone 2 fluid flow becomes more important. The fair correlation of inferred and measured heat flow along GAHY030 suggests a close connection of the disturbance of geothermal conditions in relation to anomalous BHSZ behaviour. Considering all features observed in this area, focused fluid migration forms the most reasonable explanation.
- ➔ The offset between measured and inferred heat flow, occurring even in zones without evidence for advection, might indicate that either the integrated thermal resistance [11] is overestimated or the calculated *in situ* pressure is too low and hence *in situ* equilibrium temperature from the 3-phase equilibrium curve is taken too low as well (or both).
- ➔ Several but difficult to quantify aspects may cause the discrepancy from place to place between measured and inferred heat flow. Misfits are observed especially along GAHY021 where the differences exceed both the estimated errors of the measurement and the methodology for deducing heat flow from BHSZ presence. Both methodologies are based on different parameters and measurements. Several *heat flow measurements* along this line for example suffer from highly

variable geothermal gradient measurements over the 0.5 m depth intervals [*J. Poort, pers. comm.*]. Such higher values within the upper few meters of sediment can be caused by shallow fluid flows or circulation [e.g. *Zwart et al., 1996*] with various periods [e.g. *Tryon et al., 1999*] but does not necessarily influence deeper parts of the section. Additionally, the temperature effect of purely bottom currents on heat flow measurements is unknown for Lake Baikal. Recent results *Inferred heat flow* only uses an estimate of pressure at depth, translated into equilibrium temperature. Another possibility might be the saturation degree and smaller than critical flux rates of methane from below. *Xu & Ruppel* [*1999*] conclude that a free gas zone of which the top gives rise to the reversed polarity reflection can develop well below (tens to hundreds of m) the three-phase theoretical stability limit, and thus well separated from hydrate inclusions, inducing significant errors. Also porous medium effects can play a role for *in situ* pore pressure assumptions and hence equilibrium temperature [*Clennell et al., 1999; Henry et al., 1999*], without being expressed in the probe signature. Part of the misfit between measured and inferred heat flow will also originate from the uncertainty in thermal conductivity and its extrapolation assumed in the model.

While *Golmshtok et al.* [*1997; 2000*] report an overall coincidence of inferred vs. measured heat flow with systematic differences of about 10% within the entire zones of hydrate occurrence in the Southern and Central Baikal Basins, this is not always the case in this restricted zone characterised by the irregular structures. Nevertheless, the method seems often appropriate.

4.6
Discussion: possible scenarios

The observations from the multi-disciplinary data set available obviously point towards laterally variable hydrate accumulation modes and, evidently, gas or fluid migration processes within a highly dynamic and tectonically active environment. The full scale of the acting processes is however not yet well understood. At present, only a conceptual model can be presented based on the observations and results, since several basic parameters and time scales are not known for allowing both qualitatively and quantitatively accurate modelling of the situation. Parallel lines of thoughts are being drawn and prepared for publication by *De Batist et al.*, *Van Rensbergen et al.*, and *Klerkx et al.*

4.6.1
Gas hydrate stability or instability?

The lateral variability of the HSZ on a very local scale (figure 4.18-4.22, ± 175 km²) can theoretically be either a situation of lateral changes of the hydrate stability conditions in which hydrate accumulation as observed is in equilibrium through time or a situation in which hydrate destabilisation occurs at present or occurred in the recent past. As mentioned in the introductory paragraphs, the stability of gas hydrates is dictated by specific pressure-temperature conditions, composition of the vapour phase and ionic impurities of the pore water. Hence, varying stability conditions or local destabilisation processes need to be translated into changes of at least one of these conditions.

The limited spatial extent of the zone of anomalous behaviour and its amplitude exclude several hydrate destabilising processes. *Bottom water temperature changes* with time are reported to differ only slightly from present-day conditions [*Golmshtok et al., 2000*]. Despite their time scale and dependence on heat flow in terms of hydrate stability, spatial variations of such impacts will be limited. The effect of *lake level changes* as a result of climatic changes or regional tectonism [*Colman, 1998*] will also influence the hydrate stability conditions on a regional scale and will not give rise to the local zones of irregularity. No *slide scarps* or other indications for mass wasting processes (debris

flows, slides) or sedimentary collapse structures responsible for changing the geothermal conditions and pressure distribution are observed on the acoustic sections.

The next point of importance in this debate is the *sedimentation rate* and *deposited volumes of sediments* within the area. The seismo-stratigraphic framework was worked out by *De Meersman [2000]*. Most sediment is supplied from the Selenga Delta (prograding fan units) located to the E of the study area or from the Southern border (basin-fill sediments) of the lake and is deposited in alternating sequences of variable thickness. The general pattern is one of decreasing thickness of the units towards the antithetic faults and the *Posolskaya* fault zone (N). The trend of the BHSZ e.g. along GAHY025 follows more or less the stratigraphic pattern, disrupted by the antithetic fault, but this is not the case along GAHY021. The thickness of the uppermost packages of sediments (> 100 m) seems uniform along the SSE-NNW running lines and hence its deposition will not result in lateral changes of temperature and pressure within these sedimentary sections. Thus, the influence of sedimentation can most probably be ignored as well.

Variability of the *gas composition* can also be thought responsible for changing both the heat flow inferred from the seismic data and equilibrium sub-bottom depths of hydrate stability (see §4.1). Such composition change was put forward by *Posewang & Mienert [1999]* for explaining the observed double BSR structures on the Norwegian Margin. The authors state that it is questionable whether the gas composition and migration through a nearly uniform sedimentary section can change and what the origin of such change could be. The first analyses of the composition of deeper-seated hydrates (BDP-1997) in a zone of normal BSR behaviour and those retrieved from *Malen'kiy* about 17 km more to the NE are furthermore in good agreement and hence this possibility can be ruled out most probably.

The very *local character of the anomalies and its magnitude* suggests significant energy input from below. The best alternative is a change in the sub-bottom temperature distribution coming from within the system. The primary candidate then is heat flow that can be supplied by conduction and convection. Fluids can be part of a more regional hydrothermal circulation system or flow laterally over long distances along permeable layers and hence follow more or less the local dipping stratigraphy. Sediments can contain large quantities of pore water and other fluids, and because of the high mobility and thermal capacity of water, it is capable of severely distorting the conductive heat flow. The fair correlation between inferred and measured heat flow values along GAHY030 passing *Malen'kiy* confirms the link between the anomalous BHSZ distribution and heat flow. The observed behaviour can then still be explained by either a constant heat flow through time or an episodic heat pulse and subsequent *in situ destabilisation* of the gas hydrates.

The presence of several *active fluid escape features* lined up *parallel to the active fault* but exactly in the area of the *strongest lateral change* of hydrate accumulation and free gas occurrence can hardly be considered as a coincidence. Knowing that the Baikal Rift Zone is tectonically very active [*Solonenko et al., 1997*], it is reasonable to assume that faulting and fracturing can be important processes for hydrate formation, by means of forming ideal conduits for gas supply towards the HSZ [e.g. *Booth et al., 1998; Hovland et al., 1997*]. On the other hand, recent tectonic activity can be responsible as well for disturbing the present hydrate accumulations, due to the sudden release of heat or hot water injection at the initial stability limit. It is therefore considered that the observed anomalous hydrate distribution is caused by a transient or episodic thermal pulse (or series of pulses).

4.6.2
Influence of active tectonics on gas hydrate stability

One of the key questions to be solved concerns the origin of the active fluid escape features aside the antithetic fault and why these events are only observed within this zone of anomalous hydrate occurrence. The answer probably has to be found in tectonic activity with fluid expulsion and subsequent hydrate dissociation generating a second advection cell. In the previous chapter, it was shown that small intra-basinal faults and folding do not necessarily affect the BSR continuity neither

the vertical extent of the HSZ. The data available do not evidence fluid escape features in other parts of the lake [*De Batist et al., in prep.*]. In diverse hydrate provinces, associations between fluid escape features (e.g. diapirs, mud volcanoes, pockmarks), gas hydrates, hydrate dissociation, shallow gas accumulations, excess pore pressure, faulting, slope instability, ... are often suggested for a variety of geological situations and conditions [e.g. *Hovland & Judd, 1988; Schmuck & Paull, 1993; Paull et al., 1995; Dillon et al., 1998; Mienert et al., 1998; Tryon et al., 1999; Suess et al., 1999b; Milkov, 2000; Wiprut & Zoback, 2000; Egeberg, 2000*]. Heat flow from rifting or faulting is for Lake Baikal conditions the most profound candidate to dissociate hydrates on short to long time scales.

Lake Baikal is one of the tectonically most active regions in the world. Several epicentres of earthquakes with magnitude > 5 are located within the Lake Baikal area of which some occur close to *Posolskaya* Bank [*Solonenko et al., 1997*]. In case of tectonic activity within the Southern Baikal Basin, it is reasonable to assume that the major thermo-active intra-basinal *Posolskaya* fault zone will play a central role. In the model, it is supposed that energy is released under the form of a thermal pulse from reactivation or dilatation of the *Posolskaya* fault and related minor faults, e.g. the observed antithetic fault. Heat is then supplied via frictional heat associated with slip movement along the fault segments in combination with focused pulses of hot water injected within the different faults disturbing the *in situ* temperature distribution. Both aspects are confined in time and in space and are in principal guided by the fault planes. Further seismicity can then be triggered as well by such fluid flow and can result in additional faulting and fracturing. The energy released will then also expand or spread out within the neighbouring sedimentary sections by both conduction and advection.

Once the zone of initial hydrate stability is reached, the flow will then slow down due to hydrate inclusions reducing the permeability. The flow will gradually cool due to e.g. the conversion of energy during hydrate dissociation while at the same time the flow will dissipate also laterally and further initiate hydrate dissociation along its paths. Such hydrate decomposition will create overpressure within the pore spaces of the sediments until the thermal pulse ceases or until excess pressure can dissipate, either laterally or vertically.

The sudden pulse argues for rather fast build-up of overpressures at shallow depths. The two-phase flow of free gas and pore water can result in different propagation orientations due to the buoyancy component inherent to the gas phase. This injection of excess pressure can lead to hydraulic fracturing of the overlying sediments and allow nearly-vertical upward migration of overpressured gas-rich mud. Therefore, the pressure should exceed the vertical stress on top of the overpressured cell. The hydrate gas expansion coefficient of approximately 155 volumes per volume of hydrate (STP) and the high compressibility of the gas phase is responsible for such elevated pressures. Alternatively, excess pore pressure within a gas trap can also result in sedimentary collapse, but this is not conform the data available.

Gas discharge throughout the HSZ will continue with variable intensity dependent on the pressure gradient, until the gas reservoir is depleted or the conduit is sealed. Only a fraction of the rapidly moving gas-enriched fluid discharge volume will, once within favourable stability conditions, form new gas hydrate crystals while the remainder will escape at the lake floor, resulting in the typical fluid escape features observed.

Hence, the source of the lake floor seeps is thought to be hydrate destabilisation. With time, this pulse will be completely worked out and the system will settle back to new equilibrium conditions. Such tectonically driven pulses occur episodic, but can be repeated with different magnitudes depending on the tectonic stresses and activity. The absence of temperature anomalies at the lake bed suggests that either the event did come to a halt recently or that nearly all of the energy supplied is converted into latent heat required for hydrate dissociation. The fact that the fluid escape features are clearly visible at the lake floor without significant packages of sediments draped over them, this demonstrates recent activity, what does not prove that the individual features were all active or originated at the same time.

4.6.3
Remaining questions

The hypothesis outlined above tries to explain the observed behaviour on the data sets in terms of tectonic pulses resulting in hydrate dissociation that in turn causes a second fluid flow mechanism giving rise to the fluid escape structures and cold seeps. However, the exact conditions and time scale under which such a process takes place are poorly constrained and require modelling of mass and heat flow vs. hydrate dissociation and detailed analyses of all sampled material. Quantifying these processes will be very difficult since the dynamic behaviour of the entire system as a whole including hydrate formation and dissociation is yet unknown.

The system becomes even more complicated due to its presence in an active rift zone. The picture should therefore be drawn within the full tectonic setting of the area. *Tectonic uplift* resulting in lowering the *in situ* pressures and thus forcing the system into less favourable hydrate stability conditions is thought to be of importance for hydrate stability in the Lima Basin, offshore Peru [*Von Huene & Pecher, 1999*]. There is some evidence for uplift of the *Posolskaya* bank horst, starting during the Pliocene [*Levi et al., 1997*]. The question is whether such uplift is compatible with the extension of the Baikal Rift [*Klerkx et al., in prep.*] and what the consequences are – concurrent to subsidence – for hydrate stability in this peculiar region. Furthermore, also horizontal stress components should be taken into account.

All data available, also from the winter 1999-2000 expedition of which only preliminary results were reported only very recently (VI International Conference on Gas in Marine Sediments, September 2000), should be combined to test and/or modify this hypothesis. One example, within *Malen'kiy*, anomalously high pore water Cl^- concentrations (accompanied with increased Na^+) are measured and linked to seepage of high-mineralised ground water along tectonic faults [*Granina et al., 2000*] which seems in agreement with the model presented here. The full scope of this topic cannot be revealed without detailed geochemical analyses (pore water chemistry, hydrate composition, isotopic compositions, etc.). Therefore more sampling is necessary, both in zones of regular and irregular hydrate distribution and fluid escape features.

The possible association of two of the local highs of the undulating BHSZ reflection on line GAHY021 with *Bolshoy* and *Stariy* situated approximately 2 res. 3 km N of these highs is striking but not proved to be true. Unfortunately, there is an important seismic data gap between the antithetic fault and line GAHY021. Note that these local highs are characterised by higher reflection coefficients interpreted as evidence for higher gas concentrations beneath the highs. Fluid flow cannot simply be regarded as 2D flow since fluids flow in a complex non-homogeneous pattern controlled by sediment heterogeneities and fault geometries [e.g. *Lawrence & Cornford, 1995*]. This observation might indicate migration of gases or gas-enriched fluids first to the local highs (buoyancy), trapped by hydrates and then being funnelled towards the fluid escape features, i.e. in SE-NW direction nearly perpendicular to the fault located further N. In this way, the fluid escape structures may attract fluids from the surrounding areas and form a key feature for the local hydrology, additionally disrupting the local geothermal conditions in an asymmetric way and intensifying the process running. The stratigraphic pattern characterised by the dipping strata (slopes exceeding 5°) from the *Posolskaya* fault into the deep basin might also facilitate such lateral fluid flow towards *Posolskaya*.

Other unsolved questions concern the presence of zones of anomalously deep subsidence of the high-amplitude reversed-polarity reflections interpreted to be the BHSZ and whether this is related as well to the fluid escape structures further N. The oscillating reflection is furthermore only observed on one single location, but still close to the zone of fluid escape features. The biggest anomaly is found in the vicinity of the intersection of GAHY021 and GAHY030 (see figure 4.18-4.20). This behaviour is difficult to explain, except if background heat flow in these places really is exceptionally low, a hypothesis that is contradicted by heat flow measurements along this line while in most other cases correlation between inferred and measured heat flow is much better. The deviation suggests that both deep and shallow processes are active.

An alternative for the deep anomalies can be a kind of flow mechanism extracting energy at depth from these zones towards the neighbouring sites of BHSZ up-welling (convectional cells) that may or may not be related to either the fluid escape structures or hydrate formation/dissociation cycles. Another possibility is the saturation degree and smaller than critical flux rates of methane. *Xu & Ruppel [1999]* conclude that a free gas zone of which the top gives rise to the reversed polarity reflection can develop well below the 3-phase theoretical stability limit and thus separated from hydrate inclusions. But then the question arises whether this is compatible with the continuous character of this reflection and with its crosscutting behaviour. Thus what causes gas being trapped along an irregular surface?

The nature of this unique feature will be very difficult to verify without deep drilling and without knowing accurately the partial hydrate saturation factors within the sub-surface along this line in relation with free gas zones.

4.7 Conclusions

The multi-disciplinary data set revealed the occurrence of closely-spaced normal (area 1) and anomalous features (area 2) related to gas hydrates and free gas accumulations within the Southern Baikal Basin without any topographical control on their distribution and occurrence. Fluid escape features (cold seeps) are observed on side-scan sonar data within the area where a kind of "hydrate anticline" or free gas dome is replacing the commonly expected hydrate distribution (BSR). This interface is delineated by the up-dipping high-amplitude reversed-polarity reflections at the BHSZ observed on e.g. MC92_02 and the medium-frequency airgun profiles perpendicular to the antithetic fault. This anticline is bounded to the N by an antithetic fault in the hanging wall of the large *Posolskaya* fault zone and stretches to the S near two closely spaced parallel seismic lines. One (GAHY021) is characterised by a high-amplitude oscillating negative-polarity crosscutting reflection while the other (GAHY035) shows a normal but weak BSR feature and limits the zone of inferred anomalies to the S. To the E (MC92_04) and W (area 1) of this area, normal BSR features are observed. N of the antithetic fault, a short faint BSR-like feature is observed at about mean sub-bottom depths compared to the situation in the entire study area. This BSR fades out closer to *Posolskaya*.

Comparing OBH results with modelled theoretical interval velocity curves based on empirical reference profiles reveals a partial hydrate saturation of 5-8% within a sub-bottom depth interval of 125-295 m. Indirect geophysical evidence of free gas accumulation and migration is abundant in this area, and is more pronounced than in the area 1 with normal BSR distribution. The presence of a BSR or BHSZ is indicative of free gas presence. On medium-frequency seismic profiles, negative-polarity reflections penetrate the BSR/BHSZ and point towards a meta-stable situation of seepage or accumulation of gases within the HSZ within specific stratigraphic or lithological units. Such evidence was only occasionally observed in zone 1. Other free gas pockets or enhanced reflections are characteristic for most of the acoustic sections. The order of magnitude of the reflection coefficients along the oscillating BHSZ are in agreement with those along a normal BSR event, but scattering is higher. There is a trend of increasing reflection coefficient (more negative!) under the local highs, suggesting higher concentrations of free gases compared to the lows of this reflection. Fluid escape is observed on echo-sounding, and is confirmed by the presence of a gas chimney on one acoustic section. Increasing reflection amplitudes with increasing offset (AVO) also indicates the presence of free gas beneath the reflective interface. Gas hydrate occurrence at or immediately beneath the lake bed also requires fluid migration on a regular base to form hydrates and to guarantee their chemical stability. The plumes coming out of the fluid escape structures have higher than background methane concentrations. The continuity of the BHSZ vs. enhanced reflections appears different on the one low-frequency airgun-

array line (92_02) crossing the zone of inferred anomalies, and lying rather close to some of the RCMG-1999 GAHY seismic lines. This MC line shows a distinct and continuous reversed-polarity reflection at the BHSZ that gets shallower towards *Stariy* over about 3-4 km, while the SC lines appear discontinuous. This observation suggests that the imaging of the behaviour depends on acoustic frequency used as discussed above or that the discontinuity appeared very recently, i.e. during 1992-1999...

One of the key aspects is the magnitude of the observed anomalous behaviour and its lateral variability. Differences can be in the order of hundreds of m. Vertical displacement of the BHSZ exceeds the actual fault displacement. Correlation between measured and inferred heat flow is often appropriate. Generally, heat flow measurements exceeds in most cases the inferred heat flow, even in area 1 where advective components can most probably be ruled out. This can be caused by either shallow circulation patterns or by misfits in the thermal conductivity profile assumed. Along one seismic line with anomalously deep buried BHSZ, the correlation is poor, a feature that is at present not well understood.

The presence of several venting structures (*Malen'kiy*, *Stariy* and *Bolshoy*) and the tectonic setting of the study area appear closely related to the observed typical hydrate wedge and free gas accumulations. Coincidence with elevated heat flow values and higher than normal methane concentrations in the plumes argue for a causal link between tectonic pulses, heat and focused fluid flow, hydrate destabilisation and subsequent fluid escape. In the model proposed, tectonic activity is the driving force for enhanced heat and fluid flow from depth by means of focused and branched migration through faults and fractures towards the base of initial HSZ. Heat is absorbed by the hydrate crystals starting to decompose relatively fast resulting in the generation of overpressures. If this excess pressure cannot dissipate fast enough, total vertical stress can be balanced or exceeded by the mud phase and hydraulic fracturing can occur. The gas-rich mud will rise to the surface and form the fluid escape features observed. Whether such process is powerful enough to alter the local hydrology and cause in this way the typical oscillations of the BHSZ is unclear.

Additional analyses, modelling and drilling should be carried out to validate or modify this hypothesis. At present, not sufficient details are known about e.g. the factual hydrate distribution, pore water chemistry, heat and mass flows and rate, and the tectonic activity with time. No adequate explanation is found for the oscillation of the BHSZ. Especially the lows seem anomalous while heat flow measurements show another picture. This should be a challenge for further research activities.

References

Bangs, N.L. & Brown, K.M. [1995]. *Regional heat flow in the vicinity of the Chile triple junction constrained by the depth of the bottom simulating reflection*, Proceedings of the Ocean Drilling Program, Scientific Results, **141**, 253-258 [GH].

Bohrmann, G., Greinert, J., Suess, E. & Torres, M. [1998]. *Authigenic carbonates from the Cascadia subduction zone and their relation to gas hydrate stability.* Geology, **26** (7), 647-650.

Bouriak, S., Vanneste, M. & Saoutkine, A. [2000]. *Inferred gas hydrates and clay diapirs near the Storegga slide on the southern edge of the Vøring Plateau, offshore Norway.* Marine Geology, **163**, 125-148.

Brooks, J.M., Cox, H., Bryant, W. et al. [1986]. *Association of gas hydrates and oil seepage in the Gulf of Mexico.* Organic Geochemistry, **10**, 221-234.

Clennell, M.B., Hovland, M., Booth, J., Henry, P. & Winters, P. [1999]. *Formation of natural gas hydrates in marine sediments: 1. Conceptual model of gas hydrate growth conditioned by host sediment properties.* Journal of Geophysical Research, 104 (B10), 22985-23003.

Colman, S. [1998]. *Water level changes in Lake Baikal, Siberia: Tectonism vs. Climate.* Geology, **26** (6), 531-534.

Cranston, R.E., Ginsburg, G.D., Soloviev, V.A. & Lorenson, T.D. [1994]. *Gas venting and hydrate deposits in the Okhotsk Sea.* In Gas in Marine Sediments, 2nd conference [ed. Jorgenson, N.O.], Bulletin of the Geological Society of Denmark, **41** (1), 80-85.

De Batist, M., De Meersman, K., Hus, R.& Poort, J. [in preparation]. *Lake Baikal 1999 Expedition Report.* Internal RCMG report.

De Batist, M., Klerkx, J., Vanneste, M., Poort, J., Van Rensbergen, P., De Meersman, K., Golmshtok, A.Y., Kremlev, A.N. & Khlystov, O. [in prep.]. *Tectonic activity induced gas hydrate destabilisation and gas venting in Lake Baikal, Siberia.*

De Meersman, K. [2000]. *Reflectie- en refractieseismische studie van gashydraathoudende sedimenten in het Baikal Meer, Siberië.* Unpublished M.Sc. thesis, University of Gent, pp. pp.

Dillon, W.P., Danforth, W.W., Hutchinson, D.R., Drury, R.M., Taylor, M.H. & Booth, J.S. [1998]. *Evidence of faulting related to dissociation of gas hydrate and release of methane off the southeastern United States.* in Henriet, J.P. & Mienert, J. (eds.), *Gas hydrates: relevance to world margin stability and climatic changes,* Special Publication of the Geological Society of London, 293-302.

Duchkov, A.D. & Kazantsev, S.A. [1996]. *Temperature measurement in the first underwater boreholes in Lake Baikal,* Russian Geology and Geophysics, **37** (6), 94-102.

Egeberg, P.K. [2000]. *Hydrates associated with fluid flow above salt diapirs (site 996).* In Paull, C.K. *et al.* (eds.), Proceedings of the Ocean Drilling Program, Scientific Reports, **164**, 219-228.

Egorov, A.V., Crane, K., Vogt, P.R. & Rozhkov, A.N. [1999]. *Gas hydrates that outcrop on the sea floor: stability models.* Geo-Marine Letters, **19**, 68-75.

Eldholm, O., Thiede, J. & Taylor, E. [1987]. Proceedings of the Ocean Drilling Program, initial reports, Leg **104**, College Station, TX (Ocean Drilling Program).

Ganguly, N., Spence, G.D., Chapman, N.R. & Hyndman, R.D. [2000]. *Heat flow variations from bottom-simulating reflectors on the Cascadia Margin.* Marine Geology, **164**, 53-68.

Ginsburg, G.D. [1998]. *Gas hydrate accumulation in deep water marine sediments.* in Gas hydrates: relevance to world margin stability and climatic change [Ed. J.-P. Henriet & J. Mienert], p. 51-62.

Ginsburg, G.D. & Soloviev, V.A. [1997]. *Methane migration within the sub-marine gas-hydrate stability zone under deep-water conditions.* Marine Geology, **137**, 49-57.

Golmshtok, A.Ya., Duchkov, A.D., Hutchinson, D.R., Khanukaev, S.B. & Elnikov, A.I. [1997]. *Estimation of heat flow on Baikal from seismic data on the lower boundary of the gas hydrate layer.* Russian Geology and Geophysics, **38**, 1714-1727.

Golmshtok, A.Y., Duchkov, A.D., Hutchinson, D.R. & Khanukayev, SB. [2000]. *Heat flow and gas hydrates of the Baikal Rift zone.* International Journal of Earth Sciences, **89** (2), 193-211.

Golubev, V.A. [1982]. *Geothermics of Baikal.* Nauka, Novosibirsk, pp. 150.

Golubev, V.A., Klerkx, J. & Kipfer, R. [1993]. *Heat-flow, hydrothermal vents and static stability of discharging thermal water in Lake Baikal (south-eastern Siberia).* Bulletin des Centres de recherches Exploration-Production Elf-Aquitaine, **17**, 53-65.

Granina, L., Golobokova, L., Zemskaya, T., Khlystov, O., Granin, N. & the Baikal-2000 team [2000]. *Geochemical characteristics of the surface sediments in the region of gas hydrate occurrence in Southern Lake Baikal.* in VI International Conference on Gas in Marine Sediments, St.-Petersburg, Abstract book, 37-39.

Granin, N.G., Klerkx, J., Zhdanov, A.A., Gnatovsky, R.Y. & Tcekhanovsky, V.V. [2000]. *The influence of methane venting on the hydrophysics of Lake Baikal.* in VI International Conference on Gas in Marine Sediments, St.-Petersburg, Abstract book, 40-42.

Hamilton, E.L. [1980]. *Geo-acoustic modelling of the sea floor.* Journal of the Acoustical Society of America, **68** (5), 1313-1340.

Henry, P., Thomas, M.& Clennell, M.B. [1999]. *Formation of natural gas hydrates in marine sediments: 2. Thermodynamic calculations of stability conditions in porous media.* Journal of Geophysical Research, 104 (B10), 23004-23022.

Hovland, M., Gallagher, J.W., Clennell, W.B. & Lekvan, K. [1997]. *Gas hydrate and free gas volumes in marine sediments: Example from the Niger delta front.* Marine and Petroleum Geology, 14 (3), 245-255.

Hovland, M. & Judd, A.G. [1988]. *Seabed pockmarks and seepages: impact on geology, biology and the marine environment.* Graham & Trotman Ltd., London, pp. 293.

Hutchison, I., 1985. The effects of sedimentation and compaction on oceanic heat flow. *Geophysical Journal of the Royal Astronomical Society*, **82**, 439-459.

Hyndman, R.D. & Spence, G.D. [1992]. *A seismic study of methane hydrate marine bottom simulating reflectors.* Journal of the Geophysical Research, 97 (B5), 6683-6698.

Kaul, N., Rosenberger, A. & Villinger, H. [2000]. *Comparison of measured and BSR-derived heat flow values, Makran accretionary prism, Pakistan.* Marine Geology, **164**, 37-51.

Klerkx, J., Hus, R., De Batist, M., Van Rensbergen, P. & Poort, J. [2000]. *The structural control of the methane venting area in the southern basin of Lake Baikal, Siberia.* in VI International Conference on Gas in Marine Sediments, St.-Petersburg, Abstract book, p. 57.

Klerkx, J. *et al.* [in prep.]. *Structural framework of the gas venting area in the Southern Basin of Lake Baikal.*

Kvenvolden. K.A. [1998]. *A primer on the geological occurrence of gas hydrate.* in *Gas hydrates: relevance to world margin stability and climatic change* [Ed. J.-P. Henriet & J. Mienert], p. 9-30.

Lawrence, S.R. & Cornford, C. [1995]. *Basin geofluids*, Basin Research, **7**, 1-7.

Lee, M.W., Hutchinson, D.R., Collett, T.S. & Dillon, W.P. [1996]. *Seismic velocities for hydrate-bearing sediments using weighted equation.* Journal of Geophysical Research, **101**, 20347-20358.

Levi, K.G., Miroshnichenko, A.I., San'kov, V.A., Babushkin, S.M., Larkin, G.V., Badardinov, A.A., Wong, H.K., Colman, S. & Delvaux, D. [1997]. *Active faults of the Baikal depression.* Bulletin des Centres de recherches Exploration-Production Elf-Aquitaine, **21**, 399-431.

Mienert, J., Posewang, J. & Baumann, M. [1998]. *Gas hydrates along the north-eastern Atlantic margin: possible hydrate bound margin instabilities and possible release of methane.* in Henriet, J.-P. & Mienert, J. (eds); *Gas hydrates: Relevance to world margin stability and climatic change*, Geological Society of London, Special Publication, 137, 275-291.

Milkov, A. [2000]. *Worldwide distribution of mud volcanoes and associated gas hydrates.* Marine Geology, **167**, 29-42.

Minshull, T., Singh, S. & Westbrook, G. [1994]. *Seismic velocity structure at a gas hydrate reflector, offshore western Colombia, from waveform inversion.* Journal of Geophysical Research, **99**, 4715-4734.

Nobes, D.C., Villinger, H., Davis, E.E. & Law, L.K. [1986]. *Estimation of marine sediment bulk physical properties at depth from seafloor geophysical measurements.* Journal of Geophysical Research, **91** (B14), 14033-14043.

Paull, C.K., Ussler III, W., Browske, W.S. & Spiess, F.N. [1995]. *Methane-rich plumes on the Carolina continental rise: association with gas hydrates.* Geology, **23** (1), 89-92.

Paull, C.K., Borowski, W.S., Rodriguez, N.M. & the ODP Leg 164 Shipboard Scientific Party [1998]. *Marine gas hydrate inventory: preliminary results of ODP Leg 164 and implications for gas venting and slumping associated with the Blake Ridge gas hydrate field.* in *Gas hydrates: relevance to world margin stability and climatic change* [Ed. J.-P. Henriet & J. Mienert], p. 153-160.

Peacock, D.C.P., Knipe, R.J. & Sanderson, D.J. [2000]. *Glossary of normal faults.* Journal of Structural Geology, **22**, 291-305.

Pearson, C.F., Halleck, P.M., McGulre, P.L., Hermes, R. & Mathews, M. [1983]. *Natural gas hydrate: a review of in situ properties.* Journal of Physical Chemistry, **87**, 4180-4185.

Poort, J. [2000]. *Significance of the surface heat flow in the Baikal Rift: inferences from spatial heat flow analysis and numerical modelling.* Unpublished Ph.D. thesis, Vrije Universiteit Brussel, Belgium, pp. 112.

Posewang, J. & Mienert, J. [1999]. *The enigma of double BSRs: Indicators for changes in the hydrate stability field?* Geo-Marine Letters, **19**, 157-163.

Rempel, A.W. & Buffett, B.A. [1998]. *Mathematical models of gas hydrate accumulations.* in Henriet, J.-P. & Mienert, J. (eds); *Gas hydrates: Relevance to world margin stability and climatic change*, Geological Society of London, Special Publication, 137, 63-74.

Sherstyankin, P.P. & Kuymoua, L.N. [1992]. Doklady Academii Nauk, **324** (1), 187-190 [In Russian].

Singh, S.C. & Minshull, T.A. [1994]. *Velocity structure of a gas hydrate reflector at Ocean Drilling Program Site 889 from a global seismic waveform inversion.* Journal of Geophysical Research, **99** (B12), 24221-24233.

Schmuck, E.A. & Paull, C.K. [1993]. *Evidence for gas accumulation associated with diapirism and gas hydrates at the head of the Cape Fear Slide.* Geo-Marine Letters, **13**, 145-152.

Solonenko, A., Solonenko, N., Melnikova, V & Shteiman, E. [1997]. *The seismicity and earthquake focal mechanisms of the Baikal Rift Zone.* Bulletin des Centres de recherches Exploration-Production Elf-Aquitaine, **21**, 207-231.

Spence, G.D., Minshull, T.A. & Fink, C. [1995]. *Seismic studies of methane gas hydrate, offshore Vancouver Island,* Proceedings of the Ocean Drilling Program, Scientific Results, **146**, 163-174.

Suess, E., Bohrmann, G., Greinert, J. & Lausch, E. [1999a]. *Flammable Ice.* Scientific American, November, 52-59.

Suess, E., Torres, M.E., bohrmann, G., Collier, R.W., Greinert, J., Linke, P., Rehder, G., Trehu, A., Wallmann, K., Winckler, G. & Zuleger, E. [1999b]. *Gas hydrate destabilisation: enhanced dewatering, benthic material turnover and large methane plumes at the Cascadia convergent margin.* Earth and Planetary Science Letters, **170**, 1-15.

Tinivella, U. [1999]. *A method for estimating gas hydrate and free gas concentrations in marine sediments*, Bolletino di Geofisica Teoretica ed Applicata, **40** (1), 19-30.

Tryon, M.D., Brown, K.M., Torres, M.E., Tréhu, A.M., McManus, J. & Collier, R.W. [1999]. *Measurements of transience and downward fluid flow near episodic methane vents, Hydrate Ridge, Cascadia.* Geology, **27** (12), 1075-1078.

Vanneste, M. [1999]. *Lake Baikal 1999 Expedition Proposal*, RCMG internal report, pp. 10.

Vanneste, M., De Batist, M., Golmshtok, A., Kremlev, A. & Versteeg, W. [in press]. *Multi-frequency seismic study of the gas hydrate bearing sediments in Lake Baikal, Siberia.* Marine Geology. 172 1-21

Van Rensbergen, P., De Batist, M., Klerkx, J., Poort, J., Hus, R., Vanneste, M., Granin, N. & Krinitsky, P. [2000]. *Side-scan sonar evidence of cold seeps in Lake Baikal, Siberia.* in VI International Conference on Gas in Marine Sediments, St.-Petersburg, Abstract book, 138-139.

Van Rensbergen *et al.* [in prep.]. *Sub-lacustrine mud volcanoes and cold seeps caused by dissociation of gas hydrates in Lake Baikal.*

Von Huene, R. & Pecher, I. [1999]. *Vertical tectonics and the origin of BSRs along the Peru margin.* Earth and Planetary Science Letters, **166**, 47-55.

Wiprut, D. & Zoback, M.D. [2000]. *Fault reactivation and fluid flow along a previously dormant normal fault in the northern North Sea.* Geology, **28** (7), 595-598.

Whalley, E. [1980]. *Speed of longitudinal sound in clathrate hydrates*, Journal of Geophysical Research, **85** (B5), 2539-2542.

Xu, W. & Ruppel, C. [1999]. Predicting the occurrence, distribution and evolution of methane gas hydrates in porous marine sediment. Journal of Geophysical Research, **104**, 5081-5096.

Yamano, M., Uyeda, S., Aoki, Y. & Shipley, T.H. [1982]. *Estimates of heat flow derived from gas hydrates*, Geology, **10**, 339-343.

Yuan, T., Hyndman, R.D., Spence, G.D. & Desmons, B. [1996]. *Seismic velocity increase and deep-sea gas hydrate concentration above a bottom-simulating reflector on the northern Cascadia continental slope.* Journal of Geophysical Research, **101** (B6), 13655-13671.

Zwart, G., Moore, J.C. & Cochrane, G.R. [1996]. *Variations in temperature gradients identify active faults in the Oregon Accretionary Prism.* Earth and Planetary Science Letters, **139**, 485-495.

Chapter 5

Inferred gas hydrates and clay diapirs near the Storegga Slide on the southern edge of the Vøring Plateau, offshore Norway

ELSEVIER

Marine Geology 163 (2000) 125–148

MARINE GEOLOGY
INTERNATIONAL JOURNAL OF MARINE GEOLOGY, GEOCHEMISTRY AND GEOPHYSICS

www.elsevier.nl/locate/margeo

Inferred gas hydrates and clay diapirs near the Storegga Slide on the southern edge of the Vøring Plateau, offshore Norway

S. Bouriak [a], M. Vanneste [b,*], A. Saoutkine [a]

[a] *UNESCO-MSU Centre for Marine Geology and Geophysics, Faculty of Geology, Moscow State University, Vorobjevy Gory, 119899 Moscow, Russian Federation*

[b] *Renard Centre of Marine Geology, Geology & Soil Sciences, University of Gent, Krijgslaan 281 S8, B-9000 Gent, Belgium*

Received 16 March 1999; accepted 24 September 1999

Abstract

This paper presents a new data set, including single-channel airgun seismic lines, OKEAN long-range side-scan sonar data and gravity cores, acquired on the edge of the Vøring Plateau and in the region of the Storrega Slide. The data acquisition was part of the 8th Training Through Research (TTR-8) expedition with R.V. *Professor Logachev*. The acoustic profiles clearly show two laterally separated zones characterised by the presence of bottom-simulating reflectors (BSRs) at about 350 ms TWT subbottom depth. The *lower BSR zone* is located on the slope of the Vøring Plateau in the immediate vicinity of the northern headwall of the Storegga Slide and, in some places, below the slide deposits. This zone runs parallel to the general trend of the continental slope. The spatial distribution of the *upper BSR zone*, located upslope in an area where diapir-like structures are found, does not demonstrate any topographic control. Interpretation of high-backscatter patches on the OKEAN sonographs associates the observed structures with fluid escape features on the seabed. Most of them are pockmarks, but in a few places, diapirs are cropping out and form dome-like elevations. After analysing the behaviour of the BSR (sometimes crosscutting) and its acoustic characteristics (reversed polarity), and after applying seismic inversion processing to estimate the acoustic velocity change across the BSR, this reflector is interpreted to represent the base of the local gas hydrate stability field (GHSF). This information was used to derive the regional geothermal gradient. Spatial variations of the inferred geothermal field appeared to be negligible. The observation of two separated BSR zones suggests different environmental controls for the growth of the hydrates. Enhanced reflectors observed in the intermediate zone can be explained by the presence of strata-bound free gas accumulations and migration combined with overlying permeability barriers. Therefore, a model for gas hydrate formation in relation to directional fluid migration processes, fluid escape features and the presence of diapiric structures is proposed in this paper. Our model is supported by sedimentological analyses of seafloor samples, which demonstrate the presence of stiff clays with evidence of gas migration, and by paleontological studies of the cores retrieved from the pockmarks. The presence of a BSR in the sedimentary section within the slide scar area implies the repositioning of hydrates to newly established equilibrium conditions after the slide event. This observation allows us to simply estimate an upper limit of the fluid migration velocity in the order of several cm/year. Finally, the effect of hydrate dissociation on slope instability is considered. Assuming that the in situ decomposition of hydrates due to instantaneous depressurisation is slow enough to permit the excess volume of released gas and water to be

* Corresponding author. Tel.: +32-9-264-45-90; fax: +32-9-264-49-67; e-mail: maarten.vanneste@rug.ac.be

PII: S0025-3227(99)00115-2

re-distributed through the whole sedimentary section above the paleo-BSR (with consuming heat and increasing pore pressure, dissociation tends to shift the PT-conditions back to equilibrium values), it appears that the dissociation of hydrates due to sliding would cause only 0.2% increase of the pore pressure, which would hardly contribute to further slope instability.

Keywords: gas hydrates; clay diapirs; Vøring Plateau

1. Introduction: the Storegga Slide, gas hydrates and BSRs

1.1. The Storegga Slide

The Storegga Slide situated on the passive Norwegian margin south of the Vøring Plateau is known as one of the world's biggest underwater slides. The headwall, the steepest part of the slide, is 290 km long and has an average slope gradient of 10–20°. The slide deposits are up to 450 m thick, the total run-out distance is approximately 800 km and the total displaced volume of sediments is estimated to be in the order of 5500 km^3 (Fig. 1). The slide scar area, including distal deposits, is approximately 34 000 km^2 (Bugge et al., 1987).

Based on seismic profiles, sediment samples and Gloria side-scan sonar data, Bugge et al. (1987; 1988) defined three main stages of sliding events with additional minor slides:

The first Storegga Slide occurred between 30 ka and 50 ka BP and was the largest one in terms of volume of displaced sediments. In total, about 75% of the sediments involved were deposited outside the slide scar area, i.e., below the 2700 m isobath. The first slide extends into the abyssal plain, about 350 km further downslope from the headwall. It comprises the whole slide scar area. The mobilised sediments are believed to be relatively soft, fine grained Plio-Quaternary clays. It is assumed that this mass wasting event moved in the form of a partially liquefied debris flow with enhanced pore water pressures, resulting in completely remoulded sediments (Bugge et al., 1988).

The last two major slides occurred in near succession (8–6 ka BP) and cut deeper into the more consolidated sediments in the central part of the first slide area. The deposits of the second slide are the most extensive and far-travelled: 800 km relative to the headwall in northwestern direction into the Norwegian basin. Debris flow deposits commonly occur within the area of the second slide. Furthermore, the deposits contain some large, almost undisturbed sediment units, indicating that the fluidised portion of the flow should have been relatively thick with low-permeability (Bugge et al., 1988). Probably distal deposits of this slide event are redistributed over parts of the Norwegian Sea (Bugge et al., 1987; Jansen et al., 1987).

The third event only disturbed the central and upper part of the slide scar with its headwall at 1000 m, i.e., well below that of the second slide. The deposits show an essentially blocky nature, similar to the second slide (Bugge et al., 1987, 1988).

The occurrence of gas hydrates on the Vøring Plateau and their possible relationship with the initiation of the Storegga Slide on the Norwegian shelf edge have been discussed previously (e.g., Bugge et al., 1988; Mienert et al., 1998). Bugge et al. (1987) hypothesised that the main triggering mechanism for the slides was likely to have been earthquake loading with a possible contribution of ice loading for the first slide event. The observation that inferred gas hydrates are located at the same depth as part of the gliding plane means that decomposition of hydrates may have contributed to the triggering of the slides, after an earthquake suddenly reshaped the pore pressure distribution in the sedimentary column, leading to liquefaction and weakened sediments (Bugge et al., 1987).

1.2. Gas hydrates and BSRs

Gas hydrates are ice-like mixtures of low-molecular weight gas molecules, enclosed within cages of water molecules. These structures require high pressures and low temperature conditions (e.g., Kvenvolden, 1993; Sloan, 1998). However, the main re-

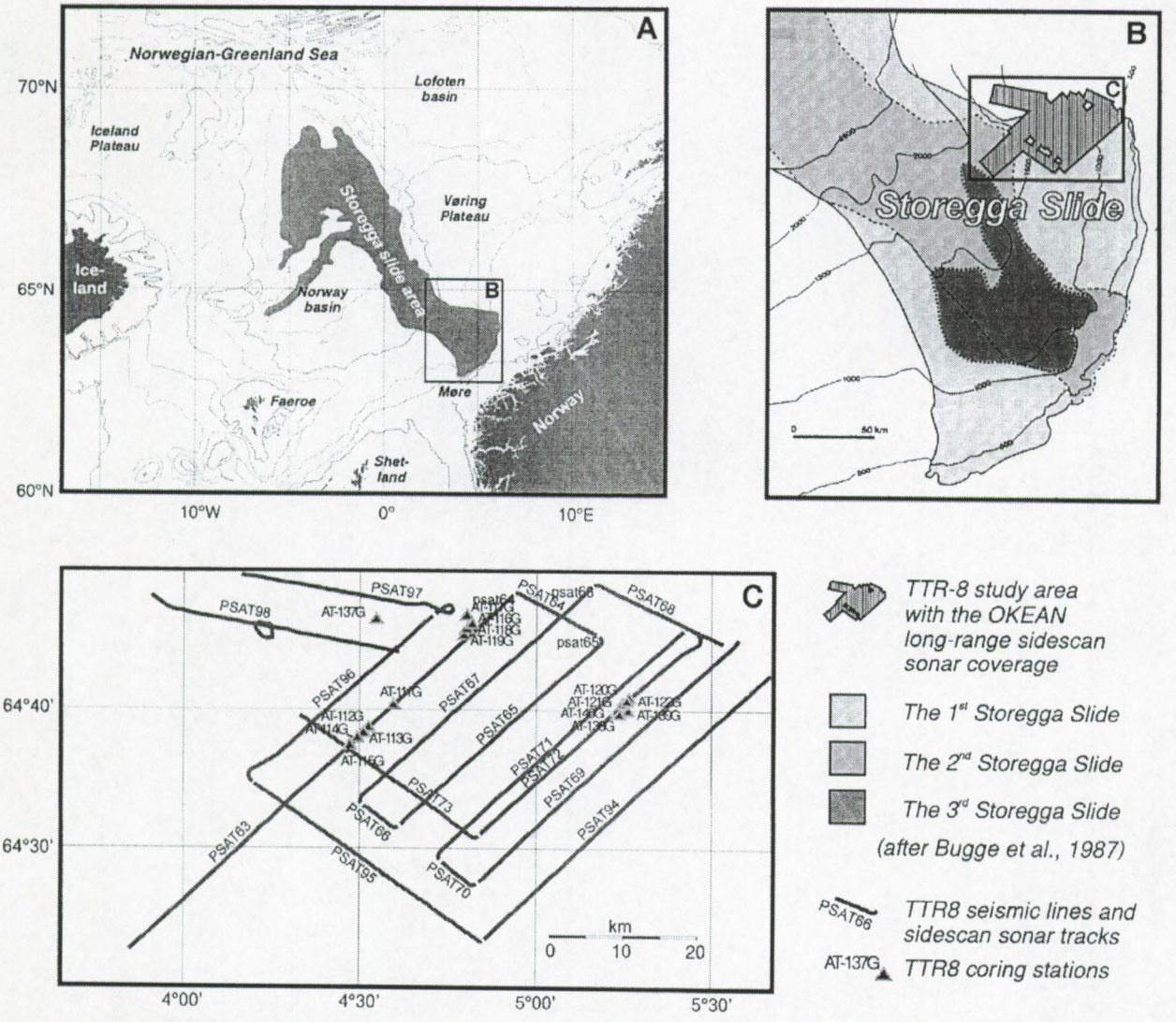

Fig. 1. Location map of the study area relative to (A) northwestern Europe and (B) the Storegga Slide (after Bugge et al., 1988), together with (C) the TTR-8 survey lines and bottom sampling stations. Seismic and OKEAN side-scan sonar data acquisition were made along the same lines.

striction for the occurrence of hydrates is the presence/supply of sufficient amounts of stabilising gas molecules (Hyndman and Davis, 1992; Rempel, 1995). Nevertheless, gas hydrates are believed to be common in continental margin areas (e.g., Mienert et al., 1998), as is confirmed by deep ocean drilling (DSDP–ODP).

Under natural conditions, the vertical extent of the gas hydrate stability field (GHSF) reaches from the seafloor to the intersection of the phase boundary with the subbottom temperature profile. The hydrates accumulate in parts of the pore spaces (typically a few percent) and in this way, their presence alters the acoustic, hydraulic and geotechnical properties of sediments (Dvorkin and Nur, 1993; Kvenvolden, 1993; Ecker et al., 1998).

On seismic records, the interface between hydrate-containing and hydrate-free sediments — which may correspond to the base of the GHSF — is often expressed as a bottom-simulating reflector (BSR). This anomalous reflector originates from the acoustic impedance contrast across an interface between

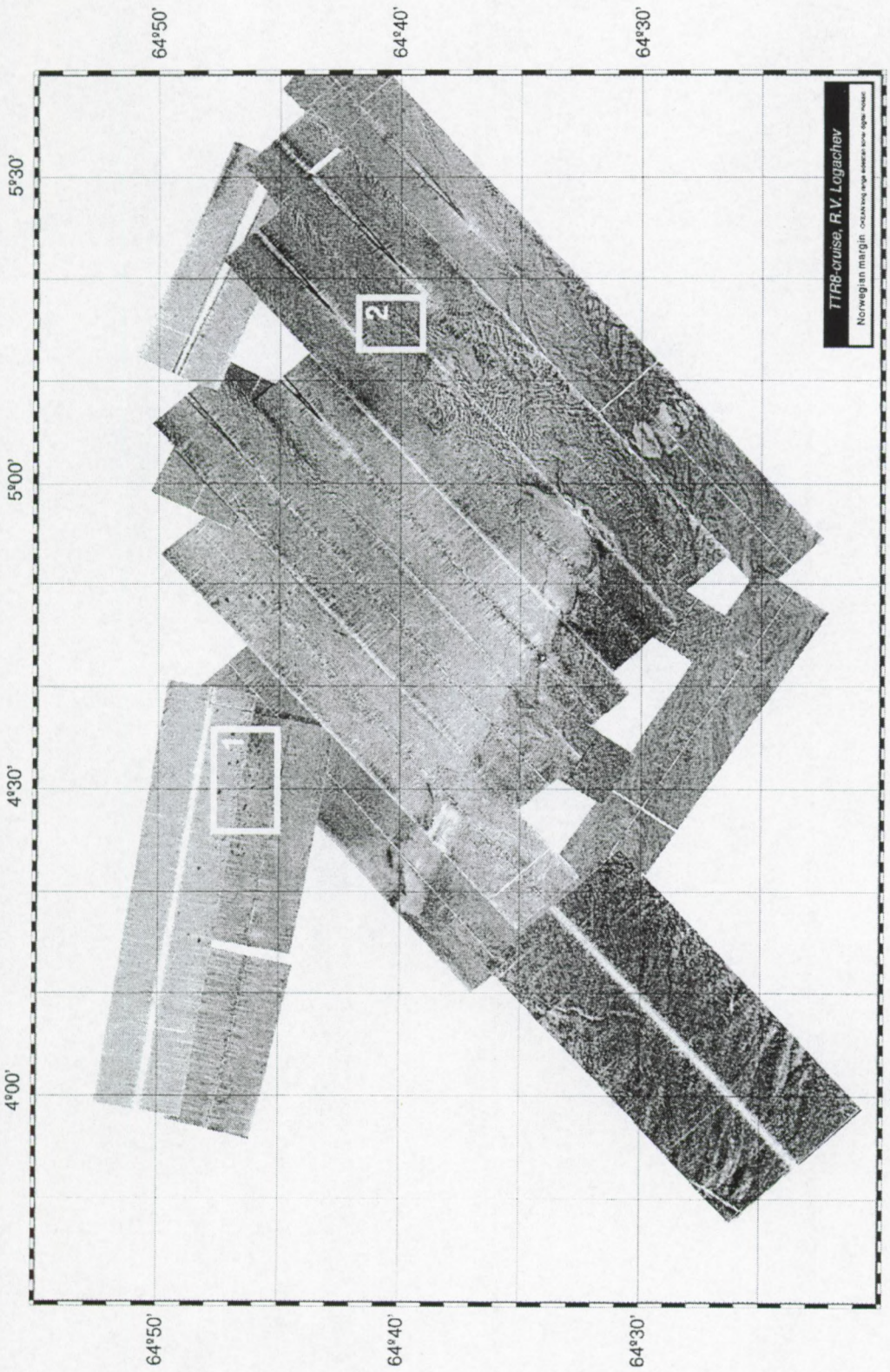

Fig. 2. Digital mosaic of the OKEAN long-range side-scan sonar imaginary. Boxes show the locations for Fig. 3.

high-velocity partially hydrate-saturated sediments above, and low-velocity probably gas-containing sediments below (Hyndman and Spence, 1992). The BSR normally mimics the seafloor topography, indicating that it is primarily temperature controlled and hence, in some regions, its presence can be used for geothermal estimations (Yamano et al., 1982). Furthermore, this high-amplitude reflector often cross-cuts the local stratigraphy and appears with negative polarity relative to the seafloor reflector (Hyndman and Spence, 1992).

1.3. Objectives of this paper

During the TTR8 cruise, carried out within the framework of the UNESCO-IOC ''Training Through Research'' (''Floating University'') Programme with R.V. *Professor Logachev*, part of the Storegga Slide area and the Vøring Plateau was investigated with a single-channel high-resolution airgun seismic reflection system, a long-range side-scan sonar and a bottom sampling programme (Fig. 1). This paper is aimed to (1) present a new multidisciplinary data set, (2) discuss the correlation between different gas and gas-hydrate related features observed, and (3) discuss their possible relevance to the submarine slide.

Analysis of the data made it possible to understand the formation mechanism of two inferred gas hydrate zones and the link with gas migration pathways, diapirs and fluid escape structures on the seafloor. Furthermore, observation of a BSR below the Storegga Slide deposits permits us to estimate the fluid migration velocity, as well as the possible contribution of gas hydrates to slope instability in the area.

2. Geological setting: Norwegian continental margin

The Norwegian-Greenland Sea is a relatively young oceanic basin, formed by seafloor spreading during the last 56 Ma. It is surrounded by passive continental margins and represents the northernmost extension of the Atlantic Ocean. The Norwegian-Greenland Sea is characterised by a peculiar hydrography of both surface (Norwegian Current, Norwegian Coastal Current) and cold dense deep or bottom (Northeast Atlantic Deep Water) water masses which are of great importance for Northern Hemisphere climate. The temperate Norwegian Current flows along the Norwegian continental margin into the Arctic ocean and plays a crucial role in the conveyor belt since the Cenozoic: its appearance and disappearance is related to the late Cenozoic glacial–interglacial cycles (Eldholm et al., 1987a; Eldholm et al., 1989a).

Based on bathymetry, morphology and structural elements, the Norwegian continental margin is subdivided into three main units: the Møre, Vøring and Lofoten-Vesterålen margin provinces (Fig. 1). The Vøring Plateau with an area of approximately 35 000 km^2 is flanked by the Lofoten basin in the North and the Norway basin in the Southwest (Eldholm et al., 1987a). It is a marginal structural high buried beneath a relatively thin veneer of Cenozoic sediments and bounded on its landward side by the Vøring Plateau Escarpment (Rabinowitz et al., 1992). Thick Cenozoic sediment accumulations characterise the area and part of the depocentre coincides with the

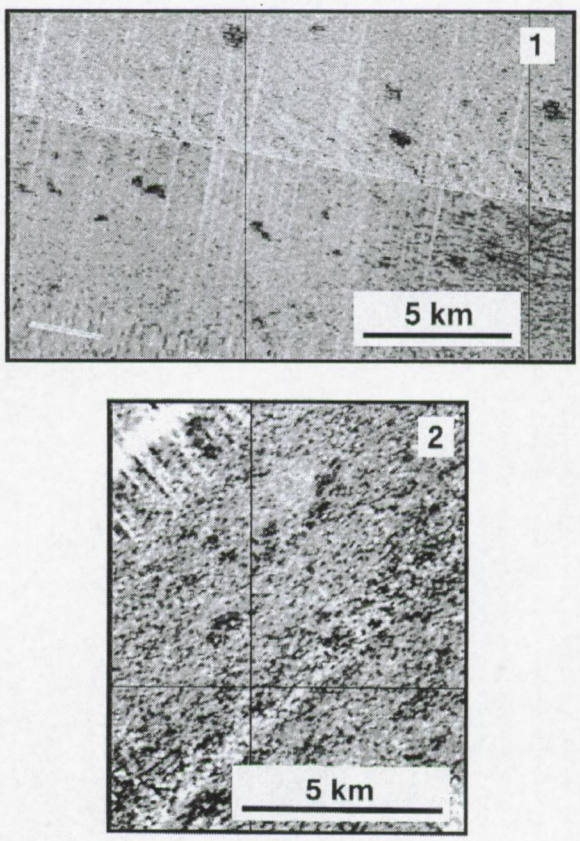

Fig. 3. Two examples of high-backscatter patches observed on the sonograph. 1 and 2 refer to the boxes in Fig. 2.

Storegga Slide area, located south of the Vøring Plateau (Jansen et al., 1987). On the marginal Vøring Plateau, diapir fields are present (Hjelstuen et al., 1997).

The potential for sediment deposition in the Norwegian-Greenland Sea responded strongly to the glacial–interglacial paleoclimatic fluctuations in the Quaternary. The regional pattern of sediment flux to the deep seafloor changed considerably (Eldholm et al., 1987a). The mainly glacial Quaternary deposits near the shelf edge in the Storegga slide area vary between 100 and over 300 m in thickness (Bugge et al., 1988).

3. Data and methods

A total of approximately 450 km of high-resolution airgun reflection seismic profiles together with OKEAN long-range side-scan sonar swath mapping of the seafloor and 15 gravity cores collected during TTR-8 expedition were examined in this study (Fig. 1).

3.1. Seismic data acquisition

The seismic system included a 2 l airgun and a single-channel hydrophone streamer with approximately 350 m offset. The data were recorded digitally (sampling interval 1 ms) within the frequency band of 50–250 Hz. The dominant frequency in water equals 180 Hz and the wavelength is 8.3 m. Only minimal processing was applied to the data to ensure a true relative amplitude recovery.

3.2. Seismic inversion procedure

A rather simple modification of a sparse-spike inversion algorithm (Russel, 1988) was applied to selected parts of the above-described seismic records. This technique and its results have previously been reported by Bouriak (1998). A reflectivity sequence is estimated for each seismic trace using an iterative procedure. Discrete reflection coefficients are added to the reflectivity sequence one by one until the error between the real trace and the synthetic trace (i.e., the convolution of the reflectivity sequence with the wavelet) is sufficiently small. The position of each reflection coefficient in the reflectivity sequence is determined by the maximum amplitude of the difference between the real trace and the synthetic one, i.e., from the position of the strongest reflection that had not yet been matched. Trial and error then yields the magnitude of each individual reflection coeffi-

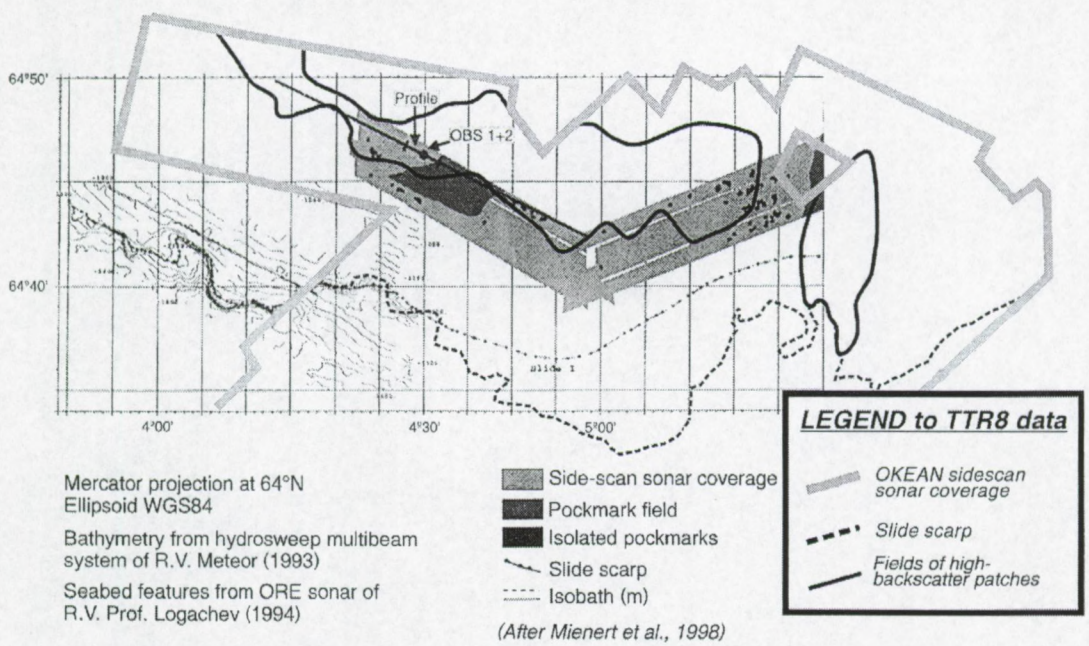

Fig. 4. Map with interpretation of side-scan sonar and hydrosweep tracks, published by Mienert et al. (1998), together with TTR-8 OKEAN mosaic interpretation. In the eastern part, the slide scarp configuration is improved using both OKEAN data and seismic data.

cient. The wavelet used for convolution is derived from the seafloor reflection for each seismic trace. The traces were reshaped to zero-phase wavelet, which allowed us to correlate the position of the individual maximum amplitudes with arrival times of different reflectors.

After proper scaling and correcting for transmission and deviation, the obtained reflectivity sequences are inverted to acoustic impedance with the recursive formula proposed by Lavergne and Willm (1977), which, in turn, was scaled into velocity with the empirical relationship between acoustic impedance and velocity proposed by Lindseth (1979). Finally, to make the result more stable and robust, the obtained ''blocky'' velocity functions were low-cut filtered to eliminate the effect of accumulation of errors, which apparently propagate through the recursive solution. As a result, this methodology only provides relative velocity information, i.e., velocity changes at major boundaries, without determining the absolute values.

3.3. Side-scan sonar survey

The OKEAN long-range side-scan sonar was operated at a frequency of 9 kHz. The swath range of the system is approximately 8 km. The OKEAN vehicle is towed at some tens of meters water depth with average speed of about 6 knots. During data processing, corrections for the varying towing speed as well as angular-variable gain were applied to compensate for spherical divergence and variations in the directional pattern of the transducers. The slant-range to ground-range corrected data were finally geographically adjusted to obtain a digital mosaic (see also Akentieva and Shashkin, 1998). The seismic and side-scan sonar data were collected simultaneously along the same lines.

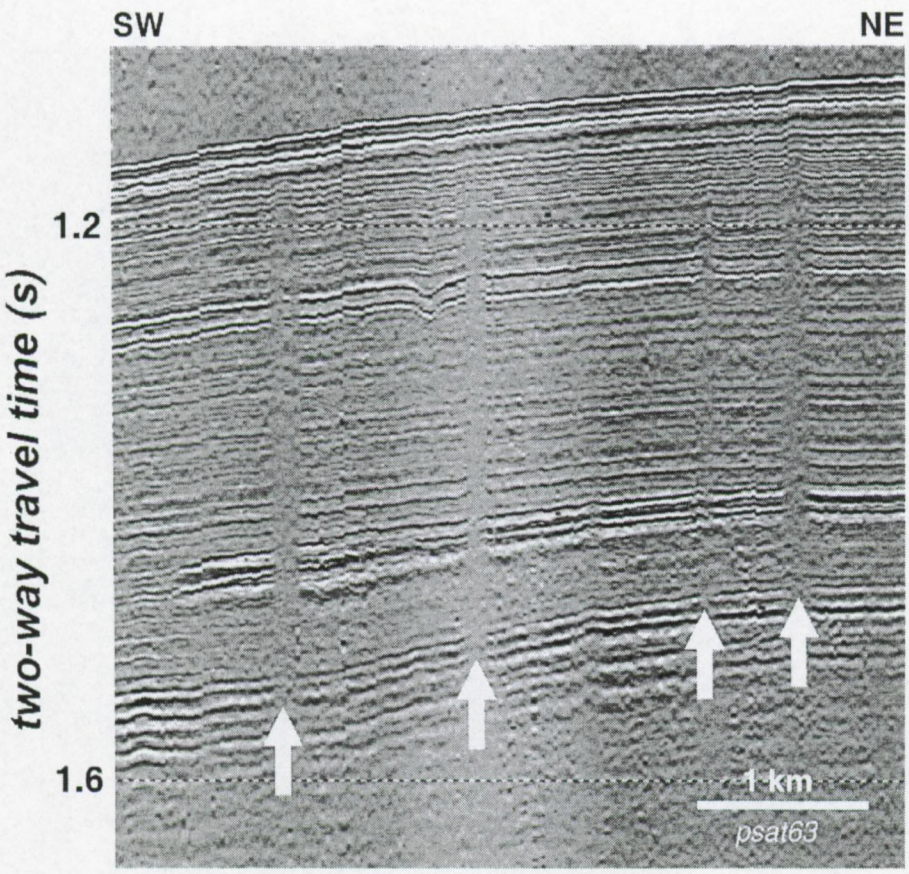

Fig. 5. Airgun seismic profile (PSAT63) showing vertical zones of acoustic wipe-outs (diapirs?) on the upper slope of the Vøring Plateau.

3.4. Sampling programme

The seafloor-sampling programme was carried out with a gravity corer (6.6 m long, 168 mm diameter, 1500 kg weight) with an inner plastic liner that allowed the collection of up to 6 m of undisturbed sediments. The ship positioning was obtained with a GPS navigation system and the locations of the coring stations relative to the features of the seafloor relief were also checked with a low-frequency (6 kHz) echosounder, which was active during all coring operations. In this work, we use visual lithological core descriptions made on board, plus micropalaeontological studies of calcareous nannofossils (coccoliths) examined in smear-slides using Olympus Light Microscope with magnification of 1000 ×. Unbroken coccoliths were identified using the system of Cenozoic calcareous nannofossils published by Bolli et al. (1985). In case of poor preservations and impossibility of precise identification of species, open nomenclature was used.

4. Observations and results

4.1. Seafloor fluid escape structures and clay diapirs

The deposits of the first Storegga Slide event and its escarpment can be clearly seen on the digital mosaic of the side-scan sonar imaginary (Fig. 2). North of the escarpment, on the upper part of the Vøring Plateau slope, numerous patches of higher backscattering were observed (Fig. 3). Their distribution fits the pockmark fields reported by Mienert et al. (1998), with allowance made for differences in operating frequencies, resolution and penetration of the high-resolution deep-towed instrument, used for that study, and the OKEAN system (Fig. 4). More specific, many of the structures observed by the high-resolution instrument are probably too small to be resolved on the OKEAN sonograph. On the other hand, the greater penetration depth of the OKEAN system allows us to observe some buried features that cannot be seen on the high-resolution data. The

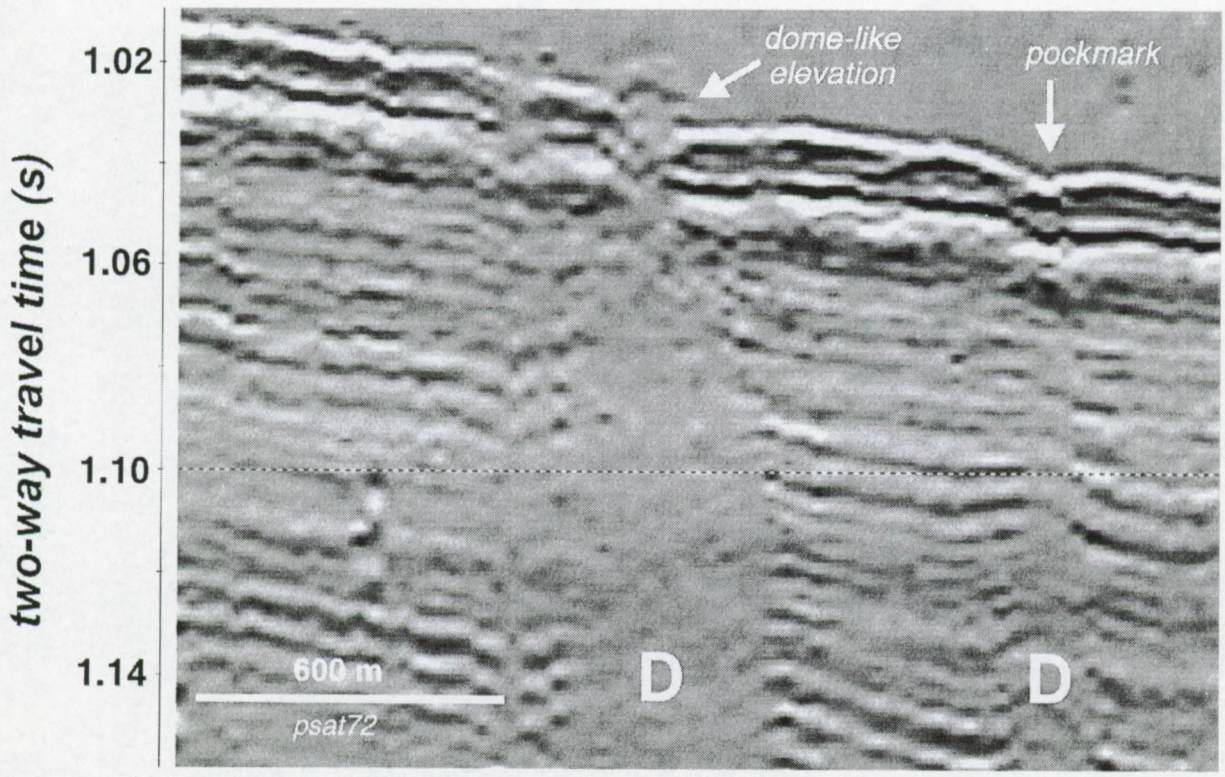

Fig. 6. Wipe-out zones (''D'') cropping out: a dome like elevation and a pockmark on the seafloor as observed on the seismic record along line PSAT72. Note the slightly up-pulling marginal reflections.

difference in operating frequencies of the two side-scan sonar sources also suggests different dimensions of scattering elements at the seafloor and in the sub-seafloor sediments, which would affect the resulting imagery most efficiently. The lower resolution and shallower towing depth of the OKEAN system does not allow us to explain the observed patches simply by seafloor topography but suggest the enhanced backscatter as being caused by local changes of the physical properties of the seafloor and sub-seafloor sediments. This can be confirmed by the presence of gas-charged sediments and carbonate crusts in all cores taken from the patches (AT-117G, 118G, 120G, 121G, 122G, 139G, and 140G).

Seismic airgun records along the same part of the slope are characterised by narrow (150–500 m in width) vertical zones of acoustic wipe-outs (Fig. 5). In vertical dimension, the ''wipe-out zones'' are traced typically for around 300 m (400 ms TWT), with their base below the penetration depth of the seismic system. Similar acoustic features were previously reported in this area by Baas et al. (1994) and Evans et al. (1996), who believed that these anomalies are caused by vertical fluid (gas?) expulsion. In two places, we noticed that these features are cropping out at the seafloor, forming dome-like elevations similar to small-scale (up to 7 m high) mud volcanic structures. In other cases, the ''wipe-out zones'' approach the seafloor and are often accompanied by small pockmarks. In deeper parts of the sedimentary section, these features are frequently characterised by up-pulling of marginal reflectors, rather suggesting vertical sediment movement than pure fluid migration processes (Fig. 6).

Nannoplankton Zones and Stratgraphic Intervals Used in the Norwegian-Greenland Sea (DSDP, Leg 38) (after Muller, 1976)

Age	Nannoplankton Zonation	Species
Quaternary	*Emiliania huxleyi*	*Coccolithus pelagicus, Cyclococcolithus leptoporus, Discolithin japonica, Emiliania huxleyi, Gephyrocapsa ericsonii, Syracosphaera pulchra*
	Gephyrocapsa oceanica	*Coccolithus pelagicus, Cyclococcolithus leptoporus, Gephyrocapsa ericsonii, Helicosphaera carterti, Syracosphaera pulchra*
Late Pliocene	*Pseudoemiliani huxleyi*	*Coccolithus pelagicus, Cyclococcolithus leptoporus, Gephyrocapsa ericsonii, Gephyrocapsa sp., Helicosphaera carterti, Helicosphaera sellii,Syracosphaera pulchra*
Early Pliocene Middle Miocene	*Reticulofenestra pseudoumbilica*	*Coccolithus pelagicus, Discolithin japonica,* ***Reticulofenestra pseudoumbilica,*** *Sphenolithus abies*
Early Miocene	*Helicosphaera ampliaera*	*Coccolithus pelagicus, Helicosphaera ampliaperta,* ***Reticulofenestra cf. pseudoumbilica***
	?	same species as in the *Spenolithus distentus* zone plus *Discolithina enormis*
Late Oligocene	*Sphenolithus ciperoensis*	
Middle Oligocene	*Sphenolithus distentus*	***Chiasmolithus altus,*** *Coccolithus abisectus, Coccolithus pelagicus,* ***Cyclococcolithus floridanus, Dictycococites dictyodus,*** *Discoaster deflandri, Sicolithina desueta, Helicosphaera euphratis, Helicosphaera perch-nielsenae,* ***Helicosphaera recta,*** *Reticulofenestra elatrata, Reticulofenestra lockeri, Sphenolithus moriformis, Zygrhablitus bijugatus*
Middle Oligocene	?	***Chiasmolithus oamaruensis, Cribrocentrum reticulatum, Cyclococcolithus luminis,*** *Discolithina pulcheroides, Isthmolithus recurvus,* ***Reticulofenestra umbilica,*** *Transversopontis obliquipons*
Early Oligocene Late Eocene	*Isthmolithus recurvus*	
Late Eocene Middle Eocene	*Reticulofenestra umbilica*	***Braarudosphaera bigelow, Reticulofenestra umbilica, Zygolithus dublus***
Early Eocene	?	***Braarudosphaera bigelow,*** *Chiasmolithus solithus,* ***Cyclococcolithus luminis, Discoaster lodensis,*** *Discoasteroides kuepperi, Discolithina pulchra, Imperiaster obscurus, Marthasteritas tribrachiatus, Micranthotithus mirabilis, Zygolithus dublus*
	Imperiaster obscurus	

bold: coccoliths found in some diapirs out-crops and pockmarks during TTR8 Leg 3.

Coccoliths founds in the TTR8 cores

Cores from diapir out-crops and pockmarks	Backgrounds cores from surroundings
AT117G *M. staurophora* (148 cm from the top) ***Chiasmolithus oamaruensis Cribocentrum cf. reticulatum, Cyclococcolithus luminis, R. umbilica, Braarudidosphaera bigelow, Discoaster lodoensis*** (394 cm from the top).	**AT111G** *Micula staurophora* (134 cm from the top)
AT118G *M. staurophora* (47 cm from the top) ***Ch. oamaruensis,Cr.cf. reticulatum, Ch. altus, Helicosphaera recta, Zigodiscus cf. dubius*** (92 cm from the top).	**AT112G** *M. staurophora* (26 cm from the top)
AT120G *M. staurophora,* (138 cm from the top)	**AT113G** *M. staurophora* (211 cm and 417 cm from the top)
AT121G *Biantolithus cf sparsus, M. staurophora,* ***R. pseudoumbilica, Dictycoccites cf. dictyodus.***	**AT114G** *M. staurophora, Reticulofenestra cf. umbilica, Discoaster sp* (357 cm from the top)
AT122G *M. staurophora*	**AT115G** *M. staurophora* (10 cm), *Chiastozigus litterarius* (259 cm from the top)
AT139G *M. staurophora,* ***B bigelow, Cr. cf. reticulatum*** (93 cm from the top)	**AT116G** *M. staurophora, Cribosphaerella sp* (336 cm from the top)
AT140G ***Ch. oamaruensis, Cyclococcolithus floridanus, R. umbilica,*** *Reticulofenestra sp.* (244 cm from the top)	**AT119G** *B. bigelow, R. pseudoumbilica, Cribocentrum sp ? (162 cm from the top) M. cf. staurophora (240 cm from the top)*
	AT138G *M. staurophora, R. pseudoumbilica* (20 cm from the top).

bold: coccoliths described in sites from Norwgian-Greenland Sea (DSDP, Leg 38)

Fig. 7. Nannoplankton zones and stratigraphic intervals used in the Norwegian-Greenland Sea (DSDP, Leg 38) (after Muller, 1978) and the pre-Quaternary nannofossils found in the TTR-8 cores.

These indirect acoustic evidences of mass transport phenomena are confirmed by analysing the core samples. Cores AT-120 and AT-121 are taken from one of the dome-like seabed elevations. The recovered sediments are mainly composed of stiff homogeneous and gas-saturated clays, which were much more consolidated than recent hemipelagic sediments. Paleontological studies of the sampled cores are summarised in Fig. 7. These studies revealed that, beside Quaternary fossils and ice-rafted debris fossils found in all the cores, the sediments taken from the dome-like elevation and pockmarks contain Tertiary fossils, mainly of Eocene to Oligocene age. In our opinion, these fossils can hardly be transported over several hundreds of meters only by fluid migration. Therefore, the observed vertical ''wipe-out zones'' should most likely be considered not as pure gas-related acoustic features, but as clay diapirs originating from formations of Tertiary (probably Eocene) age.

4.2. Seismic evidence for gas hydrates and shallow gas and implications for determining the geothermal regime

The single-channel airgun reflection seismic data collected during the TTR-8 cruise show a distinct bottom-simulating reflector at subbottom depths of approximately 350 ms TWT, as well as enhanced reflections (bright spots) indicating shallow gas accumulations. Fig. 8 shows part of a time-section along line PSAT63, on which these features — typical of the whole area — are most prominent. The high-amplitude BSR, terminating just landward of the slide scarp, mimics the seafloor topography, clearly crosscuts the local stratigraphy and appears

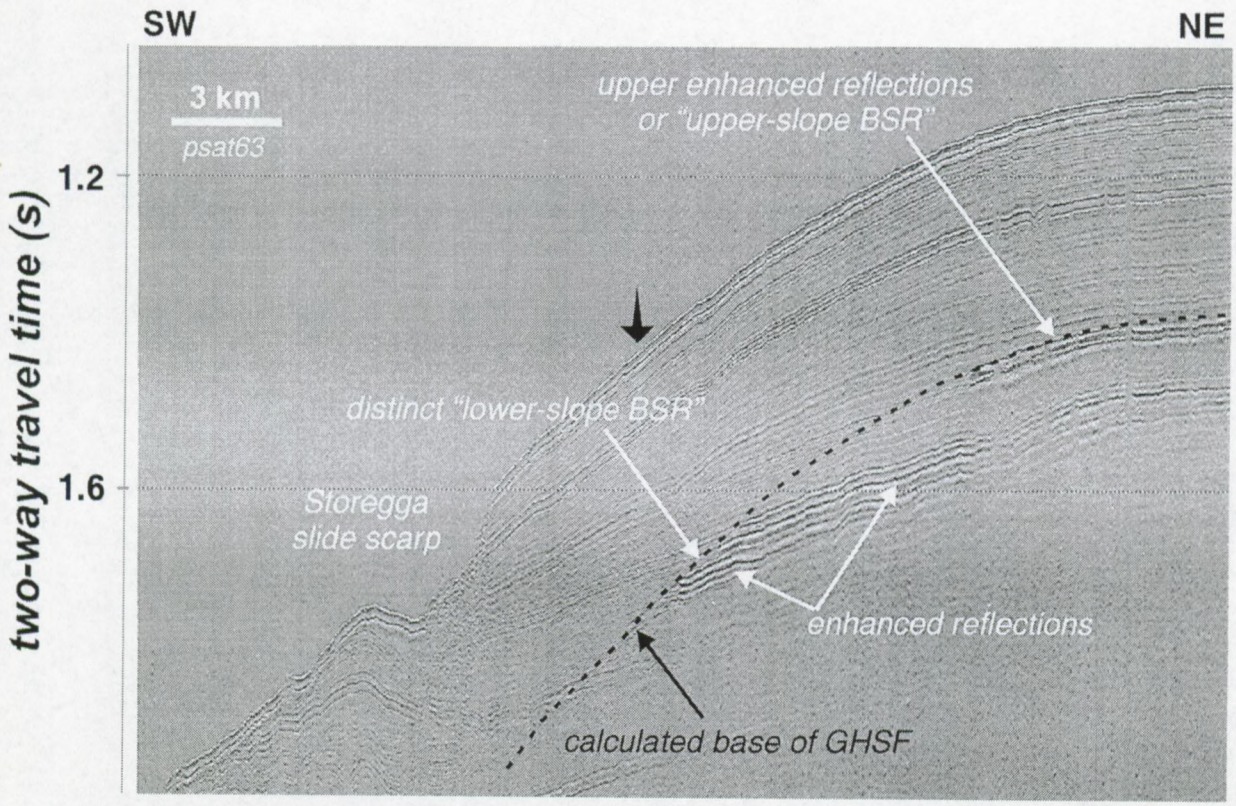

Fig. 8. Part of time-section along line PSAT63 with a clear BSR and enhanced reflections. The black dashed line respresents the calculated base of the GHSF along this line. Since the difference between the hydrostatic pressure approach (geothermal gradient of 0.0515°C/m) and lithostatic approach (geothermal gradient of 0.0558°C/m, average bulk density 1800 kg/m^3) is very small, only the lithostatic one is shown. Note that the upper enhanced reflection fits well to the GHSF base and thus is likely to be also gas hydrate related. The black arrow indicated the reference point used for geothermal calculations, and at the same time the location of the seismic traces shown in Fig. 9.

with reversed polarity relative to the seafloor reflection (Fig. 9). Slope upward in NE direction, packages of enhanced reflectors are observed. However these bright spots fade out in the diapir field further upslope.

The ''upper'' enhanced reflector on Fig. 8 also closely follows the seafloor morphology. It is seen on the upper slope at nearly the same subbottom depth as the above mentioned BSR. At first instance, this particular reflector was not considered as being linked with gas hydrates because no clear crosscutting was observed due to a sedimentation pattern that parallels the seafloor as well, although polarity analysis showed phase reversal, similar to the situation presented in Fig. 9.

BSRs were observed on all lines perpendicular to the slope in the undisturbed sediments of the Vøring Plateau, and on the three easternmost lines below the Storegga Slide deposits. Fig. 10 shows perhaps the most interesting example of the BSR observation in the area. Here, the reflector starts directly below the slide scarp and continues SW inside the slide area, simulating the present-day seafloor topography. An enhanced reflector is also seen to the NE of this BSR.

In order to derive or model the geothermal regime from the presence of BSRs on seismic records, some aspects and assumptions had to be taken into account. These are mainly based on literature study and the results published from ODP leg 104, sites 642 (67°13.5′N, 2°55.7′E), 643 (67°42.9′N, 1°02.0′E) and 644 (66°40.7′N, 4°34.6′E) located on the Vøring Plateau at 250–400 km to the N–NW of the study area (Eldholm et al., 1987b; Eldholm et al., 1989b). More details and formulas are given in Appendix A.

First of all, the BSR is assumed to correspond to the base of the GHSF and hence its subbottom position is supposed to coincide with the bulk thermodynamic 3-phase equilibrium boundary of the gas–seawater–hydrate mixture. The influence of the pore size distribution (capillary effects) throughout the GHSF and surface properties (activity) of the host material on hydrate stability is ignored. Including these effects should result in lower subbottom depths of hydrate stability (Clennell et al., 1999).

Although no hydrates have been recovered in this area, we assume a pure methane–seawater–hydrate mixture to be present since methane is by far the most abundant hydrate forming gas in nature (Kvenvolden, 1998). In contrast to the low gas content in sediments of the outer Vøring Plateau (sites 642, 643), analysis at site 644 on the inner Vøring Plateau demonstrated that the present gas is mainly isotopically light methane (> 99.9%), suggesting a biogenic origin (Kvenvolden et al., 1989).

Since the seismic data were acquired in single-channel form, no absolute velocity analysis can be performed. For estimating the subbottom position of

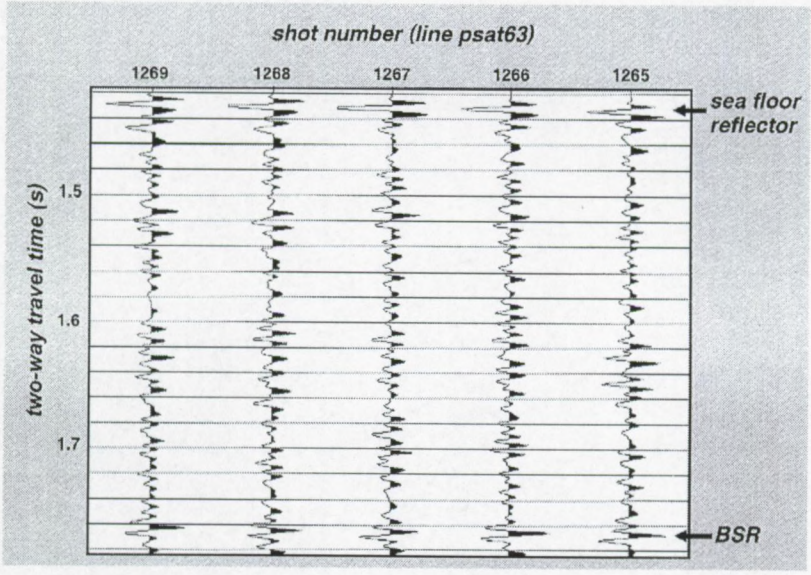

Fig. 9. Seafloor reflection and the BSR signature with reversed polarity, taken from line psat63.

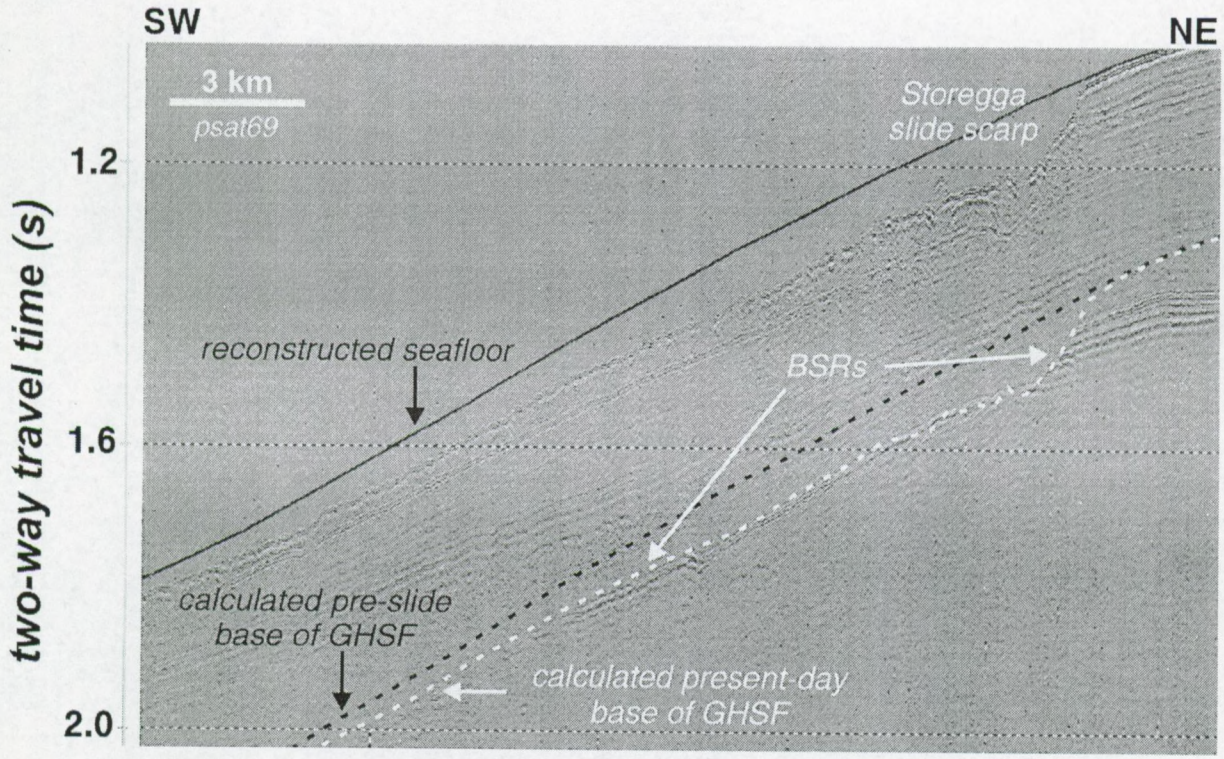

Fig. 10. Part of the seismic profile PSAT69, demonstrating a BSR below the slide scarp and deposits of the 1st Storegga Slide. Also the reconstruction of the paleo-seafloor topography along this line PSAT69, together with the calculated depths of the base of the GHSF for the present-day situation and in pre-slide seafloor conditions are shown. The intermediate position of the base of the GHSF, i.e., immediately after the slide, is not indicated since the vertical shrinking is only in the order of a few meters and hence cannot be resolved on this scale.

the BSR, an average regression equation relating the mean compressional wave velocity to subbottom depths and later to two-way travel time was determined. This equation is obtained using the p-wave velocity measurements (combined) in ODP site 642 and 643 (Eldholm et al., 1987b). Furthermore, the results are compared with the more general regression equation of Hamilton for terrigeneous sediments (Hamilton, 1980) like silt clays, turbidites and mudstone shale.

The bottom water temperature in this area is taken to be 0°C, consistent with values mentioned in Mienert et al. (1998) (''around 0 to -1°C on the mid-Norwegian slope and within the pockmark field'') and Thiede et al. (1989) (''< 0–1°C below 500 m isobath in the Eastern Norwegian Sea'').

The subbottom temperature profile was assumed to be linear with increasing depth, i.e., a steady-state situation in the sedimentary section above the base of the GHSF. Diverse factors altering the temperature gradient and thus the vertical extent of the GHSF (e.g., subsidence, compaction and continuous sedimentation, changes in bottom water temperature, sea level changes, ...) are disregarded.

Since we do not have access to accurate pore pressure profiles as a function of subbottom depth, the geothermal field and its lateral variability are investigated for both end members, i.e., the hydrostatic pore pressure distribution and the lithostatic alternative. For calculations of the lithostatic pressure, porosity changes vs. depth above the BSR were ignored and an averaged maximum saturated bulk density of 1.8 g/cm^3 was used, based on the data of ODP Leg 104 hole 644 (Eldholm et al., 1987b).

A first estimate was performed using a single BSR point on profile PSAT63, indicated on Fig. 8. The thermal gradient was found to equal 0.0515°C/m (assuming hydrostatic pore pressure distribution) or

0.0558°C/m (assuming lithostatic pore pressure). Results obtained using Hamilton's regression curve were almost identical: the calculated differences appeared to be less than 5%. Similar values for the geothermal gradient were reported by Mienert et al. (1998). These calculations — in turn — were used to delineate the theoretical GHSF in the area, for example on line PSAT63 (Fig. 8). The difference between the two approaches mentioned cannot be resolved on the seismic line, and hence, only the results of the lithostatic pressure method is shown. In either case, spatial fluctuations of the gradient within the area are negligible, as on all of the acoustic profiles the BSRs were observed at depths close to the theoretical GHSF limit.

Remarkably, the ''upper'' enhanced reflections, where these exist, also fit the same calculated lower limit of the GHSF (Fig. 8) and thus are most likely

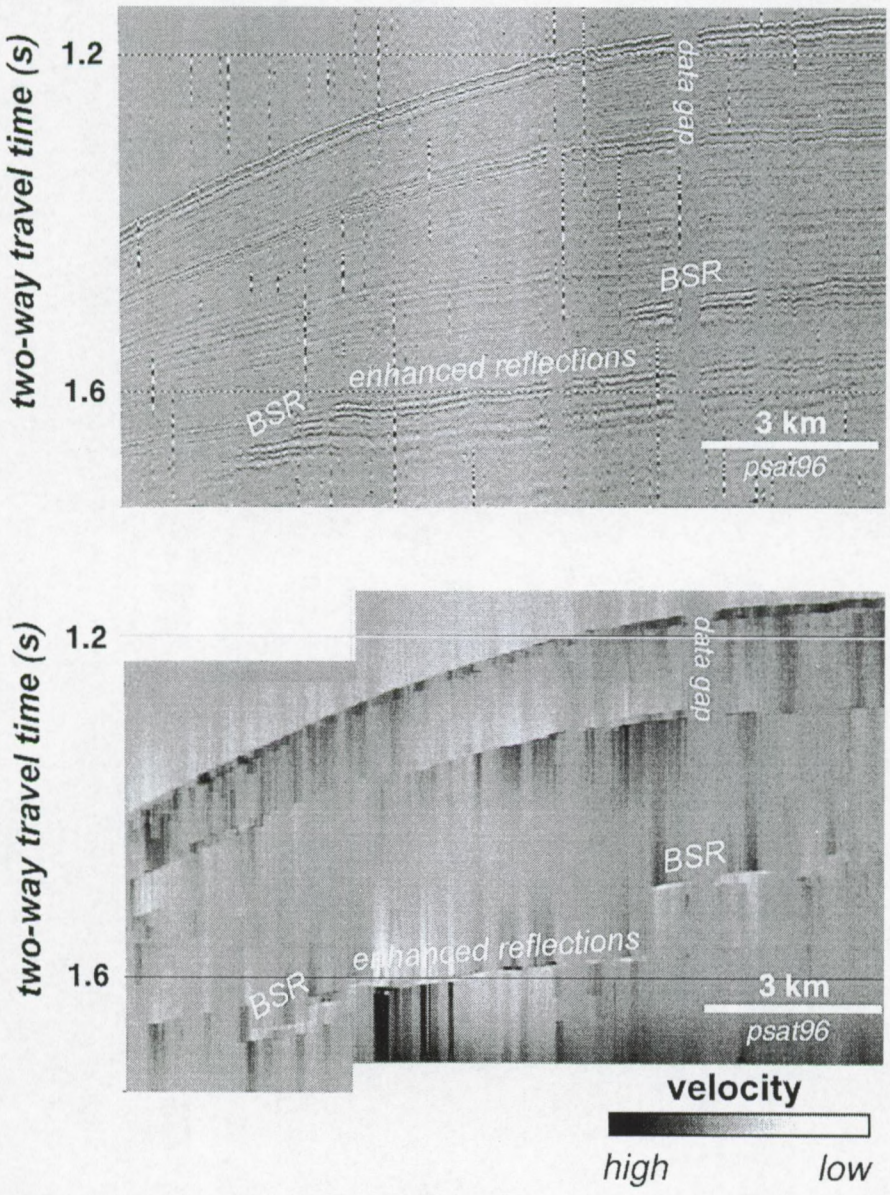

Fig. 11. Airgun profile PSAT96 with BSRs and enhanced reflections (above), and a relative velocity model derived from seismic inversion applied to the same seismic section (below).

of similar nature and should be referred to as gas hydrate BSRs too. On this figure, it is clear that both BSR occurrences coincide very well with the theoretical GHSF, while the enhanced reflectors in the intermediate zone lie below the GHSF.

The results of the seismic inversion procedure corroborate the reliability of inferring gas hydrates in two separated zones and free gas accumulations in the intermediate area for explaining the seismic observations. Both BSR events and the long continuous enhanced reflections in between of the two hydrate zones correspond to boundaries where the acoustic compressional wave velocity decreases substantially (Fig. 11). A relative velocity drop of approximately 350 m/s was found to be present at both BSR occurrences. Partial hydrate occupations of the pore spaces above the BSRs and probably some percentage of free gas below form a plausible explanation. Unfortunately, the inversion results do not allow us to estimate the total fraction of hydrates in the pore spaces and/or the volume of free gas under the GHSF. In the intermediate section, the sudden velocity drop near the enhanced reflectors seems to have a smaller magnitude, due to the lack of hydrates. However, the complex acoustic interference pattern in this area complicates the analysis and prognosis.

In the northern rim of the Storegga Slide, a high-amplitude reflector with phase reversal at approximately 375 ms TWT subbottom depth was also observed on airgun data by Mienert et al. (1998). Using high-frequency OBS measuring tools, Posewang and Mienert (1996) found a sudden velocity decrease from ±1900 m/s to values between 1300 and 1400 m/s, pointing towards the presence of free gases in a zone of 10 to 30 m under the GHSF. This confirms the results obtained with our velocity inversion.

In all cases, the BSR represents a sharp interface at the source frequency used while no reflection of the top of the hydrate layer is observed. Posewang

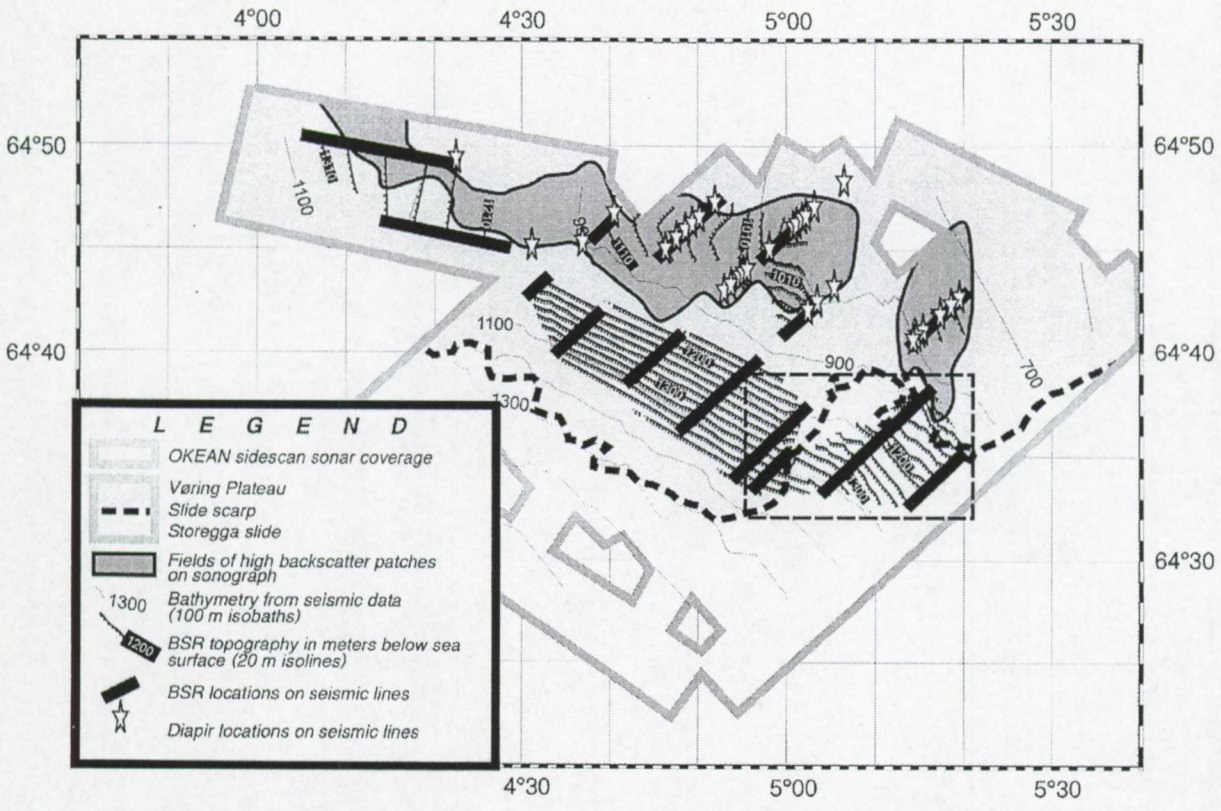

Fig. 12. Observations and interpretation of the TTR8 OKEAN long-range side-scan sonar mosaic and airgun seismic profiles. Note two separate zones of BSR distribution and the presence of BSRs in the slide area. Box shows location of Fig. 15.

and Mienert (1996) and Mienert et al. (1998) reported for the first time the occurrence of a double BSR event on one and the same acoustic cross-section in the same area. This feature is however not observed on our seismic records.

4.3. Link between inferred hydrates and fluid escape features

Fig. 12 summarises and combines all the above-described observations, showing the typical seafloor expressions and the different features observed on the seismic data.

The BSR occurrences in the study area appear to form two separated zones. One elongated zone (''lower-slope BSR'') is traced along the lower slope of the plateau and runs virtually parallel to the general trend of the slope. No fluid escape features were observed on the seafloor in this part of the area. In the southeastern part of the area within a territory of about 100 km^2, this ''lower slope BSR'' is also observed below the slide scarp and below the sediments mobilised during probably the first sliding event.

Another zone is located up slope, and is therefore referred to as ''upper-slope BSR'' zone. This zone does not demonstrate any morphological controls but fits nicely to the areas of interpreted fluid escape features observed on the OKEAN sonographs, in relation to the core analyses (see also 4.1). The diapirs, visualised on the seismic records, also seem to be related to the same areas, suggesting a close link between all these phenomena.

5. Discussion

5.1. Nature of the BSRs

In recent years, some models have been proposed to account for gas hydrate formation and accumulation and the development of BSRs in oceanic settings (Kvenvolden, 1998). In the first model, methane is assumed to be generated microbially in situ from organic matter (Claypool and Kaplan, 1974) and gas hydrate formation takes place concurrent with sedimentation. In the second model (Hyndman and Davis, 1992), gas hydrates are formed by removal of dissolved methane of biogenic or thermogenic origin derived from upwelling pore fluids as they enter the GHSF. In a third model (Minshull et al., 1994), free gas is supposed to migrate upwards through zones of higher permeability due to buoyancy, capillary forces and overpressuring mechanisms. Hydrates start to form at nucleation or growth sites and can form a seal, trapping free gas under the hydrate accumulations. As mentioned by Ginsburg and Soloviev (1997), active fluid migration can be either diffusive (percolation) or focused.

The distribution of the BSRs in this part of the Norwegian continental margin in two localised but separated zones with — most probably — different factors controlling their shape and spatial distribution contradicts the first model. In case of in situ methane formation, one would expect the zonality to be less striking, and the area of BSR distribution probably more regional and less organised. Furthermore, it is doubtful in general whether the microbial productivity and the amount of organic matter in sediments are high enough to provide sufficient amounts of methane for gas hydrate formation and accumulation (Hyndman and Davis, 1992).

The second model seems to fit better the observations. However, focused fluid flow can probably be ruled out, since there is an obvious lack of noticeable variations in the temperature gradient calculated from the BSR depths and the morphology of the BSR reflector. This suggests that the temperature profiles everywhere in the area are mainly conductive and advection of heat, normally associated with focused upward fluid fluxes, is negligible.

Therefore, we propose the following combined model of hydrate formation in this area, taking into consideration all the above mentioned observations and models. Our model, presented in Fig. 13, suggests active vertical percolation of methane in the zone of the ''lower-slope BSR''. Once the fluids enter the GHSF, the gas molecules are captured into hydrate structures, according to the model of Hyndman and Davis (1992). The effective porosity decreases due to the fractional filling of the pore spaces with hydrates, and hence, the permeability also drops, leading to a trap under which free gas can accumulate (Ecker et al., 1998). In the intermediate area between the ''lower-slope BSR'' zone and ''upper-slope BSR'' zone, a less permeable stratigraphic

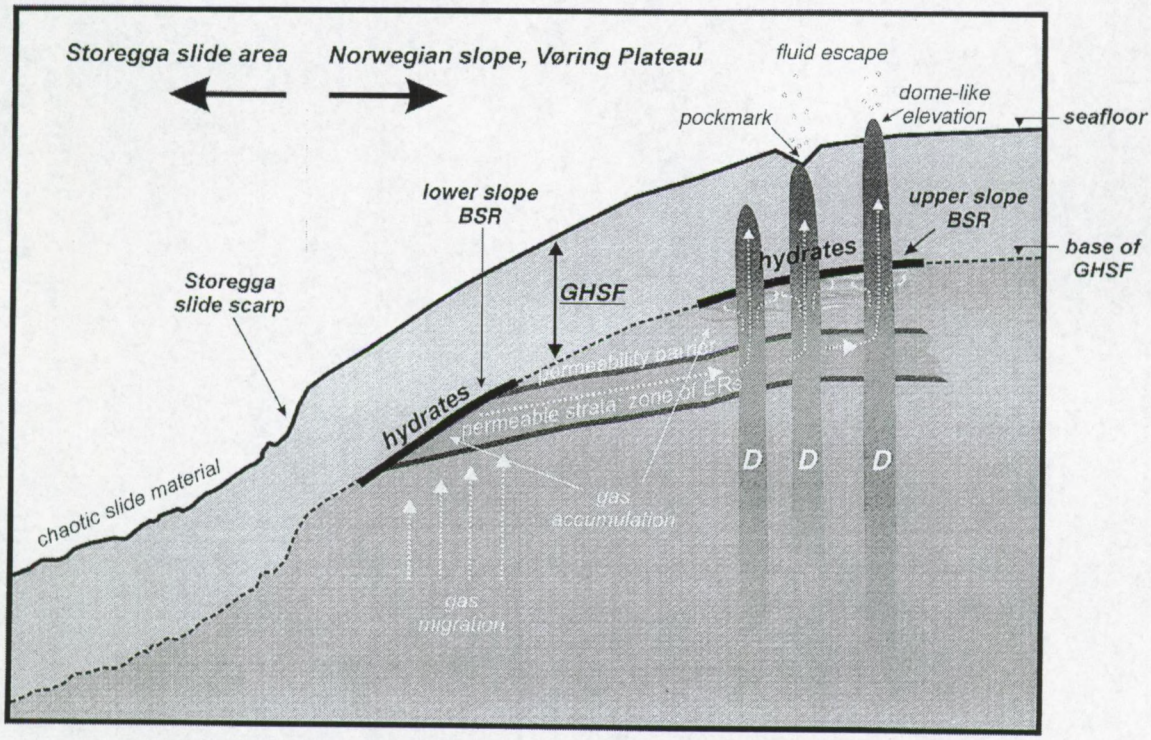

Fig. 13. A schematic model of the BSR development in the area and their link to probable clay diapirs and fluid escape features observed on the seafloor (ERs = Enhanced Reflectors).

boundary is assumed to be present below the GHSF but overlaying the enhanced reflectors, allowing free gases to accumulate or to migrate laterally towards the area characterised by the diapirs. The diapiric structures, in turn, provide possible migration pathways for further upward fluid transport to the base of the GHSF, where again hydrates can start to fill the pore spaces and thus the upper-slope diapir-related BSR formation takes place. The remaining gas, not clathrated into the hydrate structure (Clennell et al., 1999), exhausts at the seafloor creating the observed fluid escape features (pockmarks and small mud volcanoes) (Hovland and Judd, 1988), as observed on the sonographs as patches of higher backscattering.

5.2. Fluid migration velocity estimation

Based on the fact that the BSR — when observed in the sedimentary section just below the slide scarp and displaced sediments — mimics the present-day seafloor topography and, thus, appears to have already repositioned itself to the new hydrate pressure-temperature equilibrium conditions after the sliding event, it is possible to make a crude estimation of the vertical fluid migration velocity in the area of the ''lower-slope BSR''.

Using mass, momentum and energy conservation equations, it has been calculated that for a fluid velocity of 1 mm/year, the rate of hydrate formation and accumulation due to advection of methane from depth filling 1% of pore volume is of the order of 100 000 years (Rempel and Buffett, 1998; Zatsepina and Buffett, 1998). Here, we assume that a filling of 5 to 10% of the pore volume with gas hydrates is sufficient to explain the observed BSR reflection and related relative compressional wave velocity drop. Taking into account the dating of the first Storegga Slide event as 30–50 ka BP (Bugge et al., 1988), we can speculate that the subbottom fluid migration velocity in this area is of the order of at least several centimetres per year. Since, as discussed above, the conductive heat transport in the area is supposed to be by far more important than advective heat trans-

fer, this estimated quantity also represents in our opinion an upper limit for the fluid displacement rate.

5.3. Relevance of gas hydrate dissociation to further slope instability

The possible influences of sliding, and in particular the Storegga Slide events, on gas hydrate destabilisation and related liquefaction and vice versa has been actively discussed. For instance, Bugge et al. (1987) and Jansen et al. (1987) proposed gas hydrate decomposition due to earthquake agitation of sediments as one of the most likely triggering mechanisms for the Storegga Slide. Mienert et al. (1998) noticed that, as a consequence of earthquakes or mass wasting events which provoke gas hydrate to decompose due to changing thermodynamical conditions, the release of huge amounts of free gases and water in the pore space would exceed by far the volume that was previously occupied by the solid gas hydrate structure. This process can lead to — eventually drastically — increased pore pressures, facilitating further sliding. Next to that, the rapid release of methane during major slide events in coincidence with gas hydrate dissociation might have serious implications for the marine methane cycle and possibly for the global climate system (Lammers et al., 1995). Thus, any quantitative estimates of these effects are of significant interest.

The observation of BSRs inside the slide scar area and below slide deposits makes it possible to estimate how sliding could affect the gas hydrate stability in this area. It should be emphasised that such a procedure strongly depends on the assumptions made about the pore pressure distribution. In case of hydrostatic pore pressure distribution, no sliding nor earthquake would affect the overall hydrate stability.

After removal of the uppermost sediment of the seafloor, the hydrostatic pore pressure would remain unchanged since this value is only dependent on the height of the entire overlying water column.

At the same time, the seafloor is now formed by sediments initially exposed at higher temperatures due to burial under the suddenly removed sediments. The temperature difference between the seabed and the bottom water mass will cause a gradual decrease of the temperature of the ''new'' seafloor and subbottom sediments. As a consequence, the base of the GHSF will slowly move deeper into the sediments, until a new equilibrium position is reached.

This means that sliding or earthquake triggering can only force the solid hydrate structure to dissociate if excess pore pressures are present and the induced sediment failure would lead to a decrease in pore pressure. After the slide event, the theoretical base of the GHSF will then first jump immediately to a shallower subbottom depth, and only afterwards will start gradually to move deeper following the temperature decrease to the new equilibrium position (Fig. 14).

For the area of about 100 km^2 where the BSRs occur within the slide area, we have reconstructed the paleo-seafloor (i.e., the situation before the first Storegga Slide event) and calculated the position of the base of the GHSF before sliding. Fig. 10 shows an example of this reconstruction along seismic profile PSAT69. The sudden removal of the uppermost sediments caused an instantaneous decrease in lithostatic pressure (< 0.5 MPa) in the sediment column, while the in situ temperature regime at the same time is not altered. This means that the hydrates at the base of the initial stability field will fall out of the newly established pressure-induced stability field, just after the first Storegga slide event, similar as what is presented in Fig. 14. The position of the base of the GHSF immediately after the slide was then calculated, simply using the ''post-slide'' lithostatic pressure distribution and the ''pre-slide'' in situ temperature and geothermal gradient, in combination

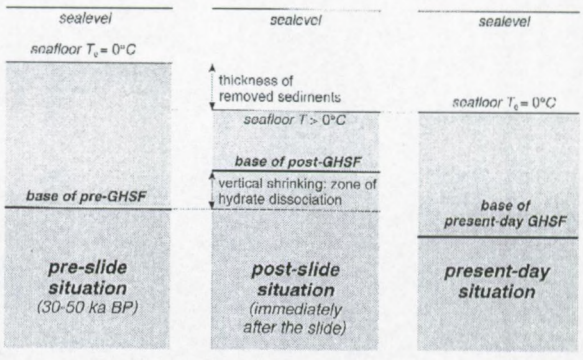

Fig. 14. Sketch of the influence of the slide event on the subbottom position of the base of the GHSF. The pre-, post and present-day situations of the vertical extent of the GHSF are shown.

with the formulas mentioned in Appendix A. A triangulation contour map of the vertical shrinking of the GHSF in this area, i.e. the thickness of that part of the initial ''pre-slide'' GHSF falling out of the ''post-slide'' GHSF, is shown in Fig. 15. The use of a lithostatic pressure assumption clearly leads to an overestimation of the calculated thickness. Even so, away from the areas directly below the escarpment where the difference is bigger, the average shrinking of the GHSF due to the slide event is in the order of only a few meters.

The total volume of sediments that was dropped out of the GHSF due to down-slope mass movement was calculated to be 41.30×10^7 m^3. The volume of sediments that remained undisturbed above the paleo-GHSF base is estimated to be 2.79×10^{10} m^3. With a maximum hydrate occupation of 10% of the pore spaces (Hovland et al., 1997) and assuming an average porosity of 50%, the total volume of dissociated hydrate due to sliding is estimated to be 2.07×10^7 m^3. At the maximum, one volume of gas hydrate yields approximately 0.8 volumes of water and 164 volumes of free gas at STP conditions (Kvenvolden, 1998). Thus, the total amount of destabilising gas hydrates in this area would release 338.66×10^7 m^3 gas and 1.65×10^7 m^3 water at STP conditions. At in situ pressures of about 13–14 MPa, the volume of released gas would not exceed approximately 2.65×10^7 m^3, due to the high compressibility of the (ideal) gas. Thus, at approximate in situ conditions, the initial volume of 2.07×10^7 m^3 of dissociating gas hydrate releases in total about 4.30×10^7 m^3 of gas and water. In other words, an excess fluid volume of approximately 2.2×10^7 m^3 needs to be redistributed in the pore spaces and will create overpressures. The crucial point in estimating the degree of these overpressures and, thus, the possible impact of hydrate decomposition on slope stability, is the time scale of the dissociation process, as the only thing needed for overpressures to dissipate through non-ideal impermeable media is sufficient time.

If one assumes that the sudden pressure decrease due to sliding will immediately dissociate all hydrate present in the zone that was dropped out of the GHSF, the released fluid volume needs to be redistributed together with the present pore fluids into the same pore volume. Hence, the excess fluid volume is 10–11%. In the most probable case when the pore fluids are considered to be mixed (small gas bubbles in pore water) and thus behaving as a single fluid phase, it is reasonable to assume that the pore pressure will also increase with approximately 10%.

However, in situ hydrate dissociation is most likely to be a slow process, and cannot be compared with the situation of hydrate decomposition during (ODP) core recovery in which the core is submitted to severe pressure reduction combined with significant temperature increase. Immediate and complete hydrate dissociation will not happen due to the sudden depressurisation caused by the slide for the

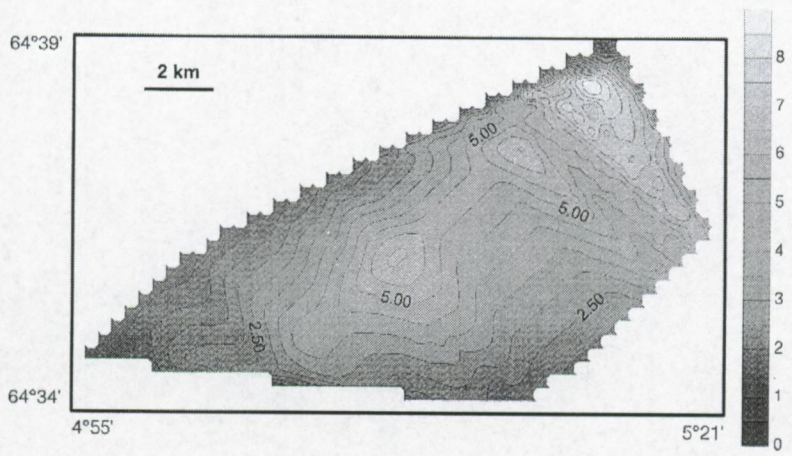

Fig. 15. The calculated thickness of the initially gas-hydrated layer which could fall out of the GHSF due to sliding within the area where the ''lower-slope BSR'' was observed below the slide deposits. Lithostatic pore pressure distribution was assumed.

following reasons. Since the pressure decrease is (nearly) instantaneous and hence much faster than heat exchange mechanisms, this process can be considered as isenthalpic depressurisation. This depressurisation will lead to a temperature drop of the gas and hydrate surface, or more specificly, it will enhance (!) the stability conditions (Sloan, 1998; pp. 549–552). From that moment, conductive heat flow from the surroundings into the hydrates is required to increase the system's temperature and will initiate hydrate dissociation. This process is limited by the rate of heat transfer, depending upon the temperature difference between the hydrate and the surrounding as well as upon geothermal properties of hydrate, host sediments and pore fluids. The partial dissociation of hydrates will then lead to a gradual pore pressure elevation. As this takes place, the heat of hydrate dissociation will be still drawn from the hydrate phase and the surrounding media, preventing the temperature from a fast increase. Thus, this gradual pressure increase at a first approximation can be considered as nearly isothermal and will shift the system back into the conditions favourable for hydrate stability. Continuous heat flow, however, now causes further dissociation, so again the pressure increases and the process starts all over again.

Quantitative estimates of this process are not available yet and additional research is necessary but it is clear that this circular process is not instantaneous at all. Moreover, in less permeable sediments, the hydrate will apparently dissociate slower than in more permeable strata because the excess pore pressure caused by partial dissociation will be dissipated slower and the system will return to hydrate stability conditions much easier.

From the above speculation about the time-scale of the in situ hydrate dissociation due to sliding, it seems to be more reasonable and correct to consider the excess fluid volume to be distributed throughout the entire section of undisturbed sediments above the inferred paleo-BSR, rather than to stay only within the pore space of the initial hydrate-containing sediments. Then, the calculated volume increase (and accordingly the pressure increase) equals only 0.2%, which — in our opinion — can hardly contribute to further regional slope instability.

Even if this is not exactly the case and the time-scale of the hydrate dissociation is, to a certain degree, overestimated, in our simplified calculations we disregarded a number of factors leading to further reduction of resulting overpressures. First, the excess pore pressure is the driving force for internal 3D fluid migration (Darcy's law). Thus, beside vertical fluid displacement, lateral migration will take place as well and the excess volume of fluids will be distributed through a larger pore space than in case when only vertical fluid migration is considered. Moreover, some volume of the migrating fluids can be exhausted through time towards the seafloor, which will also cause a release of excess pore pressure. We also ignored the volume decrease caused by the temperature difference between standard temperature (20°C) and in situ hydrate equilibrium temperature, typically around 10–15°C. Possible partial dissolution of the released gas in the released water was also disregarded. Probably more important, the change of porosity with subbottom depth is ignored as well, while the porous medium is supposed to be homogeneous. All these factors, reducing potential overpressures caused by possible in situ hydrate dissociation due to sliding, allows — in our opinion — for considering at least the order of the obtained estimation as quite reliable.

Of course, these estimates exclude by no means more complicated mechanisms or models in which the dissociation of gas hydrate effectively affects the slope stability. For instance, liquefaction or the release of active fresh water into the clayey environment of glacial/interglacial sedimentary sequence can stimulate formation of so-called ''fast clays'', leading to sediment failure. However, at least the most straightforward and simple mechanism of sliding vs. hydrate-dissociation interrelation will most likely not be considered seriously in this region. In fact, the independence of the observation of the ''lower-slope BSR'' on whether there was sliding above it or not, is itself an indirect evidence of minor, if any, relevance of the sliding to gas hydrate dissociation and vice versa.

6. Conclusions

At the edge of the Vøring Plateau near the Storegga Slide, a distinct BSR forming two laterally

separate zones was observed. The presence of shallow gas accumulations in between of these zones argues for a coupled hydrate formation mechanism in which directional gas migration plays a central role.

The ''lower-slope BSR'' is elongated virtually parallel to the general trend of the slope and is present both below the undisturbed sediments of the plateau, and below the slide scar area and slide deposits. No evidence for fluid venting through the seafloor above the BSRs is observed, except perhaps the slide scarp itself and chaotic seafloor morphology. This ''lower-slope BSR'' is characterised by clear crosscutting of the local stratigraphy and inverse polarity relative to the seafloor reflection.

The ''upper-slope BSR'' fits the area of inferred clay diapirs and is accompanied by numerous fluid escape features on the seafloor (e.g., pockmarks). The ''upper-slope BSR'' also shows reversed polarity, but no clear crosscutting is observed, due to a sedimentation pattern that also parallels the seafloor. However, its acoustic signature and subbottom position is strikingly similar to the situation in the ''lower-slope BSR'' zone. Furthermore, seismic inversion shows a significant relative velocity drop at the BSR interface. Combination of these observations and results allow us to label this reflector as a gas hydrate related BSR.

Over most of the area, the ''lower-slope BSR'' zone is connected to the ''upper-slope BSR'' zone through the presence of enhanced reflectors observed on the acoustic records in the hydrate free zone. These high-amplitude reflectors are found below the theoretical GHSF and are interpreted as indirect evidence of shallow gas accumulations.

Geothermal calculations, based on the BSR subbottom depth and the theoretical three-phase methane — seawater — hydrate equilibrium curve, suggest that the temperature gradient does not vary significantly within the area. Depending on the assumed pore pressure distribution, the geothermal gradient is calculated to be 0.051°C/m (hydrostatic pore pressure) or 0.056°C/m (lithostatic pore pressure).

A model is proposed in which active vertical percolation of gas is present within the zone of ''lower-slope BSR''. Due to the presence of vertical permeability barriers, gas migrates laterally from this region to the area of the diapirs that, in turn, provide pathways for further upward gas migration to the GHSF.

The velocity of vertical fluid migration in the ''lower-slope BSR'' zone was estimated to be at least the order of magnitude of several centimetres per year.

An estimate of possible effect of sliding or earthquake agitation of sediment on gas hydrate destabilisation, which then could facilitate further sediment failure in the area, demonstrates negative results. However, more complicated mechanisms for gas hydrate contribution to slope instability within the area (e.g., formation of ''fast clays'' due to release of active fresh water) cannot be excluded.

Acknowledgements

The authors would like to acknowledge the Scientific Party of the TTR-8 Cruise for fruitful cooperation and stimulating discussions. Personal thanks are addressed to M. Ivanov of UNESCO-MSU Centre for Marine Geosciences for his kind supervision, without which the major part of this work never could have been done. We thank our colleagues from UNESCO-MSU Centre for Marine Geosciences and Renard Centre of Marine Geology, University of Gent. G. Spence and M. Hovland are acknowledged for thoughtful comments and suggestions that undoubtedly improved the manuscript. Our collaboration has been partially supported through the Flemish Government grant RUS.97.05. M. Vanneste is funded by a Ph.D.-grant of the Flemish IWT (Brussels). We are grateful to the captain and the crew of the R.V. Professor Logachev and the technical and administrative staff of the Polar Marine Geosurvey Expedition. We acknowledge the Intergovernmental Oceanographic Commission of UNESCO, Ministry of Science and Technical Policy of the Russian Federation and all other institutes and bodies that supported the TTR-8 expedition. Guinness Breweries, Ireland are acknowledged for the excellent quality of their refreshing beverages, which were really good for us.

Appendix A. Nomenclature, parameters and formulas

A.1. Nomenclature

Symbol	Variables and constant values	Value	Unit
T	Methane–seawater–hydrate equilibrium temperature	–	°C
ρ_{bulk}	Average sediment bulk density	1800	kg m^{-3}
ρ_{sw}	Average sea water density	1025	kg m^{-3}
z	Subbottom depth	–	m
z_{BSR}	Subbottom depth of BSR	–	m
H	Water depth	–	m
$\overline{v}_p$	Mean compressional wave velocity	–	m s^{-1}
v_p	Instantaneous compressional wave velocity	–	m s^{-1}
g	Gravity acceleration	9.81	m s^{-2}
P_{atm}	Atmospheric pressure	0.101325	MPa
P	Methane–seawater–hydrate equilibrium pressure	–	MPa
P_{hydro}	Hydrostatic pressure	–	MPa
P_{lith}	Lithostatic pressure	–	MPa
t_{oneway}	Subbottom one-way travel time	–	s
t_{twoway}	Subbottom two-way travel time	–	s

A.2. Formulas

The formulas mentioned here were used to determine the geothermal field based on the presence of a BSR on the seismic profiles. Once the geothermal gradient is derived, this information is used with the same formulas for the subbottom velocity profiles and the phase boundary to calculate the vertical shrinking of the GHSF due to the sudden lithostatic pressure decrease caused by the slide event, i.e., the situation and result shown in Figs. 14 and 15.

A.2.1. Methane–seawater–hydrate equilibrium curve (Fig. 16)

$$\log P = a + bT + cT^2$$

hence:

$$T = \frac{-b + \sqrt{b^2 + 4c(\log P - a)}}{2c}$$

$a = 0.4684$ $b = 0.0401$ $c = 0.0005$

The constants a, b, c are derived after applying the method of least squares on experimental equilibrium values obtained by Dickens and Quinby-Hunt (1994). Pressure is expressed in MPa, while temperature is expressed in °C. The equation above is valid for the temperature interval $[-2, 15°C]$. The regression coefficient R^2 of this equation is 0.9994.

A.2.2. Pressure distribution

Hydrostatic pressure distribution (MPa):

$$P_{hydro} = P_{atm} + \rho_{sw} g(H + z) \times 10^{-6}$$

Lithostatic pressure distribution (MPa):

$$P_{lith} = P_{atm} + g[\rho_{sw} H + \rho_{bulk} z] \times 10^{-6}$$

In this simplified formula, the bulk density is assumed to be constant in the GHSF, so no porosity

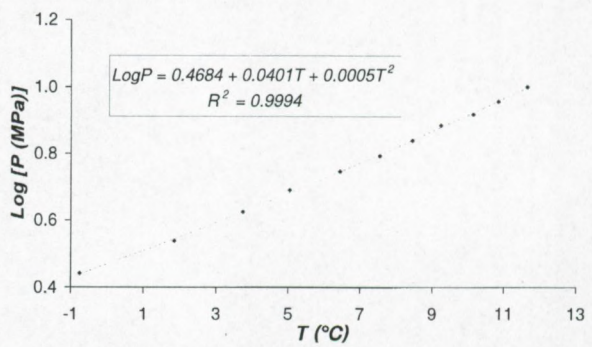

Fig. 16. Pure methane–seawater–hydrate phase boundary and equation, based on experimental data by Dickens and Quinby-Hunt (1994).

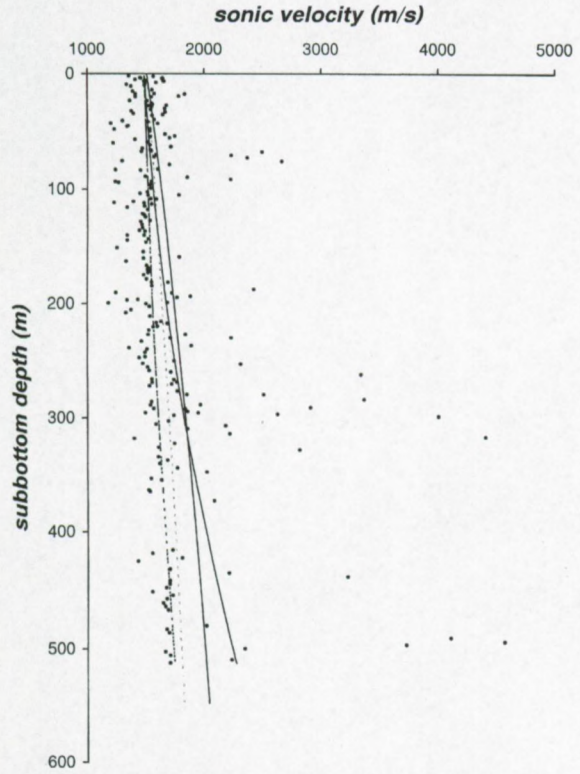

Fig. 17. Subbottom velocity profiles. The dots are measured p-wave velocities from ODP 104, site 642–643 (Eldholm et al., 1987b). The black curves represent instantaneous velocity (solid) and average velocity (dashed). The grey curves are the equivalent Hamilton's regression function (Hamilton, 1980).

changes or compaction effect is taken into account. The maximum average bulk density used, is based upon results from ODP Leg104, site 644 (Eldholm et al., 1987b).

A.2.3. Regression equations (Fig. 17)

Hamilton's equation: Mean and instantaneous compressional wave velocity (m/s) as a function of the subbottom travel time (s) for terrigeneous sediments (silt clays, turbidites, mudstone, shale) (Hamilton, 1980):

$$\bar{v}_p = 1511 + 1041 t_{oneway} - 372 t_{oneway}^2$$
$$= 1511 + 521 t_{oneway} - 93 t_{twoway}^2$$
$$v_p = 1511 + 1983 t_{oneway} - 758 t_{oneway}^2$$
$$= 1511 + 991.5 t_{twoway} - 189.5 t_{twoway}^2$$

Hamilton's equation: conversion to subbottom velocity profiles:

$$\bar{v}_p = -0.0001 z^2 + 0.6195 z + 1511$$

$$v_p = -0.0003 z^2 + 1.1063 z + 1511$$

Subbottom velocity profiles, using ODP-Leg104, site 642 and 643 (Eldholm et al., 1987b)

$$\bar{v}_p = 0.005 z^2 + 0.237 z + 1489.7 \quad R^2 = 0.8718$$

$$v_p = -0.0019 z^2 + 0.548 z + 1489.7 \quad R^2 = 0.1643$$

A.2.4. Geothermal gradient, using BSR equilibrium conditions

$$G = \frac{T - T_0}{z_{BSR}}$$

References

Akentieva, E., Shashkin, P., 1998. Technical report: OKEAN and OREtech side-scan sonars and sonograph processing. In: Kenyon, N., Ivanov, M., Akhmetzhanov, A. (Eds.), Cold Water Carbonate Mounds and Sediment Transport on the Northeast Atlantic Margin: Preliminary Results of Geological and Geophysical Investigations During the TTR-7 Cruise of R.V. Professor Logachev, 1997, 11–12.

Baas, J.H., Mienert, J., Schultheiss, P., Evans, D., 1994. Evidence of gas vents and gas hydrates in the storegga slide area (Norwegian Continental Margin). Abstracts, Gas in Marine Sediments. 3rd International Conference, NIOZ, Texel, The Netherlands, September, 1994.

Bolli, H.M., Saunders, J.B., Perch-Nielson, K., 1985. Plankton Stratigraphy. Cambridge Univ. Press.

Bouriak, S., 1998. Seismic manifestations of gas in the Sorokin trough (Black Sea): Analysis of velocity model obtained by inversion of seismic data. Abstracts, TTR7 post cruise meeting, 7–11 February, Gent, Belgium, p. 85.

Bugge, T., Befring, S., Belderson, R.H., Eidvin, T., Jansen, E., Kenyon, N.H., Holtedahl, H., Sejrup, H.P., 1987. A giant three-stage submarine slide off Norway. Geo-Mar. Lett. 7, 191–198.

Bugge, T., Belserson, R.H., Kenyon, N.H., 1988. The Storegga Slide. Philos. Trans. R. Soc. London A 325, 357–388.

Claypool, G., Kaplan, I., 1974. The origin and distribution of methane in marine sediments. In: Kaplan, I. (Ed.), Natural Gases in Marine Sediments. Plenum, New York, 99–139.

Clennell, M.B., Hovland, M., Booth, J., Henry, P., Winters, W.J., 1999. Formation of natural gas hydrates in marine sediments, part 1: conceptual model of gas hydrate growth conditioned by host sediment properties. J. Geophys. Res., in press.

Dickens, G.R., Quinby-Hunt, M.S., 1994. Methane hydrate stability in seawater. Geophys. Res. Lett. 21 (19), 2115–2118.

Dvorkin, J., Nur, A., 1993. Rock physics for characterisation of gas hydrates. In: Howell, D.G. (Ed.), The Future of Energy Gases. US Geological Survey Professional Paper, 1570, 293–298.

Ecker, C., Dvorkin, J., Nur, A., 1998. Sediments with gas hydrates: internal structure from seismic AVO. Geophysics 63 (5), 1659–1669.

Eldholm, O., Thiede, J., Taylor, E., 1987. Evolution of the Norwegian Continental margin: background and objectives. In: Eldholm, O., Thiede, J., Taylor, E., (Eds.), Proceedings of the Ocean Drilling Program. Initial reports, Leg 104, 5–25.

Eldholm, O., Thiede, J., Taylor, E., 1987. Proceedings of the ocean drilling program. Initial reports, Leg 104, Ocean Drilling Program, College Station, TX.

Eldholm, O., Thiede, J., Taylor, E., 1989. The Norwegian Continental Margin: Tectonic, volcanic and paleoenvironmental framework. In: Eldholm, O., Thiede, J., Taylor, E., et al. (Eds.), Proceedings of the Ocean Drilling Program, Scientific Results, Leg 104. Ocean Drilling Program, College Station, TX, 5–28.

Eldholm, O., Thiede, J., Taylor, E. et al., 1989. Proceedings of the Ocean Drilling Program, Scientific Results, Leg 104, Ocean Drilling Program, College Station, TX.

Evans, D., King, E.I., Kenyon, N.H., Brett, C., Wallis, D., 1996. Evidence for long-term instability in the Storegga Slide region off western Norway. Mar. Geol. 130, 281–292.

Ginsburg, G., Soloviev, V., 1997. Methane migration within the submarine gas-hydrate stability zone under deep-water conditions. Mar. Geol. 137, 49–57.

Hamilton, E.L., 1980. Geoacoustic modelling of the seafloor. J. Acoust. Soc. Am. 68 (5), 1313–1340.

Hjelstuen, B.O., Eldholm, O., Skogseid, J., 1997. Vøring Plateau diapir fields and their structural and depositional settings. Mar. Geol. 144, 33–57.

Hovland, M., Gallagher, J., Clennell, M., Lekvam, K., 1997. Gas hydrate and free gas volumes in marine sediments: Example from the Niger Delta front. Mar. Petrol. Geol. 14, 245–255.

Hovland, M., Judd, A.G., 1988. Seabed Pockmarks and Seepages: Impact on Geology, Biology and the Marine Environment. Graham and Trotman, London, p. 293.

Hyndman, R., Davis, E., 1992. A mechanism for the formation of methane hydrate and seafloor bottom-simulating reflectors by vertical fluid expulsion. J. Geophys. Res. 97 (5), 7025–7041.

Hyndman, R., Spence, G., 1992. A seismic study of methane hydrate marine bottom simulating reflectors. J. Geophys. Res. 97 (B5), 6683–6698.

Jansen, E., Befring, S., Bugge, T., Eidvin, T., Holtedahl, H., Sejrup, H.P., 1987. Large submarine slides on the Norwegian continental margin: sediments, transport and timing. Mar. Geol. 78, 77–107.

Kvenvolden, K.A., 1993. Gas hydrates: geological perspective and global change. Rev. Geophys. 31 (2), 173–187.

Kvenvolden, K.A., 1998. A primer on the geological occurrence of gas hydrate. In: Henriet, J.-P., Mienert, J (Eds.), Gas Hydrates: Relevance to World Margin Stability and Climate Change, Geological Society of London, Special Publications, 137, 9-30.

Kvenvolden, K.A., Golan-Bac, M., McDonald, T.J., Pflaum, R.C., Brooks, J.M., 1989. Hydrocarbon gases in sediments of the Vøring Plateu, Norwegian Sea. In: Eldholm, O., Thiede, J., Taylor, E., et al. (Eds.), Proceedings of the Ocean Drilling Program, Scientific Results, Leg 104, Ocean Drilling Program, College Station, TX, 291–307.

Lammers, S., Suess, E., Hovland, M., 1995. A large methane plume east of Bear Island (Barents Sea): implications for the marine methane cycle. Geologische Rundschau 84, 59–66.

Lavergne, M., Willm, C., 1977. Inversion of seismograms and pseudo velocity logs. Geophys. Prospect. 25 (2), 231–250.

Lindseth, R.O., 1979. Synthetic sonic logs — a process for stratigraphic interpretation. Geophysics 44 (1), 3–26.

Mienert, J., Posewang, J., Baumann, M., 1998. Gas hydrates along the north-eastern Atlantic margin: possible hydrate bound margin instabilities and possible release of methane. In: Henriet, J.-P., Mienert, J. (Eds.), Gas Hydrates: Relevance to World Margin Stability and Climatic Change, Geological Society of London, Special Publication, 137, 275–291.

Minshull, T.A., Singh, S.C., Westbrook, G.K., 1994. Seismic velocity structure at a gas hydrate reflector, offshore Western Columbia, from full waveform inversion. J. Geophys. Res. 99 (B3), 4715–4734.

Muller, 1978. Tertiary and Quaternary Calcareous nannoplankton in the Norwegian-Greenland Sea. In: White, S.M. (Ed.), Initial Reports of the Deep Sea Drilling Project, Leg 38, 823-841

Posewang, J., Mienert, J., 1996. Gas hydrates and free gas in sediments of the Norwegian Continental Margin: results from wide-angle seismic experiments. In: Mienert, J., Henriet, J.P. (Eds.), Gas Hydrates: Relevance to World Margins Stability and Climatic Changes, Abstract Book, 70, Gent, 18–22 September.

Rabinowitz, P.D., Baldauf, J.G., Garrison, L.E., Meyer, A.W., 1992. Ocean drilling on passive continental margins. In: Watkins, J.S., Zhiqiang, F., McMillen, K.J., (Eds.), Geology and Geophysics of Continental Margins, American Association of Petroleum Geologists, Chap. 22, 399–414.

Rempel, A., 1995. Theoretical and experimental investigations into the formation and accumulation of gas hydrates. MSc Thesis, University of British California, p. 122.

Rempel, A., Buffett, B., 1998. Mathematical models of gas hydrate accumulation. In: Henriet, J.-P., Mienert, J. (Eds.), Gas Hydrates: Relevance to World Margin Stability and Climate Change, Geological Society of London, Special Publications, 137, 63–74.

Russel, B.H., 1988 Introduction to seismic inversion methods. Society of Exploration Geophysicists, Course Notes Series, 2.

Sloan, E.D., Jr., 1998. Clathrate hydrates of natural gases, 2nd edn., Marcel Dekker, New York, p. 703.

Thiede, J., Eldholm, O., Taylor, E., 1989. Variability of Cenozoic Norwegian-Greenland Sea paleoceanography and northern hemisphere paleoclimate. in: Eldholm, O., Thiede, J., Taylor, E. et al. (Eds.), Proceedings of the Ocean Drilling Program, Scientific Results, Leg 104, Ocean Drilling Program, College Station, TX, 1067–1118.

Yamano, M., Uyeda, S., Aoki, Y., Shipley, T.H., 1982. Estimates of heat flow derived from gas hydrates. Geology 10, 339–342.

Zatsepina, O., Buffett, B., 1998. Thermodynamic conditions for the stability of gas hydrate in the seafloor. J. Geophys. Res. 103 (10), 24127–24139.

Chapter 6
Synthesis

Hydrate stability conditions and destabilisation processes

The first objective of this research project was to study the possible destabilisation processes for natural gas hydrates stored in marine or lacustrine sediments. This discussion was mainly focused on the effect of sea level changes and bottom temperature fluctuations. As an outcome of these analyses, a computer program was written to investigate the influence of both effects on naturally occurring gas hydrates through time. Combination of the pressure profile, sub-bottom temperature profile and the three-phase equilibrium equation results in an implicit dependence on sub-bottom depths. Next to that, the high variability of hydrate compositions and the wide range of the individual parameters for geological situations further necessitates a general program since the results obtained for one specific situation are not necessarily the same as for other situations. Such programs are provided with this dissertation.

Sea level drops and bottom temperature rises are both responsible for an evolution towards less favourable hydrate stability conditions. The *pressure effect* is much more pronounced in shallower water basins, for small geothermal gradients or heat flow values, for higher bottom water temperatures and evidently for higher amplitude changes of the sea level change. For bottom temperature changes to become sensible, time is required allowing the thermal pulse to penetrate the sub-surface and alter the initial equilibrium limit. The *temperature effect* initiated by changing bottom temperatures is stronger for higher amplitude changes, in shallow water basins, on longer time lags, for faster changes, for smaller geothermal gradients or heat flows. During climatic changes, sea level lowering can be combined with decreasing bottom temperatures. Hence, two opposing processes are taking place concurrently and forecasting the final result will highly depend on the typical situation of interest (time scale of pressure and temperature change, delay, water depth, amplitudes of changes). The analyses shown here illustrate that inversion can occur through time, i.e. the stability conditions can first evolve towards unfavourable conditions (upward migration) and later on to subsidence deeper within the sediments or vice versa. This is explained by the time lag required for the thermal pulse to become sensible, while pressure influences are supposed to be transferred immediately through the porous medium. Once the sea level change is completed, the thermal pulse can still be responsible for further changes of the stability limit. Another remarkable feature is that the effect of such combined processes can be different in the shallow vs. deeper parts of the basin. While in the end hydrate stability can be increased (equilibrium limit migrates deeper) at the deeper parts, less favourable conditions can remain at shallower places. The magnitude of the changes is bigger in the shallower part as well. Hence, simply stating that sea level drops during e.g. the Pleistocene forced hydrate dissociation is jumping to conclusions if bottom temperature changes are not taken into account.

A first application of this methodology revealed that methane hydrates cannot be stable at present-day conditions within the sediments of the *Magellan-Hovland* area, offshore Western Ireland, while during glacial times their extent covers the entire zone. The disappearance is fully attributed to the high-amplitude temperature change during glacial-interglacial transition that completely offsets the favourable sea level change effect. A second application was worked out for methane hydrate stability at the *Storegga Slide* area, offshore Norway. The effect of mass wasting can be considered as a sudden thermal pulse on the newly exposed sediments at the seabed. The magnitude of this pulse depends on the thickness of removed sediments with a maximum of ± 4.5°C at the headwall and fading out within the slide area. The effect on hydrate stability strictly depends on pore pressure assumption. For pure hydrostatic pressure, erosion does not alter *the in* situ pore pressure. Hence the system will simply evolve towards improved stability conditions. If lithostatic pressure is appropriate, then modelling results in a phase of dissociation at the base of hydrate stability in a restricted zone within the slide

area (< 10 m) due to the mass removal. With time, the stability limit will subside compared to the pre-slide initial situation. It is furthermore calculated that sea level fluctuations since the first *Storegga Slide* event did not result in significant changes of the evolution of the hydrate stability limit. Finally, spontaneous uplift due to buoyancy of partially hydrate-saturated sediments is not supposed to take place frequently.

Acoustic response of partially hydrate-saturated sediments

The acoustic characterisation of hydrate-bearing sediments was worked out based on multi-frequency seismic data (MC airgun-array, SC Ship and Impulse airgun, SC watergun, SC sparker) acquired in the Central and Southern Baikal Basins. Lake Baikal is, up to now, the only confined fresh water basin with both direct and indirect evidence of gas hydrates. Hydrates were retrieved by deep-drilling and shallow coring. Methane of biogenic origin is by far the most abundant gas in the hydrate structure. Areas with inferred hydrate occurrence are found symmetrically around the Selenga Delta in deeper waters (> 580 m).

The different data sets clearly reveal different images of the reflection interpreted to be the base of hydrate stability or top of gas-containing sediments (BHSZ). The acoustic data set demonstrates a high dependency of the BHSZ expression on the acquisition frequency used. The BHSZ is generally represented on MC data by a distinct polarity-reversed BSR, crosscutting the local stratigraphy and mimicking the lake floor morphology. Beneath the BHSZ, enhanced reflections often occur while amplitude blanking is present – although laterally variable and fading out upwards – above the BSR. No evidence is found neither of the upper boundary of the hydrate accumulation zone nor from the base of the free gas layer beneath. The medium- to high-frequency data are more difficult to interpret. On medium-frequency profiles, both the amplitude and continuity is less explicit. One of the high-frequency profiles is characterised by a series of enhanced or bright spots, all being part of individual reflections, while no BSR feature is discerned. These enhanced reflections terminate up-dip at about the same sub-bottom depth, and form a facies change of high-amplitude events with a blanked section. Comparison with low-frequency data reveals that this up-dip interface coincides with the BHSZ. Very-high-frequency data suffer from very variable acoustic penetration limited to about the mean sub-bottom depth of the hydrate stability limit. Often, all acoustic energy is absorbed beneath enhanced reflections. These data cannot be used unambiguously to delineate the BHSZ without careful lower-frequency control.

Indirect evidence for the presence of free gas beneath the BHSZ is abundant. AVO analyses show a significant increase in BSR reflection amplitude with increasing offset, reflection coefficients of the BSR are up to –43% of the lake floor reflection (the negative sign indicates a drop of acoustic impedance), the presence of enhanced reflections beneath the BHSZ indicates free gas, and there is a sudden drop of frequency content of the seismic signals across this event. First results of OBH analyses also demonstrate a sharp decrease in acoustic interval velocity at depths of the BHSZ. The vertical extent of the free gas zone beneath the HSZ is estimated to be in the order of a few m to a few tens of meters. The accumulation of free gas occurs in this area within specific strata beneath the HSZ. This indicates that stratigraphy and lithology are major factors controlling the migration of fluids and subsequent accumulation of free gases trapped by the hydrate boundary.

These observations illustrate that the BSR reflection amplitude depends on both vertical and horizontal resolution. These represent a specific volume giving rise to acoustic reflection. The higher the dominant frequency, the smaller this volume and the more sensible the acoustic response will be to small-scale lateral changes, inhomogeneities, irregularities,... In combination with stratigraphically and lithologically-controlled fluid migration towards the BHSZ, the absence of a BSR is then explained by the fact that the horizontal distance between the free gas containing strata exceeds the lateral resolution, and will hence not give rise to a high-amplitude reflection for this volume. Additionally, the AVO-effect is inherent to stacking of MC data, by which the increased amplitudes recorded in the far-offset channels will contribute more to the returned signal on the stacked seismic profile.

Comparison of results from deep-drilling with seismic data across the drill site show that significant amounts of hydrates can be present within the pore spaces without any acoustic expression within the entire sedimentary column. Finally, the extent of the total amount of gas hydrate in the sub-surface of Lake Baikal is estimated to contain 4.6 Gton of carbon. The Baikal hydrate reservoir is not considered to have any future economic potential.

Anomalous gas hydrate accumulations in Lake Baikal

Seismic data from the central part of the Southern Baikal Basin demonstrate that Lake Baikal represents a unique hydrate accumulation environment. Closely spaced areas reveal the presence of both normal BSRs and typical high-amplitude reflections, interpreted to represent the BHSZ based on their reversed-polarity and crosscutting behaviour combined with the coincidence with common BSR features at the intersections with other seismic profiles. Changes of the BHSZ vary over 100-150 m on a few km distance and occur independent of lake floor topography. The BHSZ forms a kind of anticline, bounded to the N by a fault structure. This typical behaviour appears to be a very local phenomenon. Within the zone of up-doming BHSZ fluid escape features are evidenced on side scan sonar data and echo-sounding, and coincide with elevated heat flow. These irregularities line up nearly parallel to an antithetic fault forming the northern rim of the zone of anomalies. Temperature variations are minimal, but methane concentrations are higher than background values. Acoustic evidence for gas accumulation and migration is abundant in this zone of anomalous BHSZ distribution.

Comparison of measured vs. inferred heat flow values shows reasonable correlation, even in zones with focused fluid discharge. In general, measured heat flow exceeds the inferred one. Along one seismic profile with typical oscillating behaviour S of the fluid escape structures, the heat flow measurements do not follow the BHSZ trend as observed and deviations are up to 40%, i.e. much higher than the estimated errors on both methods. Inferred heat flow turns out to be exceptionally low along some parts, in contradiction to the measurements. Whether this is due to fluid or heat fluxes or variations in methane concentrations and/or supply and hence critical hydrate formation conditions is unknown.

The study area lies in the hanging wall of the *Posolskaya* fault, a major thermo-active intra-basinal fault. A model is proposed in which recent tectonic activity related to movement of the *Posolskaya* fault is responsible for hydrate dissociation by injection of warmer water and heat supplied mainly via the fault zones disturbing the initially stable local geothermal field in the area. Also heat conduction and lateral fluid displacement can take place. The sudden onset of such pulses (e.g. relative to hydrate formation) suggests relatively fast build-up of overpressures. If excess pressure cannot dissipate fast enough, hydraulic fracturing can occur and nearly vertical escape of the gas rich mud phase can take place, giving rise to the observed fluid escape features. Similar processes can be repeated with time, dependent on the tectonic activity.

While this model explains qualitatively several of the observations, still some questions are unsolved and need to be investigated in the near future, taking into consideration the most recent results recently being reported. The influence of this entire process on the hydrology (*in casu* the oscillating BHSZ) is of importance.

Gas hydrates, free gas accumulations and clay diapirs offshore Norway

Unique seismic profiles were acquired during the R.V. Logachev TTR8-expedition offshore Norway in the *Storegga Slide* area. BSRs were observed in two laterally separated zones linked by the presence of shallow gas accumulations trapped beneath a low-permeability stratigraphic boundary below the local hydrate stability limit. The "lower-slope BSR" zone characterised by the crosscutting behaviour and

reversed polarity extends along some sections even below the slide scarp and within the area disturbed by the slide event. No fluid escape features are observed. The "upper-slope BSR" zone coincides with inferred clay diapirs and numerous fluid escape features at the sea floor. The BSRs lie at about the same sub-bottom depths but run nearly parallel to the stratigraphic pattern in this zone, which hampers their identification as BSRs related with free gas and/or gas hydrates. Their negative polarity and evidence of a significant drop in acoustic velocity across these reflections is indicative for a gas hydrate – free gas interface. The presence of enhanced reflections in the intermediate zone suggests that both zones of inferred hydrate occurrence are closely related. A hydrate formation model for this area is then proposed in which (vertical) active percolation of gas towards the lower-slope BSR takes place. Once entering the stability field, gas molecules are extracted from the pore fluid, form hydrates and reduce the permeability. The presence of vertical permeability barriers forces the gases to migrate laterally along stratigraphic boundaries until they reach the zone of inferred fluid escape features where the diapirs form preferential conduits for renewed vertical upward movement of gases that again can form hydrates giving rise to the "upper-slope BSR" zone. The ascending gas that is not clathrated escapes at the seabed.

The fact that the reflections are bottom-simulating illustrates the invariable geothermal conditions in the area. Geothermal gradients for the area are $0.051°C \cdot m^{-1}$ res. $0.056°C \cdot m^{-1}$, inferred from BSR observations using hydrostatic and mean lithostatic pressure distributions. Next to that, the presence of a BSR within the slide area at normally expected sub-bottom depths for these geothermal gradients, is an indirect proof that the newly established hydrate equilibrium field has been re-established well since the time of sliding. Eustatic sea level changes since the slide event only have a minor importance during re-equilibrium initiated by the sliding. This observation in combination with modelling results allowed us to estimate the internal fluid migration velocity to be in the order of a few cm per year. The lack of irregularities in the BSR structures suggests that this is as well an upper limit.

The real influence of mass wasting on the dissociation process and its contribution to further slope instability is also investigated. The key point is that pure depressurisation is a slow process for hydrate decomposition since heat needs to be extracted from the surrounding sediments. This will result in a cyclic feedback mechanism and will delay large-scale *in situ* destabilisation. At the same time, excess pressure will dissipate. In this way, the process is fundamentally different compared to the Lake Baikal situation.

Further research activities

Although this work fulfilled the main objectives, still some interesting and important topics should be taken into consideration and can form the subject of further research activities.

Modelling hydrate formation, stability and dissociation mechanisms should be significantly expanded to dynamic systems in which the entire system as a whole is considered. The succession of (short-term) bottom temperature changes should be worked out in more detail and implemented as well. Not only external processes e.g. sedimentation, subsidence, tectonic activity, isostacy, ice cap loading, bottom temperature variations, sea level fluctuations, ... but especially internal processes like energy and mass flows should be carefully investigated with emphasis on their time scale. The importance of such internally driven effects is the straightforward input of energy at the hydrate stability limit, i.e. where small changes can have the biggest impact. The influence of excess pore pressure generation due to hydrate dissociation and possible dissipation as a result of pressure or thermal pulses should be investigated in greater detail. The wide variety of geological situations and conditions does not facilitate such efforts and will result in specific thresholds or characteristics depending on local conditions. Drilling therefore can provide a tremendous amount of valuable information.

In the case of Lake Baikal, only recently a detailed multi-disciplinary data set became available and the full scale of the acting processes is not yet well understood. Studies should be carried out to explain the observed deviations between inferred and measured heat flow values for the static misfit

apparently inherent to the methodology used or to refine these methods. Especially the origin of the anomalous oscillating behaviour and deep subsidence of the BHSZ contradictory to the heat flow measurements should be addressed, regarding hydrate formation and internal flow patterns of pore water and gases. The energy budget should then be modelled. All data available and results of analyses should be investigated in order to determine the extent of the entire process, its time scale and its frequency.

Further quantitative results should be obtained from the acoustic data set, e.g. applying seismic inversion on the different groups of data, estimates of free gas content and/or partial hydrate saturation factors as a result of AVO-modelling and its lateral variation along the seismic lines and from line to line in relation to OBH/OBS and thus detailed acoustic velocity analyses. These should then be correlated as well with drilling results, if possible. A more detailed study of the attenuation mechanisms and synthetic trace modelling of the amplitude decay with depth as a function of acoustic frequency in zones of gas hydrates and free gas occurrence can also yield important information of the distribution of hydrates and free gas zones within the Baikal sediments. In this way, the estimation of carbon content of the Lake Baikal gas hydrate reservoir and underlying free gas accumulations can be significantly improved.

New seismic profiles were also recently acquired on the Norwegian continental margin and slope (TTR-10) and extend the available data set (TTR-8) further within the slope area showing more evidence of the repositioning of the HSZ since the slide event. These should be used to refine the estimates of the contribution to slope instability due to hydrate dissociation as a consequence of sliding and to modify the hydrate formation model for this area. Comparing these data with other seismic profiles from the area should be considered. New dating of the sliding even suggest that the *Storegga Slide* event might have been one single event that occurred ± 6-8 ka BP. Then, the repositioning of the BHSZ should take place extremely fast compared to the modelling exercises worked out here.

Hoofdstuk 7
Nederlandstalige samenvatting

7.1
Probleemstelling en algemeen belang van het onderzoek

7.1.1
Inleiding

Recente studies [*Raynaud et al., 1996; Watson et al., 1990*] wijzen op een toename van het methaangehalte in de atmosfeer met ongeveer 1% op jaarbasis. Aangezien CH_4 in termen van stralingsbalans 10 keer effectiever is in vergelijking met CO_2 [*Lashof & Ahuja, 1990*], is het noodzakelijk verder onderzoek te doen naar de lokalisatie van methaanreservoirs en de eventuele transfer van dit broeikasgas naar de troposfeer en de stratosfeer. Talrijke onderzoekers [o.a. *Harvey & Huang, 1995*] suggereren dat de destabilisatie van natuurlijke gashydraten, waarvan methaanhydraten de overgrote meerderheid vormen, een belangrijke bijdrage kan leveren tot de opbouw van dit atmosferisch methaan, en op die manier een rol kan spelen in lokale of zelfs globale klimatologische cycli. Evenwel blijkt de huidige kennis over de toestand en uitgebreidheid van hydraataccumulatie in sedimenten en de eventuele destabilisatiemechanismen van deze methaanreservoirs beperkt te zijn zodat verder multi-disciplinair onderzoek zich opdringt.

Gashydraten zijn ijsachtige kristalstructuren opgebouwd uit polyhedra-vormende watermoleculen die individuele gasmoleculen insluiten. Naast vrij methaan en opgelost in poriënwater zijn hydraten de derde vorm van methaan onder natuurlijke omstandigheden. Deze niet-stoïchiometrische verbindingen vormen zich doorgaans onder specifieke condities van lage temperatuur (< 25°C) en hoge druk (> 3 MPa of equivalent > 300 m waterdiepte). In natuurlijke omstandigheden is CH_4 het belangrijkste hydraatvormende gas, hoewel ook hogere koolwaterstoffen, CO_2 en H_2S kunnen voorkomen. Deze gassen vormen allemaal type-I hydraten. Daarnaast worden in de natuur nog type-II en type-H hydraten aangetroffen [*Kvenvolden, 1998*], die elk gekarakteriseerd worden door hun eigen typische stapeling van polyhedra of caviteiten per eenheidscel en dus ook specifieke evenwichtscondities hebben. Het type hydraat dat gevormd wordt, is afhankelijk van o.a. de grootte en de symmetrie van de stabiliserende gasmoleculen en de samenstelling van de gasfaze [*Sloan, 1998*].

Gashydraten worden wereldwijd aangetroffen zowel in polaire gebieden waar ze geassocieerd worden met *onshore* en *offshore* permafrost gebieden [*Collett, 1993*] als in sedimenten op de continentale hellingen en randen [e.g. *Kvenvolden, 1998;* ODP Leg 166, 164, 146, 131]. Onlangs werden deze structuren ook voor het eerst ontdekt in de sedimenten van een zoetwaterbekken, nl. het Baikalmeer in Siberië [*Kuz'min et al., 1998*]. De kritische factor voor de vorming van hydraten onder natuurlijke omstandigheden – in de veronderstelling dat de thermodynamische condities vervuld zijn – is de aanwezigheid of aanvoer van voldoende hoeveelheden gasmoleculen om de open hydraatvorm te stabiliseren. De ingesloten gassen kunnen zowel van biogene als thermogene oorsprong zijn.

Hydraataccumulaties in de poriën van oceanische of lacustriene sedimenten worden meestal indirect waargenomen door de aanwezigheid van een bodemsimulerende reflectie (BSR) op seismische profielen. Algemeen werd aangenomen dat deze reflectie de basis van de hydraatrijke zone in de sedimenten voorstelt, overeenkomend met de lokale thermodynamische evenwichtsvoorwaarden voor hydraatstabilisatie, zijnde de intersectie van het temperatuursprofiel in de bodem met de 3-fazegrens

hydraat-water-gas. De reflectie van de energie wordt veroorzaakt door het akoestisch impedantiecontrast aan een grenslaag tussen enerzijds partieel-gehydrateerde sedimenten erboven en anderzijds hydraatvrije sedimenten (met eventueel vrij gas) eronder. Deze sterke reflector volgt doorgaans de zeebodemmorfologie - en is dus in eerste instantie temperatuursgebonden -, vertoont een inverse polariteit relatief t.o.v. de zeebodemreflector en snijdt vaak primaire stratigrafische eenheden. Fysico-chemische modelleringsstudies wijzen er echter op dat deze reflectie wordt veroorzaakt aan de top van een vrije gaszone in het poreuze medium, en dat een transitiezone aanwezig kan zijn tussen de basis van de hydraataccumulatie en de top van de vrije gaszone [*Xu & Ruppel, 1999*]. Het al dan niet voorkomen van deze transitiezone is afhankelijk van de interne flux van fluïda. Toch worden vaak indirecte (akoestische) aanwijzingen gevonden voor het samenvallen van deze twee fysico-chemische grensvlakken, bij wijze van een duidelijke akoestische snelheidsinversie over de grenslaag.

Voor de vorming van methaanhydraten in sedimenten vinden we in de literatuur drie modellen terug:

- In het eerste model [*Claypool & Kaplan, 1974*] wordt verondersteld dat methaan *in situ* gegenereerd wordt door afbraak van organisch materiaal in afwezigheid van zuurstof en sulfaten binnen het thermodynamisch stabiliteitsgebied. Als de methaanconcentratie hoger ligt dan de oplosbaarheid, kunnen hydraten gevormd worden. De hydraatzone zal aandikken en de basis zal eventueel - bij continue sedimentatie - onder de stabiliteitsgrens zakken. Indien voldoende massatransportmogelijkheden aanwezig zijn, kan het vrijgekomen gas opnieuw naar het stabiliteitsgebied migreren. In dit geval zou de hydraatzone zich in principe moeten uitstrekken doorheen het volledige stabiliteitsgebied waaronder vrij gas aanwezig kan zijn.
- In het tweede model [*Hyndman & Davis, 1992*] worden hydraten gevormd door het weghalen van methaanmoleculen uit opwellende poriënfluïda aan de basis van het stabiliteitsgebied. Methaan wordt in dit geval doorgaans bacteriologisch gegenereerd op diepten onder de stabiliteitslimiet maar kan ook van thermogene oorsprong zijn. Dit heeft tot gevolg dat de gashydraten zullen accumuleren aan de basis van het stabiliteitsvenster. Vooral de scherpe afname van de oplosbaarheid van methaan eens binnen het hydraatstabiliteitsvenster speelt een belangrijke rol [*Ginsburg & Soloviev, 1997*]. Hoewel het chemische proces waarbij de gasmoleculen uit de poriënfluïda gefilterd worden niet precies gekend is, biedt dit model een afdoende verklaring voor de aanvoer van enorme hoeveelheden gassen nodig voor de vorming van hydraten.
- In het derde model [*Minshull et al., 1994*] wordt vrij gas verondersteld te migreren doorheen zones van verhoogde permeabiliteit ten gevolge van het drijfvermogen of capillaire effecten in het poreuze medium. Hydraten worden gevormd op zogenaamde nucleatiekernen, en aldus verminderen ze de porositeit en bijgevolg ook de permeabiliteit. Ten einde kan een permeabiliteitsgrens ontstaan waardoor elke vorm van migratie uitgesloten wordt. Dat leidt tot de opeenhoping van vrije gasbellen onder de fazegrens. Continue sedimentatie of subsidentie zal aanleiding geven tot veranderende evenwichtsvoorwaarden en eventueel hydraatdissociatie tot gevolg hebben, waarna het vrijgekomen gas opnieuw deel kan uitmaken van de cyclus [*Paull et al., 1994*].

In heel veel gevallen blijkt fluïdamigratie karakteristiek te zijn voor hydraatrijke gebieden [vb. *Booth et al., 1998*]. Hydraatvorming geschiedt ook preferentieel binnen relatief grotere poriën [*Ginsburg, 1998*]. Capillaire effecten kunnen de lokale evenwichtscondities verstoren en afwijkingen veroorzaken [*Clennell et al., 1999; Henry et al., 1999*]. De fysische vereiste tot het minimaliseren van de oppervlakte-energie verklaart de vorm van de hydraatinclusies in de meeste bovengehaalde kernen: nodules, gelaagde structuren, lensvormen en slechts heel uitzonderlijk massieve hydraten. Het staat vast dat de vorming van belangrijke hoeveelheden hydraten in sedimentaire middens doorgaans zeer traag gebeurt, vooral dan door de nood aan grote hoeveelheden gasmoleculen die moeten kunnen migreren [model 2/3] vanuit dieper gelegen gebieden naar het hydraatstabiliteitsgebied [*Rempel & Buffett, 1997*].

Het algemeen belang dat heden ten dage gesteld wordt in de problematiek van gashydraten is drievoudig en weerspiegelt onmiddellijk de uitgebreide industriële toepassingsmogelijkheden:

- *Energetisch aspect*: Uit de microscopische eigenschappen van de hydraatstructuren werd afgeleid dat bij standaard druk- en temperatuurscondities 1 volume hydraat met een partiële

caviteitsoccupatie van 90% in ongeveer 0.8 volumes water en 155 volumes gas ontbindt. Hieruit blijkt de enorme stockeringscapaciteit van de hydraatstructuur. Hoewel de geschatte hoeveelheden aan koolstof in hydraatvorm speculatief en onzeker zijn, convergeren de meest recente schattingen naar de grootte-orde van 10000 Gt of $2.1 \cdot 10^{16}$ m^3 [*Kvenvolden, 1998*] in mariene sedimenten en 800 Gt of $170 \cdot 10^{13}$ m^3 in permafrost gebieden [*Harvey & Huang, 1995*]. Daarnaast wordt nog verondersteld dat 10^{14} m^3 vrij gas gevangen zit onder de hydraatkap [*Sloan, 1998*]. *Ginsburg* echter suggereert dat deze hoeveelheden minstens met een factor 10 te hoog ingeschat worden [*Ginsburg, pers. comm.*]. Toch is het duidelijk dat dit medium een enorm koolstofreservoir vormt en niet langer genegeerd kan worden in de globale koolstofcyclus. Wegens het wereldwijde verspreide voorkomen van deze structuren worden hydraten dan ook steeds meer beschouwd als de energiebron van de toekomst. Recente schattingen over hydraatvolumes in enkele gebieden (Blake Ridge [*Dickens et al., 1996*], Baikal [*Vanneste et al., in press*]) tonen echter aan dat exploitatie niet overal de moeite loont.

→ *Stabiliteit van continentale randen*: Destabilisatie van gashydraten, geïnitieerd door eustatische zeespiegeldalingen of verhogingen van de bodemtemperaturen of door externe mechanismen zoals aardbevingen, kan verhoogde poriëndrukken in de sedimenten genereren. Als die overdruk niet voldoende snel dissipeert, ontstaat een instabiele toestand met verlaagde schuifweerstand. Omdat hydraten vaak aangetroffen worden op continentale hellingen en door de inwerkende zwaartekracht op de "verzwakte" sedimenten, kunnen belangrijke massaverplaatsingen plaatsgrijpen. Zo wordt bijvoorbeeld de *Storegga Slide* aan de Noorse westkust in verband gebracht met hydraatdestabilisatie geïnitieerd door een aardbeving [*Bugge et al., 1988*], hoewel een versterkend effect geinitieerd door hydraatdecompositie niet zeker blijkt [*Bouriak et al., 2000*]. De geobserveerde onderzeese afglijdingen op de continentale helling van de Beaufort Zee zouden eveneens veroorzaakt zijn door hydraatdestabilizatie volgend op een eustatische zeespiegeldaling in het Pleistoceen die tot een vermindering van de hydraatstabiliteit over een interval van 20 m leidde [*Kayen & Lee, 1991*]. Eigen onderzoek echter illustreert dat dergelijke uitspraken zeer voorbarig zijn zonder rekening te houden met temperatuurseffecten.

→ *Klimaatsgebonden aspect*: Bij klimatologische veranderingen (zeespiegelschommelingen en veranderende temperaturen van de bodemwaterstromingen) kunnen spontane verschuivingen in de evenwichtscondities voor de hydraten optreden waardoor geleidelijke destabilisatie kan voorkomen (zie vorig punt). Het vrijkomend gas zal onder bepaalde voorwaarden kunnen opgenomen worden in de atmosfeer waar het een actieve werking kan hebben als broeikasgas en dusdanig het klimaat kan beïnvloeden. Vooral wegens de gekende eigenschappen van methaan, het meest voorkomende hydraatvormende gas, als broeikasgas, kunnen oceanische en permafrost hydraataccumulaties een moeilijk in te schatten bijdrage leveren tot klimaatsveranderingen. Een wisselwerking tussen permafrost en oceanische hydraatdestabilisatie in de vorm van een positief-negatief feedback systeem [e.g. *Haq, 1993*] zou een belangrijk impact kunnen hebben op het heersende klimaat en de op punt staande veranderingen. De onzekerheden in de hedendaagse klimaatmodellen, laten echter niet toe heden te dage een definitieve conclusie uit te spreken [*Thorpe et al., 1998; Raynaud et al., 1998*].

7.1.2
Krachtlijnen van het onderzoek

Het doel van deze studie is het leveren van zowel een kwalitatieve als een kwantitatieve analyse van de mogelijke destabilisatieprocessen voor natuurlijke gashydraten in combinatie met de akoestische respons van partieel-hydraatgesatureerde sedimenten in het Baikalmeer, Siberië. Meer specifiek werden de volgende doelstellingen geformuleerd:

1. *Theoretische analyse van de klimatologische destabilisatiemechanismen van oceanische gashydraten*
2. *Analyse en prognose van de potentiële seismische respons van een zeebodem gekarakteriseerd door de aanwezigheid van hydraten*

Deze doelstellingen werden allemaal succesvol behaald en resulteerden o.a. in een aantal wetenschappelijke publicaties. Hierbij dient opgemerkt te worden dat een niet-onbelangrijke vertraging werd opgelopen wegens onvoorziene moeilijkheden om een passende akoestische dataset te verkrijgen met evidentie van hydraatzones. Zo werd de data acquisitie van het belangrijkste deel van de seismische dataset slechts tijdens de zomer van 1999 uitgevoerd. Deze studie vormt daarnaast ook de eerste stappen die het RCMG gezet heeft in de wereld van het gashydraatonderzoek.

7.2
Gevoeligheid van hydraatstabiliteitscondities

7.2.1
Inleiding

Het tweede hoofdstuk van deze doctoraatsverhandeling verwoordt de theoretische studie van de gevoeligheid van het hydraatstabiliteitsvenster onder veranderende klimatologische condities in termen van zeespiegelniveau en bodemwatertemperaturen en hun respectievelijke veranderingen. De studie gaat uit van zelfopgestelde 3-fazegrensfuncties gebaseerd op zowel theoretische als experimentele resultaten en uitgewerkt m.b.v. de methode der kleinste kwadraten. De studie maakt gebruik van enigszins vereenvoudigde situaties waarbij enkel de globale eigenschappen in rekening gebracht worden. Zo wordt verondersteld dat de drukverandering die gepaard gaat met het veranderend zeespiegelniveau zich onmiddellijk doorzet doorheen de sedimenten en dus van ogenblikkelijk belang is voor de *in situ* evenwichtscondities. Specifieke invloeden die optreden tijdens de fazetransitie of capillaire effecten worden genegeerd daar deze verondersteld worden geen noemenswaardige invloed te hebben op het tijdskader van klimatologische veranderingen en enkel een systematische afwijking tot gevolg hebben. Daarnaast wordt het medium beschouwd als een homogeen poreus medium waarin de temperatuursverdeling binnen de sedimentaire matrix niet verschillend is van deze binnen de fluïdafaze. De dichtheid van de poriënfluïda wordt ook verondersteld gelijk te zijn aan de dichtheid in de waterkolom. Indien anders vermeld, wordt hydrostatische drukverdeling in rekening gebracht en niet de lithostatische voor het bepalen van de evenwichtsdruk.

7.2.2
Programma's

De theoretische basis voor hydraatstabiliteit wordt gedefinieerd als de diepte in de sedimenten waar de heersende temperatuur de lokale evenwichtstemperatuur in het PT-diagram overschrijdt. De impliciete diepte-afhankelijkheid van het stelsel vergelijkingen (evenwichtstemperatuur, –druk, *in situ* temperatuur, drukverdeling) maakt dat dit snijpunt niet eenvoudig kan bepaald worden door het scheiden van de veranderlijken, zodat een iteratieve procedure werd opgesteld om alsnog het evenwichtspunt te bepalen. Dit punt kan overigens ook grafisch-visueel bepaald worden. Wegens de vele optredende parameters en de grote diversiteit aan mogelijke situaties werden diverse programma's geschreven die voor de gebruiker een leiddraad kunnen vormen voor een specifieke of concrete situatie die niet noodzakelijk weergegeven wordt in de tekst. De programma's laten de gebruiker bijvoorbeeld toe om zelfbepaalde of in literatuur vermelde evenwichtscoëfficiënten in te stellen of te bepalen zodat het programma niet beperkt blijft tot de studie van zuivere methaanhydraten in zout- of zoetwater. Deze programma's zijn ingesloten en vormen de ruggengraat van dit hoofdstuk. Alle formules gebruikt in de programma's worden vermeld in dit volume. Vaak worden overzichtsfiguren gemaakt waarbij iso-lijnen getoond worden in functie van diverse optredende parameters. Deze kunnen gemakkelijk gebruikt worden om in een oogopslag een vrij nauwkeurig beeld te krijgen van de specifieke en concrete situatie. Daarnaast werd een extra programma geschreven voor de studie van hydraataccumulaties in het Baikalmeer en dit werd gebruikt voor de resultaten vermeld in hoofdstuk

4. Het gebruik van de diverse programma's vereist geen additionele soft- of hardware en is geschreven voor PC platformen.

7.2.3
Resultaten en conclusies

Uit de studie blijkt dat zeespiegelschommelingen respectievelijk veranderingen van de bodemwatertemperatuur hun eigen specifieke invloed hebben op hydraatstabiliteitscondities. De tijdschaal van het gebeuren en de initiële positie van de stabiliteitsgrens blijken kritische parameters te zijn. Zuivere zeespiegelschommelingen worden verondersteld onmiddellijk in te werken en van invloed te zijn op de hydraatstabiliteit wegens de communiceerbaarheid van de poriënruimte. Temperatuursveranderingen daarentegen spelen zich af op de zeebodem terwijl de penetratie doorheen het poreus medium heel wat tijd kan vergen. Belangrijk voor hydraatdissociatie is dat de lokale condities eerst moeten evolueren tot aan de 3-faze evenwichtsvoorwaarden waarna dissociatie effectief kan optreden.

Zeespiegeldaling zal aanleiding geven tot hydraatdestabilisatie startend aan de basis. Het effect is des te belangrijker naarmate de amplitude van de zeespiegeldaling toeneemt, in ondieper water en bij kleinere geothermische gradiënt of warmtestroom. Gebruik makend van de zeespiegelcurve van *Fleming et al. [1998]* blijkt dat de amplitude van de verandering van de stabiliteitslimiet door toedoen van zeespiegeldaling kan oplopen tot ruim 100 m tijdens de laatste 210 ka, een effect dat sterk afneemt naarmate het bekken dieper wordt. Zelfs bij kleine zeespiegelschommelingen kan hydraatdissociatie optreden in een beperkt interval aan de ondergrens van de stabiliteitscondities.

Variatie van de bodemwatertemperatuur kan resulteren in zowel destabilisatie van basis naar top als omgekeerd. Het inverse proces is echter alleen van belang bij snelle temperatuurstoename in gebieden waar de kritische temperatuur overschreden wordt, dus opnieuw in ondiepe bekkens. Wat het verstoren van evenwichtscondities aan de basis betreft, moet een vertraging in de orde van jaren tot duizenden jaren in rekening gebracht worden, afhankelijk van de waterdiepte, geothermische gradiënt of warmtestroom en de amplitude van de temperatuurschommeling aan de bodem. De magnitude van de verandering van de stabiliteitsgrens kan na verloop van tijd dezelfde grootte-orde bereiken als bij zeespiegeldalingen. De situatie werd bestudeerd bij ogenblikkelijke temperatuurstoename aan de zeebodem, bij een lineaire toename van de bodemtemperatuur en in het geval van temperatuursoscillatie op de bodem.

De studie van de individuele processen geeft dus aan dat hydraatstabiliteit sterk afhankelijk is van het zeespiegelniveau en de bodemwatertemperatuur, en dat hoofdzakelijk in relatief ondiepe wateren. Deze ondiepe gebieden hebben bijgevolg een hoger risicogehalte voor hydraatdestabilisatie en eventueel massatransport (*slides, slumps, debris flows*) langsheen de continentale randen zoals bijvoorbeeld het geval is met de Noorse continentale rand. *Combinatie van beide effecten* blijkt overigens verrassende resultaten op te leveren. Stabiliteitsvoorwaarden kunnen evolueren naar eerst ongunstige en later verbeterde condities en vice versa tijdens één en hetzelfde proces van zeespiegelverandering gekoppeld aan bodemtemperatuursvariatie. Deze vaststelling heeft tot gevolg dat uit de beginsituatie niet onmiddellijk en met absolute zekerheid de eindsituatie kan voorspeld worden als er enige onzekerheid bestaat over één van de optredende parameters. Vooral de tijdschaal van beide processen en de amplitudes van de veranderingen in een specifiek gebied moeten nauwkeurig gekend zijn. Dergelijke moeilijkheden doen zich voor als twee elkaar tegenwerkende processen betreffende hydraatstabiliteit gecombineerd worden, zoals zeespiegeldaling en dalende bodemwatertemperatuur. Dit kan bijvoorbeeld het geval zijn bij uitbreiding van de ijskappen waarbij de koude bodemstromen aangezwengeld worden en zich verder kunnen uitbreiden over de zee- of oceaanbodem terwijl de zeespiegel daalt. Het ene proces kan dus eventueel het andere compenseren of overtreffen. Terwijl een dergelijk scenario in ondiepe bekkens aanleiding kan geven tot globaal minder stabiele condities kan het omgekeerde waar zijn in diepere bekkens onder dezelfde omstandigheden. Bijgevolg kan niet

zonder accurate kennis gesteld worden dat zeespiegeldaling verantwoordelijk is voor hydraatdissociatie als het geothermische regime niet of slechts minimaal in rekening wordt gebracht.

Een gecombineerde analyse van de hydraatstabiliteitscondities werd vervolgens uitgevoerd gebruik makend van de bathymetrie afgeleid uit seismische profielen in het *Magellan-Hovland* mound gebied gesitueerd ten westen van Ierland (RCMG-Belgica expedities 1997-99). De geothermische gradiënt werd afgeleid uit de literatuur, terwijl een model van lineair met diepte veranderende bodemwatertemperatuur voor de hedendaagse situatie werd opgesteld rekening houdend met de voorhanden zijnde temperatuursdata in de *Levitus* databank. In het bestudeerde gebied komen grote clusters van diverse mound-types voor. Een hypothese voor hun ontstaan werd ontwikkeld door *Henriet et al.* [*1998*] waarbij hydraatdissociatie en methaanseeps een belangrijke rol spelen en onderling verbonden zijn. De modellering van hydraatstabiliteit in dit gebied tijdens de transitie van glaciale naar interglaciale condities geeft aan dat tijdens glaciale condities het volledige gebied zich binnen de theoretische evenwichtsvoorwaarden bevindt. Bij de hedendaagse condities echter blijkt enkel de zuidelijke rand (diepste deel) binnen de stabiliteitscondities te vallen. Deze verandering is volledig te wijten aan de grote temperatuursstijging van glaciale naar interglaciale toestanden. De analyse werd uitgevoerd voor de evolutie van bodemwaterstromingen en zeespiegelstijging sinds het LGM (*Laatste Glaciale Maximum*), omdat de omstandigheden het best gedocumenteerd zijn. Gelijkaardige transities kunnen zich ook voorgedaan hebben in een verder verleden zodat de analyse niet beperkt is tot deze periode.

Verder kan erosie van sediment (*sliding, slumping*) voor de studie van de hydraatstabiliteit beschouwd worden als een speciaal geval van ogenblikkelijke verandering van de bodemwatertemperatuur. Dit werd uitgewerkt aan de hand van seismische data over de rand van de *Storegga Slide* (Noorse kust) en is ondertussen gepubliceerd [*Bouriak et al., 2000*]. Na verloop van tijd evolueert het systeem naar nieuwe evenwichtscondities die dieper in de sedimenten liggen, dus subsidentie van de evenwichtsgrens die in grootte-orde gelijk is aan de dikte van de verwijderde sedimenten op deze plaats. Afhankelijk van de veronderstelde drukverdeling (hydrostatisch – lithostatisch) kan hydraatdissociatie optreden. Enkel bij vermindering van de *in situ* druk (dus situatie met initiële overdruk) zal een tijdelijke instabiele toestand ontstaan net boven de initiële stabiliteitsgrens. Het effect blijft beperkt tot een zone van minder dan 10 m dikte die buiten de nieuwe evenwichtsgrenzen valt. Modellering van de invloed van zeespiegelveranderingen gedurende de laatste 30-50 ka (tijdstip van de eerste *Storegga Slide*) toont aan dat deze van ondergeschikt belang zijn, mede door de vertraagde inwerking van het temperatuurseffect geïnitieerd aan de bodem.

Tot slot werd ook de mogelijkheid onderzocht in hoeverre een spontane verheffing van partieel-hydraatgesatureerde sedimenten realistisch is. Daarvoor werden diverse vergelijkingen opgesteld, waaruit enkele kritische parameters konden afgeleid worden. Wegens het kleine dichtheidsverschil tussen zuivere hydraten en water en het grote verschil met de dichtheid van de sedimentaire matrix dient het bulksediment uit nagenoeg zuivere hydraten te bestaan om een dergelijke uplift mogelijk te maken. Er werd dan ook besloten dat dit proces niet in de realiteit zal voorkomen.

7.3
Akoestische respons van partieel-hydraatgesatureerde sedimenten

7.3.1
Inleiding

Het tweede deel van het doctoraatsonderzoek behelst de studie van de akoestische respons van hydraatrijke sedimenten. Het grootste deel van de akoestische dataset die daarvoor gebruikt werd, werd slechts in een laat stadium van het project verkregen. De dataset omvat meerkanaals airgun-

array seismische data, een dubbele set éénkanaals airgun data, éénkanaals watergun data en éénkanaals sparker data. De data werden deels zelf opgenomen door het *Renard Centre of Marine Geology (RCMG)*, andere werden vrijgegeven in het kader van het INTAS project 1915, of zijn gepubliceerd als USGS Open File Report [*Colman et al., 1996*]. Het totale frekwentiebereik van deze set ligt tussen 10 en 1000 Hz en is vrij uniek. De resultaten hier vermeld worden binnenkort gepubliceerd in het vaktijdschrift *Marine Geology* [*Vanneste et al., in press*]. De nadruk ligt op de frekwentie-afhankelijkheid van de typische BSR waargenomen op de diverse profielen van het Zuidelijke en Centrale Baikal Bekken.

7.3.2
Het Baikalmeer en hydraataccumulaties

Het Baikalmeer is het diepste meer ter wereld (± 1650 m) dat tevens het grootste zoetwaterreservoir vormt (20%) en is gelegen in het centrale deel van de actieve continentale Baikal rift. De ouderdom van het meer wordt op 35 Ma geschat [*Zonenshain et al., 1990*]. Het meer bestaat uit drie bekkens gescheiden door breukgebonden accomodatiezones. Sedimentaccumulaties in de bekkens is variabel, maar in de omgeving van de *Selenga delta* bedraagt de dikte van het pakket ruim 10 km [*Golmshtok et al., 2000*]. De Selenga is de belangrijkste rivier die uitmondt in het meer en is verantwoordelijk voor de aanbreng van grote hoeveelheden terrigeen en organisch materiaal. De diverse bekkens worden gekenmerkt door een bijzonder complex breukenpatroon en bijgevolg ook een lateraal zeer variabele warmtestroom [*Golubev, 1982*].

Gebruik makend van meerkanaals seismische data werden gebieden afgebakend waarin indirecte aanwezigheid van gashydraten waargenomen werd aan de hand van de observatie van een BSR [*Golmshtok et al., 1997*]. Deze gebieden blijken symmetrisch t.o.v. de *Selenga delta* te liggen. Directe evidentie voor de aanwezigheid van hydraten werd eerder toevallig bekomen tijdens het *Baikal Drilling Project* in 1997 in het axiale deel van het Zuidelijke Bekken. Evidentie werd waargenomen op dieptes van 120 en 160 meter onder de meerbodem in waterdieptes van ongeveer 1200 m. Methaan van biogene oorsprong blijkt ook hier overvloedig te zijn [*Golubev, pers. comm.*]. Ongeveer 10% van de poriënruimte bleek ingenomen door gashydraten. Tijdens een recente winterexpeditie werden nogmaals hydraten bovengehaald uit de *Malin'kiy* krater in het Zuidelijke bekken, waar tijdens de zomerexpeditie gas seepage werd waargenomen. Hydraatstalen werden bovengehaald van op 20-40 cm diepte in de sedimenten. Ook hier bleken het hoofdzakelijk methaanhydraten te zijn van biogene oorsprong [*Klerkx, pers. comm.*].

7.3.3
Data-acquisitie en verwerking

De kracht van deze studie ligt in de mogelijkheid om nagenoeg samenvallende lijnen opgenomen in verschillende akoestische frekwentieverdeling te vergelijken. Alle data werden speciaal verwerkt m.b.v. *Landmark ProMAX* software om zogenaamde *true-amplitude* profielen te verkrijgen. De processingstappen en –parameters verschillen uiteraard van set tot set wegens o.a. de frekwentieverdeling van de gebruikte bronnen. De belangrijkste stappen waren frekwentiefiltering, deconvolutie, *true amplitude recovery* (sferische correctie), *spike and noise burst edit*. De meerkanaals data werden gestacked na NMO correctie en het doorvoeren van *static headers* na het scheiden van de geluidssporen van de niet-geluidssporen binnen hetzelfde kanaal. De watergun data zijn nog behandeld met FK-filter. Attribuutanalyses werden uitgevoerd ook op de true amplitude lijnen, zoals frekwentie- en fazeplots.

7.3.4
Eigenschappen van de BSR in verschillende frekwenties

Heel wat meerkanaals lage-resolutie seismische profielen vertonen, althans met aanzienlijke laterale compressie, indirecte aanwijzingen voor de basis van de hydraataccumulatiezone en/of de top van de vrije gaszone door middel van de aanwezigheid van een BSR [*Golmshtok et al., 1997*]. Deze reflectoren worden gekenmerkt door een sterke amplitude en een inverse polariteit relatief t.o.v. de meerbodemreflectie. Helaas laten de meerkanaals seismische data ons niet toe gedetailleerde akoestische snelheidsprofielen te bekomen om de snelheidsinversie op de BSR kwantitatief uit te drukken, daar enkel de eerste drie seconden van de dataset werden uitgewisseld waardoor de typische reflectiepiek niet meer aanwezig is in de verste registratiekanalen. De zone boven de BSR kent doorgaans een verminderde reflectieamplitude (*acoustic blanking*). Heel vaak snijdt deze reflectie lithologische grensvlakken, wat duidelijk maakt dat deze typische reflectie eerder te maken heeft met de fysico-chemische eigenschappen van het poreuze medium dan wel met pure stratigrafie. In een beperkte zone onder de BSR worden dikwijls versterkte reflecties waargenomen.

Indien echter de frekwentie van de bron toeneemt, blijkt deze reflectie zich anders te gedragen. De reflectie wordt heel wat minder duidelijk, en verliest ten dele haar continuïteit, maar is meestal waarneembaar. Op de medium-frekwentie profielen worden wel diverse breuken aangetroffen in de geplooide sedimenten wat niet steeds het geval is voor de lage-resolutie profielen. De amplitude van de BSR varieert lateraal sterk en in sommige zones verdwijnt de reflectie nagenoeg volledig. Vergelijking met de lage-resolutie profielen maakt echter dat we de BSR kunnen uitkarteren langs de medium-resolutie profielen. Belangrijk is dat de basis van het stabiliteitsgebied sterker tot uitdrukking komt wanneer sedimentaire eenheden gekruist worden. Niettemin worden BSRs heel vaak aangetroffen op zowel de lage-resolutie als medium-resolutie airgun profielen terwijl een niet-onaanzienlijk aantal aparte akoestische karakteristieken worden waargenomen op andere profielen, wat uitgewerkt werd in het volgende hoofdstuk.

Op hoge-frekwentie data krijgen we een volledig ander beeld van de hydraatstabiliteitslimiet. Bijvoorbeeld het watergun profiel wordt niet langer gekenmerkt door een hoge-amplitude reflectie die de meerbodemtopografie volgt en de stratigrafie snijdt maar door een serie dicht bij elkaar liggende lokaal-versterkte reflecties met sterk variabele amplitudes die zich uitstrekt over enkele tientallen ms hoewel dit ook varieert. De bovengrens van de reeks versterkte reflecties blijkt overigens op een ongeveer constante diepte onder de meerbodem te zitten, en kan dus bodem-simulerend genoemd worden. Deze grens werd geïnterpreteerd als de basis van het stabiliteitsgebied, omdat ook nu aan een aantal typische kenmerken voldaan wordt. Hoofdzakelijk de gereduceerde amplitudes in het gebied boven deze grens zijn opvallend, terwijl versterkte reflecties onder deze grens in het oog springen. Ook hier kan het stratigrafisch patroon relatief makkelijk gevolgd worden langs beide kanten van de lokaal versterkte zones, wat duidelijk maakt dat deze versterkte reflecties deel uitmaken van gewone individuele lithologische grenslagen. De polariteit van deze versterkte reflecties blijkt ook negatief te zijn. Lithologisch-stratigrafisch gecontroleerde gasmigratie en –accumulatie worden hiervoor verantwoordelijk geacht. Overigens, de observatie van een echte BSR op dezelfde positie op een nagenoeg samenvallend lage-resolutie profiel staaft deze interpretatie.

De nog hogere-resolutie sparker data tonen op geen enkel moment een duidelijke reflectie die wijst op de aanwezigheid van hydraten. Wel worden vaak sterke onregelmatige reflecties opgemerkt waaronder plots een nagenoeg volledige absorptie van akoestische energie optreedt. Deze blijken niet steeds continu te zijn, maar kunnen verspringen van de ene naar de andere stratigrafische horizont. Vergelijking met lagere-resolutie profielen is niet evident. Zoals in het volgende hoofdstuk uitvoerig beschreven wordt, zijn er sterke variaties waargenomen in het Baikalmeer. Dit houdt is dat enkel zekerheid kan bestaan daar waar de verschillende profielen samenvallen of elkaar snijden. Er dient hier opgemerkt te worden dat de BSR vaak op de grens van de akoestische penetratie van de sparkerbron (± 350 ms) zit of dieper, terwijl dit akoestisch bereik sterk varieert van plaats tot plaats. Op veel profielen valt de basis echter onder de penetratiegrens zodat de sparker profielen niet geschikt

zijn voor het afbakenen van de hydraatstabiliteitsgrens. Desgevallend is het gebruik van dit soort data voor het bepalen van de verticale uitgebreidheid van hydraatstabiliteit speculatief.

7.3.5
Seismische data vs. diepe boring: GAHY005-006/010 vs. BDP-1997

Tijdens de laatste RCMG Baikal expeditie werden enkele seismische profielen geschoten die nagenoeg de plaats van de diepe BDP-boring (1997) doorkruisen. Wat onmiddellijk opvalt is het feit dat er geen BSR aanwezig is in de onmiddellijke nabijheid (enkele km) van de boring. Verder zijn ook geen andere akoestische anomalieën waarneembaar op deze plaats. In NE en SW richting wordt wel een reguliere, continue maar zwakke BSRs waargenomen op ongeveer 350 tot 390 ms TWTT, zijnde ruimschoots dieper dan de posities waaruit hydraten werden bovengehaald. Ook hier snijdt de BSR vaak de stratigrafie en worden versterkte reflecties waargenomen in het gebied onder de BSR.

7.3.6
Specifieke kenmerken van hydraatrijke sedimenten

Amplitude blanking wordt zeer duidelijk waargenomen op de seismische profielen van het Baikal meer, hoofdzakelijk op medium- tot hoge-resolutie data. Dit wijst op de afwezigheid van belangrijke interne reflecties of impedantiecontrasten. Op de Baikalprofielen betreft het meestal een vrij beperkte zone net boven de hydraatstabiliteitsgrens die gradueel vermindert. Dit fenomeen blijkt overigens ook lateraal te variëren. Of er een directe link bestaat met de BSR en/of partiële hydraatsaturatie is evenwel niet duidelijk. Analyse van de profielen door BDP-1997 en vergelijking met de boorresultaten geven aan dat relatief grote hoeveelheden hydraten aanwezig kunnen zijn in de sedimentaire sectie zonder aanleiding te geven tot een specifieke akoestische respons of anomalie, inclusief *blanking*. Dit laat ons toe te besluiten dat amplitudereductie niet rechtstreeks kan verbonden worden met hydraatinclusie. Daar de data verwerkt werden met het doel tot behoud van de amplitude werden geen schalingsoperatoren (AGC) gebruikt, zodat *blanking* ook niet kan veroorzaakt worden door de aanwezigheid van BSR en/of versterkte reflecties onder de BSR tijdens het processen van de data.

Lokale ***hoge-amplitude reflecties*** worden ook vaak aangetroffen bij hydraatrijke sedimenten en worden geïnterpreteerd als zijnde veroorzaakt door de aanwezigheid van vrij gas in de sedimenten onder de hydraataccumulatie wegens de schijnbare inverse polariteit. Slechts een zeer kleine hoeveelheid gas is nodig om de akoestische snelheid van de bulk sedimenten drastisch naar beneden te halen, waardoor de akoestische impedantie ook een duik maakt, wat aanleiding geeft tot een hoge-amplitude negatieve polariteitsreflectie. De aanwezigheid van dergelijke hoge-amplitude reflecties valt op bij het analyseren van de diverse datasets in het Baikalmeer. Vooral op medium- tot hoge-resolutie seismische profielen biedt deze observatie een handig middel om de basis van het hydraatstabiliteitsgebied uit te karteren, als zijnde de up-dip terminatie van dergelijke versterkte reflecties. De uitgebreidheid van deze hoge-amplitude reflecties is echter beperkt wat – afhankelijk van de stratigrafie – een maat kan zijn voor de dikte van de vrije gaslaag.

Sommige hoge-amplitude reflecties dringen overigens door de stabiliteitslimiet heen wat kan wijzen (indien negatieve polariteit) op het voorkomen van zeer lokale veranderingen van PT-voorwaarden en/of een metastabiele toestand van vrij gas binnen het stabiliteitsgebied. Dit komt echter niet frekwent voor in dit gebied. Mogelijke verklaringen zijn het optreden van tijdelijke pulsen van fluïdamigratie alsook inwerkende capillaire krachten in het poreuze medium. Deze observaties suggereren een stratigrafisch en lithologisch gecontroleerde fluïdamigratie naar de basis van het stabiliteitsvenster.

Attenuatie van akoestische energie is ook een typisch optredend fenomeen voor gasrijke sedimenten. Vooral hoog-frekwente data zijn gevoelig. De belangrijkste attenuatie-effecten zijn absorptie (conversie van akoestische energie in warmte en vervolgens dissipatie) en verspreiding aan inhomogeniteiten. In

hoeverre de BSR of hoge-amplitude reflecties onder de BSR zich gedragen als een low-pass filter, werd onderzocht aan de hand van frekwentie-analyses op de diverse datasets. Hieruit blijkt dat er zich een plotse verschuiving naar lagere frekwenties voordoet in de zone gekarakteriseerd door de BSR en/of hoge-amplitude reflecties, en dit vooral op de medium- tot hoge-resolutie profielen (airgun, watergun). De zeer-hoge-resolutie profielen (sparker) vertonen een volledige absorptie van akoestische energie op een bepaald niveau, net onder versterkte reflecties. De lage-resolutie data (airgun-array) daarentegen vertonen geen noemenswaardige attenuatie onder de BSR. Deze vaststellingen suggereren de aanwezigheid van vrij gas in een beperkte zone onder de BSR of tussen de hoge-amplitude reflecties. Dit houdt in dat lokale vrij gas accumulaties eigenlijk als een soort ***low-pass filter*** kunnen werken, en dit hoofdzakelijk voor de medium- tot hoge-resolutie data.

Verdere aanwijzingen voor de aanwezigheid van vrij gas onder de hydraataccumulaties zijn de toenemende amplitude van de reflectie bij toenemende offsetwaarden of invalshoeken, als resultaat van ***AVO-analyse*** (*amplitude vs. offset*). Daarvoor werden de seismische sporen gegenereerd als respons van een zelfde punt op de meerbodem vergeleken. De 96-kanaals hydrofoonreeks geeft aanleiding tot 24-voudige bedekking van de verschillende punten. De afstand van het eerste tot het laatste kanaal relatief t.o.v. de bron bedraagt 495 res. 2895 m. De variatie van de reflectie-amplitude met veranderende afstand is een functie van de invalshoek/afstand en is afhankelijk van de fysische eigenschappen van het reflecterende medium. Toenemende negatieve reflectie met toenemende afstand wijst op partiële hydraatoccupatie. Een gelijkaardige procedure toegepast op de data van het Baikalmeer tonen overduidelijk een dergelijke verandering, wat opnieuw een aanwijzing is voor de aanwezigheid van gas onder de grenslaag. Helaas zijn deze kwalitatieve resultaten moeilijk om te zetten in kwantitatieve resultaten wegens het gebrek aan gedetailleerde *P*- en *S*-golf snelheids- en dichtsheidsprofielen. De invloed van de directiviteit van de reeks hydrofonen werd ingebouwd in deze analyse.

Met de *multiple quotient* methode [*Warner, 1990*] werd de ***reflectiecoëfficiënt*** – een maat voor de hoeveelheid energie die gereflecteerd wordt in verhouding met de totale invallende akoestische energie – bepaald voor de meerbodemreflectie en de BSR in het kanaal met kleinste offset van profiel MC92_01. Hier werd de invalshoek (ong. 10°) verwaarloosd wat geen aanleiding geeft tot ernstige afwijkingen. Ook de relatief zwakke interne reflectoren tussen de meerbodem en de BSR worden niet in rekening gebracht. De reflectiecoëfficiënt van de meerbodem bleek gemiddeld 0.197 te zijn, terwijl voor de BSR waarden van -0.085 (-43%) bekomen werden, waarbij het min-teken uitdrukt dat het akoestisch impedantiecontrast negatief is. De laterale verandering van de reflectiecoëfficiënt langsheen het profiel werd ook bepaald. Daar waar de meerbodemamplitude relatief weinig verandert, zijn er grote schommelingen waarneembaar in het gedrag van de BSR. Op hogere-frekwentie data GAHY021 (samenvallend met MC92_01) is de reflectiecoëfficiënt een stuk lager, van zowel de meerbodemreflectie (0.139) als van de BSR (-0.049 of –34%). Laterale variatie van de reflectiecoëfficiënt kan onmogelijk verklaard worden door topografie daar de meerbodem langsheen de lijn nagenoeg perfect vlak is.

Indirecte evidentie voor de aanwezigheid van vrij gas onder het hydraatstabiliteitsveld is overvloedig aanwezig: hoge reflectiecoëfficiënt, hoge-amplitude reflecties met inverse polariteit, plotse attenuatie onder de BSR. Daarnaast zijn onlangs de eerste resultaten bekend geraakt van ***OBH-analyse*** (*ocean bottom hydrophone*) in het centrale deel van het Zuidelijke Baikal Bekken. De akoestische interval snelheid daalt sterk onder de BSR tot waarden die gelijk zijn met de bovenste sedimenten over een interval van enkele tientallen m [*De Meersman, 2000*]. Hoewel deze resultaten slechts preliminair zijn, wordt dit gedrag toch toegeschreven aan de accumulatie van vrij gas onder de BSR. De dikte van de vrije gaszone blijkt niet voldoende te zijn om een zichtbaar effect te geven op de lage-resolutie profielen, zodat de dikte wellicht slechts enkele m tot enkele tientallen m bedraagt. Ook de uitgestrektheid van de hoge-amplitude reflecties waargenomen op het watergun profiel toont aan dat de vrije gaszone beperkt is.

7.3.7
BSR continuïteit : invloed van de akoestische frekwentie

Zoals hierboven beschreven, speelt de akoestische frekwentie een duidelijke rol in het resulterende beeld van de reflectie aan de basis van de hydraatstabiliteitszone. Op lage-resolutie profielen wordt de basis van de hydraatzone waargenomen als een klassieke BSR. Indien ook op hogere-frekwentie profielen een BSR wordt waargenomen, is de reflectie-amplitude beduidend kleiner. Een verklaring voor het waargenomen gedrag dient gevonden te worden in de resolutie van de data in combinatie met het offset-afhankelijke gedrag. Bij lage frekwentie wordt een groter volume van de ondergrond gesampled en worden de fysische eigenschappen uitgemiddeld. Uiteindelijk wordt één enkel reflectiesignaal gegenereerd voor dit volume. Bij hogere frekwentie wordt dit volume een stuk kleiner terwijl kleinschalige onregelmatigheden een belangrijker effect geven (absorptie, verstrooiing). Zoals blijkt door vergelijkende studie van de meerkanaals airgun profielen en het watergun profiel dragen de individuele lokaal versterkte reflectoren of het hoge-resolutie profiel duidelijk bij tot slechts één signaal op de lage resolutie. Het feit dat niet altijd een BSR gegenereerd wordt op hogere-frekwentie profielen wijst vermoedelijk op het feit dat de transitie langs de BSR geen reguliere en eenvoudige grenslaag is. In deze optiek zal een reeks van dicht bij elkaar gelegen gasrijke strata geïdentificeerd worden als gescheiden reflecties op hoge-frekwentie data, maar zal gebundeld worden in één signaal op lage-resolutie profielen gesitueerd aan de top van de vrije gaszone. Indien de strata alternerende eigenschappen hebben (andere lithologie) en gasmigratie preferentieel geschiedt in bepaalde lagen met verhoogde permeabiliteit, dan hoeft vrij gas niet aanwezig te zijn langsheen het volledige basisvlak van hydraatstabiliteit maar enkel in beperkte zones. Als evenwel de horizontale afstand tussen de verschillende gasrijke strata groter is dan de horizontale resolutie zal geen coherente reflectie waargenomen worden en dus geen BSR. Dit staaft de redenering dat de BSR gegenereerd wordt aan de top van gasrijke sedimenten en niet noodzakelijk aan de basis van de hydraatzone. Bij de meerkanaals lage resolutie profielen wordt ook de bijdrage van de zeer sterke verre kanalen (AVO-effect) bijgevoegd in het resulterende signaal.

7.3.8
Schatting van het gashydraatreservoir in het Baikalmeer

Combinatie van de resultaten van de BDP-97 boring met het uitkarteren van zowel de laterale als verticale uitgebreidheid van het hydraatstabiliteitsvenster laten toe voor de eerste keer een schatting te doen van de grootte van het hydraatreservoir aanwezig in het Baikalmeer. Hydraten werden bovengehaald van de sedimentkolom op ongeveer 200 m van de stabiliteitslimiet in het gebied. De hydraatoccupatie van het poreuze volume bleek ongeveer 10% te zijn. Deze waarde werd als een maximum beschouwd bij de berekening. Er werd ook uitgegaan dat hydraten aanwezig zijn in het volledige gebied met indirecte evidentie voor hydraten tot op ongeveer 200 m boven het stabiliteitsgebied. Het vinden van hydraten op nagenoeg de meerbodem [*Klerkx, pers. comm.*, winter 1999-2000] wordt als uitzondering beschouwd en kan daarom achterwege gelaten worden. In beide gevallen betreft het nagenoeg zuivere methaanhydraten (> 99%).

Alle data vergaard tijdens de RCMG 1999 expeditie in het centrale deel van het Zuidelijke Baikal Bekken werden volledig geanalyseerd op de aanwezigheid van een BSR. Deze werd uitgekarteerd en het volume hydraat werd geschat uitgaande van de bovenvermelde veronderstellingen op $7.58 \cdot 10^9$ m^3 hydraat of $1.24 \cdot 10^{12}$ m^3 methaan bij STP condities. Vervolgens werden de waarden geëxtrapoleerd naar het volledige gebied waarin evidentie voor hydraten is aangetroffen in het Zuidelijke en Centrale Bekken, symmetrisch t.o.v. de *Selenga Delta*. Dit gebied is ruw geschat ongeveer 6 keer groter dan het gebied waarvoor de berekening werd uitgevoerd. Bijgevolg kan de totale hoeveelheid methaan opgeslagen in Baikal gashydraten gelimiteerd worden tot $9 \cdot 10^{12}$ m^3, of 4.6 Gton koolstof. Vrij gas onder de BSR werd niet in rekening gebracht, maar zal geen noemenswaardige stijging tot gevolg hebben. Deze hoeveelheid is slechts ongeveer 13% van de geschatte hoeveelheid hydraat aanwezig in *Blake Ridge*. Dit geeft aan dat het Baikalreservoir weinig tot geen toekomstige energiebron vormt.

7.4
Onregelmatigheden in de BSR-morfologie: gerelateerd met (neo-)tectoniek?

Het vierde hoofdstuk van dit werk behandelt de anomalieën gelinkt met de morfologie van de reflectie aan de basis van het stabiliteitsgebied of de top van de vrije gaszone zoals waargenomen op de akoestische dataset en de vergelijking tussen gededuceerde warmtestroom en werkelijke warmtestroom metingen.

7.4.1
Warmtestroom vs. seismiek: methodologie

In eerste instantie wordt de volledige methodologie om de warmtestroom te bepalen uitgaande van de zeebodem reflectie en de BSR uit de doeken gedaan. Dit gaat gepaard met conversie van *two-way travel time* naar afgelegde weg, zodat allereerst een snelheidsmodel moet gebruikt worden. Dit model werd opgesteld door *Golmshtok et al.* [*1997*] en verbindt de intervalsnelheid met de diepte onder de meerbodem. Deze relatie werd geconverteerd naar een verband tussen *two-way travel time* en diepte, en kan dan onmiddellijk toegepast worden op de akoestische dataset. Eens de diepte bekend is, kan makkelijk de *in situ* druk berekend worden, zowel hydrostatisch als lithostatisch waarbij verder gebruik gemaakt wordt van de wet van *Athy* voor de porositeitverandering met toenemende diepte en een daaraan gekoppelde gewogen dichtheidstoename. De bepaalde druk wordt vervolgens omgezet in evenwichtstemperatuur gebruik makend van de 3-faze evenwichtsvoorwaarden. De verhouding van het temperatuursverschil tussen de meerbodem en de BSR en de diepte in de sedimenten geeft dan de gemiddelde geothermische gradiënt die uiteindelijk resulteert in warmtestroom na het vermenigvuldigen met de thermische resistiviteit.

De nauwkeurigheid van deze methodologie wordt onderzocht aan de hand van enkele experimentele en theoretische snelheidscurves waarbij ruimte is voor partiële hydraatsaturatie en bijgevolg rekening gehouden wordt met snelheidstoename in het interval waarin hydraten aanwezig zijn. Het effect van hydraatinclusie wordt gemodelleerd aan de hand van de formule van *Lee*, waarbij de gewichtsfactor bepaald werd door *trial-and-error* zodat de functies in geval van een hydraatvrij medium overeenkomen met de respectievelijke referentieprofielen (*Golmshtok*, *Hamilton*). Daarnaast wordt ook het eerste resultaat van OBH metingen in de discussie betrokken en aan de hand van de modellering werd de hydraatsaturatie geschat langsheen het snelheidsprofiel. De inclusie van andere moleculen dan methaan in de hydraatstructuur zal uiteindelijk ook verschillen genereren in het finale resultaat. De grootste onnauwkeurigheid ligt echter hoogstwaarschijnlijk in het conductiviteitsprofiel. Het gebruikte profiel werd afgeleid uit een kern van ongeveer 100 m en dit verband werd lineair geëxtrapoleerd tot grotere diepten, wetend dat de gemiddelde diepte van de basis van de hydraatstabiliteitszone (BHSZ) op ruim 300 m ligt. Globaal gezien wordt de fout inherent aan de methodologie geschat op 15% van het resultaat.

De gebruikte formules stellen ons ook in staat om overzichtsfiguren te maken van de mogelijke verticale uitgebreidheid van het hydraatstabiliteitsinterval in het Baikalmeer. Dergelijke figuren werden aangemaakt voor zowel de lithostatische als hydrostatische drukverdeling en verbinden lijnen van gelijke diepte in de sedimenten of *two-way travel time* tot aan de BHSZ als functie van de warmtestroom (abscis) en de waterdiepte (ordinaat).

7.4.2
Observatie van seismische profielen, side-scan sonar: morfologie en anomalie van de BHSZ

Een 30 kHz side-scan sonar onthult de aanwezigheid van een golvende breuk dwars over het studiegebied. Verticale verplaatsing van de meerbodem bedraagt ongeveer 20 m. Deze breuk blijkt

antithetisch t.o.v. de *Posolskaya* breuk te liggen. Parallel aan deze breuk aan de zuidelijke kant lijnen een viertal semi-circulaire onregelmatigheden (*Bolshoy, Stariy, Malyutka, Malen'kiy*) zich op. Deze zijn variabel in grootte en facies en steken enkele m tot enkele tientallen m boven de meerbodem uit. Resultaten van echo-sounding duidt op fluidamigratie uit deze structuren terwijl CTD metingen in de niet-transparante plume geen noemenswaardige temperatuursanomalieën opleverden. Methaanconcentraties zijn hoger dan in het omgevend water [*De Batist et al., in prep.*].

Veel akoestische profielen worden gekenmerkt door anomalieën in vergelijking met het normale gedrag van de BHSZ zoals eerder beschreven. De anomalieën variëren van continue oscillerende hoge-amplitude reflectoren tot het schijnbaar plots onderbreken van de reflectie nabij breukzones. Dit specifieke verloop geschiedt volledig onafhankelijk van de bathymetrie. Opmerkelijk is dat het gebied waar deze typische reflecties waargenomen worden in de onmiddellijke nabijheid van een antithetische breuk – en dus de fluïdaontsnappingstructuren – ligt. Op korte afstanden kunnen belangrijke schommelingen optreden (orde 100 m), dit in tegenstelling tot het gebied besproken in hoofdstuk 3 dat net naast dit gebied ligt. Een van deze profielen, loodrecht op de breuk, vertoont een actieve gas uitsijpeling aan de meerbodem. Een tweede soort anomalie wordt gekarakteriseerd door een hoge-amplitude reflectie die oscilleert met korte golflengte (enkele km) en variabele magnitude die kan oplopen tot 150 m. Dit seismisch profiel ligt net buiten het gebied bedekt door de side-scan sonar en op enkele km van de typische structuren. Merk op dat de gemiddelde diepte van de BSR zoals besproken in hoofdstuk 3 ongeveer 400 m bedraagt, wat bijdraagt tot het anomale van een dergelijk grote variatie. Deze unieke reflecties worden toegeschreven aan de grenslaag gashydraat - vrij gas wegens de typische inverse polariteit, het snijden van de lokale stratigrafie en het feit dat ze gedeeltelijk een BSR-gedrag vertronen dat gestaag overgaat in het anomale gedrag om samen te vallen met BSRs op snijdende profielen.

Betreffende de gecontoureerde morfologie van de BHSZ als een soort anticline in dit gebied blijkt dat de breuk een duidelijke scheidingslijn vormt. Ten noorden van deze breuk richting *Posolskaya* wordt een zwakke BSR waargenomen. Over een afstand van 4 km ten zuiden van deze breuk, zijnde het gebied van de gas seeps, is de BHSZ onregelmatig, daar deze van abnormaal ondiepe posities snel terugzakt naar een dieper niveau. Op bepaalde plaatsen worden extreem diepe verzakkingen vastgesteld die verder naar het zuiden verdwijnen. Dit gebied met anomaal gedrag is beperkt tot een 175 km^2.

7.4.3
Gashydraten, vrij gas, gasmigratie?

De zopas aangehaalde overeenkomsten tussen de anomale reflecties in dit gebied in vergelijking met deze uit de aanpalende zone waarbij enkel "normale" BSRs worden aangetroffen, wijst in de richting van een causaal verband met hydraten en vrij gas in het studiegebied. Daarnaast vallen nog andere kenmerken op. Vooraleerst is er de AVO-analyse uitgewerkt in het vorige hoofdstuk maar uitgevoerd voor de oscillerende BHSZ. Ook de reflectiecoëfficiënt langsheen hetzelfde profiel werd berekend en resulteert in gelijkaardige waarden als langsheen een typisch profiel in het eerste gebied geschoten met dezelfde bron, zowel voor de meerbodemreflectie als de BHSZ. Nabij de lokale hoogten van de BHSZ blijkt de reflectiecoëfficiënt overigens een stuk groter te zijn dan op de laagten, en kan wijzen op een preferentiële gasmigratie naar en –accumulatie onder de hoogten. Ook langsheen de airgun profielen wordt een sterke attenuatie waargenomen onder de reflectie. Een belangrijk verschil met het eerder beschreven gebied is het voorkomen van veel meer reflecties met negatieve polariteit die de BHSZ doorprikken en uitmonden in de HSZ. Ook onder de BHSZ worden vaak korte stukjes van lithologische grenslagen versterkt. Een belangrijke evidentie voor gasmigratie wordt indirect geleverd door de aanwezigheid van hydraten aan de meerbodem, in één van de onregelmatige uitsijpelingsstructuren. Een dergelijk oppervlakkig voorkomen van hydraten wordt altijd gerelateerd met verhoogde gasverrijkte fluïdamigratie naar de bodem toe [e.g. *Booth et al., 1998; Ginsburg, 1998*]. Tot slot, op een meerkanaals profiel wordt in het gebied tussen *Stariy* en de antithetische breuk een

zeer chaotisch akoestisch facies waargenomen tot op de bodem. Dit geeft vermoedelijk aan dat een verhoogde gasconcentratie aanwezig is in dit gebied.

7.4.4
Berekende vs. gemeten warmtestroom

Doorheen de jaren werd een vrij uitgebreide warmtestroom dataset vergaard in de verschillende meerbekkens [*Golubev, 1982*]. Slechts een aantal van deze waarden vallen binnen het studiegebied. Tijdens de Baikal-1999 expeditie werden extra metingen uitgevoerd (KMMA – Tervuren) gebaseerd op de resultaten van de eerder uitgevoerde side-scan sonar en seismische data acquisitie. De warmtestroom werd hoofdzakelijk opgenomen langs het profiel gekarakteriseerd door de oscillerende reflectie en het profiel gekenmerkt door de seep (*Malen'kiy*). Deze waarden werden dan vergeleken met de warmtestroom afgeleid uit de eigenschappen van de BHSZ (zie hierboven). Hieruit blijkt dat er opvallend genoeg een goede correlatie bestaat tussen beide resultaten langsheen het seep-profiel, terwijl er grote verschillen (40%) worden waargenomen bij het oscillerend profiel. De resterende metingen en de *Golubev* metingen geven een behoorlijke correlatie. Het globaal beeld geeft evenwel steeds grotere waarden weer voor de gemeten warmtestroom. Dit kan verklaard worden door fluïdamigratie of ondiepe circulatie die niet in rekening gebracht wordt bij de berekende waarden maar een invloed hebben op de gemeten waarden, of door een overschatting van de thermische resistiviteit.

De incoherentie langsheen het oscillerend profiel is onverwacht, omdat ook de trend van de BHSZ niet gevolgd wordt. Evenwel dient vermeld te worden dat enkele metingen onderhevig waren aan grote variaties in temperatuursmetingen over de 0.5 m intervallen, waardoor enkele metingen minder betrouwbaar worden. Mogelijke afwijkingen van de reële situatie in vergelijking met de theoretische driefaze grens behoort ook tot de mogelijkheden. Indien de methaanflux kleiner is dan een kritische waarde kan een inverse polariteitsreflectie onstaan die een stuk dieper in de sedimenten ligt dan de evenwichtspositie [*Xu & Ruppel, 1999*]. Een afdoende verklaring voor deze discrepantie is er voorlopig nog niet. Er dient opgemerkt te worden dat een dergelijk gegeven zich slechts langs één seismisch profiel doet opvallen.

7.4.5
Scenario's

De resultaten van de multi-disciplinaire dataset illustreren een unieke verdeling van hydraten en vrije gas accumulaties binnen een actief riftgebied. Het ligt dan ook voor de hand dat tectonische inwerking een belangrijke rol kan spelen in de geobserveerde onregelmatige variaties, de seeps en vooral het zeer lokale karakter van de anomalieën. Heel wat besproken aspecten van hydraatdestabilisatie kunnen echter niet ingeroepen worden om een dergelijke verdeling teweeg te brengen. Zowel variatie van de bodemwatertemperatuur als meerspiegelschommelingen, hetzij klimatologisch of regionaal tectonisch [*Colman et al., 1998*] gestuurd, zullen een globaal effect genereren. Alhoewel de dikte van de meeste eenheden afneemt naar de breuk toe, blijkt het meest recente sedimentatiepakket vrij homogeen te zijn. Lokale tectonische verheffing is mogelijk, gerelateerd aan de *Posolskaya* breuk [*Levi et al., 1997*]. In hoeverre een dergelijk proces verenigbaar is met extensie wordt betwijfeld [*Klerkx et al., in prep.*]. Nu ligt het totale gebied volledig in de schaduw van deze breuk op enkele km afstand zodat een eventuele inwerking ook dit kleine gebied in zijn geheel zou beïnvloeden. Lokale effecten kunnen evenwel niet uitgesloten worden waarbij de verdeling van alle spanningscomponenten in rekening dient gebracht, ook de horizontale.

Een verklaring voor deze "anticlinale" vorm van de verdeling van hydraten met de aanwezigheid van de seeps en de breuken suggereert een causaal verband met tectoniek. Vooral de *Posolskaya* breuk wordt daarvoor verantwoordelijk geacht. Reactivatie van deze breuk en vervolgens de bijhorende kleinere breuken kan een belangrijke verstoring van het energiebudget teweegbrengen onder de vorm van plotse warmteoverdracht en expulsie van warmere fluïda uit dieper gelegen delen van het bekken. Dit

kan eventueel aanleiding geven tot verdere seismiciteit in het gebied. Warmtetransport geschiedt dan zowel conductief als advectief, zowel binnen de breukzones als lateraal in de aanpalende zones. Eens het hydraatstabiliteitsvenster bereikt wordt, wordt een deel van de warmte gebruikt om hydraat te dissociëren waardoor – indien dissipatie niet snel genoeg gebeurt – overdruk kan onstaan en de temperatuur van de puls sterker zal afnemen. Deze plotse injectie van verhoogde druk kan dan resulteren in het ontstaan van barsten en breuken in het overliggend sediment om dusdanig dissipatie mogelijk te maken die dan aanleiding geeft tot het onstaan van de kratervormige structuren. Gasmigratie en –ontsnapping blijft dan doorgaan tot ofwel het migratiepad afgesloten wordt of het ondiepe reservoir uitgeput raakt.

Dit model heeft zeker nog zijn tekortkomingen, en het is noodzakelijk dat de puzzel verder in elkaar wordt gepast, rekening houdend met alle nieuwe analyses en resultaten in de diverse laboratoria die de zeer recente databuit (zomer-winter 1999-2000) onderzoeken. Daarvan raken pas nu met mondjesmaat de eerste resultaten bekend, te vroeg om opgenomen te worden in dit werk.

Of er een verband bestaat tussen deze fluïdamigratiepaden en het unieke oscillerende gedrag van de BHSZ geobserveerd enkele km ten zuiden van deze structuren is een belangrijke vraag. Extra seismische profielen zouden moeten geschoten worden in dit gebied om dit aan te tonen of te ontkrachten. Desalniettemin blijken twee kraters ongeveer in het verlengde te liggen van twee toppen van de oscillerende reflectie die gekenmerkt worden door een hogere reflectiecoëfficiënt en wijzen op verhoogde concentraties van vrij gas. Het is onduidelijk of de vorming van de kraters de lokale hydrologie op een dusdanig krachtige wijze kan beïnvloeden dat een laterale fluxcomponent te berde komt, en in hoeverre dat verband houdt met het voorkomen van abnormale diepten van de BHSZ. Het voorkomen van een uitzonderlijk lage lokale warmtestroom wordt ontkracht door de warmtestroommetingen ter plaatse. Verder onderzoek en modellering van de volledige situatie dringt zich dan ook op.

7.5 Gevalsanalyse

Het vijfde hoofdstuk van deze verhandeling omvat het artikel *Inferred gas hydrates and clay diapirs near the Storegga Slide on the southern edge of the Vøring Plateau, offshore Norway* werd geschreven in nauwe samenwerking met S. Bouriak (Moscow State University) en is gepubliceerd in Marine Geology [*Bouriak et al., 2000*]. Deze publicatie had tot doel (1) het voorstellen en bespreken van een nieuwe multi-disciplinaire dataset verzameld tijdens de TTR8-expeditie met R.V. Logachev (airgun seismiek, side scan sonar, paleontologische data), (2) het analyseren van de mogelijke verbanden tussen gasmigratie en gashydraataccumulatie en (3) het onderzoeken van de mogelijke bijdrage van hydraatdissociatie door toedoen van de *Storegga Slide* tot verdere hellingsinstabiliteit in de regio. Daarvoor werd gebruik gemaakt van zowel airgun reflectie seismische data, OKEAN long-range side-scan sonar en gravity cores. De seismische data werden ook aan seismische inversie onderworpen ten einde een kwalitatief beeld te krijgen van het snelheidscontrast nabij versterkte reflecties en de BSRs.

7.5.1 Storegga Slide

De *Storegga Slide* bevindt zich op de passieve Noorse continentale rand, ten zuiden van het *Vøring Plateau*, en staat te boek als één van de grootste onderwaterafglijdingen ter wereld, met een totaal volume aan gemobiliseerd sediment van 5500 km^3 in een gebied van 34000 km^2. Drie verschillende fazen van hellingsinstabiliteit werden herkend. De eerste afglijding vond plaats tussen 50 en 30 ka BP en was de belangrijkste. De laatste twee gebeurden recentelijk en in korte opeenvolging op elkaar (8-6

ka BP) [*Bugge et al., 1988*]. Het voorkomen van hydraten en het mogelijk verband met de initiatie van de massaverplaatsing werden reeds eerder verondersteld. Daarbij zou hydraatdissociatie op diepte getriggerd worden door aardbevingen [*Bugge et al., 1988; Mienert et al., 1998*]. Vooral de observatie van BSRs in het verlengde van het glijvlak draagt daartoe bij.

7.5.2
Waarnemingen en resultaten

Fluïdasijpeling uit zeebodem

Ten noorden van de steile afglijdingswand (helling tot 10-20°) worden talrijke vlekken met verhoogde terugverstrooiing waargenomen die samenvallen met eerder gerapporteerde pockmarkvelden [*Mienert et al., 1998*]. De side-scan sonar data laten echter niet toe deze fenomenen accuraat toe te schrijven aan topografie, maar suggereren lokale veranderingen van de fysische eigenschappen van de oppervlakkige sedimenten. Dit wordt bevestigd door de aanwezigheid van gasrijke sedimenten en carbonaatkorsten in alle kernen genomen van deze vlekken. Seismische opnames over dergelijke structuren brengen aan het licht dat dit gebied samenvalt met het voorkomen van diverse smalle (150-500 m diameter) verticale zones van akoestische *wipe-outs* die zich uitspreiden tot onder de penetratielimiet van het akoestisch meetsysteem (> 400 m) en wijzen vermoedelijk op gasexpulsie. Op bepaalde plaatsen breken deze door de zeebodem door en vormen dus een koepelvormige verhoging van de zeebodem, terwijl op andere plaatsen zeebodemdepressies of *pockmarks* worden aangetroffen. Reflecties aan de rand van de *wipe-out* zones worden vaak naar boven afgebogen waardoor het lijkt alsof verticaal sedimenttransport heeft plaatsgevonden, wat gestaafd wordt door analyse van de kernen. Naast zowel kwartaire nannofossielen als *ice-rafted debris* gevonden in elke kern blijken deze genomen uit de *pockmarks* en koepels tertiaire fossielen (Eoceen, Oligoceen) te bevatten. Transport van dergelijke fossielen over honderden m vereist meer dan gas migratie, zodat deze structuren als kleidiapieren beschouwd worden.

Gas hydraten, ondiepe gasaccumulatie en implicaties voor het geothermische veld

Op de akoestische profielen worden duidelijk twee gescheiden zones gekarakteriseerd door de aanwezigheid van BSRs waargenomen. De eerste zone is gesitueerd op de helling ("*lower-slope BSR*") van het *Vøring Plateau* in de onmiddellijke nabijheid van de rand van de *Storegga Slide*, en op bepaalde plaatsen binnen het gebied verstoord door de afglijding in een gebied van ongeveer 100 km². De BSR kruist duidelijk de stratigrafie en verschijnt met inverse polariteit. In dit gebied werden geen anomale structuren in de bovenste sedimenten waargenomen (*pockmarks*, diapieren). De tweede BSR zone ligt hellingsopwaarts ("*upper-slope BSR*") in een zone gekenmerkt door diapier-achtige structuren maar valt minder op door het nagenoeg samenvallen met de stratigrafie. Polariteit is ook nu invers. Het geothermische regime werd bepaald uitgaande van een aantal veronderstellingen in een willekeurig gekozen referentiepunt. Een bodemtemperatuur van 0°C werd aangenomen, [*Mienert et al., 1998*], de BSR valt samen met de BHSZ en dus het 3-fasig evenwicht, compositie is puur methaan van biogene origine (ODP Leg 104 resultaten enkele honderden km afgelegen) en het snelheidsprofiel werd afgeleid uit dezelfde ODP Leg 104 resultaten en gecombineerd met de algemene vergelijking van *Hamilton*. De druk werd bepaald voor zowel hydrostatische als lithostatische drukverdeling. Finaal werd de temperatuurstoename met diepte als lineair beschouwd. Het uiteindelijke resultaat geeft waarden van 0.0515°C·m^{-1} (hydrostatisch) en 0.0558°C·m^{-1} (lithostatisch). Extrapolatie van deze resultaten over het gehele gebied illustreert dat de reflecties in de tweede BSR zone en binnen het gebied van de afglijding zeer goed overeenkomen met deze bepaalde positie voor de hydraatstabiliteitslimiet. Seismische inversie resulteerde vervolgens ook in een belangrijke snelheidsinversie langs deze reflecties en laat ons daarom toe deze ook te catalogeren als BSRs.

7.5.3
Discussie

Aard van de BSR

Het voorkomen van twee gescheiden zones met hydraatevidentie suggereert verschillende controlerende factoren voor hydraataccumulatie gerelateerd met fluïdamigratie en past dus niet binnen het bovenvermelde eerste model voor hydraatvorming van *Claypool & Kaplan [1974]*. De mechanismen gebaseerd op verticale fluïdamigratie zijn ook ietwat te eenvoudig zodat een gecombineerd model werd opgesteld. Het goede overeenkomen van de theoretisch berekende limiet en de BSRs in het hele gebied maakt dat intense gefocuste fluïdamigratie uitgesloten kan worden, daar deze vergelijking duidelijk illustreert dat het geothermisch regime lateraal weinig of geen veranderingen ondergaat. Hydraataccumulatie en BSR vorming in het eerste gebied ("*lower-slope*") geschiedt door actieve pseudo-verticale percolatie van opgelost methaan in poriënwater. Eens het stabiliteitsgebied bereikt wordt, worden gasmoleculen uit de fluïda gescheiden en opgenomen in de hydraatstructuur volgens het model van *Hyndman & Davis [1992]*. Dit leidt tot een vermindering van de effectieve porositeit en permeabiliteit in die zone en wordt in feite een permeabiliteitsbarrière gevormd aan de basis van het stabiliteitsvenster. Eventueel wordt overdruk gegenereerd of kan vrij gas accumuleren onder dit grensvlak. Hoge-amplitude stratigrafische reflecties die dieper liggen dan de hydraatstabiliteitslimiet in de omgeving zijn karakteristiek voor de overgansgebied tussen beide BSR-zones. De strata boven deze versterkte reflectoren worden verondersteld een verminderde permeabiliteit te hebben en zodoende verticale migratie te verhinderen. Laterale migratie van gassen langsheen deze barrière blijft evenwel tot de mogelijkheden behoren. De waargenomen diapierstructuren in het tweede gebied zijn dan weer geschikte geleidingskanalen en zorgen ervoor dat de aanwezige gassen zich verticaal kunnen verplaatsen waar ze opnieuw gehydrateerd kunnen worden als voldaan is aan de specifieke druk- en temperatuursvoorwaarden. Zodoende wordt de tweede BSR zone ontwikkeld. Gassen die niet in hydraatvorm omgezet worden door verbinding met poriënwater ontsnappen door de sedimentkolom in de oceaan. Dit kan gepaard gaan met de vorming van pockmarks.

Interne fluïdamigratiesnelheden

De aanwezigheid van een BSR in het gebied dat verstoord werd door de *Storegga Slide* impliceert dat de evenwichtscondities in de tijdspanne sinds de afglijding (30-50 ka) opnieuw hersteld zijn bij dezelfde geothermische condities. Zoals in het tweede hoofdstuk verder werd uitgewerkt, zijn de zeespiegelschommelingen sinds de afglijding van ondergeschikt belang op het repositioneren van de BSRs. Deze observatie maakt het dan mogelijk een schatting te maken van de interne migratiesnelheid, gebaseerd op de tijdschaal en theoretische modellering gebruik makend van fysico-mathematische vergelijkingen voor massa- en energiebehoud [*Rempel & Buffett, 1998*]. Er werd daarnaast verondersteld dat slechts 5 tot 10 % van het poreuze volume ingenomen wordt door hydraten, zijnde een gemiddelde waarde voor hydraataccumulatie vermeld in de literatuur [*Hovland et al., 1997*]. Als resultaat wordt de migratiesnelheid geschat in de grootte-orde van enkele cm/jaar, wat relatief veel is. Terwijl in deze zone geen BSR anomalieën werden aangetroffen, wordt het geothermische regime hoofdzakelijk geregeerd door conductie en kunnen convectie of advectie verwaarloosd worden. Bijgevolg wordt de schatting dan ook geïnterpreteerd als zijnde een bovenwaarde.

Contributie van hydraatdissociatie op verdere hellingsinstabiliteiten

Tot slot werd in dit artikel de relevantie van hydraatdissociatie bij verdere hellingsinstabiliteiten en eventueel massatransport bestudeerd. De resultaten zijn sterk afhankelijk van de veronderstelde drukverdeling binnen de sedimenten. Het massatransport heeft na verloop van tijd een positieve werking op *in situ* hydraatstabiliteit indien gerekend wordt met hydrostatische druk. Indien echter

lithostatische druk gebruikt wordt, valt door toedoen van de sedimenterosie een deel van het initiële stabiliteitsgebied buiten het nieuw ingestelde. Het drukeffect is minder dan 0.5 MPa op het maximale punt. De dikte van deze laag is maximaal nabij de rand van de afglijding (tot 10 m) en mindert hellingsafwaarts. Dit gebeuren is slechts van beperkte duur en wordt gecompenseerd door de vrij trage penetratie van de koude temperatuurspuls aan de sedimenten die na de afglijding de zeebodem vormen. In het gebied werd de paleo-situatie gereconstrueerd en vergeleken met de nieuwe situatie. Door het massatransport zou ongeveer $2 \cdot 10^7$ m^3 hydraat dissociëren zodat $339 \cdot 10^7$ m^3 vrij gas geproduceerd wordt bij STP condities, dus ongeveer $2.7 \cdot 10^7$ m^3 onder *in situ* druk (13-14 MPa) wat gecompresseerd moet worden in de vrijgekomen ruimte. De tijdschaal van het hele gebeuren speelt een belangrijke rol. Indien het dissociatieproces ogenblikkelijk gebeurt en begrensd blijft in het volume dat uit het stabiliteitsvenster valt, dan wordt een overdruk van ongeveer 10% gegenereerd. Echter, ogenblikkelijke en volledige dissociatie zal hoogstwaarschijnlijk niet plaatsvinden door toedoen van de afglijding – en dus verminderde druk – alleen, en additionele energie moet uit de directe omgeving gehaald worden (warmtestroom) om dissociatie te voltooien. Uiteindelijk komt er een cyclisch proces van instabiliteit-stabiliteit waardoor volledige dissociatie vertraagd wordt. Als uiteindelijk het overschot aan volume verdeeld wordt doorheen de volledige sedimentaire sectie boven de initiële stabiliteitsgrens, dan resulteert dit proces in een toename van de poriëndruk van slechts 0.2%. Ook de rol van 3D-fluïdamigratie veroorzaakt door drukgradiënten bij dissociatie mag niet uit het oog verloren worden. In dergelijk geval zal hydraatdissociatie geen aanleiding vormen voor verdere hellingsinstabiliteit in de regio. Daarbij dient opgemerkt te worden dat het gebruik van de lithostatische druk een overschatting tot gevolg heeft, en dat het werkelijke effect een stuk kleinschaliger kan zijn.

7.6 Toekomstperspectieven

Alhoewel de oorspronkelijke doelstellingen allemaal behaald werden, kan uiteraard niet ontkend worden dat er nog heel wat onzekerheden zijn, zowel wat theoretische modellering betreft van hydraatstabiliteit, de akoestische respons en het volledige dynamische systeem.

Bij modellering van de stabiliteit van hydraat zou moeten getracht worden een dynamisch model op te stellen dat rekening houdt met een zo volledig mogelijk geologisch systeem. De invloed van zeespiegelschommelingen en bodemtemperatuursvariatie op de theoretische stabiliteit van hydraten is behoorlijk gekend, maar dient uitgebreid te worden met de mogelijke invloeden van een veelheid aan andere optredende processen die een analyse danig kunnen bemoeilijken. Hier werd enkel rekening gehouden met klimatologische variaties in de tijd, terwijl opeenvolgende thermische pulsen met korte werking buiten beschouwing gelaten werden. Niet alleen externe factoren zoals zeespiegelschommelingen en bodemstroomvariaties of sedimentatie, erosie, isostatie, subsidentie,... maar ook en vooral de invloed van inwendige processen zoals verticale en laterale fluïdamigratie en het destabilisatieproces op zich verdienen aandacht. Het belang daarvan ligt in het energiebudget en het feit dat dergelijke processen in eerste instantie van invloed zullen zijn op de zone waarin kleine effecten tot dissociate kunnen leiden, wat aanleiding kan geven tot overdruk met alle mogelijke gevolgen van dien. De precieze werking en consequenties zijn echter onvoldoende bekend. Een extra moeilijkheid is uiteraard de grote variëteit aan geologische contexten waardoor grote verschillen kunnen en zullen optreden. Informatie uit diepe boringen lijkt dan onontbeerlijk.

Dit geldt in het bijzonder voor het Baikalmeer, waar zowel een gekende als een uitzonderlijke hydraatverdeling worden waargenomen. Onlangs werd een multi-disciplinaire dataset vergaard in het gebied met anomalieën. De resultaten dienen in elkaar gepuzzeld te worden om concrete antwoorden te vinden op de hedendaagse vragen. De meest in het oog springende zijn vragen naar de effectieve invloed van het riftproces of tectonische invloeden van hoofdzakelijk de *Posolskaya* breukzone aan de

rand van het bijzondere gebied, de origine van de anomaal diepe hydraatzones in de buurt van de fluid escape structures.

Recentelijk werden ook nieuwe seismische profielen vergaard in het *Storegga Slide* gebied (TTR-10) waarop blijkt dat de "lower-slope BSR" zich verder uitstrekt binnen het afglijdingsgebied. Deze data moeten ons toelaten zowel de schattingen als het hydraatvormingsmodel in de gescheiden zones verder uit te werken en te verfijnen. Daarbij dienen deze data ook vergeleken te worden met andere seismische profielen van het gebied.